MECHANISMS OF LONGITUDINAL DEPRESSION FORMATION IN STEEL CONTINUOUS CASTING

by

Matthew L.S. Zappulla

© Copyright by Matthew L.S. Zappulla, 2020

All Rights Reserved

A thesis submitted to the Faculty and the Board of Trustees of the Colorado School of Mines in partial fulfillment of the requirements for the degree of Doctor of Philosophy (Mechanical Engineering).

Golden, Colorado

Date _____

Signed: _____
Matthew L.S. Zappulla

Signed: _____
Dr. Brian G. Thomas
Thesis Advisor

Golden, Colorado

Date _____

Signed: _____
Dr. John C. Berger
Professor and Department Head
Department of Mechanical Engineering

ABSTRACT

In continuous casting, longitudinal cracks and depressions are some of the most dangerous defects in the cast product. Cracks and depressions can lead to substantial mitigation costs or sudden failures in the final product, and in the worst case can lead to catastrophic breakouts in an operating caster.

This work develops and applies computational models to examine and elucidate the behavior and formation mechanisms for longitudinal depression defects to relate the shape of the defect to the mechanism that caused it. The primary tools used are heat transfer solidification models coupled with a temperature-, phase-, and strain-rate-dependent, elastic-viscoplastic thermal-mechanical finite element model, including a new crack propagation methodology implemented. When possible, industrial samples and examples of the defects discussed are shown and used as qualitative and quantitative validation of the models. Longitudinal depressions in continuous casting can occur in both compression and tension conditions. Tension conditions result in partial necking of the steel shell and generally lead to the most common type of observed depression: a U-shape. In certain conditions, thinning of the shell is severe enough to allow the ferrostatic pressure to partially bend the depression back towards the mold and create a W-shape depression. Depressions can also form in severe compression, due to a partial inelastic buckling (or kneeling) of the shell, also leading to a W-shape depression.

Depressions often contain cracks, and depressions with cracks tend to be deeper and more severe in nature than their non-cracked counterparts. Based on model predictions, it has been found that the presence and growth of a crack within a depression tends to deepen a depression, thereby decreasing its width/depth aspect ratio. Additionally, it has been observed that crack proximity to the solidification front, as well as thermal disruption proximity to the meniscus, is directly related to an increase in defect severity. As a result, it

seems that many of the serious crack and depression defects commonly found in cast slabs start very close to the meniscus (as a result of some thermal disruption event) and grow along with the solidification front.

Furthermore, it has also been found that the initiation location, and the direction of crack growth, changes the appearance of the depression. The presence of a surface crack(s) is observed to distribute tensile stresses that would otherwise go into further necking of the depression. It has also been found that for depressions without a surface crack, there is a tendency to develop excess sub-surface tension and thus sub-surface hot tear macro-segregation streaks.

Additionally, cracks that start sub-surface and propagate towards the surface of the steel shell are found to adopt a shape where the surface sharply changes slope towards the base of the depression. In cases where the crack completely traveled to the surface, the corners of the crack (often thin and pointed) point away from the surface as the thin ligament gave away.

Finally, a novel methodology has been developed for real-time prediction of longitudinal depressions and defects using integrated mold temperature measurements mapped onto the surface of the as-cast slab. This methodology can be used to augment existing breakout detection systems by taking high resolution temperature data histories of discrete points on the surface of the slab to predict longitudinal bleeder type breakouts.

TABLE OF CONTENTS

ABSTRACT iii

LIST OF FIGURES xv

LIST OF TABLES xxxii

LIST OF ABBREVIATIONS xxxiii

ACKNOWLEDGMENTS xxxv

DEDICATION xxxvii

CHAPTER 1 INTRODUCTION 1

1.1 Defects in Continuous Casting 2

1.2 Research Objectives 5

1.3 Research Methodology 7

1.4 Dissertation Outline 7

CHAPTER 2 BACKGROUND 10

2.1 The Continuous Casting Process 10

2.2 Mold Heat Transfer 14

2.2.1 Fluid Flow in the Mold 14

2.2.2 Details of the Interfacial Gap 18

2.2.2.1 Slag Layer 20

2.2.2.2 Interface Resistances 21

2.2.2.3 Air-Slag Gap Formation 22

2.3 Mechanical Behavior of the Strand 23

2.3.1 Within the Mold . . . 24
2.3.2 Secondary Cooling . . . 25
2.3.3 Bulging . . . 27
2.3.4 Summary . . . 27
2.4 Defects in Continuous Casting . . . 28
2.4.1 Temperature Regions of Low Ductility . . . 29
2.4.2 Common Crack Defect Types . . . 32
2.4.3 Star Cracks . . . 34
2.4.4 Transverse Depressions and Cracks . . . 34
2.4.5 Longitudinal Depressions and Terminology . . . 36
2.4.6 Longitudinal Cracks . . . 39
2.4.7 Longitudinal Cracks Within Longitudinal Depressions . . . 40
2.4.8 Breakouts . . . 43
2.4.8.1 Transverse Sticker Breakouts . . . 43
2.4.8.2 Longitudinal Bleeder Breakouts . . . 44
2.4.8.3 Breakout Detection . . . 45
2.4.8.4 Healing a Bleeder Breakout . . . 45
2.4.9 Summary . . . 46
CHAPTER 3 MODEL FORMULATION . . . 49
3.1 Overview . . . 49
3.2 Model Domain . . . 49
3.3 Governing Equations . . . 50
3.3.1 Heat Transfer Model . . . 50

3.3.2 The Péclet number 51
3.3.3 Stress Model 52
3.4 Heat Transfer Boundary Conditions 53
3.5 Interfacial Gap Thermal Resistor Model 55
3.5.1 Overview 55
3.5.2 The Mold/Flux Interface 55
3.5.3 The Flux/Shell Interface 56
3.5.4 Solid Slag Layer 58
3.5.5 Liquid Slag Layer 59
3.5.6 The Air Gap 60
3.5.7 Total Gap Heat Transfer 61
3.5.8 Implementation 62
3.6 Reduced Order Mold Model 65
3.7 Stress Boundary Conditions 67
3.7.1 Previous Cracking Models 69
3.7.1.1 Current Cracking Model and Implementation 70
3.7.1.2 Cracking Criterion 71
3.8 Material Properties 73
3.8.1 Enthalpy and Specific Heat Capacity 74
3.8.2 Thermal Conductivity 75
3.8.3 Mass Density and Thermal Linear Expansion 77
3.8.4 Elastic Properties 79
3.8.5 Constitutive Models 80

3.9 Finite Element Implementation 81
3.10 Model Verification and Validation 82
3.10.1 Thermal-Mechanical Solidification Analytical Solution 82
3.10.2 Mesh Resolution Convergence Study 83
3.10.3 Heat Flux in the Mold 85
3.10.4 Validation of Solidification Stress Model 89
3.10.5 Heat Transfer Model Validation 92
3.10.5.1 General Resistor Model Results 93
3.10.5.2 Effect of Flux Layer Thickness 95
3.10.5.3 Effect of Flux Solidification Temperature 95
3.10.5.4 Effect of Flux Layer Thickness Variation 95
3.10.6 Mechanical Constitutive Model Validation 96
3.10.6.1 Phase-Based Constitutive Model Selection 97
3.10.6.2 Phase-Based Material Properties for Stainless Steel 97
3.10.7 Solidifying Shell Model Validation 102
3.10.7.1 Ferrite Mechanical Constitutive Model 104
3.10.7.2 Austenite Mechanical Constitutive Model 104
3.11 Computational Considerations 107
3.12 Summary 107
CHAPTER 4 3D THERMAL MECHANICAL MODEL OF SOLIDIFYING STEEL STRAND 109
4.1 Abstract 109
4.2 Introduction 109

4.3 Model Setup 110
4.4 Thermal Boundary Conditions 111
4.5 Mechanical Boundary Conditions 112
4.6 Material Properties 114
4.7 Results and Discussion 115
4.7.1 Model Validation 115
4.7.2 Initial Solidification in the Mold 117
4.7.3 Spray Cooling and Rolls 118
4.7.4 Bulging 123
4.7.5 Bending and Unbending 125
4.8 Conclusions 132
4.9 Future Work 133
4.10 Acknowledgements 133
CHAPTER 5 TATA STEEL CASE STUDY 134
5.1 Introduction 134
5.2 Benchmark Plant Measurements 135
5.3 Mold Data Mapping Methodology 137
5.3.1 Mapping Mold Data to Slab Data 138
5.3.2 Defect Visualization 139
5.4 Thermal-Mechanical Model Formulation 142
5.5 Volumetric Heat Source 143
5.6 Thermal Model Calibration and Validation 145
5.7 Thermal-Mechanical Model Results 146

5.8 Defect Appearance on Instrumentation 148
5.9 Locating Mold Thermocouples 150
5.9.1 Changes in Spacing for Small Variations in the Defect 154
5.10 Conclusions 155
5.11 Acknowledgements 157
CHAPTER 6 LONGITUDINAL DEFECT FORMATION MECHANISMS 158
6.1 Introduction 159
6.2 Computational Model Tools 161
6.3 Material Properties 165
6.3.1 Domain Size Effect 166
6.4 Defect Mechanisms 168
6.4.1 U-Shape Necking Type Depression Without Surface Cracks 168
6.4.2 U-Shape Necking Type Depression with Sub-Surface Cracking 170
6.4.2.1 Localization Effects 172
6.4.2.2 Defect Timing and Relative Severity 173
6.4.3 U-Shape Buckling Type Off-Corner Depression Due to Inadequate Taper 174
6.4.4 W-Shape Buckling Type Depression Due to Excessive Compression . 175
6.4.5 W-Shape Necking Type Depression with Surface Crack 179
6.4.6 U-Shape Grooves From Solidification Against a Slag finger/Rivulet . 180
6.4.7 V-Shape Necking Type Depression Due to Mold Scratch 184
6.4.8 U-Shape Necking Type Depression With Surface Cracks 188
6.4.9 Longitudinal Surface Cracks With Curved Corners and No Depression 193

6.4.10 Longitudinal Depression With an Opened Sub-Surface Crack With Pointed Corners . . . 193

6.5 Discussion . . . 195

6.5.1 Crack Influence on Depression Formation . . . 198

6.5.2 Depression Formation . . . 198

6.5.3 Thermal Disruption . . . 198

6.5.4 Mechanical Disruption . . . 199

6.5.5 After Initial Formation . . . 200

6.5.6 Analyzing a longitudinal defect . . . 202

6.5.7 What to Look For . . . 202

6.5.8 Differentiating Defects . . . 203

6.6 Summary . . . 203

6.7 Final Thoughts . . . 204

6.8 Acknowledgements . . . 204

CHAPTER 7 LONGITUDINAL DEPRESSION DEFECT VISUALIZATION METHODOLOGY . . . 206

7.1 Introduction . . . 206

7.2 Background . . . 207

7.3 Purpose Driven Visualization . . . 208

7.4 Grid/Mesh Visualization and Interpolation . . . 209

7.5 Color Map Selection for Scalar Fields . . . 211

7.6 Thermal Integral Methodology . . . 214

7.6.1 Mapping Mold Data to Slab Data . . . 217

7.6.2 Defect Criterion . . . 219

7.7 Implementation and Interpretation 220
7.8 Results 222
7.9 Discussion 231
7.10 Implementation Procedure For an Operating Caster 232
7.10.1 Calibration Conditions and Data 232
7.10.2 Procedure 233
7.10.2.1 Collect and Analyze Data from a Good Quality Cast 233
7.10.2.2 Generate a Standard Profile 233
7.10.2.3 Collect and Analyze Data from a Bad Quality Cast 234
7.10.2.4 Confirm the Standard Profile and Calibrate Thresholds . . . 234
7.10.2.5 Run a Blind Calibration Test 234
7.10.3 Display Setup Notes 235
7.11 Applications Beyond Continuous Casting 237
7.12 Conclusions 237
7.13 Acknowledgements 238
CHAPTER 8 CONCLUSIONS 239
8.1 Research Objectives 239
8.2 Longitudinal Defect Formation Mechanisms 240
8.3 Research Questions Answered 245
8.4 Final Thoughts 248
REFERENCES CITED 250
APPENDIX A MULTIPHYSICS MODELING OF CONTINUOUS CASTING OF STAINLESS STEEL 268

A.1 Introduction 268
A.1.1 Constitutive Modeling of Metal Solidification 269
A.1.2 Multiphysics Approaches 271
A.2 Multiphysics Model Formulation 272
A.2.1 Solidifying Shell Model 273
A.2.2 Fluid Flow Model and Fluid/Shell Interface Treatment 275
A.2.3 Mold Distortion Model 277
A.2.4 Boundary Conditions and Shell/Mold Interface Treatment 277
A.3 Viscoplastic Model of Solidifying Steel 280
A.3.1 Austenite Constitutive Model 281
A.3.2 Ferrite cCnstitutive Model 282
A.3.3 Liquid and Mushy Phase Constitutive Model 284
A.3.4 Phase-Based Constitutive Model Selection 284
A.4 Phase-Based Material Properties for Stainless Steel 285
A.5 Results and Discussion 290
A.5.1 Thermal Flow in Liquid Pool 293
A.5.2 Heat Flux in the Mold and Model Validation 296
A.5.3 Stress and Deformation in Solidifying Steel Shell 298
A.5.4 Computational Considerations 305
A.6 Conclusions 306
A.7 Future Work 307
A.8 Acknowledgements 307
APPENDIX B CON1D INPUT FILE 308

APPENDIX C ABAQUS INPUT FILES 316

C.1 Thermcouple Analysis Abaqus Input File 316

C.2 Tata Steel Cracking Model Input File 323

APPENDIX D ABAQUS FORTRAN SUBROUTINES 333

D.1 FILM for ROM mold 333

D.2 HETVAL for Negative volumetric heat generation 409

D.3 GAPCON for Resistor Model 410

D.4 MPC Cracking Subroutine 416

APPENDIX E POST-PROCESSING SCRIPTS 419

E.1 Abaqus Depression Shape Extraction Script 419

E.2 Abaqus Interpolate Thermocouple Temperatures in Single Element ROM Mold 422

APPENDIX F MATLAB SCRIPTS 425

F.1 Data File Import Function 425

F.2 Integral Method Video Script 426

APPENDIX G SELECTED LONGITUDINAL DEFECT PERSPECTIVE IMAGES 433

APPENDIX H SELECTED LONGITUDINAL DEFECT CROSS SECTION IMAGES 453

APPENDIX I SUPPLEMENTAL ELECTRONIC FILES 490

LIST OF FIGURES

Figure 1.1 Slab defect remediation by torch 2

Figure 1.2 Slab breakout shell after removal from machine 4

Figure 1.3 Examples of observed longitudinal cracks/depressions 6

Figure 2.1 Continuous casting process schematic 10

Figure 2.2 Mold region schematics(a) Diagram close up of the mold , (b) Cutaway view inside the mold 11

Figure 2.3 Thin slab caster strand inside of machine:(a) Curved secondary cooling section of thin slab caster, (b) Horizontal section of thin slab caster just before the mechanical shear 13

Figure 2.4 Shell growth phase contour mold results inside upper portion of the mold 14

Figure 2.5 Bulging thin slab shell leading to a whale outside of containment 15

Figure 2.6 Continuous caster final products: (a) Steel coils in yard waiting for transportation to customer,(b) Stacked steel slabs waiting for further processing 15

Figure 2.7 Natural mold flow patterns 17

Figure 2.8 Transient phenomena in caster meniscus region 19

Figure 2.9 Crystallinity and thickness dependent slag conductivity 21

Figure 2.10 Multi-taper mold schematic 24

Figure 2.11 Secondary cooling segment schematic 26

Figure 2.12 Example heat transfer behavior during roll contact and water sprays in secondary cooling 26

Figure 2.13 Schematic of strand bulging between rolls 28

Figure 2.14 Dendrite strength and ductility variation at high-temperature, responsible for hot tearing 30

Figure 2.15 Schematic diagram of ductility curve defining the three characteristic regions of hot ductility 31

Figure 2.16 Schematic diagram showing mechanism for transformation induced intergranular failure 33

Figure 2.17 Continuous Casting Crack Types 34

Figure 2.18 Star Cracks: (a) Typical star crack on slab surface ,(b) Multiple star cracks on the surface of a slab 35

Figure 2.19 Transverse Cracks:(a) Transverse corner crack ,(b) Transverse Midface Crack 35

Figure 2.20 Crack-like defect at centerline of hot-rolled product arising due to centerline segregation 36

Figure 2.21 Defect Terminology: (a) Slab with constant static longitudinal depression and crack along entire length, (b) Transverse slice through longitudinal depression with crack 38

Figure 2.22 Mechanism of gutter formation near mold exit due to excessive narrow face taper 38

Figure 2.23 Mechanically Based Longitudinal Defects: (a) Withdrawal roll cracks in 9 in square bloom , (b) Diagonal longitudinal sub surface cracks in a 12 in x 5 in slab (This section also shows bulging and rhomboidity) . . . 39

Figure 2.24 Longitudinal Corner Cracks: (a) Longitudinal corner crack on a 9 in square blooom , (b) Bleed on a 35.5 in x 8 in slab associated with a longitudinal corner crack 40

Figure 2.25 Observed Depression and Crack Depth Relationship 41

Figure 2.26 Severe longitudinal crack in depression (Full size undimensioned image available in appendix) 42

Figure 2.27 Longitudinal facial crack within depression on slab surface (Full size undimensioned image available in appendix) 43

Figure 2.28 Example of a sticker breakout 44

Figure 2.29 Sticker breakout detection method 45

Figure 2.30 Example of bleed contained within the mold (casting direction to the right) 46

Figure 2.31 Longitudinal bleeder related breakout shell after removal from machine (casting direction down) 47

Figure 2.32 Off-corner longitudinal depression breakout Appearance: (a) Intermittent bleeds at the base of an off-corner depression, (b) Resultant Slab breakout shell after removal from machine 47

Figure 3.1 Model domain within caster geometry 50

Figure 3.2 Heat Transfer Boundary Conditions 54

Figure 3.3 Contact interface roughness 56

Figure 3.4 Temperature dependent slag/strand interface heat transfer/resistance . . 57

Figure 3.5 Temperature dependent conductivity 58

Figure 3.6 Interfacial gap material schematic 62

Figure 3.7 Interfacial gap resistor schematic 62

Figure 3.8 Calculation flowchart for resistor model 64

Figure 3.9 Model domain for TATA Steel ROM mold calibration with heat flux and temperature contour results for matching upper thermocouple 67

Figure 3.10 Stress model boundary conditions 68

Figure 3.11 Crack growth schematic 72

Figure 3.12 Low carbon steel phase fractions 73

Figure 3.13 Temperature-dependent specific heat capacity 76

Figure 3.14 Temperature-dependent properties of 4 example steel grades including the Low Carbon steel investigated: a) Thermal conductivity b) Enthalpy c)Density d) Thermal linear expansion 78

Figure 3.15 Temperature-dependent elastic modulus of steel 80

Figure 3.16 Comparison of Weiner & Boley and Abaqus results 84

Figure 3.17 Mesh study results for low carbon steel 86

Figure 3.18 Calculated interfacial and superheat flux profiles down mold centerlines . 87

Figure 3.19 Heat flux measurements from heatup of mold cooling water 88

Figure 3.20 Thermocouple measurements: (a) locations and (b) temperature histories of thermocouples inserted on the mold wide face 88

Figure 3.21 Calculated mold and shell temperature results (wide face) with thermocouple validation 90

Figure 3.22 Shell thickness results from CON1D and Abaqus 91

Figure 3.23 Comparison of experimental and simulated force curves 92

Figure 3.24 Projected and actual heat flux profiles 94

Figure 3.25 Instantaneous and average heat flux profiles 94

Figure 3.26 Flux layer thickness variation with 800°C solidification temperature . . . 95

Figure 3.27 Effect of solidification temperature variation 96

Figure 3.28 Time varying flux thickness with 800°C solidification temperature 96

Figure 3.29 Mechanical constitutive models of austenite and ferrite for 316L stainless steel with experimental data 98

Figure 3.30 Phase fractions for 409L stainless steel 101

Figure 3.31 Thermal properties of 409L stainless steel: (a) conductivity and (b) enthalpy 102

Figure 3.32 Mechanical properties of 409L stainless steel: (a) elastic modulus, (b) density, (c) thermal linear expansion 103

Figure 3.33 δ-ferrite constitutive model results for plain carbon steel (lines) compared with measurements (symbols) by at 2 temperatures, and 3 strain rates, for two steel grades 105

Figure 3.34 Austenite constitutive model for plain carbon steel 106

Figure 4.1 Computational model domain of half-caster showing rolls, chunk domain in initial position, and mesh 111

Figure 4.2 Thermal and mechanical boundary conditions of the model 112

Figure 4.3 Secondary cooling segment schematic 113

Figure 4.4 Heat transfer behavior during roll contact and water sprays in secondary cooling 113

Figure 4.5 Example constitutive behavior for δ-Ferrite over a variety of strain rates at 1505°C 116

Figure 4.6 Example constitutive behavior for γ-Austenite over a variety of temperatures at a strain rate of 10^{-4} 116

Figure 4.7 Surface temperature variation down the caster, comparing current 3D model with previous work 117

Figure 4.8 Shell growth profile from current 3D model compared to previous work 118

Figure 4.9 Temperature and hoop stress through the strand thickness from current 3D model at several times, compared with previous work (bottom) 10 seconds below meniscus with lines to show phases 119

Figure 4.10 Wide face centerline surface hoop (z) stress (MPa) and surface temperature history in the mold 120

Figure 4.11 a) Hoop (z) stress (MPa) on the inner radius after mold exit and before unbending, b) Bulging displacement (mm) at wide face centerline between the first 3 support rolls below the mold 121

Figure 4.12 Wide face centerline results at the surface of the inner radius (marked with yellow line: a) Surface temperature, b) Hoop (z) stress, c) Bulging (X) displacement of the inner radius 122

Figure 4.13 Through-thickness x-stress contours (MPa): (a) on narrow face and (b) through centerplane before bending 124

Figure 4.14 Casting direction (Y) stress through the thickness at the wide face centerline during bending (with a liquid core): a) From a previous 2D model b) From the current 3D model 126

Figure 4.15 Casting direction (X) stress through the thickness at the wide face centerline during unbending (with a solid core): a) From a previous 2D model b) From the current 3D model 126

Figure 4.16 Hoop (z) stress through the thickness at the wide face centerline during bending under a sprayed and unsprayed region 127

Figure 4.17 Hoop (z) stress through the thickness at the wide face centerline during unbending under a sprayed and unsprayed region 128

Figure 4.18 Casting direction stress on the narrow face just before and during bending 129

Figure 4.19 Casting direction stress through the thickness along the narrow face surface during bending (indicated by white arrow in Figure 4.18) . . . 129

Figure 4.20 Stress in the casting direction on the narrow face during unbending . . 130

Figure 4.21 Stress in the casting direction through the thickness at the narrow face surface during unbending (indicated by white arrow in Figure 4.20) . . 130

Figure 4.22 Width-direction shrinkage towards the WF centerline (Z-displacement at the corners) 131

Figure 5.1 Top surface appearance of slab Z9407-101 with severe longitudinal defects off the North NF and inset image of a slab sample containing a depression that was subjected to detailed metallurgical analysis 136

Figure 5.2 Measured local temperature profiles across the mold width at specific times and locations down the mold. (a) Uniform casting conditions after the region containing the defect and (b) Before, during, and immediately after formation of the defect region with the depression. . 137

Figure 5.3 (a) Temperature profiles down the mold for the far field and the FBG sensor closest to the depression center (19 mm away) averaged over the instrumentation residence time of the depression (b) 3D plot of temperature evolution along the same single vertical line near the depression. 138

Figure 5.4 Contours that map defects over half of slab from wide face centerline to narrow face: (a) Instantaneous mold temperature, (b) Final slab surface appearance, (c) Instantaneous difference from standard temperature (d) Defect criterion based on integrated temperature drop T_{IdropF} 141

Figure 5.5 Thermal-stress model domain shown in cutaway of continuously cast slab (a), interfacial gap layers in this model (b), and numerical implementation as a thermal resistor model (c). 142

Figure 5.6 Negative Volumetric Heat Generation Function 144

Figure 5.7 (a) Temperature results from CON1D with plant measurements for FBG and thermocouples and (b) con1d output results for flux layer composition within the mold. 145

Figure 5.8 (a) Calculated heat flux profiles down mold comparing Abaqus and CON1D models; (b) Corresponding mold temperature profiles also comparing with FBG measurements. 147

Figure 5.9 Slab surface depression shape comparing model prediction with scan of sample with defect 147

Figure 5.10 Strand surface temperatures and corresponding mold surface temperatures for a 0.624 mm deep depression 148

Figure 5.11 Thermocouple Analysis Model Results at 20 s Below Meniscus (a) Heat flux profile across the surface,(b) Defect Shape 149

Figure 5.12 Thermocouple Location Analysis for $0.1°C$ Resolution 151

Figure 5.13 Thermocouple Location Analysis for $1°C$ Resolution 152

Figure 5.14 Thermocouple Location Analysis for 5°C Resolution 153

Figure 5.15 Results of 10% reduction in flux thickness at defect center for Tata Steel case: (a) Heat flux on mold hot face (Original result solid line), (b) Steel surface (Black) and mold hot face temperature (Red) 155

Figure 5.16 Depression depth change from 10% reduction in flux thickness at defect center for Tata Steel case (Original result solid line) 156

Figure 5.17 Thermocouple spacing locations from 10% reduction in flux thickness at defect center for Tata Steel case 156

Figure 6.1 Breakout shell of 0.1%C grade from slab caster with visible off-corner longitudinal depression and bleed: a) Breakout shell up to the meniscus with inset image closeup of bleed filled off-corner longitudinal depression, b) Section of corresponding off-corner depression from slab prior to breakout with visible intermittent bleeds (casting direction downwards). Note: Inset photo has been color adjusted for visualization purposes 160

Figure 6.2 Model domain within caster geometry and boundary conditions 162

Figure 6.3 Boundary conditions a) Thermal and b) Mechanical used in this work 163

Figure 6.4 Thermal disruption takes the form of reduced heat transfer: a) Gap resistor model schematic, b) Example gap composition 163

Figure 6.5 Liquid and solid isotherm locations at depression center for a 25 mm thermal disruption on the surface of solidifying shell with an example crack propagation history following, and then lagging behind the solidus isotherm 165

Figure 6.6 a) Phase Fraction solidification history for the plain low carbon steel used in this work, and b) Example values for the constitutive models used in this work including the solid γ-Austenite and δ-Ferrite phases, and the weak liquid phase 166

Figure 6.7 Domain size effect far field results: Shrinkage displacement (a) and Hoop stress through thickness (b) for 40 mm small domain and 40 mm section within 500 mm domain 167

Figure 6.8 Examples of 2 U-shaped necking type depressions, cross sections and surface views. From left to right: First: Top surface view of a longitudinal depression on a plain low carbon (0.04 %C) steel slab, Second: Transverse cross section of the same plain low carbon defect, Third and Fourth: Transverse cross section of a non-peritectic Al-Mn AHSS steel grade (0.2 %C) with a longitudinal depression 168

Figure 6.9 Deformed shape and temperature contours for 25 mm thermal disruption with applied tension of 0.03 mm/s at: a) Meniscus, b) 5 s, c) 10 s, and d) 15 s below the meniscus 169

Figure 6.10 EDS map of sub-surface hot tears with macro-segregation from a non-peritectic Al-Mn AHSS steel grade (0.2 %C) with a longitudinal depression and no surface crack 170

Figure 6.11 Examples of sub-surface crack groups with only one or two reaching the surface 171

Figure 6.12 Deformed shape and maximum principal stress (a) and strain (b) contours at 15 s below the meniscus for 25 mm thermal disruption with applied tension of 0.03 mm/s. Black horizontal lines indicate phase/temperature isotherms. (Deformation scaled 2x in Y) 172

Figure 6.13 Combined mechanism for necking localization and corresponding depression depth severity 173

Figure 6.14 Effect of thermal disruption initiation time on depression evolution: a) Depth history for varying disruption initiation times, b) Deformed shape of depression at mold exit and after cooling to near ambient, for late disruption (top) and early disruption (bottom) Note: Deformation scaled 5x 174

Figure 6.15 Example of sub-surface cracks beneath bulging gutter depression (outlined in black boxes on sulfur print) Note: Image color adjusted for clarity 175

Figure 6.16 Off-corner depression formation mechanism schematics : a) Narrow face shell bulging leading to off-corner depressions with sub surface cracks, b) Excessive taper leads to buckling of the wide face shell . . . 176

Figure 6.17 Off corner buckling depressions from overtaper 176

Figure 6.18 (a) Continuously cast billet exhibiting severe "W" shape depression after buckling within the mold , (b) Hoop stress model results for severe over-taper case with thermal disruption displaying sub-surface tension 177

Figure 6.19 Transverse section of a buckled thin slab cast AHSS prior to multiple simultaneous breakouts at longitudinal depression 179

Figure 6.20 a) Micrograph of a W-Shape depression in tension , b) Model result for a significantly thinned shell bent back towards the mold into a W-shape at 180

Figure 6.21 Abnormal shell surface as a result of solidifying against slag fingers on the mold hot face: a) Flux-related surface grooves on a breakout shell , b) Oscillation mark dips due to flux patch , c) Schematic of slag finger descending from slag rim 181

Figure 6.22 EDS analysis of a longitudinal U-shape groove defect at the midface of an Al-Mn non-peritectic Advanced High Strength Steel (0.2 %C) slab cast at 1 m/min with a high-Al slag 182

Figure 6.23 Slag finger model results: a) deformed shape with temperature contours after 30 s of solidification, b) Depression depth history 183

Figure 6.24 a) Mold surface imperfection (i.e. gouge) results in b) very straight longitudinal surface depression and/or crack. Present in all slabs cast in campaign, and always at the same location across the strand width (severity and shape of defect varies only with grade). 185

Figure 6.25 Model results for 1 mm deep and 1 mm wide scratch in mold using 0.1 mm elements: (a) Displacement contours at 4 s, (b) Unscaled deformed mesh at 4 s with phase/temperature contours, (c) Time history of depression center displacement including phase history of the depression center surface 186

Figure 6.26 Effects of mold scratch width and depth on defect formation behavior (all results shown at 30 s below meniscus) 187

Figure 6.27 Transverse section and perspective view of a defect sample from a low carbon thin slab cast just prior to breakout (a), visible long crack on broadface surface and corresponding shape/dimensional problems on NF (b) and Schematic explanation of broad face crack effects on narrow face shape problems and internal crack formation 189

Figure 6.28 Longitudinal facial crack at the base of longitudinal depression wandering across the surface of the broad face outer radius 190

Figure 6.29 Domain end displacement (shrinkage) for a 25 mm thermal disruption on the surface at of solidifying shell with and without a bleeder crack propagating along the liquidus isotherm: a) displacement vs time including crack opening displacement, b) deformed model results for no crack (left) and crack (right) cases, and c) contributions and total displacement at 30 s 192

Figure 6.30 (a) Longitudinal surface crack at the base of longitudinal depression with AHSS steel grade (0.2 %C), (b) Model results for an arrested 2.5 mm surface crack 194

Figure 6.31 a) Apparent surface crack at the base of a longitudinal depression , b) Schematic explanation of sub-surface crack propagating to surface, c) Deformed result of arrested sub-surface crack hold case at 10 s with 25 mm thermal disruption (deformations scaled 5x) 195

Figure 6.32 Heat flux and temperature results for a U shaped necking depression with and without a surface bleeder crack 196

Figure 6.33 Surface hoop stress results at depression center (black) and the far field (blue) 197

Figure 6.34 Hoop stress time history results across the surface of U shape necking depression without (a) and including a surface bleeder crack (b) for the same initial thermal disruption 197

Figure 6.35 Hoop stress time history results through the thickness for the far field (a) and depression center (b) of a U shaped necking depression 197

Figure 6.36 Model results for uniform heat transfer case with a propagating surface crack approximately following the 50% solidus isotherm 199

Figure 6.37 Deformed shape and temperature contours for 25 mm thermal disruption at 30 s with: (a) Applied compression of 0.03 mm/s, (b) Frictional tension, and (c) Applied tension of 0.03 mm/s 201

Figure 7.1 Mold sub-surface temperature 3D contour plot using hot color map with (a) and without (b) grid spacing conveying spatial information . . 210

Figure 7.2 Two-dimensional contour plots of mold sub-surface temperature in various MATLAB color maps: (a) hot (blackbody radiation), (b) jet (rainbow), (c) hsv (rainbow color map in HSV space), and (d) gray (grayscale) 213

Figure 7.3 Longitudinal depression finite element solidification model 2D contour plot showing temperature and phase fraction (deformation scaled 5x) . 214

Figure 7.4 Broadface copper instrumented FBG mold 216

Figure 7.5 Measured local temperature profile and an example standard temperature profile 150 mm below top of mold from wide face centerline to slab edge 217

Figure 7.6 Nomenclature for mold and slab geometry reference configuration used in Integral Defect methodology (shown at $t0$) 218

Figure 7.7 Contours indicating defects mapped over half of slab from wide face centerline to narrow face: (a) Instantaneous mold temperature, (b) Final slab surface appearance, (c) Instantaneous difference from standard temperature (d) Defect criterion based on integrated temperature drop, T_{IdropF}. 224

Figure 7.8 Integral Defect Methodology Heads-up Display Frame 1 227

Figure 7.9 Integral Defect Methodology Heads-up Display Frame 2 228

Figure 7.10 Integral Defect Methodology Heads-up Display Frame 3 229

Figure 7.11 Integral Defect Methodology Heads-up Display Frame 4 230

Figure 7.12 Downstream use of the T_{IDropF} methodology 236

Figure 8.1 Examples of 11 different longitudinal depression based defects (referenced previously) with specific formation mechanisms within the continuous casting mold 241

Figure A.1 Flow chart for multiphysics model 273

Figure A.2 Model domain of solidifying steel shell 274

Figure A.3 Austenite constitutive model for plain carbon steel (Wray, 1982) compared with stainless steel data 283

Figure A.4 Delta-ferrite constitutive model results for plain carbon steel (lines) compared with measurements (symbols) by (Wray, 1976) at 2 temperatures, and 3 strain rates, for two steel grades. 285

Figure A.5 Constitutive models of austenite and ferrite for 316L stainless steel with experimental data (Venugopal et al., 1993). 286

Figure A.6 Phase fractions for 409L stainless steel. 289

Figure A.7 Thermal properties of 409L stainless steel: (a) conductivity and (b) enthalpy. 291

Figure A.8 Mechanical properties of 409L stainless steel: (a) elastic modulus, (b) density, (c) thermal linear expansion. 292

Figure A.9 Molten-steel flow patterns and temperature distributions at (a) horizontal plane 180 mm below the meniscus and (b) center plane between the wide faces in the mold. 294

Figure A.10 Calculated interfacial and superheat flux profiles down mold centerlines 295

Figure A.11 Heat flux measurements from heatup of mold cooling water 296

Figure A.12 Thermocouple measurements: (a) locations and (b) temperature histories of thermocouples inserted on the mold wide face 297

Figure A.13 Calculated mold and shell temperature results (wide face) with thermocouple validation. 299

Figure A.14 Shell thickness results from CON1D and ABAQUS. 300

Figure A.15 Surface temperature and hoop stress results with superheat flux: (a) Wide face and (b) Narrow face. 301

Figure A.16 Hoop stress profile through the thickness at different times below meniscus (WF centerline from slice model). 302

Figure A.17 Hoop stress and phase profile through the thickness 60 s below the meniscus (WF centerline from slice model). 304

Figure A.18 Deformed shape with temperature contours: (a) 100 mm, (b) 200 mm, (c) 400 mm, and (d) 800 mm below meniscus. 305

Figure G.1 Multiple longitudinal depressions across slab broadface 434

Figure G.2 Multiple longitudinal depressions across slab broadface - Dimensioned . 435

Figure G.3 Multiple longitudinal cracks within a moving depression 436

Figure G.4 Multiple longitudinal cracks within a moving depression - Dimensioned 437

Figure G.5 Multiple longitudinal cracks within a moving depression 438

Figure G.6 Multiple longitudinal cracks within a moving depression - Dimensioned 439

Figure G.7 Longitudinal cracks on slab broadface, casting direction down. (scale unavailable) 440

Figure G.8 Sharp longitudinal depression on slab broadface 441

Figure G.9 Sharp longitudinal depression on slab broadface - Dimensioned 442

Figure G.10 Longitudinal crack at the base of deep U shape depression 443

Figure G.11 Longitudinal crack at the base of deep U shape depression - Dimensioned 444

Figure G.12 Longitudinal midface W-shape depression and intermittent surface cracks on a 203 mm square billet, 0.8wt%C, lubrication changed from oil to flux 445

Figure G.13 Sharp longitudinal depression with severe crack at the base wandering along slab broadface 446

Figure G.14 Sharp longitudinal depression with severe crack at the base wandering along slab broadface - Dimensioned 447

Figure G.15 Sharp longitudinal depression with severe crack at the base wandering along slab broadface 448

Figure G.16 Sharp longitudinal depression with severe crack at the base wandering along slab broadface - Dimensioned 449

Figure G.17 Sharp longitudinal depression with severe crack at the base on slab broadface 450

Figure G.18 Sharp longitudinal depression with severe crack at the base on slab broadface - Dimensioned 451

Figure G.19 Slag rim sample removed from a caster including polished light optical image (center) 452

Figure H.1 Sample micrograph cross section naming convention 453

Figure H.2 Transverse cross section from a non-peritectic Al-Mn AHSS steel grade (0.2 wt %C). Sample name: 88-403 454

Figure H.3 Transverse cross section from a non-peritectic Al-Mn AHSS steel grade (0.2 wt %C) etched with 3% Nital. Sample name: 88-403-A00 455

Figure H.4 Transverse cross section from a non-peritectic Al-Mn AHSS steel grade (0.2 wt %C) etched with 3% Nital. Sample name: 88-403-A00 - Dimensioned 456

Figure H.5 Transverse cross section from a non-peritectic Al-Mn AHSS steel grade (0.2 wt %C) etched with 3% Nital. Sample name: 88-403-A01 457

Figure H.6 Transverse cross section from a non-peritectic Al-Mn AHSS steel grade (0.2 wt %C) etched with 3% Nital. Sample name: 88-403-A01 - Dimensioned 458

Figure H.7 Transverse cross section from a non-peritectic Al-Mn AHSS steel grade (0.2 wt %C) micrograph etched with 3% Nital, with primary dendrite arm spacing, sample name: 88-403-A01 459

Figure H.8 Transverse cross section from a non-peritectic Al-Mn AHSS steel grade (0.2 wt %C) micrograph etched with 3% Nital sample name: 88-403-A02 460

Figure H.9 Transverse cross section from a non-peritectic Al-Mn AHSS steel grade (0.2 wt %C) micrograph etched with 3% Nital sample name: 88-403-A02 - Dimensioned 461

Figure H.10 Transverse cross section from a non-peritectic Al-Mn AHSS steel grade (0.2 wt %C) micrograph etched with 3% Nital, including primary dendrite arm spacing, sample name: 88-403-A02 462

Figure H.11 Transverse cross section from a non-peritectic Al-Mn AHSS steel grade (0.2 wt %C). Sample name: 91-303 463

Figure H.12 Transverse cross section from a non-peritectic Al-Mn AHSS steel grade (0.2 wt %C). Sample name: 91-303-A00 464

Figure H.13 Transverse cross section from a non-peritectic Al-Mn AHSS steel grade (0.2 wt %C). Sample name: 91-303-A00 - Dimensioned 465

Figure H.14 Transverse cross section from a non-peritectic Al-Mn AHSS steel grade (0.2 wt %C) etched with 3% Nital. Sample name: 91-303-B00 466

Figure H.15 As cast image of Low carbon steel cast at 43 in/min, 121.3" wide, 52°F superheat, and 7.16" SEN submergence depth (Sample A) 467

Figure H.16 2% Nital etched Low carbon steel cast at 43 in/min, 121.3" wide, 52°F superheat, and 7.16" SEN submergence depth (Sample A) 468

Figure H.17 2% Nital etched Low carbon steel cast at 43 in/min, 121.3" wide, 52°F superheat, and 7.16" SEN submergence depth (Sample A – Region A) . 469

Figure H.18 2% Nital etched Low carbon steel cast at 43 in/min, 121.3" wide, 52°F superheat, and 7.16" SEN submergence depth (Sample A – Region B) . 470

Figure H.19 2% Nital etched Low carbon steel cast at 43 in/min, 121.3" wide, 52°F superheat, and 7.16" SEN submergence depth (Sample A – Region C) . 471

Figure H.20 2% Nital etched Low carbon steel cast at 43 in/min, 121.3" wide, 52°F superheat, and 7.16" SEN submergence depth (Sample A – Cross Section 1-1) 472

Figure H.21 2% Nital etched Low carbon steel cast at 43 in/min, 121.3" wide, 52°F superheat, and 7.16" SEN submergence depth (Sample A – Cross Section 1-1) - Dimensioned 473

Figure H.22 2% Nital etched Low carbon steel cast at 43 in/min, 121.3" wide, 52°F superheat, and 7.16" SEN submergence depth (Sample A – Cross Section 1-2) 474

Figure H.23 2% Nital etched Low carbon steel cast at 43 in/min, 121.3" wide, 52°F superheat, and 7.16" SEN submergence depth (Sample A – Cross Section 1-2) - Dimensioned 475

Figure H.24 2% Nital etched Low carbon steel cast at 43 in/min, 121.3" wide, 52°F superheat, and 7.16" SEN submergence depth (Sample A – Cross Section 1-4) 476

Figure H.25 2% Nital etched Low carbon steel cast at 43 in/min, 121.3" wide, 52°F superheat, and 7.16" SEN submergence depth (Sample A – Cross Section 1-4) - Dimensioned 477

Figure H.26 2% Nital etched Low carbon steel cast at 43 in/min, 121.3" wide, 52°F superheat, and 7.16" SEN submergence depth (Sample B) 478

Figure H.27 2% Nital etched Low carbon steel cast at 43 in/min, 121.3" wide, 52°F superheat, and 7.16" SEN submergence depth (Sample B – Region A) . 479

Figure H.28 2% Nital etched Low carbon steel cast at 43 in/min, 121.3" wide, 52°F superheat, and 7.16" SEN submergence depth (Sample B – Region B) . 480

Figure H.29 2% Nital etched Low carbon steel cast at 43 in/min, 121.3" wide, 52°F superheat, and 7.16" SEN submergence depth (Sample B – Region C) . 481

Figure H.30 2% Nital etched Low carbon steel cast at 43 in/min, 121.3" wide, 52°F superheat, and 7.16" SEN submergence depth (Sample B – Cross Section 2-1) 482

Figure H.31 2% Nital etched Low carbon steel cast at 43 in/min, 121.3" wide, 52°F superheat, and 7.16" SEN submergence depth (Sample B – Cross Section 2-1) - Dimensioned 483

Figure H.32 2% Nital etched Low carbon steel cast at 43 in/min, 121.3" wide, 52°F superheat, and 7.16" SEN submergence depth (Sample B – Cross Section 2-2) 484

Figure H.33 2% Nital etched Low carbon steel cast at 43 in/min, 121.3" wide, 52°F superheat, and 7.16" SEN submergence depth (Sample B – Cross Section 2-2) - Dimensioned 485

Figure H.34 2% Nital etched Low carbon steel cast at 43 in/min, 121.3" wide, 52°F superheat, and 7.16" SEN submergence depth (Sample B – Cross Section 2-3) 486

Figure H.35 2% Nital etched Low carbon steel cast at 43 in/min, 121.3" wide, 52°F superheat, and 7.16" SEN submergence depth (Sample B – Cross Section 2-3) - Dimensioned 487

Figure H.36 2% Nital etched Low carbon steel cast at 43 in/min, 121.3" wide, 52°F superheat, and 7.16" SEN submergence depth (Sample B – Cross Section 2-4) 488

Figure H.37 2% Nital etched Low carbon steel cast at 43 in/min, 121.3" wide, 52°F superheat, and 7.16" SEN submergence depth (Sample B – Cross Section 2-4) - Dimensioned 489

LIST OF TABLES

Table 3.1 Tata Steel ROM mold 66

Table 3.2 Plain low-carbon steel composition 74

Table 3.3 Plain low-carbon steel transition temperatures 74

Table 3.4 Properties used in the Weiner and Boley test problem 83

Table 3.5 Gap conductivity and resistance values 93

Table 3.6 Compositions (wt.%) of steel grades 100

Table 3.7 Transition temperatures for 409L stainless steel 101

Table A.1 CON1D interfacial gap parameters 279

Table A.2 Compositions (wt.%) of steel grades used in Stainless Steel Work 289

Table A.3 Transition temperatures for 409L stainless steel. 290

LIST OF ABBREVIATIONS

Body Centered Cubic	BCC
Brittle Temperature Zone	BTZ
Casting Speed	V_C
Cohesive Zone	CZ
Crack Tip Opening Angle	CTOA
Crack Tip Opening Displacement	CTOD
Face Centered Cubic	FCC
Fiber Bragg Grating	FBG
Finite Element Analysis	FEA
Finite Element Method	FEM
High Carbon Steel	HC
Low Carbon Steel	LC
Multi-Point Constraint	MPC
Narrow Face	NF
One-Dimensional	1D
Reduced Order Model	ROM
Submerged Entry Nozzle	SEN
Three-Dimensional	3D
Two-Dimensional	2D
Ultra-Low Carbon Steel	ULC

Virtual Crack Closure Technique . . . . . VCCT

Wide Face . . . . . WF

Zero Ductility Temperature . . . . . ZDT

eXtended Finite Element Method . . . . . XFEM

ACKNOWLEDGMENTS

First and foremost, I would like to thank my advisor Prof. Brian Thomas. For taking a chance on me as an undergrad, supporting me for the better part of a decade, putting tremendous trust in me, allowing me to make my own mistakes, and fiercely arguing in even the most semantic discussions. Thank you.

I also gratefully acknowledge the financial support by the member companies of the Continuous Casting Consortium at the University of Illinois at Urbana-Champaign and the Continuous Casting Center at the Colorado School of Mines, which have included: ABB, AK Steel, ANSYS-Fluent, Baosteel, CBMM, Nippon Steel and Sumitomo Metal Corporation, Nucor, RHI Magnesita Refractories, Arcelor-Mittal, SSAB, POSTECH/POSCO, JFE Steel, and Tata Steel. I would also like to thank the Department of Mechanical Engineering at Colorado School of Mines for financial support in the form of graduate teaching fellowships. Over the years this work was additionally supported by a number of grants and funding sources. The National Science Foundation (Grant Number: CMMI-1300907) as well as part of the Blue Waters sustained-petascale computing project, which is supported by the National Science Foundation (awards OCI-0725070 and ACI-1238993) and the state of Illinois. Blue Waters is a joint effort of the University of Illinois at Urbana-Champaign and its National Center for Supercomputing Applications. Additionally, at Colorado School of Mines some funding provided by The National Science Foundation GOALI Program (Grant Number: CMMI 18-08731)

Over the course of this project I have been privileged to interact, and work, with some excellent researchers, scientists, and engineers around the world for which I am grateful: Rich Gass of ArcelorMittal Indiana-Harbor, Ken Blazek, Hongbin Yin, and Rudolf Moravec of ArcelorMittal ECRD, Joydeep Sengupta of ArcelorMittal-Dofasco, Ed Szekeres of Casting Consultants Inc., and Begoña Santillana of Tata Steel Europe. All of the extra discussion,

support, and samples you provided allowed me to complete the work I needed to.

Research is truly a team effort and I would like to thank some of the other students, visiting scholars, and researchers of the CCC that I have had the pleasure to work with over the past few years: Kenny Swartz, Eric Badger, Aravind Murali, Brendan Joyce, Gavin Hamilton, Pete Srisuk, Ramnik Singh, Prathiba Divuuri, Adnan Akhtar, Hyung-Jin Lee, Hyunjin Yang, Kun Xu, Kai Jin, Zhelin Chen, Nathan Seymour, Yonghui Li, Xialou Yan, A.S.M. Jonayat, Carly Blaes, Hamed Olia, Ghavam Azizi, Lipsa Das, Mingyi Liang, Prof. Guoming Zhu, and Keigo Toishi. Special thanks go to Nick Bresnahan for substantial work regarding sample preparation, microscopy, and dimensioning some rather frustrating images.

Particular thanks are due to Bryan Petrus, Rui Liu, and Seong-Mook Cho for many shared meals, pints of advice, and trivia with the CDC, and especially to Lance Hibbeler, without whose mentorship my project and graduate school experience would not have been nearly as successful.

Thanks also to some of my colleagues in Mechanical Engineering and across campus in Metallurgical and Materials Engineering: Ty Porter for his help with electron microscopy and metallographic preparation techniques, and Nathan Johnson, S.R.J. Likith, and Henry Geerlings for mathematical and programming discussion.

Graduate school is a weird experience, and this work would not have been possible without the support of all my friends and family, especially Linda Zappulla. Finally, tremendous thanks are due to Kayla Molnar, for keeping me grounded in reality and putting up with me and what the PhD process did to me for the last few years.

To R.L.Z., the first engineer I ever knew.

CHAPTER 1

INTRODUCTION

Steel as a manufacturing material has been a cornerstone of the industrialized world since the mid 15th century [1]. The advent of the Bessemer process in the mid 19th century kicked the industry into mass production [2], however, at the time of the patent it proved very difficult to control and the quality of the final products was far inferior to other methods which slowed it's adoption [3]. Not until the introduction of mold oscillation in the 1930's by Siegfried Junghans was the functionally continuous process industrially feasible.

Further developments in the 1950's and 60's saw the development of modern continuous casting including the successful operation of the world's first production scale continuous casting machines [3, 4]. By the 1990's the continuous casting process was the production method for the majority of the world's total crude steel. As of 2019 more than 96% of the world's steel production is produced using the continuous casting process [5], with annual production topping $\sim$1.7 billion metric tonnes. Using conservative estimates, this constitutes approximately \$1.08 trillion dollars in annual sales - of which \$1.04 trillion can be directly attributed to continuous casting.

Steel offers one of the most efficient cost-to-weight ratios of any manufacturing material and it is found everywhere from construction equipment to construction material, infrastructure to transportation, and even household appliances. However, this widespread and mature process still suffers from various defects and taking corrective action to daily problems such as longitudinal cracks and depressions requires better fundamental understanding of how the many different types of defects form, and how to recognize them

As Pierre Dauby commented in 2012: "Any [product] redo costs money... Any inspection costs money"[6]. If even $1/10^{th}$ of 1% of continuously cast steel products have a defect that requires attention or mitigation, this represents more than \$1 million dollars per day of

affected revenue. A process this critical to worldwide manufacturing and infrastructure is clearly worthy of attention.

1.1 Defects in Continuous Casting

As a defect created during initial solidification in the mold travels further in the process, each subsequent step adds value to the product and increases the wasted expense if that slab needs to be re-mediated (like in Figure 1.1) or scrapped completely. This down stream processing makes it even harder to identify causes, as each step adds a variety of different interactions that can lead to a defect. Furthermore, a defect is not necessarily the result of a single cause. Often the defect is a result of multiple interacting causes and process parameter variations, with this complexity it should come as no surprise that there is still a lot that is unknown about their exact origins.



Figure 1.1: Slab defect remediation by torch

Cracks and depression formation are serious quality defects that have affected continuous casting since its inception. The process itself is well known to have a high predisposition for generating cracks [7] of all kinds (See Figure 2.17); The high rate of heat removal results in steep temperature gradients and thus high thermal strains and stresses as the shell attempts

to expand or contract. The strand also becomes subjected to mechanical stresses from mold taper, rolls, ferrostatic pressure, and bending or straightening sections. Cracks and depressions can lead to substantial mitigation costs or sudden failures in the final product, and in the worst case can lead to catastrophic breakouts in an operating caster.

Of continuous casting defects, longitudinal depressions and longitudinal cracks, both of which are known to initiate predominately within the mold, represent a significant portion of issues. Furthermore, these defects are not as easy to recognize and understand as their known causes are much less specific than other types of defect. They are inherently more difficult to spot on instrumentation than transverse depressions & cracks, because they do not have the systematic signature of making each row of thermocouples dip as they travel down the mold during casting [8]. To further complicate things, longitudinal cracks can appear anywhere across the surface of the slab (midface, corner, off-corner) wide and narrow faces, they appear with different shapes, and with or without surface or sub-surface cracks.

For all of the cost benefits to better understand cracks and depressions, probably the single most important reason is for safety. In the harsh industrial environment of a steel plant there are thousands of ways for injuries or fatalities to occur thus, occupational safety is the prime directive of most steel manufacturers. The single most catastrophic defect that can occur at the caster is a breakout. When the shell of the steel strand ruptures during casting, exposing the molten core, thousands of gallons of liquid steel can pour out of the strand, onto the machine and the nearby plant floor. The result of a breakout is shown in Figure 1.2. In the 21st century, breakout prevention systems are in place at most casters and thankfully are set up to immediately seal the tundish off and prevent further feeding of the steel [9]. However, while these systems save countless lives, the best preventative measure is not to have a breakout at all.

About 80% of breakouts are categorized as "sticker-type" breakouts and have been discussed at length in the literature [9–12], with the remaining 20% being attributed to cracks and scum entrapment [9, 12]. A less common type of breakout is an after-effect of a longitu-



Figure 1.2: Slab breakout shell after removal from machine

dinal depression, a bleeder type breakout. Bleeder type breakouts are a result of severe shell thinning, followed by evidence of bleeders on the surface of the strand, and finally complete rupture of the solid shell. Current breakout detection systems are great at predicting sticker breakouts, a transverse phenomenon, but are not good at spotting breakouts caused by an extreme longitudinal depression. As such, more intelligent methods are needed to reliably predict, prevent, and detect longitudinal-based breakouts.

Cracks are widely known to appear at the base of depressions, and deeper and wider surface cracks are seen to generally appear at the base of deeper and wider depressions as reported in the literature [13]. However, it is observed that in many cases, depressions appear without surface cracks. This begs the question, what is the relationship between cracks and depressions?

Figure 1.3 shows a rogues gallery of some longitudinal depressions with cracks. It is clear that they all have different appearances, some more detrimental to product quality than others. By the end of this thesis, the author hopes to convince you that using the validated computational model in this work, each of these defects can be better understood based on appearance alone, as well as predict their formation within the mold.

1.2 Research Objectives

While continuous casting, and steelmaking in general, is one of the most mature processes of the industrialized world, it is clear that its complexities are vast. With continuous casting production measured in the *billions* of metric tonnes per year, any small improvement in the process leads to increases in throughput, efficiency, and cost savings. Heat transfer issues within the mold have a significant effect on final cast shape. Flux layer thickness variations, scratches on the surface of the copper (or coating), water channel scaling and clogging, premature or uneven mold wear, all of these can create local heat transfer non-uniformities. Cracks and depressions are still one of the most costly defects in continuous casting, many times resulting in scarfing (surface removal), downgrading, complete scrapping, and if accidentally shipped out, even product failures and loss of customer trust. As

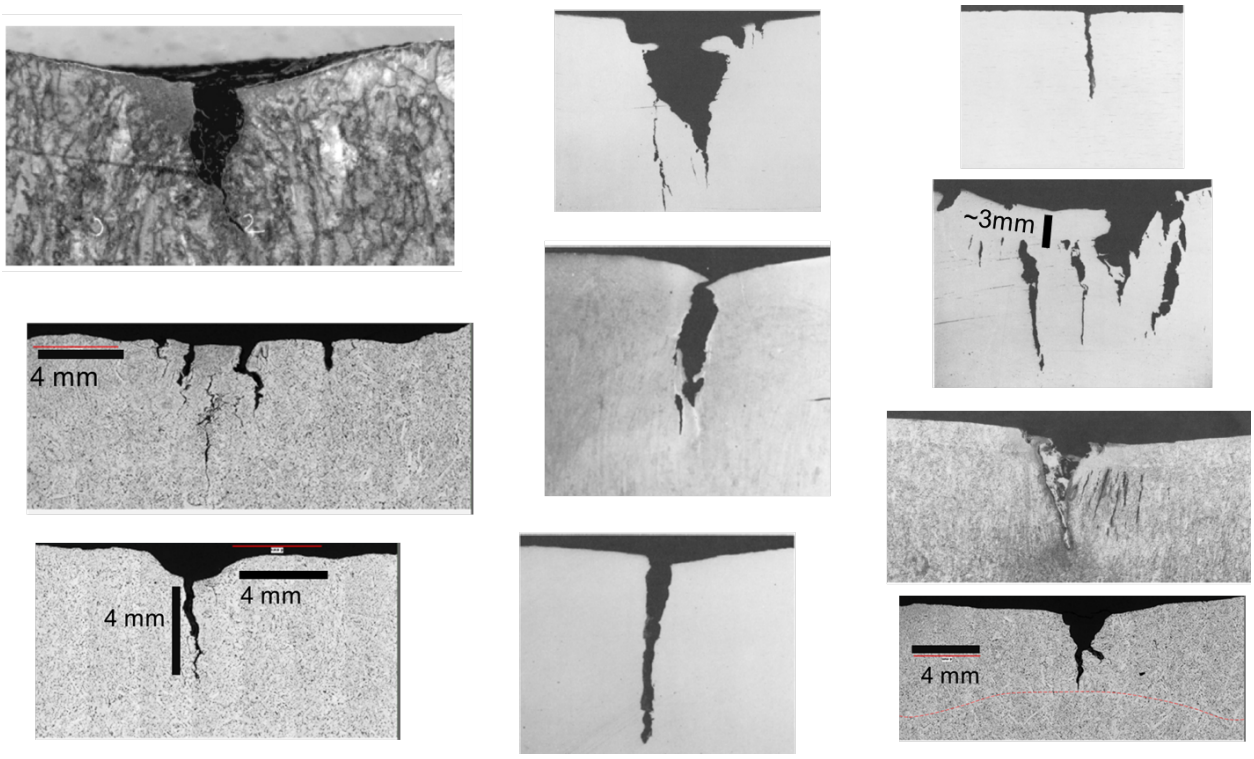


Figure 1.3: Examples of observed longitudinal cracks/depressions

technology has increased so too has our ability to limit and confine our defects to smaller sizes, and less detrimental areas. However, cracks remain an issue at many casters and while general causes are known, little is known (and proven) on the process of formation. Much of the knowledge that does exist is empirical, and there is quite a bit still unknown about the fundamental mechanisms; as such, more work is needed on the steps that can be taken when troubleshooting a caster that is producing a high amounts of them.

Previous advances have mainly come from trials at operating steel plants. But, as the process improves, and defects become more intermittent, this "trial and error" approach becomes more expensive. Modeling, more specifically computational modeling, allows engineers to take a unique real world situation, make assumptions, and distill it into its most relevant and basic parameters. By making these simplifications we can study and begin to understand the phenomena and behavior in different situations that might otherwise be extremely expensive or unrealistic to duplicate in the real world. Continuous casting research

stands to benefit greatly from computational modeling as the real process environment is so hazardous that conventional experimental techniques are often inadequate and dangerous at the temperatures and conditions that are present at an operating caster.

The objective of this work is to gain a fundamental understanding of how different types of depressions form and develop into their particular appearance. Six specific research questions are posed to fulfill the broad research objective:

- What conditions are necessary to initiate a depression?
- What are the steps in depression formation?
- How do depression shapes vary if caused by tension vs compression?
- How does a crack change the surface shape of a defect?
- Can the shape of a longitudinal defect indicate a formation mechanism?
- Can a methodology be developed to predict the likelihood of a defect?

1.3 Research Methodology

To accomplish this goal a number of thermal-mechanical finite element models were developed. Variations in thermal and mechanical boundary conditions for the models are based on plant data and process understanding; and include validation with exact plant conditions when available. Some microscopy and compositional analysis was used to confirm and quantify behavior predicted by the models. Finally, attempts are made to visually match the shape of depressions, found from plant measurements, by modeling different temperature and mechanical histories, and provide demonstrable specific casting situations that lead to the formation of the defect.

1.4 Dissertation Outline

This work is divided into 5 results and discussion chapters (3 through 7) preceded by this introduction and the following background chapter, and succeeded by a summary conclusions chapter.

Chapter 2 provides background on the continuous casting process, relevant phenomena, and further motivation for this research topic.

Chapter 3 provides thorough details on the models developed and used in this work including verification and validation. This chapter contains excerpts from a Journal of Materials Processing Technology article published in April 2020 [14]. In the journal paper, thermal fluid flow calculations were conducted by Dr. Seong-Mook Cho (advised by Prof. Brian Thomas), with contributions to stainless steel applications by Dr. Hyoung-Jun Lee (advised by Prof. Seon-Hyo Kim) and by Dr. Seid Koric. The measurements used in this work were taken at POSCO steel and compiled by Dr. Seong-Mook Cho and Dr. Hyoung-Jun Lee. While the journal paper focuses on multiphysics modeling of stainless steel, it also includes extensive model validation compared against experimental tensile test data for the different steel grades, and demonstrates the validity of the modeling methodology and material model used in this work. The full text of the paper can be found in section 8.4. Additionally, development of the thermal resistor model used in this work began during the author's progress towards a Master of Science degree, as such this chapter also contains substantial excerpts from a 2016 Masters Thesis at the University of Illinois at Urbana-Champaign [15].

Chapter 4 explores behavior within a continuous caster using a full 3D thermal-mechanical finite element model. This chapter contains a 2019 AISTech conference paper published in May 2019 [16]. The model detailed in this conference paper was developed in collaboration with Prof. Guoming Zhu.

Chapter 5 is a case study application of the models developed in this work. The case study conducted in 2018 in Ijmuiden, Holland for Tata Steel Europe, gives a complete analysis of a defect using full caster data to validate the 2D depression effect for the first time. The study also demonstrates the validity of the approach for defect identification, as well as the ability of the model to predict the final shape of a defect and match it's thermal signature.

Chapter 6 addresses a series of longitudinal depression and/or crack defects and provides detailed formation mechanisms for each one. Understanding how defects form is beneficial

for anyone that works around a caster, and to this end, it is the hope of the author to provide a useful and practical guide for anyone to get a general grasp of how and why these different types of longitudinal defects form, and in some ways how to alleviate the problems.

Chapter 7 details a new methodology developed in this work for using high resolution thermal data collected from a caster during operation to accurately predict the presence and severity of a defect on the final product surface. This chapter contains large excerpts from a featured journal cover article published in Steel Research International in April 2019 [17] and a patent filed in January of 2020 [18]. The fluid flow work in the journal paper was conducted by Dr. Seong-Mook Cho.

Chapter 8 provides a summary of the results, conclusions, and contributions from this work with respect to the specific research objectives stated.

CHAPTER 2

BACKGROUND

2.1 The Continuous Casting Process

The basic principle of the continuous casting process for steel is based on feeding liquid steel into a water cooled copper mold which is also open at the bottom as shown in Figure 2.1. Preparation of the liquid steel is conducted elsewhere in the plant inside of large ladles made of ceramic refractory material and is referred to as steelmaking and metallurgy. The final product out of secondary steelmaking and metallurgy is a ladle full of molten steel to be cast - often weighing in excess of 300 metric tonnes. The steel usually travels to the caster by a combination of torpedo or tundish cars on railroad tracks, or overhead cranes depending on the operation.

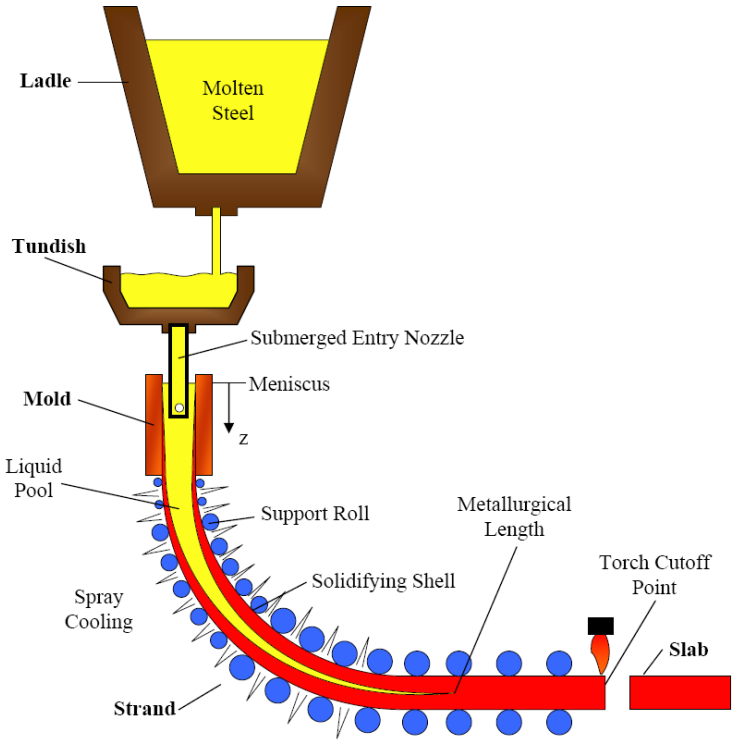
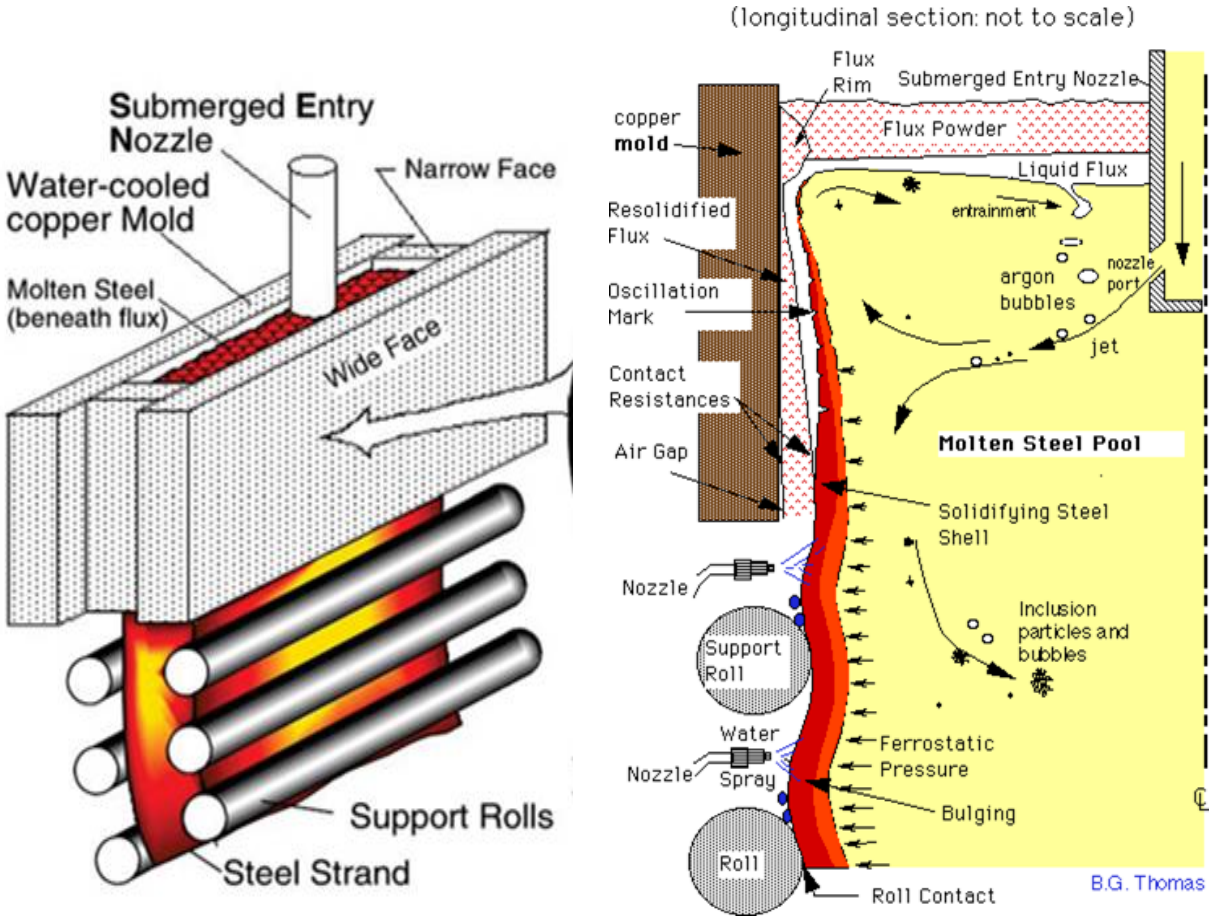


Figure 2.1: Continuous casting process schematic [19]

The molten steel is fed into a refractory lined vessel called a tundish used to regulate a steady feed of steel into the caster. The main purpose of the tundish is to act as a buffer so that the process is continuous between ladle changes, however, it also provides more opportunity for separation of oxide inclusion [20] as well as a smooth and stable pattern for flow into the mold, thereby reducing level issues near the meniscus [21]. As shown in Figure 2.2(a) liquid steel is fed from the tundish into the mold through the Submerged Entry Nozzle (SEN). The flow of molten steel into the mold is controlled by either a stopper rod in the base of the tundish or a slide-gate within the SEN assembly itself.



(a) (b)

Figure 2.2: Mold region schematics(a) Diagram close up of the mold [22], (b) Cutaway view inside the mold [22]

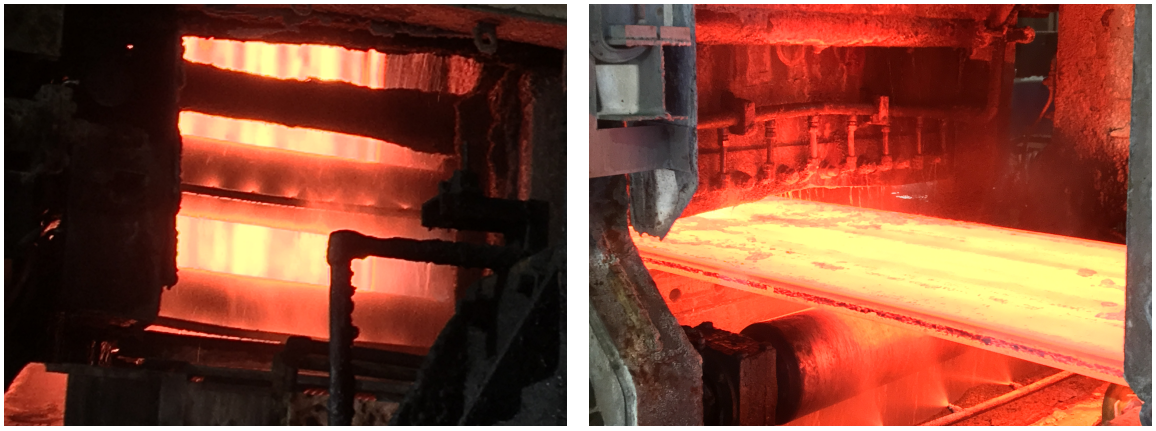
To start up the caster, a dummy bar is used to 'plug' the mold from the bottom to allow the mold to fill and an initial steel shell to solidify and support the process above. The bar is withdrawn from the machine, disconnected, and the process is then capable of continuous operation. Refractory nozzle(s) in the bottom of the tundish distribute liquid steel into the mold, and heat transfer to the water cooled copper immediately solidifies the liquid steel and begins to grow the shell. The mold is also oscillated vertically to further prevent the solidifying shell from sticking to the mold walls. As Figure 2.2(b) shows, mold flux powder is added to the free surface of the liquid steel not only to provide thermal and chemical insulation from the environment, but also act as lubricant in the interface between the solidifying shell and the copper mold.

As soon as the solidified shell is sufficiently thick to contain the liquid steel; the partially solidified section, known now as the strand, is withdrawn from the mold at a rate referred to as the casting speed, V_C, using drive rollers and is further cooled by water sprays of the secondary cooling system.

Upon exit from the mold, the hot solidified skin of the shell cannot yet withstand the hydrostatic pressure exerted by the liquid steel (ferrostatic pressure) within the shell above, and would bulge outwards if not constrained. Therefore, it is necessary to support the continuously solidifying shell using support rolls below the mold between sprays, as shown in Figure 2.3(a).

The thickness of the shell increases with distance from the meniscus down the length of the mold. Shell thickness in continuous casting follows a well accepted square root of time relationship, of the form $s = k\sqrt{t}$, as shown in section 2.1. Where s is the shell thickness, t is time, and k is a solidification rate constant. Depending on the caster and casting speed, the shell thickness can be anywhere from 15 - 45 mm thick. The strand becomes completely solid after passing several meters down the machine where the two sides of the growing shell meet. The distance from the meniscus to this location is referred to as the metallurgical length M_L and varies from caster to caster as well as casting conditions.

Metallurgical length also generally coincides with the "end of containment" which refers to the latter portion of the caster that no longer requires upper support rolls due to a fully solid section (seen in Figure 2.3(b)). As mentioned earlier, the steel shell is generally not strong enough to resist the pressure exerted by the liquid steel above and requires support. If metallurgical length is not reached very close to the end of containment, solidification defects start to occur such as hot shortness, loose center, and in the worst case scenario, a whale as shown in Figure 2.5. A whale occurs when the ferrostatic pressure of the liquid from above bulges the broadface shell of the strand outwards between rolls. Whales are a serious problem for production as well as from a safety standpoint, as it is essentially a large pinched pocket full of molten steel. Production generally has to stop, and the whale needs to be cooled completely before it can be cut out of the machine.



(a) (b)

Figure 2.3: Thin slab caster strand inside of machine:(a) Curved secondary cooling section of thin slab caster, (b) Horizontal section of thin slab caster just before the mechanical shear

In the ideal operating conditions, once the strand exits containment it is completely solid and the final cast product can be cut to length by an oxy-acetylene torch. The torch generally travels with the strand at the casting speed, or in some cases, the slab is cut off using a mechanical shear. Finally, depending on the type of rolling operation and product, the slab may enter immediately into a tunnel furnace for immediate processing (*i.e.* a thin-

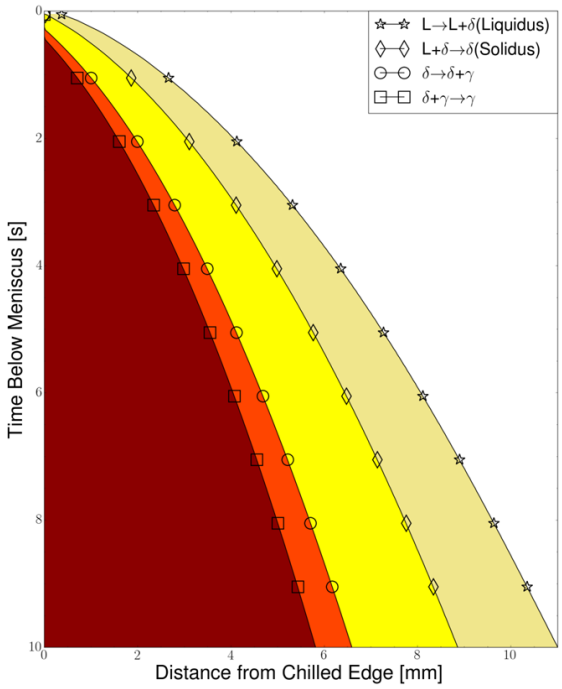


Figure 2.4: Shell growth phase contour mold results inside upper portion of the mold

slab minimill) directly into coiled sheet (as in Figure 2.6(a)). Another option is stacking and transportation to a storage area for holding until further processing as seen in Figure 2.6(b).

2.2 Mold Heat Transfer

As described previously, molten steel is delivered to the caster from the tundish through the SEN and into the mold. During solidification the heat must be removed in a uniform and efficient manner to ensure the best quality of final product.

2.2.1 Fluid Flow in the Mold

In all but the most pristine conditions, the result of most flow patterns can affect the quality of the slag layer as well as meniscus behavior, both of which are critical for initial solidification and thus the quality of the final product. As a result, mold flow and SEN design is the subject of substantial industry research within steel companies and vendors alike. It is well established that the molten steel flow pattern in the mold resulting from conventional bifurcated SENs is not of any one type [24]. Flow patterns can be single or double roll,



Figure 2.5: Bulging thin slab shell leading to a whale outside of containment [23]



(a) (b)

Figure 2.6: Continuous caster final products: (a) Steel coils in yard waiting for transportation to customer,(b) Stacked steel slabs waiting for further processing

stable or unstable, symmetric or unsymmetric, deep, shallow or somewhere in between and just unpredictable. Furthermore, the specific effects on steel quality are not well known and difficult to narrow down to a particular pattern as they also vary with slab width, casting speed, argon flow rate, and SEN angle/immersion depth, and particularly small changes in these parameters.

Diagrams of 3 "natural" types of flow pattern are shown in Figure 2.7. On the left a stable (permanent) double roll is shown, this is the most desirable pattern for mold fluid flow. A stable double roll pattern has equal distribution of molten slag over the entire width of the mold, and generally has the best casting conditions leading to the best quality defect-free steel product. In the middle, a completely unstable roll pattern is shown; characterized by vortexing at the meniscus, substantially uneven molten slag layer thicknesses, and high mold level fluctuations. These problems lead to mold powder slivers, uneven shell solidification, and longitudinal cracks. On the right a stable single roll flow pattern is shown, characterized by thinning of the molten slag layer at the SEN, and strong downward flow opposing the float removal of inclusions and argon gas bubbles. This tends to cause longitudinal broad face cracks, pencil pipe defects and sub-surface inclusions.

To further complicate things, the strength of the roll pattern may or may not be consistent, and also has varying effects on meniscus behavior. A strong double roll pattern tends to have high meniscus velocities and level fluctuations as well as thinning of the liquid slag layer near the narrow faces. Thinning near the narrow faces may cause lubrication issues (sometimes sticker alarms), high amounts of mold powder entrained into the liquid, and mold powder slivers in the final product. On the other hand, a weak double roll pattern is characterized by cold meniscus temperatures, slow velocities, and inefficient washing of the solidification front, conditions that often lead to long hooks, sub-surface inclusions, and slag patches on slab surfaces [6].

Of these conditions, the worst is the "permanently unstable" flow pattern, which generates the most chaotic turbulence, which is most responsible for rare events, such as large level

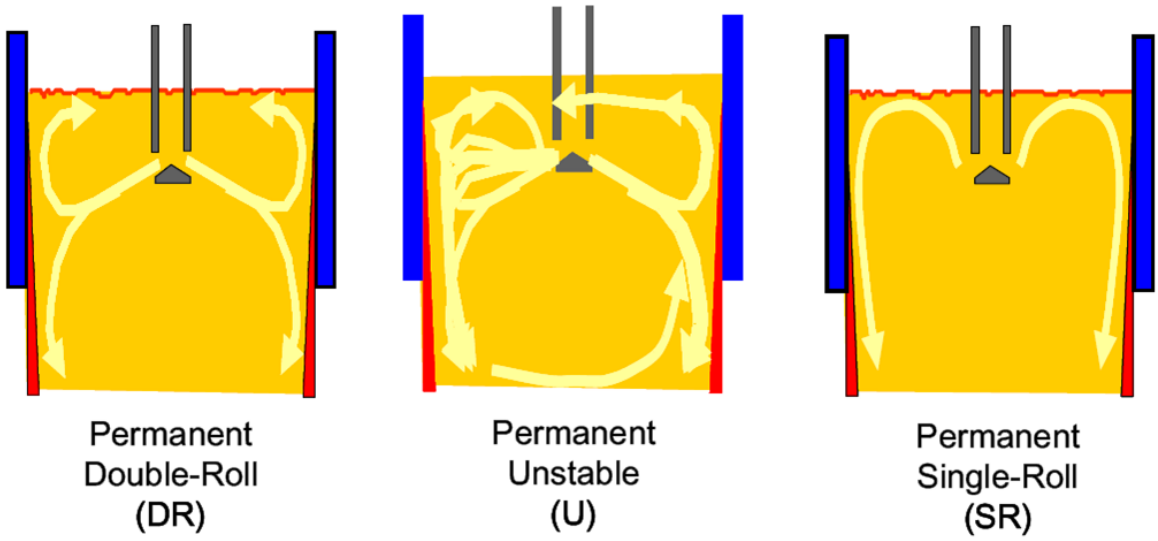


Figure 2.7: Three natural steel flow patterns in the mold [24]

fluctuations. Prior work, using a thermal stress model of the shell near the meniscus, showed that a fluid flow fluctuation (level drop) is capable of causing a tensile hoop stress in the shell [25]. At this location, such a tensile stress could initiate a longitudinal crack at a weakened location in the shell (*i.e.* thermal disruption center). As described, the result of most flow patterns, changes between flow pattern types, or even small changes within a given pattern, can lead to substantial differences in the behavior of the meniscus and quality of the slag layer as well as severe level fluctuations. As a result, these changes can lead to thermal disruption of the shell, which for this work will be considered an interruption to the consistent uniform heat transfer behavior around the circumference of the strand.

It is sometimes pointed out in the literature that unstable flow patterns and large changes in meniscus flow velocities are statistically associated with defects in the final coiled product[6, 24, 26]. However, it is also often implied that there is a relationship between unstable flow patterns and longitudinal cracks and depression based on this association; thus a thermal disruption could also have a longitudinal surface crack. What this connection neglects is to separate the aspects of inclusion based defects versus longitudinal defect. As such, while we know that fluid flow affects longitudinal defects, the actual relationship

between unstable fluid flow patterns and longitudinal cracks and depressions still remains unclear and of substantial interest.

2.2.2 Details of the Interfacial Gap

In continuous casting, heat removal from the steel shell in the mold is controlled mainly by the heat conduction across the interface between the shell and the copper mold. As the liquid steel solidifies against the four walls of the water-cooled copper mold, the solidifying shell ideally does not come into direct contact with the mold copper. Mold powder is added to the free surface of the liquid steel, melts and flows between the steel shell and the mold wall to act as a lubricant. The re-solidified mold powder, or slag, adjacent to the mold wall cools and greatly increases in viscosity, thus acting like a solid. It is thicker near and just above the meniscus, where it is called the 'slag rim'. Depending on temperature, cooling rate, and cooling history, this slag layer may have a structure that is glassy, crystalline, or a combination as shown in Figure 2.8. As long as the strand surface temperature remains above the slag crystallization temperature, the layer will remain liquid and provide lubrication for the shell as it moves downward. If the strand surface temperature is at or below the crystallization temperature, the slag layers are solid, so it is difficult for molten slag to fill in to accommodate any mismatch between the mold taper and the strand shrinkage, which means an air gap may form within the gap.

As the shell travels down the mold and solidifies it shrinks due to phase changes and thermal contraction. If the taper calculation is not adequate, shrinkage of the strand may cause an air gap to form in the space between the shell and the mold. The gap may also be affected by mold distortion warping the copper out of it's expected shape as it heats up during use. The size of the gap is particularly important when exploring positions near the corner where geometry effects and shell strength outweigh ferrostatic pressure.

It has been estimated that within the mold, the gap alone accounts for as much as 84% of the total resistance to heat transfer from the molten steel to the cooling water, while the growing steel shell, mold wall and the mold/cooling water interface accounts for the balance

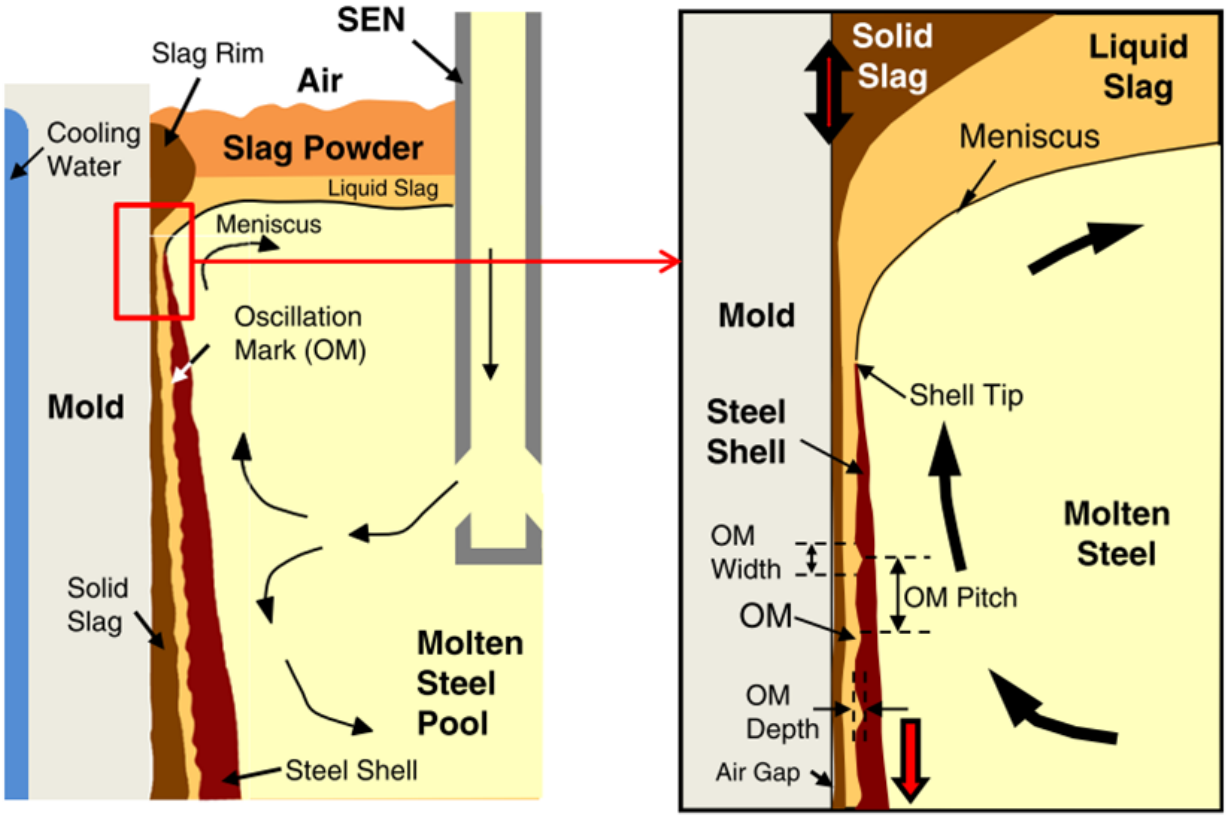


Figure 2.8: Transient phenomena in caster meniscus region [27]

of 16% [28]. Thus, the behavior of heat removal in the mold is dependent largely on the behavior of the gap. In an ideal casting, the mold gap is filled entirely with slag in either solid or liquid form. The slag provides lubrication between the moving shell and mold as well as aiding in heat transfer. If there is a disruption or non-uniformity in this lubricating layer, such as the formation of an air gap, the heat transfer will be strongly affected and potentially create local hot spots. Local hot spots and reheating are widely regarded to be one of the major causes for surface defects such as longitudinal cracks and depressions [13, 29].

2.2.2.1 Slag Layer

As discussed above, mold powder is added to the free surface of the liquid steel. The mold powder on the top surface melts and forms a slag pool above the meniscus. As the steel is cast, liquid slag flows down around the sides providing the desired lubrication within the gap and solidifying as it moves below the meniscus. The powder can either be a mechanical mixture of fine grain oxides, or a pre-melted and granulated mixture. Important properties such as: viscosity, basicity, melt temperature, melting rate and degree of crystallization are strongly related to the composition of the powder [4]. The composition of the casting powder may change throughout the casting due to reactions between steel and slag. As the composition changes, the essential properties of the slag will also change leading to variations in layer thickness, crystallinity, thermal conductivity, and resistance as shown in Figure 2.9 [30].

The casting powder has several functions: Protect the metal from oxidation, Thermally isolate the upper surface to prevent meniscus solidification, Absorb inclusions from the melt and dissolve them, Lubricate the surface between mold and shell, Allow for uniform heat removal, Define the meniscus shape by determining the metal/slag interfacial tension. Further details on mold powders and slag behavior can be found in the literature. [4, 28, 31, 32].

There is some dispute in the literature and practice on what exactly the distribution of the liquid and solid layers is. Plant practice has also shown that there is often liquid slag captured at mold exit, while still others report completely solid layers; while both scenarios

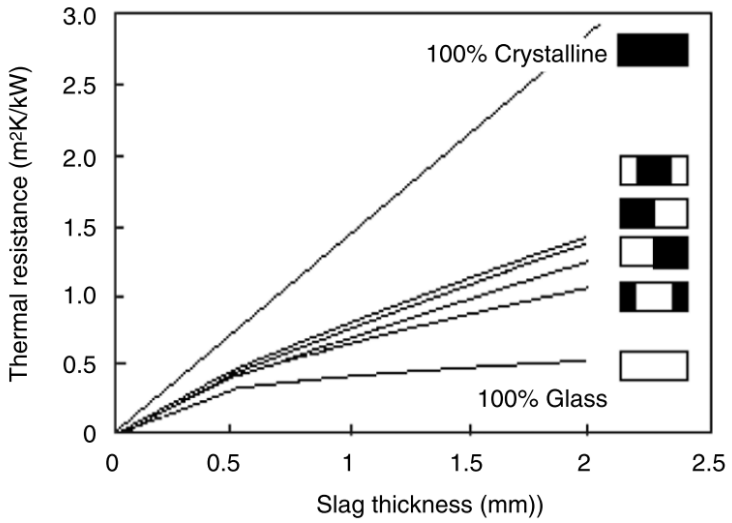


Figure 2.9: Crystallinity and thickness dependent slag conductivity [31]

do occur, the details remain unclear. The properties of liquid slag are complicated, which makes conclusive data difficult to find. Reported values of liquid conductivity in the literature vary from 0.5 to 3 W K/m [18,20,21]. In addition, slag conductivity exhibits the hysteresis effect, though in general the liquid layer tends to decrease with distance below the meniscus as the shell temperature drops. Within the liquid slag layer, both conduction and radiation play a role. The radiation effect has been shown to contribute up to 30% of the total heat flux in the liquid layer but removal of this effect only reduced the total heat flux in the mold by ∼10% [33].

2.2.2.2 Interface Resistances

Interface resistances have a significant contribution relative to the total resistance of the gap [30, 34]. The two most important interfaces are the interface between the copper mold and the flux layer, and the flux layer with the shell. The Mold-Flux interface is the interaction between the copper mold surface and the solid layer of flux it is in contact with. The Flux-Shell interface is the interaction between the liquid or solid layer of flux and the shell surface. In the upper part of the mold this interface almost always includes a liquid layer, however depending on conditions, this layer may have become fully solid by mold exit.

The Mold-Flux interfacial resistance is largely a property of the particular mold powder used, as the surface roughness is related to its crystallization behavior as well as its transition temperatures [31, 32]. The Mold-Flux interfacial resistance increases with the crystallinity of a given flux. The resistance increase from this change is due to the increased surface roughness with the mold surface when it solidifies (*i.e.* the uneven surface creates an equivalent air gap). The change in crystallinity has also been shown to somewhat increase with thickness of the slag layer [30]. Prior works have treated this interface as temperature or thickness dependent, reducing the resistance with distance from the meniscus [33] or with increasing thickness [30].

Similar to the Mold-Flux interface, the Flux-Shell interface resistance increases greatly as the temperature drops below the slag crystallization temperature. Data discussed in the literature [35, 36] relates the variation in heat transfer with temperature, and represents a large resistance relative to the total, while also being highly interface temperature dependent.

2.2.2.3 Air-Slag Gap Formation

Shrinkage of the steel shell away from the mold walls may increase contact resistances or air gaps, which act as a further resistance to heat flow, especially after the slag is completely solid and unable to flow into the gaps. The surface roughness depends on the tendency of the steel shell to 'ripple' during solidification at the meniscus to form an uneven surface with deep oscillation marks. The appearance of the surface depends on the oscillation practice, the slag-rim shape and properties, the strength of the steel grade relative to the ferrostatic pressure, mold taper, and mold distortion.

If conditions within the mold allow for it, an air gap can form. Additionally, if there is a liquid layer of slag present in the gap above the T_{Sol} temperature, the air gap may instead be filled with liquid slag. This condition is based on the assumption that liquid slag from above the gap location would flow downwards to fill in this gap. The thermal conductivity of the air gap is dependent on composition of the gas [37]. Prior work assumes values for air [35] as well as a 20% hydrogen mixture [37] using binary conductivity mixture rules [38].

2.3 Mechanical Behavior of the Strand

As the molten steel solidifies against the mold walls and moves down through the caster to the shear, the strand experiences an extremely complicated thermal and mechanical loading history, which is directly related to the design of the particular caster[1]. In general, casters have a fixed thickness dictated by their unique and specific design geometry. The narrow face and wide face copper molds of the caster domain are vertical and held fixed at predetermined taper angles. Many casters are capable of online width changes and taper adjustments, particularly common in thin slab casters; however, some casters operate on a fixed width during casting.

Setting the taper is critical to final product quality as bulging in the mold can directly lead to bleeds and breakout (as described later in this chapter). While it is not a common practice, it is well accepted that the optimal taper is parabolic in shape [39–41] as shown in Figure 2.10. While machining parabolic narrow faces is a difficult task, other ideas such as grooved molds, and multi-taper profiles have been explored. Most modern casters use vertical molds that require bending and unbending of the strand. Curved molds eliminate the need to bend the strand, as they cast directly into an arc, but still require unbending/straightening, and are more prone to particle, inclusion, and bubble capture on the inner radius due to the curvature of the mold.

Below the mold, machine taper and changing caster radii, including straight and curved segments for bending and unbending change based on the specific caster geometry. Individual support rolls are fixed in space from translation but are allowed to freely rotate around their center. Spaced throughout the machine are a number of motorized drive rolls to maintain appropriate withdrawal/casting speed during operation. Control problems with drive rolls can lead to tension or compression in different parts of the strand during the cast. Damage to the body or surface of the rolls can cause them to apply unexpected loads and displacements

[1]The full publication, including complete illustrative figures, for the 3D thermal-mechanical model of the strand within the caster can be found in Chapter 4 [16]

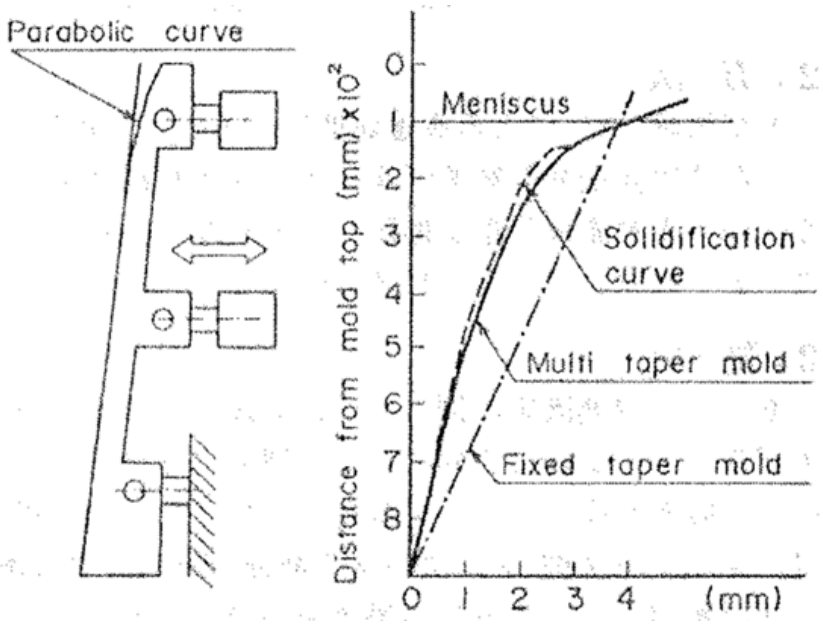


Figure 2.10: Multi-taper mold schematic [39]

to the strand as it passes between them.

2.3.1 Within the Mold

Thermal-mechanical behavior in the mold is important to subsequent behavior below the mold and surface crack formation. Fast cooling of the shell surface generates a brief period of tensile stress during initial solidification in the mold [15]. Then, with no external loading as the shell continues to grow, internal cooling and shrinkage, accompanied by slower cooling of the surface, causes compressive stress to develop at the surface in the cooler and stronger material. The compressive surface stress then increases to tension towards the solidification front.

Proper mold care is important to minimize cracks. Improper over-taper may push on the weak shell and distort it, which is more common towards mold exit. Improper under-taper (usually occurring towards the middle of the mold) or improper sub-mold support, can allow the strand to move around or bulge from ferrostatic pressure. Irregular mold oscillation can result in deeper oscillation marks and potentially slag becoming stuck between the mold and

shell. Mold wear and thermal distortion is known to change the taper over the life of the mold and if this is not accounted for when setting the taper, unintended bad practices may occur.

Each of these mechanical mold issues can also mean deviation from uniform heat transfer, which can cause local reheating and weakening of the shell. Reheating is significant for a number of reasons, not just related to the strength of the material. If the temperature change is significant enough, a phase transformation may take place. Ill-timed phase transformations can mean not only a thinner shell is present, but in the case of reheating from γ-austenite, the potential appearance of a weak δ-ferrite phase surrounded by colder and much stronger γ-austenite.

2.3.2 Secondary Cooling

On mold exit, the strand enters the secondary cooling zones and experiences alternating periods of: water spray/air mist cooling (convection), roll contact (thermal contact conductance), and slower, ambient-temperature cooling in the regions that are sheltered beneath the rolls (convection and radiation), as shown in Figure 2.11 and Figure 2.12.

Temperature results have shown that the strand surface typically exits the mold above $\sim$1100 °C, depending on the specific casting conditions. As a result of 2-dimensional cooling, the corners are the coldest region around the strand perimeter at any given distance below the meniscus. The wide faces then experience some slight reheating before the first spray zone followed by periodic fluctuations in surface temperature, as the strand surface passes beneath the rolls and sprays, removing substantially more heat than the sheltered regions in between. The differences in heat removal are shown in Figure 2.12.

The spray cooling regions exhibit the largest cooling and lowest surface temperatures, while the adjacent regions (rolls and ambient) experience reheating. As temperature changes (both up and down) cause thermal stress, the hoop stresses oscillate between tension and compression according to the spray cooling, roll contact, and in-between regions. Sudden cooling of the strand surfaces by the sprays causes local contraction of that portion of the

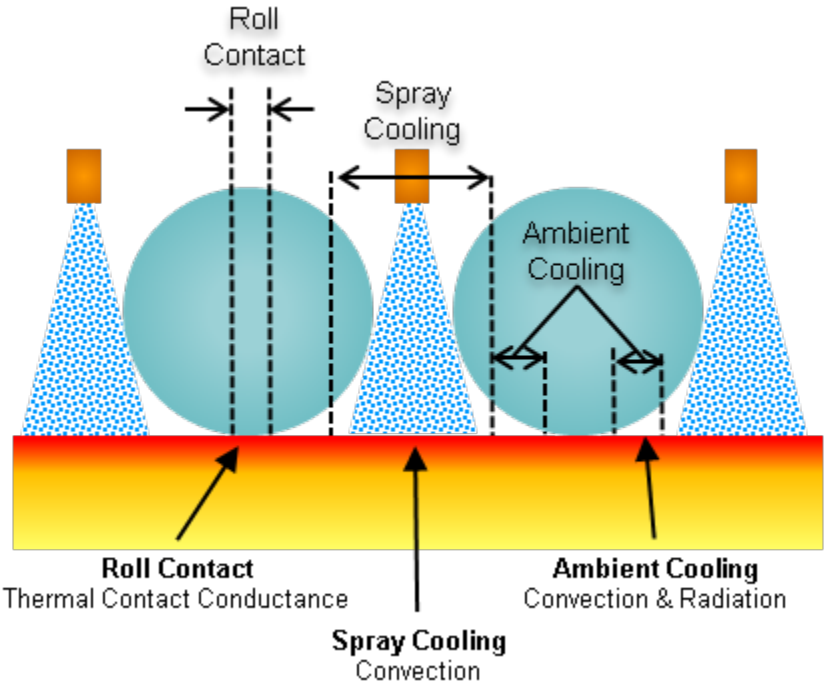


Figure 2.11: Secondary cooling segment schematic

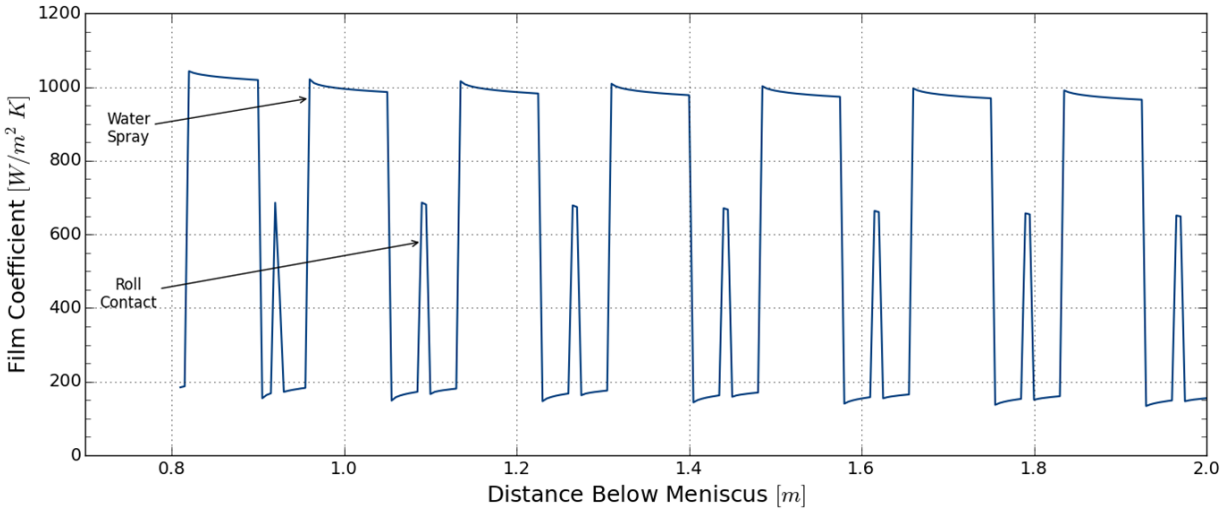


Figure 2.12: Example heat transfer behavior during roll contact and water sprays in secondary cooling

surface. Mechanical constraint by the surrounding, hotter, surface and sub-surface opposes contraction, so the result is tension beneath the sprays in both the casting direction and strand circumference (hoop) directions. As the coldest and strongest part of the strand, the corners and narrow faces experience the highest stresses during the casting process. As a result of their strength, improper machine taper (tapering through the thickness versus the width) has the potential to cause unnecessary extra difficulties, such as premature roll wear, shape problems, and slab defects like off-corner cracking.

2.3.3 Bulging

Bulging occurs in continuous casting as the internal ferrostatic pressure from the molten core pushes the solid shell outwards against the constraint of the support rolls in the caster. Deformation outwards between rolls increases when the shell is hot and thin, the roll spacing is too large, or there is roll misalignment. A schematic of bulging behavior within the support rolls section is shown in Figure 2.13. Bulging can lead to many quality problems including unstable mold level fluctuations, transverse cracking, segregation, as well as undue stress on the containment portion of the caster. Very slight bulging is generally observed between rolls on most of the wide face shell away from the corners. The corners tend not to be affected due to the mechanical constraint of the colder Narrow Face (NF). Bulging magnitudes in an appropriately aligned caster are typically less than a few tenths of a millimeter, depending on the roll pitch. Many casters accomplish this low bulging with the use of small-diameter split-rolls across the width, which enable a smaller roll pitch than a full width roll would require.

2.3.4 Summary

For the harsh industrial environment they operate in, continuous casters are surprisingly precise machines. Caster practices are carefully designed for every grade or grade family based on the specific geometry and setup of a given caster. Bending, unbending, and spray practices must be carefully timed and adjusted to provide the necessary cooling while also

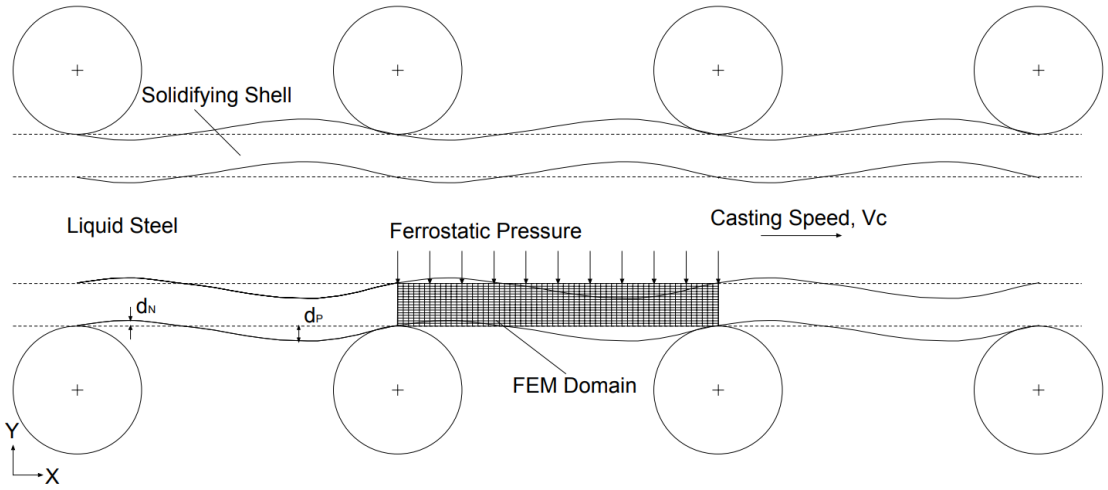


Figure 2.13: Schematic of strand bulging between rolls [42]

avoiding ductility troughs. Slight roll misalignments down to the tenth of a millimeter in any direction can cause a caster to suddenly start making cracked slabs. Typically, once the slab has reached metallurgical length, it subsequently exits containment. Depending on the operation, the slab may immediately enter a tunnel furnace for heating prior to hot rolling, or it may be transported to a slab storage yard. In the downstream process a given slab may be moved by crane, train, truck, or a combination. Each step adds another opportunity for the slab to be unintentionally damaged, mishandled, or dropped. However, any cracking or defects that become apparent after exit from the caster are all but guaranteed to have been generated within the machine - often during initial solidification. Complete description and discussion of thermal-mechanical behavior of the strand within the caster can be found in section 3.12.

2.4 Defects in Continuous Casting

Much of the existing open literature in continuous casting focuses on defects in a general sense, few address longitudinal defects specifically, and none nail down direct formation mechanisms. For a proper discussion of longitudinal depressions and cracks, clear definitions and terminology differentiating it from other defects are necessary.

Cracks in the continuous casting of steel require two different phenomena acting at the same time in order to initiate: metallurgical embrittlement and tensile stress. Tensile stresses can be roughly classified as thermal or mechanical and can be oriented transverse (in the casting direction) or longitudinal (towards the mold faces). Withdrawal of the strand tends to cause axial mechanical stress which is often the basis for transverse cracking, while thermal stresses around the circumference of the strand tend to be the cause of longitudinal cracking. Metallurgical embrittlement includes a variety of mechanisms, but often can be predicted according to ratios of alloying elements, certain ranges of composition, and specific ranges of temperature [43–45]. Most importantly, all steel grades have temperature ranges where they experience a significant lack of ductility.

2.4.1 Temperature Regions of Low Ductility

Firstly, at high temperature involving the mushy zone during solidification, low strength and ductility are often associated with the presence of liquid films in interdendritic spaces, a schematic of which is shown in Figure 2.14. These films are known to be highly segregated, have depressed solidus temperatures, and thus are not as strong as the dendrites themselves [7]. When tension across the mushy zone (containing the dendritic solidification front) pulls the liquid films between the dendrites apart, equilibrium requires liquid feeding to fill the space. Available liquid comes from the region surrounding the dendrites which tends to have higher concentrations of alloying elements as they are rejected to the solute from solidification of the dendrites. Thus, on the dendrite scale, hot tearing in this case eventually appears as segregation streaks in the final product.

If liquid feeding is not possible or inadequate, the tension on the dendrites can locally drop the pressure in the liquid. and allow gases (often hydrogen) to be pulled out of solution. This results in visible subsurface crack formation. If this occurs near the surface of the casting, especially at the low liquid fractions near to the solidus isotherm, then the hot tear can grow to the surface as an open crack. These types of hot tears can be readily observed with macroscopically visible dendrite tips within these cracks. Heavy oxidation within these cracks

appears during subsequent processing as oxide inclusions (slivers) which are detrimental to the final product quality. Ductility typically drops to only about one percent (macroscopic strain) in this region, which is responsible for cracks via the mechanism of hot tearing.

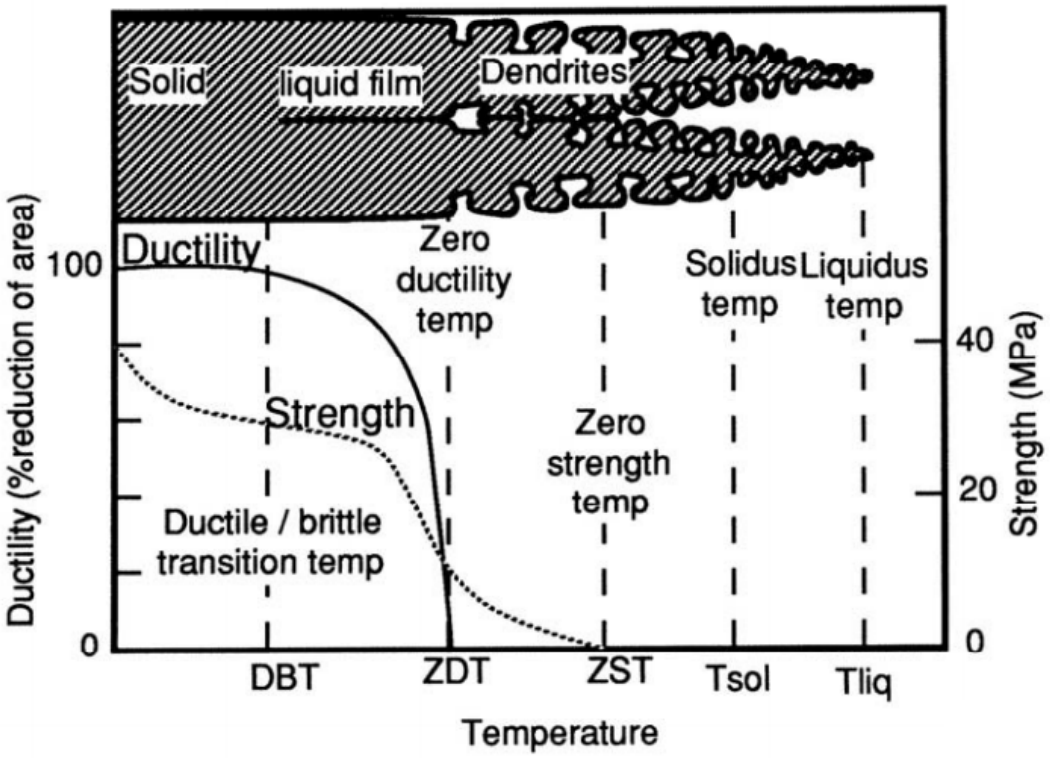


Figure 2.14: Dendrite strength and ductility variation at high-temperature, responsible for hot tearing [44]

Secondly, at intermediate temperatures, there is a ductility trough where the austenite grain boundaries become embrittled and fail, especially if they have ferrite networks that concentrate the strain. Ductility is greatly reduced, but still significant (20-40%). These two different ranges of hot ductility behaviour in steel are shown in Figure 2.15 [44]. In this work, the behavior of interest is primarily: the semi-solid hot tearing low ductility region (a) and the combined lower temperature region (b,d,e,f) in which low ductility intergranular failures often occur [44, 45].

A number of prior studies have examined thermal-mechanical properties and cracking during solidification and conducted reviews on the topic [43] particularly hot ductility in

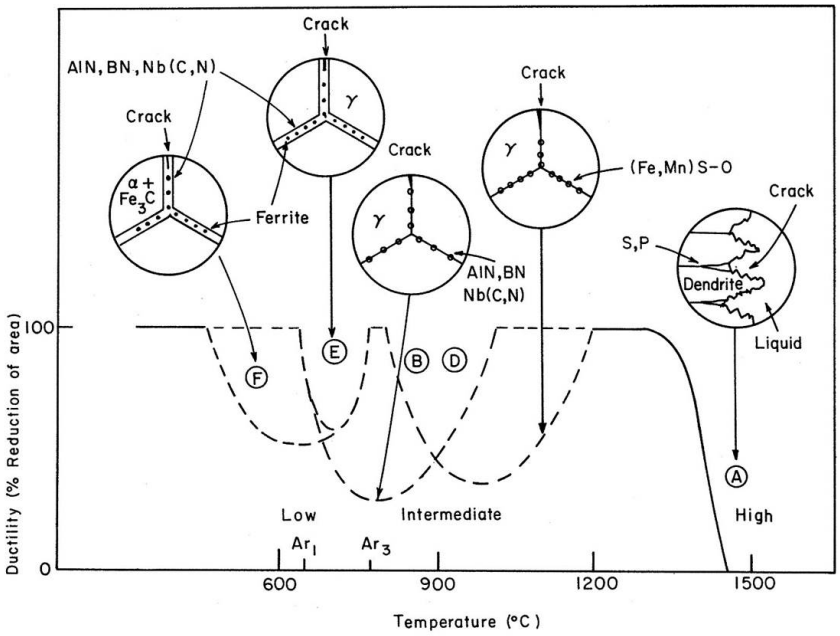


Figure 2.15: Schematic diagram of ductility curve defining the three characteristic regions of hot ductility [44]

continuous casting conditions [46]. Further studies have examined how to relate hot ductility and transverse cracking [45] and the effects of precipitates on cracking behavior [47]. In addition to the hot tearing and intermediate-temperature ductility troughs, there are also lower temperature ductility troughs and other mechanisms which are not of interest in this work.

Compositional effects are often discussed qualitatively in the literature, such as the observation that lower manganese to sulfur ratios as well as elevated levels of aluminum, nitrogen, sulfur, and copper can result in more cracks. The literature includes a variety of compositional heuristics for crack formation, but the peritectic phase transformation associated with the iron-carbon phase diagram is the most prevalent trend. Cracks are more likely in peritectic steels, found between the limit of carbon solubility in δ-ferrite, 0.09%C, and the peritectic composition of 0.16%C, depending on other alloying elements.

The peritectic range of steel grades is known to have a variety of difficulties associated with casting due to their complex behavior during solidification, solid-state phase transfor-

mations, and subsequent rippled shell surface [48]. While these ripples can provide strong sites for crack initiation they would likely lead to transverse cracks in operations with controlled oscillation and horizontal oscillation marks. This suggests that longitudinal cracks in peritectic steels may be caused by other secondary factors. Rapid solidification and phase change shrinkage can be quite large in the case of peritectic steels and because of this, the shell may lose contact with the wall. This loss of contact can result in shell thinning, and thus lead to cracking further down the mold, as local shell regions change phase at different times. The ultra-low carbon range is also expected to have a predisposition to cracking, potentially due to the long duration of the δ-ferrite to γ-austenite transition period. The general occurrence and predisposition is known, but the exact formation mechanism is still not understood.

Intergranular failures in the intermediate-temperature low ductility trough arise as a result of stress and strain concentrations at the austenite boundaries. They are caused either by the presence of films of the softer deformation induced ferrite enveloping the austenite grains, or by grain boundary sliding in the austenite. Both failure mechanisms are enhanced by the presence of grain boundary precipitates and inclusions (the finer, the more detrimental), coarser grain sizes, and lower strain rates [45]. Intergranular failure can occur at a stage in the austenite to ferrite transformation when a thin film of ferrite has formed around the austenite grains (Figure 2.16). As flow stress is a strong function of temperature, and at a given temperature ferrite is almost an order of magnitude weaker than austenite, this translates into low flow stresses compared with the austenite, and therefore to strain concentration in the ferrite film. This leads to microvoid formation, and a ductile failure at the microscopic scale, but with small strain to failure at the macroscale. Harmful precipiates include (Fe,Mn)S and (Nb,Al,Ti)N precipitates in the austenite grain boundaries.

2.4.2 Common Crack Defect Types

In 1967 The British Iron and Steel Research Association (BISRA) put out a manual illustrating and describing the most common defects at the time [49]. In the late 1970s,

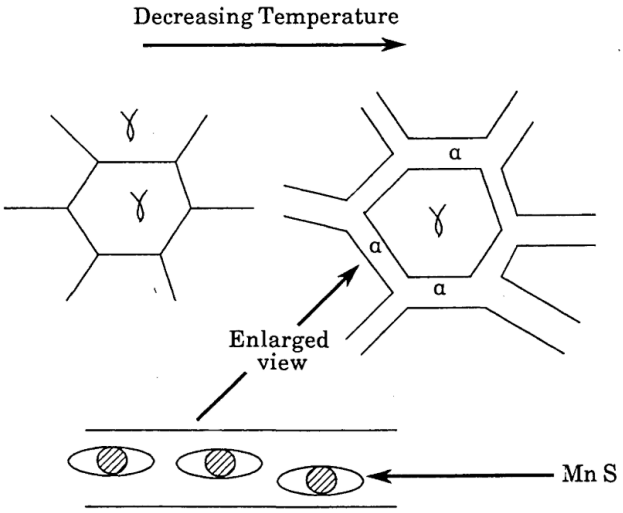


Figure 2.16: Schematic diagram showing mechanism for transformation induced intergranular failure [45]

Brimacombe and colleagues put out a seminal paper called: "Crack Formation in the Continuous Casting of Steel" focusing on more specific details regarding defect formation. Since then, there have been almost no broad and comprehensive defect guides published in the open literature. Most companies have internal reporting mechanisms for defect and root cause analysis, especially with regards to breakouts. Some companies even have internal literature and archives for learning purposes, but in general, steel companies do not discuss casting defects externally, and rarely publish more than one or two images. For accessibility, many of the following images are reprinted from various other sources, including BISRA and Brimacombe, along with many other defect images collected and/or taken by the author. In addition, every effort is made to provide the steel grade, casting conditions, and defect dimensions as available.

Figure 2.17 shows a variety of types of cracks and defects that are generally seen in continuous casting. As the figure shows, there are different types located all around the slab. Each has associated characteristics, and some are identifiable down to the mechanism. Cracks are not the only type of defect in continuous casting, in this work a defect will be considered: A shortcoming, imperfection, flaw, or abnormality that impairs quality, function, or utility.

Thus for this work a defect includes, transverse and longitudinal, internal and surface, cracks and depressions.

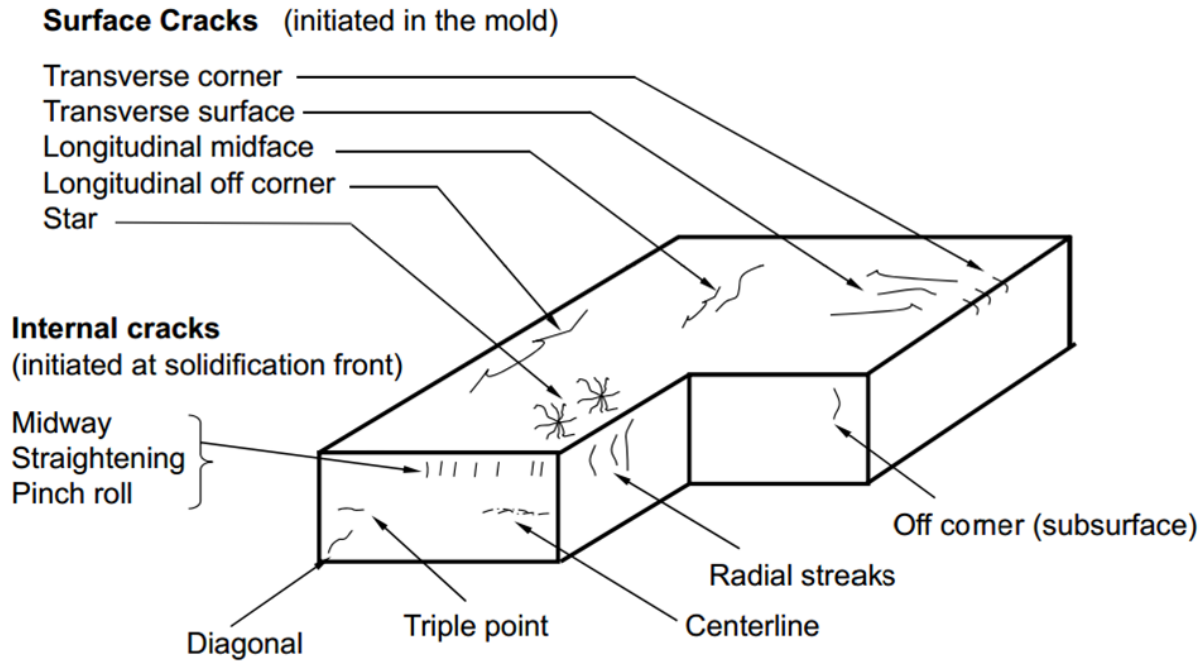


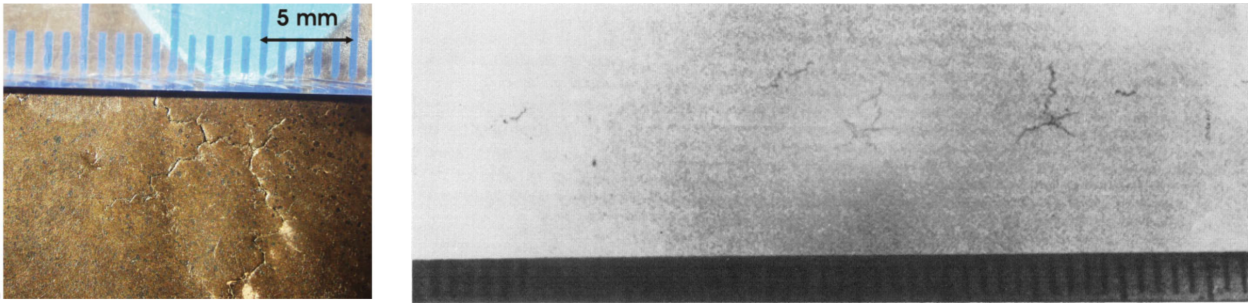
Figure 2.17: Continuous Casting Crack Types [50]

2.4.3 Star Cracks

Star cracks are one of the easier defects to recognize as they are usually surface cracks that follow paths along grain boundaries, due to embrittlement, as a result of elevated levels of copper, often due to pickup from the mold itself or sometimes to compositional problems in the melt. These compositional issues can also lead to changes in the ductility trough for a given grade and are often associated with transverse cracking. An example of star cracks are shown in Figure 2.18(a) and Figure 2.18(b).

2.4.4 Transverse Depressions and Cracks

Transverse depressions are common in continuous casting as the formation of oscillation marks are part of the process. Consistent and even oscillation marks do not tend to be



(a) (b)

Figure 2.18: Star Cracks: (a) Typical star crack on slab surface [51],(b) Multiple star cracks on the surface of a slab [52]

an issue, but disruptions to mold oscillation behavior or friction within the mold can cause uneven and intermittent deeper oscillation marks. Generally, transverse cracks are found at the base of these oscillation marks (transverse depressions), which present an opportunity for a stress concentration, and thus transverse cracks are strongly tied to mechanical conditions within the caster. Ill-timed bending or unbending while the surface of the strand is within a ductility trough is a common cause of transverse cracks that needs to be avoided when designing caster cooling practices, as was the case in Figure 2.19(a) and Figure 2.19(b). Mechanical conditions also sometimes result in radial streaks, as the solidification fronts experience excess tensile stresses during the bending and unbending processes.



(a) (b)

Figure 2.19: Transverse Cracks:(a) Transverse corner crack [40],(b) Transverse Midface Crack [52]

Another type of transverse cracking is centerline cracking, which is often related to compositional segregation, and broadface support issues, occasionally resulting in center looseness due to shrinkage (lack of liquid feeding) where the two sides of the slab are not completely continuous across the centerline. An example of centerline cracking is shown in Figure 2.20. In many cases, the cavity cannot be closed through the rolling process and presents itself as a defect. Additionally, centerline cracking commonly occurs when the strand is unbent in a crack sensitive (low ductility) range.



Figure 2.20: Crack-like defect at centerline of hot-rolled product arising due to centerline segregation[53]

2.4.5 Longitudinal Depressions and Terminology

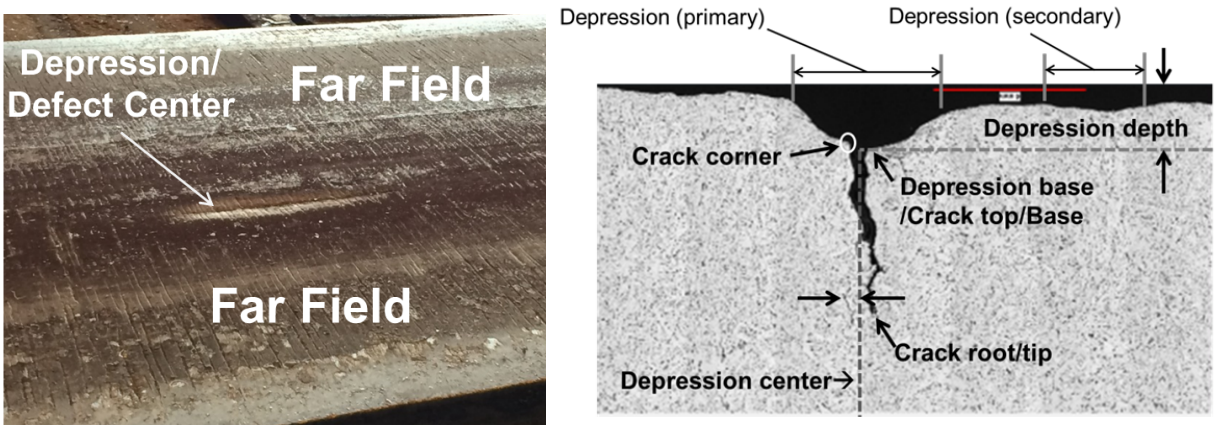
A previous definition given for a longitudinal depression is "A channel-shaped depression on the face of the product, running in the direction of the axis" [49]. While this definition is a good start, some further detail is required, and for this work, a surface depression will be considered: A depressed (lowered) portion of the shell/strand surface as compared to the surrounding far field surface appearance. Certain longitudinal depressions are not necessarily problematic. For example, gutter type depressions are often the result of bulging or buckling of the off-corner region of the broadface shell and corner rotation. Only in cases where subsurface cracks appear is this problematic and thus, it has been found that generally only crack sensitive grades have this problem. Additionally, very wide and shallow (*i.e.* high aspect ratio) gutter usually does not have these cracks.

The most fundamental root cause of the initiation of longitudinal depressions is a local decrease in heat transfer out of the steel shell. This decrease in heat transfer can occur for a number of reasons, many of which are related to mold flux such as: slight differences in flux composition from bag to bag, chemical flux contamination, moisture infiltration, and debris within the flux. Conditions within the gap are not the only potential cause; scratches or imperfections on the hot face of the copper can have a tremendous effect on the thermal gap. Additionally, behavior within the copper can be problematic as well, such as severe scaling, water channel clogging, or improper thermocouple design.

In this work, the depth of a depression will be taken as the vertical distance between the surface at the apparent center point of the defect and the far field surface. The depressions modeled in this work are considered to be symmetrical about the center of the depression and, if present, the crack. The width of a depression is assumed to be the location where the vertical distance to the far field surface is equal to 10% of the depression depth. Crack lengths will be assumed to be the distance from the base of the depression to the end of the visible macroscale crack tip. There are some situations where a crack has evidence of microscale level continuation but for this work that will be largely ignored.

In addition to these descriptions, some terminology needs to be clarified further with figures. An example of a longitudinal surface depression is shown in Figure 2.21(a), which illustrates what is meant by the term "far field", and is used to describe the broad face strand regions away from the defect. A cross section of a longitudinal depression with a crack is shown in Figure 2.21(b).

For discussion and readability using industrially relevant terminology, a portion of this work will be referring to the “buckling” of the steel shell. However, in this work the author does not mean "buckling" in the traditional solid mechanics sense (*i.e.* not purely elastic compression loading leading to Euler buckling). In the context of this work, the term “buckling” should be understood to mean “inelastic buckling” or “kneeling”, as described in the mechanics literature [54]. The term buckling has also been used previously in the steel



(a) (b)

Figure 2.21: Defect Terminology: (a) Slab with constant static longitudinal depression and crack along entire length, (b) Transverse slice through longitudinal depression with crack

industry to describe gutter type depression defects which are a specific subset of longitudinal depressions as shown in Figure 2.22. Gutter refers to a specific type of longitudinal depression in the off corner region of the broad face. Gutter is primarily caused by local buckling of the broadface shell near the narrow face as a result of excessive taper and corner rotation [55].

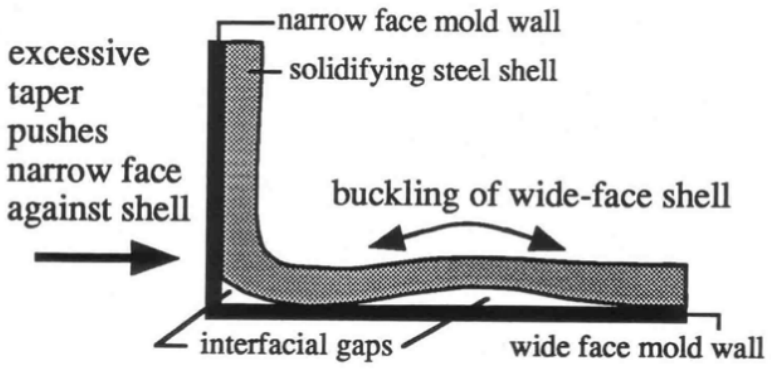


Figure 2.22: Mechanism of gutter formation near mold exit due to excessive narrow face taper[44]

2.4.6 Longitudinal Cracks

Unlike the previously mentioned defects, understanding of longitudinal cracks is much more limited. As mentioned before, cracks can be surface or sub-surface and corner, off-corner, or facial. A litany of operating factors is brought up in discussion of longitudinal crack causes: mold conditions like inadequate taper, improper water cooling, and mold wear; sub-mold conditions like over or under cooling, support type below the mold, poor alignments; and even metal stream impingement, slab geometry changes, high pour temperatures and compositional effects [13].

Some longitudinal cracks are slightly easier to understand and troubleshoot, this is particularly true of mechanically based defects. Midway, straightening, pinch roll, diagonal, and triple point cracks are tied to problems with support roll alignment, excessive pressure, and the timing of ductility troughs or solidification fronts meeting on the interior of the strand. Examples of two types of support roll cracks are shown in Figure 2.23.

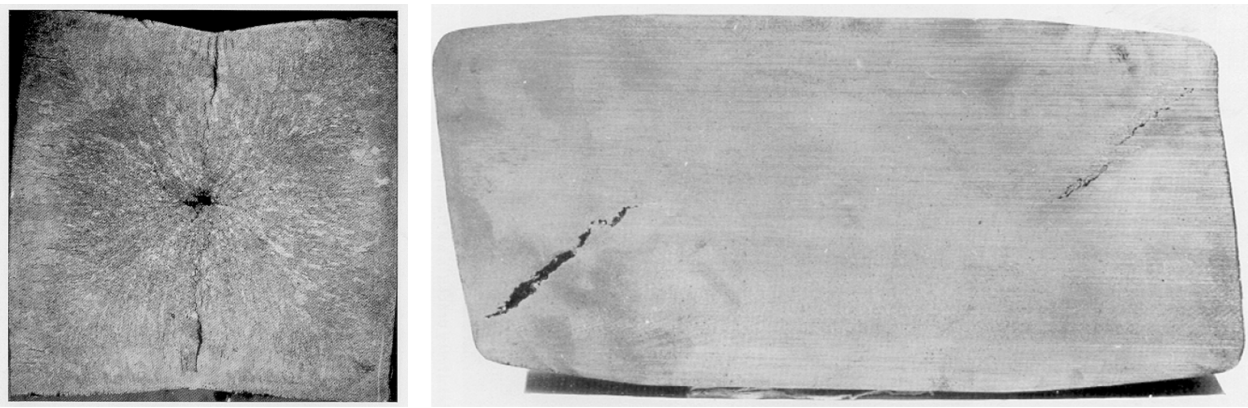
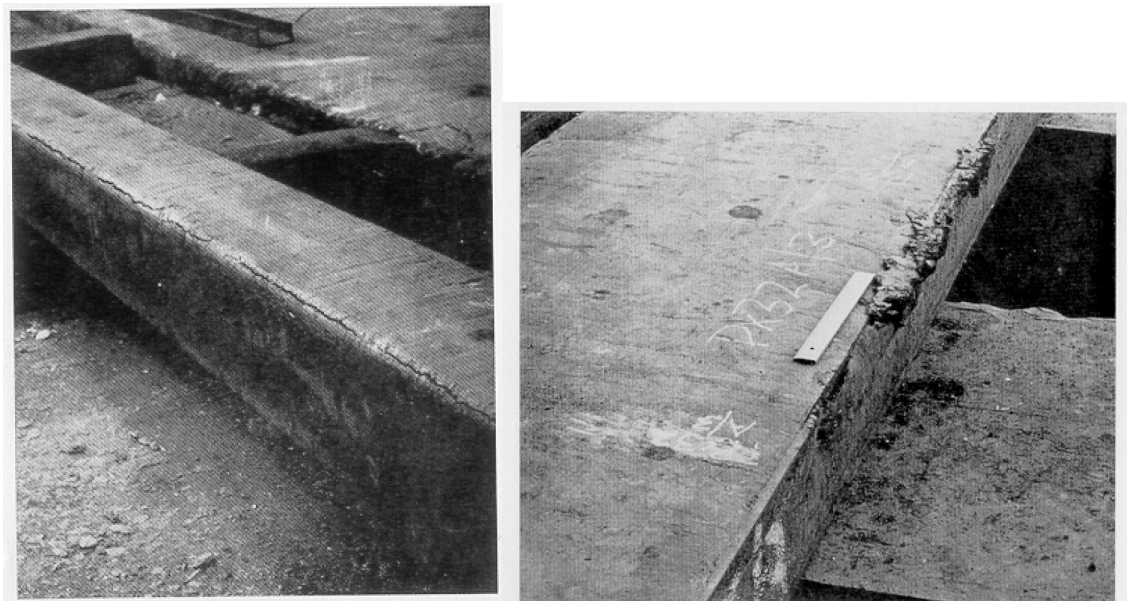


Figure 2.23: Mechanically Based Longitudinal Defects: (a) Withdrawal roll cracks in 9 in square bloom [49], (b) Diagonal longitudinal sub surface cracks in a 12 in x 5 in slab (This section also shows bulging and rhomboidity) [49]

In addition to support and withdrawal based defects, other mechanical longitudinal problems can arise particularly at the corners of cast slabs and billets. Corner cracks (Figure 2.24(a)) are understood to appear as a result of the complex two-dimensional loading

and heat transfer that the corner region experiences, as well as lubrication and mold distortions [52]. Furthermore, the lower temperatures lead to changes in timing for low ductility relative to the rest of the slab surface.

With low ductility and mechanical loading applied at the corners, sometimes bulging of narrow face in combination with thermal shrinkage, corner cracking is often problematic when casting grades between 0.15 and 0.23 wt%C. In more severe scenarios, longitudinal corner cracks can also lead to bleeds, where liquid steel is able to leak and "bleed" from the interior out of the shell. An example of a longitudinal corner crack with a bleed is shown in Figure 2.24(b)



(a) (b)

Figure 2.24: Longitudinal Corner Cracks: (a) Longitudinal corner crack on a 9 in square blooom [49], (b) Bleed on a 35.5 in x 8 in slab associated with a longitudinal corner crack [49]

2.4.7 Longitudinal Cracks Within Longitudinal Depressions

It has been previously discussed in the literature that longitudinal depressions and longitudinal cracks are strongly associated with each other. Additionally it has been detailed extensively that in general larger depressions are found with larger cracks as shown in Fig-

ure 2.25 [56], where the higher position of the unfilled circle (deeper depression) corresponds to a higher position of the unfilled square (longer crack). However, it is unclear what the relationship is between depression formation and crack appearance.

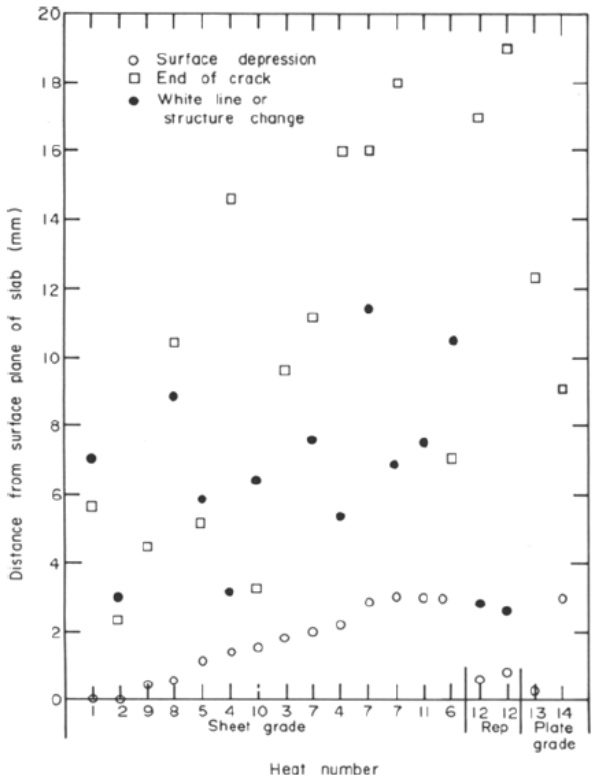


Fig. 5—Depth of crack, surface depression and white line (or structure change) below surface plane of slab for different heats.

Figure 2.25: Observed Depression and Crack Depth Relationship [7]

Sometimes the cracks are present along the entire depression, other times, they are intermittent as in the example shown in Figure 2.26. In this case a longitudinal depression was found along a significant length of a slab, and a crack was observed to appear intermittently along the length within the depression. It is also clear from the image that the crack wandered across the width of the depression. Note that the depression width can be observed based on the presence/visibility of deeper oscillation marks where they were not able to be smoothed out by the support rolls.

Depressions can also wander across the width of a slab as shown in Figure 2.27 though it is also apparent from the image that the crack did follow along with the depression for its entire length and did not move elsewhere.

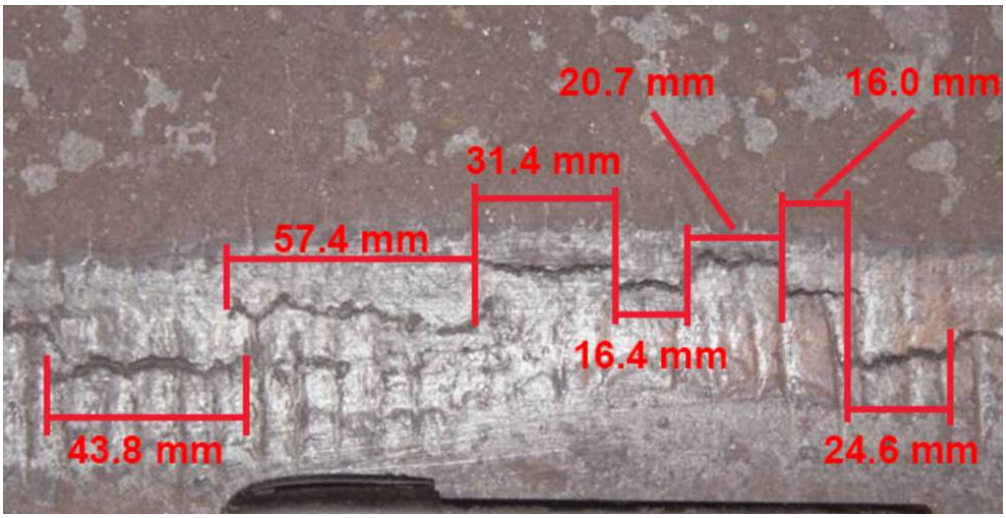


Figure 2.26: Severe longitudinal crack in depression (Full size undimensioned image available in appendix)

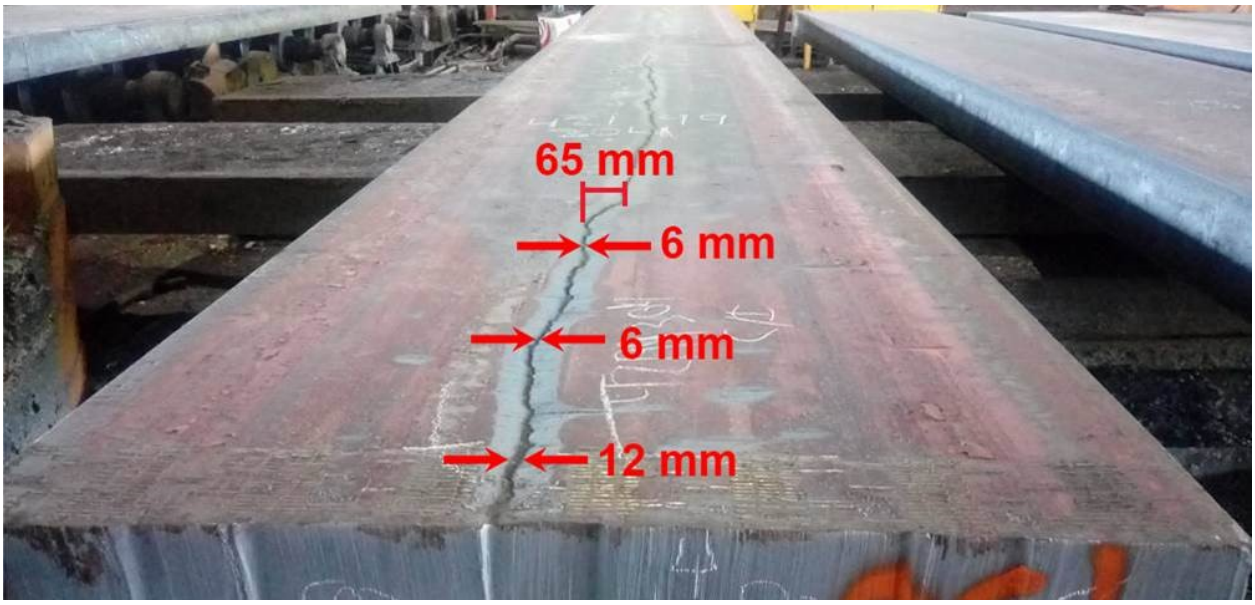


Figure 2.27: Longitudinal facial crack within depression on slab surface (Full size undimensioned image available in appendix)

2.4.8 Breakouts

Breakouts occur where cracks penetrate through to the surface because the local shell falls below a critical thickness. Local shell thickness can be reduced from gap formation, either by mechanical forces lifting the shell from the mold surface or from fluid-flow related effects, such as variations in slag layer thickness (either too thick or too thin).

2.4.8.1 Transverse Sticker Breakouts

The most common type of breakout is known as a sticker breakout. Sticker breakouts occur when a transverse crack opens up and some of the molten core leaks out of the crack and sticks to the shell. As the strand continues to be withdrawn from the machine, the molten steel continually solidifies against the mold, sticks, and is torn. An example of a sticker type breakout is shown in Figure 2.28. Modern breakout detection systems are set up to catch this type of breakout by analyzing the TCs with an inversion algorithm. When a sticker breakout is detected, the machine goes into what is often referred to as sticker slowdown speed. Sticker slowdown speed is in the realm of 0.1 m/min, and the hope is that

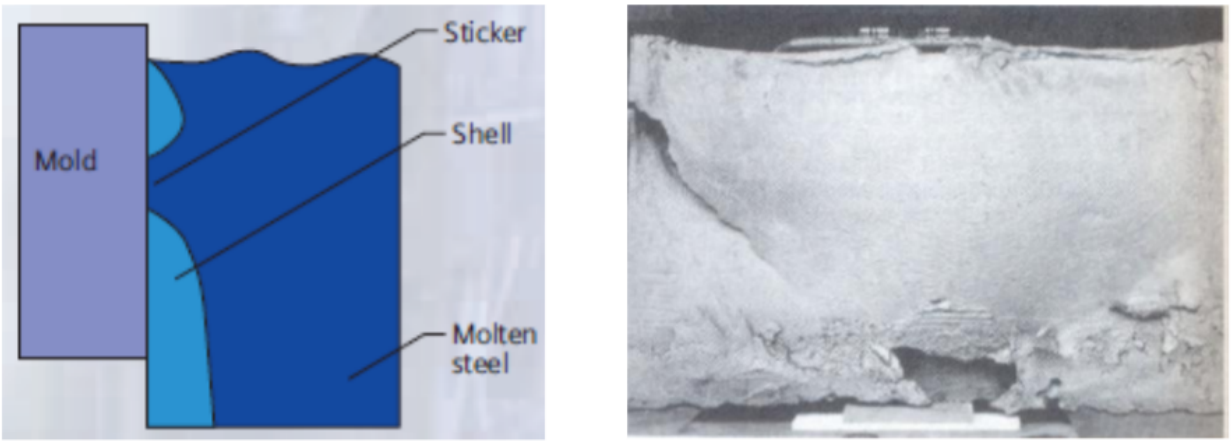


Figure 2.28: Example of a sticker breakout [40]

this significant slowdown will be enough for the stuck upper portion of the shell to re-attach and solidify against the lower portion of the shell that is separated from. Sticker slowdown speed is not to be confused with creep speed which is often is the realm of 0.01 m/min. Creep speed is used when the caster must be stopped, however, complete stoppage of the machine with the strand still inside is not an option. If the caster were to come to a complete stop, the support rolls would stop rotating and the portion of the roll surface in contact with the strand would heat up and expand, severely damaging the rolls and warping them into a banana shape. Upon subsequent re-start of the caster, these warped rolls would damage not only the machine, but also the strand.

2.4.8.2 Longitudinal Bleeder Breakouts

About 80% of breakouts are categorized as sticker-type breakouts and have been discussed in the literature [9–12], with the remaining 20% being attributed to cracks and scum entrapment [9, 12]. A less common type of breakout is an after-effect of a longitudinal crack, a bleeder type breakout. Examples of bleeder type breakouts are shown in Figure 2.30 and Figure 2.31. Bleeder type breakouts are the result of longitudinal crack (often at the base of a longitudinal depression), leading to small intermittent bleeds that heal, a full bleed inside the mold, and finally a breakout as the bleeder exits the mold and completely ruptures

the solid shell.

2.4.8.3 Breakout Detection

Breakout detection generally functions by looking for cases of inverted thermocouples, meaning that below the sticker, temperatures appear to be increasing instead of decreasing as expected, this is shown in Figure 2.29. Current breakout detection systems are designed and tested at predicting sticker breakouts, a transverse phenomenon, but are not good at spotting breakouts caused by an extreme longitudinal depression. As such, more intelligent methods are needed to reliably predict, prevent, and detect longitudinal-based breakouts.

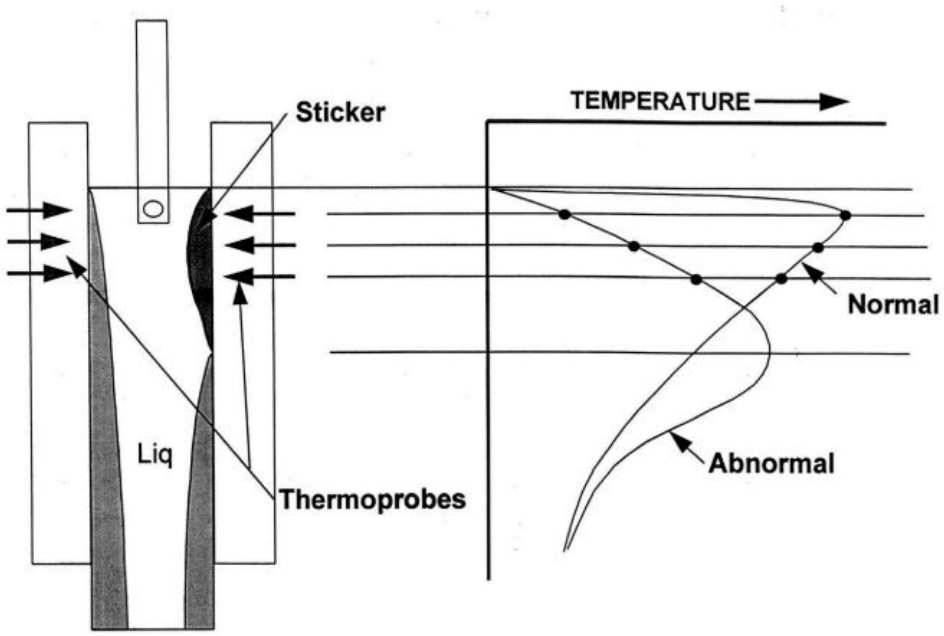


Figure 2.29: Sticker breakout detection method [57, 58]

2.4.8.4 Healing a Bleeder Breakout

Prior to a bleeder type breakout, there is a possibility of the bleed healing (fresh steel emerging from, solidifying, and sealing the hole/crack) within the mold. When this occurs, the surface appearance looks similar to Figure 2.30 or Figure 2.32(a), where molten steel leaked out and filled in low spots on the shell surface (oscillation marks) or created a small

local lump as it solidified.

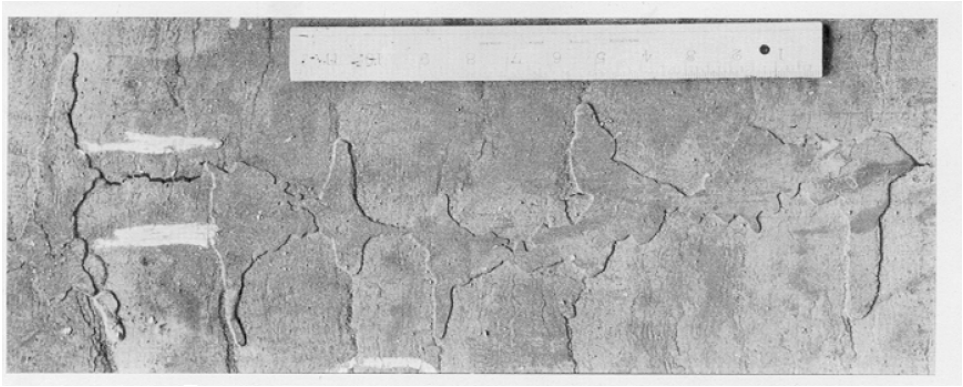


Figure 2.30: Example of bleed contained within the mold [40] (casting direction to the right)

In severe cases, where the bleed is not able to heal, it can lead to a complete breakout of the shell. An example of this type of breakout is shown in Figure 2.31, which is a slab breakout shell from a heat cast in 2015 (Figure 2.32(a) and Figure 2.32(b) are all from the same breakout investigation). The slabs prior to the breakout had some shape problems on the broadface lengths, and the subsequent investigation revealed that overtapering of the mold led to an off-corner depression (buckling gutter), severe shell thinning, intermittent bleeds, and finally a full breakout.

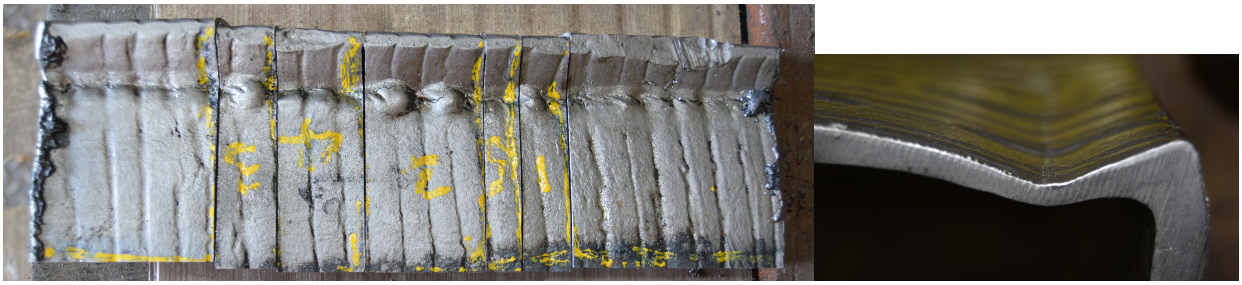
Note that in Figure 2.32(a) the gutter was deep enough that the bleed did not get smoothed down by contacting the mold as in Figure 2.30, or rolled out by the support rolls below. Additionally, this means that the oscillation marks are still quite deep. Also note that in Figure 2.32(b), the deepest part of the gutter depression directly corresponds with the thinnest portion of the shell as a result of the reduced heat transfer. The thinned portion is also the location where the shell reached its critical breakout thickness first.

2.4.9 Summary

As described above, defects in the continuous casting process, particularly longitudinal defects, are significant in that many common data collection methods are not able to capture their behavior in a way that allows mitigation if they should be leading to a bleeder type



Figure 2.31: Longitudinal bleeder related breakout shell after removal from machine (casting direction down)



(a) (b)

Figure 2.32: Off-corner longitudinal depression breakout Appearance: (a) Intermittent bleeds at the base of an off-corner depression, (b) Resultant Slab breakout shell after removal from machine

breakout. Furthermore, quite little is still known about the specific formation mechanisms of longitudinal defects. This work explores, in detail, the mechanisms and generation of longitudinal depressions and cracks, and introduces methods for identification, better understanding, and prediction.

CHAPTER 3

MODEL FORMULATION

3.1 Overview

This work utilizes a combination of computational models to simulate and analyze a variety of longitudinal defects. Multiple iterations of the same general thermal-mechanical finite element model are used to study the temperature and shape development of specific thermal-mechanical conditions within the caster. Appropriate thermal boundary conditions for these models are derived and implemented from a series of other numerical models to provide realistic conditions informed by plant measurements. For the low carbon steel primarily studied in this work, a non-linear material model including temperature-, phase-, and carbon content-dependent elastic–viscoplastic constitutive effects was used. Developed in this work is also a multi-point constraint (MPC) model that allows for dynamic boundary condition modification during coupled thermal-mechancal models and the opening of cracks along the boundary of the model. This works also includes a new implementation of a previously developed Reduced Order Model (ROM) mold to allow for calculation for mold temperatures within the finite element model.

3.2 Model Domain

The primary model domain for this work consists of a 2D transverse slice, in the X-Y plane, on the wide face of the steel strand away from the corner region, as shown in Figure 3.1. The slice is initially at uniform temperature, chosen to be the temperature of the steel at the level of the meniscus. This is usually the steel liquidus temperature plus some approximate value for superheat taken from CFD models, plant data, or the literature. For the plain low carbon steel used in this work the initial domain temperature is 1532°C unless otherwise stated. One surface of the domain is in thermal and mechanical contact with the mold. The thermal boundary condition between the steel domain and the mold

domain is a coupled gap conduction model, which allows for air gap formation behavior as well as disrupted (non-uniform) heat transfer across the surface.

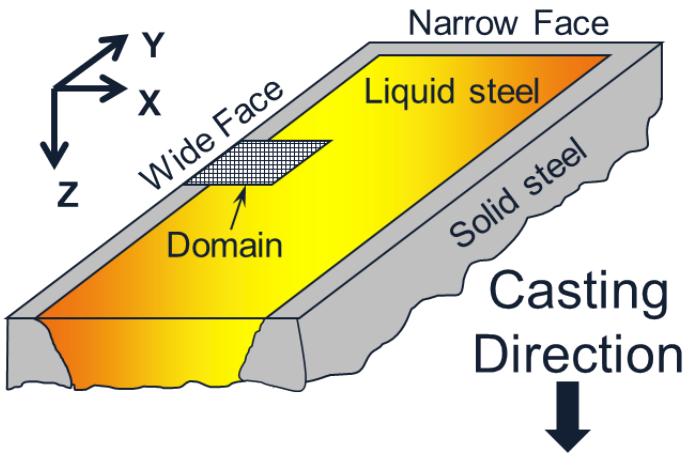


Figure 3.1: Model domain within caster geometry

3.3 Governing Equations

3.3.1 Heat Transfer Model

Assuming fourier law heat conduction, and no internal heat generation or deformation heating (viscious dissipation) effects, the energy equation simplifies to the form of eq. (3.1).

$$\rho\left(\frac{\partial H}{\partial t}\right) = \nabla \cdot (k\nabla T) \tag{3.1}$$

where, H is the specific enthalpy, ρ is density, k is thermal conductivity, T is temperature, t is time. Expansion of the material derivative D term yields independent time temperature and velocity terms:

$$\frac{DT}{Dt} = \frac{\partial T}{\partial t} + V_x\frac{\partial T}{\partial x} + V_y\frac{\partial T}{\partial y} + V_z\frac{\partial T}{\partial z} \tag{3.2}$$

where, V_x, V_y, V_z are velocity components in the: x direction perpendicular to the mold surface, y horizontal direction tangential to the mold surface, and z the casting directions.

$$\rho\left(\frac{\partial H(T)}{\partial T}\right)\left(\frac{\partial T}{\partial t}\right)=\frac{\partial}{\partial x}\left(k(T)\frac{\partial T}{\partial x}\right)+\frac{\partial}{\partial y}\left(k(T)\frac{\partial T}{\partial y}\right)=\nabla\cdot(k(T)\nabla T) \tag{3.3}$$

$$\rho\frac{\partial H}{\partial t}=\nabla\cdot(k(T)\nabla T) \tag{3.4}$$

The continuous casting process is assumed to be operating at steady state with no speed changes, thus the transient term $\frac{\partial T}{\partial t}$ is equal to zero and drops out.

The $2-D$ transient heat conduction given by eq. (3.1) is solved for the temperature distribution which is then fed into the mechanical analysis.

3.3.2 The Péclet number

The Péclet number (Pe) given by eq. (3.5) is a class of dimensionless numbers [59] relevant in the study of transport phenomena in a continuum. Named after the French physicist Jean Claude Eugène Péclet, it is a representative ratio of the rate of advection to the rate of diffusion. For this model, advection is caused by strand movement at the casting speed, and diffusion is due to the thermal diffusivity of the steel given by eq. (3.6).

$$Pe=\frac{Lu}{\alpha} \tag{3.5}$$

where α is thermal diffusivity, L is a characteristic length, u is characteristic velocity,

$$\alpha=\frac{k}{\rho c_p} \tag{3.6}$$

thus,

$$Pe=\frac{Lu}{\frac{k}{\rho c_p}} \tag{3.7}$$

Substituting eq. (3.7) with casting parameters, it becomes:

$$Pe = \frac{LV_C}{\frac{k}{\rho c_p}} \tag{3.8}$$

Where L is the distance below the meniscus taken below as mold exit, V_c is the casting speed, k is the thermal conductivity, ρ is the mass density, and C_p is the specific heat capacity.

$$\begin{aligned} V_C &= 3\text{m/min} & L &= 1\text{m} \\ k &= 33\text{W K/m} & \rho &= 7500\text{kg/m}^3 \\ C_p &= 661\text{J K/kg} & H_f &= 272\text{kJ/kg} \\ \Delta T &= 500^\circ\text{C} \end{aligned}$$

The assumption of advection domination can be seen, even for very short times. Even for casting speeds as low as 1 m/min, by 0.25 seconds advection is already 3 orders of magnitude greater than conduction by mold exit. This time below meniscus directly translates to the distance below meniscus as a result of the constant casting speed.

$$Pe = \frac{LV_c}{\left(\frac{k}{\rho c_p}\right)} = \frac{1(\text{m}) \times 3(\text{m/min})}{\frac{33(\text{w/m}\times\text{K})}{7500(\text{kg/m}^3)\times 661(\text{J/kg}\times\text{K})}} = 7.5 \times 10^3 \tag{3.9}$$

With negligible heat conduction in the casting direction, a Lagrangian domain may be used to analyze the heat transfer in the solidifying shell. This approximation essentially transforms the physical z - direction into a temporal quantity, which is valid while the process remains at steady state.

3.3.3 Stress Model

During initial solidification the thermal-mechanical strains are on the order of only a few percent. Thus, the small strain assumption was adopted for this work. This assumption is supported by previous solidification model results [60]. The out-of-plane (z-direction) stress is characterized by a state of generalized plane strain, where slices are constrained to remain planar by continuity.

The general governing equation for the static problem is given by the force equilibrium balance in eq. (3.10),

$$\nabla \cdot \underline{\underline{\sigma}} + b = 0 \tag{3.10}$$

where $\underline{\underline{\sigma}}$ is the second order Cauchy stress tensor, and b is an applied traction.

The rate form decomposition of the total strain is divided into elastic, inelastic, and thermal components,

$$\dot{\varepsilon} = \dot{\varepsilon}_{el} + \dot{\varepsilon}_{ie} + \dot{\varepsilon}_{th} \tag{3.11}$$

where inelastic strain includes the combined effects of plastic strain and creep. The stress and elastic strain rates then are related by the isotropic elasticity constants based on the temperature-dependent elastic modulus and Poisson ratio. The thermal strain term depends on the isotropic temperature-dependent thermal expansion α coefficient tensor, found from the temperature-dependent density and the evolving temperature distribution from the transient thermal model. Even though there is no explicit yield condition, inelastic effects are assumed to follow J2 plasticity with isotropic hardening, and the inelastic strain rate is found assuming the Prandtl-Reuss equations. Further details of the stress model, including details of the solution methods are included in Appendix A.

3.4 Heat Transfer Boundary Conditions

Figure 3.2 shows the model domain with thermal boundary conditions applied. The rectangular model domain is in thermal contact with the surface of the mold, through a gap conduction model implemented in the GAPCON subroutine in Abaqus, while all 3 other sides of the domain are thermally unconstrained and considered to be insulated. As shown in the figure, the subroutine is only applied on the lower surface of the domain. The subroutine allows for definition of spatial and temporal heat transfer profiles across the width and down the length (time) of the mold. This is accomplished by defining variations in the total slag

layer thickness in time and space; full details of which are included in section 3.5. The gap conduction model is applied for this particular work to create a thermal disruption on the left side of the domain by including what can be considered an effective air gap, or a reduction in the heat transfer abilities of the slag layer. Shown in Figure 3.2, the flux layer thickness is uniform across a majority of the domain, at the depression centerline the flux adopts a larger thickness representing the thermal disruption. Between the two areas, the thickness varies linearly.

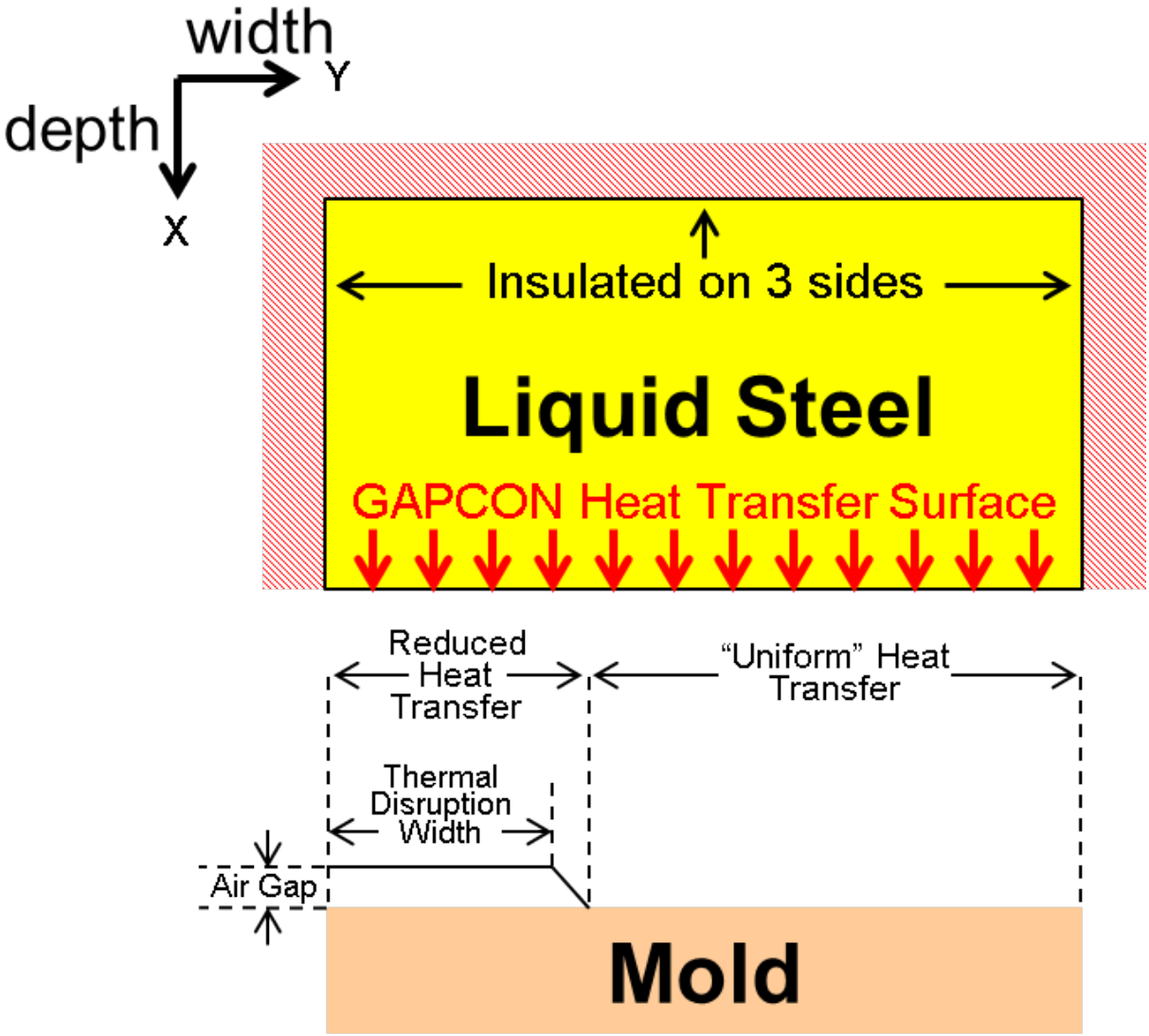


Figure 3.2: Heat Transfer Boundary Conditions

3.5 Interfacial Gap Thermal Resistor Model

3.5.1 Overview

A explained in section 1.4, in continuous casting, as the liquid steel solidifies against the four walls of the water-cooled copper mold, the solidifying shell ideally does not come into direct contact with the mold copper and instead most of the heat transfer is controlled by the interfacial gap between the two materials. In this work a coupled model of formation is desired and therefore it becomes necessary to define the heat transfer across the interracial gap in terms of thickness, conductivity, and displacement.

3.5.2 The Mold/Flux Interface

This interfacial resistance is largely a property of the particular mold powder as the surface roughness is related to its crystallization behavior as well as its transition temperatures [61]. The mold/slag interfacial resistance increases with crystallinity of the flux due to increased density of solid phase in the form of surface roughness on mold side (equivalent to air gap) and also increases with thickness of the slag layer [30]. Prior works have treated this interface as temperature or thickness dependent, reducing the resistance with distance from the meniscus [33] or with increasing thickness [30]. However, for this work, a fixed value of $h_{Mold} = 2500\ \mathrm{W\,K/m^2}$ was used for this Mold/Slag interfacial heat transfer coefficient which is in line with reported values [30]. The value of mold flux interface thermal resistance is given by eq. (3.12). Because the resistance value for this interface is fixed, calculation of the interface temperature, T_{mc}, is trivial according to eq. (3.13).

$$R_{Mold} = \frac{1}{h_{Mold}} \tag{3.12}$$

$$T_{mc} = T_{mold} + (T_{shell} - T_{mold})\frac{R_{contact}}{R_{total}} \tag{3.13}$$

3.5.3 The Flux/Shell Interface

Similar to the Mold/Slag interface, the slag strand interface resistance increases greatly as the temperature drops below the slag crystallization temperature. Non-uniformities in the flatness of the shell surface shown in Figure 3.3 are incorporated into the model through this interface resistance. Experimental data discussed in the literature, [35, 36] included in Figure 3.4, shows the variation in heat transfer with temperature. As this represents a large resistor relative to the total, and being highly temperature dependent on the interface temperature a fixed value was not used for this interface.

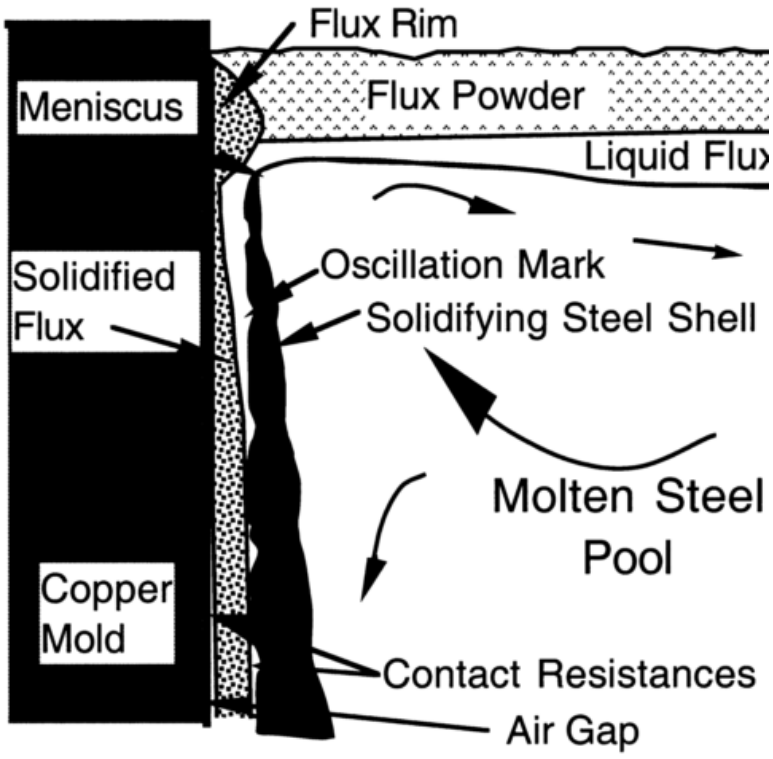


Figure 3.3: Contact interface roughness [34]

The interface resistance between the liquid slag and the solid steel shell is temperature dependent. The data points for the resistance were taken from the literature [35] and a curve

fit was applied as shown in Figure 3.4. Hysteresis was not accounted for in calculation for this interface.

Flux-Strand Interface Temperature		
°C		W/m²·K
Temperature		$h_{Interface}$
Crystal	1030	1000
Softening	1150	2000
Solidus	1511	10000
Liquidus	1529	20000

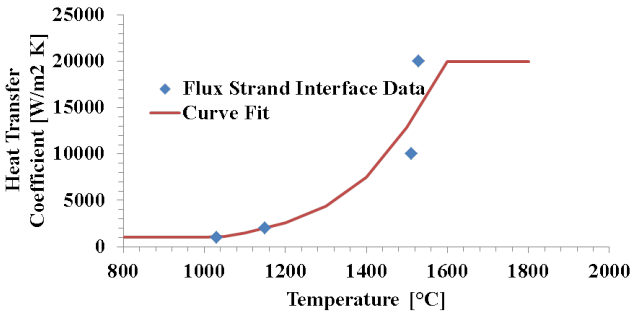


Figure 3.4: Temperature dependent slag/strand interface heat transfer/resistance [35]

The flux/shell interface temperature, T_{ls}, is calculated using eq. (3.14). Deriving a smooth function for this temperature dependent behavior proved somewhat difficult but an exponential function, eq. (3.15), was chosen. The corresponding resistance value for the interface is calculated by eq. (3.16).

Due to the non-physical implications of the exponential function on the upper and lower end, the interfacial coefficient was bounded. If $h_{Shell} < 1,000$ W K/m^2 , $h_{Shell} = 1,000$W K/m^2. This lower bound represents some theoretical oscillation mark/surface roughness opposition to heat transfer when the temperature is low enough. If $h_{Shell} > 20,000$ W K/m^2 , $h_{Shell} = 20,000$W K/m^2. This upper bound representing some degree of "perfect" contact and preventing numerical issues as it were to approach infinity.

$$T_{ls} = T_{mc} + (T_{shell} - T_{mold})\frac{R_{sol} + R_{liq} + R_{rad}}{R_{total}} \tag{3.14}$$

$$h_{shell} = 3.8981e^{0.0054T_{ls}} \tag{3.15}$$

$$R_{shell} = \frac{1}{h_{shell}} \tag{3.16}$$

3.5.4 Solid Slag Layer

The molten slag flowing into the gap travels downwards with the strand during casting and gradually solidifies against the copper mold. A solidification temperature T_{Sol} is chosen for this model, a value of 650°C is used initially with variations explored in a parametric study. Reported values of critical flux temperatures vary widely across the literature and even between similar fluxes. They are still the subject of much research, and the chosen value falls within a range of values found in the literature from experimental data sets [27, 33, 35]. Flux powder contains air which gives the mixture a low conductivity, ~0.3 W K/m [62]. As the powder heats, sinters, coalesces, and melts, the air disappears so its thermal conductivity gradually increases as shown in Figure 3.5 [27].

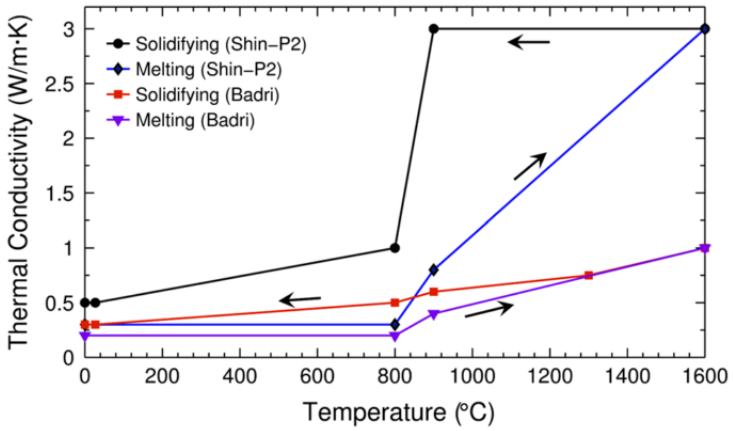


Figure 3.5: Temperature dependent conductivity [27]

The solid flux layer thickness D_{Sol} is calculated according to eq. (3.17) as a fraction of the total gap thickness with a linear relationship between the chosen flux solidification temperature T_{Sol} and the interface temperatures T_{LS} and T_{MC} given by eq. (3.14) and eq. (3.13) respectively.

$$D_{sol} = (T_{crystal} - T_{mc})\frac{D_{gap}}{T_{ls} - T_{mc}} \tag{3.17}$$

This model uses a fixed conductivity value of $k_{Sol} = 0.5$ W K/m for the solid slag layer, this conductivity value is specifically lower than that of liquid slag and similar to values

reported in the literature for solid slag which show decreasing conductivity with decreasing temperature [27]. Solid flux layer resistance R_{Sol} is calculated according to eq. (3.18) using the fixed value chosen for k_{Sol}.

$$R_{sol} = \frac{D_{sol}}{k_{sol}} \tag{3.18}$$

3.5.5 Liquid Slag Layer

The properties of liquid slag are complicated, which makes conclusive data difficult to find. Reported values of liquid conductivity in the literature vary from 0.5 to 3 W K/m [18,20,21] in addition, slag conductivity exhibits the hysteresis effect. Within the slag, the liquid layer is assumed to be solidifying with distance from the meniscus as the shell temperature drops. Thus for the purposes of this work, the hysteris effect is ignored, a fixed value is used, and it is assumed that once the liquid layer disappears, re-melting does not occur.

Within the liquid slag layer both conduction and radiation play a role. The radiation effect has been shown to contribute up to 30% of the total heat flux across the liquid layer, but removal of this effect only reduced the total heat flux in the mold by ∼10% [33]. Some previous work has utilized a partially linearized form of the 4^{th} order radiation equation [36], however, in this work radiation was accounted for by an appropriate increase in liquid slag conductivity. The thickness of the liquid layer, D_{Liq}, is calculated based on the defined flux gap size, D_{Gap}, and the solid layer thickness, D_{Sol}, according to eq. (3.19).

$$D_{liq} = D_{gap} - D_{sol} \tag{3.19}$$

A constant thermal conductivity value for $k_{Liq} = 3$ W K/m is used based on previous work appearing in the literature [27]. Thermal resistance of the liquid layer R_{Liq} is calculated using this fixed value according to eq. (3.20).

$$R_{liq} = \frac{D_{liq}}{k_{liq}} \tag{3.20}$$

This work assumes that a decrease in conductivity is balanced by the increase in radiation at higher temperatures [27], which agrees with the other models [63] and the measurement of constant conductivity in molten slag systems [62]. It has further been noted that heat transfer within an amorphous glassy material is lower than that of a crystalline material. A minimum threshold value for liquid layer thickness is chosen to ease numerical difficulties and prevent wildly large values for heat transfer coefficient. This thickness, $D_{LiquidThresh}$, is chosen to be 0.01 mm for this work which represents a maximum h value to be $20,000$ $\mathrm{W\,K/m^2}$, values used in the literature have been in this range [36].

3.5.6 The Air Gap

As discussed previously, if conditions within the mold allow for it, an air gap can form. The size of the air gap is an output of the stress model in the form of displacement of the shell surface nodes from the mold. To help the numerical solution, a minimum threshold value $D_{AirThresh} = 0.001$ mm is adopted to prevent non-physical behavior associated with very small gaps (displacements).

Additionally, if there is a liquid layer of slag present in the gap above the chosen T_{Sol} temperature, the air gap is given to be filled with liquid slag. This condition is based on the assumption that liquid slag from above the gap location would flow downwards to fill in this gap.

The thermal conductivity of the air gap is dependent on composition of the gas [37]. Prior work has values assumed for air [35] as well as a 20% hydrogen mixture [37] using the binary conductivity mixture rules [38]. For this work a fixed value for conductivity $k_{Air} = 0.06$ $\mathrm{W\,K/m}$ is used for the air gap [61]. This value is consistent with low temperature values for a high hydrogen environment found in the literature [37]. A temperature dependent conductivity value is left for future work. The thermal resistance of the air gap is given by eq. (3.21).

$$R_{Air} = \frac{D_{Air}}{0.06} \tag{3.21}$$

3.5.7 Total Gap Heat Transfer

The heat transfer model is dependent on the 5 resistant components in the gap described above: the mold/slag interface, the air gap, the solid slag layer, the liquid slag layer, and the slag/steel interface. Combining eqs. (3.12), (3.16), (3.18), (3.20) and (3.21) into eq. (3.22) yields eq. (3.23) and an effective thermal resistor model represented by Figure 3.6 and Figure 3.7.

Heat conduction depends on the thermal resistances and time-averaged thickness profiles down the mold of the different layers of materials contained in the gap. For the purposes of this model, we are concerned primarily with the general deformation behavior of the solidifying shell, as such a number of simplifications will be made:

In addition to those discussed above, some simplifying assumptions were made for this model:

- The potential buildup of scale, and/or resulting blockage, within the water channels was neglected, thus we will assume that the mold is operating at steady state with constant temperature T_{Mold} =150°C
- The distribution of liquid and solid slag will be assumed linear between the interface temperatures
- As mold slags are mixtures they do not have a singular transition temperature. While there is some debate on the minimum percentage of liquid slag that would fill in an air gap, for the purposes of this work, 60% liquid slag will be assumed to fill in an air gap.
- The latent heat evolved by liquid-slag solidification is less than 3% of the heat transferred across the gap, so it is neglected in this model. [64]
- Oscillation marks and prescribed surface shape non-uniformity are neglected
- Interface resistances are not dependent on flux layer thickness

$$R_{total} = R_{Mold} + R_{Air} + R_{Sol} + R_{Liq} + R_{Shell} \tag{3.22}$$

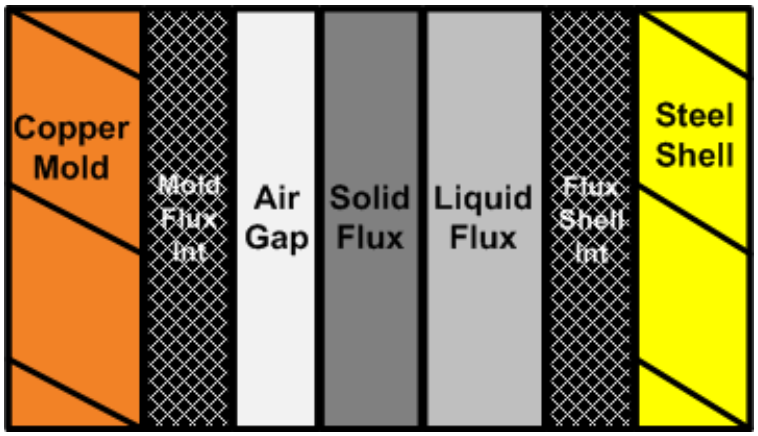


Figure 3.6: Interfacial gap material schematic

$$R_{total} = \frac{1}{h_{Mold}} + \frac{D_{Liq}}{k_{Liq}} + \frac{D_{sol}}{k_{Sol}} + \frac{D_{Air}}{k_{Air}} + \frac{1}{h_{Shell}} \tag{3.23}$$

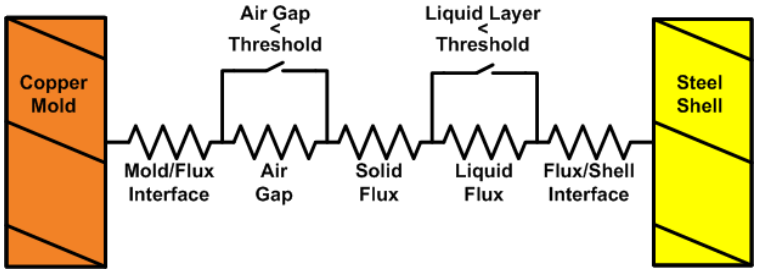


Figure 3.7: Interfacial gap resistor schematic

3.5.8 Implementation

The model was first implemented in Microsoft Excel for troubleshooting and proof of concept and subsequently implemented into the Fortran subroutine GAPCON for use in Abaqus to couple the steel shell and mold thermal behavior. The flowchart for operation can be found in Figure 3.8. The primary inputs of interest to the subroutine from Abaqus are the temperatures of the slave and master surfaces. For inclusion of the coupled model results and potential air gap formation, the distance of the surfaces from each other is also needed. The surface displacement is first converted to meters from the millimeter units of

the model. If this value is larger than the threshold size for air gap formation, the resistance is calculated according to eq. (3.15), if it is less than the threshold, the resistance is set to 0.

The fixed value for the mold/flux interface resistance is calculated according to eq. (3.12).

On the first call to the program, initial values for the interfacial temperatures are set to approximate values. In addition, we programmatically assume that the gap is half liquid and half solid so that a starting total resistance can be approximated. As iterations will be performed, these values need only to be reasonable for the initial conditions.

The model then checks if the solidification flag has been thrown indicating that in a previous increment, the entire slag layer solidified. If the entire slag layer has become solid, it is assumed that it will remain solid, a simplified calculation is performed, and iterations are skipped.

If the solidification flag has not been thrown, the program enters the iteration loop. The loop begins with calculation of the shell interface resistance according to the previously calculated interface temperature. As discussed, this value is bounded, and if it is found to be outside of the bounds, it is set equal to the appropriate value.

Based on the newly calculated interface resistance, a new total resistance is calculated and used to calculate new interface temperatures. The flux layer calculation is then performed using these new interface temperatures to find the size of the solid slag layer. If the liquid slag layer is found to be smaller than the threshold size set by the user, the entire gap is assumed to be solid, otherwise the remaining gap space is assumed to be liquid. The loop counter is incremented by one, and the loop repeats. When all iterations have been performed, the loop exits. If the temperature of the shell is below 1400°C (chosen to reduce the likelihood of an accidental flag trip too early in the simulation) AND the entire slag layer is solid, the solidification flag is tripped.

Finally, the gap resistance is totaled, converted to heat transfer coefficient, and output to Abaqus.

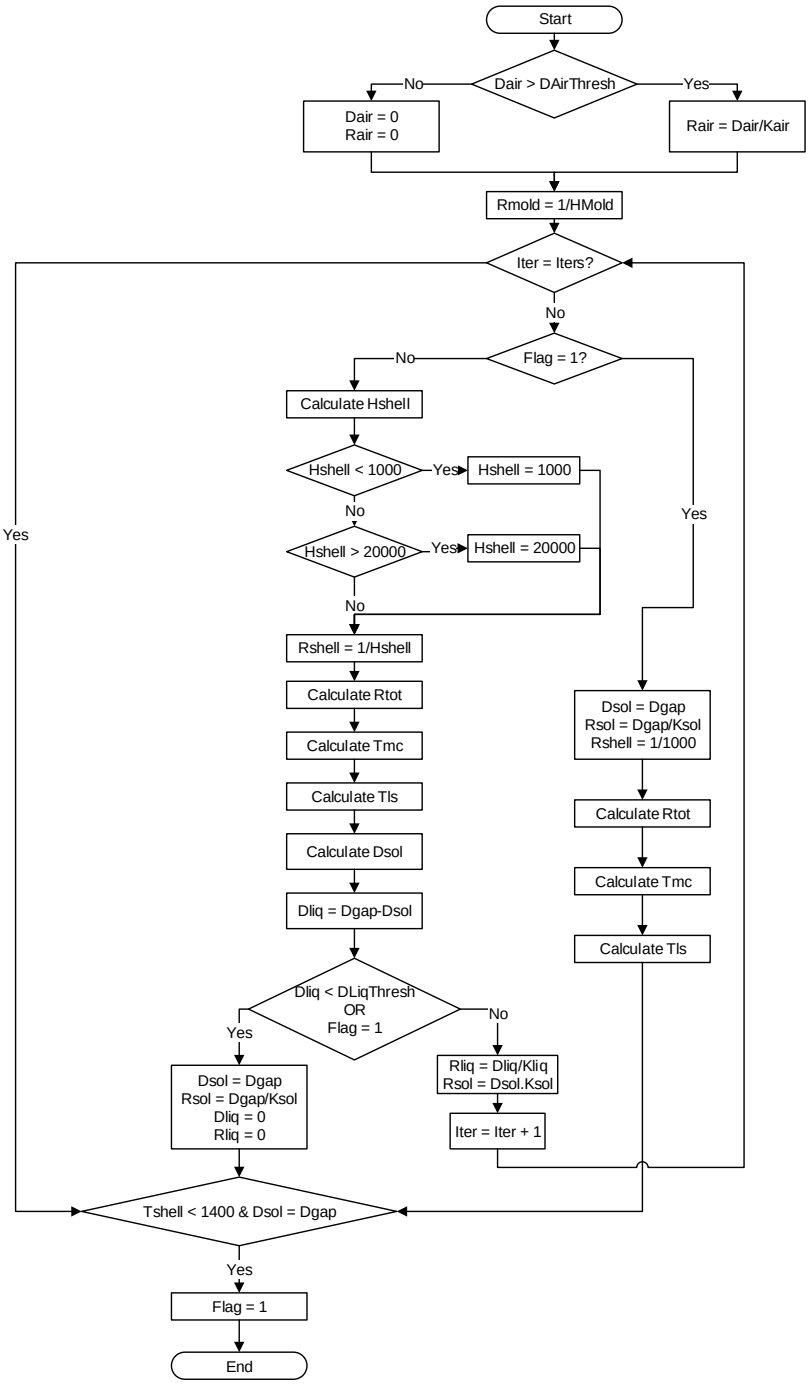


Figure 3.8: Calculation flowchart for resistor model

3.6 Reduced Order Mold Model

To allow easier prediction of accurate mold temperatures, a reduced order mold model was implemented based on previously published and validated work [65]. The ROM mold works by calibrating the thickness of a simplified effective copper mold that allows for the temperature to match plant measurements at a predefined calibrated thermocouple depth. This simplistic method was shown to match well with plant data in multiple cases when calibrated correctly. Use of the ROM mold is necessary to avoid using a complete 3D strand section and mold. Recent work has shown that type of 3D model to be numerically taxing even with highly simplified material properties and a very coarse mesh, taking nearly 1 month of wall clock time to simulate a short section [16].

In this work, the ROM mold was implemented using a single row of finite elements given basic properties of the mold material with a fixed thermal conductivity of 312 W K/m.

On the back side of the mold a variable convection condition is applied using the Abaqus subroutine FILM to include the heat removal from the mold by the circulating cooling water channels. Full details can be found in the literature [66] and section D.1. Validation of proper model setup was performed in this work by matching the example problems geometry, boundary conditions, and results, given in the original work. Calibration of the model in this work was carried out based on the method provided in the literature and the detailed data provided by Tata Steel regarding their mold geometry. A 3D symmetric section of the mold was generated and used for the calibration. The domain is shown in Figure 3.9 with the final contour results for heat flux and temperature located at the calibration location for the upper thermocouples within the copper mold. Detailed parameters used in the calibration can be found in Table 3.1. In the more general cases where the ROM mold is not being used, instead a fixed simplified rectangular mold geometry is used with the temperature of the mold copper fixed to be 150°C.

Table 3.1: Tata Steel ROM mold

Parameter	**Value**	**Unit**
Thermal Conductivity	33	[W K/m]
Total Mold Width	2210	[mm]
Approx Cast Width	1310	[mm]
Percent Of Mold Width Used	59.3	[%]
Small Channel Width	5	[mm]
Small Channel Radius	2.5	[mm]
Small Channel Length	15.5	[mm]
Large Channel Width	5	[mm]
Large Channel Radius	2.5	[mm]
Large Channel Length	18.5	[mm]
Water Channel Length	850	[mm]
Number Of Small Channels	63	[-]
Number Of Large Channels	42	[-]
Small Channel Area Round	87.3125	[mm^2]
Large Channel Area Round	102.3125	[mm^2]
Total Small Channel Area	5500.6875	[mm^2]
Total Large Channel Area	4297.125	[mm^2]
Total Cross Section Area	9797.8125	[mm^2]
Avg Cross Sectional Area	93.3125	[mm^2]
Small Channel Perimeter	38.85	[mm]
Large Channel Perimeter	44.85	[mm]
Total Small Channel Perimeter	2447.55	[mm]
Total Large Channel Perimeter	1883.7	[mm]
Total Cross Section Perimeter	4331.25	[mm]
Avg Perimeter	41.25	[mm]
Physical Hydraulic D	9.048	[mm]

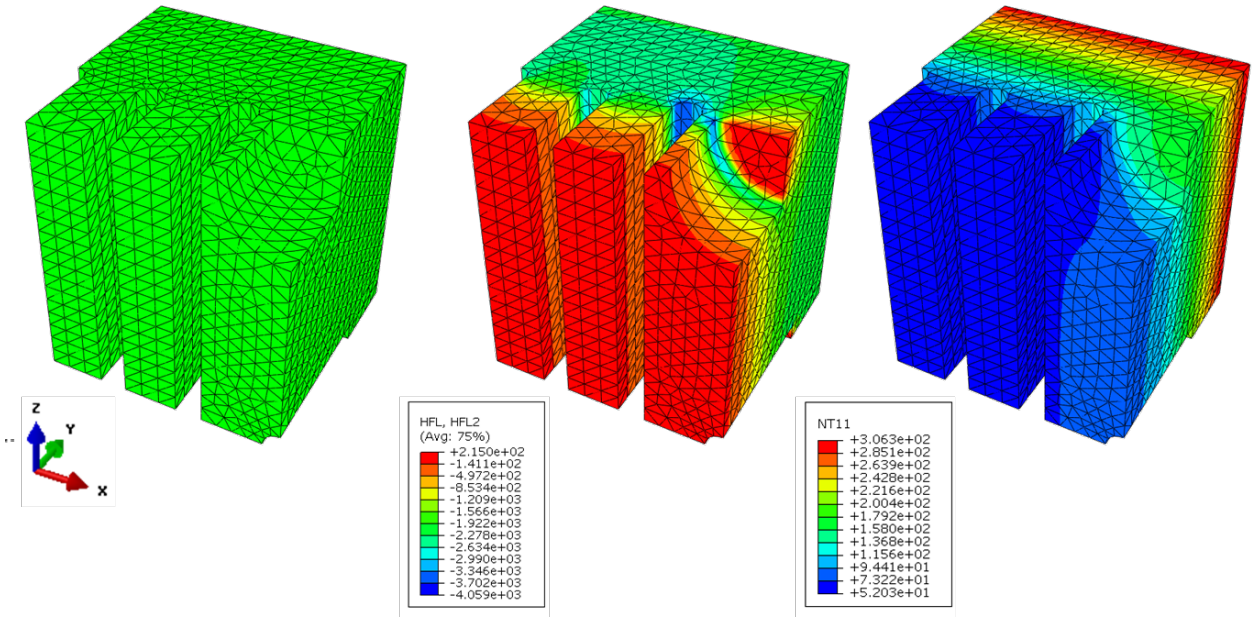


Figure 3.9: Model domain for TATA Steel ROM mold calibration with heat flux and temperature contour results for matching upper thermocouple

3.7 Stress Boundary Conditions

Figure 3.10 shows the model domain with mechanical boundary conditions applied. The left and right boundaries of the domain are symmetry planes and must remain planar. The left side is fixed in the Y direction and only allowed to displace towards or away from the mold in the X direction, the left side is required to move as a straight line, the top surface is unconstrained and remains stress free.

Ferrostatic pressure in the liquid steel pool, that pushes the continuously solidifying shell towards the contact surfaces of the mold, is implemented into the solidifying steel shell model via the Abaqus DLOAD subroutine as a distributed load which increases linearly with vertical distance (time) down the mold. Ferrostatic pressure is applied on the bottom surface of the domain as shown in Figure 3.10, increasing with time and starting from zero at the meniscus. The value increases linearly proportional to time according to: $P_{Ferro} = \rho g V_c t$, where ρ is the density, g is the gravitational constant, V_c is the casting speed, and t is the time below meniscus. This method of handling ferrostatic pressure pulling on the surface as

opposed to pushing from the liquid has been confirmed previously by the author [15].

Mechanical interaction between the shell and the mold contact surfaces is accounted for using coulomb friction with a factor of $\mu = 0.15$ based on measurements for solid slag on copper [33]. Sliding contact that permits gap formation without permitting penetration is enforced using the hard contact algorithm in Abaqus with the mold hotface as the "master" surface and the shell exterior as the "slave" surface. All nodes of the mold are held fixed in both X and Y directions, and the surface is considered the non-deformable rigid master while the steel surface is the deformable slave surface.

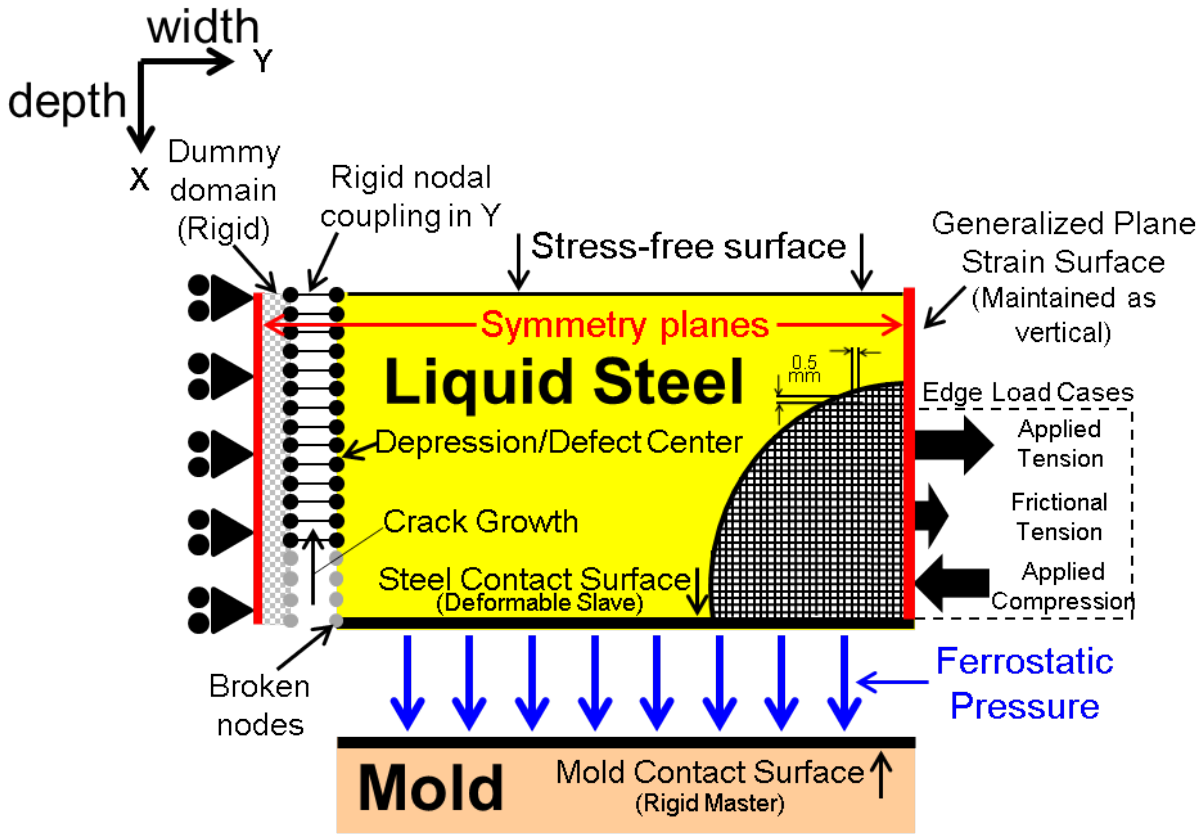


Figure 3.10: Stress model boundary conditions

3.7.1 Previous Cracking Models

Creating a crack within the model domain represents a discontinuity within the traditional finite element method but it has been around for quite some time in various forms [67]. A variety of methods have been utilized by others, particularly with respect to composites and laminates where their interest is primarily in delamination behavior. These groups often take advantage of methods already accepted within the FEM framework, such as Virtual Crack Closure Technique (VCCT) and Cohesive Zone (CZ) approaches, both of which have reached sufficient maturity to be available in several commercial simulation software packages (including Abaqus) [68]. Other more home-grown implementations have taken on a few forms, one example is using a user element to generate a spring element with a variable very high stiffness to enforce the boundary condition [69]. The primary issue with many of these methods is that they require knowledge of the fracture behavior, such as energy release rate for VCCT, CTOA, CTOD, or at least some data regarding loading and growth history. At the temperatures of interest in the solidification range, data like this is all but non-existent and extremely difficult to get experimentally.

Modeling stationary discontinuities, such as a crack, with the conventional finite element method requires that the mesh conforms to the geometric discontinuities. Creating a conforming mesh can be quite difficult. Modeling a growing crack is even more cumbersome because the mesh must be updated continuously to match the geometry of the discontinuity as the crack progresses. This is one of the reasons for the development of the eXtended Finite Element Method (XFEM).

Modeling discontinuities, such as cracks, as an enriched feature is commonly referred to as the extended finite element method (XFEM). The extended finite element method was first introduced by [70], and is an extension of the conventional finite element method [71]. The method allows the presence of discontinuities in an element by enriching degrees of freedom with special displacement functions, and does not require the mesh to match the geometry of the discontinuities. It is a very attractive and effective way to simulate initiation

and propagation of a discrete crack along an arbitrary, solution-dependent path without the requirement of remeshing. It further allows for surface based cohesive behavior, contour integral evaluations for an arbitrary stationary surface crack without the need to define the conforming mesh around the crack tip, allows contact interaction of cracked element surfaces, allows the application of distributed pressure loads to the cracked element surfaces, allows the output of some surface variables on the cracked element surfaces, and allows both material and geometrical nonlinearity [66].

While this certainly seems like a very attractive tool, the method is available only for first-order solid continuum elements, and second-order stress/displacement tetrahedron elements, and furthermore, the XFEM implementation within Abaqus does not currently support the fully coupled temperature-displacement analysis that is required to model the defects in this work.

3.7.1.1 Current Cracking Model and Implementation

The crack model methodology used in this work is based on time-dependent release of connections between pairs of nodes. This imposes the crack to follow a predefined and prescribed path along the symmetry plane according to a chosen criterion. To accomplish the release of nodes, a multi-point constraint (MPC) Abaqus subroutine was created based on a method called nodal release [72]. In this work, while we are concerned with the behavior of the crack, we are more interested in how the crack affects the evolving shape and stresses associated with of the longitudinal depression defect, thus the details of the crack initiation and conditions for propagation are not modeled explicitly based on coupling with the evolving thermal and mechanical models. Instead, the crack history is assumed apriori, such as shown in Figure 3.11.

The MPC subroutine was coded in *nodal* mode, which allows for programmatic changes to behavior at each node involved in the constraint. Figure 3.11 shows a schematic representation of the MPC subroutine active in the model. A dummy domain part is generated in the model the same length (in the X direction) as the liquid steel domain and meshed

with the same resolution. Instead of applying the symmetry boundary condition directly to the steel domain, the boundary condition is applied on the dummy domain (*i.e.* all nodes in the dummy domain are constrained in X and Y). This constraint essentially renders the material model of the dummy domain irrelevant as none of the nodes will displace in the Y direction and the dummy domain will behave as a rigid body. For all models, the initial condition is for all of the nodes along the depression/defect center to be coupled in the Y direction to the rigid dummy domain. When the evaluated criterion is met, the node is released (its constraint is removed), it becomes a broken node, and creates a free surface, as shown in Figure 3.11

The specific nodal relationship between the group of nodes on the dummy domain and the steel domain is a shared Y location. Furthermore, the nodal constraints between the dummy domain and the steel domain are specifically setup to allow stress free translation in the X direction (*i.e.* no individual node on the steel domain is required to stay at the same X position as a corresponding node on the dummy domain).

3.7.1.2 Cracking Criterion

The cracking criterion used for propagating the crack in this work is roughly based on hot tearing, where the crack continuously follows along somewhere in the solid-rich mushy zone as it moves deeper into the solidifying shell. To break apart the nodes eq. (3.24) is defined, a priori, to place the propagation path within the domain where desired (shown in Figure 3.11).

$$C = a + b\sqrt{t} \tag{3.24}$$

where, a and b are empirical parameters chosen to give the desired profile and offset from the solidus isotherm, and t is the time below meniscus. This function, eq. (3.24), is evaluated at each time step and each node along the boundary involved in the constraint on the left side of the domain. According to eq. (3.24), if the location of the crack front is greater than or

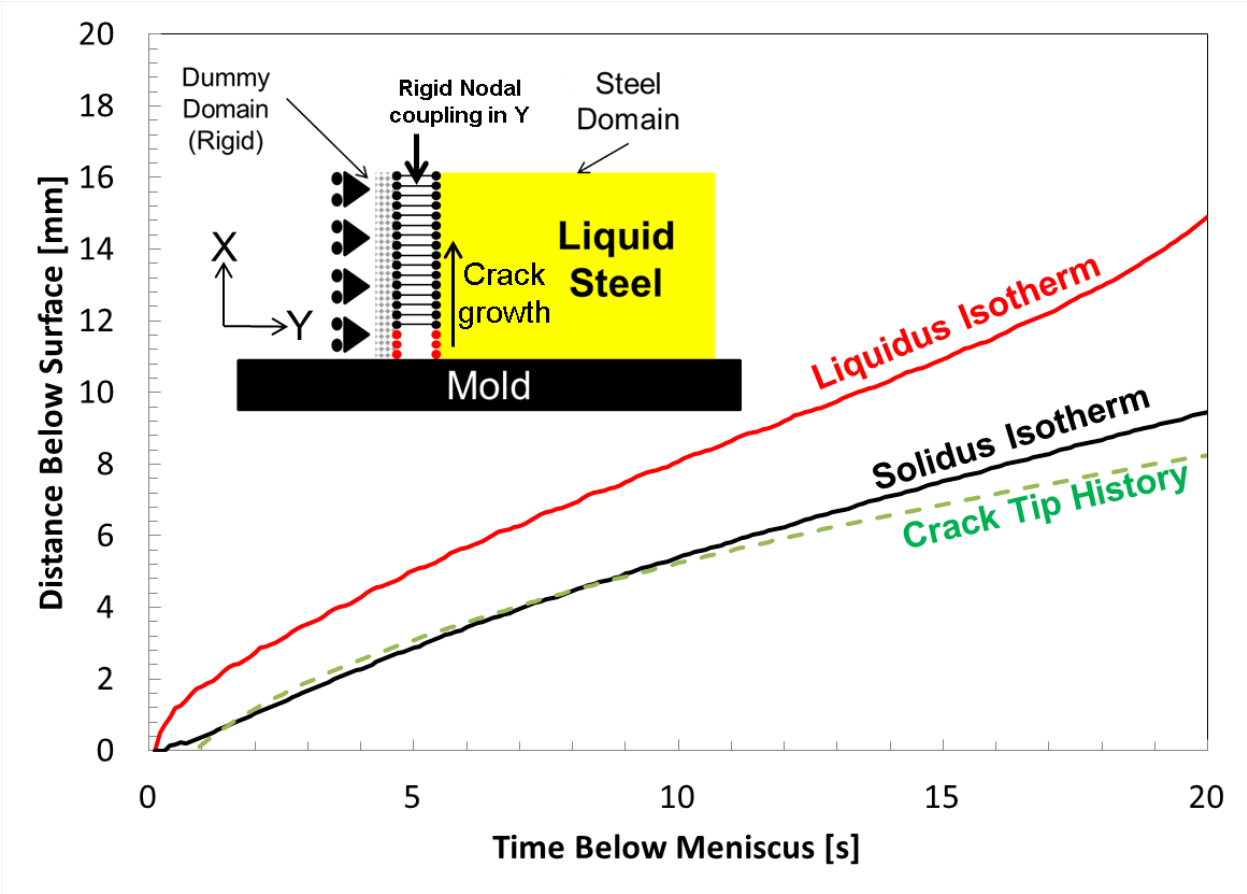


Figure 3.11: Crack growth schematic

equal to the distance of a given node along the boundary (from the steel surface), the MPC subroutine turns that node relationship off and that node is no longer constrained by the dummy domain position in the Y direction. A complete example case MPC subroutine used for this work is included in section C.2 and complete details on the operation of the MPC subroutine can be found in the literature [66].

3.8 Material Properties

The primary grade chosen for this work is a $0.04wt\%C$ plain low carbon steel, with phase fraction history shown in Figure 3.12. The composition for this steel grade is given in Table 3.2 and the transition temperatures detailed in Table 3.3.

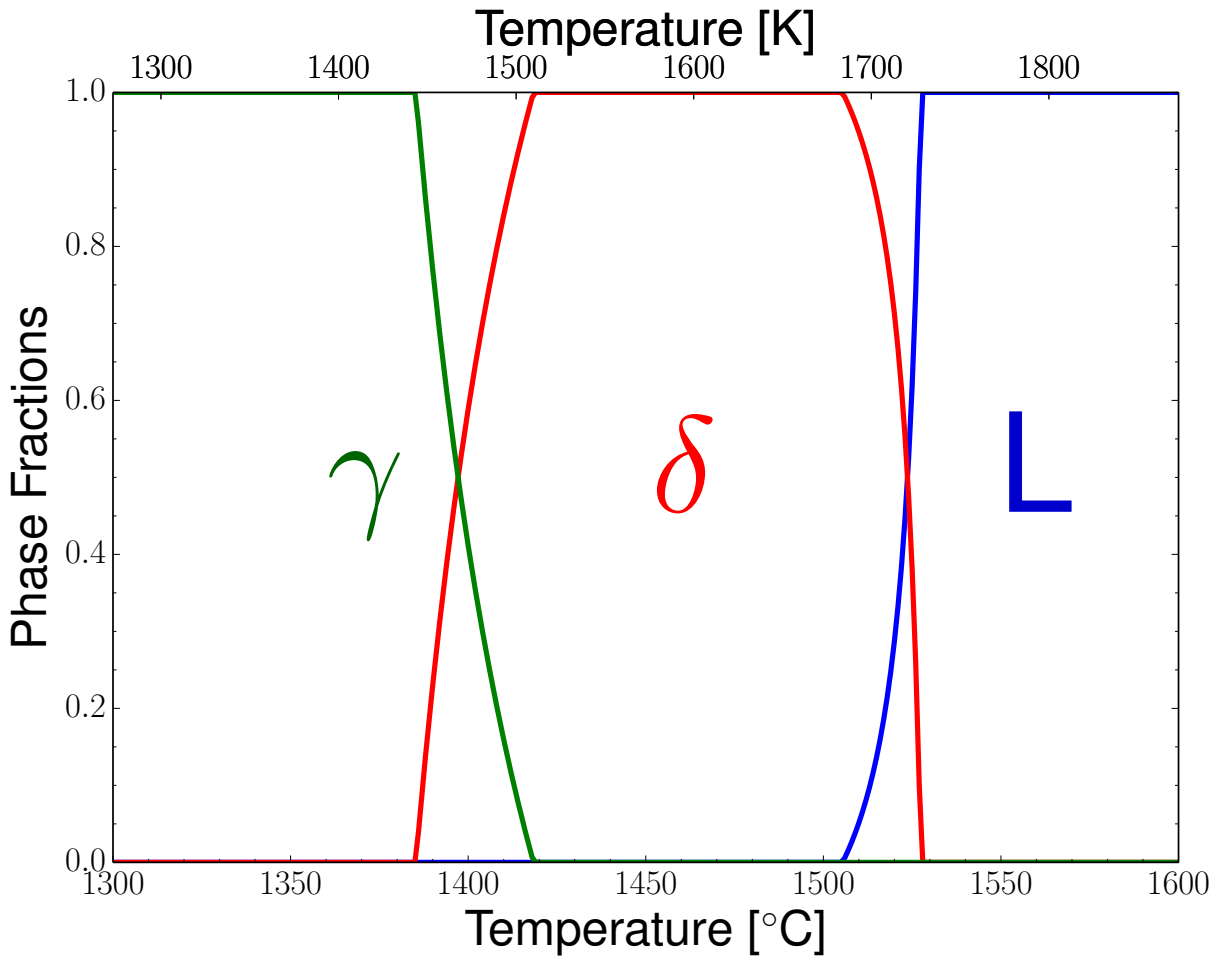


Figure 3.12: Low carbon steel phase fractions

Table 3.2: Plain low-carbon steel composition

Element	**Wt %**
Carbon	0.040 %
Aluminum	0.040 %
Chromium	0.010 %
Copper	0.010 %
Manganese	0.200 %
Nickel	0.010 %
Phosphorus	0.010 %
Sulphur	0.010 %
Silicon	0.020 %
Titanium	0.050 %
Iron	Balance

Table 3.3: Plain low-carbon steel transition temperatures

Transition	**Temperature**
Austenite End	695°C
Austenite Start	1418°C
Delta Ferrite End	1385°C
Delta Ferrite Start	1505°C
Solidus	1505°C
Mushy Zone	23°C
Liquidus	1528°C
Pour Temperature	1532°C

3.8.1 Enthalpy and Specific Heat Capacity

The specific enthalpy, H (J/kg), curve used to relate heat content and temperature in this work, is obtained by integrating the specific heat curve C_P fitted from measured data compiled by Harste [73] as given in eqs. (3.26) to (3.28) and (3.31). Figure 3.13 shows the specific heat capacity, and Figure 3.14 shows the enthalpy for four example grades including the low carbon steel examined in this work. The enthalpy values used are weighted according to the fraction presence of each phase as shown in eq. (3.25). Values vary based on

temperature and the phase of the steel. It is worth noting that while the latent heats for each of the grades is very similar, it is not identical, and the distribution of release based on temperature is also not the same. The equations used for each phase [73] are shown in eqs. (3.26) to (3.28) and (3.31).

$$H[kJ/Kg] = H_L f_L + H_\delta f_\delta + H_\gamma f_\gamma + H_\alpha f_\alpha \tag{3.25}$$

Where temperature T is given in Kelvin.

$$H_L = 824.6T - 104642.3 + \Delta H^l_{mix} \tag{3.26}$$
$$H_\delta = 0.8872T^2 + 441.39T + 50882.3 \tag{3.27}$$
$$H_\gamma = 0.07489T^2 + 429.849T + 93453.72 + \Delta H^\gamma_{mix} \tag{3.28}$$

where,

$$\Delta H^l_{mix} = 18125(\%C) + 1966120\frac{(\%C)^2}{43.839(\%C) + 1201.1} \tag{3.29}$$
$$\Delta H^\gamma_{mix} = 36601(\%C) + 1907930\frac{(\%C)^2}{43.839(\%C) + 1201.1} \tag{3.30}$$

$$H_\alpha = \begin{cases} 5188T^{-1} - 86 + 0.505T & \\ \quad -6.55\times10^{-5}T^2 + 1.5\times10^{-7}T^3 & T \leq 800 \\ 5188T^{-1} - 86 + 0.505T & \\ \quad -6.55\times10^{-5}T^2 + 1.5\times10^{-7}T^3 & 800 < T \leq 1000 \\ 5188T^{-1} - 86 + 0.505T & \\ \quad -6.55\times10^{-5}T^2 + 1.5\times10^{-7}T^3 & 1000 < T \leq 1042 \\ 5188T^{-1} - 86 + 0.505T & \\ \quad -6.55\times10^{-5}T^2 + 1.5\times10^{-7}T^3 & 1042 < T \leq 1060 \\ -10.068T + 2.9934\times10^{-3}T^2 & \\ \quad -5.21766\times10^6T^{-1} + 12.822 & 1060 < T \leq 1184 \end{cases} \tag{3.31}$$

3.8.2 Thermal Conductivity

The temperature and grade dependent conductivity functions for plain carbon steel phases is fitted from measured data compiled by Harste [73] and is given by eqs. (3.32)

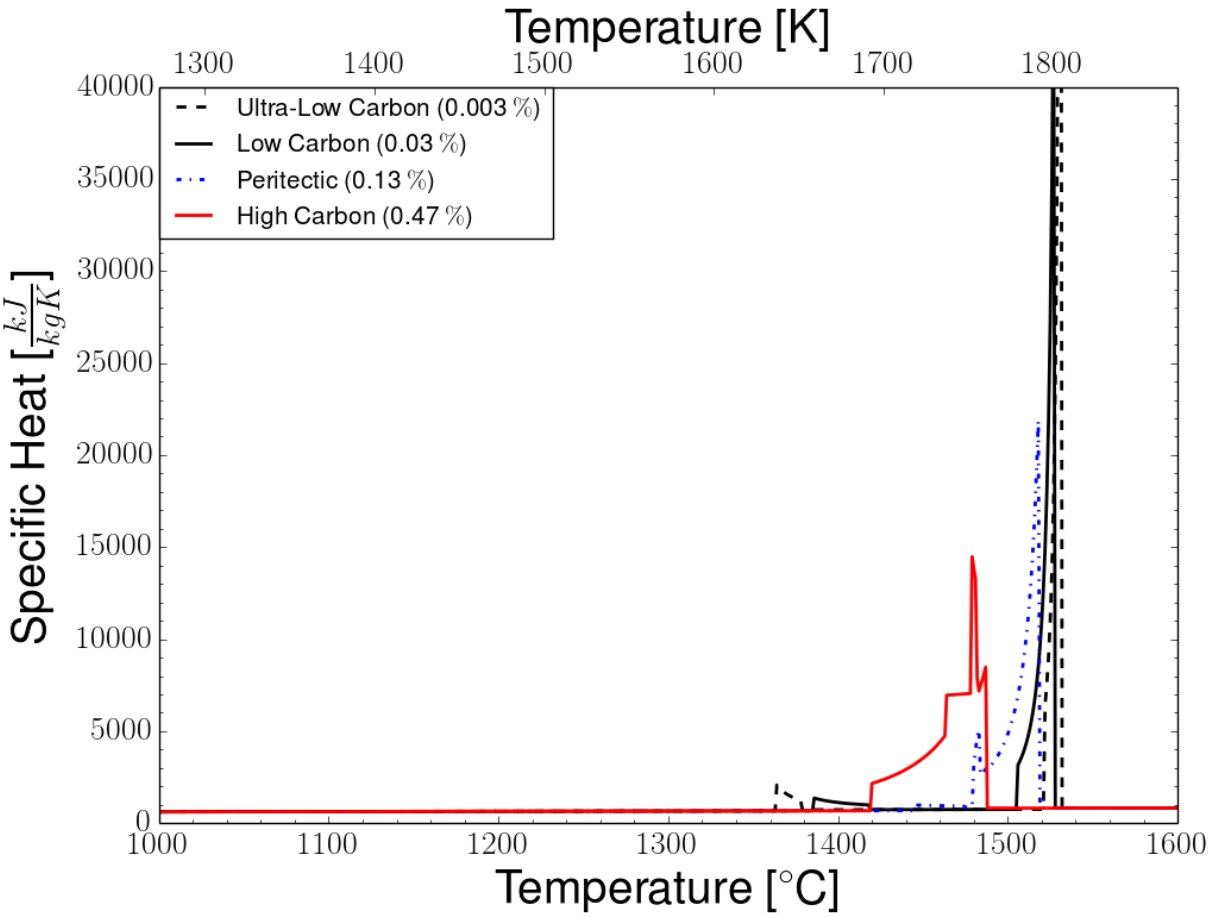


Figure 3.13: Temperature-dependent specific heat capacity

and (3.35). Figure 3.14 shows the conductivity for four example grades including the low carbon steel examined in this work. The conductivity, k (W K/m), increases linearly through the mushy zone to the liquid by a factor of 6.5 to partly account for the effect of convection due to flow in the liquid steel pool [74]. A small difference in shell thickness is noted when this is not included, but for the purposes of this work is negligible.

$$k_l = 39.0 \tag{3.32}$$

$$k_\delta = (21.6 + 0.00835T)(1 - F_1(C\%^{F_2})) \tag{3.33}$$

$$k_\gamma = 20.14 + 0.00931T \tag{3.34}$$

where,

$$F_1 = 0.425 - 0.0004385T \tag{3.35}$$

$$F_2 = 0.209 - 0.00109T \tag{3.36}$$

3.8.3 Mass Density and Thermal Linear Expansion

Mass density, ρ ((kg/m^3)), is calculated by weighted phase fraction of all of the phases given by eq. (3.39). Experimental data taken from the work of Jablonka et al. [75] and compiled by Jimbo and Cramb [76]. The thermal linear-expansion function is obtained from solid-phase density measurements compiled by Harste [73] and liquid density measurements by Jimbo and Cramb [76]. A simple mixture rule is applied to obtain the overall density from the values of the different phases. Figure 3.14 shows the density and thermal linear-expansion curves for four example grades including the low carbon steel examined in this work, choosing the reference temperature, T_0, to be the 1507°C [77].

$$\alpha_L = \sqrt[3]{\frac{\rho_{T_0}}{\rho_T}} - 1 \tag{3.37}$$

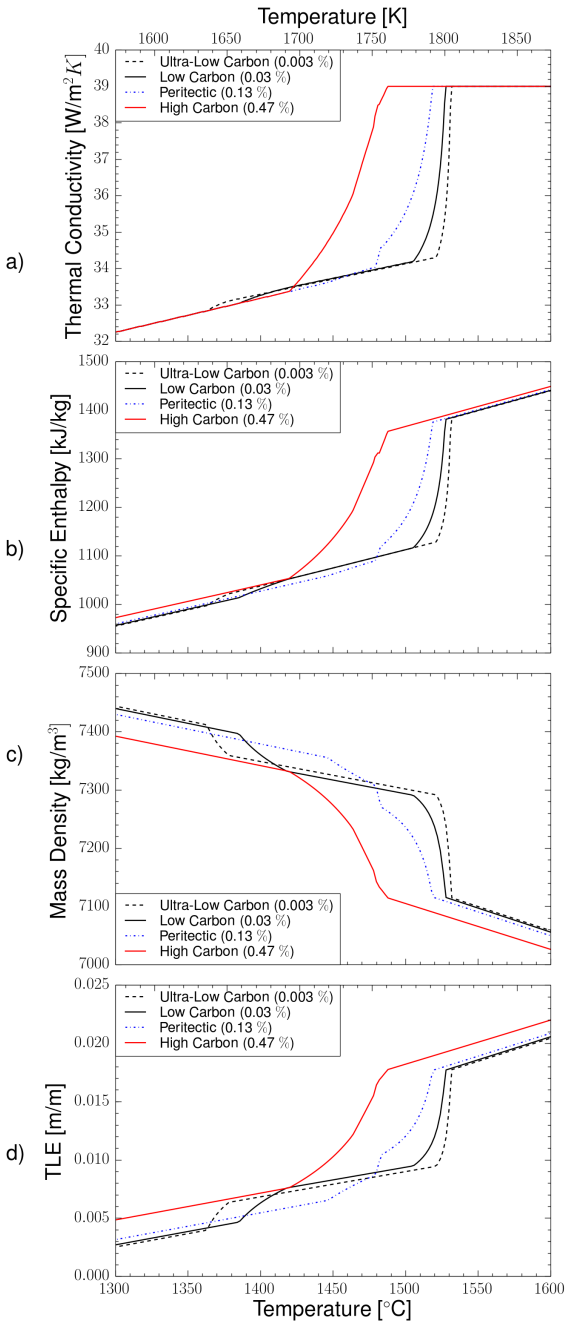


Figure 3.14: Temperature-dependent properties of 4 example steel grades including the Low Carbon steel investigated: a) Thermal conductivity b) Enthalpy c)Density d) Thermal linear expansion

$$\rho_l = 7100 - 73.2C_C - (0.828 - 0.0874C_C)(T - 1550) \tag{3.38a}$$

$$\rho_\delta = \frac{100(8011 - 0.47T)}{(100 - C_C)(1 + 0.013C_C)^3} \tag{3.38b}$$

$$\rho_\gamma = \frac{100(8106 - 0.51T)}{(100 - C_C)(1 + 0.008C_C)^3} \tag{3.38c}$$

$$\rho_\alpha = 7881 - 0.324T - 3 \times 10^{-5}T^2 \tag{3.38d}$$

$$\rho_T[\text{kg/m}^3] = \rho_l f_l + \rho_\delta f_\delta + \rho_\gamma f_\gamma + \rho_\alpha f_\alpha \tag{3.39}$$

Where α_L is the Thermal Linear Expansion coefficient and the density ρ_{T_0} is the density at the reference temperature T_0. For this work ρ_{T_0} is taken to be 7400 kg/m^3 .

3.8.4 Elastic Properties

The temperature-dependent elastic-modulus curve used in this model is a stepwise linear fit of measurements by Mizukami et al. [78], given in Figure 3.15.

The liquid is modeled as a weak perfectly plastic solid. The elastic modulus of the liquid region was given the value of 0.01MPa, and the Poisson ratio is constant at $\nu = 0.3$. The measured Poisson ratio that approaches 0.5 at high temperatures is achieved with this model, by considering the large extent of incompressible creep strain ($\nu = 0.5$) that accompanies the elastic strain during the test [79]. Incorrectly incorporating part of the volume conserved plastic behavior, where $\nu = 0.5$, into the elastic has been found to be likely to cause numerical difficulty for the solver [77].

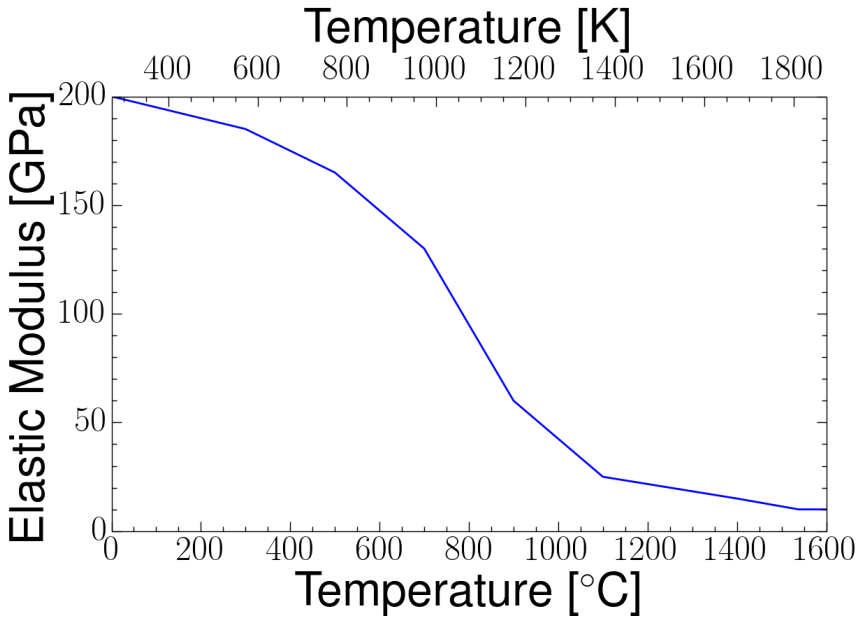


Figure 3.15: Temperature-dependent elastic modulus of steel

3.8.5 Constitutive Models

Two constitutive models relating the stress-strain relationship are utilized in this work. These equations were developed to match tensile-test measurements of Wray [80] and creep-test data of Suzuki et al [81]. The details of these two models can be found in [82] and [83] respectively. The ferrite and austenite phases are not of comparable strength. Ferrite is approximately an order of magnitude weaker than austenite of the same temperature, because of this a weighted mixture rule is not appropriate in regions with the much weaker phase when the softer material dominates the net mechanical behavior. In previous works where these two constitutive equations were utilized, eq. (3.41) was in effect when there was less than 10% of either ferrite phase, otherwise eq. (3.40) was used. This work also uses this method. Improving upon this transition method is left for future work.

Two different constitutive equations are used to model the behavior of solidifying steel. eq. (3.40) is the Zhu Modified Power law [82] and is used for ferrite.

$$\dot{\bar{\epsilon}}_{in-\delta}[1/s] = 0.1 F_\delta |F_\delta|^{n-1} \tag{3.40}$$

where,

$$F_\delta = \frac{C\overline{\sigma}}{f_C(\frac{T(K)}{300})^{-5.52}(1+1000|\overline{\epsilon}_{in}|)^m}$$
$$f_C = 1.3678 \times 10^4 C_C^{-5.56\times10^{-2}}$$
$$m = -9.4156 \times 10^{-5} T(K) + 0.349501$$
$$n = (1.617 \times 10^{-4} T(K) - 0.06166)^{-1}$$

C represents the sign on the 3 dimensional stress tensor [84], and C_C is the wt.% carbon. Equation eq. (3.41) is the Kozlowski model III [83] which is used for austenite.

$$\dot{\overline{\epsilon}}_{in-\gamma}[1/s] = f_C|F_\gamma|^{f_3-1}F_\gamma exp(\frac{-4.465\times10^4}{T(K)}) \tag{3.41}$$

where,

$$F_\gamma = C\overline{\sigma} - f_1\epsilon_{in}|\epsilon_{in}|^{f_2-1}$$
$$f_1 = 130.5 - 5.128 \times 10^{-3} T(K)$$
$$f_2 = -0.6289 + 1.114 \times 10^{-3} T(K)$$
$$f_3 = 8.132 - 1.54 \times 10^{-3} T(K)$$
$$f_C = 4.655 \times 10^4 + 7.14 \times 10^4 C_C + 1.2 \times 10^5 C_C^2$$

The liquid and mushy zones are modeled with an isotropic elastic-perfectly-plastic rate-independent constitutive model, using a small, constant yield stress of 0.01 MPa, whenever temperature exceeds the solidus temperature.

3.9 Finite Element Implementation

A schematic of the general mesh used in this work is shown within Figure 3.10. The model uses CPEG4HT elements in Abaqus: Two-dimensional, piecewise linear, continuum, generalized plane strain, 4 node, diffusive heat transfer, hybrid elements. Unless otherwise stated, the steel domain was divided into 0.5 mm square elements for a total of 3200 elements.

3.10 Model Verification and Validation

Computational modeling provides a powerful tool for approximating real-world systems, however, they rarely exactly imitate the real world due to various assumptions and simplifications. With this in mind, accurate modeling requires two, different, very important steps that are sometimes overlooked: verification and validation. First, a newly developed model needs to be verified against a known or analytical solution, this is how we establish that the proper behaviors are being captured. This step also includes a mesh convergence study to ensure mesh independent results output. Second, a verified model then needs to be validated (often involving calibration) by matching a detailed real-world example demonstrating that it is truly representative of the problem in question.

3.10.1 Thermal-Mechanical Solidification Analytical Solution

Proper model verification requires a test problem with a known solution [15]. An important analytical solution for the generation of thermal stresses in a general one-dimensional metal solidification process was derived by Weiner and Boley [85] using a simple elastic rate-independent plastic constitutive model. The semi-infinite pure material elastic perfectly plastic plate domain is constrained against bending but otherwise free to shrink. We use it here as an ideal problem to validate our solidification stress model. The constants and parameters used to approximate the behavior of our problem for this simplified validation problem can be found in Table 3.4. For the Weiner and Boley model a mushy zone is included just enough for numerical stability, and is approximately negligible.

Results of the numerical and analytical solution are shown in Figure 3.16, the temperature and stress are plotted along the lower edge of the domain starting from the chilled end towards the free end. As expected, the temperature in the liquid remains constant, while the temperature distribution through the solid decreases with time. The stress profile shows behavior that indicates compression at the surface moving towards tension at the solidification front.

Table 3.4: Properties used in the Weiner and Boley test problem

Property	Value	Unit
Thermal Conductivity	33	W K/m
Density	7500	kg/m^3
Young"s Modulus (Solid)	4000	MPa
Young"s Modulus (liquid)	1400	MPa
Poisson"s Ratio	0.3	-
Thermal Expansion	$2x10^{-5}$	1/K
Pour Temperature	1769	K
Fixed Wall Temperature	1273	K
Liquidus Temperature	1768.1	K
Solidification Temperature	1768	K
Solidus Temperature	1767.9	K
Latent Heat	272	kJ/kg
Specific Heat	661	J K/kg

The surface of the shell is quenched immediately. This causes the domain to shrink locally. Initially the domain is allowed to shrink freely, unconstrained by the lack of strength in the primarily liquid domain. The liquid has negligible strength, and thus carries no stress. As time progresses, the rest of the domain cools and attempts to shrink. Relative to the solidified surface, the interior of the domain is still weaker and as it attempts to shrink remains opposed by the stronger material at the surface. This tends to generate compression at the surface, and to maintain equilibrium, generates sub-surface tension.

Comparing the results shown in Figure 3.16, the numerical results match the analytical solution and methodology is validated.

3.10.2 Mesh Resolution Convergence Study

A mesh study was conducted to verify that the model was converging to a proper solution, changing only the number of elements through the solidification direction (x). The domain width was chosen to maintain 3 elements through the thickness and an aspect ratio of 1. (*i.e.* the 10-elements case has 4mm square elements, giving a 12mm wide domain). Figure 3.17 shows results for 6 different mesh refinements after 10s of solidification; these results indicate

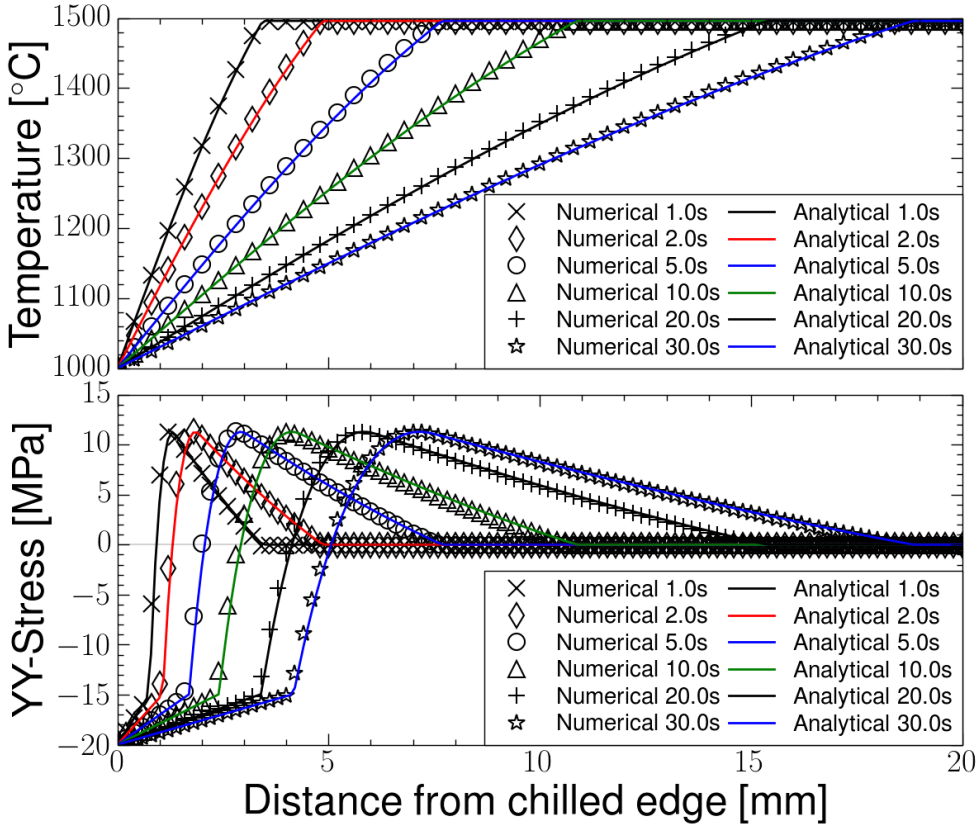


Figure 3.16: Comparison of Weiner & Boley and Abaqus predicted temperature and stress distributions through the shell

that while 1, 2.5, and 4 mm elements can accurately reproduce the temperature history, shown in Figure 3.17(a), a more refined mesh is necessary to properly resolve the stress and strain behavior, shown in Figure 3.17(b-d).

While 4 mm elements capture the behavior of compression at the surface, and tension towards the solidification front, the problem becomes the low number of elements through the mushy zone. The size of the mushy zone is strongly grade dependent and can vary by almost an order of magnitude. For the LC steel shown, the mushy zone at 10 s is only $\sim$2 mm wide and with elements close to that size, the mushy zone could be contained within a single element. The phase transformation regions raise similar problems and are often thinner than the mushy zone. For the LC steel, the δ-ferrite to austenite region is 1 mm wide, and the 1 mm elements just barely capture the details. The inelastic strain, shown in Figure 3.17(d), demonstrates that 4 mm elements capture the general behavior in the austenite near the surface, but indicate the presence of strain throughout the mushy zone and also into the liquid.

For all of the reasons discussed, element size selection is extremely important for a solidification model. It becomes notably more important when interested in the solidification front or any phase transformation region. For this work an element size of 0.5 mm was chosen providing a balance between speed of calculation and capture of relevant phenomena [41]. In certain situations a highly refined mesh of 0.1 mm was used to more accurately capture quantitative stress and strain values.

3.10.3 Heat Flux in the Mold

Measurements were obtained from the operating caster to enable calibration and validation of the heat transfer model. This includes the measured heatup of the cooling water between entering and leaving the mold wide faces and narrow faces and the measured temperatures from thermocouples in the mold walls during $\sim$3 hours of nearly steady casting in the real plant. Figure 3.19 shows time histories of average heat flux leaving the mold, which are calculated from the water heatup, knowing the water flow rate and total mold surface

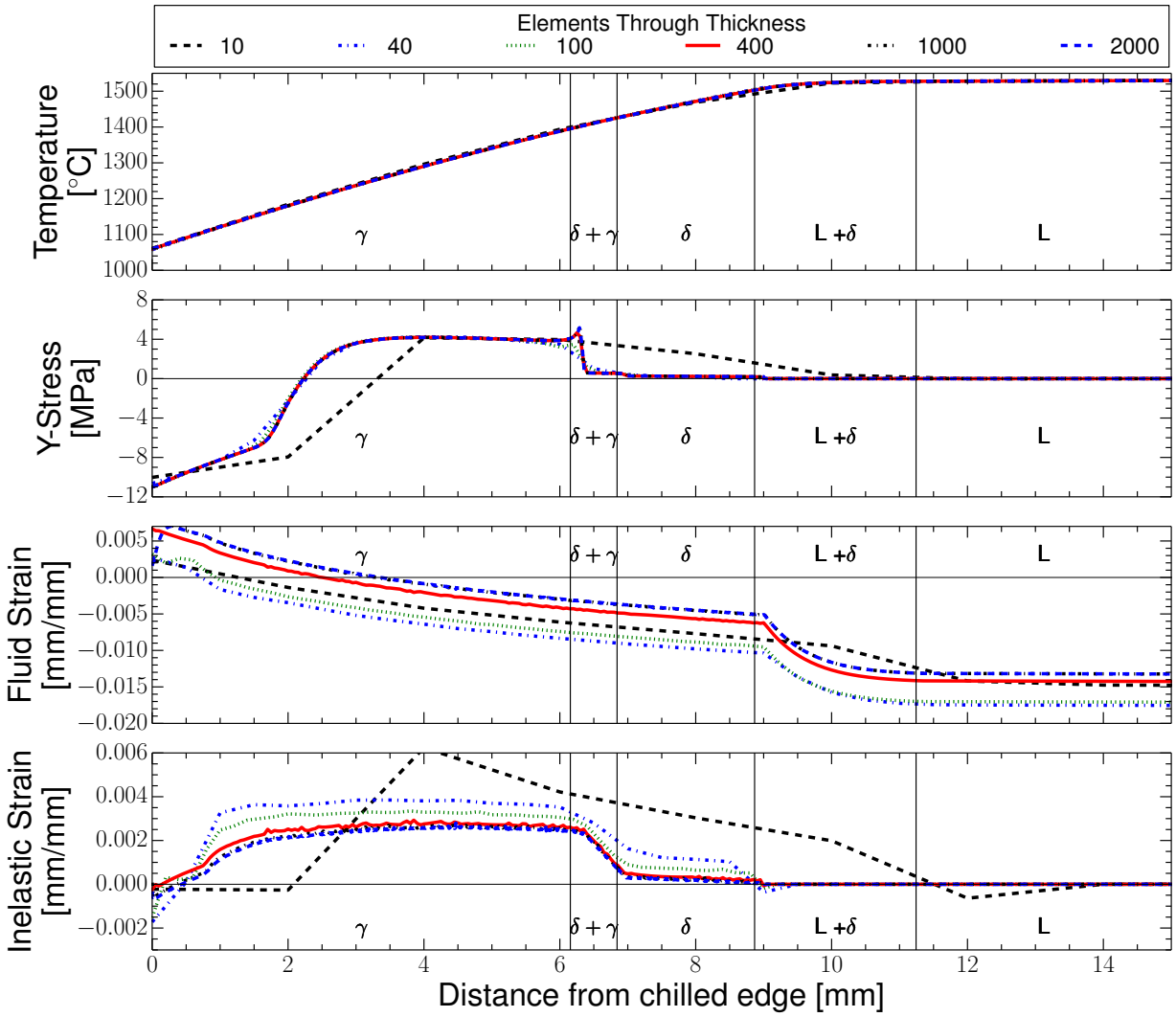


Figure 3.17: Mesh study results through shell thickness for low carbon steel (0.045%C)—10s below meniscus a) Temperature b) Y-Stress c) Fluid Strain d) Inelastic Strain

area. The time averages of these heat fluxes are also given.

Figure 3.20 shows plant measurements from 13 thermocouples (TCs) located 110 mm below the meniscus, and 20 mm beneath the mold hot face. The time- and spatial- averages of these temperature histories are also included in Figure 3.20(b). The thermocouple data of TCs 4-10 located in the central wide face region away from the corners average 120.4°C with standard deviation of 3.7°C.

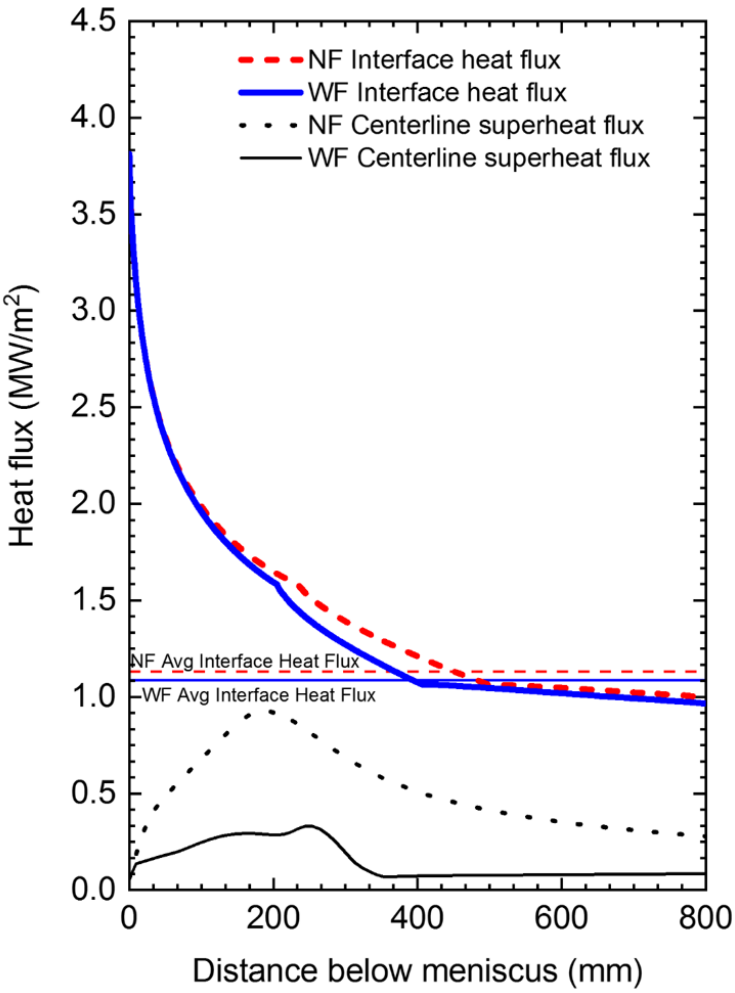


Figure 3.18: Calculated interfacial and superheat flux profiles down mold centerlines

The average heat flux across the interface between the steel shell and the mold hot face predicted by the CON1D model, is calculated by integrating the interface heat flux profile along the casting direction, shown in Figure 3.18, and dividing by the total mold

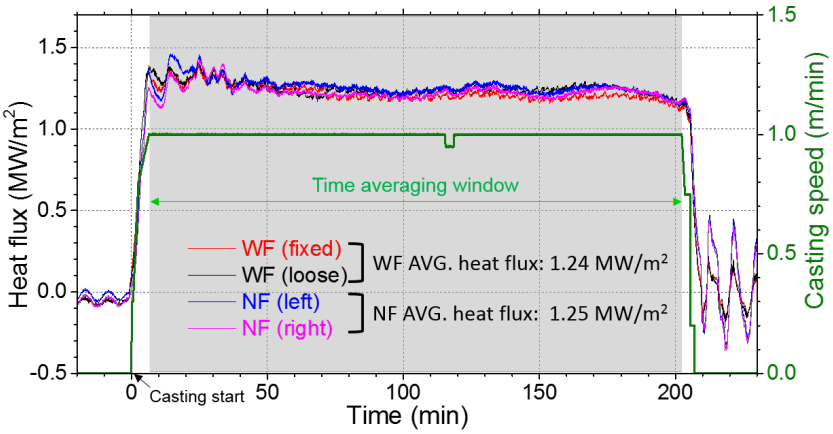


Figure 3.19: Heat flux measurements from heatup of mold cooling water

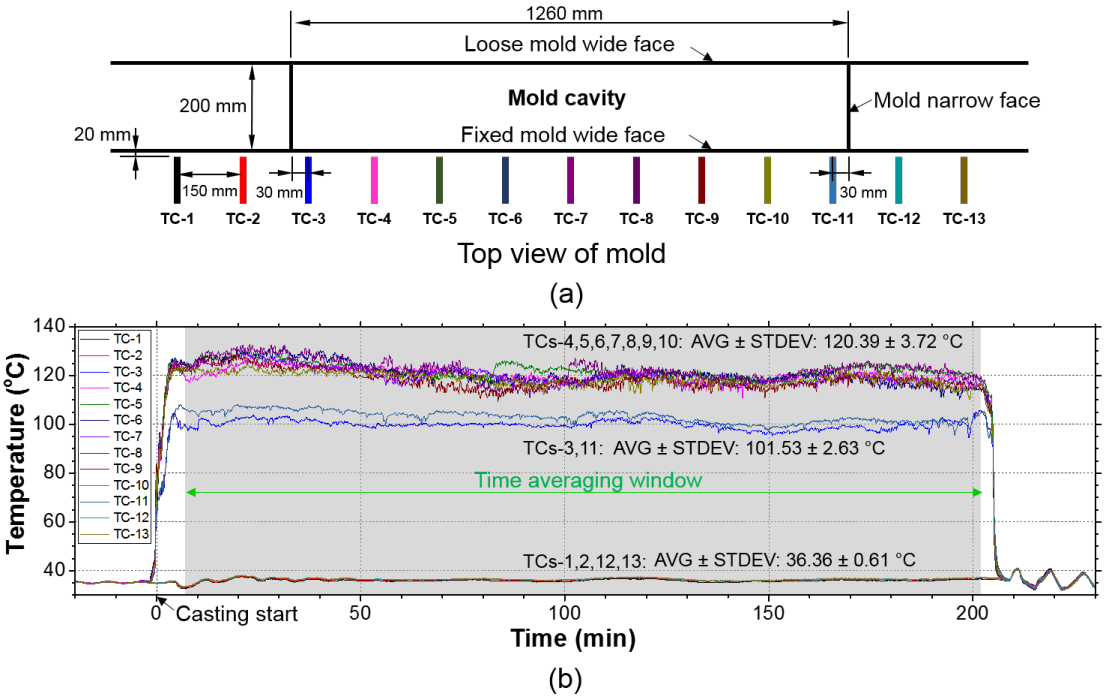


Figure 3.20: Thermocouple measurements: (a) locations and (b) temperature histories of thermocouples inserted on the mold wide face

length (900 mm) and width. These calculated average heat fluxes agree reasonably with the measurements: WF: 1.10 (predicted) vs. 1.24 (measured) MW/m^2 and NF: 1.15 (predicted) vs. 1.25 (measured) MW/m^2. Furthermore, the temperature in the mold wide face predicted at the thermocouple location exactly matches the measured average thermocouple data, as shown in Figure 3.21. Matching both average mold heat flux and thermocouple temperatures in the upper mold is significant because it suggests that the entire heat flux profile cannot be too far from reality. This was achieved by careful adjustment of model thermal parameters in Table A.1 such as fv.

The non-uniform superheat distributions, caused by the mold flow pattern, results in local thinning and temperature variations in the solidifying steel shell which greatly affects thermal stress behavior in the shell, and quality of the final steel products. As described previously, the superheat profile on the narrow-face centerline is higher than on the wide face, which makes the shell thickness of the narrow face substantially thinner than the wide face, as shown in Figure 3.22. This is also influenced by heat transfer through the interfacial gap between the steel shell and mold contact surface.

Figure 3.20 shows that the shell surface temperature starts to decrease faster at ∼400 mm below the meniscus, which is accompanied by corresponding decreases in slope of the mold wall temperatures. This is due to decreasing gap thickness, from better contact between the steel shell and the mold surfaces at that location. The model predictions of both shell thickness and mold temperature profiles are quantitatively verified by comparing the models (CON1D and Abaqus), in addition to the validation of CON1D with plant measurements already discussed.

3.10.4 Validation of Solidification Stress Model

Validation of solidification stress models at the relevant temperatures is quite difficult. Experimentally it is complicated, but prior work has demonstrated that it is possible to measure these stresses/forces using the Submerged Split Chill Contraction (SSCC) test. The SSCC test can measure forces in a solidifying steel shell under controlled conditions that

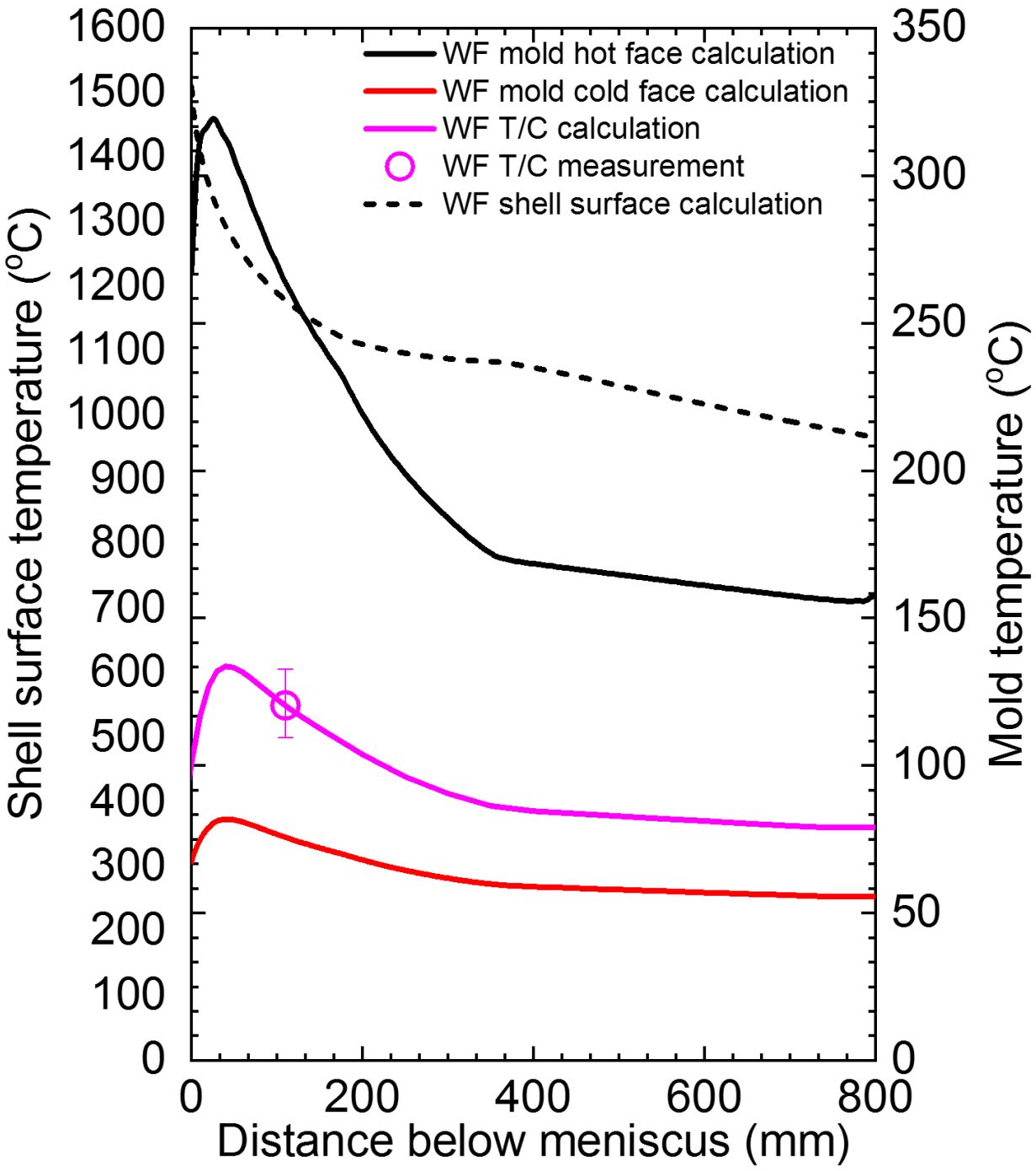


Figure 3.21: Calculated mold and shell temperature results (wide face) with thermocouple validation

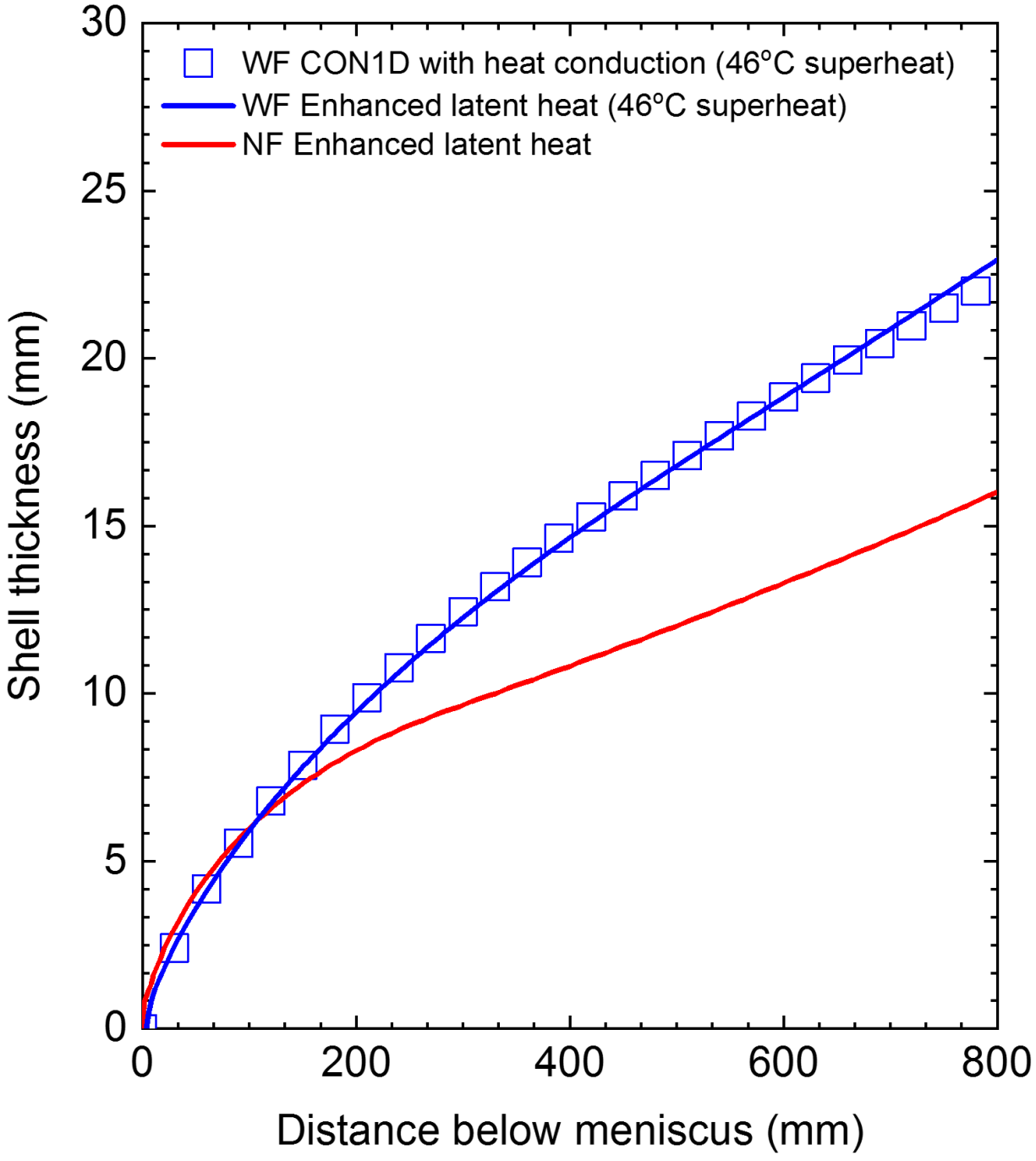


Figure 3.22: Shell thickness results from CON1D and Abaqus

match those of commercial casting processes. A computational model of the test was developed and applied to the experimental setup. The model successfully matched measurements of 1) temperature history; 2) shell thickness; 3) solidification force (shown in Figure 3.23; and 4) failure location. In addition, the model reveals the stress and strain profiles through the shell thickness. The SSCC test and validated model together is a powerful analysis tool for mechanical behavior, hot tear crack formation and other phenomena in solidification processes [86].

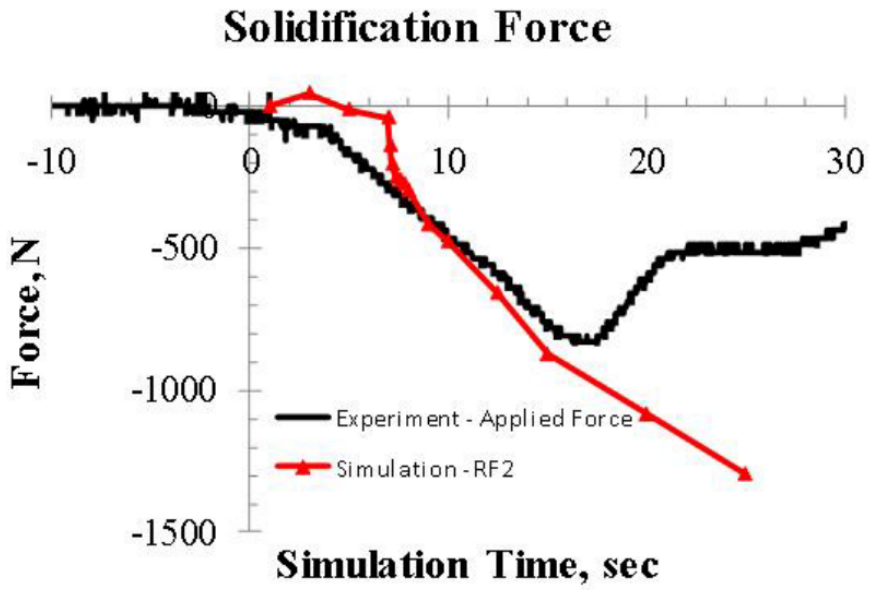


Figure 3.23: Comparison of experimental and simulated force curves[86]

3.10.5 Heat Transfer Model Validation

In this work, a resistor model is used to calculate heat transport across the interfacial gap. To find accurate interfacial heat fluxes, measurements of mold thermocouple temperatures and heat flux from water heatup are needed. For some previous models [87], an inverse heat conduction problem (IHCP) is solved to match the surface boundary conditions with specific plant measurements. In the current work, the two-way thermal-mechanical coupling between the solidifying steel shell and mold is modeled in detail to find the heat transferred

across the interfacial gap between the mold and steel shell, which depends strongly on the local gap distance calculated from the mechanical solution. Measurements are used here for model calibration and validation.

3.10.5.1 General Resistor Model Results

Working up to the full model, some simplified versions were created to verify expected behavior. Uniform flux thickness results in uniform heat transfer across the surface, it is non-uniformity in flux thickness that creates heat transfer variations and local hot/cold spots. These local hot spots are known to result in displacement from the surface as the steel shell begins to reheat. Before induced air gaps can be examined, uniform thicknesses were studied. For models with no air gap or a defined air gap the shell surface was constrained to remain fixed in the x direction within the stress model and ferrostatic pressure was not applied.

Using a uniform total flux layer thickness of 2mm with no air gap, a first model was simulated using the values found in Table 3.5. Results of this comparison are shown in Figure 3.24, differences between Excel and Abaqus results at early times are purely numerical and are ignored. In general both the calculated resistance and resultant heat flux have infinity norm error on the order of less than 2%. Results indicate values of approximately 4.5 MW/m^2 at the meniscus gradually decreasing to 1.3 MW/m^2 at 30 s. This decreasing behavior is to be expected, and the values do not appear unreasonable based on prior work of the author [41], and values that appear in the literature as shown in Figure 3.25.

Table 3.5: Gap conductivity and resistance values

Location	Conductivity/Conductance	Resistance
	W/(m K)/W/(m^2 K)	m^2 K/W
Mold/Flux Interface	33 (h_{mold})	0.0004
Air Gap	0.06 (k_{Air})	D_{Air}/0.06
Solid Flux Layer	0.5 (k_{Sol})	D_{Sol}/0.5
Liquid Flux Layer	3.0 (k_{Liq})	D_{Liq}/3.0
Flux/Shell Interface	$3.98e^{0.0054T_{ls}}$ (h_{shell})	$\frac{1}{3.98e^{0.0054T_{ls}}}$

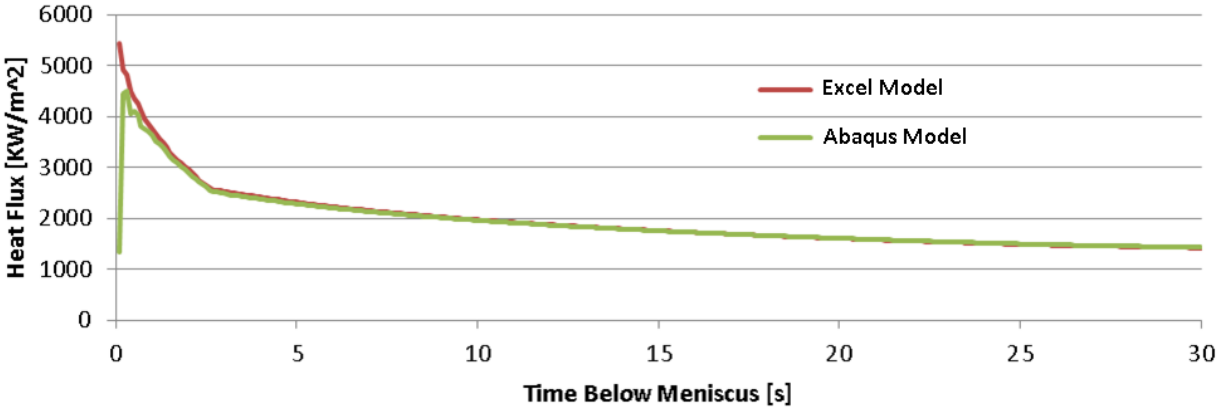


Figure 3.24: Projected and actual heat flux profiles

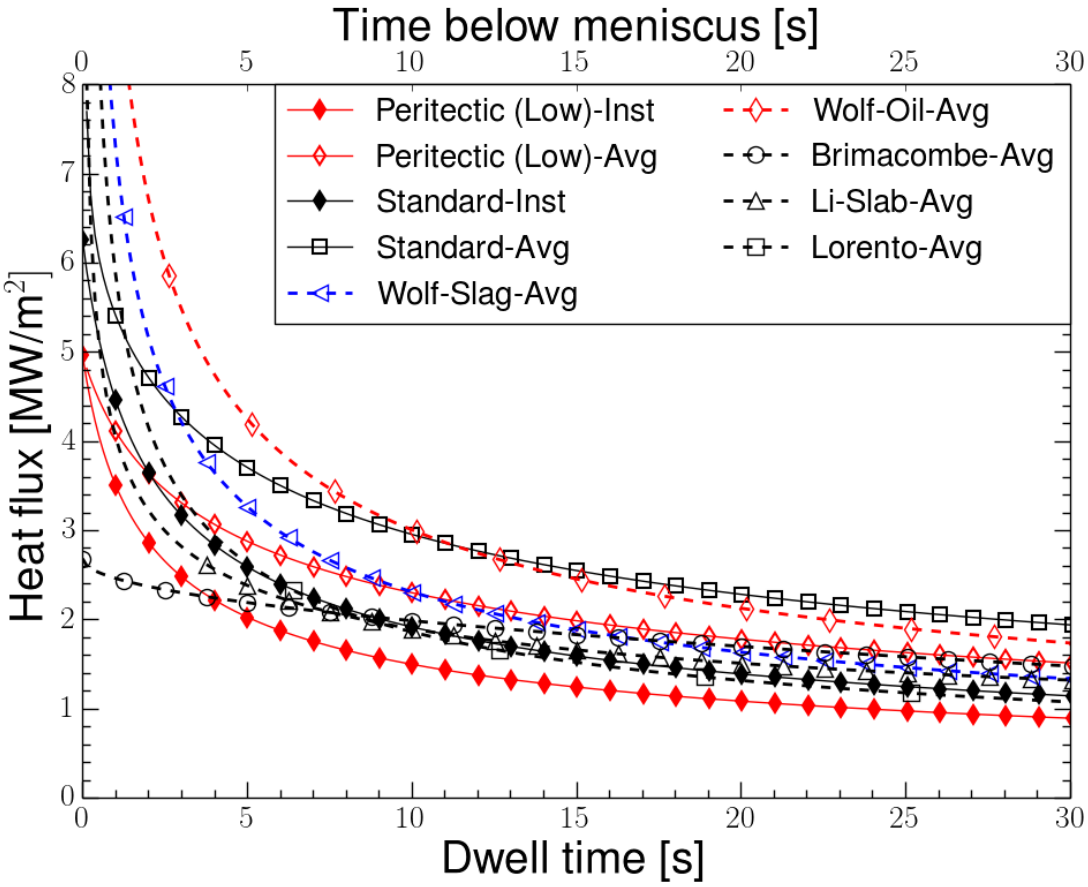


Figure 3.25: Instantaneous and average heat flux profiles

3.10.5.2 Effect of Flux Layer Thickness

Studies were carried out using a constant total flux layer thickness shown in Figure 3.26. It was observed that with all other properties fixed, as flux layer thickness increased, heat flux across the interface dropped. The change from 0.5 mm to 2 mm resulted in a continuous difference of about 1000 W K/m with a fixed solidification temperature of 800°C.

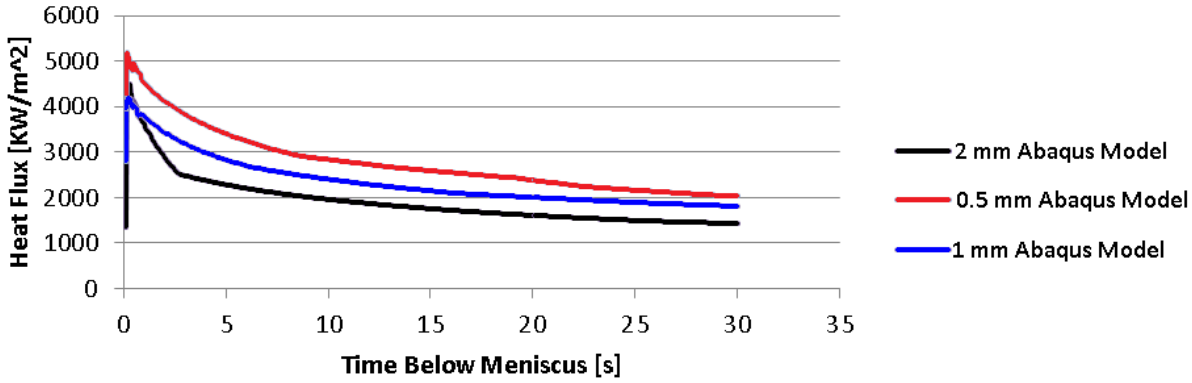


Figure 3.26: Flux layer thickness variation with 800°C solidification temperature

3.10.5.3 Effect of Flux Solidification Temperature

Studies were conducted using a fixed flux layer thickness while varying the solidification temperature of the slag layer. The thickness was fixed at 2 mm, and the solidification temperature was varied according to values found in the literature 650°C, 800°C, 1030°C. Results, shown in Figure 3.27, indicate that as solidification temperature decreases, the interface heat flux rises. This is consistent with expectations as the higher conductivity liquid layer persists in the gap longer which lowers the total resistance within the gap.

3.10.5.4 Effect of Flux Layer Thickness Variation

Studies were conducted with the flux thickness varying with time/distance below the meniscus. Results are shown in Figure 3.28. The 2mm thickness with a solidification temperature of 800°C was compared to a variation of 2mm at the meniscus decreasing linearly to 1 mm at mold exit. The varying flux thickness is shown to have a corresponding increase in

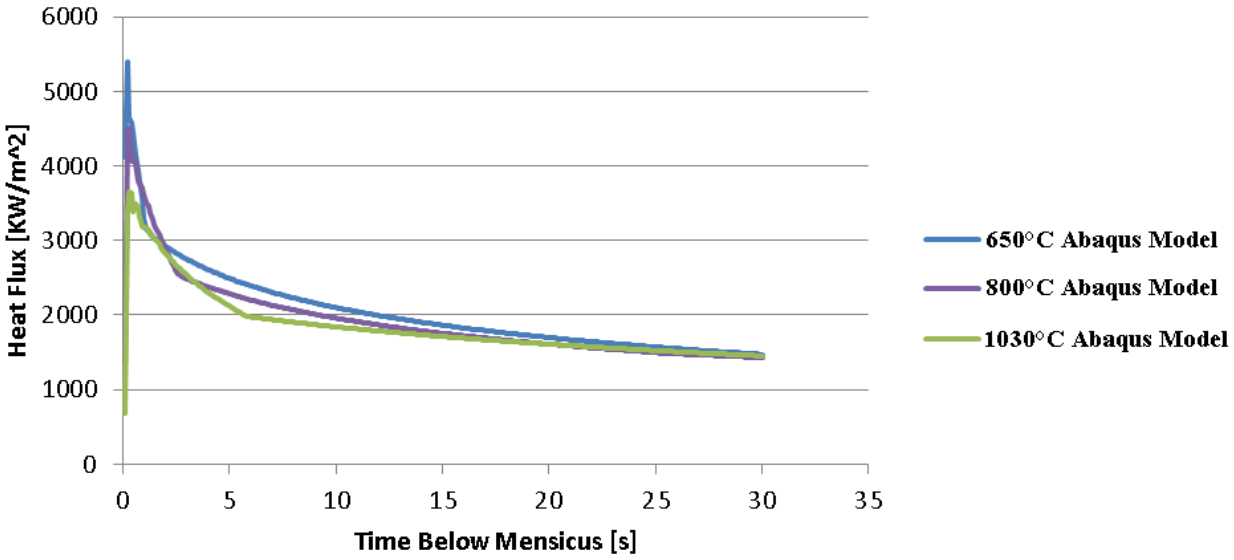


Figure 3.27: Effect of solidification temperature variation

heat flux as the mold flux thickness decreases. The difference in heat flux is more pronounced after 5 s.

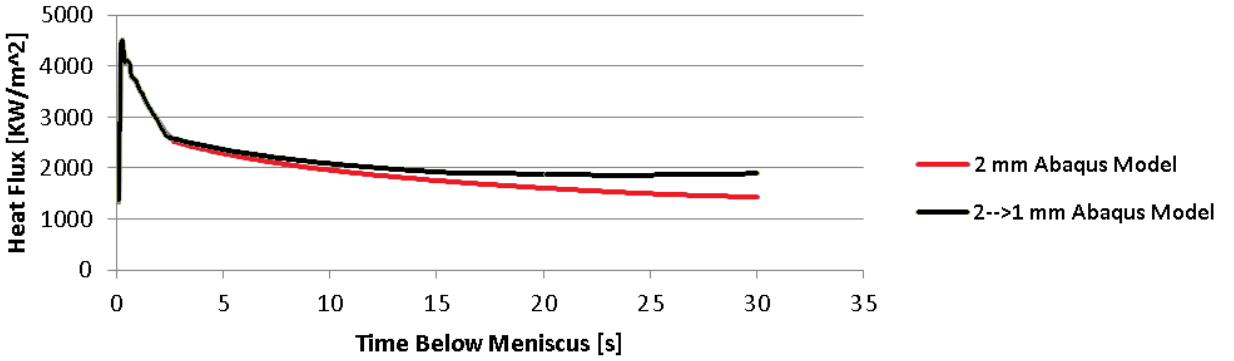


Figure 3.28: Time varying flux thickness with 800°C solidification temperature

3.10.6 Mechanical Constitutive Model Validation

The steel grade used in this work is based around a nominal low carbon composition used previously [15]. Extensive validation of the mechanical constitutive model has been previously conducted and further validation using a stainless steel was recently published by the author, as such, the validation in this section will focus on the stainless steel from that

work [88]. The entire publication can be found in section 8.4.

3.10.6.1 Phase-Based Constitutive Model Selection

As different steel phases have greatly different mechanical properties, the choice of constitutive model in this work depends on the phase-fraction evolution with temperature of the particular steel grade of interest, and the transition between phases, as described by [41]. In two-phase regions, most thermal and mechanical properties are modeled based on a simple weighted average summation based on phase fraction. Constitutive equations are handled differently.

In austenite/ferrite mixtures, the Zhu model for ferrite is applied in the solid when the ferrite volume fraction exceeds 10%. Otherwise, the Kozlowski austenite model is used. This criterion was chosen over a mixture law based on phase fractions, because time-dependent inelastic response in the ferrite phase governs the local mechanical behavior if the ferrite domain is unbroken. The previous work of [89] found that a transition of 10% matched quite well with a more complicated transitional model using an Eshelby tensor with multiple phases. Details on the method devised to integrate these highly nonlinear constitutive equations are explained in [90], and were implemented via the UMAT subroutine in Abaqus.

Figure 3.29 shows the results of both constitutive models, integrated for the same conditions as data measured by [91] for 316L stainless steel. The austenite is observed to be about 10X stronger than the corresponding ferrite, and the Kozlowski model agrees with the measured data.

3.10.6.2 Phase-Based Material Properties for Stainless Steel

Due to the many different types of steel, comprehensive mechanical-property experimental-data for the range of high temperatures, low strains, and low strain rates of interest in casting processes is difficult to find for any given steel grade. Although plain carbon steels are defined by their carbon content, they also contain up to several weight percent of many other alloying elements, which depend heavily on the specific grade. Higher alloy steels such as

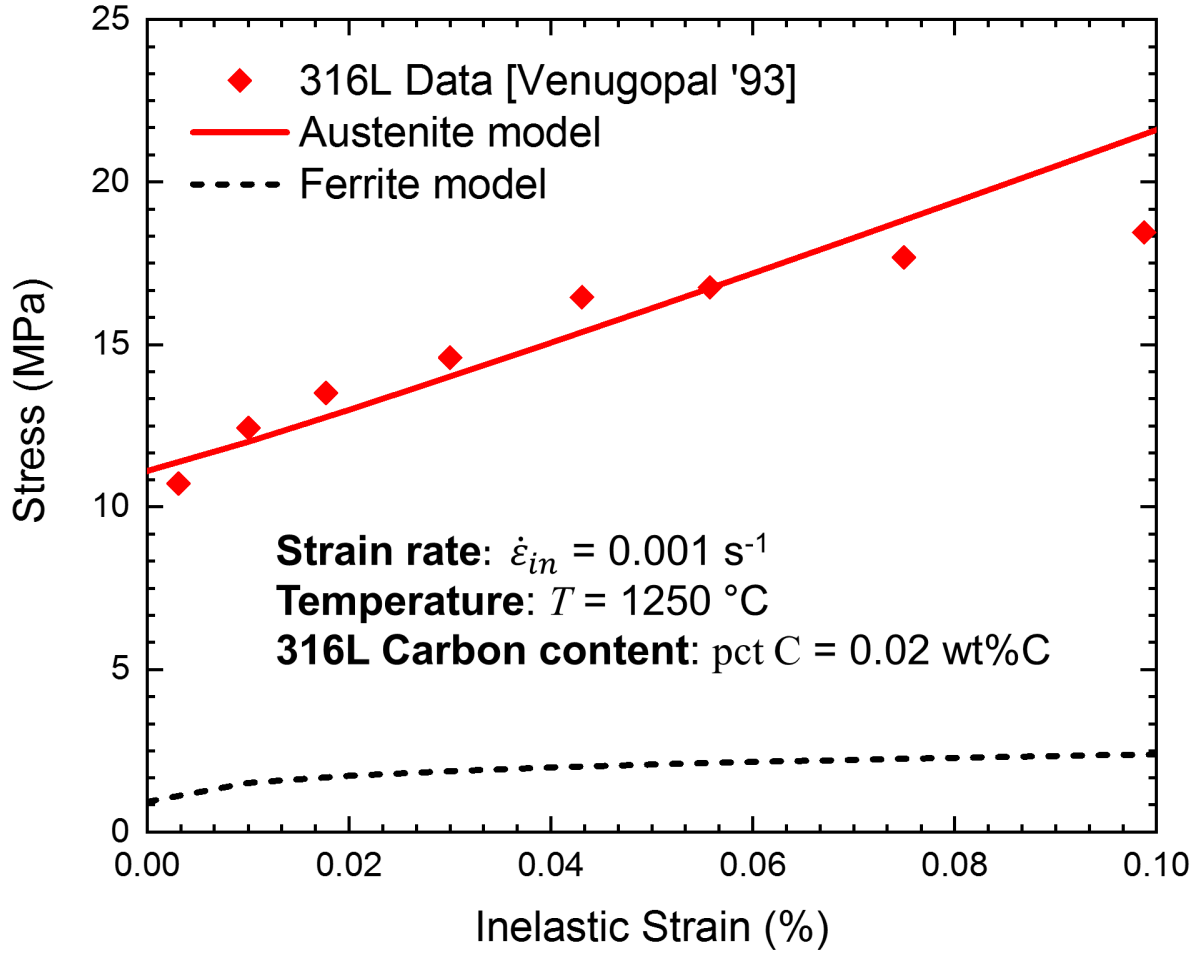


Figure 3.29: Mechanical constitutive models of austenite and ferrite for 316L stainless steel with experimental data [91]

next generation Advanced High-Strength Steels, tool steels, and stainless steels have substantially higher amounts of specific alloying elements (such as Si, Mn, Cr, and Ni) in order to achieve specific enhanced properties such as ductility-to-strength ratio, hardenability, hot working strength, and corrosion resistance.

Originally fit to data for specific plain carbon steels, both the austenite and ferrite models of the Kozlowski-Zhu constitutive laws exhibit reasonably good agreement with tensile-test data for other types of steel when the temperature, strain rate, and phase evolution are the same. Figure 3.34, which shows the austenite constitutive model and some of its plain-carbon fitting data, also compares the predictions of this model with tensile-test measurements for 316L stainless steel obtained by [91] at the appropriate temperature and strain rate. As also shown in Figure 3.29, the agreement is remarkable and significant, considering the very different composition of this steel. Furthermore, Figure 3.33, which shows the δ-ferrite constitutive model and some of its fitting data, also compares the predictions of this model with tensile-test measurements for a high-silicon electrical steel, which falls in the ferrite regime. Again, a very close fit is obtained for this very different steel grade.

Very little mechanical property data can be found for specific steels at elevated temperatures. High temperature stress-strain data for the temperature-, strain-, and strain-rate conditions encountered during continuous casting for 409L could not be found in the literature. However, while high temperature steel properties depend on composition, the specific phase at a given temperature is substantially more relevant to its behavior as shown by the results presented above. Therefore, finding the proper phase diagram, more specifically the phase fraction history of a given steel grade, and using phase specific constitutive equations is a sufficient and more convenient method for determining mechanical behavior during solidification, without the necessity of performing complete mechanical testing in this regime. This method has been previously validated by [86] comparing predictions using the Kozlowski-Zhu constitutive laws with force measurements in solidifying steel shells. Other similar studies, including those by [92] and [41] have applied this approach to investigate various aspects of

the continuous casting process.

Based on its composition shown in Table 3.6, the evolution of the volume fractions of each phase with temperature during solidification and cooling of 409L stainless steel are shown in Figure 3.30, calculated from the appropriate multi-dimensional equilibrium phase diagram based on free-energy minimization with JMatPro [93]. Specific transformation temperatures are given in Table 3.7.

Table 3.6: Compositions (wt.%) of steel grades

Grade	**Plain Carbon 1 [80]**	**Plain Carbon 2 [94]**	**Electrical** [94]	**316 SS** [91]	**409L SS**
C	0.051	0.028	0.017	0.02	0.005
Mn	0.82	0.01	0.01	1.7	0.27
Si	0.28	0.006	3.01	0.77	0.54
S	0.018	0.004	0.004	0.007	0.001
P	0.001	0.001	0.001	0.04	0.0224
Cr	-	-	-	18.2	11.2
Ni	-	-	-	11.6	0.1
Al	$<$0.002	0.001	0.002	-	0.003
Ti	-	-	-	-	0.22
N	0.001	0.001	0.003	-	0.008

Compared to plain carbon steel grades, the phase history of 409L stainless has substantially different austenite and ferrite regions. Whereas in plain low-carbon steels, solidification to δ-ferrite is followed by complete transformation into austenite, in this particular ferritic stainless steel, ferrite is still stable all the way to room temperature. Figure 3.30 shows that the cooling steel only partially transforms into austenite, reaching a maximum austenite fraction of about 60% at $\sim$1000°C, followed by a complete transition back into ferrite.

The temperature-dependent thermal properties: conductivity and enthalpy, shown in Figure 3.31, are calculated by JMatPro [93] and input into Abaqus subroutines. The temperature-dependent elastic modulus, density, and thermal linear expansion are shown in Figure 3.32.

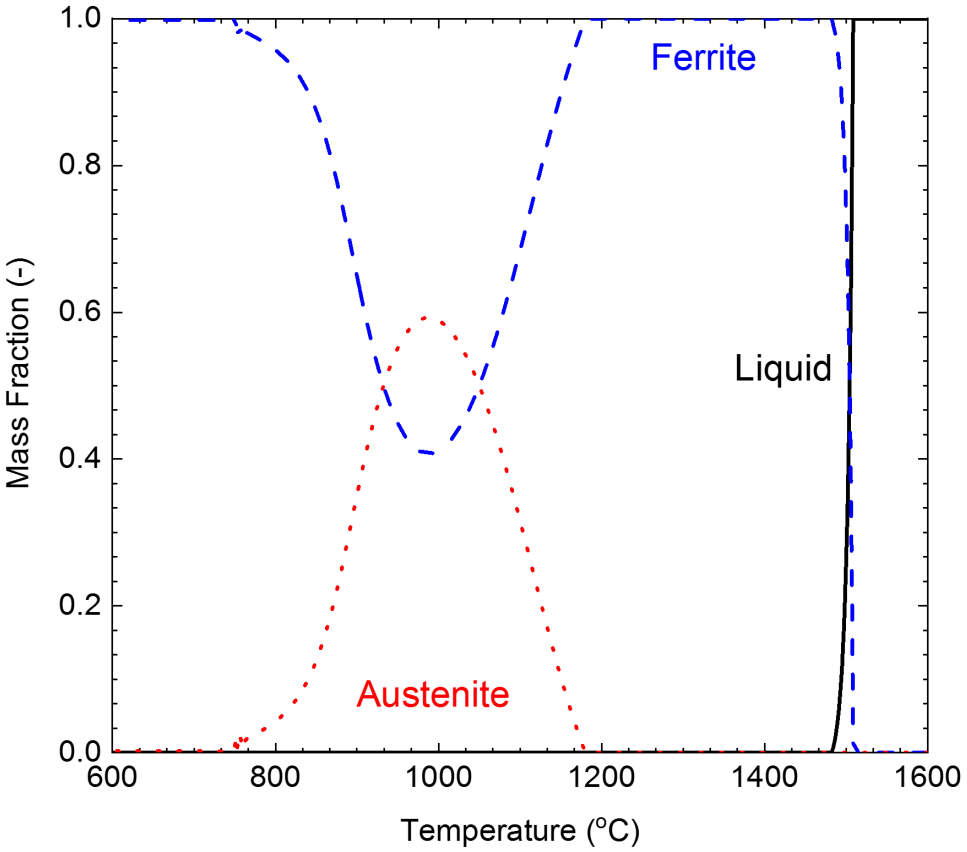


Figure 3.30: Phase fractions for 409L stainless steel

Table 3.7: Transition temperatures for 409L stainless steel

Pour temp.	1555.00°C
Liquidus temp.	1508.63°C
Solidus temp.	1481.93°C
Mushy zone	26.7°C
Austenite start	1180°C
Austenite end	753°C

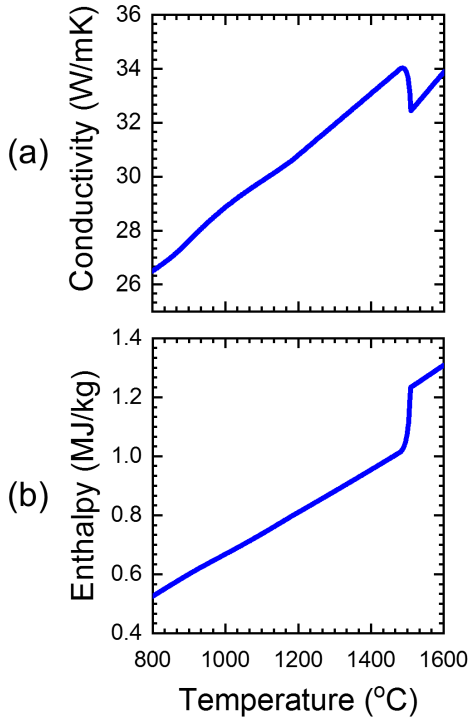


Figure 3.31: Thermal properties of 409L stainless steel: (a) conductivity and (b) enthalpy

Decreasing temperature leads to increases in density and elastic modulus as the crystal structure become more tightly packed and stiffer. In addition, as the steel changes phase from δ-ferrite to γ-austenite, and thus from body-centered-cubic to close-packed face-centered-cubic, the atomic packing fraction also increases, so the density further increases, as the lattice spacing becomes smaller. This is accompanied by corresponding decreases in the thermal linear expansion, which is inversely related to the cube root of the density at a given temperature.

3.10.7 Solidifying Shell Model Validation

In many solidification processes, such as the continuous casting of steel, one dimension of the casting is much longer than the others, and is otherwise unconstrained. In this case, it is quite reasonable to apply a condition of generalized plane strain (also called 2.5D model) in the long casting direction (z), and to solve a two-dimensional thermo-mechanical problem in the transverse (x-y) plane. It has been previously demonstrated how this condition enables a

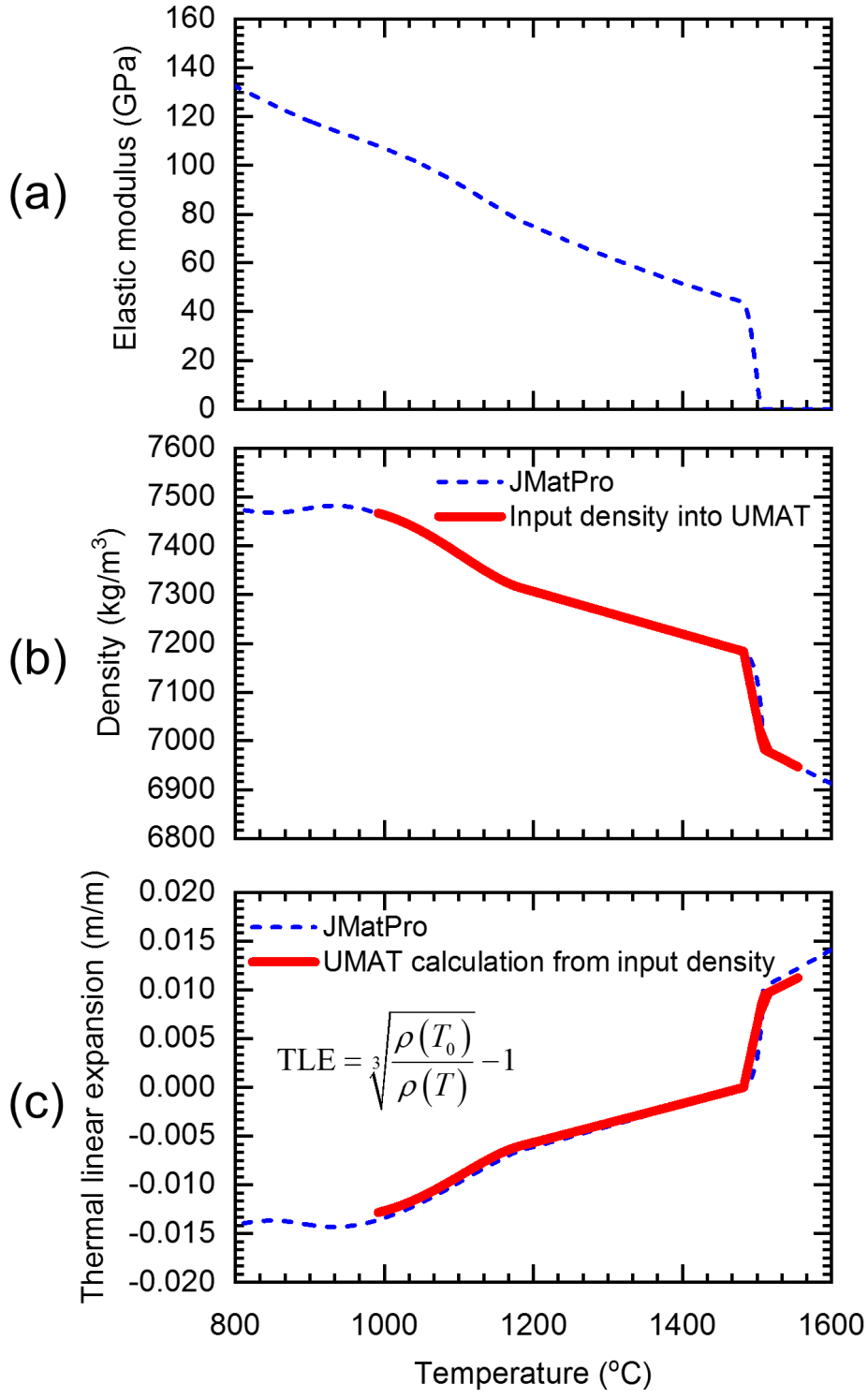


Figure 3.32: Mechanical properties of 409L stainless steel: (a) elastic modulus, (b) density, (c) thermal linear expansion

two-dimensional computation to accurately produce the complete three-dimensional thermal-stress state, so long as there is no axial bending, as in the case here[84].

A transverse Lagrangian generalized-plane-strain two-dimensional (2D) slice model is applied to simulate the solidifying steel shell in the slab mold during continuous casting, which travels down the mold at the casting velocity. This approach avoids unnecessary and computationally intensive calculation of the liquid behavior away from the mold wall. More importantly, it avoids non-physical mass conservation by enabling shrinkage of the un-modeled liquid region due to pushing fluid out of the slice.

A "1D-slice" shell model was used to verify thermal stress behavior in simplified conditions. This slice model is seen as a thin strip "drilled" into the solidifying shell, and assumes uniform solidification and full contact with the mold wall[95].

The strains during solidification are typically small (2%), but the capability to handle finite rotations is necessary to model some parts of the shell in a continuous-casting process.

3.10.7.1 Ferrite Mechanical Constitutive Model

For the δ-ferrite phase, a power law constitutive model proposed by [82], is implemented, as given in eq. (3.40). This model was fitted to match tensile-test measurements of plain carbon steel made by [94]. Figure 3.33 shows this ferrite model integrated within the relevant low strain range for a variety of constant temperatures and strain rates. For the same conditions, this phase is almost an order of magnitude weaker than austenite. As with the austenite model, the form of the ferrite model is also restrictive to accommodate kinematic hardening and the Bauschinger effect in reverse and cyclic loading, which increases the difficulty of fitting the model to the data. Compositions for all steel grades discussed in this work can be found in Table 2.

3.10.7.2 Austenite Mechanical Constitutive Model

For the austenite phase, a unified formulation proposed by [83] is used, which matches both the creep test data of [96] and the tensile test data measured by [80]:

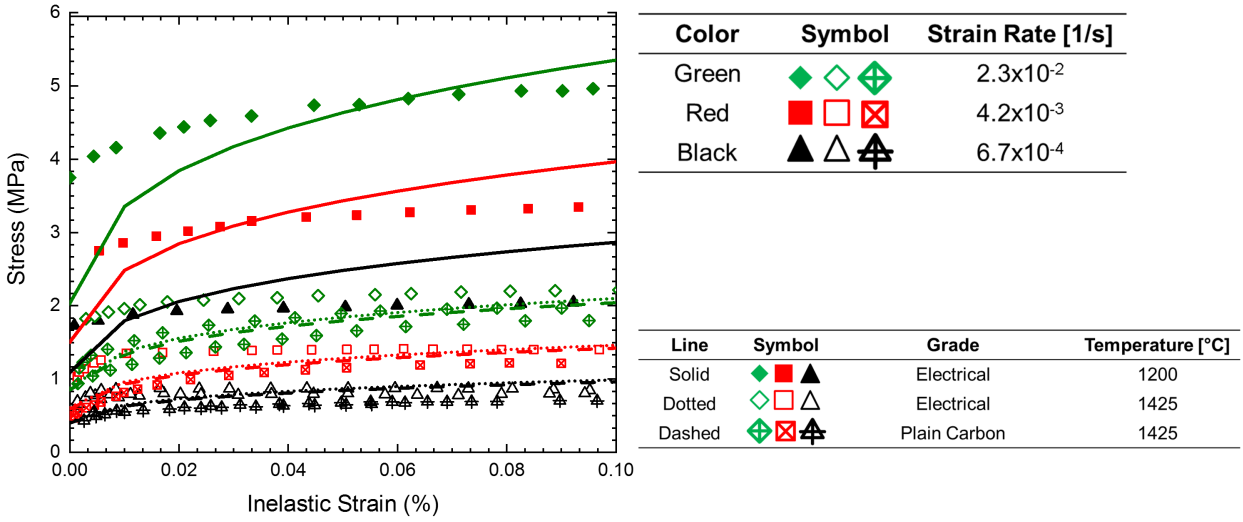


Figure 3.33: δ-ferrite constitutive model results for plain carbon steel (lines) compared with measurements (symbols) by [94] at 2 temperatures, and 3 strain rates, for two steel grades

$$
\begin{aligned}
&\dot{\bar{\varepsilon}}_{ie}[\mathrm{sec}^{-1}] = f_C\left(\bar{\sigma}[MPa] - f_1\,\bar{\varepsilon}_{ie}|\bar{\varepsilon}_{ie}|^{f2-1}\right)^{f3}\exp\left(-\frac{Q}{T[K]}\right)\\
&where:\\
&Q = 44,465\\
&f_1 = 130.5 - 5.128\times 10^{-3}T[K]\\
&f_2 = -0.6289 + 1.114\times 10^{-3}T[K]\\
&f_3 = 8.132 - 1.54\times 10^{-3}T[K]\\
&f_C = 46,550 + 71,400(\%C) + 12,000(\%C)^2
\end{aligned}
\tag{3.42}
$$

where Q is an activation energy constant, $\bar{\sigma}$ (MPa) is Von Mises effective stress, empirical functions f_1 ,f_2 ,f_3 ,f_c depend on absolute temperature K , and %C is carbon content (weight percent), which is one of the ways that steel grade (composition) is represented. [97] showed that eq. (3.42) allows an algorithmic approximation of kinematic hardening, where $\bar{\sigma}$ and $\dot{\bar{\varepsilon}}_{ie}$ are signed according to the largest principal stress and strain rate component respectively. They demonstrated reasonable agreement with some cyclic fatigue test data at high temperatures.

Originally fitted to tensile-test and creep data for plain carbon steel, Figure 3.34 compares the Kozlowski model III constitutive equation with data points measured for plain

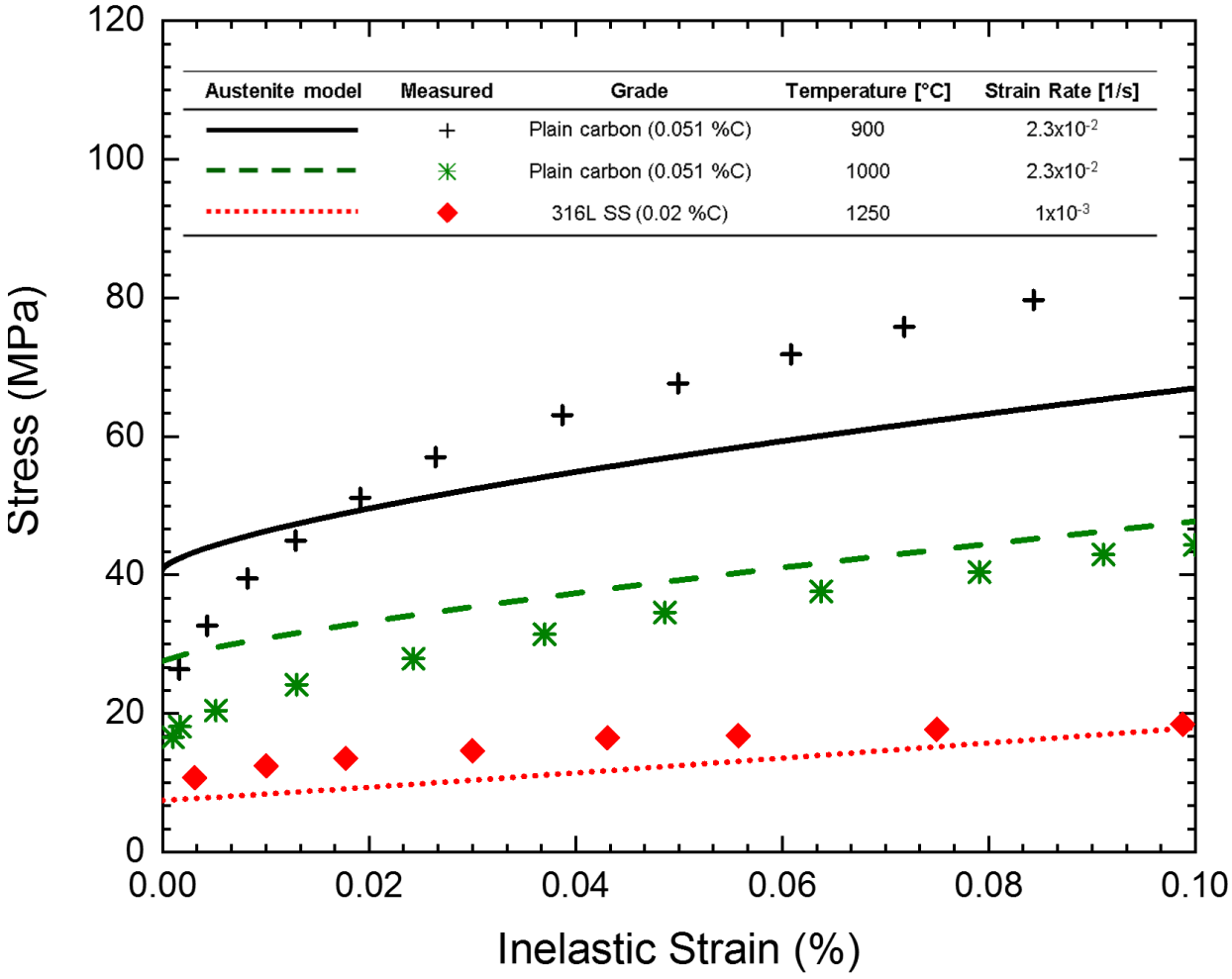


Figure 3.34: Austenite constitutive model for plain carbon steel (Wray, 1982) compared with stainless steel data

carbon steel at two different temperatures [80]. The form of this austenite constitutive model is rather restrictive to allow inclusion of realistic behavior during cyclic loading, such as kinematic hardening, the Bauschinger effect and other realistic behavior in cyclic loading.

3.11 Computational Considerations

The majority of this work was conducted on two different Dell T7900 series workstations both with 64GB of DDR3 SDRAM, Intel Xeon Silver 4110 2.1GHz CPUS and 32 cores. Depending on the exact conditions, the initial 30 s coupled model takes approximately 8 hrs to run. Including the crack model into the simulation adds extra expense and raises run time to approximately 12 hrs. The secondary cooling model, used to bring the domain down to "room temperature" for final shape analysis is substantially faster and takes only about 1-2 hrs. Due to the way that Abaqus handles subroutines, it would appear that parallelization of this particular implicit model is not as valuable as hoped. As long as the job does not get split across more than one machine (or node on HPC system) in general, speedups can be seen if the model is large enough. However, partially due to the necessary use of flags indicating flux layer solidification in the GAPCON subroutine, it was found that this model works best on standalone workstations with multiple cores sharing the same memory.

3.12 Summary

A series of numerical models have been developed to study the thermal-mechanical behavior of depression and crack formation behavior during steel solidification in the continuous casting mold. The models feature phase-dependent constitutive equations using elastic-viscoplastic constitutive models for the austenite, ferrite, and liquid phases during the solidification process, which are tightly coupled with phase fraction calculations, as well as with highly nonlinear temperature-dependent properties. A reduced order mold model has been implemented to predict the temperature response of the copper in far field conditions as well as near defects. Constitutive equations, which were originally fitted from data for plain carbon steel, are shown to reproduce tensile-test measurements for stainless steels as well,

so long as the phase, temperature, and strain rate are the same. While high temperature steel properties depend greatly on composition, the specific phase at a given temperature is the reason for this behavior. Using phase-specific constitutive equations is a sufficient and more convenient method to determine mechanical behavior of solidifying steel without the need for complete mechanical testing data in this difficult regime.

CHAPTER 4

3D THERMAL MECHANICAL MODEL OF SOLIDIFYING STEEL STRAND

4.1 Abstract

The thermal-mechanical behavior of a chunk of the strand in a thick slab caster is simulated from initial solidification to the end of the caster, including spray cooling and roll contact using a fully three-dimensional transient Lagrangian finite-element model. The model features efficient linearizations of phase-, temperature-, carbon content-, and strain-rate-dependent, constitutive equations; as well as temperature-dependent thermal properties. Surface temperature drops and tensile hoop stresses during spray region impingement, outer-radius tension during bending, inner-radius tension during unbending, and bulging between rolls are quantified. Slab corners are observed to experience higher stresses, due to their lower temperature producing higher strength, and provide extra mechanical constraints where the narrow and wide face shells meet.

4.2 Introduction

In harsh environments such as steel continuous casting, computational modeling is an important tool for process understanding and improvement. Thermal-mechanical models are important to understanding the formation of cracks, depression, and other related casting defects. Large scale and highly refined models are computationally expensive and difficult to validate, however, especially in three dimensions (3D). Lots of information can be obtained from simplified 2D models, as many previous works are. However, 3D models introduce the ability to explore more phenomena such as corner effects, stresses in the casting direction, and the complicated behavior in the bending and unbending regions. Some previous 3D models have focused on solidification in casters but with an emphasis on grain morphology as related to hot tearing [98]. Some models have used a combined 2D and 3D technique in multiphase simulations [99, 100], however these models are mostly relegated to the mold region and

neglect the rest of the caster. A small subset of work has explored bulging [42, 101–103] or unbending [104, 105] and a few studied both together [106–108]. Furthermore in many cases these are simplified or limited in dimension, domain, simulation length, or application. While many of these models have focused on stresses in secondary cooling, some have also explored the heat transfer in smaller scale models and laboratory studies[109–111]. The large models sometimes neglect much in the way of heat transfer from spray cooling and roll contacts making it difficult to study the effects of non-uniformities that can drastically affect the cyclic loading that the strand surface experiences [112]. Some recent 3D models have examined heat transfer and stress in a slab caster, but the stress calculation and solidification stress models were uncoupled [113]. Another focused specifically on individual sprays, heat transfer and solidification, but neglected stresses [114].

This work follows a 3D chunk of steel from its molten state, as it moves down through the caster, and experiences primary solidification in the mold, secondary cooling in the spray zones, along with interactions with the support rolls, bending and unbending, and bulging between rolls as a result of ferrostatic pressure. The model includes phase-, temperature-, carbon content-, and strain-rate-dependent, constitutive equations; as well as temperature-dependent thermal properties.

4.3 Model Setup

The 3D model of a thick slab caster was developed in LS-DYNA [115] using a combined Lagrangian and Eulerian reference methodology. In this methodology, the Eulerian domain of the caster (mold walls and support-roll surfaces) is fixed in space, which provides the mechanical contact boundary conditions for the Lagrangian domain of the strand chunk, which travels down through the caster at the typical constant casting speed of 1.04 m/min. As shown in Figure 4.1, the model includes a 2.4 m long chunk of the strand that is 1000 mm wide and 158 mm thick, assuming symmetry about the vertical centerplane through the strand thickness, so only half (500 mm) of the width is simulated. As the initial condition, the strand chunk is completely liquid, positioned above the meniscus level in the mold, as

shown in the second frame of Figure 4.1. This chunk travels down through the 0.8 m working mold length and 16 m of the secondary cooling zones.

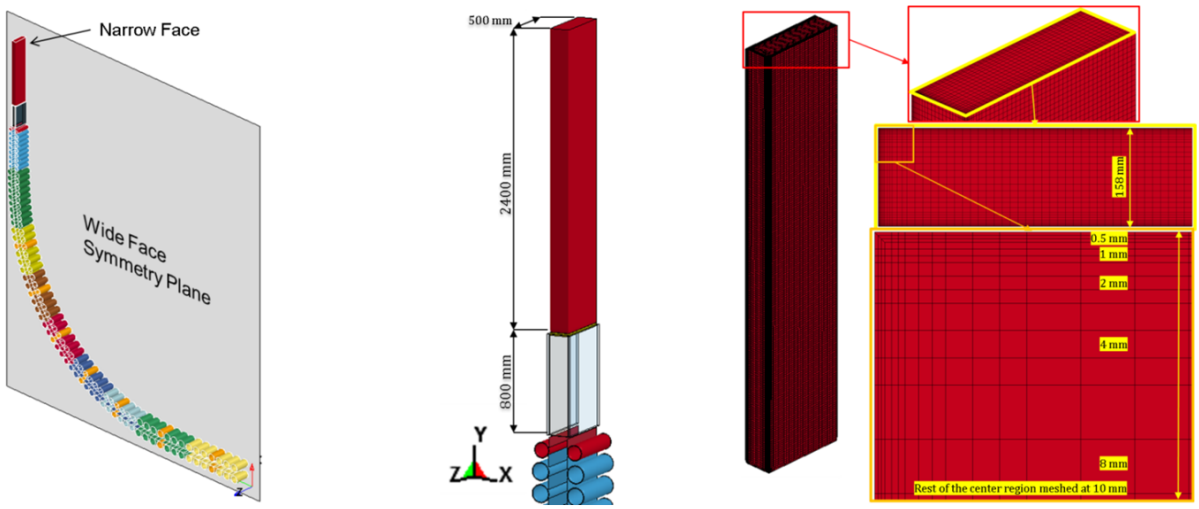


Figure 4.1: Computational model domain of half-caster showing rolls, chunk domain in initial position, and mesh

4.4 Thermal Boundary Conditions

The initial temperature of the entire strand is set to 1550°C, representing the pour temperature of molten steel entering the mold at the meniscus, as shown in Figure 4.2. Each node in the domain above the meniscus stays fixed at the pour temperature until the time when it enters the working mold region, at which time its temperature degree-of-freedom is enabled. The initial temperature of the dummy bar is set to 700°C. Heat transfer within the mold is imposed using thermal contact conductance and a fixed mold temperature of 200°C.

On mold exit, the strand domain enters secondary cooling zones and experiences alternating periods of: water spray / air mist cooling (convection), roll contact (thermal contact conductance), and slower, ambient-temperature cooling in the regions that are sheltered beneath the rolls (convection and radiation), as shown in Figure 4.3. The impacted spray water is held fixed at 25°C, the rolls are at 300°C, and ambient temperature is 40°C. In the model, spray cooling convection is applied at specific regions of the strand surface, according

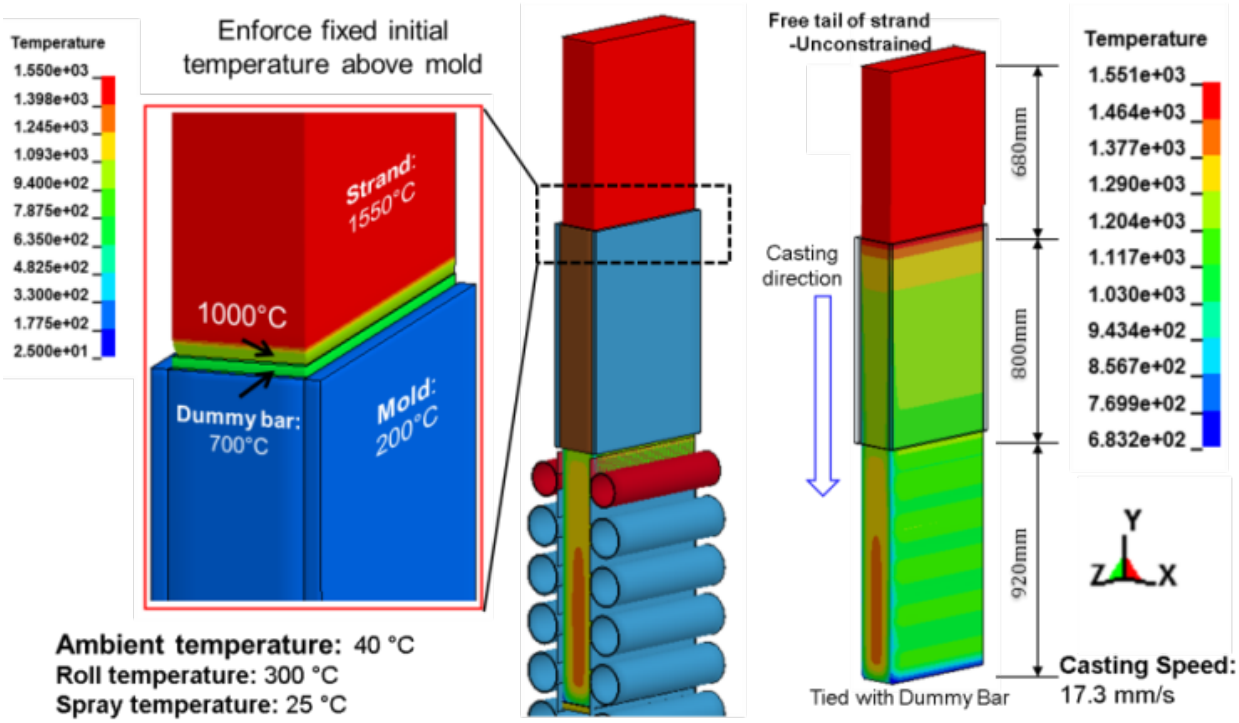


Figure 4.2: Thermal and mechanical boundary conditions of the model

to the estimated effective area of the impacted region beneath each spray nozzle. A meshed region was created for each effective spray area, which is fixed in space, and interacts only thermally, and not mechanically, with the chunk domain. That thermal interaction involves applying the convection of that particular spray to the adjacent portion of the moving strand surface, while it is within view.

4.5 Mechanical Boundary Conditions

The narrow face and wide face mold of the caster domain are vertical and held completely fixed in both space and time. Taper is not applied in the mold. Below the mold, machine taper and changing caster radii, including straight and curved segments for bending and unbending are all applied by fixing the locations of the roll surfaces, based on the caster geometry. Individual rolls are held fixed from translation but are allowed to freely rotate around their center. In this preliminary work, all rolls thus are treated as support rolls and not drive rolls, which may affect the axial stresses. The outside surface of each roll is

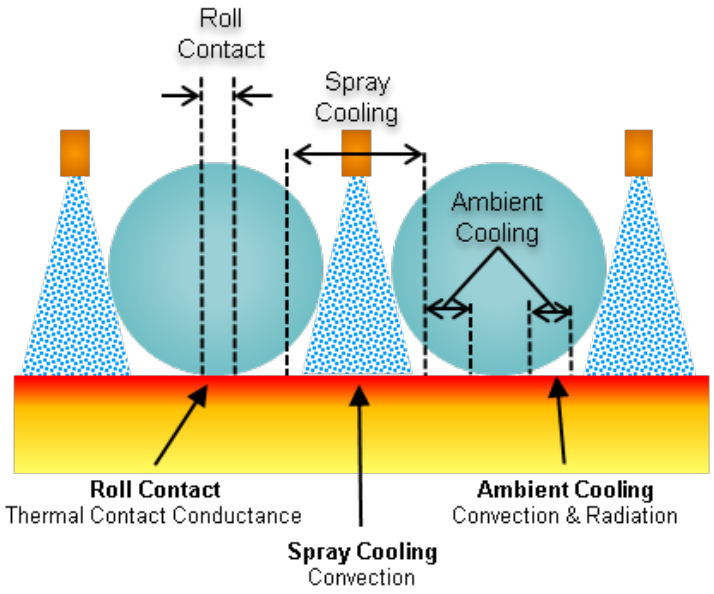


Figure 4.3: Secondary cooling segment schematic

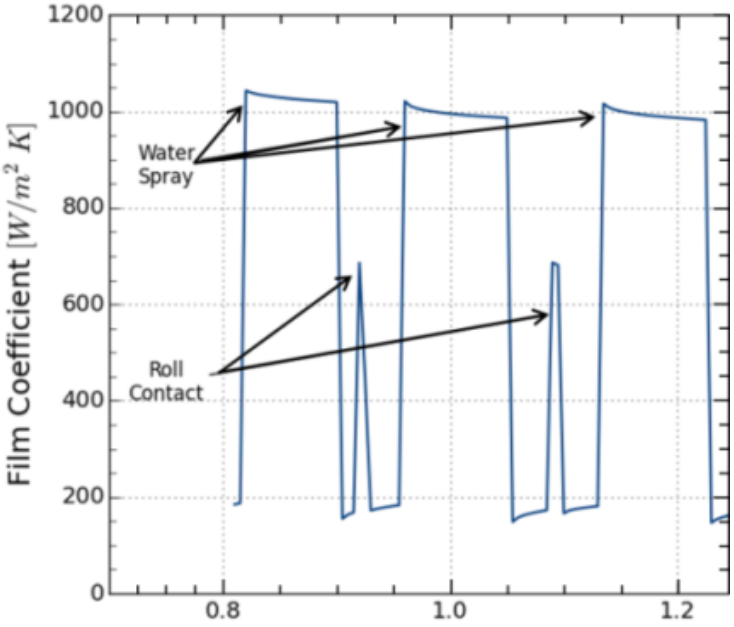


Figure 4.4: Heat transfer behavior during roll contact and water sprays in secondary cooling

allowed to contact the surface of the strand chunk without penetration. To reduce computational complexity, rolls on the inner and outer radii were only given contact constraints with their corresponding strand surface (*i.e.* inner radius rolls only "see" the inner radius strand surface).

The dummy bar follows a predefined path down the caster at the casting speed of 17.3 mm/s to pull and guide the strand at the correct orientation for steady casting. The dummy bar and strand chunk travel together down the caster through the vertical mold section, bending and unbending, and horizontally out of the caster. The position of the dummy bar at a given time is fixed, based on the casting speed and non-linear arc length calculations based on the caster geometry. Nodes on the bottom of the strand domain are attached to corresponding nodes on the dummy bar domain surface, using "tie constraint" equations. Each node of the strand bottom and dummy bar top surfaces is given an individual local coordinate system, in order to constrain only the degrees of freedom in the casting direction. This enables the large rotations of the strand chunk as its orientation changes, due mainly to rigid body motion, as it moves through the caster during the simulation. This is equivalent to a mechanical symmetry condition applied to the bottom surface of the chunk domain, keeping this planar section perpendicular to the casting direction at all times.

In contrast to the special set of constraints at the strand bottom surface, the top surface of the chunk domain is unconstrained (zero force boundary condition). This allows the entire chunk domain to deform (e.g. liquid to be squeezed in and out) and thus prevents non-physical mass conservation of the domain. These constraint conditions are critical to achieving reasonable mechanical behavior and stress results from the simulation.

4.6 Material Properties

During solidification and cooling in this process, the thermal-mechanical properties of the steel vary considerably with temperature and additionally, constitutive models are needed to convert between stress and strain. Material properties such as density, elastic modulus, thermal conductivity, enthalpy, and specific heat are taken from previous work [41]. In

this work, an elastic-plastic formulation was adopted, using stress-strain curves for each temperature and phase (liquid, delta-ferrite, austenite) that are strain-rate dependent.

Three different constitutive models were used to define the constitutive property data, based on the three phases of steel, liquid, delta-ferrite, and gamma-austenite. Liquid was modeled as an elastic perfectly plastic weak solid with a yield stress of 10 kPa. For ferrite, the Zhu-power law model was used [17], and for austenite, the Kozlowski model III was used [83]. Examples of the constitutive data are plotted in Figure 4.5 and Figure 4.6, for a variety of strains, strain rates, and temperatures, of both solid phases. This model uses a stress-strain form of the constitutive behavior rather than the inelastic-creep type formulation used in prior work [41] but produces similar results.

For a model of this size, efficiency is critical, to help ease the computational difficulty and solve time. Thus, the thermal and mechanical material properties used in this work are a tabular version of data generated from the equations given in previously validated modeling work [41]. Using tables with discrete data for a variety of strains, strain rates, and temperatures LS-Dyna interpolates between the values to find the relevant property. The simulation presented in this work involved a 700,000 node finite-element mesh of 3D thermal-mechanical brick elements, and was solved with LS-Dyna on a workstation computer in $\sim$3 weeks.

4.7 Results and Discussion

4.7.1 Model Validation

Temperature results from the model are shown in Figure 4.7 to Figure 4.9. The temperature profile down the caster, the shell growth profile, and the metallurgical length all match remarkably well with prior calculations for the same caster, which was previously shown to match with plant measurements [112].

Stress profiles taken at the WF centerline (symmetry plane) are shown in Figure 4.9 and match both qualitatively with accepted solidification stress behavior [85] and quantitatively with previous work using simplified slice models of similar composition and conditions [15,

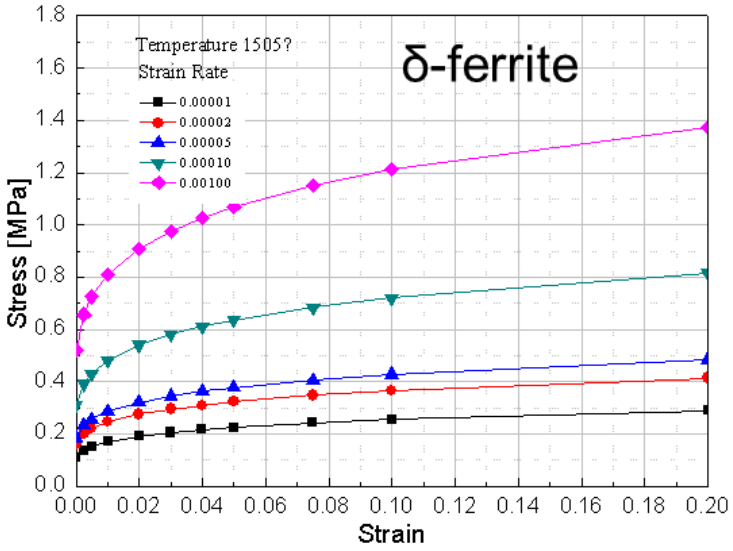


Figure 4.5: Example constitutive behavior for δ-Ferrite over a variety of strain rates at 1505°C [17]

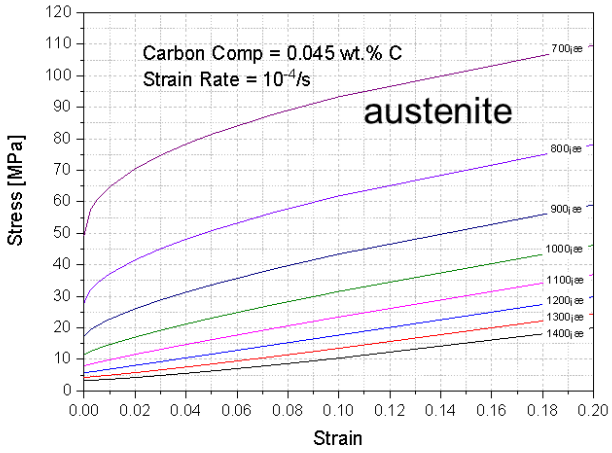


Figure 4.6: Example constitutive behavior for γ-Austenite over a variety of temperatures at a strain rate of 10^{-4} [17]

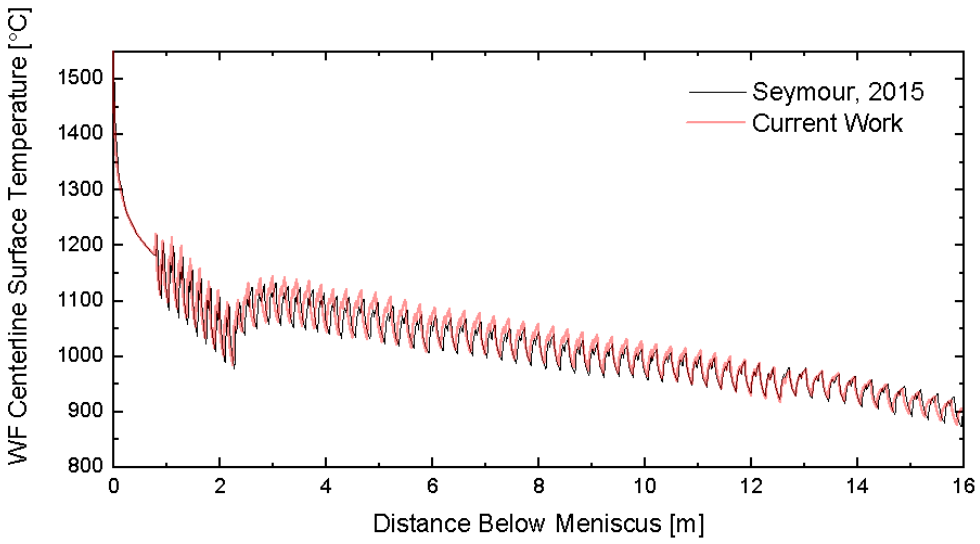


Figure 4.7: Surface temperature variation down the caster, comparing current 3D model with previous work [112]

41, 112].

4.7.2 Initial Solidification in the Mold

Thermal-mechanical behavior in the mold is important to subsequent behavior below the mold and surface crack formation. As discussed in previous work [41], fast cooling of the shell surface generates a brief period of tensile stress during early solidification in the mold. As the shell continues to grow, internal cooling and shrinkage accompanied by slower cooling of the surface then causes compressive stress at the surface, increasing to tension towards the solidification front, and dropping to zero in the liquid. This well-known behavior [41], can be observed in Figure 4.9 and Figure 4.10. Figure 4.10 shows that the hoop stress (tangential to the strand surface) increases to over 5 MPa in tension before dropping to ∼10 MPa in compression. The second tensile peak is likely due to the shrinkage that accompanies a temporary increase in surface cooling at ∼150 mm below the meniscus. This confirms the sensitivity of the hoop-stress condition at the surface to surface cooling conditions, as reported in recent work on stainless steel using a 2D transverse slice model [17].

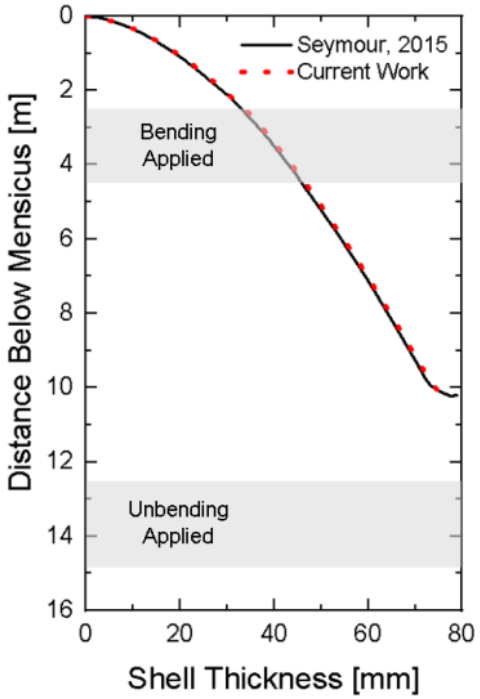


Figure 4.8: Shell growth profile from current 3D model compared to previous work [112]

4.7.3 Spray Cooling and Rolls

Temperature results in Figure 4.7 show that the strand surface exits the mold just under 1200°C. The narrow faces then experience prolonged reheating before persistent continuous cooling again (the modeled typical caster does not have NF sprays). As a result of 2-dimensional cooling, the corners are the coldest region around the strand perimeter at any given distance below the meniscus. The wide faces then experience some slight reheating before the first spray zone. This is followed by periodic fluctuations in surface temperature as the strand surface passes beneath the rolls and sprays, which remove substantially more heat than the sheltered regions in between, as shown in Figure 4.3 and Figure 4.4. Visible in Figure 4.7, detail of these fluctuations are shown in Figure 4.12a. The spray cooling regions exhibit the largest cooling and lowest surface temperatures, while the adjacent regions (rolls and ambient) experience reheating.

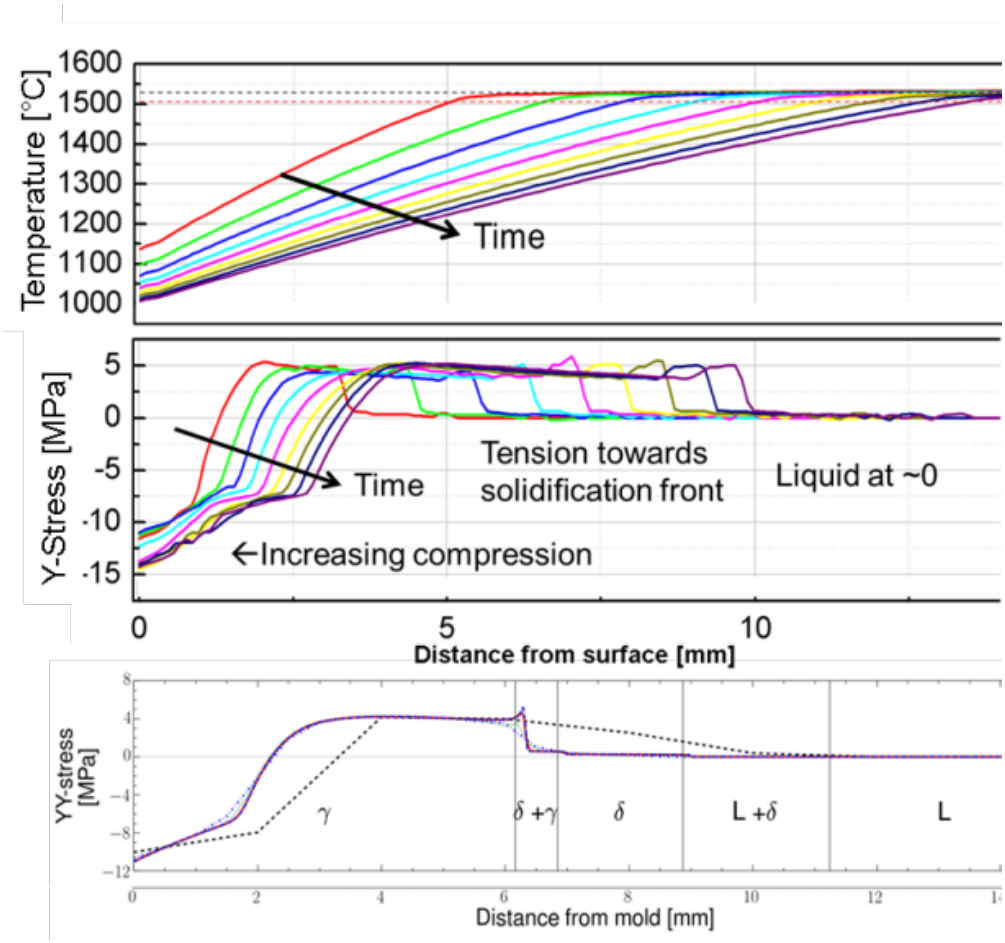


Figure 4.9: Temperature and hoop stress through the strand thickness from current 3D model at several times, compared with previous work (bottom) 10 seconds below meniscus with lines to show phases [41]

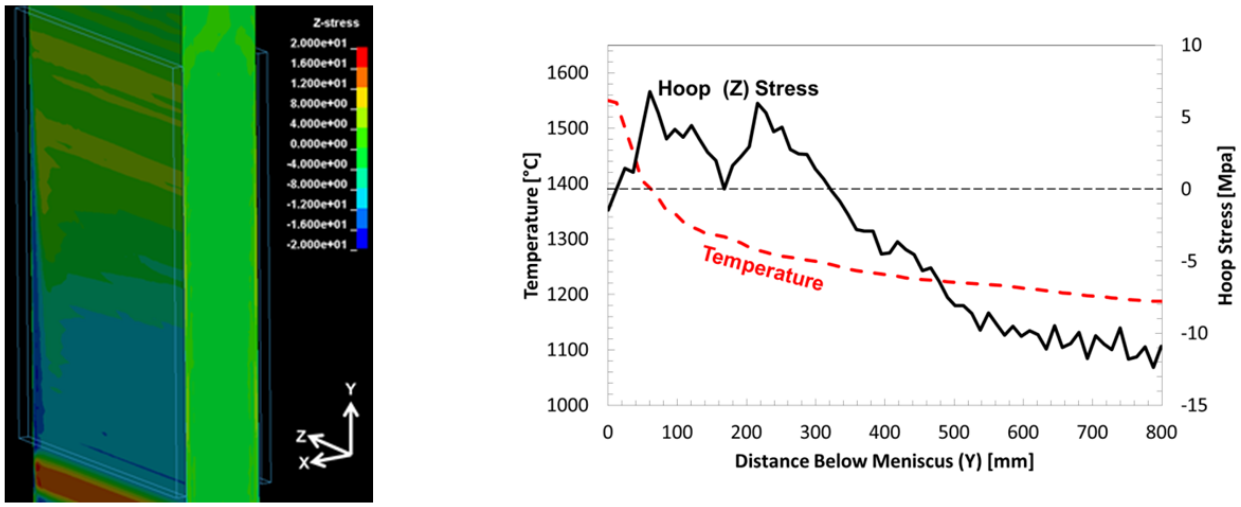


Figure 4.10: Wide face centerline surface hoop (z) stress (MPa) and surface temperature history in the mold

As temperature changes are the cause of thermal stress, the hoop stresses are seen in Figure 4.12b to fluctuate according to the spray cooling, roll contact, and in-between regions. As described in the previous section, the strand surface exiting the mold is in compression. Sudden cooling of the strand surface by the sprays causes local contraction of that portion of the surface. Mechanical constraint by the surrounding hotter surface and sub-surface opposes contraction, so the result is tension beneath the sprays in both the casting direction and strand circumference (hoop) directions, as shown in Figure 4.11a and Figure 4.12b. Complementary compression is induced beneath the sprayed region of the strand surface, as well as a slight decrease in the tension near the solidification front. Figure 4.12b shows that the tensile hoop stress resulting from the sprays is approximately 15 MPa, prior to bending, with the magnitude increasing with distance below mold. This behavior has been noted in previous work [103], [112]. The qualitative behavior of alternating tension and compression with and without sprays is present throughout the roll containment portion of the caster with increasing magnitude with distance below the mold.

Figure 4.13 shows the through-thickness-stress (X-Stress) through the thickness of the strand, prior to bending. This stress is only significant near the corners and on the narrow

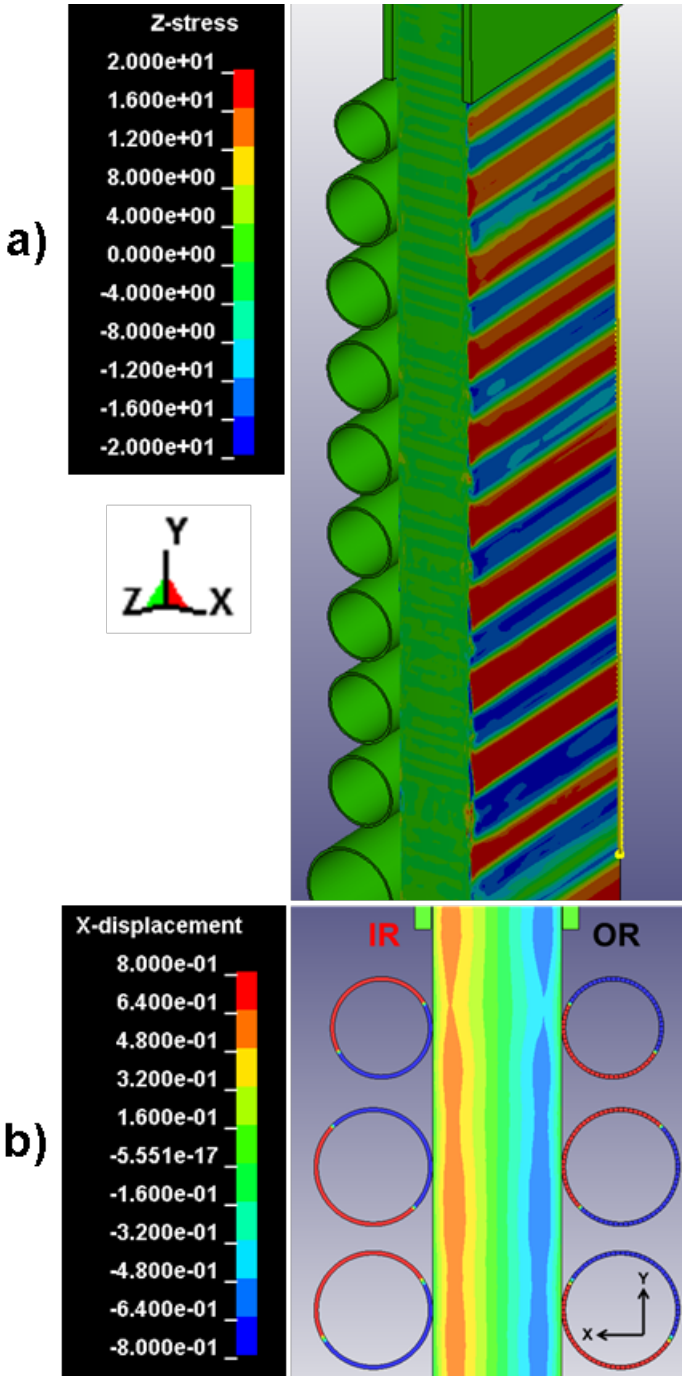


Figure 4.11: a) Hoop (z) stress (MPa) on the inner radius after mold exit and before unbending, b) Bulging displacement (mm) at wide face centerline between the first 3 support rolls below the mold

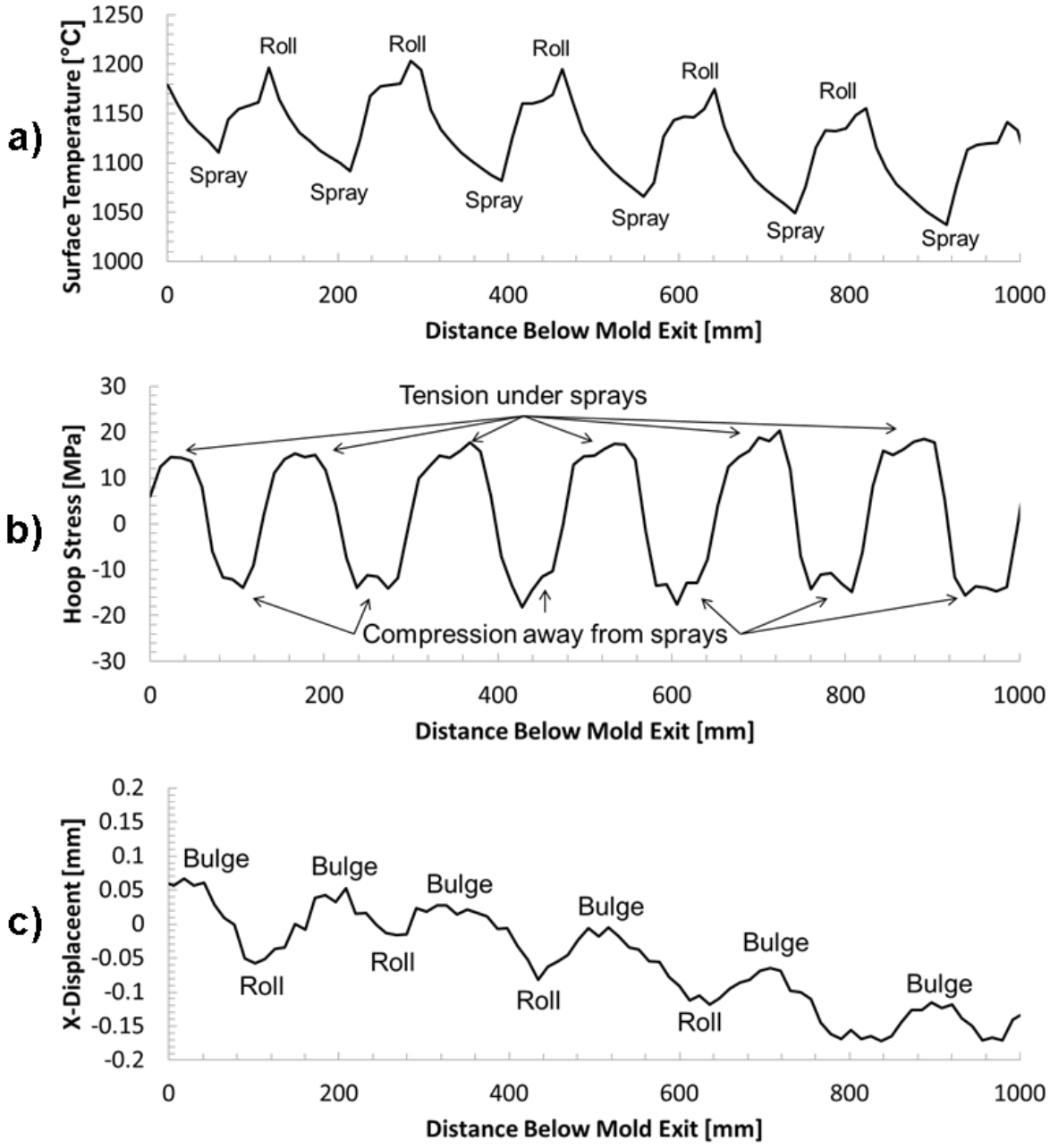


Figure 4.12: Wide face centerline results at the surface of the inner radius (marked with yellow line: a) Surface temperature, b) Hoop (z) stress, c) Bulging (X) displacement of the inner radius

face. Figure 4.13a shows that this X-Stress reaches a peak compressive stress directly under each roll right at the corner region. The corresponding stress plot at the wideface centerplane, Figure 4.13b shows negligible through-thickness stress, as the liquid interior provides no resistance to deformation.

The high stresses in the narrow face, Figure 4.13a, are caused by the machine taper in this upper portion of the caster being slightly too large and squeezing the strand. While the low (ambient) temperature of the rolls, and their accompanying cooling, shrinkage, and tension-generating effects [112], are included in the model, the mechanical squeezing effect of the rolls was larger in this case. Tension is also observed in the regions surrounding the compression to balance out the forces, these tensile regions may be prone to corner cracking depending on the temperature history of the strand and the brittle temperature regions of the grade being cast. As the coldest part of the slab, the corners experience the highest stresses during the casting process. The narrow faces also experience high stress because of improper machine taper which has the potential to cause unnecessary extra difficulties such as premature roll wear, shape problems and off-corner cracking.

4.7.4 Bulging

Bulging occurs in continuous casting as the internal ferrostatic pressure from the molten core pushes the solid shell outwards against the constraint of the support rolls in the caster. Deformation outwards between rolls increases when the shell is hot and thin, the roll spacing is too large, or if there is roll misalignment. Bulging can lead to many quality problems including unstable mold level fluctuations, transverse cracking, segregation, as well as undue stress on the containment portion of the caster. Bulging is observed between rolls on most of the wide face shell, away from the corners which mechanically constrain the edges of the WF from bulging. As seen in Figure 4.11b and Figure 4.12c, bulging between the first 3 support rolls is only $\sim$0.15 mm. This is due to the efficient use of small-diameter, split-rolls in this caster, which enable a small roll pitch. There is some bulging present in the mold, as this model does not include any taper of the wide face coppers. However, machine taper of the

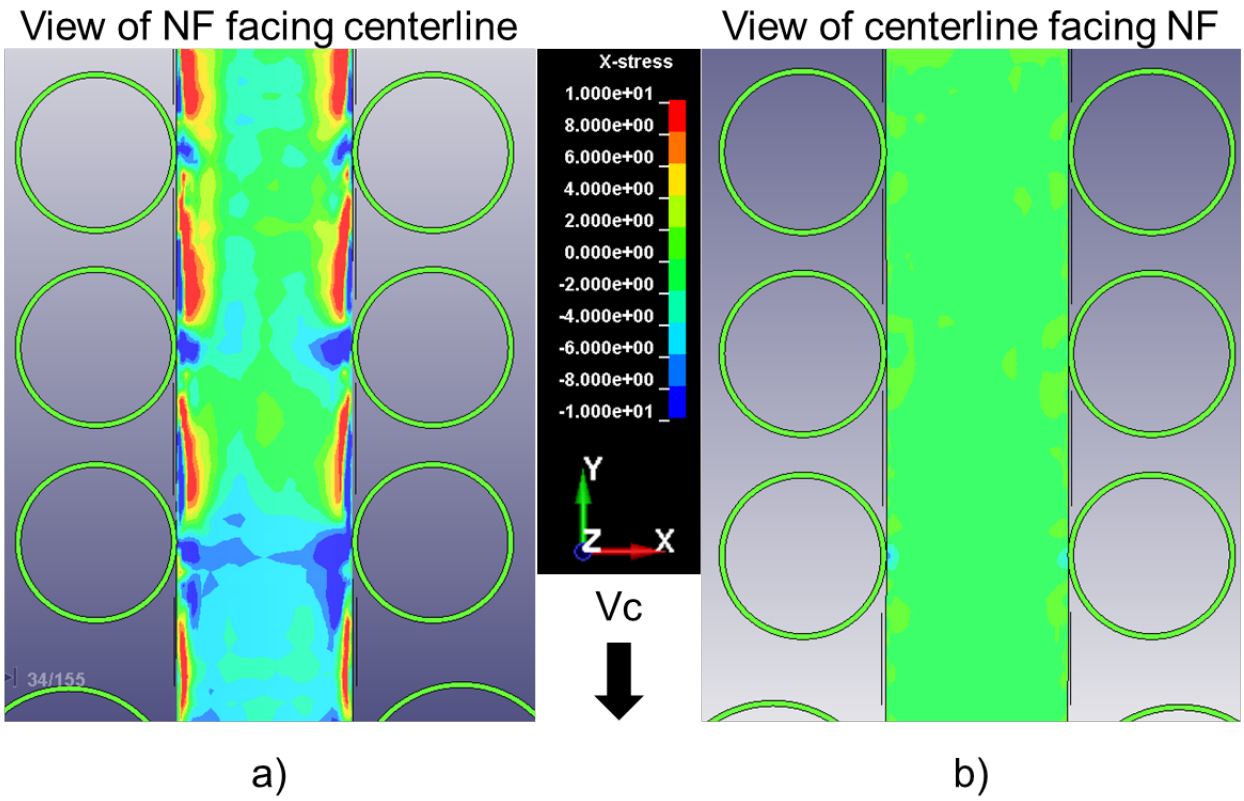


Figure 4.13: Through-thickness x-stress contours (MPa): (a) on narrow face and (b) through centerplane before bending

rolls down the caster is included, which causes the general downward slope of Figure 4.12c. Recall that the machine taper in this caster caused the through-thickness stress observed in Figure 4.13.

4.7.5 Bending and Unbending

The strand in this vertical-mold caster experiences multipoint bending into the constant radius of the caster arc, followed later by unbending after the entire strand has solidified. This introduces complex stress states to the strand, which are captured by the 3D model. During mechanical bending of the 4-sided box-shaped solid shell with its liquid core, the shell on the inner radius of the wideface is forced into compression, with corresponding tension generated in the outer radius shell. These stresses are highest in the casting direction, as expected from Euler-Bernoulli beam behavior. These casting-direction stresses are shown in Figure 4.14 through the strand thickness at the wide face centerline. The results from a previous 2D model with a highly refined mesh (a) and the current 3D model (b) show that this mechanical effect generally dominates over the superimposed alternating tension and compression experienced by the shells on the inner and outer radius, due to the alternating surface temperatures caused by the sprays and rolls. The central liquid region naturally remains at nearly zero stress. Note that there are also some minor variations in the stress profile caused by the marginal mesh resolution of the current 3D model.

Unbending is experienced later by the strand, after moving through the constant-machine-radius majority of the contained region of the caster. Note that as the strand orientation changes from vertical during bending to horizontal during unbending, the casting-direction stress changes from Y to X. Figure 4.15 shows casting direction (X) stress through the thickness at the wide face centerline during unbending, again for the previous model (a), and the current work (b) which again show a reasonable qualitative match. As expected from beam theory, the stress profile reverses to compression near the outer radius and tension near the inner radius. At this time, the strand is completely solid in this caster, so the stresses are expected to be higher, as the results show, and they generally increase continuously from

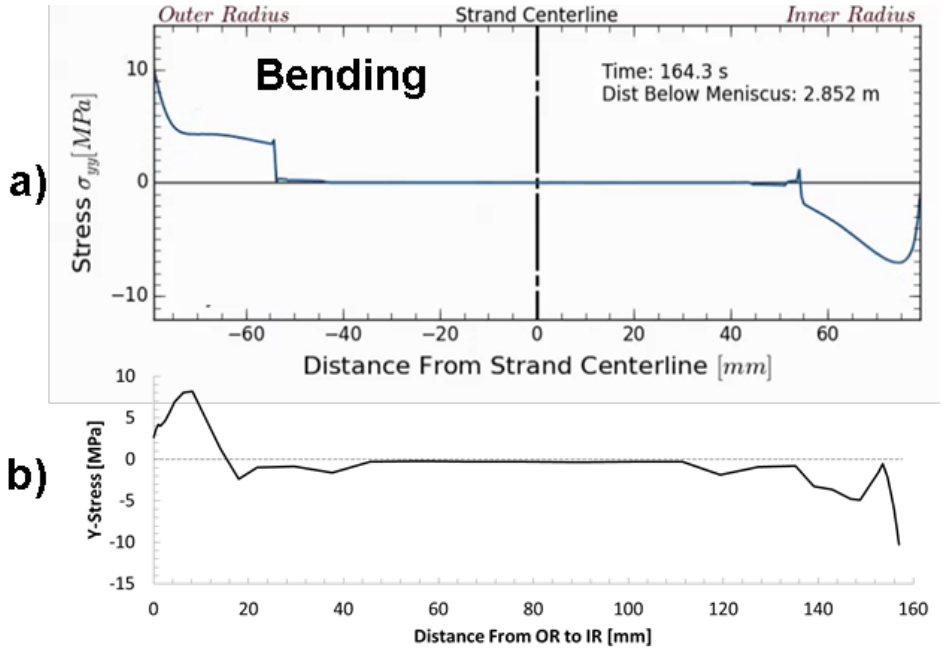


Figure 4.14: Casting direction (Y) stress through the thickness at the wide face centerline during bending (with a liquid core): a) From a previous 2D model [112] b) From the current 3D model

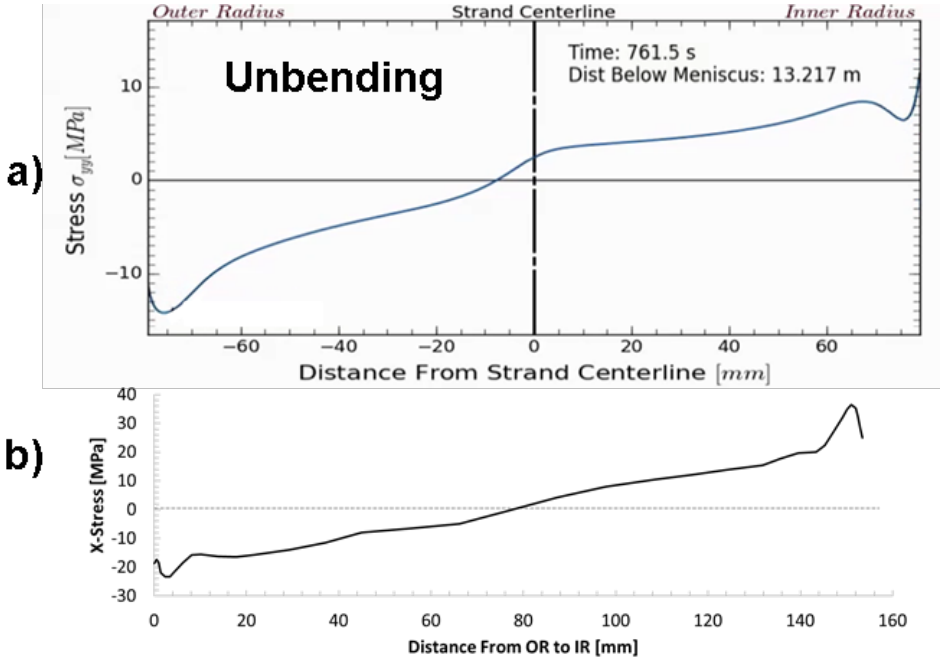


Figure 4.15: Casting direction (X) stress through the thickness at the wide face centerline during unbending (with a solid core): a) From a previous 2D model [112] b) From the current 3D model

compression at the outer radius towards tension at the inner radius. Local stress very near to the strand surfaces jump sharply between tension and compression according to the local condition of cooling or reheating at the strand surface. Figure 4.16 and Figure 4.17 show hoop (Z width direction) stress at the wide face centerline, underneath and away from a spray, during bending and unbending respectively. The tension induced by the rapid cooling from sprays is enough to completely reverse the stress behavior and drive the surface of the strand into tension. Note that tension developing beneath the sprays at the surface in the width direction (Z-stress in Figure 4.17) is higher than in the casting direction (X-stress in Figure 4.15). This is because the fan-shaped sprays cause a wider region of the strand to shrink in the width direction.

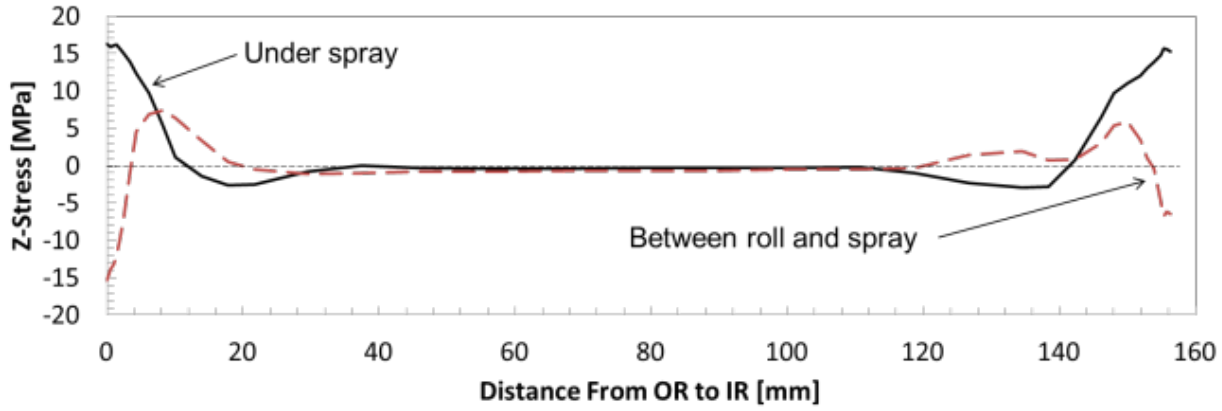


Figure 4.16: Hoop (z) stress through the thickness at the wide face centerline during bending under a sprayed and unsprayed region

The effect of bending and unbending on casting-direction stress development at the narrow face surfaces is shown in Figure 4.18 to Figure 4.21. Generally, the behavior matches expectations for bending and unbending a single beam with a solid core: the inner radius gets compressed and the outer radius experiences tension during bending; and the opposite occurring during unbending. However, the distribution of these stresses is slightly more complicated, especially near the corners, owing to the additional effects of the alternating tension and compression from the spray cooling regions, and the local compression beneath

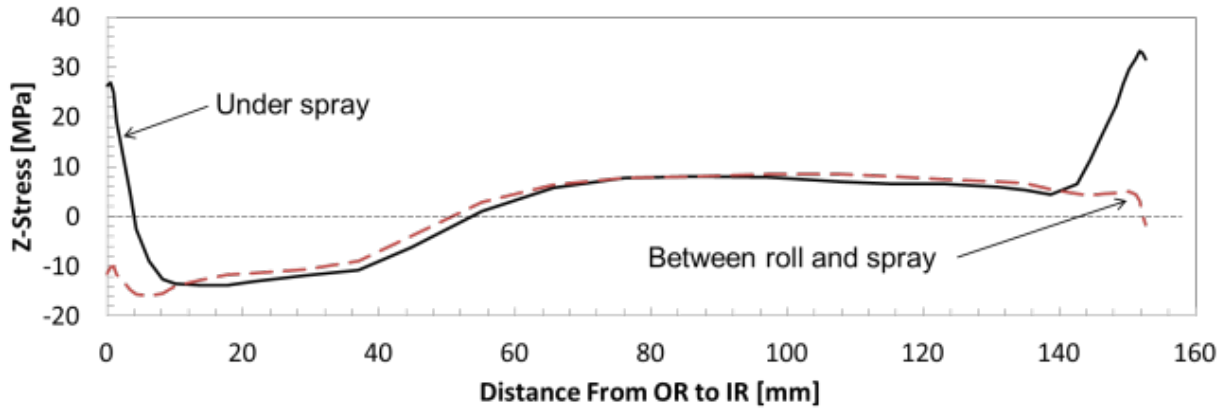


Figure 4.17: Hoop (z) stress through the thickness at the wide face centerline during unbending under a sprayed and unsprayed region

the rolls due to squeezing from the machine taper.

Due to the lower temperatures, as well as the extra constraint, the narrow faces experience higher stresses than the center, especially during bending. This can be seen by comparing the magnitudes of the casting direction stress at the narrow face in Figure 4.19 with the corresponding magnitudes at the centerline in Figure 4.14. In bending, mostly symmetrical compressive stress is observed near individual rolls with the peaks found on either side of the roll contact.

The stress in the casting directions at the narrow face during unbending experiences much higher tension on the inner radius and compression on the outer radius. Again, the magnitudes of the casting direction stress at the narrow face, Figure 4.21, are substantially higher than that at the centerline, Figure 4.15. The tensile stress on the inner radius is centered around the second roll of the unbending section, as shown in Figure 4.20, which suggests that most of the work of unbending is being accomplished by the first two rolls in the segment.

Bending and unbending also affects the shape of the strand. During casting, the entire strand is trying to shrink towards the center of the cross section. This is shown for the width direction in Figure 4.22, where both corners (at the narrow face) are observed to shrink

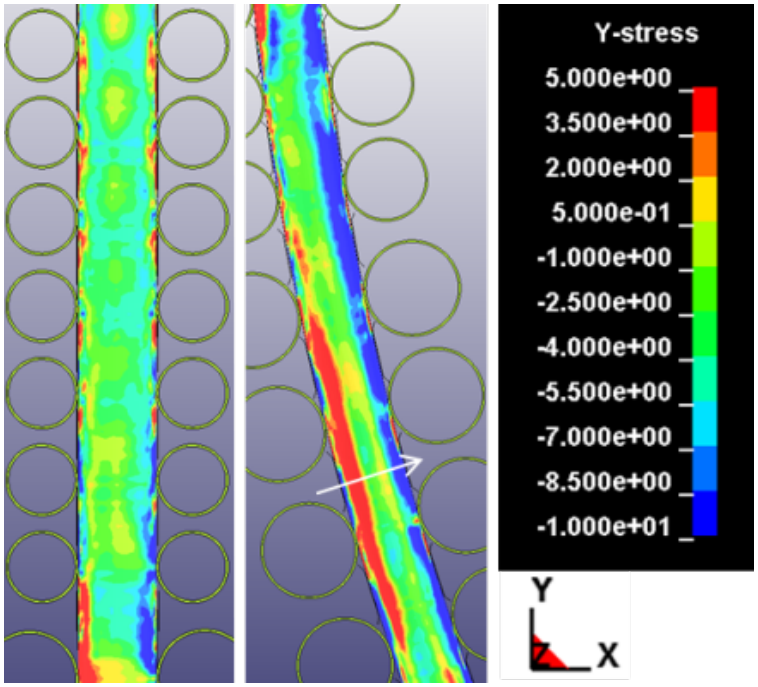


Figure 4.18: Casting direction stress on the narrow face just before and during bending

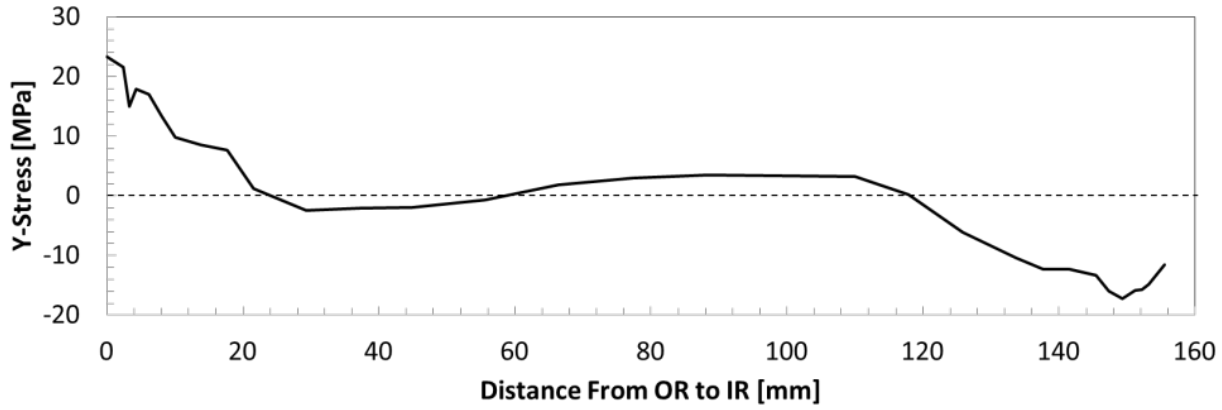


Figure 4.19: Casting direction stress through the thickness along the narrow face surface during bending (indicated by white arrow in Figure 4.18)

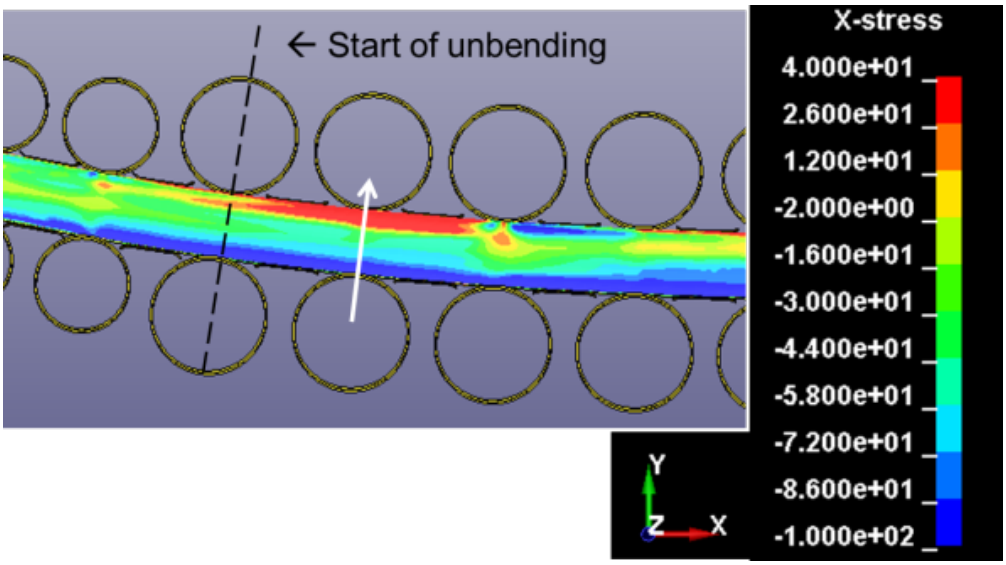


Figure 4.20: Stress in the casting direction on the narrow face during unbending

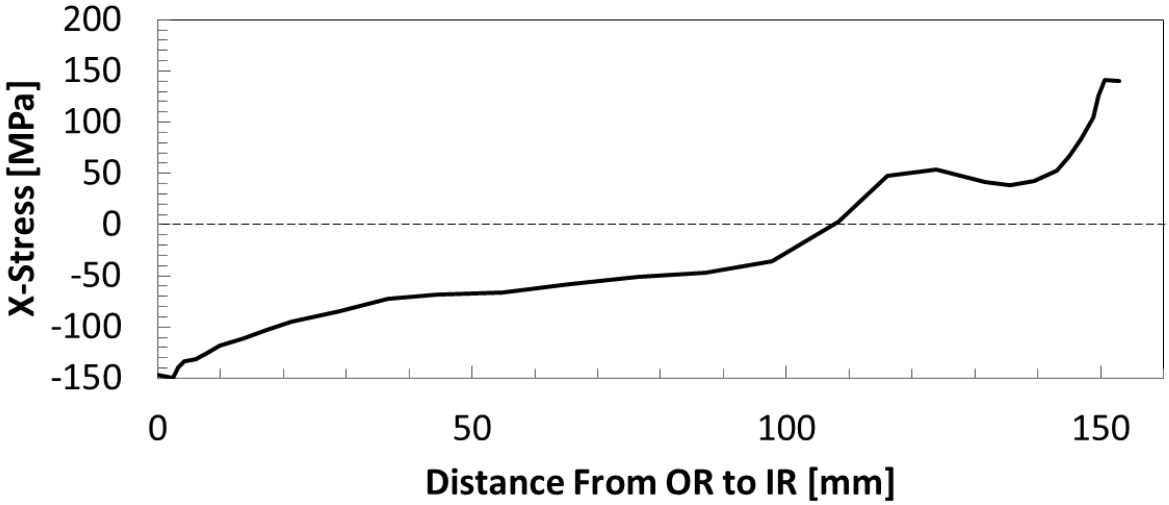


Figure 4.21: Stress in the casting direction through the thickness at the narrow face surface during unbending (indicated by white arrow in Figure 4.20)

(negative displacement). The inner and outer radii behave differently, however. During bending, as the inner radius surface is being compressed in the casting direction, it tries to expand in the width direction, in an attempt to conserve volume (surface area). At the same time, as the outer radius is stretched in the casting direction, it consequently shrinks slightly in the width direction. This deformation results in a trapezoidal cross sectional shape (wider inner radius) as the strand attempts to conserve volume. The accompanying contribution of this behavior to the width-direction hoop stress appears to be less than the effect of the sprays. Finally, during unbending, the trapezoid shape tries to reverse with the opposite behavior: contraction of the strand inner-radius width and expansion of the outer radius. Owing to the strand being totally solid, this only partially occurs, and a slight trapezoidal shape remains in the final slab. The accompanying result of this unbending effect does lead to a general reversal of stress in the strand interior, as Figure 4.17 shows compressive hoop stress towards the outer radius and tensile hoop stress towards the inner radius.

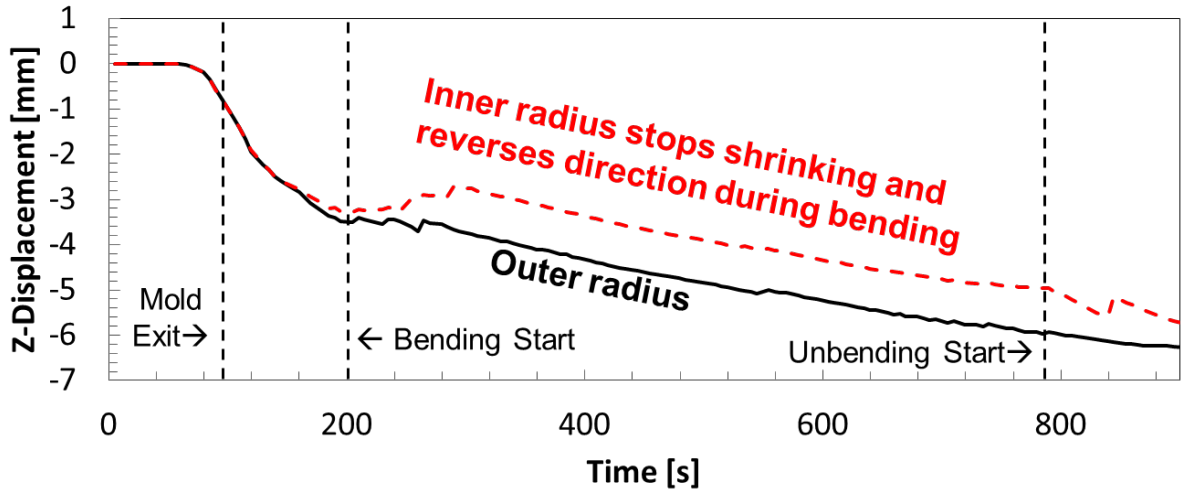


Figure 4.22: Width-direction shrinkage towards the WF centerline (Z-displacement at the corners)

4.8 Conclusions

A fully three-dimensional transient Lagrangian thermal-mechanical finite-element model of the entire continuous slab casting process has been developed using LS-Dyna. The model has been applied to simulate the behavior of a 2.4 m long chunk of the strand in a typical thick slab caster from initial solidification in the mold, through secondary cooling and containment, past final solidification at the metallurgical length, and includes the effects of spray cooling, bulging between rolls, bending and unbending, machine taper, and other important phenomena. Relevant results of the model are compared to previously conducted 2D work [112] and found to match quite well qualitatively with predictions.

The model results illustrate the surface temperature drops, and the accompanying shrinkage and tensile hoop stresses that develop as periodic bands across the wide-face surfaces due to spray water impingement, and the corresponding compression bands that arise in the unsprayed regions near roll contact. The outer-radius tension during bending, inner-radius tension during unbending, and bulging between rolls are also simulated. The strand corners experience the highest stresses due to their lower temperature (higher strength) and more mechanical constraint form surrounding material. Squeezing due to machine taper generates slight compression peaks beneath regions of roll contact, but only near the narrow faces when there is a liquid core. During bending, the strand exhibits beam bending behavior, with tension on the OR and compression on the IR, with the opposite trends appearing during unbending with substantially higher magnitude. It is also found that on bending, the shape of the cross section of the strand changes from a rectangle into a trapezoid with a wider inside radius, which persists past final solidification and unbending. It is also seen that each segment has a characteristic stress behavior related to the configuration of the water sprays and the rolls.

4.9 Future Work

This model is a first attempt to include the important phenomena that govern thermal-mechanical behavior in the entire continuous-slab casting process into a single comprehensive model. Much future work and analysis is needed, however. The quantitative accuracy of the current model is limited by mesh discretization issues, as the element size is too coarse. In addition to improving mesh refinement, the length of simulated chunk should be increased, in order to simulate stress evolution properly through startup to steady-casting conditions. Exploring novel operational practices such as compression casting is possible with this type of model and is intended as future work already underway. The model has great potential to study important phenomena, including bulging based on roll pitch and segment length, soft reduction practices, steel grade effects, and extending the model to investigate crack formation, segregation, and other issues that affect steel continuous casting.

4.10 Acknowledgements

The authors wish to thank the members of the Continuous Casting Center at the Colorado School of Mines as well as The China Scholarship Council (No.201606465036) for providing financial support. Additionally, the authors would like to acknowledge the contribution of Nathan Seymour for his 2D modeling work on this topic.

CHAPTER 5

TATA STEEL CASE STUDY

Cracks and depressions in steel continuous casting often start during initial solidification in the mold and evolve later in the process. To understand the mechanism(s) of formation of these defects, a finite-element model of transient thermal-mechanical behavior during steel solidification has been developed and applied to simulate longitudinal depressions. The thermal model features a detailed analysis of heat transfer across the interfacial gap, which is fully coupled with a thermal-mechanical elastic-viscoplastic finite-element model that calculates the evolving size and shape of surface depressions. The results are compared with analysis of a sample with a longitudinal surface depression and crack from a commercial continuously cast slab. In this scenario, a thermal event caused a local drop in heat transfer, followed by frictional tension on the domain due to slab shrinkage, led to shell necking and the formation of a localized U-shaped depression. Finally, a new visualization methodology has been developed to better reveal defect formation in real time, such as longitudinal depressions, which persist as they move down the mold at the casting speed.

5.1 Introduction

Quality during continuous casting is greatly affected by heat transfer across the interfacial gap between the copper mold walls and the steel strand, which governs initial solidification of the steel shell and the formation of surface cracks and other defects [41, 95, 116]. Previous work has shown that cracks correlate with high and/or variable heat flux in the mold, especially near the meniscus region [117]. Thus, quality monitoring systems routinely include the measured mold heat flux signal, based on heat up of the cooling water as it passes through the mold as well [118, 119] as well as other methods [9, 119, 120]. Combining advanced computational modeling with careful plant measurements and forensic analysis of defects is

an important methodology to identify how the defects form. Online visualization of real-time measurements is a useful tool to identify defect formation, hopefully in time to take corrective action, and is better if augmented by calculations based on the defect formation mechanism. This paper presents benchmark measurements obtained during continuous casting when longitudinal depressions and cracks formed, and compares the measurements with corresponding predictions of a thermal-stress model.

5.2 Benchmark Plant Measurements

On June 18, 2017, a campaign of low-carbon steel was cast at ∼1.4 m/min at slab caster 21 at Tata Steel Europe in Ijmuiden, Netherlands. For this campaign, the loose broad face mold copper was instrumented with a 38 x 70 grid of fiber Bragg grating thermocouples that recorded temperature histories at more than 2000 locations [121]. The instrumented region extended across the entire mold width from above the meniscus (90 mm below top of mold) to 285 mm below the meniscus. Although such molds are complex, and expensive to make and maintain, this new methodology enables faster response time, and smaller spacing between sensors than conventional thermocouples, which can be presented in real time, and recorded with high resolution [122, 123]. Figure 5.1 shows severe longitudinal depressions and cracks in a ∼1300 mm-wide slab, which is a relatively rare occurrence. Of particular interest is the depression at ∼265 mm from the North narrow face, (-394 mm from the strand centerline), which is about 250 mm long.

Figure 5.2 shows the instantaneous temperature profiles measured across the mold subsurface at several times during the casting campaign, which correspond to the ∼25 s time period that the 250 mm-long longitudinal depression of interest was in the instrumented portion of the mold. The resolution of the data is indicated by the straight line segments plotted between measured points, which are sufficiently dense to capture the real profile behavior under most conditions. Figure 5.2(a) shows typical steady-state temperatures across and down the mold after conditions returned to normal. As expected, temperatures in the mold generally decrease with distance below the meniscus, and steeply decrease towards the

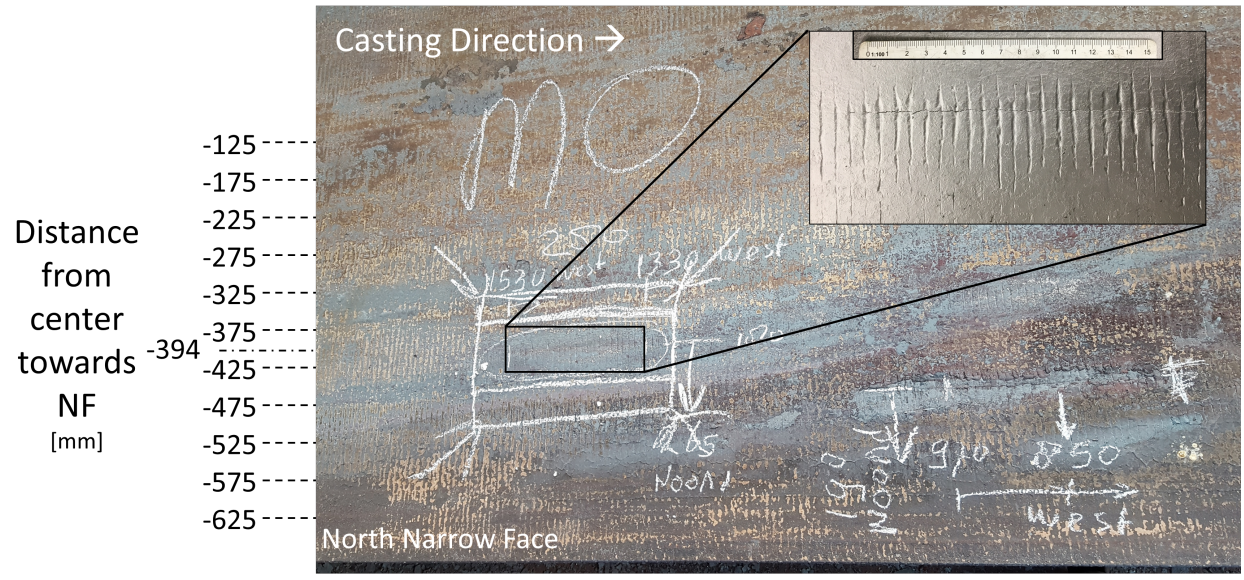


Figure 5.1: Top surface appearance of slab Z9407-101 with severe longitudinal defects off the North NF and inset image of a slab sample containing a depression that was subjected to detailed metallurgical analysis

narrow faces, (strand corner), indicating the cast width of the strand. Most importantly, temperatures recorded near to the depression location are lower. Figure 5.2(b) shows temperatures before, during, and after the residence time of the defect in the mold. It reveals a region of lower temperature that persisted across the mold width during the transient time that the depression developed, which is the general thermal signature of this type of defect. This temperature dip is partly due to the thermal event that initiated the defect and partly due to the consequent drop in heat transfer across the locally larger interfacial gap between the strand and mold wall, which thus experiences a larger thermal resistance. These temperature variations also fluctuate in time.

The center of the depression at -394 mm in Figure 5.1, shown as a dashed vertical line in Figure 5.2(b), passed between two columns of FBG sensors at -375 and -425 mm from the broad face center. A time average of the temperature history over the 30s duration of the depression is shown as a red line in Figure 5.3(b), taken at the FBG sensor column at -375 mm from the wideface centerline, which was closest (19 mm away) to the depression center (solid vertical line in Figure 5.2(b)). Instantaneous time-averaged far field temperatures were

taken at +475mm (opposite side of the slab) and are shown in black in Figure 5.3(a). This temperature profile quantifies the significant drop in temperature from above the meniscus to the end of instrumentation, where it approaches back to the far field value.

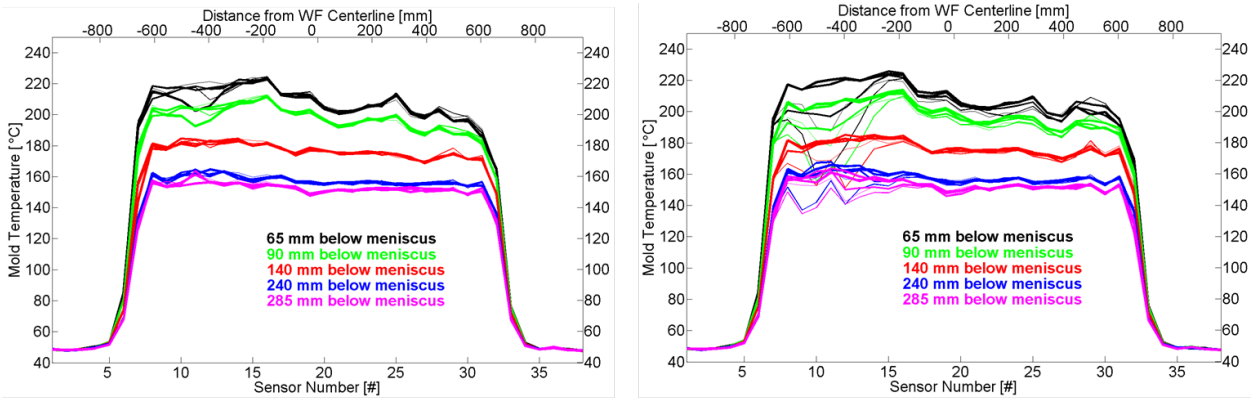
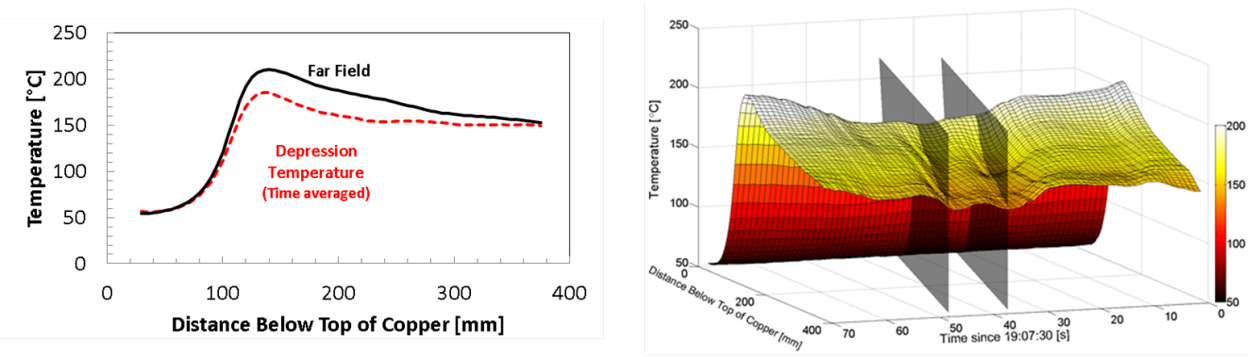


Figure 5.2: Measured local temperature profiles across the mold width at specific times and locations down the mold. (a) Uniform casting conditions after the region containing the defect and (b) Before, during, and immediately after formation of the defect region with the depression.

5.3 Mold Data Mapping Methodology

A new methodology has been developed to better enable operators to interpret continuous online measurement of dense mold temperature data to detect formation of longitudinal defects [18]. Figure 5.3(b) shows a 3D surface plot of temperatures down the mold for 70 s surrounding the residence time of the surface depression. Lines of constant time run parallel to the axis of distance down the mold. Temperatures are taken from the same vertical line of FBG sensors ∼19 mm from the depression center. In this figure, movement in the casting direction at 25 mm/s of two points down the strand in the depression is visualized by two translucent vertical planes, spaced 11s apart. The oldest data is sliced by the right plane, where the shell starts at the meniscus (back right) at 22 s and exits at 37 s.

In Figure 5.3(b), there are clearly visible valleys in the temperature plot, delineated by the vertical planes. These temperature valleys represent the time duration of this depression.



(a) (b)

Figure 5.3: (a) Temperature profiles down the mold for the far field and the FBG sensor closest to the depression center (19 mm away) averaged over the instrumentation residence time of the depression (b) 3D plot of temperature evolution along the same single vertical line near the depression.

The angled nature of the valleys matches close to the casting speed planes, which indicates that the depression started at the meniscus and then translated down the strand at the casting speed. The steep gradient near the meniscus on the right plane indicates that the depression formed rapidly; temperatures stayed depressed for 11s until the left translucent plane, and then gradually returned to far field conditions. Slight changes in the shape of the valley indicate that the depression shape changed with time, growing rapidly when it first formed, stagnating for a short distance, continuing to grow, and finally receding and disappearing.

5.3.1 Mapping Mold Data to Slab Data

The translating nature of defect formation, shown in the previous section, suggests a better methodology to visualize the formation of defects in the mold. With the high sampling frequency and spatial resolution of FBG molds, it is possible to track detailed time histories that correspond with points on the slab surface moving down the mold at the casting speed, by matching position down the strand according to the time it was adjacent to a given distance down the mold. Then, the instantaneous drop in temperature at a given measured point in the mold surface is found by subtracting TStandard , which is a 2D array of standard

temperatures at the instrumented points of the mold, calculated previously by averaging data when no defects occurred, according to the given steel grade and casting conditions:

$$\Delta T(t) = \min(0, T_{\text{Mold}}(x_{Slab}, y_{Slab} - \int_{t_0}^{t} V_c(t_i)dt_i, t) - T_{\text{Standard}}(x_{Slab}, y_{Slab} - \int_{t_0}^{t} V_c(t_i)dt_i)) \quad (5.1)$$

While a location of interest on the slab surface, y_{Slab}, is within the instrumented region of the mold, $t_{Enter} < t < t_{Exit}$, the criterion, T_{IDrop}, evolves with time by integrating the history of the temperature drop at that moving location:

$$T_{IDrop}(x_{slab}, y_{slab}, t) = \int_{t_{Enter}}^{t} \Delta T(t_i)dt_i \quad (5.2)$$

where tEnter is the time when the location, y_{Slab}, enters the instrumented mold region, $y_{Slab} = y_{Moldtop}$.

Large values of T_{IDrop} at the end of the instrumented region indicate regions of the slab surface which have experienced a mold temperature history that is cooler than standard conditions. This indicates lower heat flux across the interfacial gap and a hotter shell temperature. This is often due to surface depressions, which often lead to cracks, owing to a locally hotter shell. These regions can be tracked, subjected to extra inspection, and perhaps downgraded. This methodology and criterion can be applied to systems with arbitrary spacing of the measurement points, provided there is enough spatial resolution to achieve reasonable accuracy. A contour map of this criterion indicates regions on the strand surface that have experienced prolonged, periods of temperature drops relative to the standard profile, likely due to a surface depression. Details of this methodology are provided elsewhere [18].

5.3.2 Defect Visualization

A console display setup for post-mortem (forensic) defect analysis using this new defect indicator is suggested in Figure 5.4. Figure 5.4(a) shows the instantaneous contour map in the instrumented region displayed by the sensors at the current time, using a blackbody color

map without interpolation. Figure 5.4(b) shows a top-down photograph (adjusted to remove perspective) of the final surface appearance of the region of the cast slab corresponding to the temperatures in Figure 5.4(a) at the time it resided in the instrumented region in the mold. The translucent gray rectangle at the top indicates that portion of the image which was above the meniscus level at that time. Figure 5.4(c) shows a contour plot of the instantaneous deviations between the standard and current temperatures for each location in the array. Values are always negative or zero, because depression defects always tend to lower mold temperature. Increased negative values indicate deeper depressions. Figure 5.4(d) shows an example of the output results from the new methodology, obtained by accumulating the results in Figure 5.4(c) for 11 s (245 mm past the bottom of the instrumented region), according to the new defect criterion function. The time period spent within the instrumented region of the mold is represented by the space between the thick black horizontal lines, labeled top and bottom of instrumentation. Once a surface location passes out of the instrumented region, the contours are fixed, and the calculation for that surface point is completed. Again, increasingly negative numbers indicate higher likelihood of surface quality problems. The longitudinal depression at the left of Figure 5.4(b) is clearly visualized in Figure 5.4(d), but is hardly noticeable in the raw temperature data. This illustrates the value of this new defect identification methodology, which is described in detail elsewhere [17].

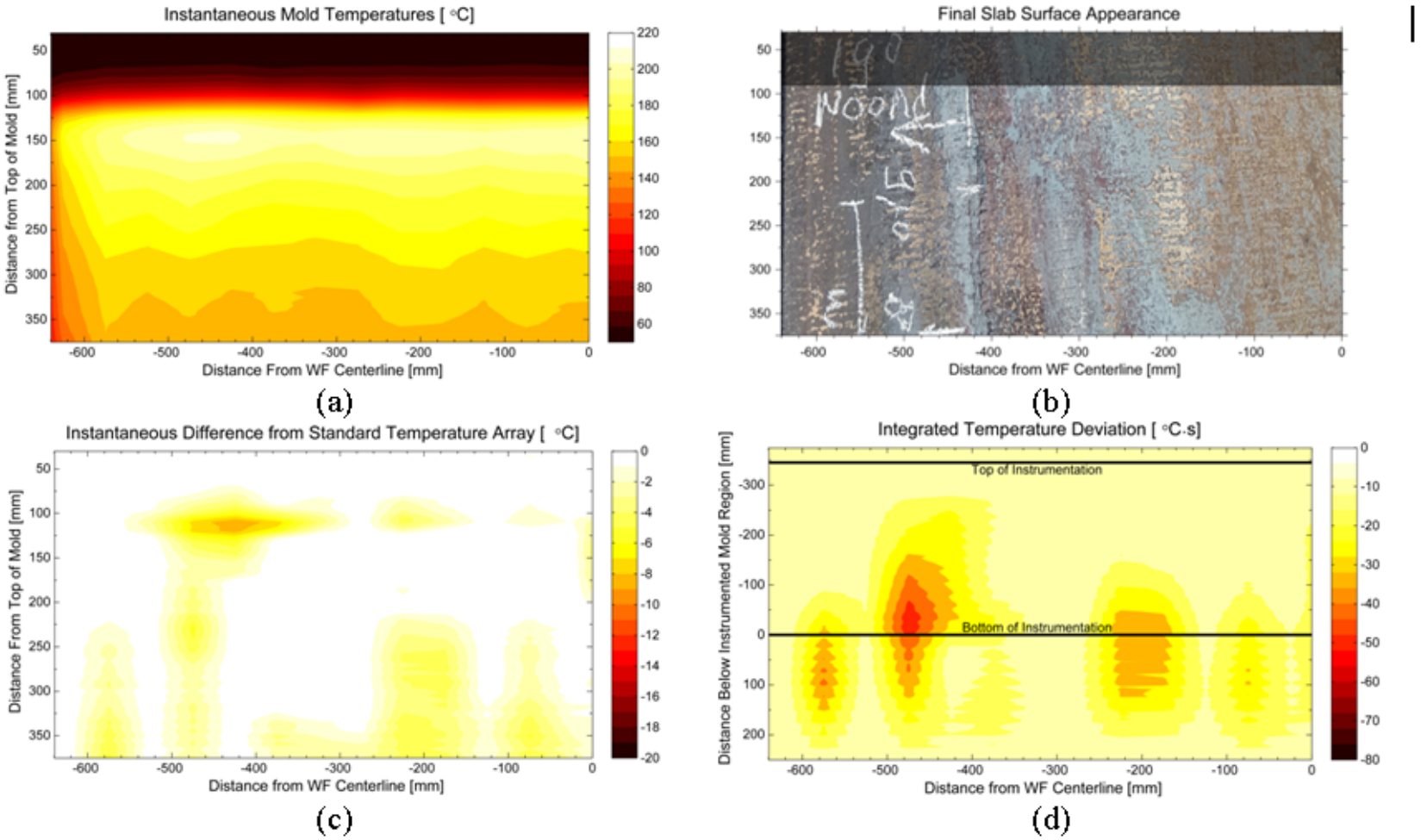


Figure 5.4: Contours that map defects over half of slab from wide face centerline to narrow face: (a) Instantaneous mold temperature, (b) Final slab surface appearance, (c) Instantaneous difference from standard temperature (d) Defect criterion based on integrated temperature drop T_{IdropF}

5.4 Thermal-Mechanical Model Formulation

The thermal-mechanical model in this work focuses on a two-dimensional (2-D) slice through the solidifying steel shell in a state of generalized plane strain in both x and z directions [95], as it moves down the mold at the casting speed in a Lagrangian reference frame. The model solves the transient heat conduction and momentum equations to predict the temperature, displacement, strain, and stress histories of the shell. The governing equations are solved using the finite-element method in ABAQUS/Standard (implicit). The transient analysis uses coupled-temperature displacement elements and step-wise coupling between the thermal and mechanical calculations. The 20 mm thick x 40 mm wide simulation domain, shown in Figure 5.5(a), represents a portion of the solidifying shell somewhere along the broad face away from the corner.

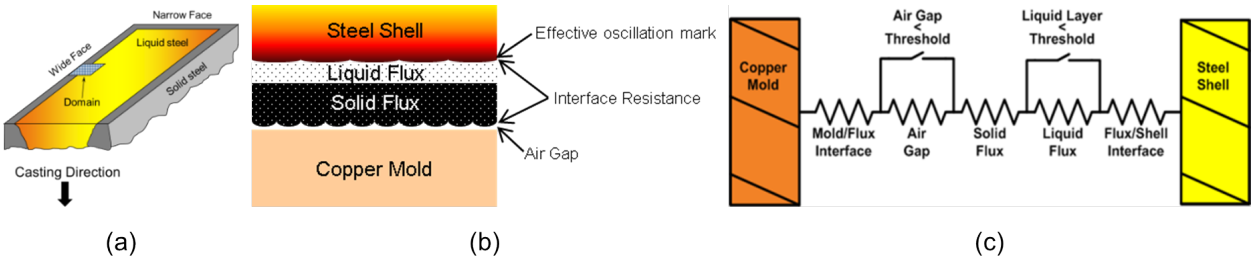


Figure 5.5: Thermal-stress model domain shown in cutaway of continuously cast slab (a), interfacial gap layers in this model (b), and numerical implementation as a thermal resistor model (c).

The model is applied here to the case with FBG measurements shown in the previous section. The initial temperature is set to the reported tundish temperature, 1554°C in the steel, and 100°C in the mold. Coupling between the solidifying shell and the copper mold was accomplished using a GAPCON subroutine. Given the mold hot face and steel shell surface temperatures, and the total gap thickness calculated by the mechanical model at each time step, the thermal model calculates appropriate local solid and liquid layer thicknesses using: flux solidification temperature 1045°C, and resistances (mm^2 K/mW) of the different layers comprising the gap: the mold/slag interface, 0.0004, air gap, $D_{Air}/0.06$, solid slag layer,

$D_{Sol}/3.0$, liquid slag layer, $D_{Liq}/1.0$, and slag/shell interface, $0.251exp(-0.0054Tls)$. D_{Air}, D_{Sol}, and D_{Liq} are thicknesses of the air gap, solid slag, and liquid slag layers respectively, and T_{ls} is the temperature of the liquid slag/steel shell interface. The slag/shell interface resistance is non-linear and numerically constrained between 1,000 and 20,000 W/K.

To calculate accurate mold temperatures, a Reduced Order Model (ROM) of the mold was applied [65]. Modeled as a single row of elements along the width, the ROM mold has a calibrated thickness of 28.35 mm to account for water slots in the transverse direction. A constant thermal conductivity of 315 W K/m and variable convection boundary condition is applied to the mold cold face.

The displacement and stress state of the model is calculated by solving the static stress equilibrium equations including frictional contact with $\mu = 0.15$. Details of this model, including the elastic-visco-plastic constitutive behavior with different temperature-, and composition-dependent properties in each of the steel phases: liquid, δ-ferrite, and γ-austenite can be found elsewhere [41, 95, 116].

5.5 Volumetric Heat Source

To allow easier prediction of accurate mold temperatures, a reduced order mold model was implemented based on previously published and validated work [65]. The ROM mold works by calibrating the thickness of a simplified effective copper mold that allows for the temperature to match plant measurements at a predefined calibrated thermocouple depth. This simplistic method was shown to match well with plant data in multiple cases when calibrated correctly. Use of the ROM mold is necessary to avoid using a complete 3D strand section and mold which recent work has shown to be numerically taxing even with highly simplified material properties and a very coarse mesh, this type of model can take nearly 1 month of wall clock time to execute [16].

In this work, the ROM mold was implemented using a single row of finite elements given basic properties of the mold material with a fixed thermal conductivity of 312 W K/m. In order to mimic the full 3D behavior of the copper mold heat removal, specifically the

axial temperature gradients in the mold, which are in the undiscretized axial direction, a negative volumetric heat generation term was used on the material. This value changes with time/distance below the meniscus according to eq. (5.3) and plotted in Figure 5.6.

$$Qdot = ((0.13 * T_{Mold}^{1.18}) - erf(t/6.0)) \tag{5.3}$$

where T_{Mold} is the temperature of the mold material at any calculation point, erf is the error function given by:

$$erf(x) = \frac{2}{\sqrt{\pi}} \int_0^x e^{-t^2} dt$$

, and t is the time below the meniscus.

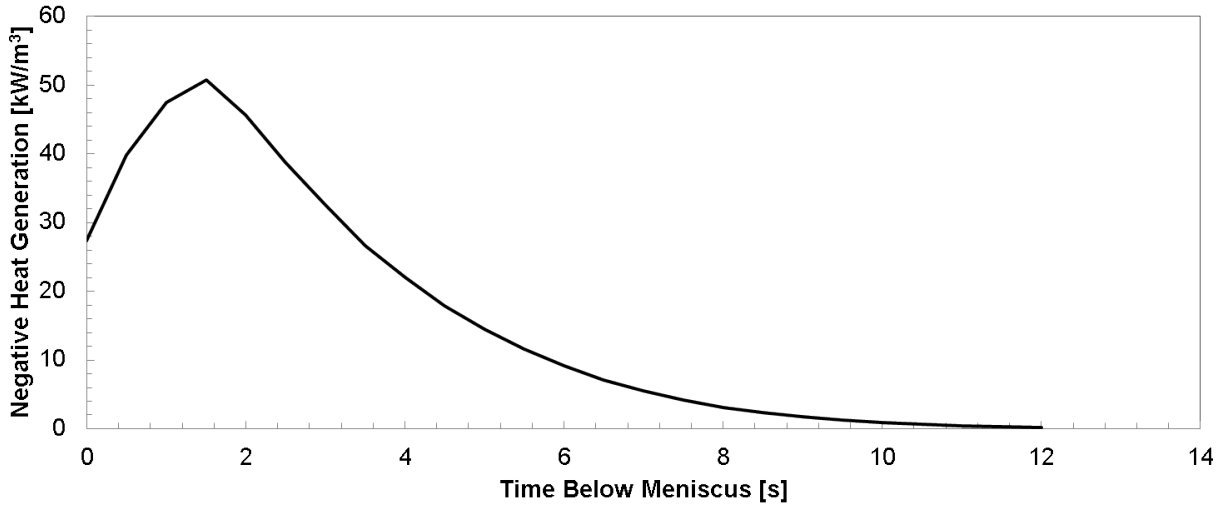


Figure 5.6: Negative Volumetric Heat Generation Function

This time varying heat removal allows for the additional removal of heat from the meniscus region in the 3D mold that would otherwise be neglected in the 2D mold in this work and would cause unrealistically high temperatures in the meniscus and near-meniscus region. This term transforms the 2D slice heat-transfer model into a 3D model with calibration to match the real 3D mold heat transfer. This procedure is implemented using the HETVAL material subroutine within Abaqus. Details of this subroutine can be found in the literature [66] and section D.2. On the back side of the mold a variable convection condition is

applied using the Abaqus subroutine FILM to include the heat removal from the mold by the circulating cooling water channels. Full details can be found in the literature [66] and section D.1. Validation of proper model setup was performed in this work by matching the example problems geometry, boundary conditions, and results, given in the original work. Calibration of the model in this work was carried out based on the method provided in the literature and the detailed data provided by the steel plant. In the more general cases where the ROM mold is not being used, instead a fixed mold geometry is used with the temperature of the mold copper fixed to be 150°C.

5.6 Thermal Model Calibration and Validation

First, the continuous-casting heat transfer model, CON1D [64] was calibrated to match both the heat flux measured from heat up of the mold cooling water, FBG temperature measurements at the far field, and two rows of embedded thermocouples, as shown in Figure 5.7(a). For these far-field conditions, CON1D suggests a flux layer thickness profile down the gap, as shown in Figure 5.7(b).

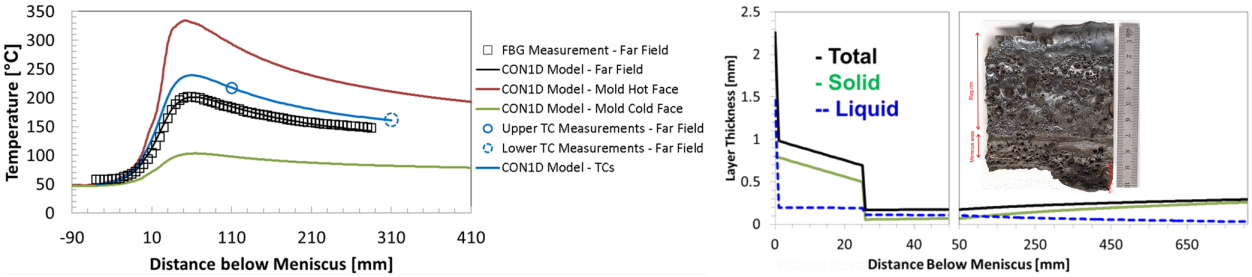


Figure 5.7: (a) Temperature results from CON1D with plant measurements for FBG and thermocouples and (b) con1d output results for flux layer composition within the mold.

Of particular interest is that Figure 5.7(b) indicates the presence of a significantly thicker layer of flux extending to 26 mm below the farfield meniscus; Slag thickness then decreases to ∼0.2 mm and gradually increases with distance down the mold. The extended slag rim, of ∼1 mm thickness, retards heat transfer in the meniscus region, and delays initial

formation of the shell below the farfield meniscus. It is needed to enable CON1D to match the plant measurements. This provides strong evidence that such extended slag rims during casting are real. This is further supported by anecdotal evidence from this particular facility where several extended slag rims with similar thickness profiles were found after casting. Furthermore, an example of such a slag rim is shown in the inset image shown in Figure 5.7(b) from a different caster at the same plant. A larger image of this slag rim can be found in the appendix (Figure G.19).

After calibration of CON1D with measurements, the GAPCON model in Abaqus was adjusted to match CON1D. Due to the 2D nature of the model, axial heat conduction is neglected. Instead, a negative volumetric heat generation was applied, decreasing from -25 W/m^3 to zero over the first 10 s. Figure 5.8(a) shows the match with the farfield CON1D heat flux profile, and Figure 5.8(b) shows a comparison with the corresponding mold temperatures, including the FBG data. Note that the peak heat flux appears over 20 mm below the farfield meniscus, owing to the extended meniscus slag rim discussed previously. Results from the Abaqus model are also compared with the FBG sensor data 19 mm away from the depression center. Figure 5.8(a) shows that the heat flux profile in the depression center is substantially lower than that of the far field. This is due to the extra thermal resistance created in that region, in addition to the consequent physical opening of the depression, which was assumed to create an air gap. Figure 5.8(b) shows a substantially higher peak temperature predicted by the Abaqus model near the meniscus, which is a modeling artifact due to missing copper above the meniscus that removes heat axially and leads to the smoother and lower temperatures of the FBG and CON1D profiles in this plot.

5.7 Thermal-Mechanical Model Results

Depression shape results of the thermal-mechanical model are compared with a digital microscope scan and measurements of the sample in Figure 5.9. The ∼4 mm deep crack is indicated by the vertical dashed line. The inset compares a micrograph cross section through the depression (right) with the predicted shape (left). The model slightly overpredicts the

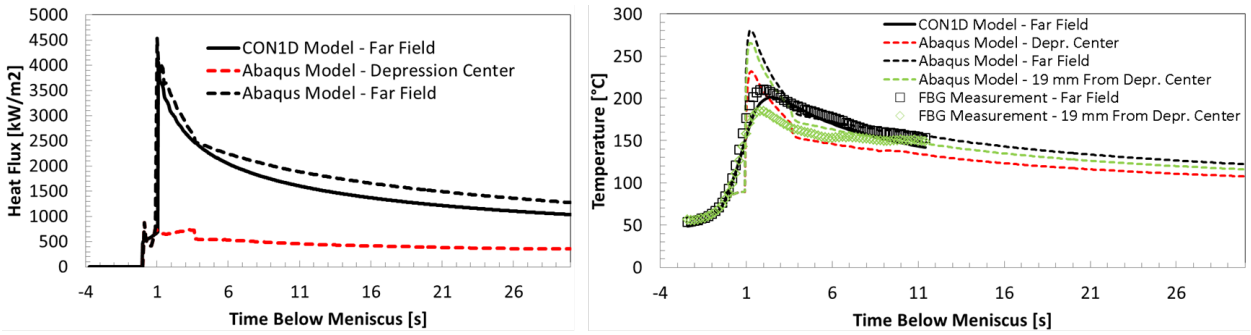


Figure 5.8: (a) Calculated heat flux profiles down mold comparing Abaqus and CON1D models; (b) Corresponding mold temperature profiles also comparing with FBG measurements.

depression depth, likely due to overprediction of the temperature gradient near the meniscus (Figure 5.8(b)), which is due to incomplete incorporation of the axial heat flow near the meniscus into the Abaqus slice model. Additonally, during casting, scale formation occurs on the surface of the steel shell. This layer forms as the strand surface oxidizes and interacts with the environment. Assuming a scale layer of 0.3 mm (within the appropriate range of scale thickness [124]) makes the final depression shape slightly shallower as some of the surface is removed.

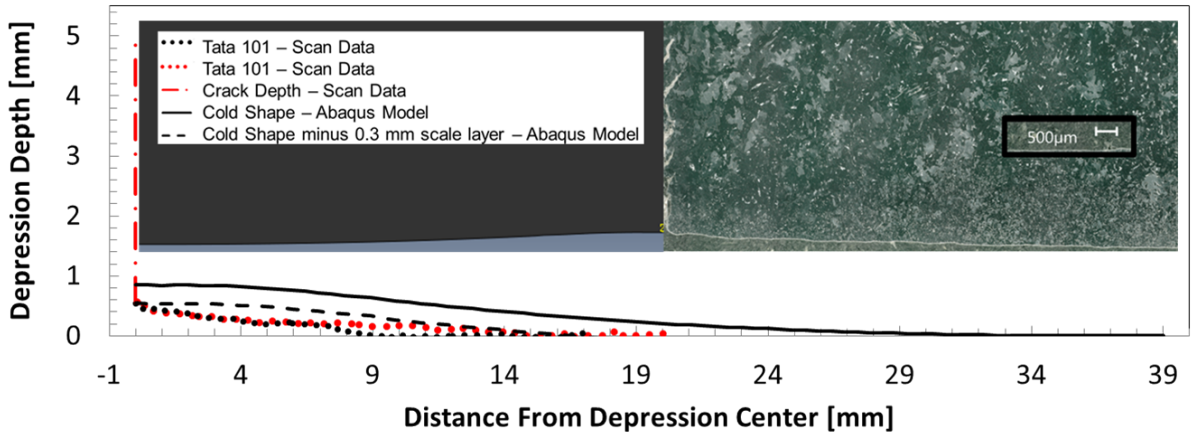


Figure 5.9: Slab surface depression shape comparing model prediction with scan of sample with defect

5.8 Defect Appearance on Instrumentation

Longitudinal depressions on the surface of the strand represent a local hot spot on the steel. Reduced heat removal, as a result of separation from the mold, leads to local heat up as continued heat addition from the molten core raises the temperature and thins out the shell. This drop in heat transfer out of the shell, combined with the continued heat removal by the mold cooling water, actually leads to the opposite behavior within the mold. As the drop in heat addition to the mold from the strand causes temperatures in that region of the mold to drop. This behavior can be observed by instrumentation on the mold, as shown in Figure 5.10, where the steel surface temperature at the defect centerline is higher than the far field, and the corresponding mold temperatures have the opposite trend.

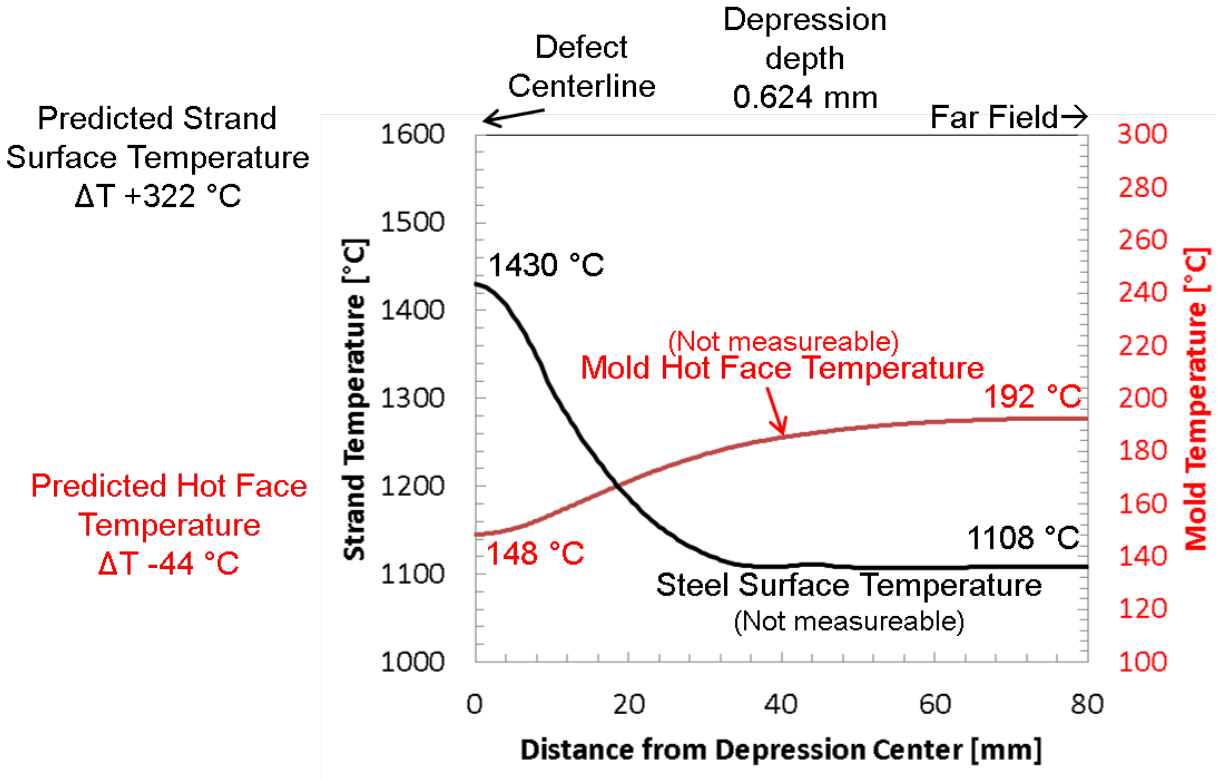
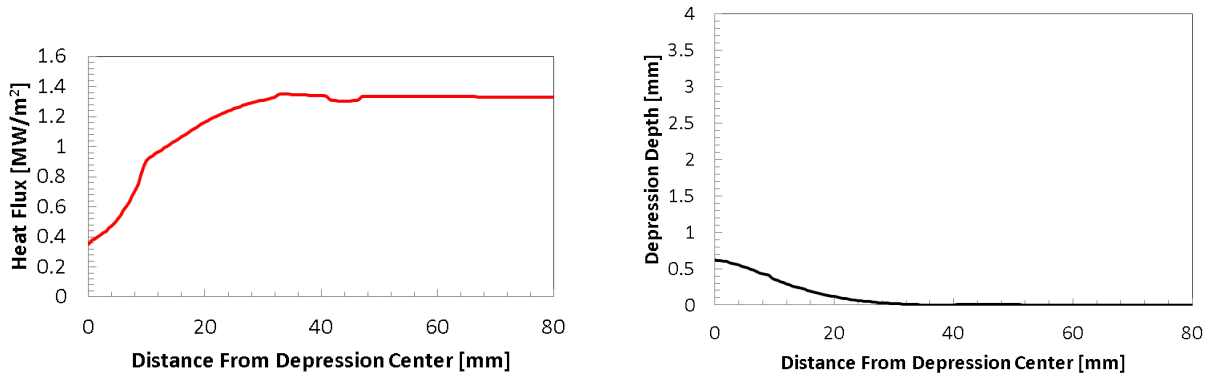


Figure 5.10: Strand surface temperatures and corresponding mold surface temperatures for a 0.624 mm deep depression

The appearance of longitudinal depressions (i.e. mold separation) is observable on sufficiently refined instruments as a local drop in temperature compared to the far field [17]. The example shown in Figure 5.10, has a depression with a depth of 0.624 mm which is more than 320°C hotter than the far field at the strand surface, while the mold hot face registers a 44°C drop in temperature at the same location.

The model used for the calculations here is an 80 mm domain without a crack. The thermal disruption is the same as the one described previously in this chapter. The wider domain is selected to ensure that the far field temperature is reached regardless of the final size of the depression. The vertical line at 40 mm and 80 mm is fixed in the Y direction, this boundary condition makes the 80 mm domain equivalent to the 40 mm domain under a high friction/hold mechanical condition. The following results are shown at 20 s below the meniscus, with a depression shape as shown in Figure 5.11(b) and a heat flux as shown in Figure 5.11(a).



(a) (b)

Figure 5.11: Thermocouple Analysis Model Results at 20 s Below Meniscus (a) Heat flux profile across the surface,(b) Defect Shape

Unfortunately, strand and mold surface temperatures are not observable in practice and thus this understanding is only useful as a theoretical tool. However, using the reduced order mold model developed previously [65] and implemented in this work, the mold temperatures at a possible thermocouple depth can be predicted using the calibrated 28.35 mm ROM

mold.

5.9 Locating Mold Thermocouples

Placement of mold thermocouples is part of mold design and is easy to dismiss as simple as long as it satisfies the needs of breakout prevention. However, it is clear from this work that careful selection of thermocouple locations can make it possible to catch longitudinal depressions. There are cost and heat transfer tradeoffs in selecting locations and spacing. With this in mind, in order to catch longitudinal depressions no matter where they are across the strand perimeter, careful selection of spacing between fibers around the mold perimeter and depth below the hot face must be made. In addition to spacing, the resolution of the sensors need to be taken into account. Thermocouple resolution refers to the ability of a thermocouple to observe a real temperature variation caused by a depression to stand out over the noise, both electrical fluctuations in the sensor system as well as typical temporal and spatial temperature variations around the mold perimeter. Results for the previous case study, and model simulation involving the Tata Steel thin-slab caster, a 0.624 mm deep and 48 mm wide, U-shaped necking-type depression, with a $\sim$72% drop in heat flux from far field to the depression center, are used for the following thermocouple analysis

In general, heat flow within the mold occurs across the minimum possible one-dimensional path between the solidifying liquid steel core and the mold cooling water. In the ideal circumstance, the heat transfer is completely uniform around the mold at a given position below the meniscus. However, as discussed in this work, longitudinal defects are associated with heat transfer variations around the mold perimeter. These variations create corresponding temperature gradients across the strand and across the surface of the mold. As shown in Figure 5.10, as the heat travels across the gap from the strand surface to the mold hot face the temperature variation is smaller. Though it is still clearly visible, the resultant temperature difference on the mold hot face between defect center and the far field drops by more than 85% compared to the temperature variations on the strand surface. Furthermore, as the heat travels from the mold hot face through the high-conductivity copper, which rapidly

diffuses the heat, these gradients are further filtered and all variations appear even smaller. This filtering behavior can be observed in Figure 5.12 to Figure 5.14 by comparing the values for the three different thermocouple depths calculated at each resolution.

Starting with the results of the 0.1°C resolution thermocouple analysis (Figure 5.12), the filtering effect can be explored. For a thermocouple depth of 5 mm below the hot face, the temperature of a thermocouple aligned directly across from the depression center is observed to be ∼134°C while a thermocouple at the far field measures ∼170°C, which represents a 22% drop. For a thermocouple depth of 10 mm below the hot face, the temperature at depression center is observed to be ∼121°C while the far field temperature is measured at ∼150°C, representing a 20% drop. For a thermocouple depth of 13.37 mm below the hot face, the temperature at depression center is observed to be ∼112°C while the far field temperature is measured at ∼137°C, representing a 18% drop. Note that the depth of 13.37 mm is actually the calibrated offset depth for a 15 mm deep placement of thermocouple using the 3D ROM mold for this analysis. As such, the 5 and 10 mm depths are slightly further from the hot face than the real locations that they represent, as well.

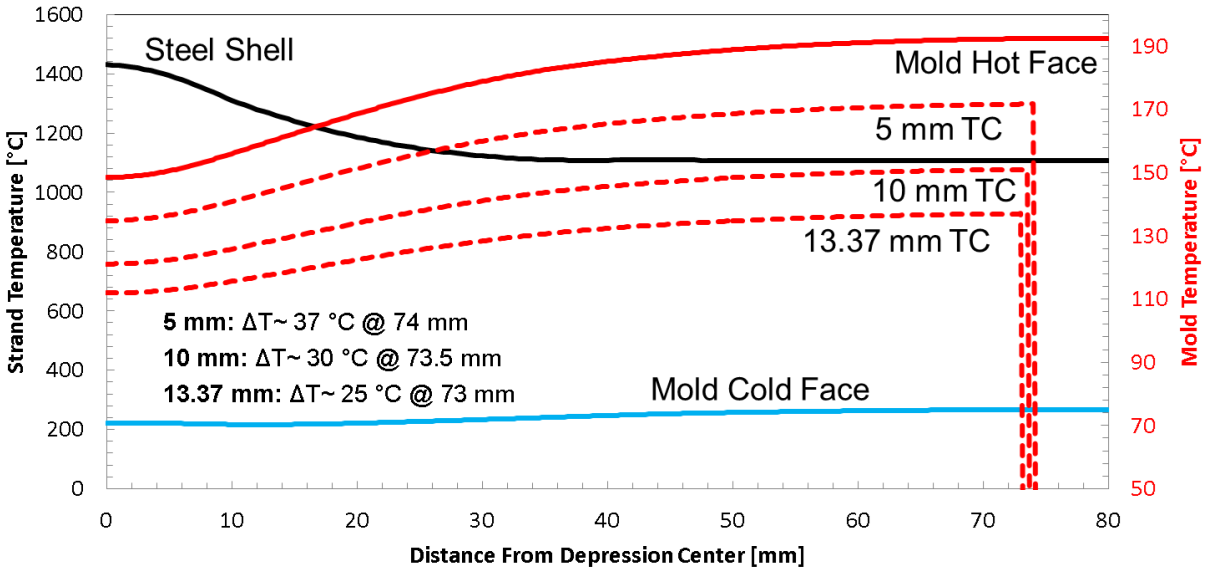


Figure 5.12: Thermocouple Location Analysis for 0.1°C Resolution

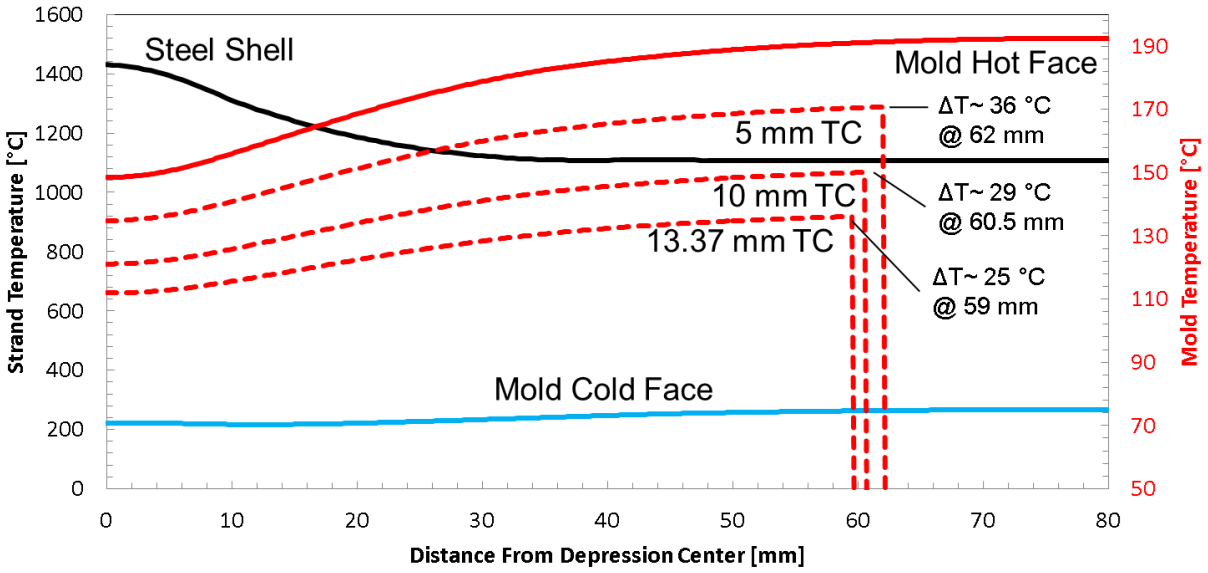


Figure 5.13: Thermocouple Location Analysis for $1°C$ Resolution

For a thermocouple with a larger resolution of 5°C (Figure 5.14), this changes slightly. For a thermocouple depth of 5 mm below the hot face, the temperature at depression center is observed to be ∼134°C while the far field temperature is measured at ∼166°C, representing a 20 % drop. For a thermocouple depth of 10 mm below the hot face, the temperature at depression center is observed to be ∼121°C while the far field temperature is measured at ∼146°C, representing a 17 % drop. For a thermocouple depth of 13.37 mm below the hot face, the temperature at depression center is observed to be ∼112°C while the far field temperature is measured at ∼132°C, representing a 15 % drop.

One purpose of sensors such as thermocouples is to recognize variations across the surface. From the results it is clear that as a thermocouple is placed further away from the mold hot face and strand surface the observable temperature difference decreases significantly. Depending on the spacing of the sensor (assuming a perfect sensor signal) the observed temperature deviation can be reduced by as much as 93% from the strand surface and 54% from the mold hot face by the time the thermocouple depth is reached. Specifically, the spacing of sensors needs to be small enough that observable temperature differences are

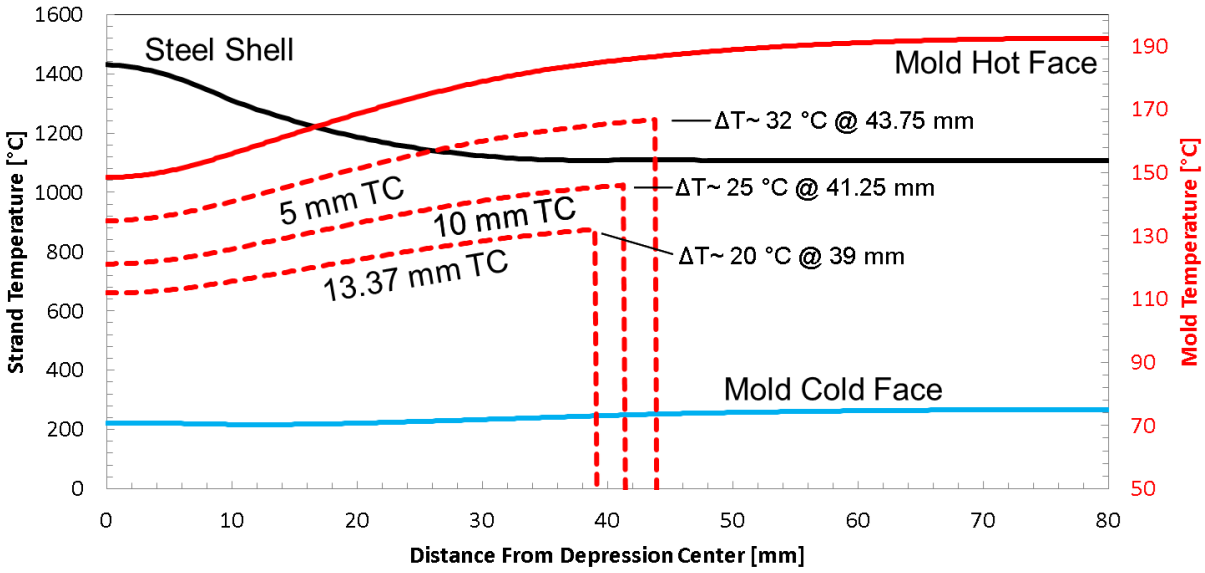


Figure 5.14: Thermocouple Location Analysis for 5°C Resolution

greater than the resolution of the sensor.

However, it should be noted that there is a diminishing benefit to bringing temperature measurement devices closer to the mold hot face. The damping of the variations through the copper would seem to suggest that the best case is having temperature measurements as close to the mold hot face as physically possible. However, it is important to consider not just the potential maintenance costs of having sensors that much closer to the hot face (by affecting the number of times that a mold can be resurfaced), but also that with increasing distance from the surface, the sensor is affected by temperature changes across a larger area of the surface.

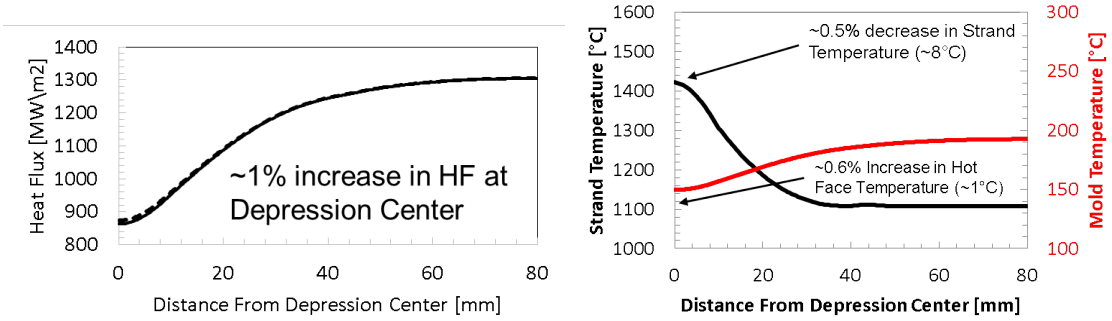
As sensors are placed closer to the surface, they are able to more quickly react to their immediate surroundings, but they lose some ability to sense these changes in 2D that occur through the thickness of the mold copper. Specifically, for sensors closer to the surface, there is less filtering by the copper, but the variations from a misaligned depression (not directly aligned with a sensor) must propagate with a more horizontal component, so it becomes harder for the sensor to see them. These two factors almost exactly cancel out. Keeping the

sensors further below the hot face surface actually enables them to better measure changes that may be occurring across the mold or between sensors. This can help lower maintenance costs as well as the disruption to mold heat transfer caused by rerouting water channels. However, results of this analysis show that placing thermocouples closer to the hot face surface only slightly increased the width that they are able to be affected by depressions. Meaning that the two effects mostly cancel out and that the maximum spacing for a given defect changes very little for variations in depth. Thus for a given resolution, depth, and selected minimum size of acceptable thermal disruption (defect), there is an optimal spacing for thermocouple placement that can be chosen using this type of analysis.

For the defect evaluated in this chapter, and for thermocouples placed 15 mm below the hot face, the ideal horizontal spacing should be 146 mm for a 0.1°C resolution, 118 mm for a 1°C resolution, and 78 mm for a 5°C resolution; and by moving closer to the hot face (*i.e.* the 5 mm case), these spacings change by a maximum of only 8 mm for the low resolution case (5°C). These results are for a particular scenario of longitudinal depression in a specific mold, however, in the real operation, the resolution must be determined according to the size of the deviation caused by the defect, in addition to the transient thermal fluctuations that naturally occur in the process.

5.9.1 Changes in Spacing for Small Variations in the Defect

The following analysis includes a small change to the original defect discussed above to explore the spacing prediction provided. With all other variables fixed, the total flux layer thickness at depression center was decreased by 10%. The decrease in flux layer thickness should increase the effective heat flux, decrease the strand surface temperature, and increase the mold temperature. As shown in Figure 5.15(a) and Figure 5.15(b), the change in effective flux thickness resulted in an ∼1% increase in heat flux at the center of the depression. The increase in heat flux locally reduces the strand surface temperature by about 8°C, and only increases the hot face temperature by ∼1°C.



(a) (b)

Figure 5.15: Results of 10% reduction in flux thickness at defect center for Tata Steel case: (a) Heat flux on mold hot face (Original result solid line), (b) Steel surface (Black) and mold hot face temperature (Red)

While the apparent changes in heat transfer are rather small, it is observed that the depression depth increased by ∼5% with a negligible change in width (Figure 5.16). This indicates that the increase in heat transfer that otherwise would have made the depression shallower was somewhat cancelled out by the effective increase in the air gap

As previously mentioned, changes in depths of thermocouple placement lead to differences in optimal horizontal spacing for a given defect. Results of the 10% reduction in flux thickness at defect center are shown in Figure 5.17 for a 5°C resolution. For thermocouples placed 15 mm below the hot face, the ideal horizontal spacing should be 77.5 mm, moving closer to the hot face spacing increases to 81.5 mm (10 mm depth) and finally up to 87 mm (5 mm depth). Compared to the original defect, the optimal spacing changes only about 1 mm for every depth, indicating that for this size and type defect the optimal spacing is not very sensitive to small changes in the heat transfer and that spacing would still be able to pick up the defect.

5.10 Conclusions

New models and visualization methods have been developed to enable new insights into the continuous casting solidification process, specifically revealing how temperature differ-

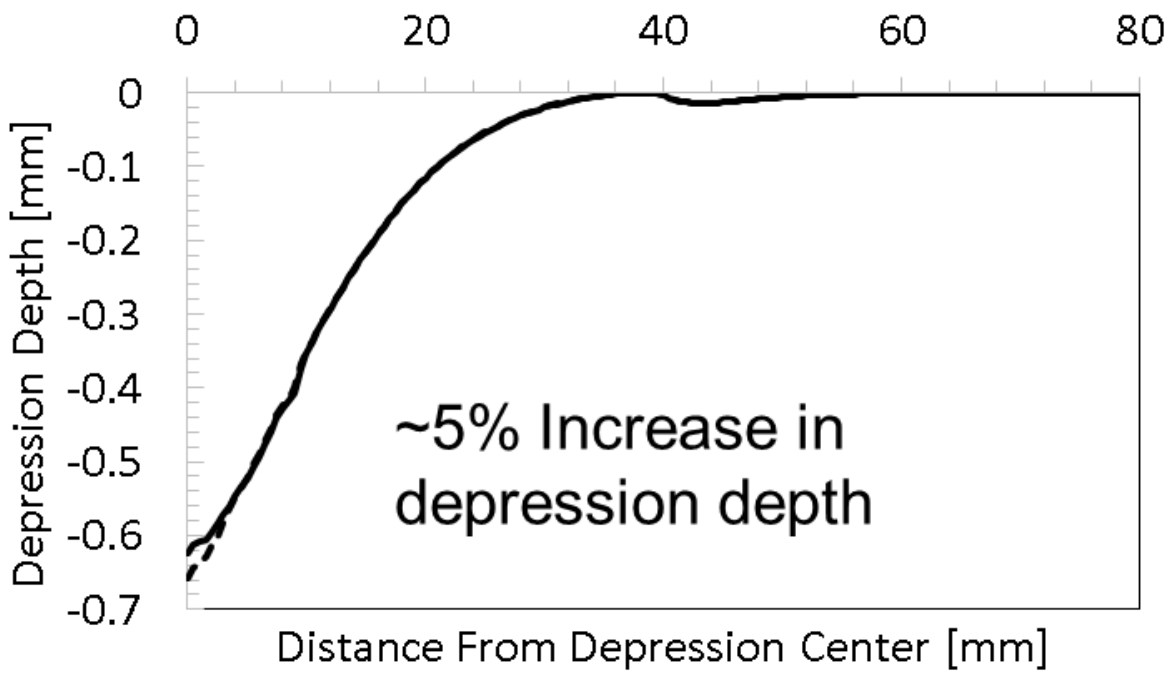


Figure 5.16: Depression depth change from 10% reduction in flux thickness at defect center for Tata Steel case (Original result solid line)

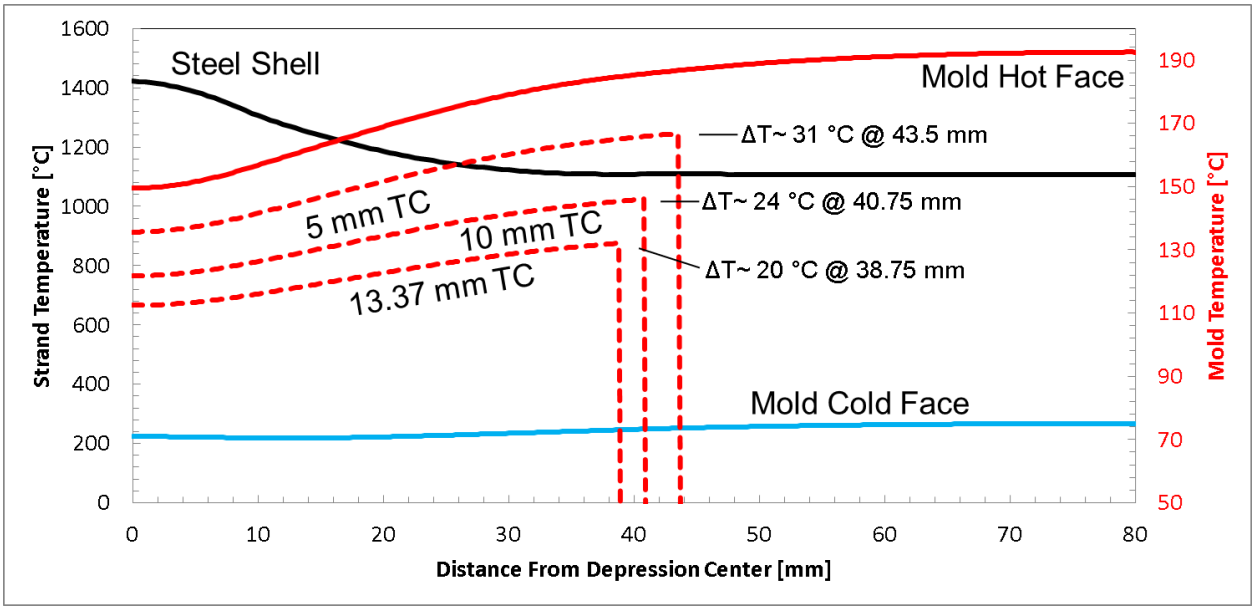


Figure 5.17: Thermocouple spacing locations from 10% reduction in flux thickness at defect center for Tata Steel case

ences are related to longitudinal defect formation. A new computational thermal-stress model has been developed to investigate longitudinal surface defects, as well as to predict the corresponding mold temperatures. Results show that one possible scenario for the specific longitudinal crack and depression defect studied in this case was a ∼20 mm wide local thermal disruption, combined with a crack and some applied tension which led to a necking style depression and a U-shape defect with a crack at the base. Furthermore, this work has provided a detailed analysis of placement for temperature sensing devices within a continuous casting mold allowing for better selection of spacing and depth for a desired defect detection capability.

5.11 Acknowledgements

Particular thanks for this project are extended to: Begoña Santillana, Mathias Mul, Ton Spierings, Stephen Carless, Gert Abbel, Dirk Van Der Plas, Arnoud Kamperman, of Tata Steel Europe, and Martin Seden of ABB.

CHAPTER 6

LONGITUDINAL DEFECT FORMATION MECHANISMS

Longitudinal cracks and depressions are a very important class of defects in continuous-cast products, and also cause breakouts which are not detected by conventional breakout-detection systems. This work investigates the formation of longitudinal depressions, with and without cracks, using a thermal-mechanical model of steel solidification, and relates specific formation mechanisms with the different shapes of the depressions. Several samples of longitudinal defects from commercial slabs are presented as qualitative and quantitative validation of some of the model predictions. Longitudinal depressions in continuous casting can occur in both compression and tension conditions. Tension, such as caused by excessive transverse friction in the mold, can result in partial necking of the shell, leading to the most common type of observed depression - a U-shape. In certain conditions, thinning of the shell is severe enough to further allow the ferrostatic pressure to partially bend the depression and create a W-shape depression. Compression condition depressions are more subtle and much less noticeable when they do occur, and may result in a partial buckling of the shell, also leading to a W-shape depression. Depressions with narrow surface cracks tend to be more V-shaped and are substantially deeper than their non-cracked counterparts, having lower width/depth aspect ratios. Sometimes, however, surface cracks widen to absorb the strain, resulting in higher aspect ratio depressions, or even an otherwise flat slab surface. Finally, depressions without surface cracks tend to have higher width/depth aspect ratios, and sometimes have sub-surface hot tears present, which relieve some of the tension on the solidification front and result in sub-surface macro-segregation streaks. Such sub-surface cracks sometimes may penetrate to the surface, propagating along prior-austenite grain boundaries, and resulting in complex-shaped surface crack openings.

6.1 Introduction

As of 2019, more than 96% of world steel production uses the continuous casting process [5], with production topping ∼1.7 billion metric tonnes and a value of over one trillion dollars in annual sales directly attributed to continuous casting. Within the industry it is well understood that "Any [product] redo costs money... Any inspection costs money" [6]. If even 1/10th of 1% of continuously cast steel products have a defect that requires extra handling or remediation this represents over $1 million dollars per day. Longitudinal depressions and longitudinal cracks represent a substantial amount of continuous casting defects – both of which are known to initiate during initial solidification in the mold. Each subsequent processing step increases the cost if that slab needs to be remediated or scrapped.

Beyond the cost benefits, safety is an even more important reason to better understand depressions and cracks. Breakouts occur where cracks penetrate the surface of the solidifying shell because the local shell falls below a critical thickness, and thousands of liters of molten steel can pour out of the strand and onto the machine and nearby plant floor. Local shell thickness can be reduced due to formation of an excessive interfacial gap between the shell and the mold, either by mechanical forces lifting the shell from the mold surface or from fluid-flow related effects such as variations in slag layer thickness (either too thick or too thin).

Modern breakout prevention systems are in place at most casters and, thankfully, are set up to immediately seal the tundish off and prevent further feeding of the steel [9]. Current breakout detection systems are great at predicting sticker breakouts, which are well understood and easily identified by their classic V-shape which evolves in the casting direction, using algorithms based on identifying primarily transverse time-related changes [9, 11, 12, 125–127]. However, these systems are not very good at spotting breakouts caused by a longitudinal depressions/bleeds or cracks. Thus, better methods are needed to reliably predict, prevent, and detect longitudinal-based breakouts.

Longitudinal-based breakouts are characterized by a longitudinal depression, that evolves into a bleeder, and ultimately into a through-thickness longitudinal crack and a breakout. A longitudinal bleed is characterized by intermittent leaking of molten steel, out of small holes within a longitudinal depression, without full rupture of the strand. The steel is forced through cracks in the shell by the ferrostatic pressure, and in the less serious cases, solidifies against the surface of the strand sealing the crack. In the more serious sustained bleeder case, the longitudinal depression thinning out the shell and allowing for the formation of holes persists and repeated bleeds occur, likely increasing in size and severity, and finally lead to a complete rupture of the solid shell; an example of such a bleeder type breakout is shown in Figure 6.1.



Figure 6.1: Breakout shell of 0.1%C grade from slab caster with visible off-corner longitudinal depression and bleed: a) Breakout shell up to the meniscus with inset image closeup of bleed filled off-corner longitudinal depression, b) Section of corresponding off-corner depression from slab prior to breakout with visible intermittent bleeds (casting direction downwards). Note: Inset photo has been color adjusted for visualization purposes

Severe shell thinning and bleeders are often very closely related to longitudinal cracks and depressions, and while they are one of the most commonly seen defects, still quite little is

known about their formation mechanisms. This chapter of the work will explore in detail the different formation mechanisms of longitudinal depressions - specifically the initiation and growth of depressions, as well as the effect of crack presence on their behavior. The purpose of this work is to provide a practical guide to understanding how different types of depressions form on a caster. Furthermore, the relationship between the formation mechanism and the depression appearance will be emphasized, to aid in troubleshooting. Additionally, gaining a better grasp of how these longitudinal defects form and behave is a closer step towards eliminating them from the cast product entirely.

This work will focus primarily on disruptive behaviors starting at and near the meniscus with the fundamental goal of understanding what the specific steps in the formation mechanisms for a given defects.

6.2 Computational Model Tools

This chapter applies the computational thermal-mechanical finite-element model that was described and validated in the previous chapters. The models simulate and analyze a variety of specific longitudinal defects involving depressions and cracks. The model first solves the heat conduction equation for the temperature distribution, followed by the mechanical equilibrium, constitutive, and strain displacement relationship for the deformed shape, strains, and stresses. The domain for this model consists of a two-dimensional (2D) transverse slice through a small, local portion, of the wide face of the steel strand away from the corner region, as shown in Figure 6.2. The slice is initially at uniform temperature, chosen to be the approximate temperature of the steel at the level of the meniscus; in this work the temperature is set to 1532°C which is approximately 5°C above the liquidus temperature. One surface of the domain is in thermal and mechanical contact with the mold.

The thermal boundary condition between the steel domain and the mold domain is a coupled gap conduction model as shown in Figure 6.3, which allows for air gap formation behavior as well as disrupted (non-uniform) heat transfer across the surface. Every case starts with some type of initial thermal or mechanical disruption at the meniscus. Most of

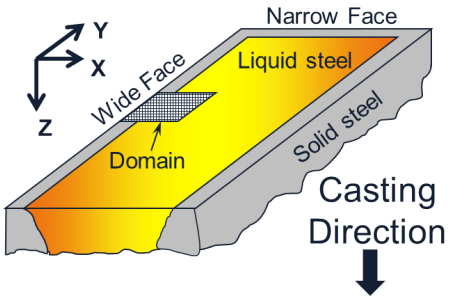


Figure 6.2: Model domain within caster geometry and boundary conditions

the models below use a 25 mm wide thermal disruption with an additional 1 mm of flux added into the gap conduction model, as a base case unless otherwise stated. In certain conditions, such as the W-shape tension depression, "thicker" disruptions (more heat flux drop) were used to create the conditions. Further details of the gap model are discussed in chapter 3 and Chapter 5. The other 3 boundaries on the 2D slice are thermally insulated based on physical conditions in the caster and desired symmetry.

A thermal disruption is a local deviation from uniform heat transfer around the perimeter of the slab at the meniscus. This might be caused by a large level fluctuation in the mold caused by the turbulent fluid flow, a local non-uniformity in slag infiltration at the meniscus, or another event during oscillation at the meniscus, as discussed previously in Chapter 2. A mechanical disruption is a local deviation in surface shape of either the strand surface (such as a depression or crack) or of the mold surface (such as a gouge or scratch). A surface depression is a depressed (lowered) portion of the shell/strand/slab surface as compared to the surrounding far field surface appearance.

The gap model includes the thermal behavior of solidifying mold flux as well as the interface resistances due to roughness between the steel shell and liquid flux as well as the solid flux and the copper mold as shown in Figure 6.4.

The mechanical boundary conditions on the model are shown in Figure 6.3b. Symmetry planes can be found on the left and right sides of the domain, both of which are given boundary conditions which enforce them to remain as straight vertical lines throughout the

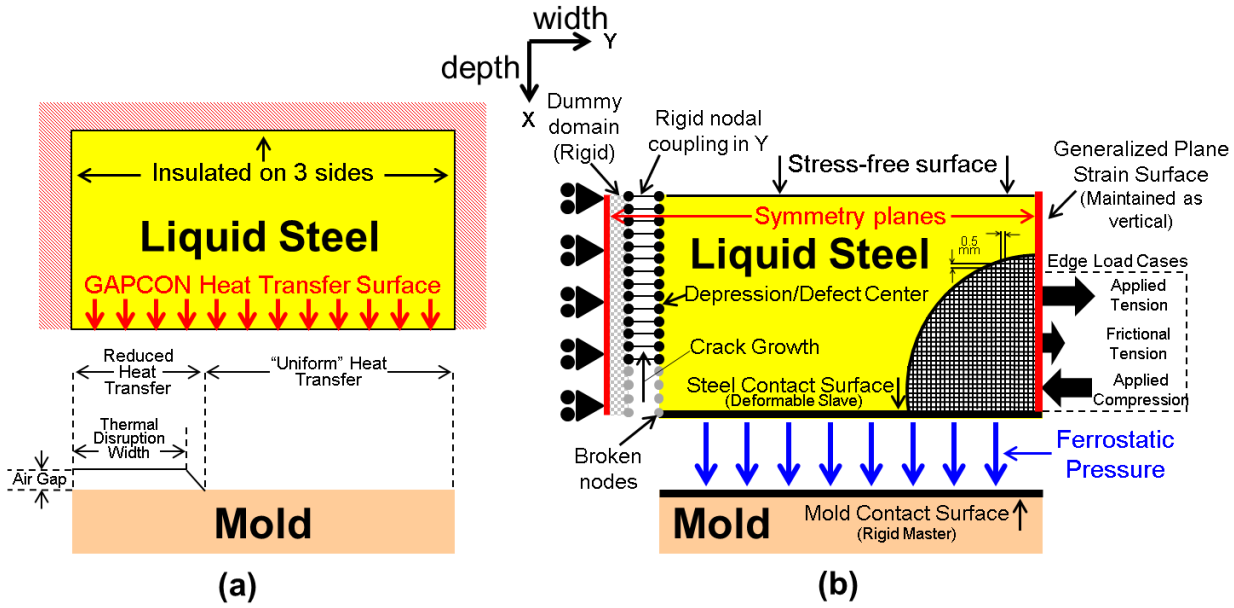


Figure 6.3: Boundary conditions a) Thermal and b) Mechanical used in this work

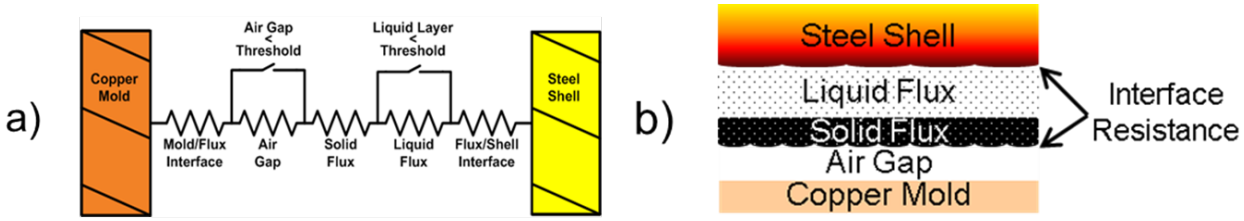


Figure 6.4: Thermal disruption takes the form of reduced heat transfer: a) Gap resistor model schematic, b) Example gap composition

simulation. Movement (displacement) of points (nodes) on the left boundary are fixed to zero in the horizontal (Y direction), parallel to the mold surface, while the right boundary is free to displace, or to have a loading condition applied to simulate phenomena such as tension from bulging and/or high friction, or compression from mold overtaper conditions. The bottom surface of the domain is pulled into mechanical contact with the mold by the ferrostatic pressure applied on the bottom of the domain according to the time history of the casting [15]. The mold is a thin rectangular domain that remains fixed in time and space throughout the simulations. The top surface boundary of the steel is stress free, and unconstrained.

An extension of the previously discussed thermal-mechanical finite-element model was developed for this work to study the effect of crack propagation history on defect shape. Cracks were created in some simulations using a special procedure by creating a rigid coupling to a dummy domain on the left symmetry plane and allowing nodes to release according to a predefined criterion. The inset in the upper left of Figure 6.5 shows the crack propagation path along the symmetry plane on the left of the model domain. As the model slice moves from the meniscus down through the mold (increasing time), nodes separate from the rigid symmetry plane according to a defined history. The freed surface is then able to deform according to the stress state in the region. Crack propagation histories are imposed a-priori, such as the example shown in Figure 6.5. As the (mechanical) crack history is defined a-priori, and the thermal and mechanical models are coupled, the crack history is able to influence the thermal solution through the gap conduction displacement coupling relationship.

The plot in Figure 6.5 shows typical simulations results for the evolution of the liquidus and solidus isotherms (or shell locations) in solid red and black lines respectively. An example of the nonlinear crack tip propagation/growth history is as shown by the green dashed line. Full details of this model can be found in the literature [88]. Complete details of this are discussed in Chapter 3.

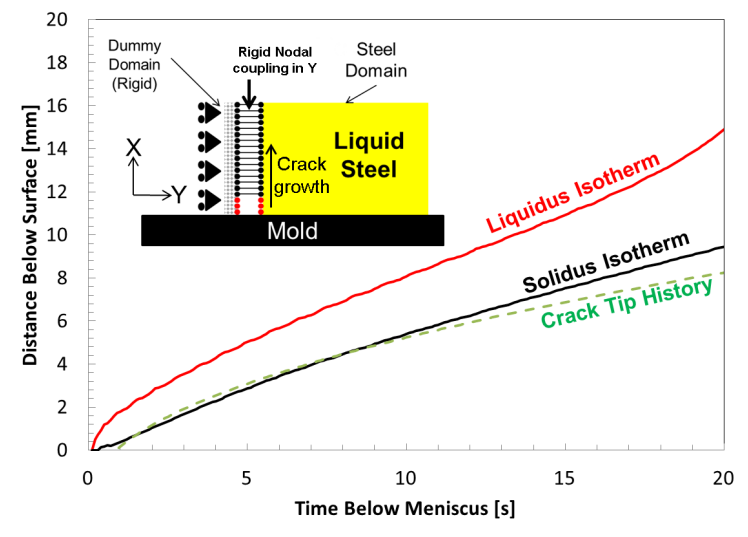


Figure 6.5: Liquid and solid isotherm locations at depression center for a 25 mm thermal disruption on the surface of solidifying shell with an example crack propagation history following, and then lagging behind the solidus isotherm

6.3 Material Properties

To enable evaluation of results, most simulations in this work use properties for a plain low-carbon steel (0.04 wt% C) as an example grade, with phase fraction history as shown in Figure 6.6. For this grade, liquid solidifies completely into δ-ferrite, followed by complete transformation into γ-austenite. The thermal behavior of other grades is expected to be very similar. The model predicted mechanical behavior for other grades depends mainly on the phase fraction history. The solidification stress behavior for stainless steels, advanced high-strength steels, and peritectic steel grades differs as discussed elsewhere [17, 41]. In two-phase regions, most thermal and mechanical properties are modeled based on a simple weighted phase fraction summation, with the constitutive equations handled differently. To model the liquid and mushy zones before solidification, an isotropic elastic-perfectly-plastic rate-independent constitutive model, with a small yield stress of $\sigma_{Yield} = 10kPa$, is used when the temperature is above the solidus temperature. The Zhu power law ferrite model [17] is applied in the solid whenever the volume fraction of ferrite is more than 10%, and the Kozlowski III austenite model [83] is applied otherwise.

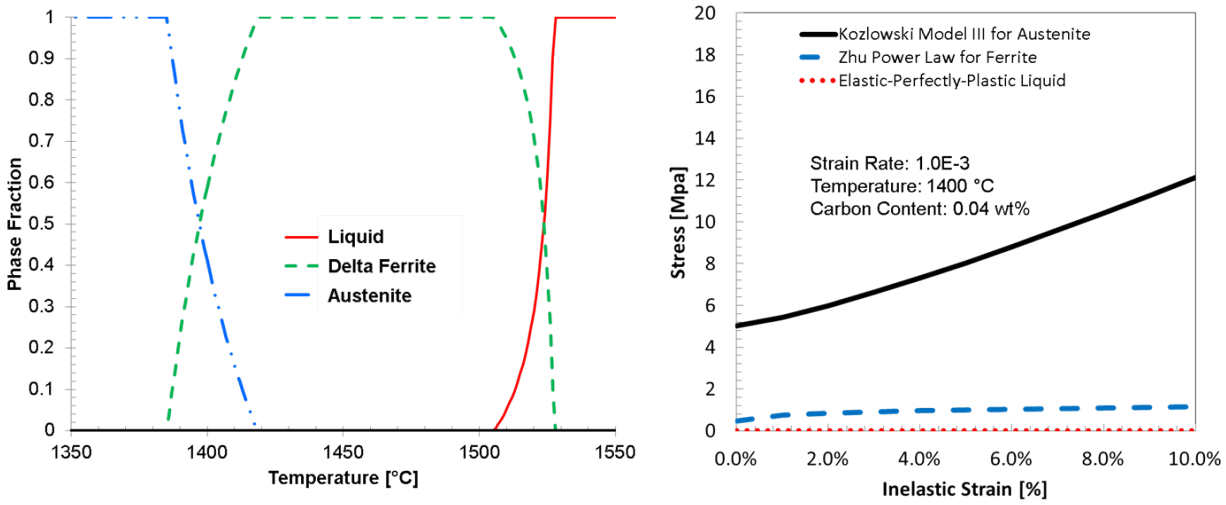


Figure 6.6: a) Phase Fraction solidification history for the plain low carbon steel used in this work, and b) Example values for the constitutive models used in this work including the solid γ-Austenite and δ-Ferrite phases, and the weak liquid phase

The ferrite phase of steel is almost one order of magnitude weaker than austenite for the same temperature and strain conditions; this can be observed in the example model calculations Figure 6.6, which shows results for both solid constitutive models, along with the liquid phase.

6.3.1 Domain Size Effect

An assumption made in this work, is that the far field behavior of the steel shell can be captured and imposed onto a smaller domain, as an applied tension, or according to the friction in the mold. In the large domain, hoop tensile stress towards the center is higher, and can partially help explain why wider casters are often found to have higher propensity for creating longitudinal defects. This is partially due to the larger area for variability in frictional and lubrication behavior within the mold as well as the larger areas for shrinkage to apply local tension on specific areas towards the center. Figure 6.7 shows the far field results of the small 40 mm domain primarily used in this work along with the results at 40 mm in the full size 500 mm domain simulation.

Figure 6.7a shows that after approximately 1.3 s, the shrinkage profile of the small domain very closely matches the behavior of the larger domain. The behavior very near to the meniscus is complicated and involves substantial fluid flow effects as discussed previously. The exact meniscus behavior is not the subject of this work, thus only the relative shrinkage results after 1.3 s are shown.

Figure 6.7b shows the far field hoop stress behavior through the thickness at 20 s for both domain sizes. As the plot shows, through-thickness hoop stress is nearly identical in both domains. Results of this study indicate that using the smaller domain to explore behavior on a larger scale is valid. Furthermore, applications of tension to the small domain (in excess of frictional tension) can easily allow for analysis of conditions towards the center in the larger scale model without the computational expense.

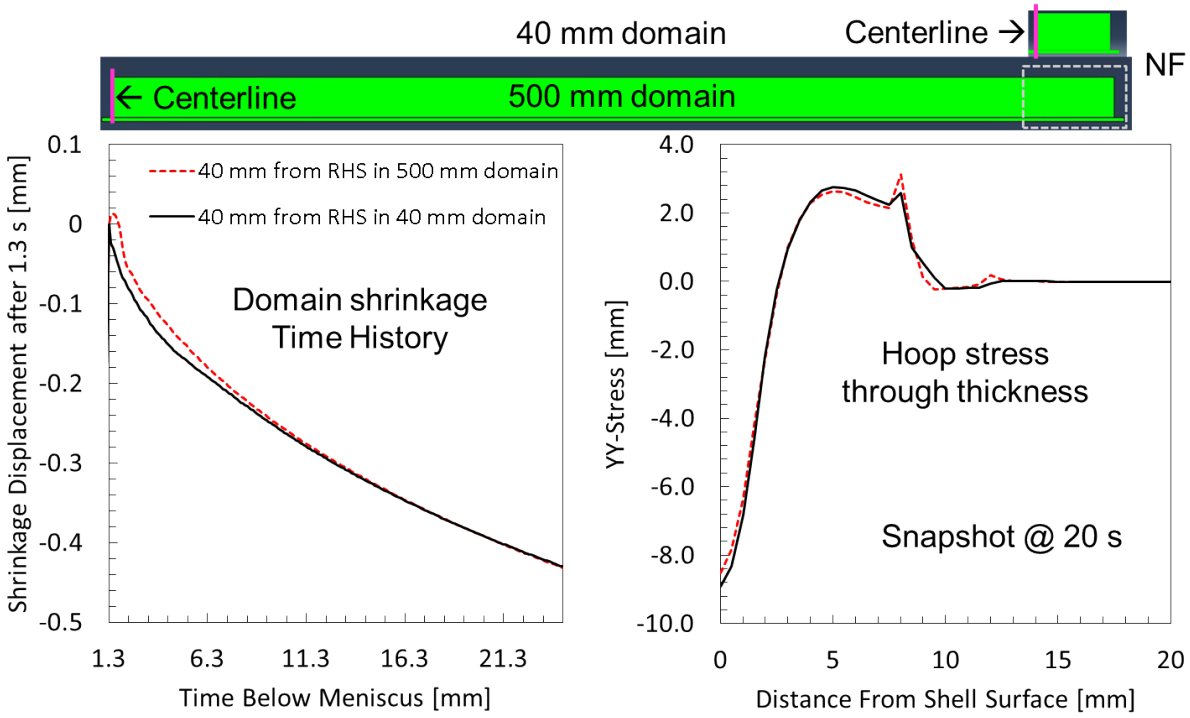


Figure 6.7: Domain size effect far field results: Shrinkage displacement (a) and Hoop stress through thickness (b) for 40 mm small domain and 40 mm section within 500 mm domain

For an unabridged description of each of the models mentioned in this section, including material property validation, please refer to the literature [15, 17, 41, 95, 128, 129].

6.4 Defect Mechanisms

The next sections present example manifestations of longitudinal depressions and cracks, together with model simulation results and a detailed explanation of the mechanism believed responsible for its formation. When possible, photographs of slab samples containing defects believed to arise from this mechanism are also provided.

6.4.1 U-Shape Necking Type Depression Without Surface Cracks

One of the most commonly observed types of depression has a U-shape with no visible surface crack. This type of defect is characterized by a smooth U-shaped surface depression. Their shape can range from shallow and wide (high width/depth aspect ratio up to ∼200 to deep and narrow, with lower aspect ratio (down to ∼5). Two examples of longitudinal depressions without surface cracks from two different steel grades and casters are shown in Figure 6.8.

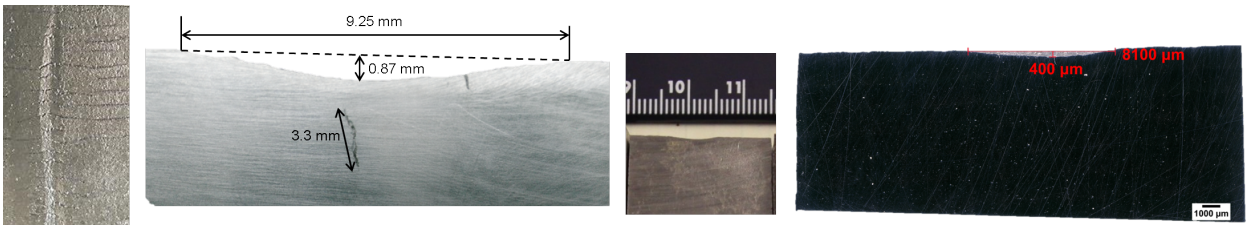


Figure 6.8: Examples of 2 U-shaped necking type depressions, cross sections and surface views. From left to right: First: Top surface view of a longitudinal depression on a plain low carbon (0.04 %C) steel slab, Second: Transverse cross section of the same plain low carbon defect, Third and Fourth: Transverse cross section of a non-peritectic Al-Mn AHSS steel grade (0.2 %C) with a longitudinal depression

The formation mechanism for U-shaped depressions is illustrated in Figure 6.9, which shows the deformed shape and temperature contours for a particular model simulation. In this simulation, a thermal disruption of 25 mm wide, 1 mm of additional slag and a constant tensile strain rate displacement of 0.03 mm/s was applied to the right side of the 40 mm wide domain. As the shell starts to grow, the local thermal disruption causes a reduction in heat transfer across the gap near the left symmetry plane, where the depression center

eventually forms, and where the highest reduction and highest strand surface temperatures are found. Uniform heat transfer at the far field away from the depression proceeds, and the colder stronger shell at the far field shrinks against friction from the mold and applies tension on the shell. Localization of the tension occurs at the weakest part of the shell, the thin depression center, leading to necking and separation from the mold surface. Separation from the mold surface leads to a further decrease in the heat transfer in this region and continued necking. Tensile strain is concentrated in the necked region, and bending causes a slightly higher strain at the solidification front. When this exceeds the critical strain for the given steel grade, a sub-surface crack is predicted to form, directly beneath the deepest part of the depression.

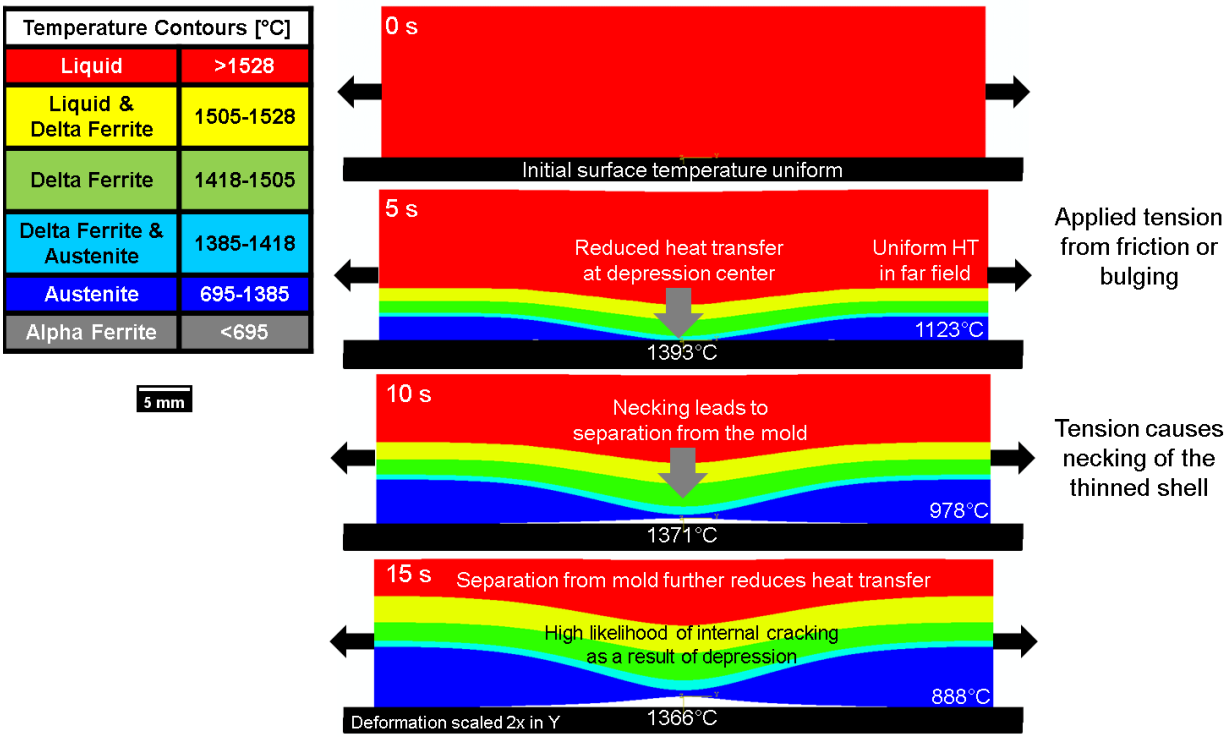


Figure 6.9: Deformed shape and temperature contours for 25 mm thermal disruption with applied tension of 0.03 mm/s at: a) Meniscus, b) 5 s, c) 10 s, and d) 15 s below the meniscus

6.4.2 U-Shape Necking Type Depression with Sub-Surface Cracking

Depressions with obvious surface cracks are readily associated with quality problems and downgraded for remediation. However, slabs with surface depressions and no visible surface cracks may still have quality issues. During solidification, there is already tension at the solidification front as the colder steel at the surface shrinks. It is well accepted that too much tension near the solidification front can lead to hot tears and macro-segregation as a result of liquid feeding problems. The formation of a depression leads to increases in tensile stresses throughout the cross section of the shell, including at the solidification front. For this reason, it is not a surprise that evidence has been found linking sub-surface cracks and sub surface macro segregation streaks in samples with non-surface-cracked longitudinal surface depressions. As shown in Figure 6.10, evidence of MnS as well as MnSi are observed below a surface depression without a crack. It is also believed that the presence of a surface crack would likely not change the appearance of the segregation at this location.

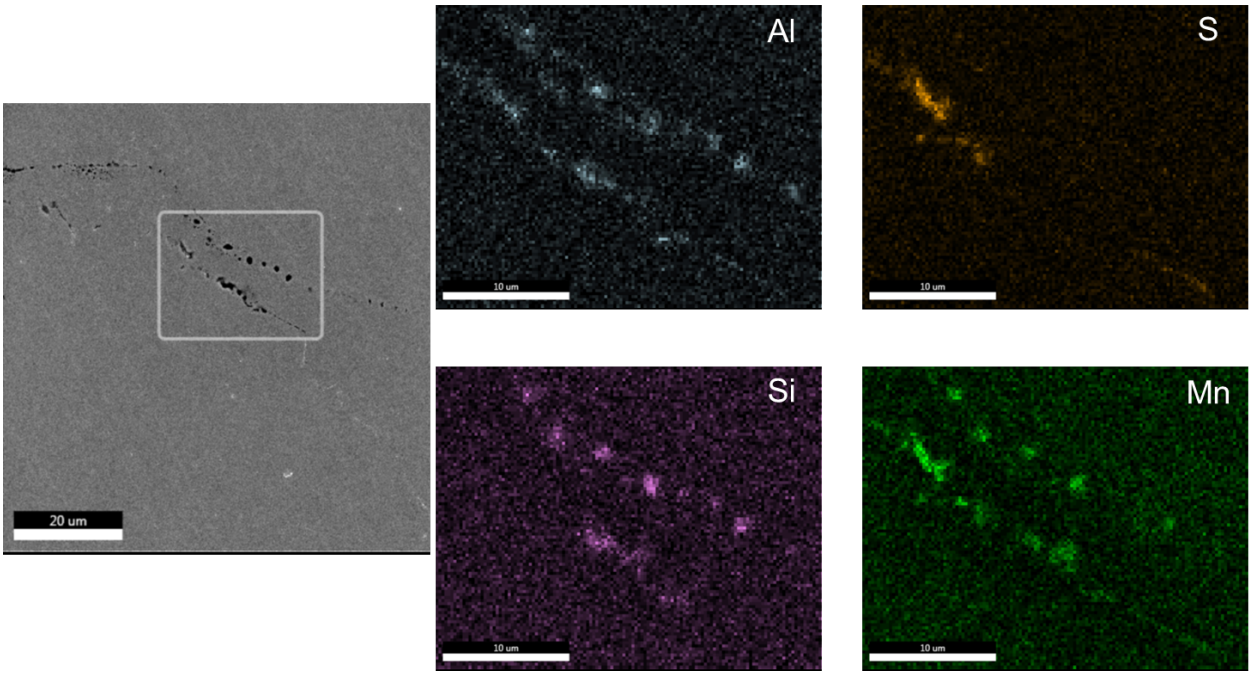


Figure 6.10: EDS map of sub-surface hot tears with macro-segregation from a non-peritectic Al-Mn AHSS steel grade (0.2 %C) with a longitudinal depression and no surface crack

Propagation of a sub-surface crack to the surface is advantageous in relieving the tension that is going into necking of the shell, and if multiple cracks are present, rupture to the surface is usually enough to retard the growth of the other sub-surface cracks and further open the surfaced crack instead. This is likely why sub-surface cracks are often found in groups (Figure 6.11), with usually just one of them propagating all the way up to the surface.

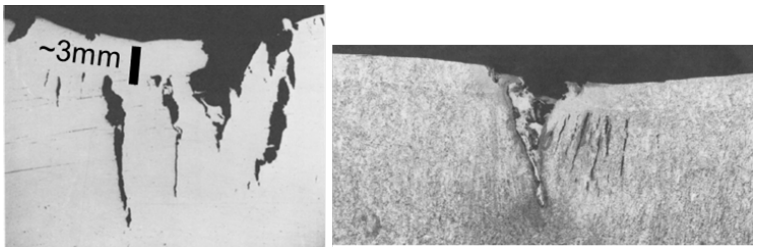


Figure 6.11: Examples of sub-surface crack groups with only one or two reaching the surface [7]

During the formation and growth of the U-shaped depression, tension localizes towards the center of the defect. However, while the localized tension raises the stress through the cross section, sub-surface cracking occurs as a result of exceeding the critical strain and not high stress. The critical strain is quite small and depends largely on composition. It has been reported that values between 2% and 8% provide sufficient strain for internal cracking in low carbon steel grades [130]. Figure 6.12 shows the maximum principal stress and strain for the 25 mm thermal disruption case at 15 s below the meniscus. In both images the top two black horizontal curved lines represent the liquidus (upper) and solidus (lower) isotherms. While the maximum principal stress is only $\sim$0.23 MPa, the maximum principal strain is $\sim$4.6%, which is well within the critical cracking strain. Lower width/depth aspect ratios are associated with sub-surface cracking, as the increased depth of the depression is associated with increased bending, which increases tension near the solidification front, causing hot tear(s), which draw in interdendritic liquid from the surroundings and result in a region of macro-segregation, with the shape of a crack.

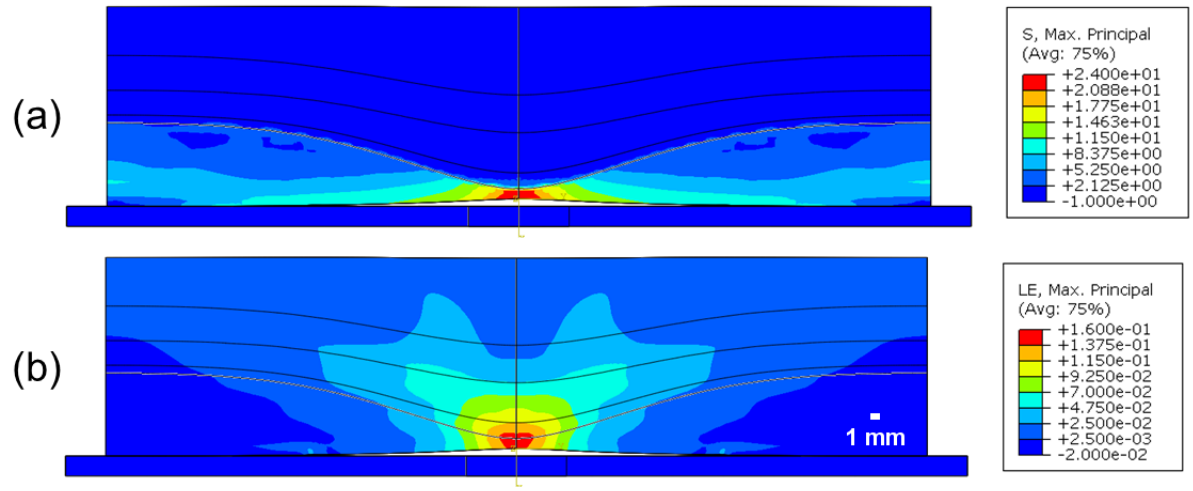


Figure 6.12: Deformed shape and maximum principal stress (a) and strain (b) contours at 15 s below the meniscus for 25 mm thermal disruption with applied tension of 0.03 mm/s. Black horizontal lines indicate phase/temperature isotherms. (Deformation scaled 2x in Y)

6.4.2.1 Localization Effects

The size of the thermal disruption region has a notable effect on the depression severity. Figure 6.13 shows the results of a frictional tension parametric study with varying widths of the thermal disruption. Formation of this type of depression depends on two different mechanisms operating together: increased local temperature due to the gap (which weakens the steel shell), and local concentration of the strain, which increases with increasing friction and contact length. If the thermal disruption is very narrow, then 2-D heat transfer around the thermally-disrupted region is possible, and the temperature increase in the depression bottom is small. However, if the thermal disruption is very wide, then the local frictional tensile strain becomes less, because the contact region between the strand and the mold decreases, for a fixed domain size. Thus, the severity of strain concentration is reduced. The deepest depression, (and corresponding most likelihood for a sub-surface crack) is for a critical intermediate condition, which depends on casting conditions, such as cast width.

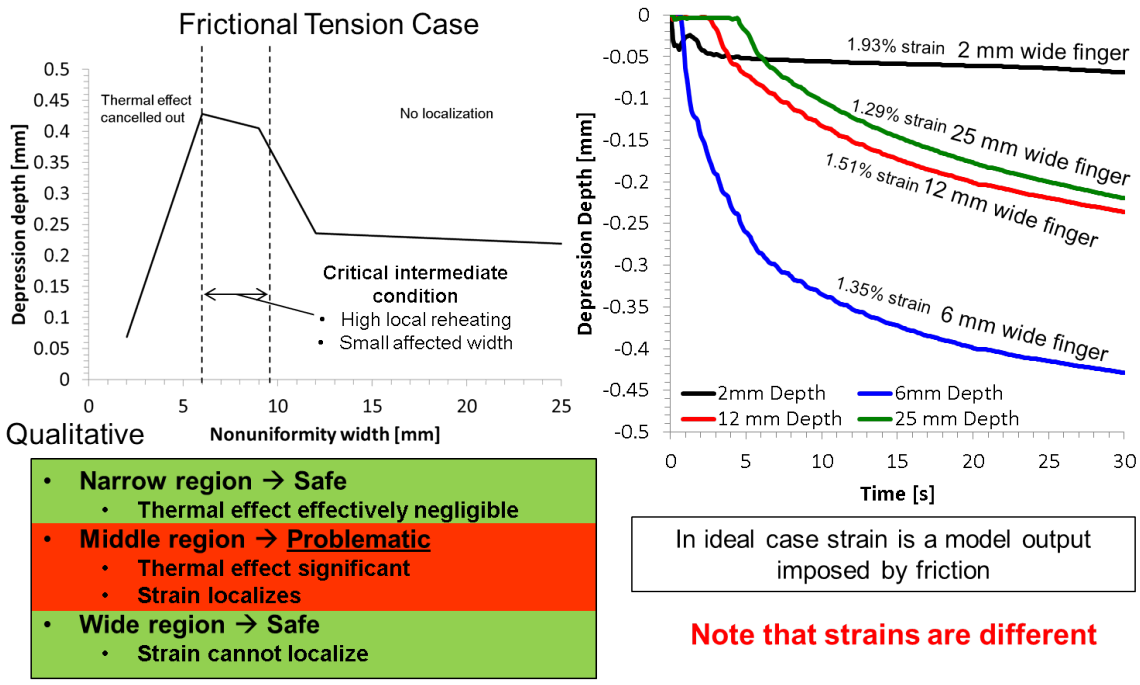


Figure 6.13: Combined mechanism for necking localization and corresponding depression depth severity

6.4.2.2 Defect Timing and Relative Severity

Figure 6.14 shows the results of a parametric study examining the effect of the thermal disruption start location; as well as the final deformed shapes, both at mold exit, and after cooling to near ambient. It has been found that the depression stops growing once the surface temperature reaches ~700°C. Figure 6.14a shows that delaying the start of the thermal disruption to a lower distance below the meniscus causes the depth of the resultant depression to decrease. Figure 6.14b shows the final depression depth, which is substantially deeper than at mold exit. Furthermore, the depression is always much deeper when the disruption starts closer to the meniscus. This finding is consistent with the accepted understanding that longitudinal depressions and cracks tend to initiate close to the meniscus.

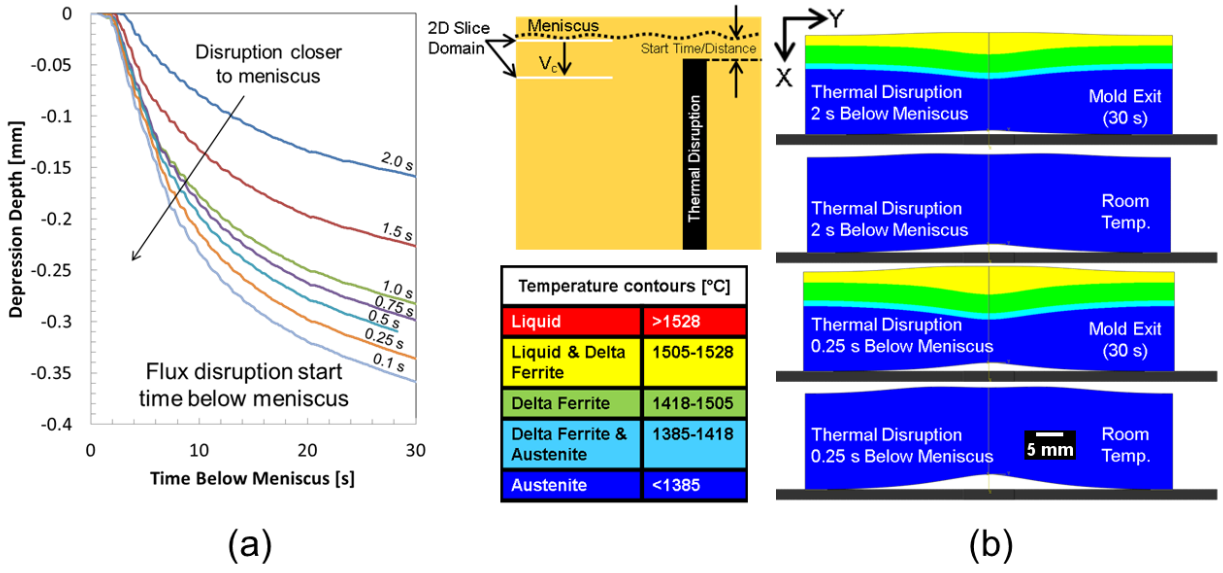


Figure 6.14: Effect of thermal disruption initiation time on depression evolution: a) Depth history for varying disruption initiation times, b) Deformed shape of depression at mold exit and after cooling to near ambient, for late disruption (top) and early disruption (bottom) [131] Note: Deformation scaled 5x

6.4.3 U-Shape Buckling Type Off-Corner Depression Due to Inadequate Taper

Another type of depression, which is relatively well understood, is off-corner, U-shape depressions. Previous work has shown these depressions may arise due to either excessive or insufficient taper of the narrow faces of the mold [55]. They are only problematic when accompanied by sub-surface cracks, such as shown in Figure 6.15 They are particularly common on the inside radius of the strand, especially in curved mold casters [55].

The formation mechanism of these depression defects involves two stages. Firstly, a thermal disruption at the meniscus often leads to lower heat transfer and a thin spot on the shell in the off-corner region. This disruption is often caused by turbulent flow problems that create standing waves in the mold. Insufficient taper then removes the support provided by the narrow face and allows the shell on the narrow faces to bulge outwards from the ferrostatic pressure. As shown schematically in Figure 6.16a, the narrow-face bulging is greatest at the center of the narrow face, and leads to rotation of the corners towards the center of the



Figure 6.15: Example of sub-surface cracks beneath bulging gutter depression (outlined in black boxes on sulfur print) [50] Note: Image color adjusted for clarity

strand, pivoting around the weak, thin region of the shell. This rotation pulls the off-corner region of the wide face shell surface inwards, growing into a gradual, U-shaped depression that persists in the final slab, where it is often referred to as “gutter”. The second stage of the mechanism that forms this type of longitudinal depression can also arise due to excessive narrow face taper. As shown schematically in Figure 6.16b, excessive taper of the narrow face molds forces the shell inwards and compresses the broadface shell. As the narrow face moves inwards, the corner behavior can change the force application direction enough to help buckle the broadface shell at the off corner region.

Off-corner depressions caused by this mechanism are likely to be deeper and more severe, with lower aspect ratios, such as pictured in Figure 6.17. In this work "buckling" refers to non-uniform compression of the solidifying shell, when the applied load results in movement away from the mold, often caused by overtapering of the narrow face coppers, and should be understood to mean “inelastic buckling” or “kneeling” [54].

6.4.4 W-Shape Buckling Type Depression Due to Excessive Compression

This type of defect is shown in Figure 6.18a and is characterized by two (or more) wide and shallow depressions on the broadface surface. In this particular case the depressions

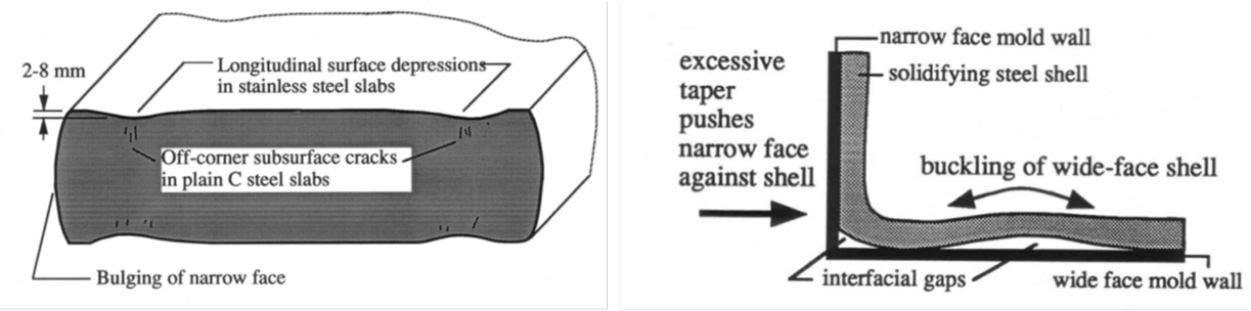


Figure 6.16: Off-corner depression formation mechanism schematics [55]: a) Narrow face shell bulging leading to off-corner depressions with sub surface cracks, b) Excessive taper leads to buckling of the wide face shell



Figure 6.17: Off corner buckling depressions from overtaper

vary slightly in severity along the length of the billet and also wander side to side slightly. As shown in Figure 6.18, the W-shape depression is primarily related to the application of compressive stresses leading to buckling of the shell. For example, the billet shown in Figure 6.18a was cast in a billet mold that was switched from oil casting to slag casting, without a change in taper [132, 133]. However, slag casting has lower heat transfer that oil, which means less shrinkage of the strand, and the billet became stuck in the mold. To remove the billet, the drive rolls were turned up and the strand was forcibly removed from the caster. As the strand was driven out of the machine, it was subjected to high levels of compression across the broad faces due to the fixed width of the mold which caused the surface to buckle.

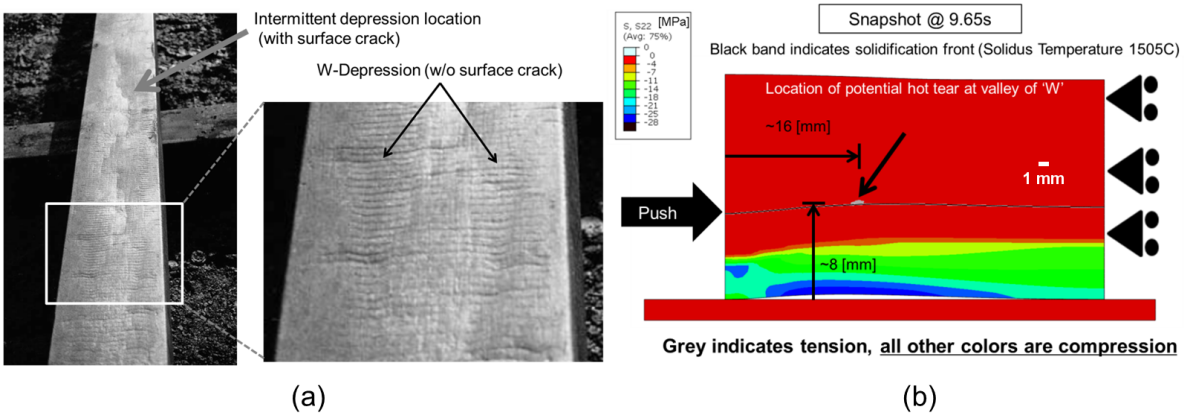


Figure 6.18: (a) Continuously cast billet exhibiting severe "W" shape depression after buckling within the mold [132, 133], (b) Hoop stress model results for severe over-taper case with thermal disruption displaying sub-surface tension

This type of depression is a result of compression and buckling on the broadface. As the strand shrinks, over taper of the mold forces the narrow faces inwards and imposes compression on the broadfaces. A local disruption in heat transfer creates a weaker spot in the shell, and if the compression is high enough, the broadface shell will buckle and bend under the load. As the sub-surface yields, the location of peak stress at the solidification stress moves around and can lead to wandering of the depression side to side across the strand

This type of depression is rarely described in previous literature, and may be difficult to spot because during normal operation, the strand usually does not experience the high compressive stresses necessary to cause it. Overtapering the mold is a common practice, and understandable because it is safer for maintaining heat transfer and avoiding breakouts than undertapering. Usually, the compressive stresses from slight overtapering during steady conditions are low enough that any buckling of the shell would be extremely minor and any warping of the surface would be removed as soon as the section reached the support rolls. Additionally, a W-shape depression requires some yielding of the sub surface to allow it to deepen. This may bend the shell, creating tensile stress on the solidification front, and leading to surface hot tears. These sub-surface cracks may be recognized because they may cause the strand surface to have intermittent, locally deeper, even V-shaped portions in one or both of the two depressions of the W. As usual, the cracks follow the prior austenite grain boundaries, and become filled with solute enriched with alloys leading to macro-segregation defects beneath the surface. It is also possible that sub-surface cracks form before the forces become large enough to cause the double-depression W-shape across the broad face, so instead the depression is manifested as a single wide and shallow U-shape.

The W-shape buckling style depression is also common in thin slab casters, especially those with funnel molds, due to the complex geometries, change in circumference down the funnel portion of the mold, which are susceptible to inadequate taper design. For example, Figure 6.19 shows a cross section from a thin-slab caster that buckled during casting. It has been shown, based on longitudinal crack location and frequency analysis, that proper taper and funnel design are critical to final product quality [134]. Overtapering of a funnel mold can cause the shell to separate away from the mold at the inner curve/shoulder location (curve closest to the wide face centerline), while the inner flat region remains in contact. Undertapering is likely to lead to bulging of the shell, and could lead to separation at the inner flat region as well as the inner curve as the shell is stretched around the outer curve. Both of these scenarios can lead to shell thinning, surface depressions caused by buckling,

and eventually to a breakout. In certain situations there is even the potential for multiple simultaneous breakouts as was the case with Figure 6.19. These depression defects can be avoided by proper taper design based on the specific grade being cast.

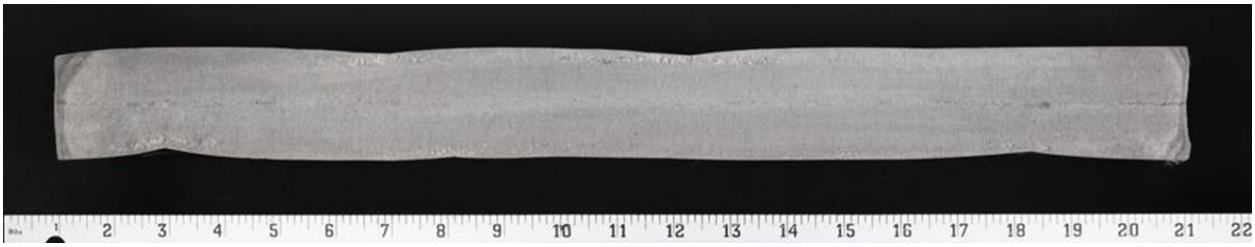


Figure 6.19: Transverse section of a buckled thin slab cast AHSS prior to multiple simultaneous breakouts at longitudinal depression

6.4.5 W-Shape Necking Type Depression with Surface Crack

While the U-shape is the most common style of depression, and is due to necking in tension of the shell, a second type of depression is possible with tension. Figure 6.20a shows a micrograph of a W-shaped depression that is believed to have evolved from a U-shaped depression as a result of significant shell thinning and the action of ferrostatic pressure on the shell. Additionally, surface cracks can be observed at the depression center, where increased tension would be experienced as a result of bending of the shell as it is pushed back towards the mold from its initially necked depressed position. Figure 6.20b, shows results from a model simulation of this type of depression. Note the significantly thinned austenite layer, as well as solid shell, compared to the previously shown results for U-shape depressions. Initially a U shape necking depression starts to form. However, the significant shell thinning at the base of the depression keeps the surface so weak that ferrostatic pressure pushing outwards from the liquid core is able to maintain a smaller gap between the defect center and the mold surface while the depressions to the side of the defect center bend and continue to neck. If sufficiently high strain is reached (particularly if a low ductility trough is encountered) then a surface crack is likely to form at the defect center.

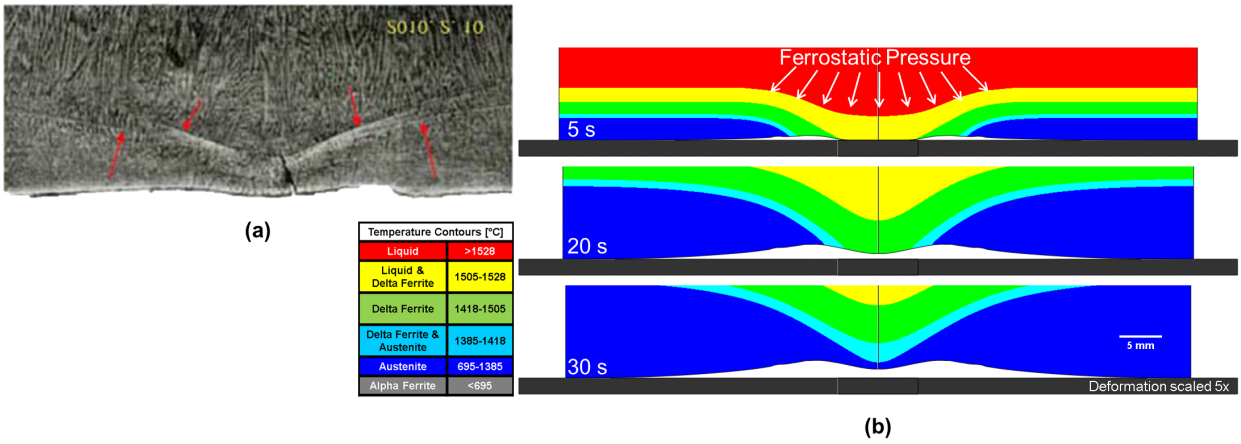


Figure 6.20: a) Micrograph of a W-Shape depression in tension [135], b) Model result for a significantly thinned shell bent back towards the mold into a W-shape at

6.4.6 U-Shape Grooves From Solidification Against a Slag finger/Rivulet

In contrast with most of the depression types previously discussed, some longitudinal depression defects are manifested as almost straight, vertical grooves down the strand surface. One of these types, shown in Figure 6.21, is caused by part of the solid flux layer at the slag rim sticking to the mold wall and growing downwards with an appearance similar to an icicle, although its appearance can only sometimes be seen on the mold wall after the end of the casting sequence. On a local level, a small chunk of solid slag becomes caught in the scratch and protrudes past the surface of the copper creating an uneven surface for solidification to occur. The slag scab creates a local reduction in heat flux due to the thicker flux layer. Depending on behavior of the flux the scab may grow or be eroded away. Once in the gap, the unmelted slag chunk creates a local artifact for the shell to solidify around. A slag finger stuck to the mold has two different important effects: thermal and mechanical. Firstly, the slag finger creates an additional layer of slag, which lowers the local thermal conductivity of the interfacial gap, even if it is very thin. This local insulation acts as a thermal disruption that leads to a locally thinned shell, with related behaviors similar to previously-discussed depression types. Secondly, the space taken by the finger creates an uneven surface for solidification to occur. This naturally causes the local shape of the shell

that solidifies around it at the meniscus to match the finger shape, thereby directly creating an impression/depression on the strand surface (mechanical effect). Although these two consequences of a slag finger always act together, their importance varies according to the slag finger shape. The final shape of this type of defect is indicative of the original shape of the slag finger. Results of the models shown in Figure 6.21 convey that the change in shape of the initially created depression changes only slightly after the shell begins to solidify around it. Frictional or additional tension on the broadface surface causes similar necking phenomena as described before. Depending on the severity of the tension a slight reduction in depth of the depression is expected and a widening of the original shape. This is especially likely in the case of a shorter slag finger.

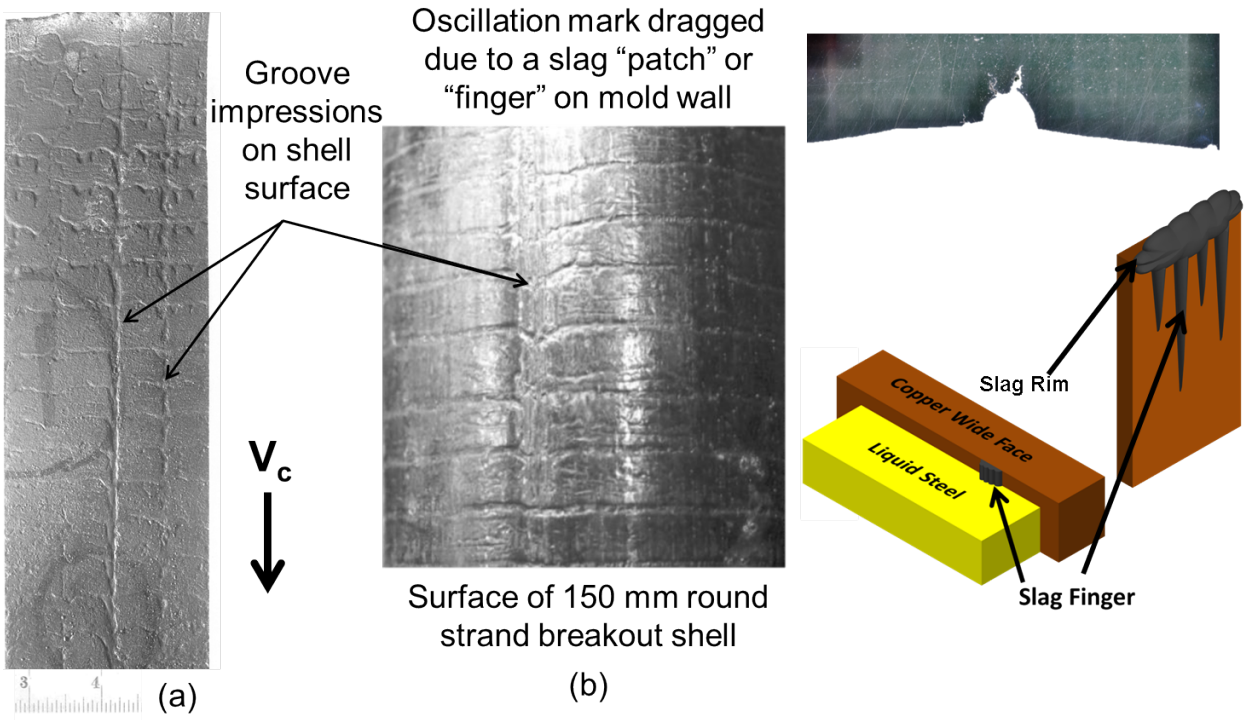


Figure 6.21: Abnormal shell surface as a result of solidifying against slag fingers on the mold hot face: a) Flux-related surface grooves on a breakout shell [136], b) Oscillation mark dips due to flux patch [136], c) Schematic of slag finger descending from slag rim

Figure 6.22 shows a transverse cross section of one of these slag related longitudinal groove defects found at the midface of an Advanced High Strength Steel (0.2 %C, high Mn)

slab cast at 1 m/min with a high-aluminum slag. Electron Dispersive Spectroscopy (EDS) area scans of a portion of the cracked surface region reveals high pickup of aluminum from the slag as well as penetration of sulfur, silicon, and calcium present deep into the cracks indicating the presence of slag at high temperatures allowing for increased diffusion into the shell.

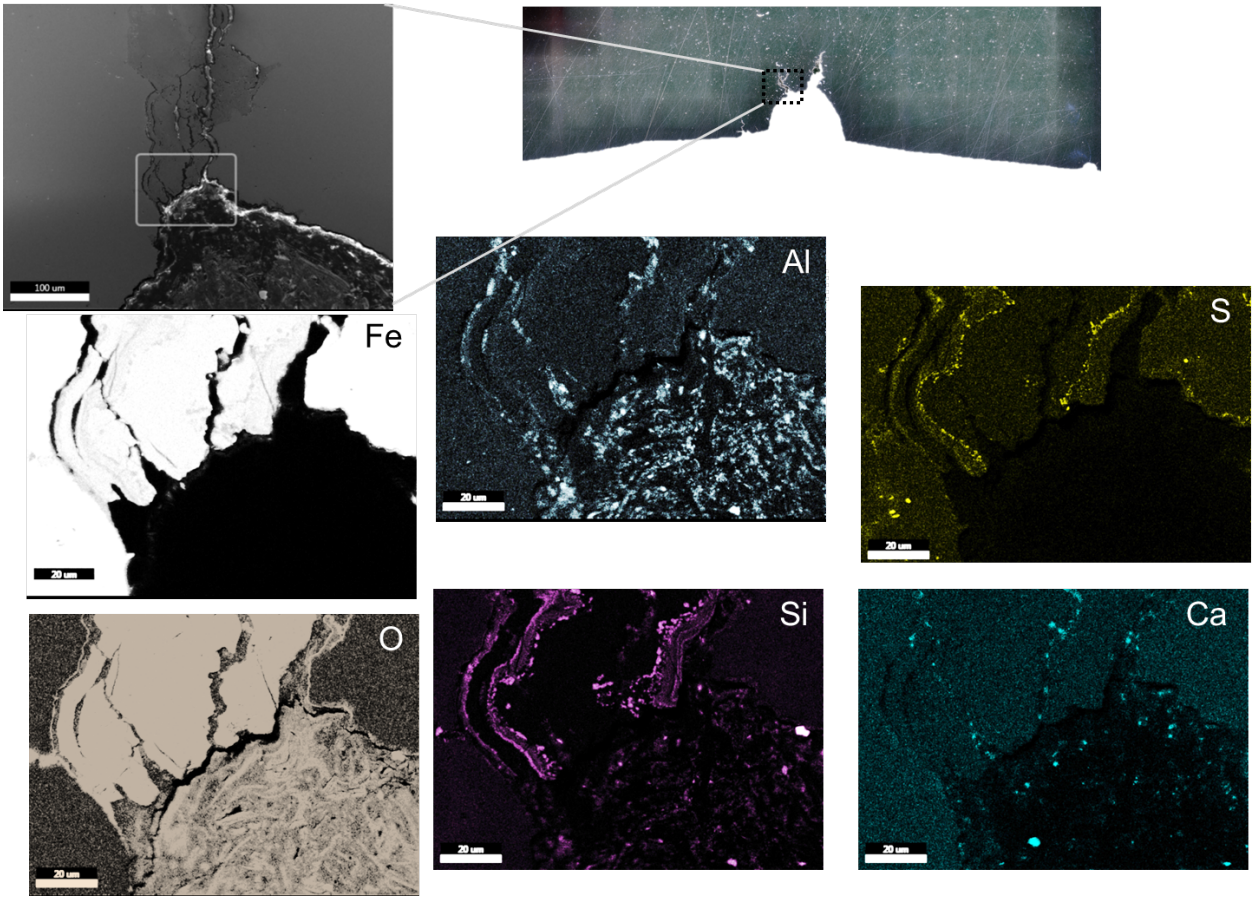


Figure 6.22: EDS analysis of a longitudinal U-shape groove defect at the midface of an Al-Mn non-peritectic Advanced High Strength Steel (0.2 %C) slab cast at 1 m/min with a high-Al slag

Results of the model in Figure 6.23 show that the depression is more severe if the finger disappears sooner, i.e. an "empty" space is created sooner. The lower the conductivity of the material filling the space, the worse the defect will likely be. The depth of the slag finger defect is initially the same as the finger itself. As the finger gradually shrinks with distance down the mold, ferrostatic pressure may be able to push the thin and weak shell in the

depression back towards the mold wall. Eventually, however, frictional tension may cause necking via the same mechanism that causes U-shaped necking depressions. Once a local depression has formed, the lower the conductivity of the material filling the space, the worse the defect will likely be. Thus, slag fingers or rivulets that end abruptly a short distance down below the meniscus may be more problematic. This is because the downward-moving depression in the shell for this case may suddenly experience an air gap, with greatly reduced heat transfer, that is much more severe than the retarded heat transfer experienced when it was adjacent to the slag finger. Such a gap could cause reheating of the local surface, leading to severe necking, crack formation at the solidification front, and a deep, V-shaped (low aspect ratio) depression that represents a severe quality problem.

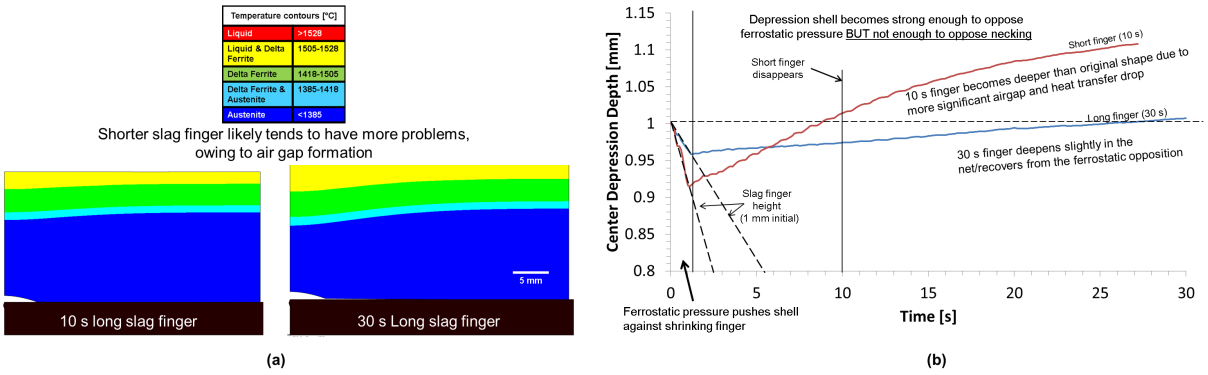


Figure 6.23: Slag finger model results: a) deformed shape with temperature contours after 30 s of solidification, b) Depression depth history

Avoiding this type of depression simply requires preventing the formation of slag fingers. There are many potential causes of the slag finger. A slight scratch or scratches in the mold surface would entrap slag. Alternatively, excessive viscosity of the slag, due to local composition problems, such as caused by excessive alumina pickup from inclusion-laden steel could produce such behavior. Or, it could be related to excessive turbulence in the fluid flow near the meniscus and slag infiltration problems. Issues with startup slag and extra shrinkage of the initial shell during startup could lead to slag fingers [137].

6.4.7 V-Shape Necking Type Depression Due to Mold Scratch

Another type of straight, vertical, depression can be caused by a scratch in the mold surface near the meniscus. Sometimes during casting or maintenance, mechanical equipment can scratch, gouge, or scrape the surface of the copper mold. This may or may not penetrate any coating present, but it may create a depression in the mold surface, which can locally disrupt heat transfer and solidification.

Two scenarios are possible depending on the size of the mold scratch, as well as the properties of the specific slag in use. Firstly, the scratch may be large enough that liquid mold slag can infiltrate into to fill the scratch. This slag solidifies in the scratch to create a fixed local region of reduced heat transfer, as the gap at the scratch becomes effectively thicker due to the added flux. Secondly, the scratch may be either too small or the flux viscosity and/or temperature does not allow it to infiltrate into the space for some reason and the scratch is effectively filled with gas (air). The scratch creates a fixed local region of reduced heat transfer from the insulating effect of the gas

Both scenarios will effectively result in the same defect appearance. The longitudinal defect is likely to manifest as a very straight, continuous, sharp (low aspect ratio) V-shaped depression on the slab surface located at one static location across the strand perimeter, such as the several images of the same example shown in Figure 6.24b and Figure 6.24C. This defect is likely to appear on all slabs in all heats, with varying severity, until the mold is removed from service.

Due to the low aspect ratio, increased tensile stress is seen near the defect while the rest of the surface is in compression. Crack sensitive grades are likely to be found with cracks at the base of the depressions. Additionally, there is a high likelihood of sub-surface hot tear cracks due to increased tensile stresses as the surface depression forms inwards. Increases in casting speed or slab thickness will exacerbate these difficulties.

As the defect starts to form, the shell is briefly pushed towards the crack in the mold. This depends on the shape of the crack and also the local shell thickness. In the case of

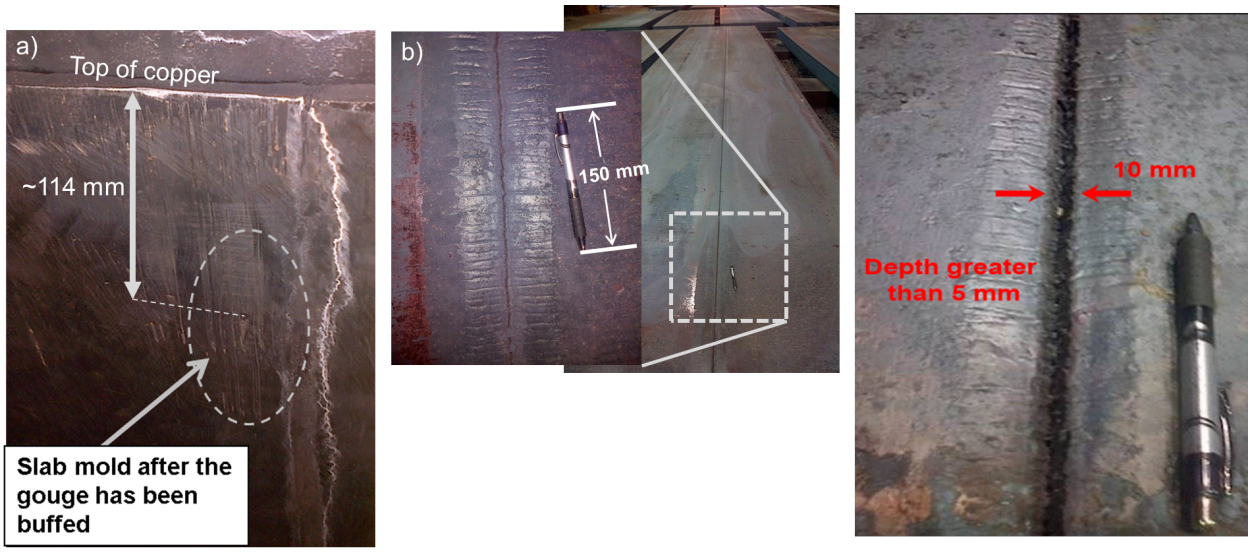


Figure 6.24: a) Mold surface imperfection (i.e. gouge) results in b) very straight longitudinal surface depression and/or crack. Present in all slabs cast in campaign, and always at the same location across the strand width (severity and shape of defect varies only with grade).

this model, the shell was briefly pushed towards the mold until the shell shrinkage overcame the force of the ferrostatic pressure and began to neck and pull away from the mold surface. The defect formed is a fairly sharp, v shape depression. The thickness of the total solid shell only varies by about 0.25 mm at the depression center, however the defect center surface is still at 1387°C. As Figure 6.25 shows, the local shell at the center of the defect is still transforming from ferrite to austenite even after 2 seconds when the rest of the shell has transformed. This difference in phase, and corresponding differences in strength cause high levels of stress to localize at the defect center in excess of 1 MPa. Based on the values in the literature [138], and depending on tramp element content (P, S), this is likely to be enough to initiate a crack in a plain low carbon steel.

Results of a study exploring width and depth changes is shown in Figure 6.26. Results indicate that the severity of the V-shaped depression is directly affected by the change in depth of the scratch, without an appreciable change in the width of the defect. This is likely due to the tremendous drop in heat transfer as a result of the increased air/slag gap from the scratch.

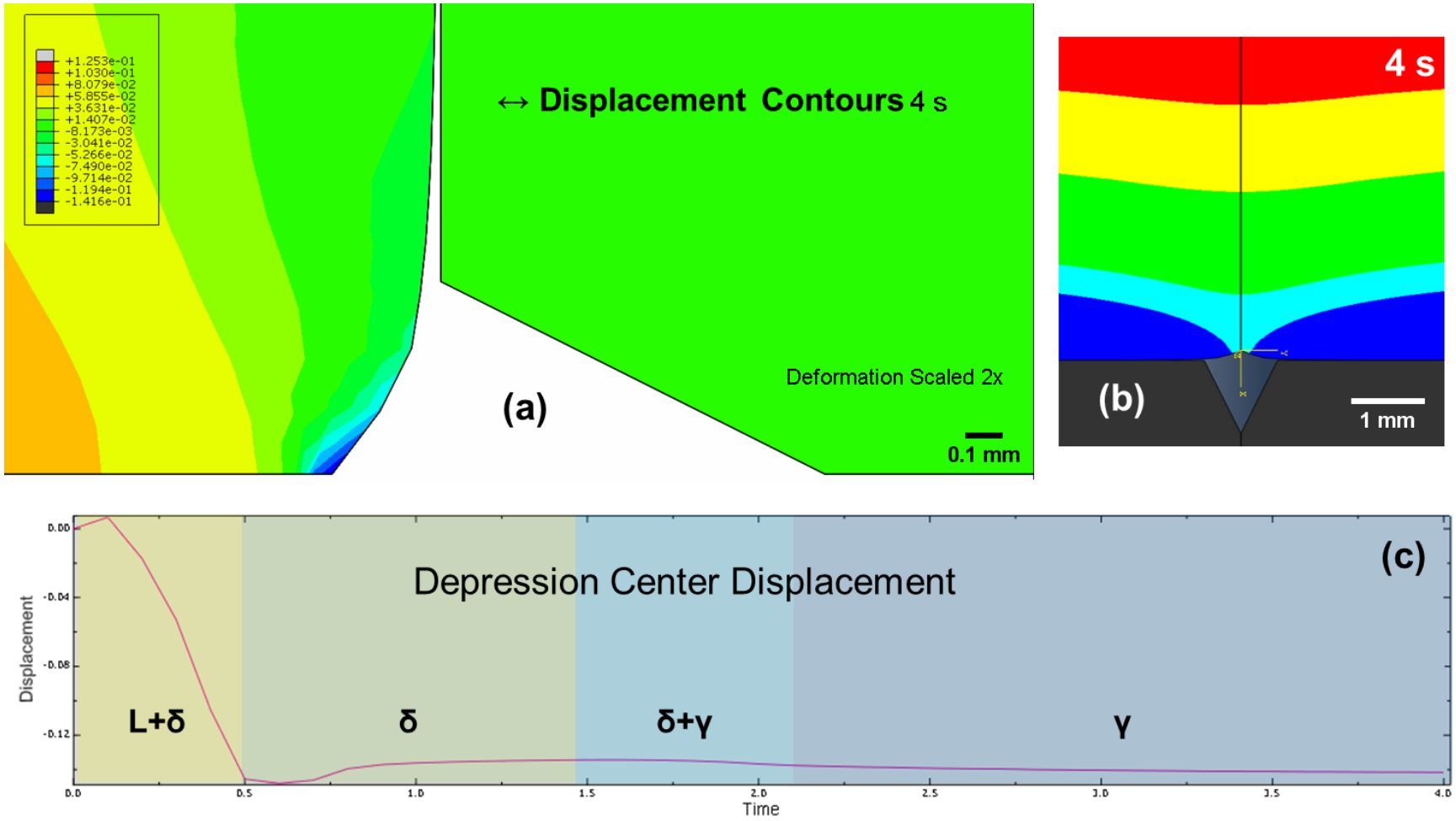


Figure 6.25: Model results for 1 mm deep and 1 mm wide scratch in mold using 0.1 mm elements: (a) Displacement contours at 4 s, (b) Unscaled deformed mesh at 4 s with phase/temperature contours, (c) Time history of depression center displacement including phase history of the depression center surface

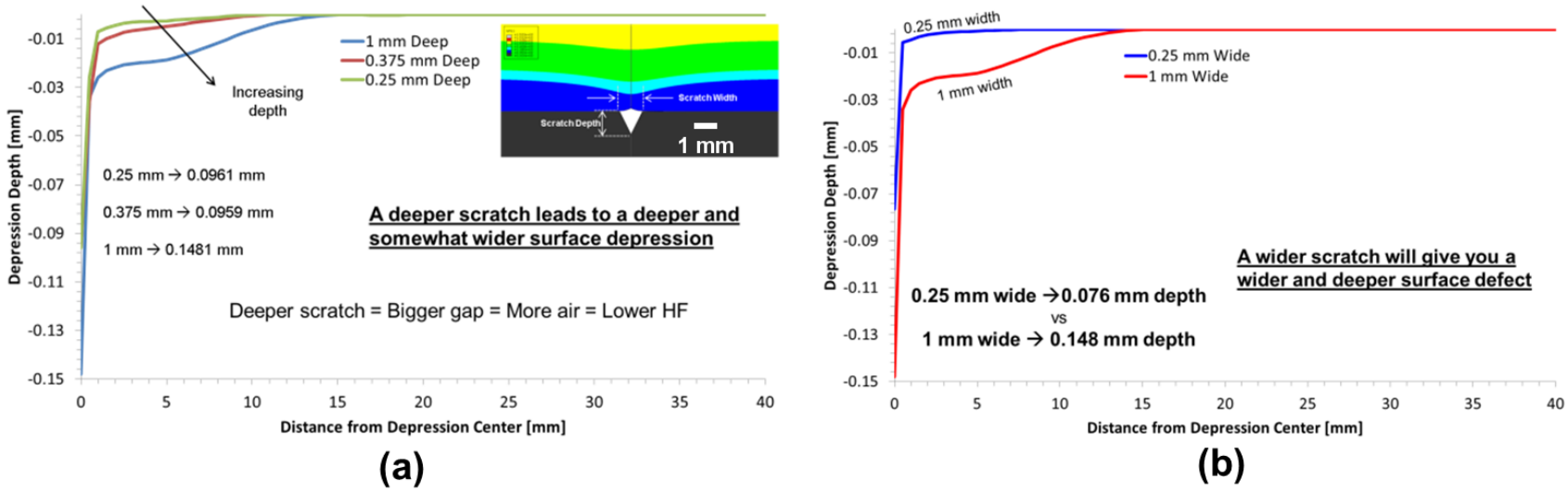


Figure 6.26: Effects of mold scratch width and depth on defect formation behavior (all results shown at 30 s below meniscus)

The severity of long defects, as a result of a mold scratch, varies significantly depending on the distance down the mold that the scratch starts. Scratches that start within the first few seconds below the meniscus are the most detrimental. Depending on the casting speed, this may be within the first hundred millimeters of the meniscus for traditional slab casters, or within the first few hundred millimeters for thin slab operations, which operate at higher speed. The effect of the scratch decreases substantially as the shell thickness increases with dwell time; thus, scratches towards the bottom of the mold are unlikely to cause any problems. Thus, the severity of the depression provides an indication about the size and location of the mold scratch/defect.

6.4.8 U-Shape Necking Type Depression With Surface Cracks

Another type of U-shape depression caused by necking is shown in Figure 6.27a, which shows severe, very wide, surface cracks (∼3mm. This is a low carbon steel cast on a thin slab caster at over 6m/min. The sample shown was taken from the slab just prior to a breakout. Multiple intermittent surface cracks similar to the one shown were found in the slabs leading up to the breakout. The little circular depressions on the sample surface are from molten steel droplets from the breakout that occurred above the sample, that were rolled into the slab surface. More importantly, the severe surface crack shown eventually penetrated from the surface into the mushy zone and directly led to the breakout. Intermittent surface cracks can be seen in Figure 6.27a, where the total width of the surface cracks observed on the broad face (∼3mm) can be seen to match with the width of shape asymmetry experienced on the narrow face.

Figure 6.27b shows a schematic to explain this particular defect. During casting, the broadface inner radius experienced high friction and potential sticking at the corner. This is believed to have led to the initiation of a crack while the shell was still very thin. Within the crack of the sample shown, dendrites are visible on the surface, indicating that this crack extended to somewhere within the mushy region, where there was interdendritic liquid present. As the shell continued to solidify, the outer radius continued to shrink, while the

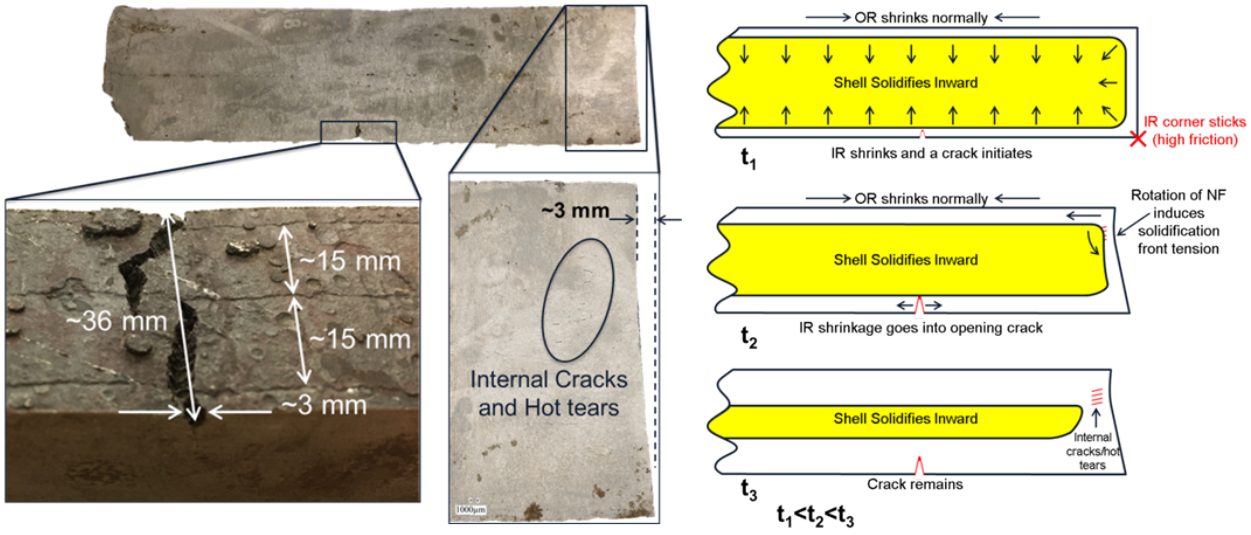


Figure 6.27: Transverse section and perspective view of a defect sample from a low carbon thin slab cast just prior to breakout (a), visible long crack on broadface surface and corresponding shape/dimensional problems on NF [50] (b) and Schematic explanation of broad face crack effects on narrow face shape problems and internal crack formation

inner radius shrinkage instead concentrated into extending the opening of the surface cracks. As the inner radius was not shrinking, the continued shrinkage of the outer radius led to corner rotation. This generated tension near the solidification front towards the outer radius of the narrow face shell, causing hot tears and macro segregation streaks at that location. The intermittent nature of the severe cracks on the sample, as well as the entire slab leading up to the breakout, indicate the precarious nature of this breakout scenario. Each one of these cracks had the potential to crack all the way through the shell to the liquid core.

In this specific sample, high friction, lubrication problems, and the thermal disruption were created by high fluid flow velocities generating a standing wave across the meniscus. The standing wave was confirmed by oscillation mark profile variation of more than 20 mm from the wide face centerline to the narrow face. As a result of the standing wave, slag pooled away from the narrow face, making infiltration of molten slag into the gap difficult towards the narrow faces, and causing bad lubrication there. In addition to the surface profile and lubrication issues, severe level fluctuations at the transition of the standing wave likely created the necessary thermal disruption to initiate this defect [50].

As visible in the sample (Figure 6.27a), the previously discussed thin slab breakout crack defect appeared intermittently at similar, but not identical, locations across the surface. This behavior is in contrast to the previously mentioned "static" crack (Figure 6.24) that appears consistently at the same location across the broad face. It should be noted that most of the defects mentioned are found all across the broadface and often wander around. Another example of this wandering behavior is shown in the longitudinal facial crack within a depression in Figure 6.28. This behavior is also apparent in the buckling type depression (Figure 6.17) where the exact location of the depressions wanders slightly from side to side and varies slightly in depth. This is particularly likely as sub-surface cracking occurs, and subsequently relieves stress, in different locations and depths below the defects.

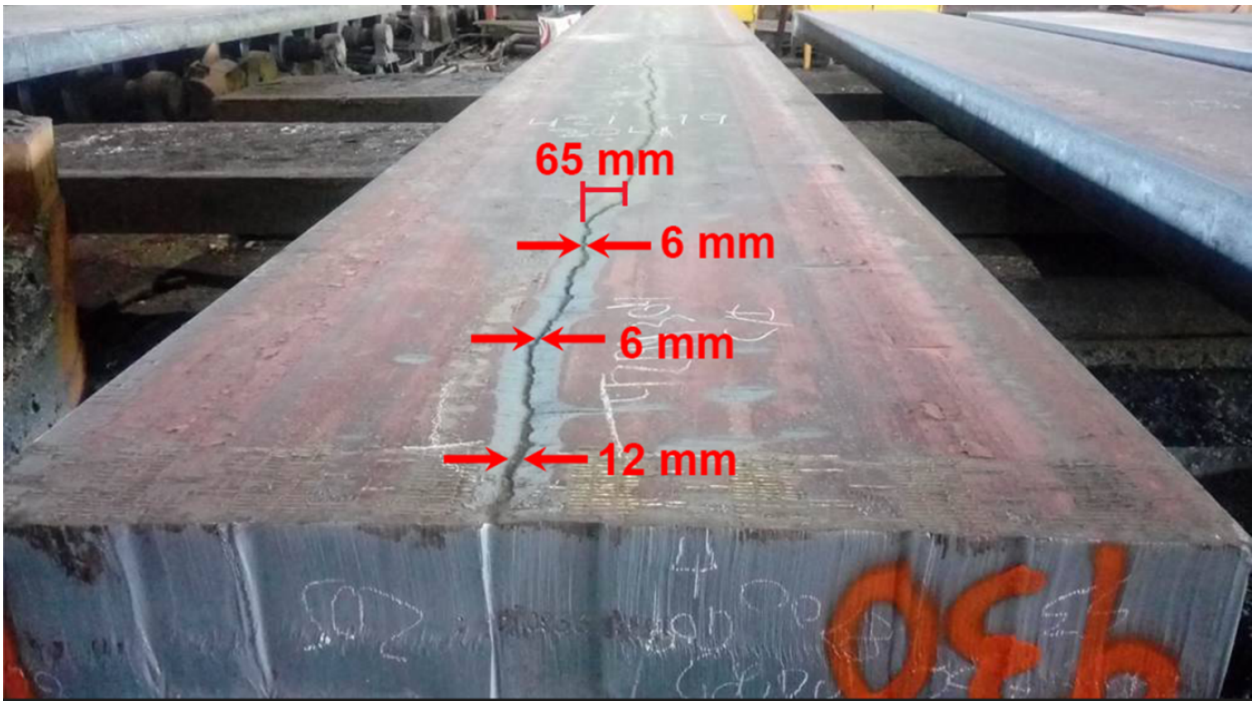


Figure 6.28: Longitudinal facial crack at the base of longitudinal depression wandering across the surface of the broad face outer radius

While the presence of a surface crack has been shown to change the appearance of the final longitudinal depression in the strand surface, depending on the severity and type of crack, consequences can be further reaching even to the point of causing shape problems for

the entire slab. As shown in Figure 6.29, for identical conditions, the presence of a bleeder type crack within a depression can reduce the shrinkage of the strand broad face by more than 80%. While the un-cracked model shrank ∼1.29% over 30 s, the bleeder cracked model shrank significantly less, only about 0.26%. Accounting for this difference in the cracked model with only 20% shrinkage of the non-cracked condition, 72% of the intended shrinkage went into displacement of the crack opening, while the remaining ∼8% in reduced shrinkage can be attributed to the higher overall temperature of the depression.

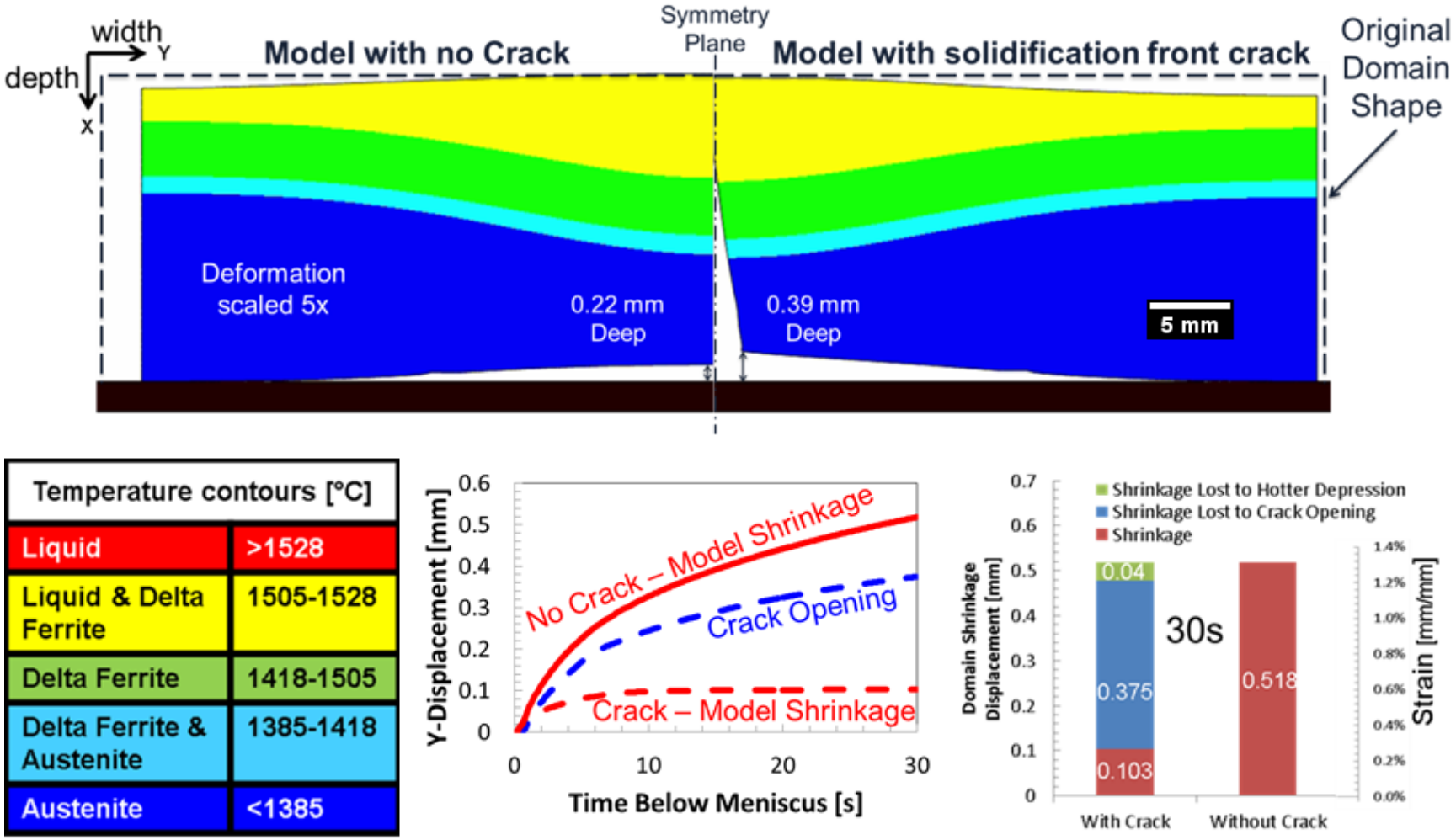


Figure 6.29: Domain end displacement (shrinkage) for a 25 mm thermal disruption on the surface at of solidifying shell with and without a bleeder crack propagating along the liquidus isotherm: a) displacement vs time including crack opening displacement, b) deformed model results for no crack (left) and crack (right) cases, and c) contributions and total displacement at 30 s

6.4.9 Longitudinal Surface Cracks With Curved Corners and No Depression

Sometimes, surface cracks appear with negligible surface depressions. The shape of the corners of these cracks can provide insight into its formation mechanism. Figure 6.30 shows initially the defect starts to form via the same mechanism as the U-shape necking depression. Early during this process, however, some disruptive event at the meniscus initiates a crack at the surface of the slab (as mentioned in the fluid flow section of Chapter 2). This is very likely at the center of the initial depression, where the shell is the hottest and weakest and strain is highest. Upon initiation of the crack, some of the tension that originally would have gone into further necking of the shell and deepening of the depression, instead goes into the opening of the crack. As the crack corners are now separated at the surface, the shell on both sides continues to try to shrink. With a new free surface and lack of constraint, this shrinkage of the shell on both sides of the crack pulls the corner outwards, and the corners rotate slightly, protruding slightly outward, relative to the far-field. This mechanism is illustrated clearly in the simulation results shown in Figure 6.30b

6.4.10 Longitudinal Depression With an Opened Sub-Surface Crack With Pointed Corners

A related type of surface crack is found at the root of some V-shaped longitudinal depressions and is shown in Figure 6.31. As with the previous example, this defect starts as a U-shape necking depression. In this case, however, a sub-surface crack initiates, (rather than a surface crack). This sub-surface crack propagates towards the strand surface, owing to the increased tension across the entire crack. The shell ligament closest to the surface narrows and concentrates the tensile stress. This narrow region is now carrying tensile load and the necking localizes even further into the pre-existing depression as it heats up more. Depending on the steel grade, this can be particularly problematic if the defect locally enters an intermediate low ductility trough due to the temperature change. In this case the appearance of the fracture surface is likely to be quite brittle and jagged. Eventually, the crack may propagate all the way to the surface and the corners of the crack are likely to

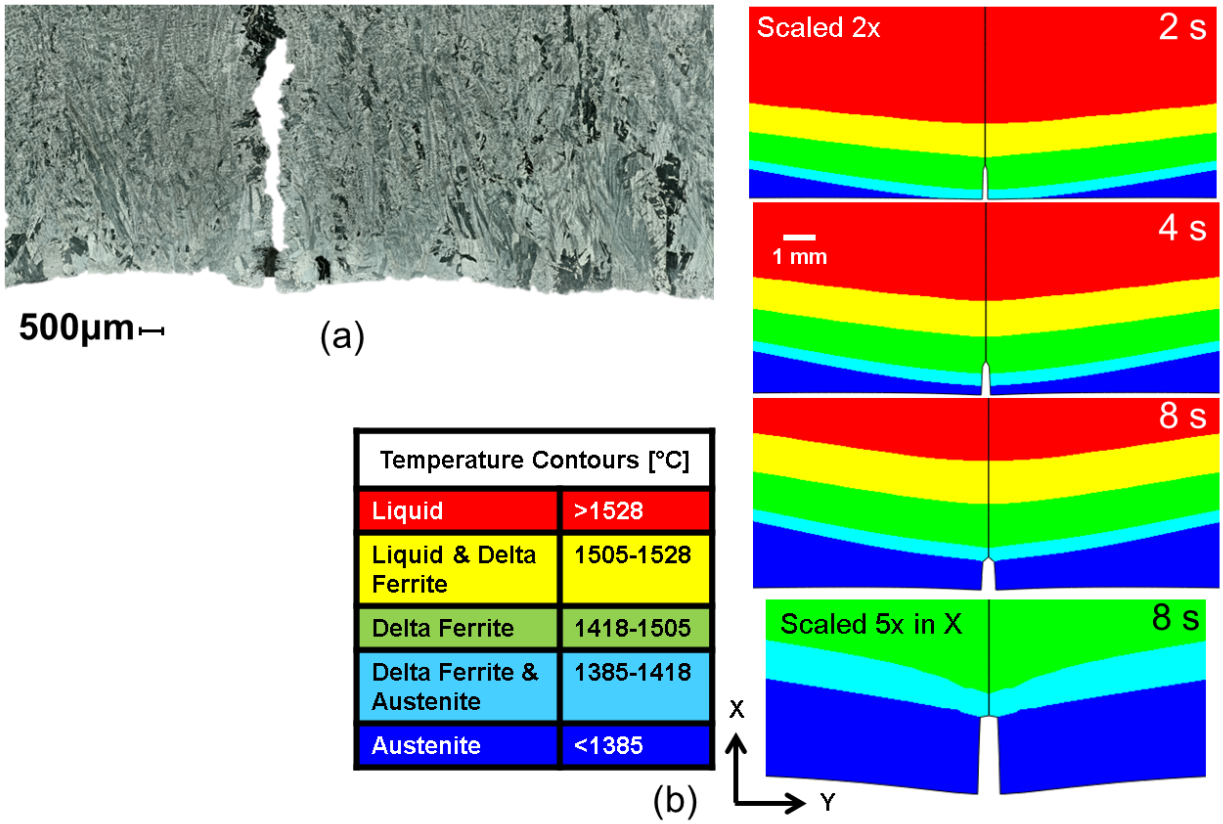


Figure 6.30: (a) Longitudinal surface crack at the base of longitudinal depression with AHSS steel grade (0.2 %C), (b) Model results for an arrested 2.5 mm surface crack

adopt an appearance where they point inwards back along the propagation path.

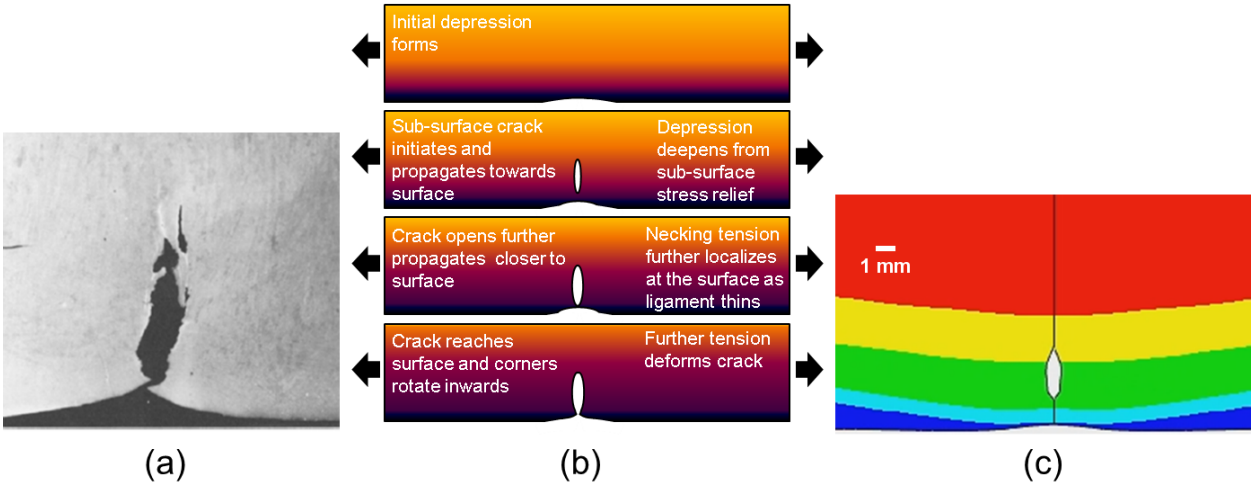


Figure 6.31: a) Apparent surface crack at the base of a longitudinal depression [7], b) Schematic explanation of sub-surface crack propagating to surface, c) Deformed result of arrested sub-surface crack hold case at 10 s with 25 mm thermal disruption (deformations scaled 5x)

When possible, taking slab samples and sectioning down to an individual defect can be very valuable. In most cases it may not even be necessary to fully polish and etch the sample to get a better understanding of the defect. As discussed above, the corners of the crack at the surface have different appearances depending on the crack growth direction, this may help in analysis at-a-glance as surface scale on the hot slab may make observation somewhat difficult until the slab has cooled down.

6.5 Discussion

Figure 6.32 shows heat transfer results for a U shaped necking depression with and without a surface bleeder crack. As the figure shows, the presence of a crack causes a slight drop in heat flux at the depression center from the un cracked condition. This is a result of the deepening of the depression from corner rotation and sub surface shrinkage of the crack corner during solidification of the shell. The drop in heat flux causes a corresponding increase in temperature of the cracked condition as shown in Figure 6.32b, where the cracked

depression center is ∼50°C hotter at 30 seconds. The figure also shows that the far field is blind to the existence and change in heat transfer created by the cracking at depression center.

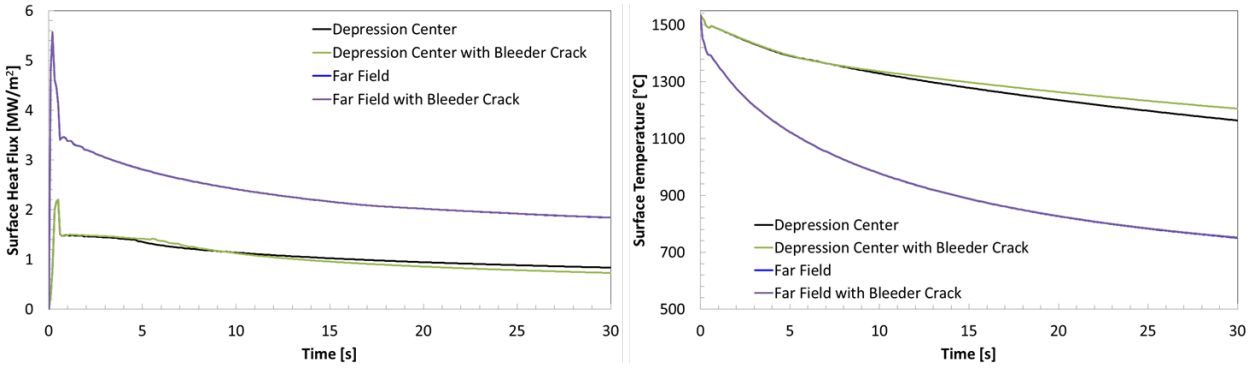


Figure 6.32: Heat flux and temperature results for a U shaped necking depression with and without a surface bleeder crack

Figure 6.33 shows the surface hoop stress results for the far field and the center of the depression. The behavior of the far field follows the expectation from prior work of the author and the literature where a brief period of tensile stress is observed at short times followed by increasing compression as the sub surface of the shell shrinks in opposition to the colder surface. In uniform heat transfer conditions it has been previously demonstrated that the entire surface will be in uniform compression equal to the far field stress value. The depression center experiences similar behavior, however, the depression center has substantially less compressive stress as a result of the tensile stresses imposed by frictional interaction with the mold surface leading to necking of the shell.

Figure 6.34 shows the hoop stress history results of a U-shape necking depression with a surface bleeder crack and Figure 6.35 shows hoop stress time history results through the shell thickness at the far field (b) and depression center (b). The qualitative behavior is similar, but the magnitudes of compressive stress are substantially different. Note that the free surface of the crack creates a stress free condition at depression center in Figure 6.34b.

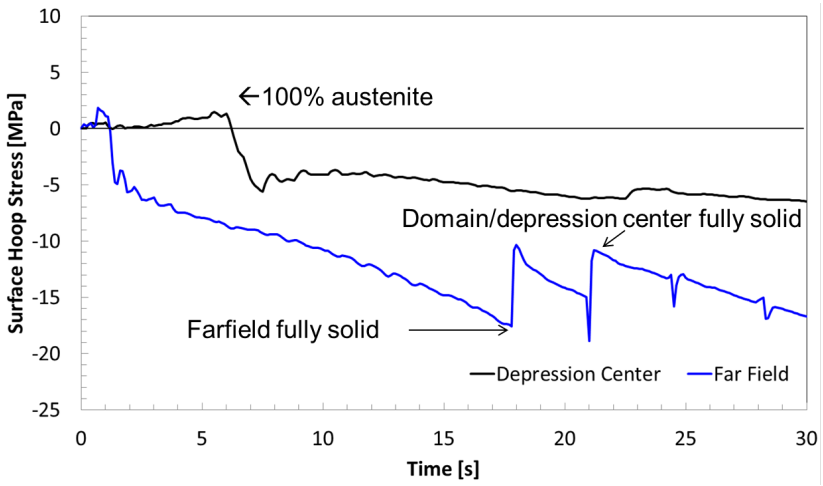


Figure 6.33: Surface hoop stress results at depression center (black) and the far field (blue)

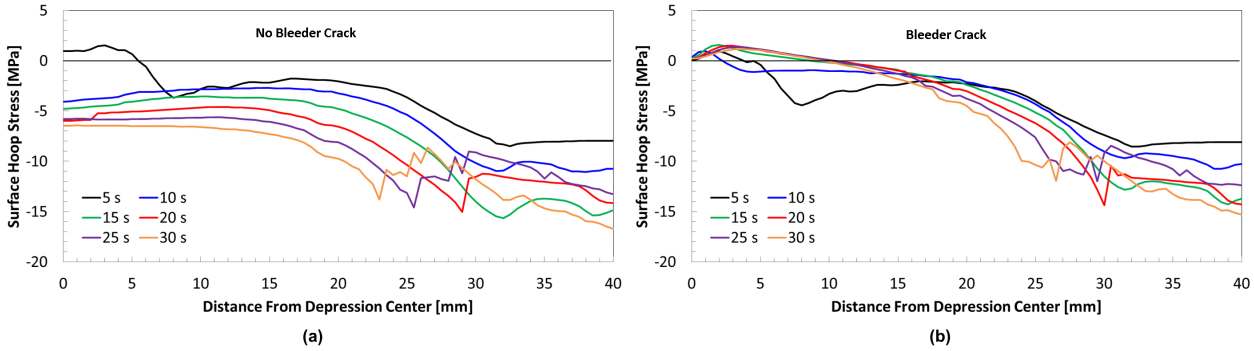


Figure 6.34: Hoop stress time history results across the surface of U shape necking depression without (a) and including a surface bleeder crack (b) for the same initial thermal disruption

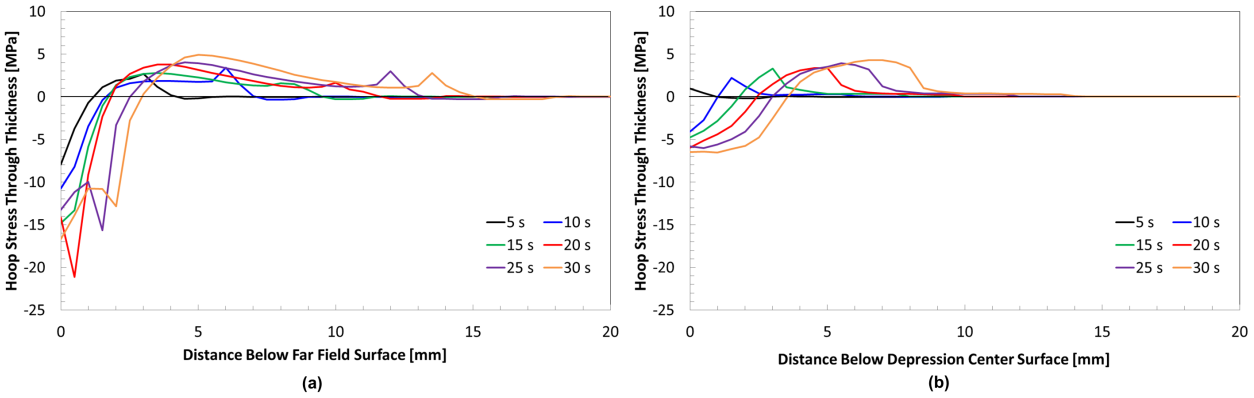


Figure 6.35: Hoop stress time history results through the thickness for the far field (a) and depression center (b) of a U shaped necking depression

6.5.1 Crack Influence on Depression Formation

As mentioned before, continuous casting as a process tends to have a high propensity for cracks. Cracks on their own represent a significant quality problem depending on the severity, however, what is less studied and understood is the relationship between cracks and depressions. It has been observed in the literature that cracks appear at the base of the more severe depressions [13]. In this work, the presence and growth of cracks has been shown to change the shape and severity of depressions, and depending on the crack propagation history, the overall defect shape takes on different appearances.

Figure 6.36 shows the model results of a uniform heat transfer model with 1 mm uniform flux layer thickness, no thermal disruption, and a propagating surface crack. The presence of a crack in the absence of a thermal disruption is capable of creating the mechanical effect (separation from the mold) necessary to start the depression growth feedback cycle. In this example, a surface crack propagates within the mushy zone at approximately 50% solid fraction. As in the other situations previously described, the crack opening and sub surface shrinkage causes rotation of the crack corner and deepening of the depression. The lack of initial thermal disruption does not seem to be an issue as the opening of the crack separates the shell surface from the mold hot face and creates an air gap. Other crack scenarios were run in the course of this work and the results show that unless the surface crack penetrates through to the mushy zone, a surface crack alone is not enough to cause a depression to form.

6.5.2 Depression Formation

A depression can be initiated as a result of either a mechanical and/or thermal disruption, and the behavior is generally the same as one type of disruption is followed by the other.

6.5.3 Thermal Disruption

In the case of a thermal disruption, changes to the heat transfer in a region of the strand can lead to higher local surface temperatures. Higher temperatures will lead to localized

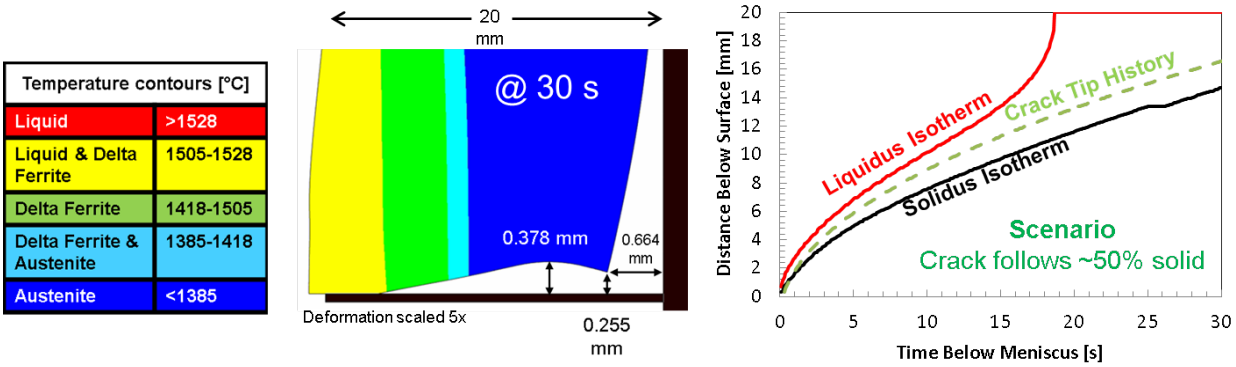


Figure 6.36: Model results for uniform heat transfer case with a propagating surface crack approximately following the 50% solidus isotherm

thinning of the solid shell. Thinning of the solid shell, combined with further cooling and contraction of the surrounding material will lead to localization of tensile stresses as the rest of the shell attempts to shrink and contract. Higher temperatures are directly associated with lower strength and the localized tensile stresses will result in necking phenomena, initiating a mechanical disruption to the surface of the shell.

6.5.4 Mechanical Disruption

In the case of a mechanical disruption, a slight disturbance to the surface profile or shape of the solidifying shell can lead to the appearance of a surface region further in distance to the mold hot face than the surrounding area. As long as this disruption is large enough, this depressed area, will experience reduced heat removal from the mold, leading to a thermal disruption. As before, the depressed region will be hotter than the rest of the surface being cooled. Lower strength and the continued cooling of the surrounding material will lead to tensile strain being applied to the depressed surface region. The load applied to the hotter and weaker region will result in yielding and necking of this area and deepening/worsening of the depression.

6.5.5 After Initial Formation

Once a longitudinal depression forms within the solid shell, natural ferrostatic pressure is generally not strong enough to put the surface back into contact with the mold. Furthermore, if the depression is a result of necking, the dimensions of the strand no longer match the intended shape, thus flattening out the depression requires fighting not only the strength of the weakened/thinned depressed region, but also the surrounding material – and the slab is likely to have shape problems. Upon exit from the mold further cooling of the strand is accomplished with hydraulic or air mist water sprays. The continued cooling of the strand in the presence of a depression leads to a given defect almost doubling in depth with a negligible change in width. Figure 6.37 shows the behavior of the same 25 mm thermal disruption in three different mechanical loading conditions. Of particular interest is the change in austenite layer thickness within the solid shell. As mentioned before, there is a tendency to overtaper (applied compression) casters when possible. This is in contrast to allowing an undertaper (applied tension) situation. As shown in Figure 6.37, overtapering a caster actually reduces the defect severity of a given thermal disruption by reducing the retardation of the austenite shell growth at depression center.

The only modeled situation found to remove a formed depression was a severe reduction in heat transfer across the entire surface of the domain which allowed for reheating of the far field, for homogenization of the surface temperature, and to a lesser degree shell thickness. The reheating of the far field was found to cause some expansion which, along with ferrostatic pressure, allowed for the depressed region to move back closer to the mold. This situation may sound similar to sticker slow down speed, to heal a potential sticker breakout, but this action is not practical for a far less severe defect during normal caster operation and thus it should be assumed that once a depression has been formed the only method for removal is downstream intervention and remediation if the defect is severe enough.

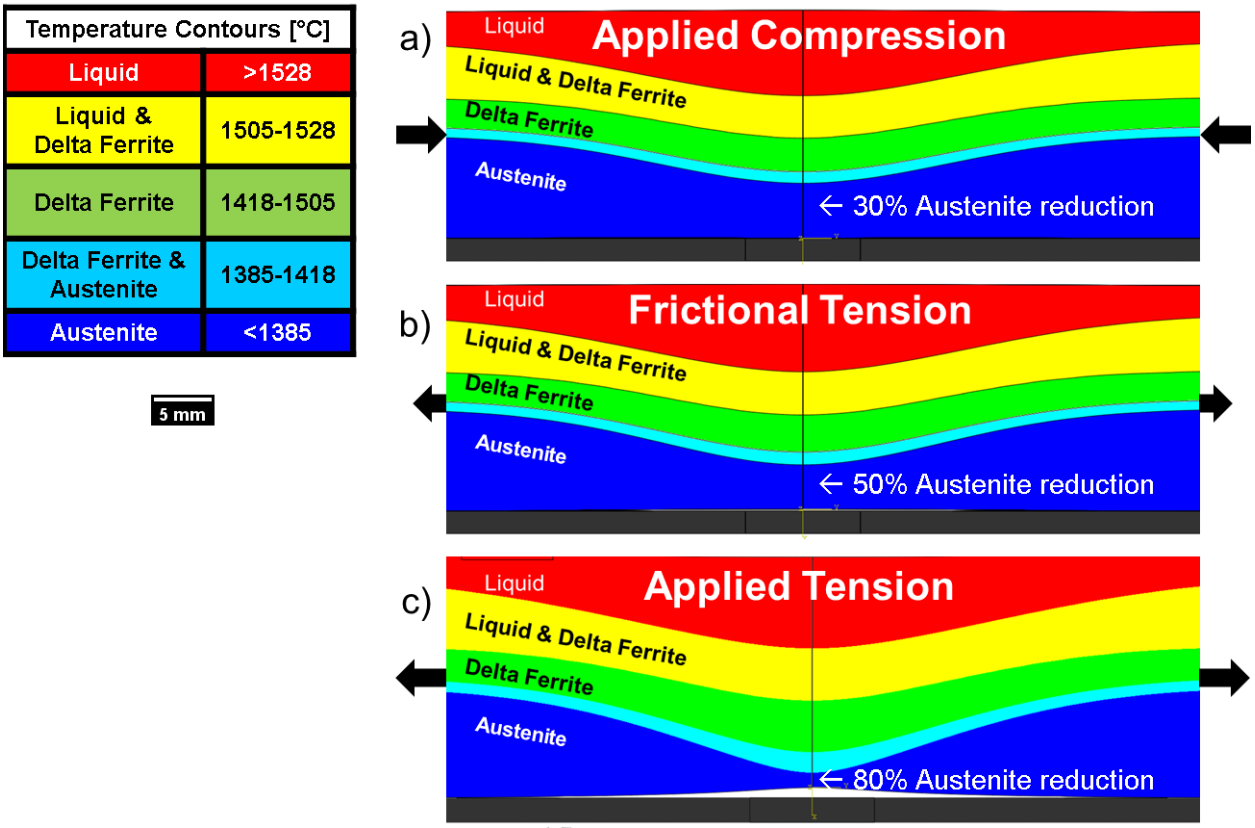


Figure 6.37: Deformed shape and temperature contours for 25 mm thermal disruption at 30 s with: (a) Applied compression of 0.03 mm/s, (b) Frictional tension, and (c) Applied tension of 0.03 mm/s

6.5.6 Analyzing a longitudinal defect

Product quality is critical to the success of every steel company. Inspection and observation of the steel occurs at multiple points along the production line and can take a variety of forms: thermal monitors at mold exit, pyrometers placed within containment, laser profilometers and length gauges after torch cut; or as simple as an inspection stand with an employee taking notes by hand. Regardless of the method, all of these steps are taken to better understand and track the quality of the product as early in the process as possible. It should also be understood when approaching a defect investigation that subsequent processing, specifically rolling, will change the appearance of the initial defect from its as-cast appearance. In plant operations, even a dedicated inspection station is likely to have some difficulty in discerning defects at a distance, furthermore, the scale layers on the slab make it substantially more difficult to differentiate what type of defect we may be looking at or if there is a crack present.

6.5.7 What to Look For

For purposes of this discussion lets focus on an as-cast slab inspection occurring after the slab has cooled enough to be safely interacted with. Once a depression exits the mold, the strand enters secondary cooling and the support rolls. As the still hot strand travels through the support rolls, the rolls deform the strand and act to smooth out the surface. For a uniform surface (i.e. no depression) the oscillation marks tend to disappear with this deformation; however the deformation is not very much and thus depressions on the surface of the broad face tend to protect the oscillation marks and leave them still visible. Changes in grade mixes bring challenges to any caster as new practices need to be designed for the best quality product. During the process of practice trials it is important to remember that certain grades, even those not particularly crack sensitive, do have multiple ductility troughs. Intense reheating and temperature differences at the base of severe depressions may be enough to bring the steel locally into a brittle temperature region. So while the

region may initially neck, changes in practice can change the local temperatures enough that a crack may form. This has been previously pointed out in the literature with regards to instantaneous ductility differences through the shell thickness during casting [139].

6.5.8 Differentiating Defects

It is clear that discerning the presence of a defect on the surface of the strand is possible, and the likely signatures or appearances of different types may be able to be induced from the existing knowledge. For example, in the case of a severe depression we expect there to be a dip in the local temperature of the mold. If this depression were to develop a bleed, it is highly likely that high resolution sensors would show a region of lower temperature with a hot spot towards the center where the shell would be the thinnest and the bleed is most likely to occur. Similarly, this type of signature may also appear in the case of the Tension w-shape depression, where the center of the depression may come back into contact with the mold. At this point it is unclear whether it is possible to differentiate a long depression from a crack, or a depression containing a crack, using mold temperature readings alone. The lack of mold data together with quality information makes this difficult, but this will change in the coming years. To further complicate the issue, it has also been found that the formation of a crack without an initial thermal disruption is capable of generating enough of a mechanical disruption leading to a thermal disruption and a depression. Finally, the general behavior of defect formation is likely similar, but care should be taken with interpretation for large alloy or grade differences (i.e. Advanced High-Strength Steels, peritectic steel grades, etc.).

6.6 Summary

- On crack sensitive grades, visible depressions warrant closer examination if it is for critical applications as sub-surface cracks and macro-segregation streaks may be present
- If pronounced oscillation marks are visible on only a limited portion of a slab, it is likely that this region contains a depression

- Slabs identified to have significant shape problems should be inspected for the presence of cracks
- Cracks cause pre-existing depressions to deepen, not from continued necking, but from rotation and thermal shrinkage
- If cracking with bleeds are found, this is likely indicative of a near breakout
- Reheating at the base of depressions may be enough to bring the steel locally back into a brittle temperature region depending on the steel grade. Thus grade/grade family specific spray practices that put the strand surface too close to a ductility trough run the risk of generating cracks if any heat transfer disruptions are significant
- As FBG molds become more common, much more extensive and detailed data will become available and narrowing down signatures will become easier

6.7 Final Thoughts

With the significant pressure on casting operations to increase efficiency, throughput, and product quality all at the same time, defect analysis can seem painstaking and not always practical. However, improvements across the board can be seen if better understanding of the defects specific to a given caster can be identified and examined. Highly instrumented molds, such as FBG, have been gaining popularity in recent years. As they become more common, a tremendous amount of detailed data will be generated, more than has ever been accessible before. Processing through this data, along with quality reports, line inspections, and defect analysis, will allow for extracting more detailed signatures of specific defects. All of this has the potential to dramatically improve the understanding and overall product quality of a given caster, its specific product mix, and the industry as a whole.

6.8 Acknowledgements

The author would like to thank the member companies of the Continuous Casting Center at the Colorado School of Mines for their financial support as well as their substantial

involvement in sample procurement for this project. Specific thanks are extended to: Rich Gass, Hongbin Yin, Kenneth Blazek (Ret.), and Rudolf Moravec, of ArcelorMittal ECRD; Joydeep Sengupta and Jackie Leung of ArcelorMittal Dofasco; Gert Abel, Begoña Santillana, Dirk Van Der Plas, Arnoud Kamperman, Stephen Carless of Tata Steel Europe; Sunday Abraham, Rick Bodnar (Ret.), and Xiaoxu Zhu of SSAB Iowa; and Ron O'Malley of Missouri Science and Technology University (formerly of Nucor Steel). Additional thanks to Nicholas Bresnahan for his metallography and microscopy work.

CHAPTER 7

LONGITUDINAL DEPRESSION DEFECT VISUALIZATION METHODOLOGY

This chapter introduces a novel methodology developed during the course of this work for processing high-resolution temperature data taken within a continuous casting mold to predict longitudinal defect formation in real-time (or near-real time forensic analysis of defects) In this method, temperature data is tracked at specific locations on (or near to) the moving material surface over a time period and processed to determine an integrated temperature deviation for each location. This integrated temperature deviation, in units of K s or $^{\circ}C \cdot s$, shows where the temperature history of a given material point is less than an expected standard temperature for a prolonged period. High values of this deviation are indicative of a longitudinal defect. The integrated temperature deviation data simplifies multiple sensor readings recorded over a time interval into a single value at each point on the moving material (steel strand) surface. The amplification of the history by integration into a singular value makes defects much more apparent to an operator, thus enabling the operator to take corrective action in real time. Corrective action could be as simple as changing a parameter of the continuous manufacturing process, (such as lowering the casting speed), or marking the defective portion of the slab to be set aside for further inspection, remediation, or recycling.

This method has applications in other manufacturing processes outside of continuous casting and can be extended to other materials as well. This method also has the ability to supplement existing break out protection systems by adding the ability to detect potential longitudinal bleeder breakouts.

7.1 Introduction

Based on the previously described mechanisms and the advancements in temperature sensors for the continuous casting process, the obvious question becomes: How can one

relate the formation mechanisms and interpret measurements in real-time to react and take meaningful action? The previous chapters have discussed both the formation mechanism and the temperature signatures of such a defect in a post-mortem scenario, but what is more powerful is the ability to put this methodology online for real time operation. This chapter will tie these two concepts together and allow for defect identification based on detailed temperature measurements and visualizing them online. The ultimate goal of this is creating a tool for preventing severe longitudinal cracks/depression and longitudinally based breakouts that are not currently captured by conventional breakout prevention systems.

7.2 Background

Many continuous manufacturing processes, such as the continuous casting of steel, occur in harsh environments where experiments are difficult and often times impossible. In many situations, direct data collection during the continuous manufacturing process is impossible, and even indirect data collection is difficult. Thus, the detection of defects formed during operation is extremely difficult and usually involves the interpretation of indirect measurements and data. For example, in the continuous casting of steel, one of the most important indirect methods is the measurement of temperature inside the mold of the continuous casting system.

Current techniques for temperature measurement inside the mold typically involve monitoring the average heat flux based on the amount of heat absorbed by cooling water or based on embedded thermocouples in the copper walls of the mold; however, thermocouples have many problems such as interference from electromagnetics used in the vicinity and contact problems, so thermocouples provide only qualitative signals. Further still, thermocouples cannot be placed too tightly together in close proximity without disrupting the heat transfer through the mold, as their placement directly affects the path of cooling water slots. Recently, fiber Bragg grating (FBG) temperature measurement systems have been placed into molds. FBG molds can measure very high density temperatures across the entire length and width of the mold, without disrupting heat transfer, and with better accuracy.

However, even with improved sensing, current data analysis and visualization of the data simply displays the raw temperature data or a simple variation thereof. Then, an operator views the data and identifies defects based on experience. There is ample opportunity for human error with prior art systems. For instance, even an experienced operator may not detect a relatively small, but consistent moving temperature drop that corresponds to a defect on a surface of the material. With these shortcomings in mind, a methodology is developed and introduced for the processing of high-density data from temperature sensors to better analyze and visualize potential quality issues on the surface of a continuously cast slab.

7.3 Purpose Driven Visualization

The best visualization methods are adapted to meet particular objectives. If the objective is to entertain and inspire, or to show general trends, the ideal visualizations will be very different than if the goal is to accurately convey quantitative information in real time. The display of abstract tensor variables, such as stress, should differ from the display of readily-observed scalar variables such as temperature, which can benefit from a physically-based visualization scheme.

The mesh resolution needed to convey results that are pleasing to the human eye often differs from what is best for numerical methods, and vice-versa. For example, a well refined and efficient finite-element mesh that yields good numerical accuracy for stress analysis throughout a given domain typically has a very biased mesh with large elements in most regions and tiny elements near corners, geometry changes, and areas of interest. Meshing that same domain for computer generated images for visualizing temperature or rendering light reflections, for example, would look substantially different.

Finding effective ways to post-process the results to visualize the phenomena is very problem specific. Prior process understanding can help to narrow down the important variables, orientations, and parameters to display that best convey the insights contained in the information. It usually helps to pay attention to the underlying physics when visualizing

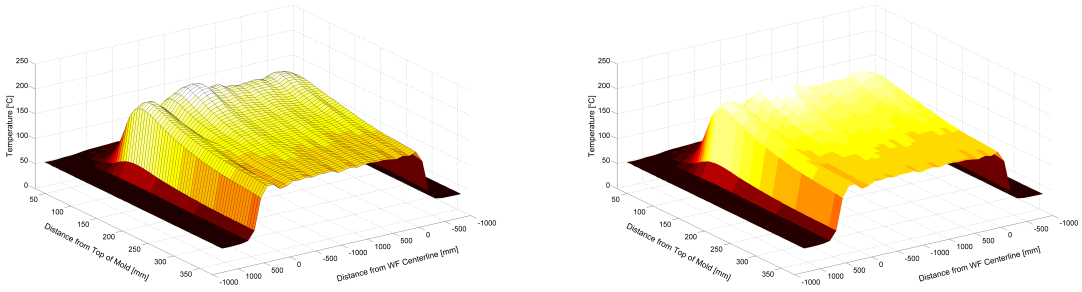
data. For example, orienting the domain so that gravity always acts downwards usually makes it intuitively easier to understand the results. Bounding a color map according to limits that are physically achievable in the process is another way to make results easier to see. Maintaining the true aspect ratios of the part domain or geometry in a schematic is always best, unless there is a good reason to distort the domain to focus on a particular result. Such physically-based visualizations convey the data in a way that is spatially accurate, and enables realistic interpretation to extract fundamental understanding needed to make process improvements easier to accomplish.

7.4 Grid/Mesh Visualization and Interpolation

For a model simulation, the first purpose of visualization should be to determine if the simulation results are reasonable. Most computational methodologies, including finite-volume and finite-element methods, involve a grid of cells or a mesh of the domain, and nodal points. The discretization boundaries between the cells or elements should be sufficiently refined as to have no influence on the results. If any vestige of the grid/mesh can be discerned in the results, this indicates a potential problem with the accuracy. Thus, it is often useful to overlay the grid/mesh onto contour plots of the field-variable results in order to distinguish real physical phenomena from mesh-related artifacts. Once the grid/mesh resolution has been established to be sufficient, and the results to be accurate, there is no need to plot the grid/mesh. Indeed, a properly-refined grid/mesh will typically be too dense to see through, and showing it will likely distract the reader from the display of information.

Similarly, grid information can also benefit the initial display of measurements. Measured data in many engineering processes is now becoming dense enough to plot contour maps of field variables. However, if the distance between measurements is still too large, important phenomena may be missed, and the contours may not accurately represent the field variable being measured. Additionally, it is important to be able to troubleshoot sensor systems and identify anomalies in individual or groups of sensors. Showing the grid in the visualization can help with these issues.

Default settings for plots in many commercial packages, such as MATLAB [140], often add grid spacing to the contour plots. In some cases this is desirable, such as shown in Figure 7.1(a) versus Figure 7.1(b), where the grid discretization conveys the exact spatial locations of the collected temperature data. Other scenarios where this might be useful are when space is limited and showing the grid also conveys something about the finite element mesh resolution, such as during a mesh refinement study. When attempting to turn off the grid spacing in a program such as MATLAB, one should be wary of associated setting changes, which also affect the data displayed, such as shading: this is a common situation that often also turns on interpolation.



(a) (b)

Figure 7.1: Mold sub-surface temperature 3D contour plot using hot color map with (a) and without (b) grid spacing conveying spatial information

For both model results and measurements, it is best to plot values at the points of greatest accuracy (e.g. cell centers in finite-difference methods, integration points in finite-element results, and actual points from measured data) and then to connect them with straight lines. However, once a mesh is sufficiently refined that the contours, represented as line segments, appear smooth, plotting at other locations, such as at nodes, is acceptable. Some post processing software performs non-linear interpolation between the actual calculated or measured points. This is often not appropriate, as it adds unintended artifacts to the displayed results, especially when the interpolation method does not match the model or data. While interpolation is usually intended to make smoother and more appealing visuals,

this is actually a disservice because it obscures the real physical phenomena from mesh related artifacts. Deviations that would indicate accuracy problems due to an insufficiently-refined grid may be suppressed. Thus, using interpolation to suppress the "wiggles" is ill-advised [141].

Moreover, minor glitches in the data sometimes become magnified by an inappropriate interpolation method. For example, in order to achieve a continuous curve, a cubic spline interpolation of data with a single outlying point may produce a kinked line that extends far outside the range of all of the data points. The resulting new extreme peaks may mislead the viewer to believe that some real physical behavior is responsible for a new trend that actually does not exist. To avoid such problems, the safest interpolation method, if a continuous line is desired, is to represent the real data points with symbols, and to connect them with straight lines. This accurately conveys the information without misleading the reader. This methodology is readily extended to visualize data in multiple dimensions, such as adding a third spatial dimension or time.

7.5 Color Map Selection for Scalar Fields

Color map selection can be a surprisingly complex task which often requires balancing a variety of conflicting goals such as user preference, standard convention, and practicality [142, 143]. There are many color maps in existence today, and substantial discussions in the literature with regard to efficacy [144]. What is generally agreed upon, is that some color maps are better than others at conveying particular types of data, and if care is not taken, it is easy to choose poorly [145]. Color map selection is often chosen with little thought, taking the software default during post processing of data. While taking the default color map might be an easy choice, it is often not the best for conveying the particular information at hand. Stopping for a moment to consider other color-map options can be very beneficial.

For many applications that involve temperature, including steel continuous casting, one of the most intuitive and useful color maps is blackbody radiation. This color map is derived from the colors emitted due to black body radiation from a hot object at elevated temper-

ature. The exact wavelengths of light observed in nature are adjusted to have a constant increase in brightness throughout and to be perceptually uniform. Liquid (or the hottest color of interest) is usually denoted as white, while the darkest solid is denoted as black. The contrast allows for easy understanding of the temperature field, and its physical basis makes it intuitive, because it matches human experience.

Rainbow color maps are popular, perhaps because of the misconception that the range of colors is complete, enabling the widest possible range to convey the data. However, research has repeatedly shown that the rainbow color map is rarely the optimal choice for data display due to: its tendency to confuse natural perceptual ordering, its uncontrolled luminance variation, and its regions with limited perceptual change, but significant change in represented value [146]. Figure 7.2 shows the same 2D temperature data set shown in Figure 7.1 using four different color maps, plotted with MATLAB [140]. While it is still possible to discern [temperature] changes and trends in the rainbow (Figure 7.2(b)) and hsv (Figure 7.2(c)) color maps, it is far less intuitive than the blackbody (Figure 7.2(a)) and gray (Figure 7.2(d)) maps.

Continuously-changing color maps can be difficult to read accurately, because it is difficult for the human eye to distinguish between subtle changes in color. Instead, using discrete bands, sometimes referred to as "color banding," can provide distinct, thin boundaries between the colored regions, which correspond with specific values given in the legend. In addition to enabling more accurate reading of the contour map, these lines may also have physical significance. For example, each color in Figure 7.3 represents a different material phase, so the contour lines represent phase-change interfaces.

Using discrete and obviously different colors to distinguish regions, certain times heavy contrast is desired and makes choosing colors across the spectrum not only helpful, but often preferred. Figure 7.3 shows phase fraction and temperature results from a 2D Lagrangian solidification model of longitudinal depression formation; details of this model can be found elsewhere [41, 128]. This custom color map was chosen for intuitive reading and understand-

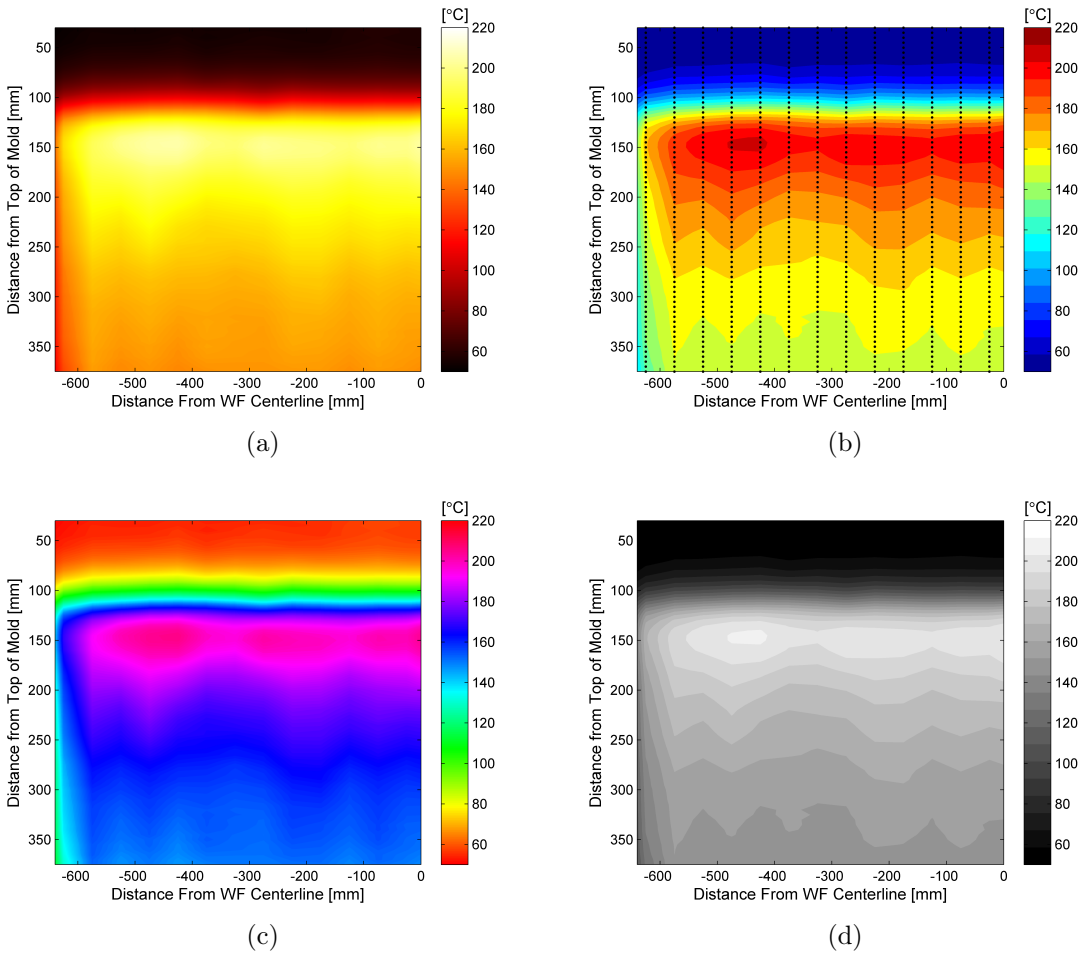


Figure 7.2: Two-dimensional contour plots of mold sub-surface temperature in various MATLAB color maps: (a) hot (blackbody radiation), (b) jet (rainbow), (c) hsv (rainbow color map in HSV space), and (d) gray (grayscale)

ing. The two highest temperature regions both contain liquid and are given colors with higher perceived temperatures (red and yellow). Red and yellow were chosen over orange to accentuate the change in phase more clearly. The lower temperature, fully solid regions, use cooler perceptual colors (green, teal, and blue), again chosen to be different enough to provide contrast accentuating the different phases. The displacements are scaled 5x equally in both X and Y in order to see the surface depression shape more clearly, while preserving the aspect ratio of all of the layer thicknesses as well as the surface depression shape. Finally, a thin vertical line shows the symmetry plane.

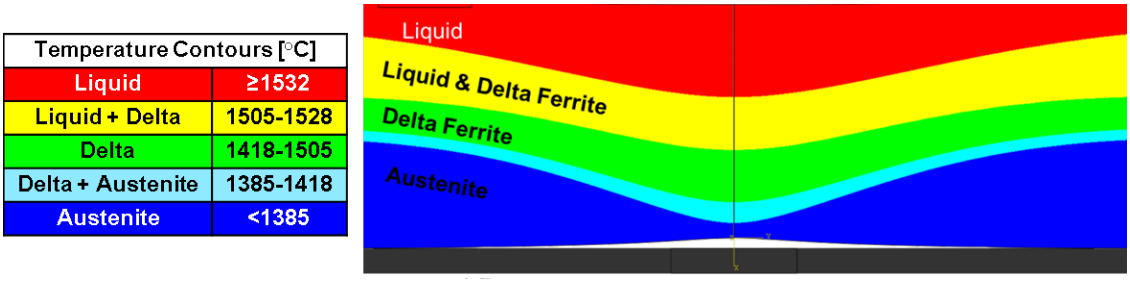


Figure 7.3: Longitudinal depression finite element solidification model 2D contour plot showing temperature and phase fraction (deformation scaled 5x)

Commercial packages which feature results presentation, such as ABAQUS [147], ANSYS Fluent [148], matplotlib [149], ParaView [150], MATLAB [140], and Tecplot [151] are excellent tools when used properly. However they can produce confusing results as a consequence of non-optimal post processing decisions, such as unfortunate choices for color maps and plot colors. Each program is capable of applying good color maps, but taking the default is rarely the best method for conveying results.

7.6 Thermal Integral Methodology

The extraction of knowledge contained in large data sets can be aided by enhancement of features or new variables which best convey that information. This section presents a new methodology to enhance the interpretation of continuous online measurement of dense mold temperature data to aid operators in detecting impending formation of longitudinal defects.

Ideally, in continuous processes, conditions should remain constant at essentially steady state. In reality, changes are always occurring on many different length and time scales, and the operation can be transient in many different ways. It is important to know when such changes are normal, or when they are significant and worsening, requiring corrective action by the operator. Thus, caster operations at all plants provide monitors to show the operator many important process variables and their thresholds or limits, which are often portrayed as lines across the top and bottom of the screen, to convey the windows of acceptable operation to stay within.

Typical variables include casting speed, mold heat flux, steel composition aims, tundish superheat, SEN submergence, spray water flow rates, surface pyrometer temperatures, and level profile in the mold to convey fluctuations. These metrics (and differences between the current value and the acceptable thresholds) are tracked during casting and examined continuously in the operations pulpit.

Quality during continuous casting is greatly affected by heat transfer across the interfacial gap between the copper mold walls and the steel strand, which governs initial solidification of the steel shell and the formation of surface cracks and other defects[15, 95, 128]. Previous work has shown that cracks correlate with high and/or variable heat flux in the mold, especially near the meniscus region [117]. Thus, quality monitoring systems routinely include the measured mold heat flux signal, based on heat up of the cooling water as it passes through the mold [119, 152] as well as other methods [9, 119, 120].

Recently, it has become possible to obtain dense temperature measurements in the mold. This is accomplished with Fiber Bragg Gratings, which can measure temperature at more than 2000 locations within the mold using fibers embedded inside the copper plates [121, 153]. Though manufacturing and maintaining these specialized molds is complex, numerous advantages over traditional thermocouples are seen. Particularly faster response time, and smaller spacing between sensors, which enables the presentation, in real time, of transient temperatures within the mold in higher resolution [122, 123]. The instrumented broadface

copper mold used in this work is shown in Figure 7.4.



Figure 7.4: Broadface copper instrumented FBG mold

An example of an instantaneous temperature profile measured across the mold subsurface is shown in Figure 7.5. The resolution of the data is indicated by the straight line segments plotted between measured points, which are sufficiently dense to capture the real profile behavior under most conditions. This figure also shows two horizontal lines, which represent the typical average of temperatures measured for this steel grade at this casting speed at this distance down the mold (full plot width line), and the local minimum (shorter line).

One purpose of displaying the evolving temperature map is to enable operators to spot the formation of surface defects, such as longitudinal depressions and cracks, during slab residence time in the mold. In addition to mechanical conditions, their formation is often linked to thermal variations in the mold, usually reductions in heat transfer. Reduction in heat transfer within the mold region leads to elevated temperatures on the surface of the slab, and lower temperatures seen by the mold surface; this is particularly notable when these

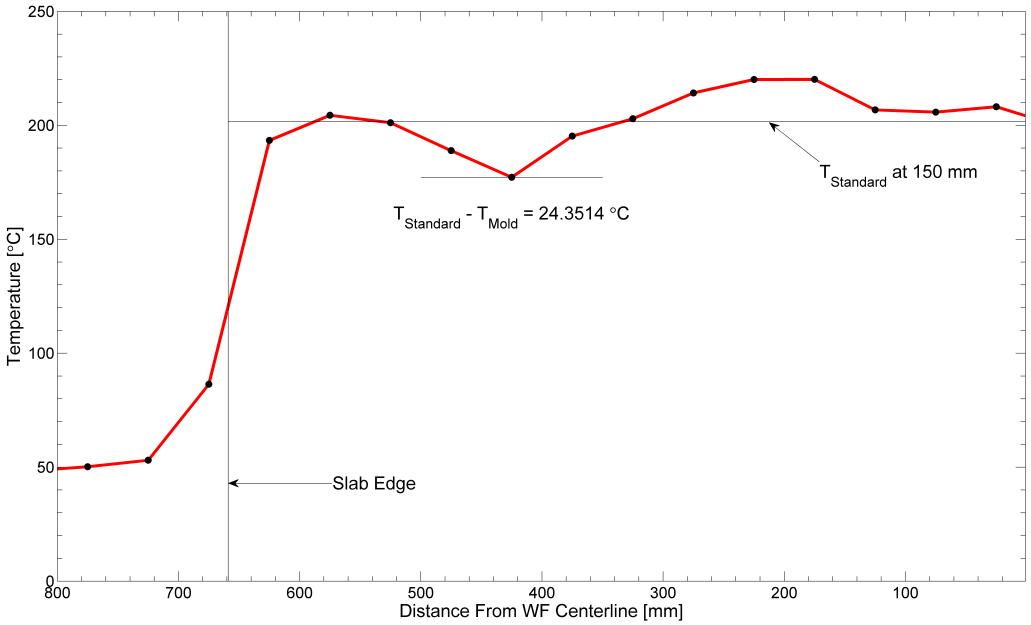


Figure 7.5: Measured local temperature profile and an example standard temperature profile 150 mm below top of mold from wide face centerline to slab edge

defects are present. These defects typically form close to the meniscus, and grow on the slab as they move vertically down the mold at the casting speed [152]. This consistently vertical motion suggests a physically-based methodology to improve understanding of the resultant signals. Specifically of interest is the relative drop within the entire instrumented region of the mold between the standard temperature profile and the instantaneous temperature profile. The difference is then summed according to the residence time of the slab surface at that location down the mold.

7.6.1 Mapping Mold Data to Slab Data

To translate, or map, the temperature readings, or data, from the mold to the slab material there is a unique spatial and temporal mapping of mold temperature data, $T_{Mold}(x_{Mold}, y_{Mold}, t)$, to slab temperature, $T_{Slab}(x_{Slab}, y_{Slab}, t)$, according to the time, location, and casting speed history. As shown in Figure 7.6, y_{Mold}, is the distance up the mold subsurface from the reference location, y_{Mold0}, which is located at the bottom of the instrumented region where

temperature data is measured; and y_{Slab} is distance along the slab, opposite to the casting direction, from y_{Slab0}, which is a reference location fixed on the slab that aligns with the bottom of the instrumented region at the reference starting time, ($y_{Slab} = y_{Mold}$ at $t = t_0$). For a given mold, the horizontal locations on the slab and mold, measured from a fixed horizontal reference such as the mold centerline, are identical ($x_{Slab} = x_{Mold}$).

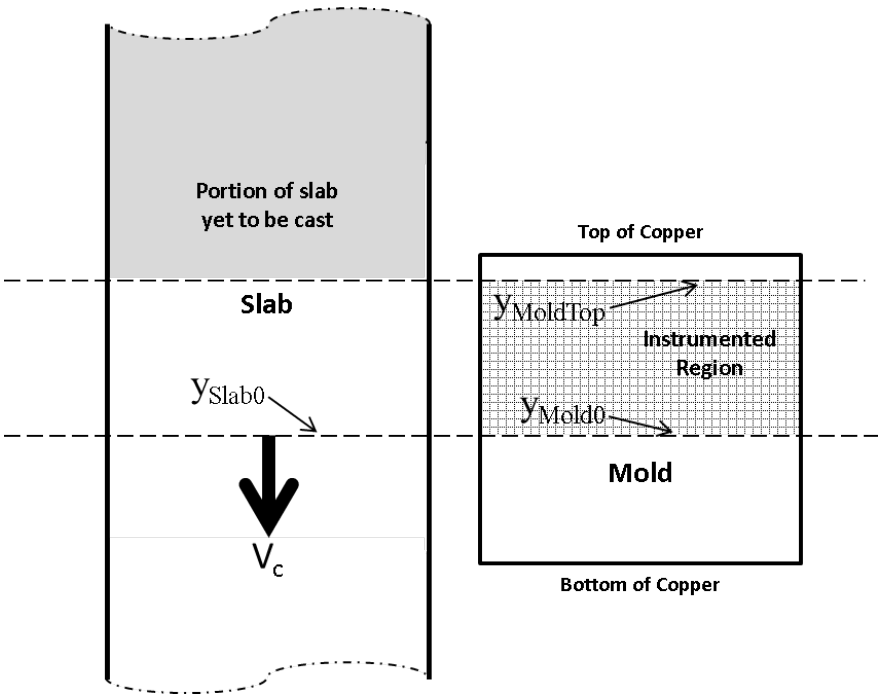


Figure 7.6: Nomenclature for mold and slab geometry reference configuration used in Integral Defect methodology (shown at $t0$)

At any given time, t, the vertical location of any specific point of interest down the slab surface, y_{Slab}, is related to the point in the mold it is currently adjacent to, y_{Mold}, according to eq. (7.1).

$$y_{Slab}(t) = y_{Mold} + \int_{t_0}^{t} V_c(t_i)dt_i \tag{7.1}$$

where the last term in this equation is the vertical distance traveled downward by the slab location since the reference starting time at t_0, and V_c, is the casting speed, which also may vary with time. For a constant casting speed eq. (7.1) simplifies to eq. (7.2).

$$y_{Slab}(t) = y_{Mold} + V_c * (t - t_0) \tag{7.2}$$

Mapping mold temperature to slab temperature, according to eq. (7.1) gives eq. (7.3).

$$T_{slab}(x_{Slab}, y_{Slab}, t) = T_{Mold}(x_{Mold},\ y_{Mold} + \int_{t_0}^{t} V_c(t_i)dt_i,\ t) \tag{7.3}$$

7.6.2 Defect Criterion

The following criterion helps to identify cracks and other defects associated with longitudinal depressions by indicating regions on the strand surface that have experienced multiple, or prolonged, periods of temperature drops relative to the standard profile. The drop in the current temperature at any given measured point in the mold subsurface, relative to the standard temperature at that location is given by eq. (7.4).

$$\Delta T(t) = \min(0, T_{\text{Mold}}(x_{\text{Mold}}, y_{\text{Mold}}, t) - T_{\text{Standard}}(x_{\text{Mold}}, y_{\text{Mold}}) + a) \tag{7.4}$$

where $T_{Standard}$ is a 2D array of standard temperatures at the instrumented points of the mold, calculated previously by averaging data when no defects occurred, according to the given steel grade and casting conditions. The constant, a, is a threshold value that could be used to filter random variations in T (currently set to 0). This particular example criterion ignores temperature increases, because they are not believed to help heal any of the longitudinal defects discussed in this work. In a more general sense, particularly in implementation of this method in a different process, physical property increases are a valid criterion. Inserting eq. (7.3) into eq. (7.4) gives eq. (7.5).

$$\Delta T(t) = \min(0, T_{\text{Mold}}(x_{Slab}, y_{Slab} - \int_{t_0}^{t} V_c(t_i)dt_i, t) - T_{\text{Standard}}(x_{Slab}, y_{Slab} - \int_{t_0}^{t} V_c(t_i)dt_i)) \tag{7.5}$$

While a location of interest on the slab surface, y_{Slab}, is within the instrumented region of the mold, $t_{Enter} < t < t_{Exit}$, the criterion, T_{IDrop}, also called the "integrated physical property deviation", evolves with time by integrating the history of the temperature drop at that

moving location as given by eq. (7.6).

$$T_{IDrop}(x_{slab}, y_{slab}, t) = \int_{t_{Enter}}^{t} \Delta T(t_i) dt_i \tag{7.6}$$

where t_{Enter} is the time when the location, y_{Slab}, enters the instrumented mold region, $y_{Slab} = y_{Moldtop}$. This time is typically known from recorded data for the slab, heat, and time, and can also be calculated using the reference time, t_0, the length of the instrumented region, $y_{MoldTop} - y - Mold0$, and the casting speed history with eq. (7.7).

$$y_{Slab} - y_{MoldTop} = \int_{t_0}^{t_{Enter}} V_C(t_i) dt_i \tag{7.7}$$

For a constant casting (or relative material movement) speed, this simplifies to eq. (7.8).

$$t_{Enter} = t_0 + \frac{y_{Slab} - y_{MoldTop}}{V_C} \tag{7.8}$$

Once the location of interest, y_{Slab}, passes out of the instrumented region, $y_{Slab} >= y_{Mold0}$, at time, $t >= t_{Exit}$, $T_{IDropF}(x_{Slab}, y_{Slab}, t)$ is no longer time dependent and has reached its final constant value, $T_{IDropF}(x_{Slab}, y_{Slab})$. This is found by setting $t = t_{Exit}$ in eq. (7.6), where t_{Exit} is the time when the location of interest reaches the last instrumented point in the mold, as in eq. (7.9).

$$y_{MoldTop} - y_{Mold0} = \int_{t_{Enter}}^{t_{Exit}} V_C(t_i) dt_i \tag{7.9}$$

For a constant casting speed, and knowing t_{Enter}, from eq. (7.7), eq. (7.9) simplifies to eq. (7.10).

$$t_{Exit} = t_{Enter} + \frac{y_{MoldTop} - y_{Mold0}}{V_c} \tag{7.10}$$

7.7 Implementation and Interpretation

The equations given in the previous section are well-suited for computational implementation. For an arbitrary casting speed history, eqs. (7.7) and (7.9) each require solving a definite integral for the upper integration limit. This is readily accomplished with an incremental time-marching procedure. Similarly, eq. (7.6) can be represented as a summation as in eq. (7.11).

$$T_{IDrop}(x_{slab}, y_{slab}, t) = \sum_{t=t_{Enter}}^{t_{Exit}} \Delta T(t) \tag{7.11}$$

After substitution with eq. (7.5), eq. (7.11) gives eq. (7.12).

$$\begin{aligned} T_{IDropF}(x_{slab}, y_{slab}, t) = \\ \sum_{t=t_{Enter}}^{t_{Exit}} \min(0, T_{\text{Mold}}(x_{Mold}, y_{Mold} \\ + \int_{t_0}^{t} V_c(t_i)dt_i, t) - T_{\text{Standard}}(x_{Mold}, y_{Mold} + \int_{t_0}^{t} V_c(t_i)dt_i)) \end{aligned} \tag{7.12}$$

The definite integrals contained within eq. (7.12) can again be solved incrementally. As eq. (7.11) is evaluated for a location of interest, y_{Slab}, at increasing time, t, (using constant time steps of 1 s in this work) the value of T_{IDrop} at each point on the slab surface, starting at zero, evolves with time while moving through the instrumented region, and retains its final value upon exiting that region, T_{IDropF} [128].

According to this criterion, only temperature drops contribute to the integral, as temperature increases are believed not to cancel out previous temperature drops [116, 128]. A low heat flux, followed by a return to "standard" heat flux at a given location on the slab surface, is better than staying below the standard for a prolonged period, which is reflected in a lower value of T_{IDropF}; however, actually increasing above the standard profile is not likely to compensate for prior decreases. On the contrary, such increases might further exacerbate defect formation, as previous work has correlated mold temperature fluctuations with increasing incidence of transverse [152] and longitudinal [154] crack and depression appearance. Prior to the defect criterion in this current work, strand movement has not been taken into account, only specific locations in the mold were considered in previous work.

Large values of T_{IDropF} indicate regions of the slab surface which have experienced a mold temperature history that is cooler than standard conditions. This indicates lower heat flux across the interfacial gap and a hotter shell temperature. While low heat flux can occur due

to local mold slag variations, it is often due to surface depressions, sometimes including an air layer within the interfacial gap between the shell and mold. These low heat flux depression regions see higher slab surface temperature and often lead to cracks. These regions can be tracked, subjected to extra inspection, and perhaps downgraded. This methodology and criterion can be applied to systems with arbitrary spacing of the measurement points, provided there is enough spatial resolution to achieve reasonable accuracy.

The result of eq. (7.12), T_{IDropF}, is a 2D array of values representing the accumulated temperature drop of each location on the slab surface as it passes through the instrumented mold region. When plotted properly, as in Figure 7.7(d), this contour map indicates regions on the strand surface that have experienced multiple, or prolonged, periods of temperature drops relative to the standard profile.

7.8 Results

An example of an instantaneous snapshot of all of the measured data recorded on the inner radius wide face of the mold, using a continuous, blackbody, temperature map is shown in Figure 7.7(a). This temperature map provides a more direct local indication of heat transfer across the interfacial gap than a simple line plot at a given depth. However, the 2D contour plot creates a new problem. The real-time information needed to evaluate the behavior is evolving in both time and space and can no longer be easily displayed as being simply above or below a single signal. The operator is now challenged to perceive any important differences between the current values, and threshold limits without guides (upper and lower bounds).

To resolve this problem, the current work proposes a direct portrayal of the differences between the current and standard conditions, magnified to facilitate the visualization of defect formation. Seeing these differences is difficult for several reasons. In display of the current signal, it is tempting to filter out the noise (small fluctuations in temperature), to make real "large" variations easier to perceive. However, some of the small changes contribute valuable information. The second challenge is to find a reasonable set of standard conditions,

as displaying a range is no longer an option. Finally, augmenting the difference between current and standard conditions requires knowing which differences are real, based on the reason that they are being displayed.

Figure 7.7 shows a recommended console display setup for forensic analysis of a longitudinal defect after casting. The defect is shown along with the new defect indicator applied on half of the continuously cast slab. Figure 7.7(a-c) share a common y-axis spanning the 345 mm instrumented region within the mold, while this same region is represented between the thick horizontal lines in Figure 7.7(d). Figure 7.7(a) shows the instantaneous contour map in the instrumented region collected by the sensors at the current time, using the blackbody color map without interpolation. It is important that this contour map use strictly linear interpolation; other interpolation methods, such as cubic splines, risk creating artificial over- and under-shoots of the data. These extrema may accidentally wash out issues with sensors or other problems and distract from the more subtle changes, which are the real temperature deviations.

Figure 7.8 to Figure 7.11 show a sequence of four frames from the video of Figure 7.7 with increasing time. The sequence shows four different times and readings as the slab material, and a location on the slab material, pass through an instrumented region of a mold.

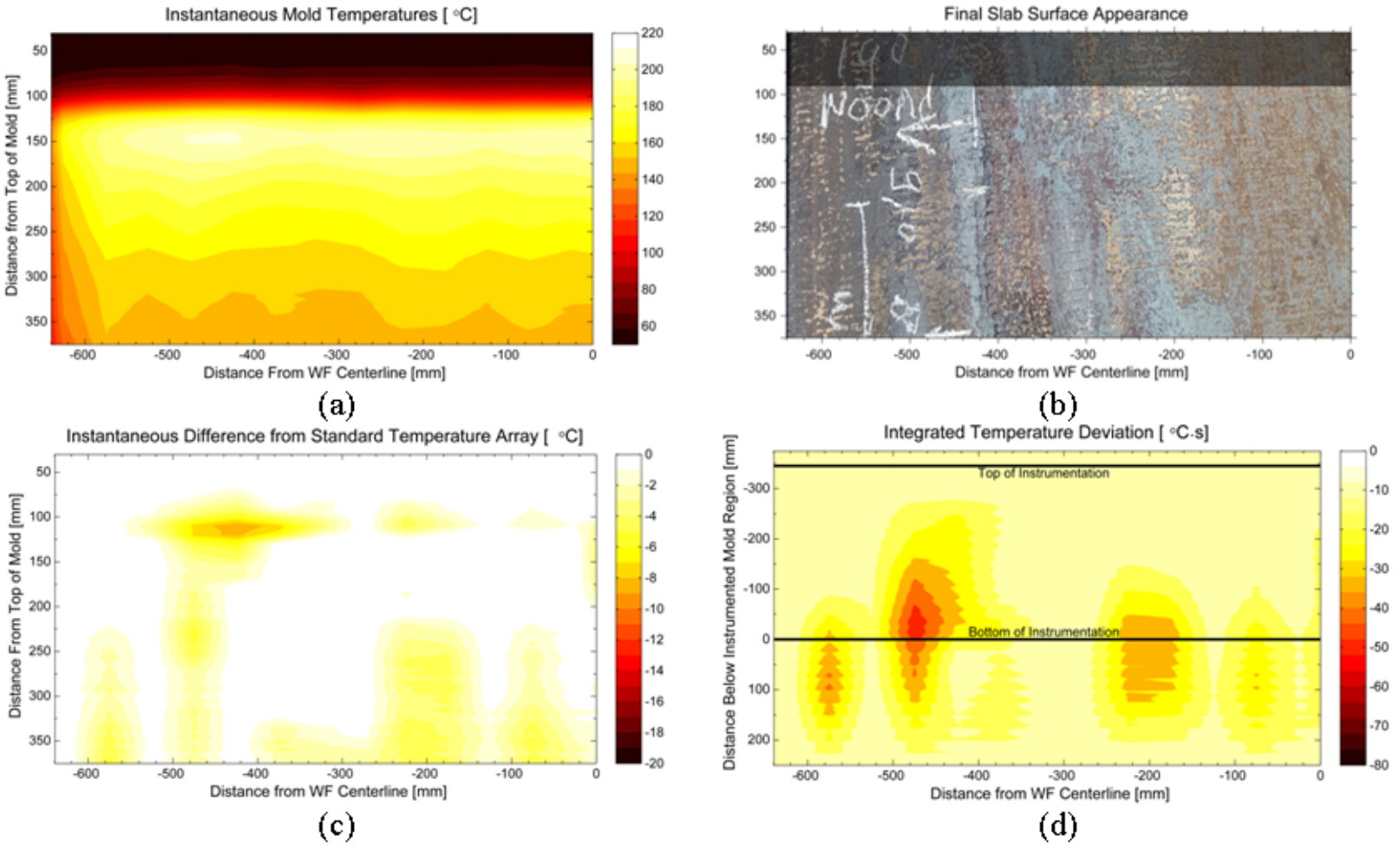


Figure 7.7: Contours indicating defects mapped over half of slab from wide face centerline to narrow face: (a) Instantaneous mold temperature, (b) Final slab surface appearance, (c) Instantaneous difference from standard temperature (d) Defect criterion based on integrated temperature drop, T_{IdropF}.

Figure 7.7(b) shows a plan view photograph (adjusted to remove perspective) of the final surface appearance of the region of the cast slab corresponding to the temperatures in Figure 7.7(a) at the time it matched the instrumented region in the mold. The translucent gray rectangle at the top indicates that portion of the image which was above the meniscus level at that time. While this image requires careful reconstruction, seeing how the measured temperatures line up with eventual surface quality problems is a helpful means of using this methodology to elucidate how defects form. Once this has been accomplished, and the results map in Figure 7.7(c) has been determined to properly indicate defects for a given set of operating conditions, according to downstream product evaluations, then a real-time version of this display in the mold can be created, without Figure 7.7(b). This would enable operators to make decisions in real time to correct evolving surface defects apparent in the results map. Additionally, instead of eliminating Figure 7.7(b) in the display window, including a surface reconstruction scan taken by an inspection device located somewhere closer to exit of the mold could be included to allow confirmation of surface problems predicted by the model.

Figure 7.7(c) shows a linearly interpolated contour plot of the instantaneous deviations between the standard and current temperatures for each location in the array. Values on this plot always have a negative or zero value, as discussed previously. Zero indicates that temperature history experienced at that location was within the specified threshold of the standard temperature profile. Increasingly negative values indicate larger temperature drops This frame is presented to contrast with the others, and is not meant to be included in the display on the operator's control room

Figure 7.7(d) shows an example of the output results from this methodology, obtained by accumulating the results in Figure 7.7(c) for 11 s (245 mm past the bottom of the instrumented region), according to the new defect criterion function in eq. (7.6). The time period spent within the instrumented region of the mold is represented by the space between the thick black horizontal lines labeled top and bottom of instrumentation. Once a surface location passes out of the instrumented region, the contours are fixed, and the calculation

for that surface point is completed; in the video this can be seen by the data in Figure 7.7(d) compressing in the vertical (casting) direction. Values in this contour plot also take on a negative or zero value, where increasingly negative numbers indicate higher likelihood of surface quality problems. The longitudinal depression (dark spot) seen at the bottom left of Figure 7.7(b) is clearly visualized in Figure 7.7(d), while it is hardly noticeable in the raw temperature data in Figure 7.7(a). A video of Figure 7.7 can be found in the supplemental files.

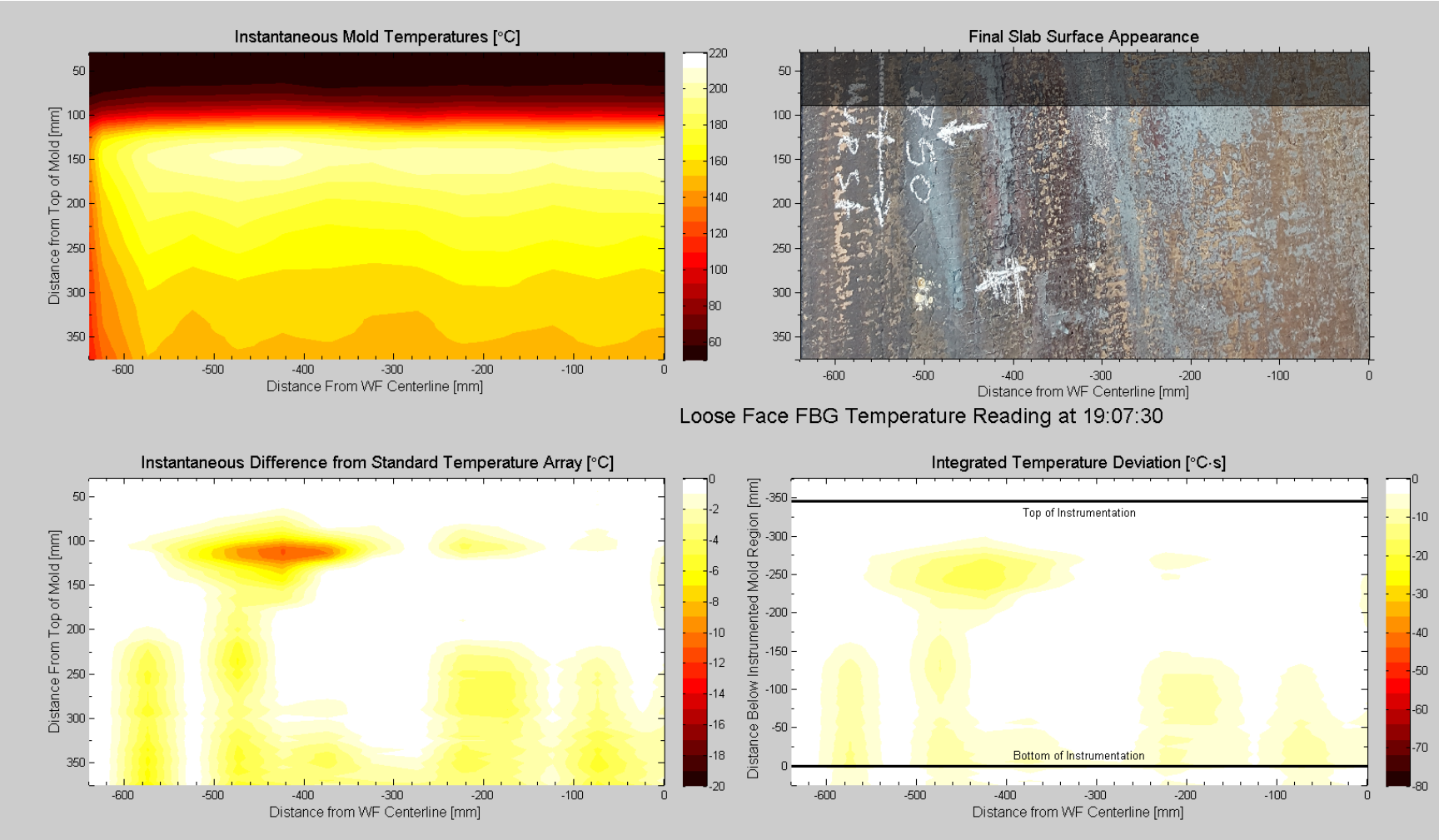


Figure 7.8: Integral Defect Methodology Heads-up Display Frame 1

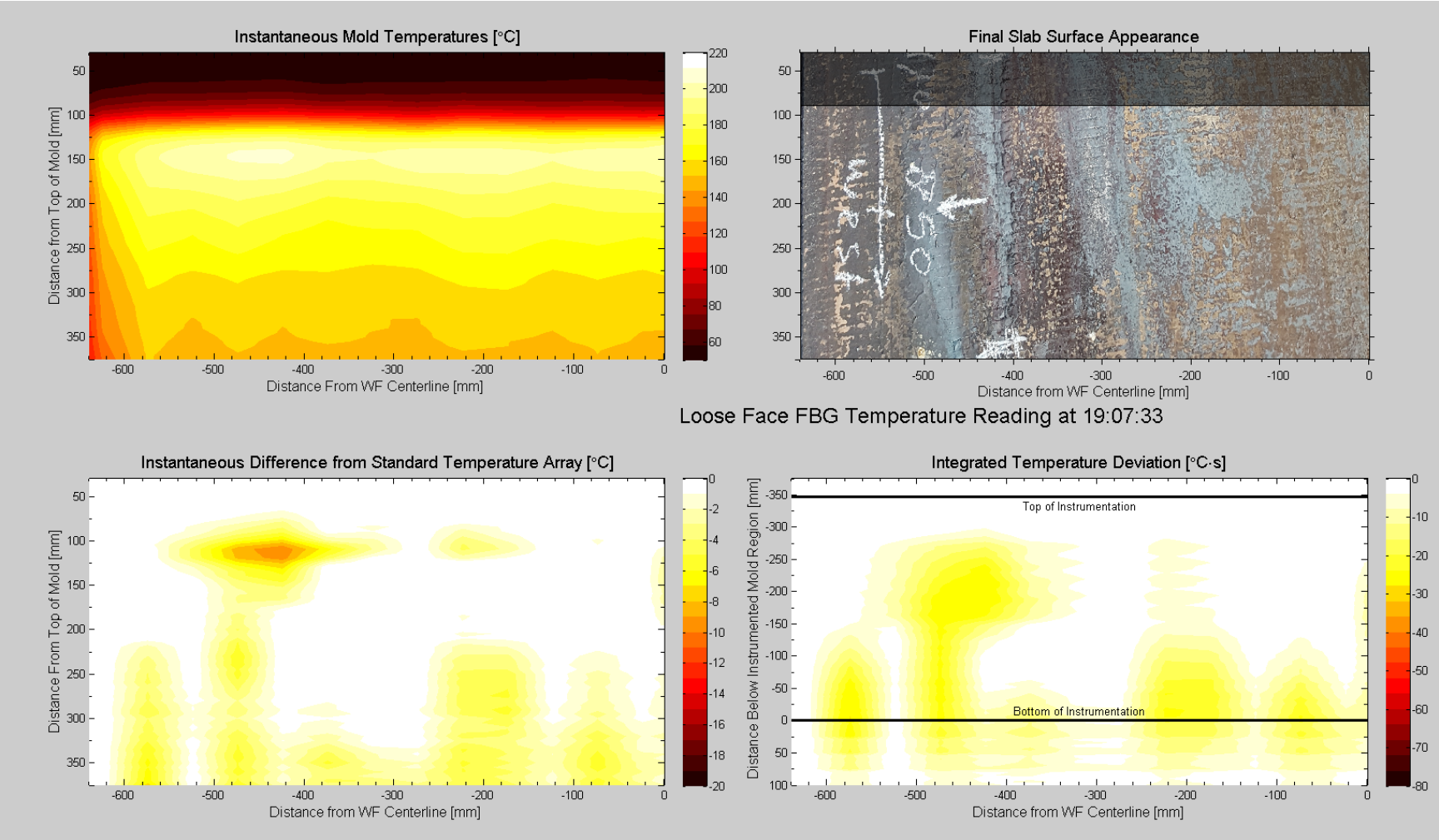


Figure 7.9: Integral Defect Methodology Heads-up Display Frame 2

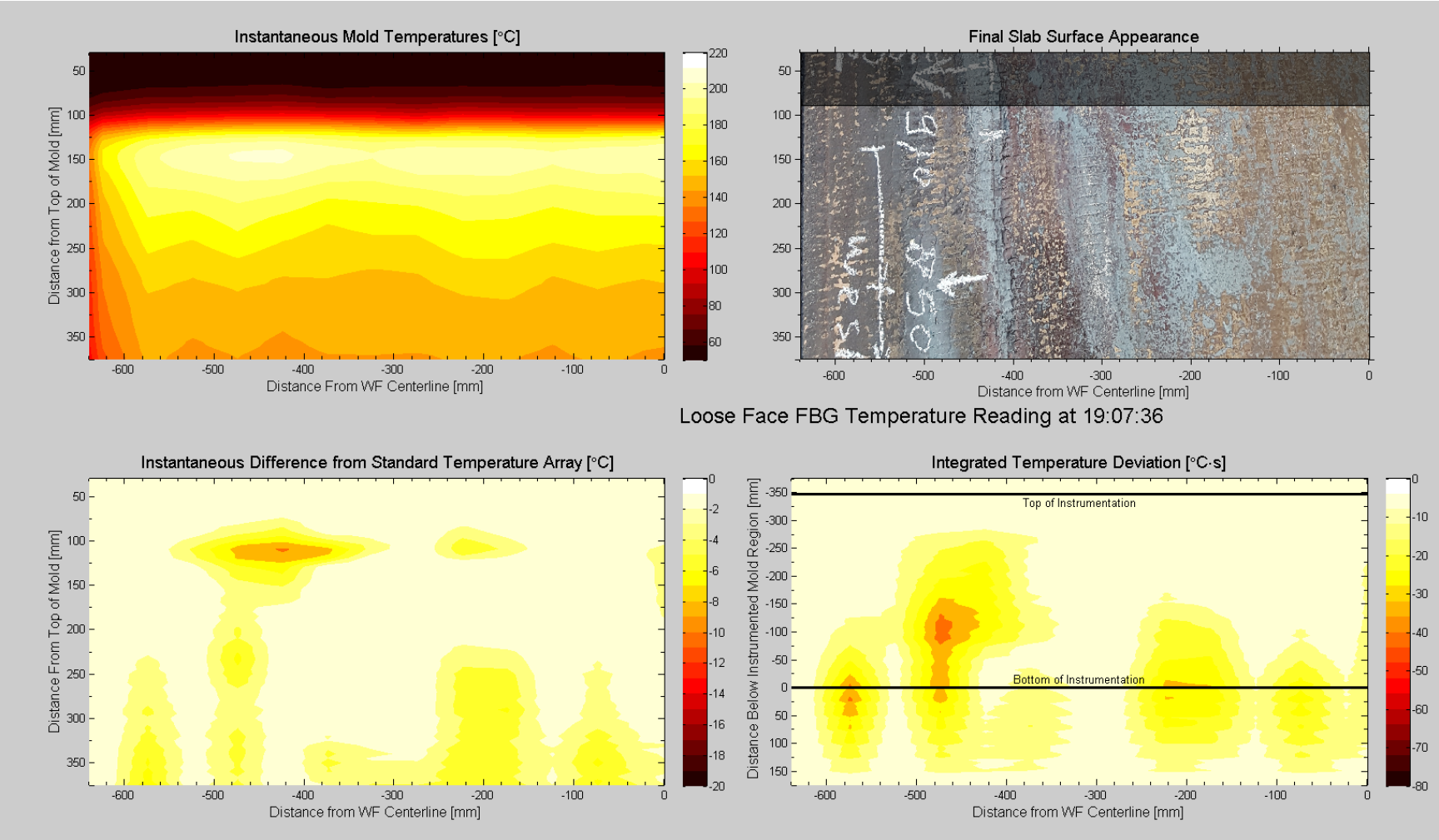


Figure 7.10: Integral Defect Methodology Heads-up Display Frame 3

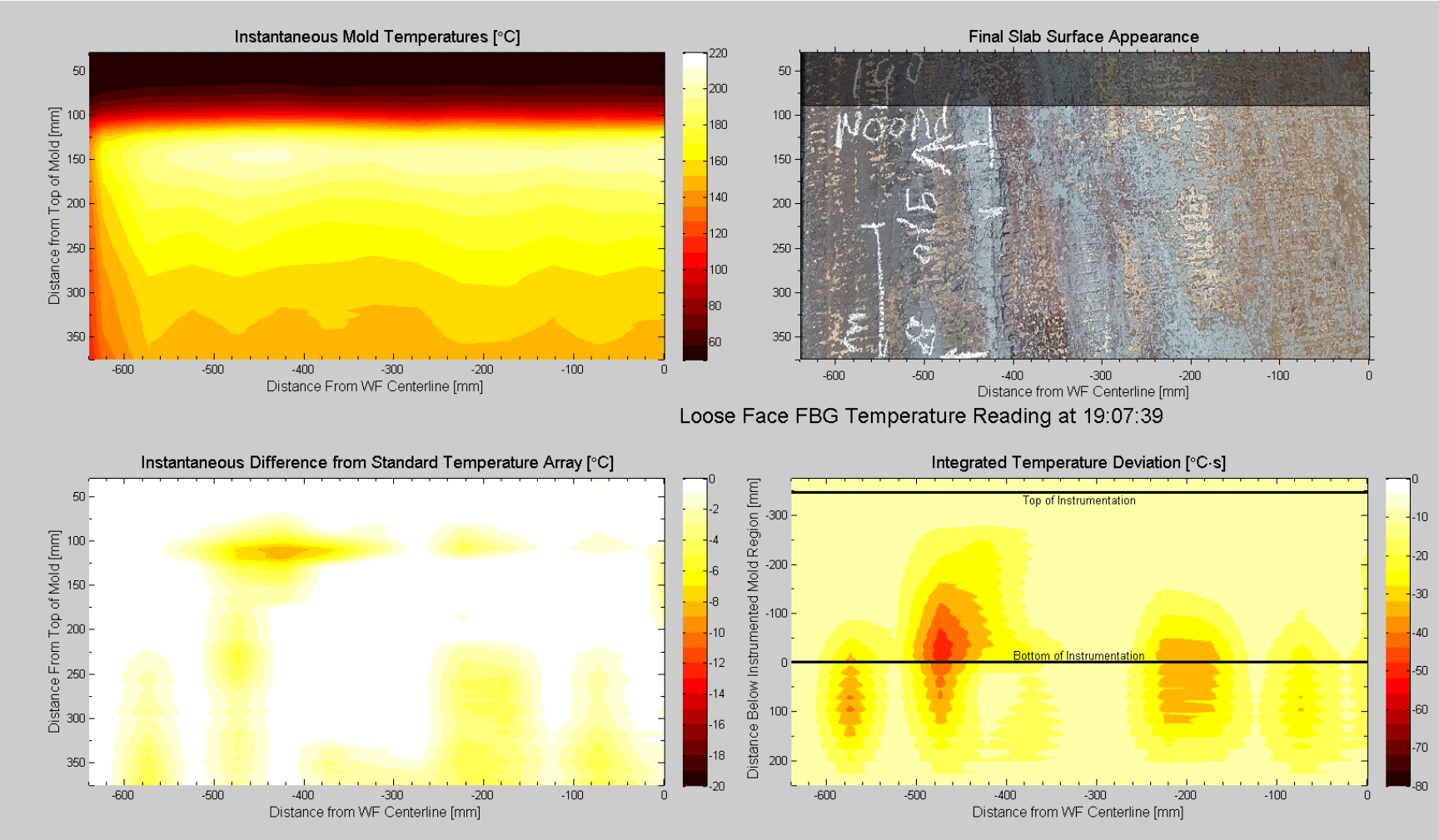


Figure 7.11: Integral Defect Methodology Heads-up Display Frame 4

7.9 Discussion

As described before, the top right image in Figure 7.7 is taken after the defect and slab has exited the machine and cooled down, and thus is not likely possible in real-time. For online operation in real time, a streaming image taken with laser or optical scanners (either of the slab surface shape exiting the caster, or of the rolled coil) might be matched with the corresponding mold temperature images taken previously and offset, and be used to evaluate quality and dispositioning (shipping or downgrading) of the steel product. The new images showing the integrated temperature drops could be helpful in the determination of slab or coil downgrading. Time offsetting the view of these results allows for including the time history of travel for the slab through secondary cooling and a tunnel furnace (in the case of an integrated thin slab casting operation).

This new method tracks and amplifies small temperature changes, so the standard profiles are very sensitive to casting conditions: grade being cast, casting speed, superheat, mold powder, mold geometry, and flow conditions, which vary from caster to caster. In addition to careful tracking and updating of the averages which represent standard conditions, natural variations not related to defect formation may need to be filtered, which would require adjusting the threshold temperature drop, a.

High thermal gradients near the meniscus region and near the slab corners make these areas very sensitive to minor temperature variations. Although level fluctuations may contribute to surface quality problems, their effects cause large T_{IDrop} values across the top of the mold. Similarly, the cooler corners cause large T_{IDrop} values down the region adjacent to the narrow face edges, especially when automated width changes and sensor spacing issues make the exact location of the corner difficult to determine. For these reasons, it may be necessary to truncate the top and side portions of the instrumented region, only using data below the meniscus at y_{Enter}, and away from the narrow faces.

Depending on the depth and response time of the temperature measurements, further tuning may be needed to implement this methodology into a given steel plant. The new

field variable, T_{IDropF}, requires sufficiently high density thermal data collection in the mold to capture the thermal signature of the strand surface defects. This method will work for any type of temperature measurement (thermocouple, laser, fiber, etc.) with the limitation being that fewer sensor locations will reduce the accuracy and prediction ability of the method to some degree. A set of only a few rows of breakout detection thermocouples in the casting direction does not provide enough information/history for each discrete slab location to produce accurate, useful results. While the method *will* still work with molds that are instrumented only for breakout detection, it is substantially limited by the lack of sensor data (*i.e.* the typical operation with only two rows of thermocouples provides only two points vertically).

Each additional sensor in the vertical direction (direction of travel) allows for another data point in the summation calculation, increasing the amplification and reliability of the integrated temperature deviation measurements. Additionally, this method is not actually measuring the temperature of the strand directly; it is an *indirect* quality measure from the mold temperatures corresponding to the strand temperatures. As such, this method functions irrespective of the depth of thermocouples as long as they are consistently set. Inconsistencies in the placement depth and subsequent changes in measurement can have unintended negative consequences on the previously established standard profile.

7.10 Implementation Procedure For an Operating Caster

For a given caster, initial setup of the system will require interfacing with the existing caster data collection system. Subsequent additions for other grades and caster practices should be an easy addition.

7.10.1 Calibration Conditions and Data

This method requires only a few pieces of information about the cast, but each piece is critical. Time-stamped temperature data is required for every available sensor in the mold. Casting speed data with time, heat, and slab signatures are needed to match the data

accurately with the output slab quality. Inaccuracies of a few millimeters are acceptable, but more than a few hundred can be problematic, as it is necessary to map the time and temperature history down to a specific location on each slab in a heat. For the initial calibration, the spatial accuracy is extremely important, but once the system is set up for a given grade it then depends on the desired level of system accuracy (*i.e.* this slab only has a small defective region in a specific location vs somewhere on a given slab is defective and thus the whole slab needs to be examined) and the system calibration may not be as important.

Any steel grade may be selected for implementing this methodology. However, it is advantageous to choose a steel grade that is common in the caster product mix and occasionally problematic. Commonality is important in making sure that enough data can be collected to establish a steady-state period of quality production to generate a good standard profile for the system. It will also be necessary to visually inspect a few slabs from the heats used to calibrate, both of good quality and bad quality (they do not need to be the same heat, but casting conditions should be as close as possible).

7.10.2 Procedure

7.10.2.1 Collect and Analyze Data from a Good Quality Cast

The methodology requires enough high quality slabs at a given set of casting conditions to establish what the standard profile should be for those conditions.

7.10.2.2 Generate a Standard Profile

The standard profile is one of the most critical parts of this system and is unique to every caster, mold, and sensor configuration. Taking the time average of each individual sensor to build the profile may be enough, or even taking the time average of one very stable column of sensors and establishing that for the entire circumference. For example, an asymmetric flow pattern may cause one side of the mold to have a slightly higher meniscus location and offset the vertical temperature profile non-uniformly across the width. Furthermore, unstable roll

pattern changes will likely add in a time transient history to the standard profile. While it is possible to configure the standard profile to have a time history, the unpredictable aspect of the roll pattern would likely make this inadvisable.

7.10.2.3 Collect and Analyze Data from a Bad Quality Cast

Once a good-quality data set has been established, it is necessary to generate a bad quality data set for particular types of quality problems. Both casts need to be at approximately the same casting speed. (*i.e.* avoid startups or slow downs for the calibration steps). It is especially important that the surface quality of the slabs be tracked for this step, images of the actually cast surface quality are the best option.

7.10.2.4 Confirm the Standard Profile and Calibrate Thresholds

Run the system setup for the previously generated standard profile (from the good casting condition) for the known bad casting condition. A successful run of this cast through the system should indicate areas on the slab that are defective (cracked or depressed) and correspond to the general areas found to have defects during the inspection. Calibration of the defect criterion threshold is based around trying to eliminate false positives (indications of a defect when there is none), narrow the system spatial accuracy for the observed defect locations, without eliminating too many areas with minor defects (*i.e.* the threshold cannot be so high as to neglect many serious cracks and/or depressions).

7.10.2.5 Run a Blind Calibration Test

The final step of implementing the procedure for a new grade and casting condition is a controlled blind test. The best method might be to have a second operator select a heat with some known issues and do a slab inspection[2]. It is important to test both the positive and negative outcomes of the procedure. Ideally, 2-5 slabs will be selected for analysis with an undisclosed amount of defects on at least half of the slabs. It is necessary to either save

[2]Note that the purpose of the blind study is to help prevent any bias, but this step can easily be conducted by a single person.

the slabs for inspection later (this may not be feasible) or to take detailed and dimensioned images of the slab surfaces for later comparison to the model output. At this stage it is critical that carefully dimensioned images of the slabs be taken, and areas with significant defects be noted. At the same time that the slab analysis is being conducted, the model should be run over the data set from the heat in question. If the the operator using model is successfully able to identify a majority of the severe defects then it should be considered calibrated. With enough good data sets, it may also be possible to apply machine learning to recognize when a given set of image sequences indicates a real defect in the product.

7.10.3 Display Setup Notes

The specific implementation of this system on a given caster has a lot of options in terms of how display will be used in the operations pulpit. Detailed here is an example of one setup that the author thinks would be useful. The primary Heads Up Display (HUD) for this method was previously shown in Figure 7.7 and described above. The primary system is concerned with the current conditions within the mold and can be handled by the main caster operator. This is the system that should be associated with any methods attached to breakout detection of longitudinal bleeder breakouts. However, it may also be helpful to have a secondary HUD for surface conditions and inspection located further downstream. For example, placing a surface profiling tool just before the coiler or scanning the slab as it enters the first set of rolls after the tunnel furnace. Profiling or scanning tools located further downstream (*i.e.* at the coiler) would follow the same procedure, but with a larger time offset to the screen readout similar to Figure 7.12.

A useful scenario example for this could be envisioned for a thin slab caster operation with a funnel mold.The procedure for a given steel grade may say that if observations are made that long cracks are starting to appear, the mold taper should be reduced. However, long defects in a funnel mold are especially difficult to discern in terms of over or under taper (partially due to the shape of the funnel mold). Specifically, defects will appear in both under and over taper conditions as a result of varying locations around the circumference of

separation from the mold inner or outer funnel curvature, and the margin between may be small. Correlating the location of long defects on the broad face surface in terms of location can be difficult (*i.e.* subjective definitions for off-corner, middle, etc.). Observations of defects appearing on the secondary offset display likely correlate to mold behavior during the casting, as such, having a display showing the current scan image/profile along with the properly time-offset display from the mold conditions when it was cast would be beneficial. This type of view can aid in decision making to try and eliminate the defects. One option that could be useful for properly identifying which region of the funnel mold is producing defects, is the use of an overlay. The overlay of lines could be on a display in the pulpit, or a laser could be projected onto the steel surface directly indicating where the current inner and outer radii of the mold are. This is especially useful in determining if a taper increase or decrease is more beneficial.

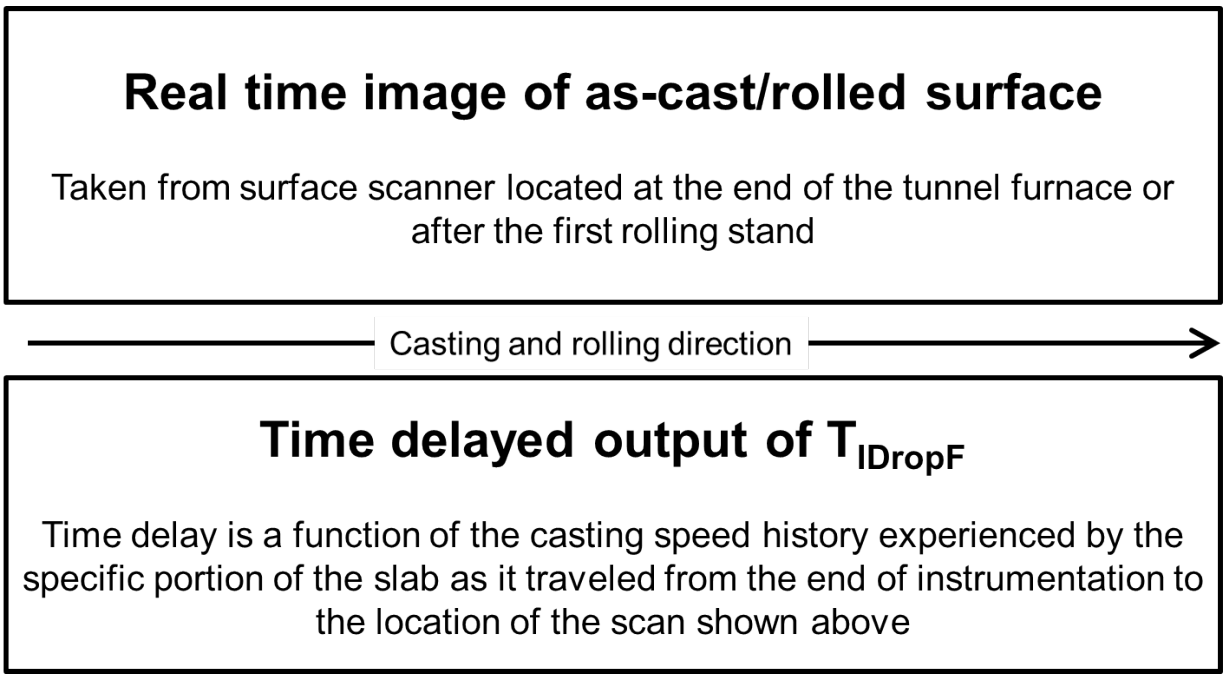


Figure 7.12: Downstream use of the T_{IDropF} methodology

7.11 Applications Beyond Continuous Casting

One of the more important aspects of this methodology is that it can apply to a wide range of applications. The methodology, in part, can be described as translating between and eulerian and langrangian reference frame in the continuous casting process. Specifically, mapping the eulerian mold time temperature history to the langrangian slab time temperature and location history. Continuous casting of steel is the original developed purpose, but even more generally it is the material passing through the instrumented mold. Taking that a further step back, this method is applicable for a material passing a second material where sensors can detect measurable physical properties. The measured properties vary but could include: position, capacitance, color, electrical conductivity or impedance, luminescence, opacity, permeability, pressure, refractive index, specific heat, temperature, etc.

As such, this method can be used for detecting defects in any manufacturing process which includes a material moving past an equipment structure in which at least two sensors are oriented in the direction of material movement. The sensor readings of the local physical property can be used, either directly or indirectly. For example, It is not necessary to measure the temperature of the actual slab material of interest as long as the indirectly measured values from the mold are representative of the material behavior of interest. As long as these conditions are met, the material or process in question is irrelevant and the method can still be applied.

7.12 Conclusions

Post processing and visualization of results is a crucial aspect of computational modeling and analysis of sensor data. If done correctly, substantial amounts of information can be condensed into a few simple images or videos to convey the important insights into the process. In this work, some recommendations are made for color maps, viewing orientations, and other aspects of visualization of 2D and 3D results relevant to materials processing, including scalar field variables such as temperature, vectors such as velocity, and tensors

such as stress. In most cases, a default rainbow color map is not as intuitive as data-specific color map, such as blackbody radiation for temperature and diverging Red-Blue for stress.

Finally, a new methodology is introduced to visualize defect formation from high density temperature data recorded in a continuous casting mold. The likelihood of surface quality problems can be predicted based on an integrated temperature drop relative to a standardized temperature profile, T_{IDrop}. When calibrated properly, this method can enable real-time monitoring of surface quality issues inside the mold during the commercial continuous casting process.

7.13 Acknowledgements

Special thanks for this project are due to Begoña Santillana, Mathias Mul, Ton Spierings, Stephen Carless, Gert Abbel, Dirk Van Der Plas, Arnoud Kamperman, of Tata Steel Europe, and Martin Seden of ABB. All of whom were instrumental in gathering the data and samples for this project, as well as allowing the author to visit and work at the Tata Steel Europe Facility in Ijmuiden.

CHAPTER 8

CONCLUSIONS

Continuously casting is a corner stone of steel production around the world. The large production scale and industry size mean that even small improvements, in efficiency or quality, to this mature process can have tremendous economic impacts. Longitudinal cracks and depressions are a very important class of defects in continuously-cast products, and also cause breakouts which are not usually detectable by existing conventional breakout-detection systems. This work has investigated the formation of longitudinal depressions, with and without cracks, using a thermal-mechanical model of steel solidification, and related specific formation mechanisms with the different shapes of the depressions. Several samples of longitudinal defects from commercial slabs have been presented as qualitative and quantitative validation of some of the model predictions. A detailed case study was performed using high resolution temperature measurements from a continuous casting mold along with a corresponding defect. With this detailed information and the previously developed modeling framework, a visualization and prediction method was created. This novel visualization method allows for the connection between solidification temperature measurements and longitudinal defects for the first time. Furthermore, this methodology has been extended to create an exciting method which allows for online real-time longitudinal defect formation prediction in a functioning continuous caster.

8.1 Research Objectives

This work has focused on gaining a fundamental understanding of how different types of depressions form and develop into their particular appearance. To accomplish this, six specific research questions were laid out to address this broad research objective:

1. What conditions are necessary to initiate a depression?
2. What are the steps in depression formation?

3. How do depression shapes vary if caused by tension vs compression?
4. How does a crack change the surface shape of a defect?
5. Can the shape of a longitudinal defect indicate a formation mechanism?
6. Can a methodology be developed to predict the likelihood of a defect?

From the results of this work, answers to these questions can be offered.

8.2 Longitudinal Defect Formation Mechanisms

As described previously, a series of models were developed to explore defect mechanisms. Longitudinal depressions in continuous casting can occur in both compression and tension conditions. Tension, such as caused by excessive transverse friction in the mold, can result in partial necking of the shell, leading to the most common type of observed depression - a U-shape. In certain conditions, thinning of the shell is severe enough to further allow the ferrostatic pressure to partially bend the depression and create a W-shape depression. Compression condition depressions are more subtle and much less noticeable when they do occur, and may result in a partial buckling of the shell, also leading to a W-shape depression. Depressions with narrow surface cracks tend to be more V-shaped and are substantially deeper than their non-cracked counterparts, having lower width/depth aspect ratios. Sometimes, however, surface cracks widen to absorb the strain, resulting in higher aspect ratio depressions, or even an otherwise flat surface. Finally, depressions without surface cracks tend to have higher width/depth aspect ratios, and sometimes have sub-surface hot tears present, which relieve some of the tension on the solidification front and result in sub-surface macro-segregation streaks. Such sub-surface cracks sometimes may penetrate to the surface, propagating along prior-austenite grain boundaries, and resulting in complex-shaped surface crack openings. Based on these findings, a series of longitudinal defect formation mechanisms were examined and matched with industrial samples.

Shown in Figure 8.1 are 11 different industrial samples of continuously cast longitudinal depression based defects. From the results presented in this work each of these defects can be characterized by a specific formation mechanism within the continuous casting mold.

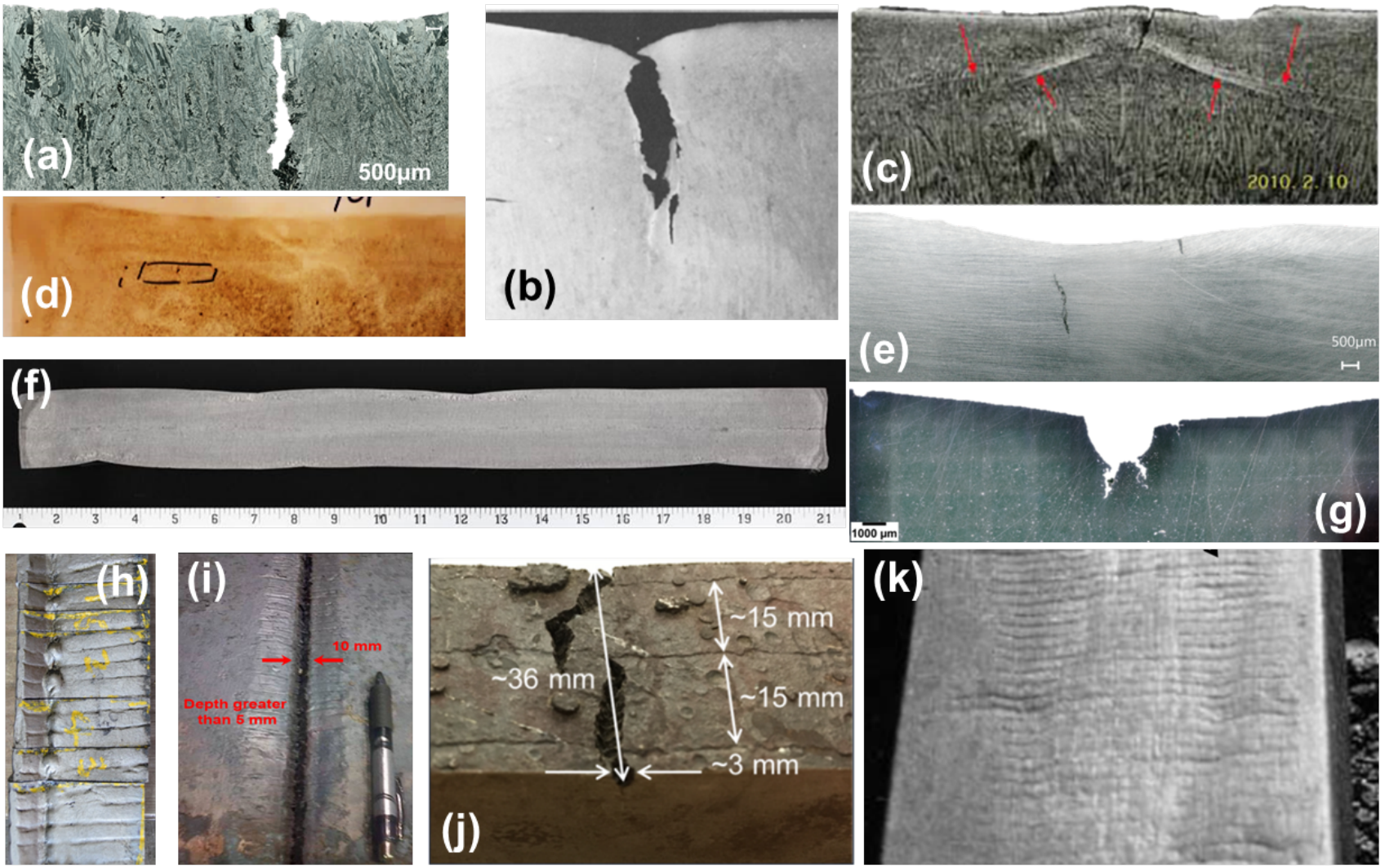


Figure 8.1: Examples of 11 different longitudinal depression based defects (referenced previously) with specific formation mechanisms within the continuous casting mold

Figure 8.1a is an example of a longitudinal surface crack with curved corners and no depression. Sometimes, surface cracks appear with negligible surface depressions. This defect likely starts the same way as the U-shape necking depression. Early during this process, however, local embrittlement and tensile stress concentration initiates a crack at the surface of the slab, very likely at the center of the initiating depression where the shell is the hottest and weakest and strain is highest. After initiation of the crack, some of the tension that originally would have gone into further necking of the shell and deepening of the depression, instead goes into opening of the crack. As the crack corners are now separated at the surface, the shell on both sides continues to try to shrink. With a new free surface and lack of constraint, this shrinkage of the shell on both sides of the crack pulls the corner outwards, and the corners rotate slightly, protruding slightly outward, relative to the far-field.

Figure 8.1b is an example of a longitudinal depression with an opened sub-surface crack with pointed corners. In contrast to Figure 8.1a, this defect starts as a U-shape necking depression. Then a crack initiates, likely sub-surface rather than a surface crack. This crack propagates towards the strand surface (likely along the prior austenite grain boundaries), owing to increased tension across the entire crack and intermediate temperature embrittlement of the thin ligament of shell between the crack and the surface. As this ligament thins, tensile stress concentrates, localizes and necks, and eventually fails, thus enabling the crack to propagate all the way to the surface. That strain concentration and necking deforms the corners to point inwards towards each other, or even back along the propagation path (away from the surface).

Figure 8.1c is an example of a W-shape necking type depression with surface crack. This is believed to have evolved from a U-shape depression as a result of significant shell thinning and the action of ferrostatic pressure pushing down on the thinnest shell in the middle of the depression. The associated bending while being pushed back towards the mold initiates tension at the surface, which opens up a surface crack at the defect center.

Figure 8.1d is an example of a U-shape buckling type off-corner depression, likely due to under-taper of the mold narrow faces. The formation mechanism of these depression defects involves two stages. Firstly, a thermal disruption at the meniscus often leads to lower heat transfer and a thin spot on the shell in the off-corner region. Insufficient taper then allows the narrow-face shell to bulge outwards from the ferrostatic pressure. This bulging of the narrow face leads to rotation of the corners, pivoting around the weak thin region of the shell, and then pulling the off-corner region of the wide face shell surface inwards, growing into a gradual, (shallow) U-shaped depression that persists in the final slab, where it is often referred to as "gutter".

Figure 8.1e is an example of a U-shape necking type depression without surface cracks. In this mechanism, a local thermal disruption causes a reduction in heat transfer and shell thinning, uniform heat transfer at the far field away from the depression proceeds, and this colder stronger shell shrinks against friction from the mold and applies tension. Localization of the tension occurs at the weakest part of the shell, the thin depression center, leading to necking and separation from the mold surface. Separation from the mold surface leads to a further decrease in the heat transfer in this region and continued necking. Tensile strain is concentrated in the necked region, and bending causes a slightly higher strain at the solidification front, which makes this type of defect prone to sub-surface hot tearing and macro-segregation, which causes the observed subsurface crack.

Figure 8.1f is likely an example of a W-shape depression due to overtaper and buckling. This W-shape buckling style depression is common in thin slab casters, especially those with funnel molds, due to the complex geometries, and changes in circumference down the funnel portion of the mold, which are susceptible to inadequate taper design. Overtapering of a funnel mold can cause the shell to separate away from the mold, especially at the inner curve (shoulder) location. These depression defects can be avoided by proper taper design based on the specific grade being cast and the funnel geometry of the given caster. This mechanism was the direct cause of a breakout in the sample shown.

Figure 8.1g is an example of a U-shape grooves from solidification against a slag finger/rivulet. In the mechanism for this defect, a small amount of slag becomes caught in the scratch, solidifies, and protrudes past the surface of the copper, creating an uneven surface for solidification to occur in addition to a local reduction in heat flux due to the thicker flux layer (*i.e.* thermal disruption). This causes the local shape of the shell that solidifies around it at the meniscus to match the finger shape, thereby directly creating an impression/depression on the strand surface (mechanical effect). Then the far-field shrinkage of the strand applies tension onto this very-low aspect ratio (∼1:1) depression created by the slag rivulet, which generates surface cracks at the depression root. This defect can be recognized by its being very straight, with a specific shape depression due to the slag rivulet.

Figure 8.1h is an example of a U-shape buckling type off-corner depression due to overtaper. In the mechanism for this defect, excessive taper of the narrow face molds forces the narrow face shell inwards and compresses the broadface shell. As the narrow face moves inwards, the corner behavior can change the force application direction enough to help buckle the broadface shell at the off corner region. Off-corner depressions caused by this mechanism are likely to be deeper and more severe, with lower aspect ratios. This mechanism was the direct cause of a longitudinal bleed, followed by a breakout in the sample slab shown.

Figure 8.1i is an example of a V-shape necking type depression due to a mold scratch. During casting or maintenance, mechanical equipment can scratch, gouge, or scrape the surface of the copper mold. These surface aberrations are especially problematic very close to the meniscus. Such a mold scratch creates a mechanical disruption in the mold surface which can significantly lower heat transfer locally. The local disruption to heat transfer thins the shell and allows for localization of far field tension from shrinkage. This defect manifests as a very straight, continuous, sharp (very low aspect ratio) V-shaped depression on the slab surface. This is in contrast to the slag rivulet which leaves an imprint in the shell, and is located at one static location across the strand perimeter.

Figure 8.1j is an example of a U-shape necking type depression with surface cracks. In the mechanism for this defect, during casting the broadface inner radius experienced high friction and potential sticking at the corner, due to excessive turbulent fluid flow, which also caused a thermal disruption at the meniscus. This is believed to have led to the initiation of a crack while the shell was still very thin. As the shell continued to solidify, the outer radius continued to shrink, while the inner radius shrinkage instead concentrated into extending the opening width of the surface cracks. As the inner radius was not shrinking, the continued shrinkage of the outer radius led to corner rotation. This generated tension near the solidification front towards the outer radius of the narrow face shell, causing hot tears and macro segregation streaks at that location. This mechanism was the direct cause of a breakout in the sample shown. This defect is characterized by its very shallow depression, and very wide surface cracks.

Figure 8.1k is an example of a W-shape buckling type depression due to excessive compression (over-taper). This depression is a result of compression and buckling on the broadface due to excessive narrow-face taper which exceeded the shrinkage profile of the steel. A local disruption in heat transfer may initiate a weaker spot in the shell, and if the compression is high enough, the inward bending may cause enough strain at the solidification front to cause subsurface cracks. In addition to its W-shape, this defect can be recognized by the wandering of the depression from side to side, as it progresses down the length of the slab.

8.3 Research Questions Answered

1. What conditions are necessary to initiate a depression?

Depressions are largely related to thermal disruption and non-uniformity of heat transfer in the mold. The minimum size of the thermal disruption needed to generate a depression depends entirely on casting conditions. Results from this work give some insight into why wider casters are often found to have more longitudinal defects, it is also likely that the minimum size thermal disruption needed for a depression in a wider caster is smaller than a

narrower caster, due to the imposed friction from the larger broadfaces. While it is possible for a depression to initiate as a result of a mechanical disruption (i.e. mold scratch/gouge, surface imperfection) the relevant aspect of this situation is that the mechanical disruption causes a thermal disruption which inevitably leads to the depression. It is generally necessary for the rest of the slab to shrink and apply tension to a localized area in order to neck the depression appropriately. A second possibility is uniform heat transfer and the initiation of a crack. The appearance of a crack in an otherwise uniformly thick shell allows the shell surface (at the crack corner) to start rotating and separate from the mold. This separation then leads to heat transfer reduction similar to the previously described case.

2. What are the steps in depression formation?

The steps in depression formation vary slightly depending on the specific type as described in the previous section. However, in most cases, the formation of a depression (without an initial crack) first requires a disruption to the uniform heat transfer around the circumference of the mold at or very near to the meniscus. If that disruption takes the form of a crack, then an initial thermal disruption is not necessary; a drop in heat transfer and corresponding depression will often develop as a result of the crack rotating away from the surface of the mold, creating an air gap.

3. How do depression shapes vary if caused by tension versus compression?

The most common type of depression is the U-shape depression, which tends to form in tension. A less common style of depression is the W-shape depression, which predominantly occurs in compression. However, if significant enough shell thinning occurs in the tension scenario, it is possible that a W shape depression will form. In general, compression related longitudinal defects are shallower (ie. higher in width/depth aspect ratio) than tension based necking type defect. However, it does seem that sometimes, off corner buckling depressions can be rather severe, with low aspect ratios, and very severe subsurface cracks.

4. How does a crack change the appearance of a depression defect?

The presence of a surface crack at the base of a depression causes the depression to become significantly deeper, with a lower width/depth aspect ratio, than a non cracked depression, also transforming it from a U-shape to a V-shape. This is largely due to the crack enabling independent rotation of the two parts of the shell as the crack propagates through the hot material. This is somewhat contrary to some prior thought; the presence of a deep depression does not necessarily mean that it has a higher propensity for a deep crack. What is more likely is that the crack itself helped make that depression deeper. In the case that reheating at the base of a depression may also bring the defect back to a low ductility temperature potentially allowing for a crack to initiate, the crack would then deepen the depression. Furthermore, if the crack opening is significant (likely a bleeder type crack), it is quite likely that a breakout was narrowly avoided and that the cracked side broadface width will be larger than an uncracked side. On the other hand, if a significant crack initiates early in the depression formation process or after a significant shell is built up, any applied tension that would have deepened the depression, goes into opening of the crack instead of necking.

5. Can the final observed shape of a longitudinal defect indicate its formation mechanism?

Differentiating between different longitudinal defects after they have formed is generally quite difficult due to the influencing factors and the number of steps between formation and analysis. However, using the tools developed in this work, significant progress has been made towards the identification of formation mechanisms, as described in the previous section. In addition to the appearance of the defect itself, some additional information can be helpful in defect analysis. For example: the condition of the copper molds (i.e. premature wear at certain points), narrow face thermocouples indicating whether the strand was or was not in contact at certain locations down the mold, casting speed and taper adjustment histories. Each extra piece of information that can be associated with a given defect can help in post-mortem analysis.

6. Can a methodology be developed to detect the formation of a longitudinal defect during the process?

In the most general sense, a longitudinal depression will appear to the mold as a cold spot due to reduced heat transfer across the gap. Using high spatial and temporal resolution sensors within the casting mold allows for extensive new insight into the process and potentially observe these local temperatures fluctuations with better accuracy. By using these measurements, amplified by the methodology developed in this work, it should be possible to visualize the formation of a longitudinal defect in real time, and to take corrective action. Furthermore, for the first time this method makes it possible to predict longitudinal based bleeder breakout behaviors which would be a substantial addition to existing breakout prevention systems that currently focus on mainly transverse-based methodologies to detect sticker breakouts.

8.4 Final Thoughts

As described in this work it is clear that discerning the presence of a defect on the surface of the strand is possible, and the appearances of defects can be matched to formation mechanisms. Some additional conclusions can also be made from this work:

- On crack sensitive grades, visible depressions warrant closer examination if it is for critical applications as sub-surface cracks and macro-segregation streaks may be present.
- If pronounced oscillation marks are visible on only a limited portion of a slab, it is likely that this region contains a depression
- Slabs identified to have significant shape problems should be inspected for the presence of cracks
- Cracks cause pre-existing depressions to deepen, not from continued necking, but from rotation and shrinkage

- If cracking with bleeds are found, this is likely indicative of a near breakout
- Reheating at the base of depressions may be enough to bring the steel locally back into a brittle temperature region depending on the steel grade. Grade/grade family specific spray practices that put the strand surface too close to a ductility trough run the risk of generating cracks if heat transfer disruptions are significant
- As FBG molds become more common, much more extensive and detailed data will become available making it easier to narrow down more specific defect signatures
- While the formation mechanisms are likely very similar, substantial changes in solidification path (i.e. AHSS, peritectic steel grades) will influence defect behavior

With the significant pressure on casting operations to increase efficiency, throughput, and product quality all at the same time, defect analysis can seem painstaking and not always practical. However, improvements across the board can be seen if better understanding of the defects specific to a given caster can be identified and examined. As discussed, highly instrumented molds, such as FBG, are gaining popularity in recent years. As they become more common, a tremendous amount of more extensive and detailed data will be generated than has ever been accessible before. Processing the new data through the lens of this work and the new defect prediction methodology, along with quality reports, line inspections, and defect analysis, will allow for extracting more detailed signatures of specific defects at the plant. Finally, informed with this new information the logical extension of this work and the new data will allow for quantitative progress incorporating the knowledge of these mechanisms and their temperature signature for online real-time prediction of specific defects before they even exit the caster.

REFERENCES CITED

[1] Joseph S. Spoerl. A Brief History of Iron and Steel Production. http://www.anselm.edu/homepage/dbanach/h-carnegie-steel.htm, 2013. URL http://www.anselm.edu/homepage/dbanach/h-carnegie-steel.htm.

[2] H Bessemer. The Bessemer Steel Works At Troy. *The Journal of The Franklin Institute*, pages 82–83, 1845.

[3] Shozo Mizoguchi, Tetsuro Ohashi, and Tsuyoshi Saeki. Continuous Casting of Steel. *Annual Review Material Science*, pages 151–169, 1981.

[4] Jessica Elfsberg. *Oscillation Mark Formation in Continuous Casting Processes*. PhD thesis, Royal Institute of Technology, 2003.

[5] World Steel Association. Steel Statistical Yearbook 2017. Technical report, World Steel Association, 2017. URL https://www.worldsteel.org/en/dam/jcr:3e275c73-6f11-4e7f-a5d8-23d9bc5c508f/Steel+Statistical+Yearbook+2017.pdf.

[6] Pierre H Dauby. Continuous Casting: Make better steel and more of it! *Revue de Metallurgie*, 109(2):113–136, 2012. doi: 10.1051/metal/2012011.

[7] J.K. Brimacombe and K. Sorimachi. Crack formation in the continuous casting of steel. *Metallurgical and Materials Transactions B*, 8(2):489–505, 1977. ISSN 03602141. doi: 10.1007/BF02696937.

[8] Brian G. Thomas, M. Jenkins, and R. B. Mahapatra. Investigation of Strand Surface Defects Using Mold Instrumentation and Modelling. *Ironmaking & Steelmaking*, 31 (6):485–494, 2004.

[9] William H Emling. Breakout Prevention. In Alan W. Cramb, editor, *The Making, Shaping and Treating of Steel: Casting Volume*, chapter 19. AISE Steel Foundation, Pittsburgh, PA, 2003.

[10] K.E. Blazek, Oscar Lanzi, Phil L Gano, and Dale L Kellogg. Calculation of the peritectic range for steel alloys. In *AISTech - Iron and Steel Technology Conference Proceedings*, volume 5, pages 80–85, 2008.

[11] S Nafisi, C D Souza, L Collins, E.S. Szekeres, and P O Box. Breakout Prevention Challenges AISTech 2011 Proceedings - Volume I AISTech 2011 Proceedings - Volume I. In *AISTech - Iron and Steel Technology Conference Proceedings*, volume I, pages 1609–1617, 2011.

[12] Akira Tsuneoka, Wataru Ohashi, Seisuke Ishitobi, Tohri Kataoka, and Masami Tenma. Measurement and Control System of Solidification In Continuous Casting Mold. In *Steelmaking Conference Proceedings*, pages 3–10, 1985. ISBN 0932897029.

[13] J.K. Brimacombe, F. Weinberg, and E. B. Hawbolt. Formation of Longitudinal , Midface Cracks in Continuously-Cast Slabs. *Metallurgical and Materials Transactions B*, 10:279–292, 1979.

[14] Matthew L.S. Zappulla, Seong-Mook Cho, Seid Koric, Hyoung-Jun Lee, Seon-Hyo Kim, and Brian G. Thomas. Multiphysics modeling of continuous casting of stainless steel. *Journal of Materials Processing Technology*, page 116469, nov 2019. ISSN 09240136. doi: 10.1016/j.jmatprotec.2019.116469. URL `https://linkinghub.elsevier.com/retrieve/pii/S092401361930442X`.

[15] Matthew L.S. Zappulla. *Grade Effects on Thermal-Mechanical Behavior During the Initial Solidification of Continuously Cast Steels*. M.s., Masters Thesis, The University of Illinois at Urbana-Champaign, 2016.

[16] M L S Zappulla, G Zhu, and B G Thomas. 3D Thermal-Mechanical Model of Solidifying Steel Strand. In *AISTech 2019 Proceedings*, number 5, pages 2175–2186, 2019. doi: 10.33313/377/.

[17] Matthew L.S. Zappulla, Seong Mook Cho, and Brian G. Thomas. Visualization of Steel Continuous Casting Including a New Integral Method for Post-Processing Temperature Data. *Steel Research International*, 90(4), 2019. ISSN 16113683. doi: 10.1002/srin.201800540.

[18] Matthew L. S. Zappulla and Brian G. Thomas. Identification of Defects in a Metal Slab Made from Continuous Casting, 2019.

[19] Brian G. Thomas. Introduction to Continuous Casting. http://ccc.mechse.uiuc.edu/introduction/concast.html, 2020. URL `http://ccc.mechse.uiuc.edu/introduction/concast.html`.

[20] A.W. Cramb, Ravi Rastogi, and Roger L Maddalena. Nozzle Clogging. In *Making, Shaping and Treating of Steel*, chapter 10, pages 1–17. AISE Steel Foundation, Pittsburgh, PA, 2002.

[21] L.C. Hibbeler and Brian G. Thomas. Mold Slag Entrainment Mechanisms in Continuous Casting Molds. In *AISTech - Iron and Steel Technology Conference Proceedings*, pages 1215–1230, 2013.

[22] Brian G. Thomas. Continuous Casting Consortium. Online. URL `http://ccc.illinois.edu/index.html`.

[23] B. Santillana and Ton Spierings. Private Communication - Tata Steel Europe R&D. Private Communication.

[24] Siebo Kunstreich, Pierre H Dauby, Sung-kwan Baek, and Sang-min Lee. Multi – Mode Ems in Thick Slab Caster Molds and Effect on Coil Quality and Machine Performance. *European Conference on Continuous Casting*, 2005.

[25] Brian G. Thomas and H Zhu. Thermal Distortion of Solidifying Shell Near Meniscus in Continuous Casting of Steel. In *JIM-TMS Solidification Science and Procesing Conference*, pages 197–208, Honolulu, HI, USA, 1995. The Minerals, Metals & Materials Society.

[26] Pierre H. Dauby. Continuous casting: Make better steel and more of it. *Revue de Metallurgie. Cahiers D'Informations Techniques*, 109(2):113–136, 2012. ISSN 11563141. doi: 10.1051/metal/2012011.

[27] A. S M Jonayat and Brian G. Thomas. Transient Thermo-fluid Model of Meniscus Behavior and Slag Consumption in Steel Continuous Casting. *Metallurgical and Materials Transactions B*, 45B(5):1842–1864, 2014. ISSN 10735615. doi: 10.1007/s11663-014-0097-9.

[28] Seizo Watanabe, Kazuo Harada, and Fujita Hitoshi-Shiro. Continuous Casting. *Tetsu-to-Hagané*, 58(11):S393, 1972.

[29] I.V. Samarasekera and Cindy Chow. Continuous Casting of Steel Billets. In *Making, Shaping and Treating of Steel*, chapter 18, pages 1–46. AISE Steel Foundation, Pittsburgh, PA, 11th edition, 2002.

[30] Jungwook Cho, Hiroyuki Shibata, Toshihiko Emi, and Mikio Suzuki. Thermal Resistance at the Interface between Mold Flux Film and Mold for Continuous Casting of Steels. *ISIJ International*, 38(5):440–446, 1998. ISSN 0915-1559. doi: 10.2355/isijinternational.38.440. URL `http://joi.jlc.jst.go.jp/JST.Journalarchive/isijinternational1989/38.440?from=CrossRef`.

[31] Kenneth C. Mills, A.B. Fox, Z. Li, and R.P. Thackray. Performance and properties of mould fluxes. *Ironmaking & Steelmaking*, 32(1):26–34, 2005. ISSN 03019233. doi: 10.1179/174328105X15788.

[32] Kenneth C Mills. Mold Powders for Continuous Casting. In *The Making, Shaping, and Treating of Steel*, chapter 9, pages 1–41. AISE Steel Foundation, 2003.

[33] Ya Meng, Brian G. Thomas, Andreas A. Polycarpou, A. Prasad, and H. Henein. Mould Slag Property Measurements To Characterize Cc Mould – Shell Gap Phenomena. *Canadian Metallurgical Quarterly*, 45(1):79–94, 2006. ISSN 00084433. doi: 10.1179/000844306794409129.

[34] David T. Stone and Brian G. Thomas. Measurement and modeling of heat transfer across interfacial mold flux layers. *Canadian Metallurgical Quarterly*, 38(5):363–375, 1999. ISSN 00084433. doi: 10.1016/S0008-4433(99)00028-2.

[35] J. K. Park, Brian G. Thomas, and I.V. Samarasekera. Analysis of thermomechanical behaviour in billet casting with different mould corner radii. *Ironmaking & Steelmaking*, 29(5):359–375, 2002. ISSN 03019233. doi: 10.1179/030192302225004601.

[36] A. Moitra, Brian G. Thomas, and W.R. Storkman. Thermo-Mechanical Model of Steel Shell Behavior in the Continuous Casting Mold. In *TMS Annual Meeting*, pages 1–31, San Diego, CA, 1992. The Minerals, Metals & Materials Society.

[37] J. E. Kelly, K. P. Michalek, T. G. O'connor, Brian G. Thomas, and J. A. Dantzig. Initial development of thermal and stress fields in continuously cast steel billets. *Metallurgical and Materials Transactions A*, 19(10):2589–2602, 1988. ISSN 0360-2133. doi: 10.1007/BF02645486. URL `http://link.springer.com/10.1007/BF02645486`.

[38] Adrian Bejan. *Convection Heat Transfer*. John Wiley & Sons, Inc., Hoboken, NJ, USA, fourth edition, 2013. ISBN 9781118671627. doi: 10.1002/9781118671627. URL `http://doi.wiley.com/10.1002/9781118671627`.

[39] T. Murakami and H. Kashima-cho. Improvements of Longitudinal Corner Cracks at High-Speed Casting. In *Current Advances in Materials and Processes: Report of the ISIJ Meeting*, volume 5, page 1291, Tokyo, 1992. Iron and Steel Institute of Japan, Iron and Steel Institute of Japan.

[40] Pabitra Palai. Casting Defects in Slab. Technical report, Tata Steel India, Jamshedpur, 2011.

[41] Matthew L.S. Zappulla and Brian G. Thomas. Thermal-mechanical model of depression formation in steel continuous casting. In *Minerals, Metals and Materials Series*, volume Part F6, pages 501–510, San Diego, CA, 2017. The Minerals, Metals & Materials Society. ISBN 9783319514925. doi: 10.1007/978-3-319-51493-2_48. URL `http://link.springer.com/10.1007/978-3-319-51493-2http://link.springer.com/10.1007/978-3-319-51493-2{_}48`.

[42] Lan Yu. *FEM Analysis of Bulging Between Rolls in Continuous Casting*. M.s., Masters Thesis, The University of Illinois at Urbana-Champaign, 2000.

[43] M.B. Santillana. *Thermo-mechanical properties and cracking during solidification of thin slab cast steel, Ph.D. Thesis*. Ph.d. thesis, Ph.D. Thesis, Delft University of Technology, 2013.

[44] Brian G. Thomas, J.K. Brimacombe, and I.V. Samarasekera. The Formation of Panel Cracks in Steel Ingots: A State-of-the-Art Review, I. Hot Ductility of Steel. *Transactions of the Iron and Steel Society*, 7(10):7–20, 1986.

[45] B. Mintz, S. Yue, and J. J. Jonas. Hot ductility of steels and its relationship to the problem of transverse cracking during continuous casting. *International Materials Reviews*, 36(1):187–220, jan 1991. ISSN 0950-6608. doi: 10.1179/imr.1991.36.1.187. URL `http://www.tandfonline.com/doi/full/10.1179/imr.1991.36.1.187`.

[46] W.T. Lankford. Some considerations of strength and ductility in the continuous-casting process. *Metallurgical Transactions*, 3(6):1331–1357, jun 1972. ISSN 0360-2133. doi: 10.1007/BF02643017. URL `http://link.springer.com/10.1007/BF02643017`.

[47] E.T. Turkdogan. consequences of microsegregation during solidification of steel: subsurface-blowhole formation oxysulfide and precipitation. In *International Iron and Steel Congress: Process Technology Proceedings*, pages 767–775, 1986.

[48] Suk Chun Moon, Rian Dippenaar, and Seong Yeon Kim. The peritectic phase transition of steel during the initial stages of solidification in the mold. *Iron and Steel Technology*, 12(10):111–121, 2015. ISSN 15470423.

[49] British Iron and Steel Research Association (BISRA). Definitions and Causes of Continuous Casting Defects. Technical report, The Iron and Steel Institute, London, England, 1967.

[50] Brian Gordon Thomas. Private Communication. Private Communication, 2020.

[51] M. Herrera-Trejo, J. J. Ruiz, M. Castro-Roman, and H. Solis. Star cracks in continuously cast peritectic steel slabs. *Ironmaking and Steelmaking*, 37(6):452–457, 2010. ISSN 03019233. doi: 10.1179/174328109X445651.

[52] J.K. Brimacombe and K. Sorimachi. Crack Formation in the continuous casting of steel. *Metallurgical and Materials Transactions B*, 8B, 1977.

[53] Diptak Bhattacharya, T. K. Roy, and Vinay V. Mahashabde. A Study to Establish Correlation Between Intercolumnar Cracks in Slabs and Off-Center Defects in Hot-Rolled Products. *Journal of Failure Analysis and Prevention*, 16(1):95–103, 2016. ISSN 15477029. doi: 10.1007/s11668-015-0050-5.

[54] F. R. Shanley. Inelastic Column Theory. *Journal of the Aeronautical Sciences*, 14(5): 261–268, may 1947. ISSN 1936-9956. doi: 10.2514/8.1346. URL `https://arc.aiaa.org/doi/10.2514/8.1346`.

[55] Brian G. Thomas, A. Moitra, and R. McDavid. Simulation of longitudinal off - corner depressions in continuously - cast steel slabs. *Iron and Steelmaker (ISS Transactions)*, 23(4):143–156, 1996.

[56] J.K. Brimacombe, F. Weinberg, and E. B. Hawbolt. Formation of longitudinal, midface cracks in continuously-cast slabs. *Metallurgical and Materials Transactions B*, 10(2): 279–292, 1979. ISSN 03602141. doi: 10.1007/BF02652472.

[57] E.S. Szekeres. Personal Communication. Technical report, Casting Consultants Inc., 1993.

[58] Brian G. Thomas. On-line Detection of Quality Problems in Continuous Casting of Steel. In *Materials Science and Technology*, pages 29–44, Chicago, 2003. ISBN 0873395611.

[59] J. A. Dantzig and Charles L. Tucker III. *Modeling in Materials Processing*. Cambridge University Press, 2001. ISBN 978-0521779234.

[60] Seid Koric and Brian G. Thomas. Thermo-mechanical models of steel solidification based on two elastic visco-plastic constitutive laws. *journal of materials processing technology*, 7(1-3):408–418, 2008. ISSN 09240136. doi: 10.1016/j.jmatprotec.2007.06.060. URL `http://www.sciencedirect.com/science/article/pii/S092401360700636X`.

[61] Seid Koric, Lance C. Hibbeler, Rui Liu, and Brian G. Thomas. Multiphysics Model of Metal Solidification on the Continuum Level. *Numerical Heat Transfer, Part B: Fundamentals*, 58(6):371–392, dec 2010. ISSN 1040-7790. doi: 10.1080/10407790.2011.540954. URL `http://www.tandfonline.com/doi/abs/10.1080/10407790.2011.540954`.

[62] Hiroki Hasegawa, Hiromichi Ohta, Hiroyuki Shibata, and Yoshio Waseda. Recent development in the investigation on thermal conductivity of silicate melts. *High Temperature Materials and Processes*, 31(4-5):491–499, 2012. ISSN 03346455. doi: 10.1515/htmp-2012-0085.

[63] R M Mcdavid and Brian G. Thomas. Flow and Thermal Behavior of the Top Surface Flux / Powder Layers in Continuous Casting Molds. *Metallurgical and Materials Transactions B*, 27(4):672–685, 1996.

[64] Ya Meng and Brian Gordon Thomas. Heat-transfer and solidification model of continuous slab casting: CON1D. *Metallurgical and Materials Transactions B*, 34(5):685–705, oct 2003. ISSN 1073-5615. doi: 10.1007/s11663-003-0040-y. URL `http://link.springer.com/article/10.1007/s11663-003-0040-yhttp://link.springer.com/10.1007/s11663-003-0040-y`.

[65] Lance C. Hibbeler, Melody M. Chin See, Junya Iwasaki, Kenneth E Swartz, Ronald J. O'Malley, and Brian G. Thomas. A reduced-order model of mould heat transfer in the continuous casting of steel. *Applied Mathematical Modelling*, 40(19-20):8530–8551, oct 2016. ISSN 0307904X. doi: 10.1016/j.apm.2016.04.002. URL `https://linkinghub.elsevier.com/retrieve/pii/S0307904X16302025`.

[66] ABAQUS. *ABAQUS 6.13 Documentation Collection*. DS SIMULIA Corp, Providence, RI, 2013.

[67] V. B. Watwood. The finite element method for prediction of crack behavior. *Nuclear Engineering and Design*, 11(2):323–332, 1970. ISSN 00295493. doi: 10.1016/0029-5493(70)90155-X.

[68] Nelson Vieira De Carvalho, R. Krueger, Gerald E. Mabson, and L. R. Deobald. Combining progressive nodal release with the virtual crack closure technique to model fatigue delamination growth without re-meshing. *AIAA/ASCE/AHS/ASC Structures, Structural Dynamics, and Materials Conference, 2018*, (210049), 2018. doi: 10.2514/6.2018-1468.

[69] Sunghwan Jung. *Growing Crack Analyses Using Nodal release Technique*. Master of science, Massachusetts Insitute of Technology, 1995.

[70] T. Belytschko and T. Black. Elastic crack growth in finite elements with minimal remeshing. *International Journal for Numerical Methods in Engineering*, 45(5):601–620, jun 1999. ISSN 0029-5981. doi: 10.1002/(SICI)1097-0207(19990620)45:5<601::AID-NME598>3.0.CO;2-S.

[71] J. M. Melenk and I. Babuška. The partition of unity finite element method: Basic theory and applications. *Computer Methods in Applied Mechanics and Engineering*, 139(1-4):289–314, 1996. ISSN 00457825. doi: 10.1016/S0045-7825(96)01087-0.

[72] H. Liebowitz and E. T. Moyer. Finite element methods in fracture mechanics. *Computers and Structures*, 31(1):1–9, 1989. ISSN 00457949. doi: 10.1016/0045-7949(89)90160-0.

[73] K. Harste. *Investigation of the shrinkage and the origin of mechanical tension during the solidification and successive cooling of cylindrical bars of Fe-C alloys, Ph.D. Thesis*. PhD thesis, Technischen Universität Clausthal, 1989.

[74] E.A. Mizikar. Mathematical heat transfer model for solidification of continuously cast steel slabs. *Transactions of the Metallurgical Society of AIME*, 239:1747–1753, 1967.

[75] A. Jablonka, K. Harste, and K. Schwerdtfeger. Thermomechanical properties of iron and iron-carbon alloys: density and thermal contraction. *Steel research*, 62(1):24–33, 1991. ISSN 0177-4832.

[76] I. Jimbo and A.W. Cramb. The density of liquid iron-carbon alloys. *Metallurgical and Materials Transactions B*, 24B(1):5–10, 1993. ISSN 03602141. doi: 10.1007/BF02657866.

[77] Simulia. *Analysis User' s Manual: User Subroutines and Parametric Studies*, volume VI. DS SIMULIA Corp, 2011.

[78] H. Mizukami, Kakuichi Murakami, and Y Miyashita. Elastic modulus of steels at high temperature. *Journal of the Iron and Steel Institute of Japan*, 63(146), 1977.

[79] Brian G. Thomas, I.V. Samarasekera, and J.K. Brimacombe. Mathematical model of the thermal processing of steel ingots: Part II. Stress model. *Metallurgical and Materials Transactions B*, 18B(1):131–147, 1987. ISSN 0360-2141. doi: 10.1007/BF02658438. URL `http://link.springer.com/10.1007/BF02658438`.

[80] P.J. Wray. Effect of Carbon Content on the Plastic Flow of Plain Carbon Steels at Elevated Temperatures. *Metallurgical and Materials Transactions A*, 13(1):125–134, 1982.

[81] Hirowo G. Suzuki, Satoshi Nishimura, and Shigehiro Yamaguchi. Characteristics of Hot Ductility in Steels Subjected to the Melting and Solidification. *Transactions of the Iron and Steel Institute of Japan*, 22(1):48–56, 1982. ISSN 0021-1583. doi: 10.2355/isijinternational1966.22.48.

[82] H. Zhu. *Coupled Thermo-Mechanical Finite-Element Model With Application to Initial Soldification.* PhD thesis, Ph.D. Thesis, The University of Illinois at Urbana-Champaign, 1996.

[83] Patrick F. Kozlowski, Brian G. Thomas, Jean A. Azzi, and Hao Wang. Simple constitutive equations for steel at high temperature. *Metallurgical Transactions A*, 23(3):903–918, mar 1992. ISSN 0360-2133. doi: 10.1007/BF02675567. URL `http://link.springer.com/10.1007/BF02675567{%}5Cnpapers3://publication/doi/10.1007/BF02675567http://link.springer.com/10.1007/BF02675567`.

[84] Seid Koric, L.C. Hibbeler, and Brian G. Thomas. Explicit coupled thermo-mechanical finite element model of steel solidification. *International Journal for Numerical Methods in Engineering*, 78(1):1–31, 2009. ISSN 00295981. doi: 10.1002/nme.2476. URL http://doi.wiley.com/10.1002/nme.2476.

[85] J.H. Weiner and B.A. Boley. Elasto-plastic thermal stresses in a solidifying body. *Journal of the Mechanics and Physics of Solids*, 1(3):145–154, 1963. ISSN 00225096. doi: 10.1016/0022-5096(63)90049-8. URL http://www.sciencedirect.com/science/article/pii/0022509663900498http://linkinghub.elsevier.com/retrieve/pii/0022509663900498.

[86] M. Rowan, Brian G. Thomas, R. Pierer, and C. Bernhard. Measuring mechanical behavior of steel during solidification: Modeling the SSCC test. *Metallurgical and Materials Transactions B*, 42B(4):837–851, 2011. ISSN 10735615. doi: 10.1007/s11663-010-9470-5.

[87] Kelvin H Cheung and P Chris Pistorius. Effect of Mold Flux on Reheating Scale – Austenitic Stainless Steel Slabs AISTech 2011 Proceedings - Volume I AISTech 2011 Proceedings - Volume I. In *AISTech - Iron and Steel Technology Conference Proceedings*, volume I, pages 1319–1326, 2011.

[88] Matthew L.S. Zappulla. *Zappulla PhD Dissertation - Thermal-Mechanical Modeling of Longitudinal Depression Formation in Continuous Casting*. Phd dissertation, Colorado School of Mines, 2020.

[89] L.C. Hibbeler and Brian G. Thomas. Micromechanical Model for the Delta Ferrite-to-Austenite Transition. Technical report, CCC Annual Meeting, CCC Report, Urbana, Illinois, 2011.

[90] Seid Koric. *Efficient Thermo-Mechanical Model for Solidification Processes and its Applications in Steel Continuous Casting*. PhD thesis, The University of Illinois at Urbana-Champaign, 2006. URL http://scholar.google.com/scholar?hl=en{&}btnG=Search{&}q=intitle:EFFICIENT+THERMO-MECHANICAL+MODEL+FOR+SOLIDIFICATION+PROCESSES+AND+ITS+APPLICATIONS+IN+STEEL+CONTINUOUS+CASTING{#}3.

[91] S. Venugopal, S. L. Mannan, and Y. V R K Prasad. Processing map for hot working of stainless steel type AISI 316L. *Materials Science and Technology*, 9 (10):899–906, oct 1993. ISSN 0267-0836. doi: 10.1179/mst.1993.9.10.899. URL http://www.tandfonline.com/doi/full/10.1179/mst.1993.9.10.899.

[92] Seid Koric, Lance C. L.C. Hibbeler, Rui Liu, and Brian G. Thomas. Multiphysics Model of Metal Solidification on the Continuum Level. *Numerical Heat Transfer, Part B: Fundamentals*, 58(October 2013):37–41, dec 2010. ISSN 1040-7790. doi: 10.1080/10407790.2011.540954. URL http://www.tandfonline.com/doi/abs/10.1080/10407790.2011.540954.

[93] Senta Software Ltd. JMatPro, Guildford, United Kingdom, 2016.

[94] Peter J. Wray. Plastic deformation of delta-ferritic iron at intermediate strain rates. *Metallurgical Transactions A*, 7(10):1621–1627, 1976. ISSN 03602133. doi: 10.1007/BF02817878.

[95] Matthew L.S. Zappulla, Lance C. Hibbeler, and Brian G. Thomas. Effect of Grade on Thermal–Mechanical Behavior of Steel During Initial Solidification. *Metallurgical and Materials Transactions A*, 48(8):3777–3793, aug 2017. ISSN 1073-5623. doi: 10.1007/s11661-017-4112-z. URL http://link.springer.com/10.1007/s11661-017-4112-zhttp://link.springer.com/10.1007/978-3-319-51493-2{_}48.

[96] T Suzuki, Karl-Hermann Tacke, K Wuennenberg, and K Schwerdtfeger. Creep properties of steel at continuous casting temperatures. *Ironmaking and Steelmaking*, 15:90–100, 1988.

[97] C. Li and Brian G. Thomas. Thermomechanical finite-element model of shell behavior in continuous casting of steel. *Metallurgical and Materials Transactions B*, 35B(6):1151–1172, 2004. ISSN 1073-5615. doi: 10.1007/s11663-004-0071-z. URL http://link.springer.com/10.1007/s11663-004-0071-z.

[98] Yi Feng and A B Phillion. A 3D Meso-Scale Solidification Model for Steels. In *AISTech - Iron and Steel Technology Conference Proceedings*, volume 1, pages 2663–2670, 2018.

[99] A. Teskeredžić, I. Demirdžić, and S. Muzaferija. Numerical Method For Heat Transfer, Fluid Flow, And Stress Analysis In Phase-Change Problems. *Numerical Heat Transfer, Part B: Fundamentals*, 42(5):437–459, nov 2002. ISSN 1040-7790. doi: 10.1080/10407790190054021. URL http://www.tandfonline.com/doi/abs/10.1080/10407790190054021.

[100] Brian G. Thomas and M. K. Okelman. Implementation Of Temperature and Strain Micro-Sensors into a Casting Mold Surface. In *Sensors, Sampling, and Simulation for Process Control*, pages 127–134. 2011. ISBN 9781118036181. doi: 10.1002/9781118061800.ch15.

[101] J.B. Dalin and J.L. Chenot. Finite element computation of bulging in continuously cast steel with a viscoplastic model. *International Journal for Numerical Methods in Engineering*, 25(1):147–163, 1988. doi: 10.1002/nme.1620250113.

[102] Akihiko Yoshii and Shigefumi Kihara. Analysis of Bulging in Continuously Cast Slabs by Bending Theory of Continuous Beam. *Transactions of the Iron and Steel Institute of Japan*, 26(10):891–894, 1986.

[103] M. Bellet and V.D. Fachinotti. ALE method for solidification modelling. *Computer Methods in Applied Mechanics and Engineering*, 193(39-41 SPEC. ISS.):4355–4381, 2004. ISSN 00457825. doi: 10.1016/j.cma.2003.11.016.

[104] K.H. Tacke. Multi-Beam Model for Strand Straightening in Continuous Casting. *Ironmaking & Steelmaking*, 12(2):87–94, 1985.

[105] K Schwaha, E Till, J Stulik, and B Lindorfer. Continuous Strand Bending and Straightening with Voest Alpine Concept - A Comparative Study. In *Continuous casting '85 : Proceedings of the international conference*, pages 4.1–4.3, London, England, 1985. The Institute of Metals.

[106] M. Uehara, I. V. Samarasekera, and J. K. Brimacombe. MATHEMATICAL MODELLING OF UNBENDING OF CONTINUOUS CAST STEEL SLABS. *Ironmaking and Steelmaking*, 13(3):138–153, 1986. ISSN 03019233.

[107] F Pascon and A.M. Habraken. Finite element study of the effect of some local defects on the risk of transverse cracking in continuous casting of steel slabs. *Computer Methods in Applied Mechanics and Engineering*, 196(21-24):2285–2299, apr 2007. ISSN 00457825. doi: 10.1016/j.cma.2006.07.017. URL `https://linkinghub.elsevier.com/retrieve/pii/S0045782507000163`.

[108] M. Deisinger and Karl-Hermann Tacke. Unbending of Continuously Cast Slabs with Liquid Core. *Ironmaking & Steelmaking*, 24(4):321–328, 1997.

[109] Hongbo Zhao, Jingwei Hao, Zhaojie Teng, Shusen Cheng, and Shoufeng Huo. Development and Application of the Integral Digital Operating Platform for Blast Furnace in. In *AISTech - Iron and Steel Technology Conference Proceedings*, pages 603–610, 2014.

[110] Rudolf Moravec, K.E. Blazek, Jaroslav Horsky, Clint Graham, Steve Fiegle, Tom Dombovic, and Tim Kaurich. Coupling Of Solidification model And Heat Transfer Coefficients to Have Valuable Tool for Slab Surface Temperatures Prediction. In *InSteelCon*, number July, pages 1–9, 2011.

[111] Jaroslav Horsky and Jana Ondrouskova. Analysis of Directly Measured Heat Transfer Coefficients During Special Experiments to Provide Better Understanding of Secondary Cooling During Continuous Casting Process. In *AISTech - Iron and Steel Technology Conference Proceedings*, 2013. ISBN 9781935117339.

[112] Nathan M. Seymour. *Thermo-Mechanical Behaviorof Steel in the Continuous Casting Process From Meniscus to Caster Exit*. Masters, Masters Thesis, The University of Illinois at Urbana-Champaign, 2016.

[113] R Hardin, P Du, and C Beckermann. Three-dimensional Simulation of Heat Transfer and Stresses in a Steel Slab Caster. In *InSteelCon*, number July, pages 1–6, 2011.

[114] R.A. Hardin and C. Beckermann. Heat Transfer and Solidification Modeling of Continuous Steel Slab Casting. In *Proceedings of the 2nd International Symposium on the Recent Developments in Plate Steels*, pages 21–31, Warrendale, PA, 2018. Association for Iron and Steel Technology (AIST).

[115] Livermore Software Technology Corporation. LS-DYNA, 2015.

[116] Matthew L. S. Zappulla and Brian G. Thomas. Surface defect formation in steel continuous casting. In *THERMEC' 2018*, Paris, France, 2018.

[117] Masayuki Kawamoto, Yuichi Tsukaguchi, Norihiro Nishida, Takashi Kanazawa, and Sei Hiraki. Improvement of the Initial Stage of Solidification by Using Mild Cooling Mold Powder. *ISIJ International*, 37(2):134–139, 1997. ISSN 0915-1559. doi: 10.2355/isijinternational.37.134. URL `http://joi.jlc.jst.go.jp/JST.Journalarchive/isijinternational1989/37.134?from=CrossRef`.

[118] Ashok Kumar. Novel Synthesis and Fabrication of Hybrid Coatings for Manufacturing. *Science And Technology*.

[119] Jiayun Zhang, Qifeng Shu, and Shoukun Wei. Prediction of Surface Tension in Molten Metallic and Ionic Systems. In *Slag Symposium*, volume 22, 2000. doi: 10.1515/HTMP.2003.22.5-6.395.

[120] Gelu Ovidiu Tirian, Ioan Filip, and Gabriela Proştean. Adaptive control system for continuous steel casting based on neural networks and fuzzy logic. *Neurocomputing*, 125:236–245, 2014. ISSN 09252312. doi: 10.1016/j.neucom.2012.11.052.

[121] Ton Spierings, Arnoud Kamperman, Herman Hengeveld, Jan Kromhout, and Edward Dekker. Development and Application of Fiber Bragg Gratings for Slab Casting. *AISTech 2017 Proceedings*, pages 1655–1664, 2017. ISSN 15516997.

[122] Adam B Badri and A.W. Cramb. Heat Flux Calculations From Thermocouples - What Can Be Measured? In *Steelmaking Conference Proceedings*, pages 65–76, Warrendale, PA, 2002. Iron and Steel Society.

[123] Brian G. Thomas, Seid Koric, L.C. Hibbeler, and R. Liu. Multiphysics Model of Continuous Casting of Steel Beam-Blanks. In *InSteelCon*, volume 56, pages 1–10, 2011.

[124] M.M. Wolf. ISS Keeping Current - In-Depth Educational Series: Scale Formation And Descaling In Continuous Casting And Hot Rolling. Technical report, Iron and Steel Society, 2001.

[125] Yuchiro Kato, Koji Harada, Toshiyuki Kajitani, and Koji Saito. Mechanism of Sticker Breakouts in Continuous Casting of Silicon Killed Steel. In *European Conference on Continuous Casting*, 2008.

[126] K.E. Blazek, O. Lanzi, and H. Yin. Boron effects on the solidification of steel during continuous casting. In *AISTech - Iron and Steel Technology Conference Proceedings*, volume 105, pages 609–625, Pittsburgh, PA, 2008. doi: 10.1051/metal:2009005.

[127] Kenneth E. Blazek and Ismael G. Saucedo. Characterization of the Formation, Propagation, and Recovery of Sticker/Hanger Type Breakouts. *ISIJ International*, 30(6): 435–443, 1990. ISSN 09151559. doi: 10.2355/isijinternational.30.435.

[128] Matthew L.S. Zappulla. CCC Annual Report. Technical report, CCC Annual Meeting, 2018.

[129] Matthew L.S. Zappulla. Modeling of Depression Formation during Solidification in the Mold. Technical report, CCC Annual Meeting, 2015.

[130] Y.M. Won, Tae-jung Yeo, Dong Jin Seol, and Kyu Hwan Oh. A new criterion for internal crack formation in continuously cast steels. *Metallurgical and Materials Transactions B*, 31(4):779–794, 2000. ISSN 1073-5615. doi: 10.1007/s11663-000-0115-y.

[131] Matthew L.S. Zappulla and Brian Gordon Thomas. Continuous Casting Center Report. Technical report, Colorado School of Mines, Golden, Colorado, 2018.

[132] I.V. Samarasekera. Longitudinal Midface Depression. Private Communication, 2015.

[133] C. A. Pinheiro, I.V. Samarasekera, J.K. Brimacombe, and B.N. Walker. Mould heat transfer and continuously cast billet quality with mould flux lubrication Part 1 Mould heat transfer. *Ironmaking & Steelmaking*, 27(1):37–54, feb 2000. ISSN 0301-9233. doi: 10.1179/030192300677363. URL `http://www.maneyonline.com/doi/abs/10.1179/030192300677363`.

[134] L.C. Hibbeler and Brian G. Thomas. Longitudinal face crack prediction with thermo-mechanical models of thin slabs in funnel moulds. *la metallurgia ...*, pages 1–16, 2009. URL `http://www.gruppofrattura.it/pdf/ext/AIM/Anno2009/febbraio2009.pdf`.

[135] Ron OMalley. W-Shape Longitudinal Depression. Private Communication, 2019.

[136] E.S. Szekeres. Brimacombe Course Notes, 2015.

[137] M.S. Jenkins, S.R. Story, and R.H. Davies. Defining Air-Mist Nozzle Operating Conditions for Optimum Spray Cooling Performance. In *Procedings of the Nineteenth Australasian Chemical Engineering Conference*, pages 161–169, Newcastle, 1991.

[138] Dong Jin Seol, Young Mok Won, Kyu Hwan Oh, Yong Chang Shin, and Chang Hee Yim. Mechanical Behavior of Carbon Steels in the Temperature Range of Mushy Zone. *ISIJ International*, 40(4):356–363, 2000. ISSN 0915-1559. doi: 10.2355/isijinternational.40.356.

[139] J.K. Brimacombe, F. Weinberg, and E. B. Hawbolt. Formation of Longitudinal , Midface Cracks in Continuously-Cast Slabs. *Metallurgical and Materials Transactions B*, 10, 1979.

[140] Mathworks. *MATLAB - Mathworks - MATLAB & Simulink*. 2016.

[141] Philip M. Gresho and Robert L. Lee. Don't suppress the wiggles-They're telling you something! *Computers and Fluids*, 9(2):223–253, 1981. ISSN 00457930. doi: 10.1016/0045-7930(81)90026-8.

[142] Alexandru C. Telea. *Data Visualization - Principles and Practice*. 2014. ISBN 0470222808; 9780470222805. doi: 10.1002/9780470417409.ch2.

[143] L.D. Bergman, B.E. Rogowitz, and L.A. Treinish. A rule-based tool for assisting colormap selection. In *Proceedings Visualization '95*, pages 118–125,, 1995. ISBN 0-8186-7187-4. doi: 1070-2385/95. URL `http://ieeexplore.ieee.org/document/480803/`.

[144] Liang Zhou and Charles D. Hansen. A Survey of Colormaps in Visualization. *IEEE Transactions on Visualization and Computer Graphics*, 22(8):2051–2069, aug 2016. ISSN 1077-2626. doi: 10.1109/TVCG.2015.2489649. URL `http://ieeexplore.ieee.org/document/7305807/`.

[145] Kenneth Moreland. Why We Use Bad Color Maps and What You Can Do About It. *Electronic Imaging*, 2016(16):1–6, feb 2016. ISSN 2470-1173. doi: 10.2352/ISSN.2470-1173.2016.16.HVEI-133. URL http://dx.doi.org/10.2352/issn.2470-1173.2016.16.hvei-133http://www.ingentaconnect.com/content/10.2352/ISSN.2470-1173.2016.16.HVEI-133.

[146] David Borland and Russell M. Taylor. Rainbow color map (still) considered harmful. *IEEE Computer Graphics and Applications*, 27(2):14–17, 2007. ISSN 02721716. doi: 10.1109/MCG.2007.323435.

[147] ABAQUS. *ABAQUS 6.13 Theory Manual*. DS SIMULIA Corp, Providence, RI, 2013. URL http://www.3ds.com/products-services/simulia/support/documentation/.

[148] ANSYS Inc. *Fluent User Manuals*. Canonsburg, Pennsylvania, 17 edition, 2016.

[149] John D. Hunter. Matplotlib: A 2D graphics environment. *Computing in Science and Engineering*, 2007. ISSN 15219615. doi: 10.1109/MCSE.2007.55.

[150] Amy Henderson. *The ParaView Guide: A Parallel Visualization Application*. 2004. ISBN 9781930934146. doi: citeulike-article-id:4375994.

[151] Tecplot Inc. *Tecplot 360 EX User's Manual*. Bellevue, WA, 2018.

[152] S. Kumar, B N Walker, I V Samarasekera, and J K Brimacombe. Chaos at the meniscus–the genesis of defects in continuously cast steel billets. *Process Technology*, 13:119–141, 1993. URL http://www.csa.com/partners/viewrecord.php?requester=gs{&}collection=TRD{&}recid=199605511062MD{&}q=chaos+at+the+meniscus+{&}uid=788490814{&}setcookie=yes.

[153] G. Hedin, A. Kamperman, M. Seden, K. Frojdh, and J. Pejnefors. Exploring opportunities in mold temperature monitoring utilizing fiber Bragg gratings. In *5th International Conference on Process Development in Ironmaking and Steelmaking*, number June, Luleå, Sweden, 2016.

[154] D Stewart, P N Hewitt, and L Peeters. The Prediction of Longitudinal Cracking During Slab Casting. In *Steelmaking Conference Proceedings*, pages 207–214, Warrendale, PA, 1996. ISS.

[155] J. O. Kristiansson. Thermal stresses in the early stage of solidification of steel. *Journal of Thermal Stresses*, 1982. ISSN 1521074X. doi: 10.1080/01495738208942153.

[156] T. Inoue and D. Y. Ju. Analysis of solidification and viscoplastic stresses incorporating a moving boundary: an application to simulation of the centrifugal casting process. *Journal of Thermal Stresses*, 15(1):109–128, jan 1992. ISSN 0149-5739. doi: 10.1080/01495739208946124. URL http://www.tandfonline.com/doi/abs/10.1080/01495739208946124.

[157] Diego J. Celentano. *A thermomechanical model with microstructure evolution for aluminium alloy casting processes*, volume 18. 2002. ISBN 5626817522. doi: 10.1016/S0749-6419(01)00075-4.

[158] Daniel Paquet, Piyush Dondeti, and Somnath Ghosh. Dual-stage nested homogenization for rate-dependent anisotropic elasto-plasticity model of dendritic cast aluminum alloys. *International Journal of Plasticity*, 27(10):1677–1701, 2011. ISSN 07496419. doi: 10.1016/j.ijplas.2011.02.002. URL http://dx.doi.org/10.1016/j.ijplas.2011.02.002.

[159] L. Anand. Constitutive Equations for the Rate-Dependent Deformation of Metals at Elevated Temperatures. *Journal of Engineering Materials and Technology*, 104(1):12, 1982. ISSN 00944289. doi: 10.1115/1.3225028.

[160] A. E. Huespe, A. Cardona, N. Nigro, and V. Fachinotti. Visco-plastic constitutive models of steel at high temperature. *Journal of Materials Processing Technology*, 102 (1):143–152, 2000. ISSN 09240136. doi: 10.1016/S0924-0136(00)00442-8.

[161] D Li, M A Wells, S L Cockcroft, J E Ives, and D Jin. Accurate temperature measurement during water quench operations characterized by boiling water heat transfer. In *Materials Science and Technology*, volume 2, pages 125–136, New Orleans, 2004.

[162] Joanna R Groza, Shackelford, Enrique J. Lavernia, and Powers. *Materials Processing Handbook*. CRC Press, mar 2007. ISBN 978-0-8493-3216-6. doi: 10.1201/9781420004823. URL https://www.taylorfrancis.com/books/9781420004823.

[163] A. R. Safari, M. R. Forouzan, and M. Shamanian. Thermo-viscoplastic constitutive equation of austenitic stainless steel 310s. *Computational Materials Science*, 68:402–407, 2013. ISSN 09270256. doi: 10.1016/j.commatsci.2012.10.039. URL http://dx.doi.org/10.1016/j.commatsci.2012.10.039.

[164] Qin Qin, Mingliang Tian, Jinmiao Pu, and Jianlin Huang. Constitutive investigation based on the time-hardening model for AH36 material in continuous casting process. *Advances in Mechanical Engineering*, 10(1):168781401775068, jan 2018. ISSN 1687-8140. doi: 10.1177/1687814017750680. URL http://journals.sagepub.com/doi/10.1177/1687814017750680.

[165] R. Pierer, C Bernard, and C. Chimani. Evaluation of Common Constitutive Equations for Solidifying Steel. *BHM*, 150(5):1–13, 2005. URL file://hermes26/SCC/CMF/RefManager+Pdffiles.

[166] Jung-Eui Lee, Tae-Jung Yeo, Kyu Hwan OH, Jong-Kyu Yoon, and U-Sok Yoon. Prediction of cracks in continuously cast steel beam blank through fully coupled analysis of fluid flow, heat transfer, and deformation behavior of a solidifying shell. *Metallurgical and Materials Transactions A*, 31(1):225–237, jan 2000. ISSN 1073-5623. doi: 10.1007/s11661-000-0067-5. URL http://dx.doi.org/10.1007/s11661-000-0067-5http://link.springer.com/10.1007/s11661-000-0067-5.

[167] G. Palumbo, A. Piccininni, V. Piglionico, P. Guglielmi, D. Sorgente, and L. Tricarico. Modelling residual stresses in sand-cast superduplex stainless steel. *Journal of Materials Processing Technology*, 217:253–261, 2015. ISSN 09240136. doi: 10.1016/j.jmatprotec.2014.11.006. URL http://dx.doi.org/10.1016/j.jmatprotec.2014.11.006.

[168] ABAQUS. *ABAQUS 6.13 Subroutine Manual*. DS SIMULIA Corp, Providence, RI, 2013. URL http://www.3ds.com/products-services/simulia/support/documentation/.

[169] Zhongsen Yuan and Frank Mucciardi. Novel Sensor for Continuous Temperature Monitoring in Harsh Environments AISTech 2004 Proceedings - Volume I AISTech 2004 Proceedings - Volume I. In *AISTech - Iron and Steel Technology Conference Proceedings*, volume I, pages 809–820, 2004.

[170] B.E. Launder and D.B. Spalding. The numerical computation of turbulent flows. *Computer Methods in Applied Mechanics and Engineering*, 3(2):269–289, 1974. ISSN 00457825. doi: 10.1016/0045-7825(74)90029-2.

[171] J. A. Dantzig. LANDING AN ACADEMIC JOB The process and the pitfalls. *Industrial Engineering*, pages 1–28, 2001.

[172] L.C. Hibbeler and Brian G. Thomas. The Thermal Distortion of a Funnel Mold. In *AISTech - Iron and Steel Technology Conference Proceedings*, pages 1–10, 2012. URL http://link.springer.com/article/10.1007/s11663-012-9696-5.

[173] Hacı Mehmet Sahin, Kadir Kocatepe, Ramazan Kayıkcı, and Neşet Akar. Determination of unidirectional heat transfer coefficient during unsteady-state solidification at metal casting–chill interface. *Energy Conversion and Management*, 47(1):19–34, jan 2006. ISSN 01968904. doi: 10.1016/j.enconman.2005.03.021. URL https://linkinghub.elsevier.com/retrieve/pii/S0196890405000816.

[174] A.M. Lush, G Weber, and L Anand. An implicit time-integration procedure for a set of internal variable constitutive equations for isotropic elasto-viscoplasticity. *International Journal of Plasticity*, 5(5):521–549, jan 1989. ISSN 07496419. doi: 10.1016/0749-6419(89)90012-0. URL `http://linkinghub.elsevier.com/retrieve/pii/0749641989900120`.

[175] C. Li and Brian G. Thomas. Maximum casting speed for continuous cast steel billets based on sub-mold bulging computation. In *85th Steelmaking Conference Proceedings*, pages 109–130, Warrendale, PA, 2002. Iron and Steel Society. URL `http://ccc.illinois.edu/PDFFiles/Publications/02{_}newest.pdf`.

[176] Brian G. Thomas and C. Ojeda. Ideal taper prediction for slab casting. In *ISS Steelmaking Conference*, pages 295–308, Indianapolis, IN, 2003. ISS-AIME. URL `http://ccc.illinois.edu/PDFFiles/Publications/03{_}ISS2003{_}ThomasBG{_}final{_}post.pdf`.

[177] Sushil Gupta and Veena Sahajwalla. Devolatilization and Cracking Behaviour of Australian Lumpy Coals at High Temperatures. In *AISTech - Iron and Steel Technology Conference Proceedings*, 2007.

APPENDIX A

MULTIPHYSICS MODELING OF CONTINUOUS CASTING OF STAINLESS STEEL

During the solidification of stainless steel, the mechanical behavior of the solidifying shell follows nonlinear elastic-viscoplastic constitutive laws depending on metallurgical phase fraction calculations (liquid, ferrite and austenite). A multiphysics model that couples thermal-mechanical behavior in a Lagrangian reference frame, including both classical time-independent plasticity and creep, with turbulent fluid flow in the liquid phase in an Eulerian frame is applied to determine realistic temperature and stress distributions in the solidifying shell of stainless steel in a commercial continuous caster. Compositional effects are incorporated through the use of phase diagrams to define the phase fraction variations with temperature during the process. The behavior at these high temperatures can be adequately captured using specific constitutive equations for each phase and careful decisions about switching between them. Results for a 409L ferritic stainless steel show that, due to its phase fraction history, solidification stresses differ significantly from those in plain carbon steels. Specifically, they include a secondary sub-surface compression peak due to phase change expansion between γ-austenite and δ-ferrite through the thickness of the shell.

A.1 Introduction

While developments in advanced manufacturing processes, such as metal-based additive manufacturing are ongoing, the manufacturing field is still dominated by more traditional metal solidification processes, such as: ingot and foundry casting, welding, and particularly continuous casting. Advancement of these mature processes depends on improved quantitative understanding, such as that gained from advanced computational models. These processes are driven by many coupled phenomena, including heat transfer, fluid flow with turbulence, phase transformations, thermal distortion, and thermo-mechanical stress development.

Over 96% of the world's steel is made with the continuous casting process, according to recent statistics by [5]. Experiments are limited due to the harsh conditions inside the liquid and solidifying steel, and the many process variables which affect the complex phenomena in the process. Thus, numerical modeling presents an ideal tool to better understand and help to find ways to reduce defects, increase productivity, and improve this important process. Tremendous advances in high performance computing technology and numerical algorithms in the last 25 years have enabled more realistic and accurate modeling of liquid steel flow and the solidifying shell, but finding multiphysics computational approaches that are both efficient and accurate remains a big challenge. Chronic defects affecting this process include cracking and surface depression problems, which often correspond to mismatches between solidification contraction and mold taper. [41] have shown how this can increase the size of the solid shell/mold interfacial gap, which reduces heat transfer between the mold plate and steel shell, leading to locally hot and thin portions of the shell. These thin spots cause stress concentration, resulting in depressions, longitudinal cracks, and sometimes even breakouts, due to ferrostatic pressure from the liquid pool exerted onto the thin and weakened shell at mold exit.

Elastic, rate-independent plastic constitutive models are generally adequate for engineering purposes at ambient temperatures for most metallic materials. However, at high temperatures, most metal alloys exhibit time-dependent inelastic behavior, similar to a viscous fluid, and solidification adds further complication. Therefore, better constitutive models are needed to describe the elastic-viscoplastic behavior during metal solidification processes such as the continuous casting of steel.

A.1.1 Constitutive Modeling of Metal Solidification

An important analytical solution for the generation of thermal stresses in a general one-dimensional metal solidification process was derived by [85] using a simple elastic rate-independent plastic constitutive model. [155] later added a creep law to account for the time-dependent inelastic behavior at high temperatures. In the last two decades, more funda-

mental but computationally demanding viscoplastic models, with and without yield surfaces, have been used to model realistic vertical-type semi-continuous aluminum direct-chill (DC) casting and steel continuous-casting processes. [156] used a modification of Perzyna's constitutive equation to model elastic-viscoplastic constitutive behavior during aluminum DC casting.[157] derived a yield-surface-based viscoplastic model with microstructure evolution and applied it to aluminum casting. [158] incorporated rate-dependent behavior by using a viscoplastic model based on overstress in their homogenization model of cast aluminum alloys.

Unified viscoplastic constitutive models, which treat rate-independent plastic strain and rate-dependent creep together as inelastic strain, are particularly popular in steel casting. [159] developed the first such model based on several evolving internal state variables, that has been used in several thermo-mechanical models of metals on elevated temperatures. A decade later, [83] introduced a simple constitutive equation to model the γ-austenite phase of steel, relating inelastic strain, as a single structure parameter, to strain rate, stress, temperature, and steel grade via carbon content. To model the weaker, body-centered cubic (BCC) δ-ferrite phase of steel, [82] devised a power law based constitutive model to incorporate the much higher creep rates of this phase, compared to the stronger, face-centered cubic (FCC) austenite phase. These constitutive models have been popular since their inception, having been either used or reviewed in many steel solidification papers, such as by [160], [161], [90], [162], [163], [164]. [160] and later [60] compared the Anand and Kozlowski-Zhu models against steel solidification experiments and found similar behavior for both models; although the Kozlowski-Zhu model produced results much closer to experiments for low carbon steels. [165] also found that the Kozlowski model agreed well with several other steel solidification constitutive models and experiments.

In order to efficiently incorporate these highly nonlinear constitutive models at the local level (integration points), [90] incorporated a bounded Newton-Raphson method at the integration points, into the global-level finite-element solution methodology in ABAQUS,

which provided a tenfold performance increase in solving solidification thermo-mechanical problems. This approach is used in the current work. [84] later developed an explicit finite-element formulation of this method, and showed its benefits over the implicit method for large three-dimensional solidification problems with regard to high performance computing.

A.1.2 Multiphysics Approaches

Turbulent fluid flow of molten steel with heat advection and thermo-mechanical behavior of the solidifying shell are traditionally modeled independently, with separate numerical methods (finite volume vs. finite element) and reference frames (Eulerian vs. Lagrangian). [166] followed by [99] have applied full coupling of these phenomena in a multiphysics frame on simplified casting geometries, but did not compare results with either analytical solutions or experiments. Another multiphysics approach to couple these phenomena is to focus on the solidification front to separate the fluid flow and thermal-mechanical models. The temporal and spatial distribution of superheat flux calculated to exit the solidification-front walls of the domain used by the thermal turbulent flow simulation can be implemented into the thermo-mechanical model of the solidifying steel shell growing in the mold region with a domain that includes only a portion of the fluid region. Because the mechanical behavior has minimal influence on the fluid flow, the two models are only one-way coupled, which enables significant computational savings.

[61] devised and validated a new enhanced latent heat method to introduce spatial and temporal superheat flux data into a Lagrangian thermal-mechanical finite-element model of the solidifying shell and mold. The new modeling approach was demonstrated by [92] via simulation of the multiphysics phenomena in a commercial continuous beam-blank casting of carbon steel grades, and the predictions show good matches with both an analytical solution to a one-dimensional test problem and with plant measurements of shell thickness profiles from a commercial caster. For thermo-mechanical modeling of stainless steel alloys, most previous works have focused on various phenomena lower than solidification temperatures while only [167] and [163] have treated solidification of stainless steel grades but without any

coupling with the fluid flow physics.

Regardless of the method, multiphysics modeling of solidification processes is a complex task. Phase-transformation laws are strongly dependent on chemical composition, and often differ between heating and cooling. Another issue is the lack of reliable thermo-mechanical properties in the literature for stainless steel at high temperature and low strain rate, which often leads to neglecting the phase dependence of the steel properties. We believe that this paper presents the first complete macro-scale model of stainless steel casting that couples thermal-mechanical analysis in solidifying stainless steel, based on thermo-elastic-viscoplastic phase dependent constitutive laws, with the turbulent thermal fluid flow of liquid steel, and thermo-mechanical deformation of the mold. This work presents a combined multiphysics modeling methodology for solidification processes, featuring a constitutive model where the compositional effects depend only on the phase fraction evolution, as well as a procedure to capture the important effects of heat transfer, turbulent fluid flow, and solidification on the thermal-mechanical behavior.

A.2 Multiphysics Model Formulation

The solidifying steel shell behavior is simulated here with a sophisticated, but computationally intensive, multiphysics model with several sub-models incorporating together a thermal-mechanical model of the solidifying steel shell (Section 2.1), a turbulent thermal fluid flow model of the liquid steel (Section 2.2), and a model of thermal distortion of the mold (Section 2.3), as shown in Figure A.1. In addition to their mechanical coupling, the shell and mold models are coupled thermally via a detailed model of the interfacial gap (Section 2.4). A validated heat transfer-solidification model CON1D, described by [64], is used to provide the initial shell thickness profile for the fluid flow model and initial heat fluxes for the mold distortion model. The calculated heat fluxes due to the effect of superheat transport in the turbulent fluid flow model are incorporated into the thermo-mechanical model via the enhanced latent heat method, described in more detail in Section 2.2. In addition to this thermal coupling, the mechanical effect of fluid flow on the deformation of the so-

lidified shell is considered by applying the ferrostatic pressure load that pushes the newly solidifying shell toward the mold, discussed in Section 2.4. Since the improved shell profile from thermo-mechanical model has little effect on superheat results in the fluid flow model, a single iteration of this model system is often sufficient to produce accurate multiphysics results.

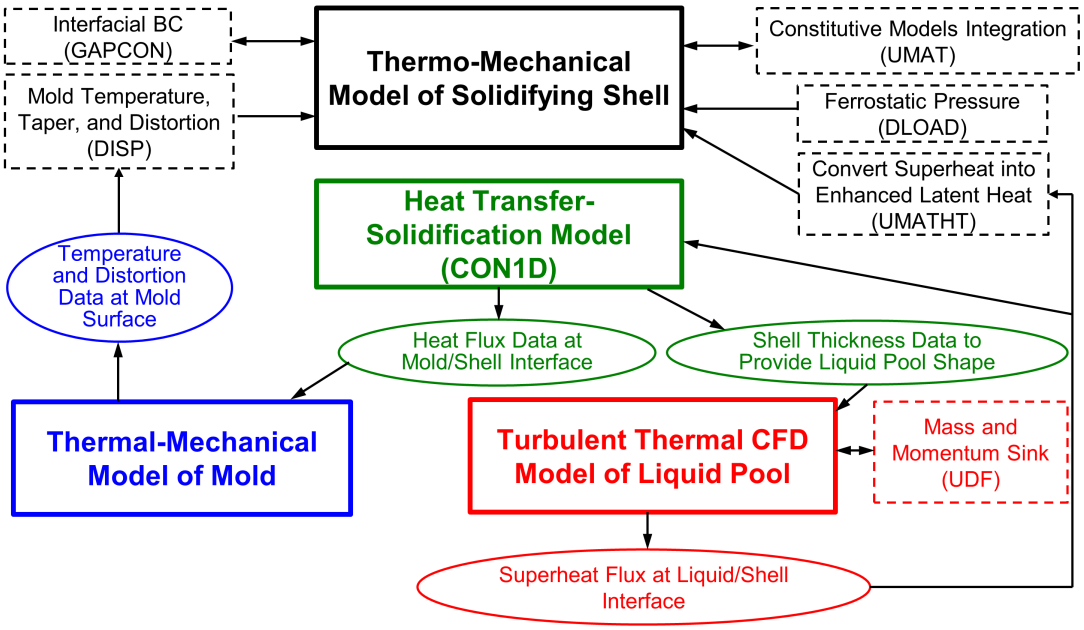


Figure A.1: Flow chart for multiphysics model

A.2.1 Solidifying Shell Model

In many solidification processes, such as the continuous casting of steel, one dimension of the casting is much longer than the others, and is otherwise unconstrained. In this case, it is quite reasonable to apply a condition of generalized plane strain (also called 2.5D model) in the long casting direction (z), and to solve a two-dimensional thermo-mechanical problem in the transverse (x-y) plane. [84] and others have demonstrated how this condition enables a

two-dimensional computation to accurately produce the complete three-dimensional thermo-stress state, so long as there is no axial bending, as in the case here. A transverse Lagrangian generalized-plane-strain two-dimensional (2D) slice model, shown in Figure A.2, is applied to simulate the solidifying steel shell in the slab mold during continuous casting, which travels down the mold at the casting velocity. The domain is an L-shape of a strand section next to the mold wall which is thick enough to model double the expected thickness of the solidifying shell at mold exit. This approach avoids unnecessary and computationally intensive calculation of the liquid behavior away from the mold wall. More importantly, it avoids non-physical mass conservation by enabling shrinkage of the un-modeled liquid region due to pushing fluid out of the slice. From the work of [95], a second "1D-slice" shell model was used to verify thermal stress behavior in simplified conditions. This slice model is seen as a thin strip "drilled" into the solidifying shell, and assumes uniform solidification and full contact with the mold wall.

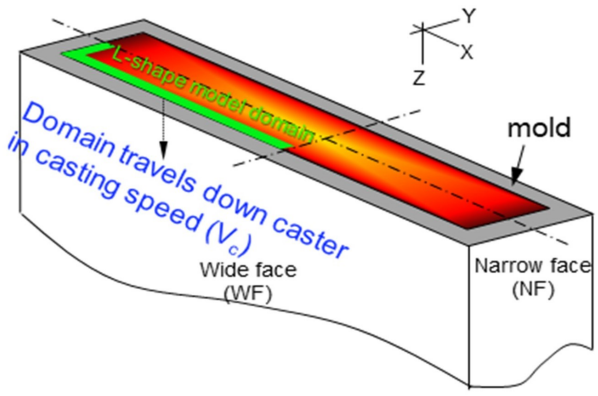


Figure A.2: Model domain of solidifying steel shell

In the Lagrangian reference frame, the temperature distribution in the strand is obtained from numerical solution of the three-dimensional (3D) transient heat conduction equation:

$$\rho\left(\frac{\partial H}{\partial t}\right) = \nabla \cdot (k\nabla T) \tag{A.1}$$

where ρ is the mass density, H is specific enthalpy, which includes the latent heat of phase transformations (solidification, and δ-ferrite to γ-austenite), and k is the isotropic thermal conductivity. All of these properties are highly temperature dependent. The strains during solidification are typically small (2%), but the capability to handle finite rotations is necessary to model some parts of the shell in a continuous-casting process. The quasi-static equilibrium equation describes the mechanical behavior of the strand:

$$\nabla \cdot \sigma(x) + b = 0 \tag{A.2}$$

where σ is the Cauchy stress tensor and b is the body force density vector due to gravity. These equations were solved in a fixed finite-element mesh using the commercial stress software, ABAQUS [168].

A.2.2 Fluid Flow Model and Fluid/Shell Interface Treatment

A 3D thermal turbulent fluid flow model of molten steel pool is solved in an Eulerian reference frame for velocity and temperature fields, and superheat flux distributions at the steel shell front. The model domain includes the tundish bottom, nozzle, and top three-meters of the molten steel pool both in the strand and mold. The continuity equation that represents the mass conservation of the molten steel is given as follows:

$$\rho \left(\nabla \cdot v \right) = S_m \tag{A.3}$$

where ρ is the mass density of liquid steel and v is time-average velocity, and S_m is a mass sink to model the liquid lost due to crossing the solidification front. This term is applied only to the computational cells on the solidification front, according to the methodology of [169]. Momentum conservation is satisfied by solving the time-averaged momentum balance:

$$\rho \left[\frac{\partial v}{\partial t} + v \cdot (\nabla v) \right] = \nabla \cdot \sigma + S_{mom} \tag{A.4}$$

where the Cauchy stress σ is represented by the standard constitutive relationship for turbulence:

$$\sigma = C_{\mu}\frac{K^2}{\in}\left(\nabla v + (\nabla v)^T\right) - pI \tag{A.5}$$

where P is pressure, constant is 0.09; K is turbulent kinetic energy, and is its dissipation rate, which are found by solving two additional partial differential equations according to the standard model by [170]. S_{mom} is a momentum sink term added to the same interface cells as Sm to account for solidification of the molten steel as explained by [169]. Boundary conditions are fixed velocity at the inlet, no-slip conditions on the top surface beneath the slag layer, and on the walls which represent the solidification front, and pressure outlet conditions at the strand exit. The energy conservation equation for molten steel flow, which includes advection terms into section A.2.1, is:

$$\rho\left[\frac{\partial H}{\partial t} + v \cdot \nabla H\right] = \nabla \cdot (k\nabla T) \tag{A.6}$$

Temperature was fixed to the liquidus temperature on the domain boundaries representing the solidification front that surrounds the liquid pool. These equations were solved using the commercial Computational Fluid Dynamics (CFD) software package, ANSYS Fluent [148] According to the method of [92], additional latent heat is calculated to represent superheat flux transported by the molten steel flow to the solidification front, based on the Stefan interface condition:

$$\Delta H_f = \frac{q''_{super}}{\rho_{solid}\ |v_{interface}|} \tag{A.7}$$

This is additional latent heat added to the enthalpy in section A.2.1 via a user subroutine UMATHT in [168]. The discrete data of the superheat flux distribution, that is calculated at the boundaries of the 3-D Eulerian fluid flow model, is converted via multi-dimensional

interpolation to a function of space and time (or distance below meniscus) for the mushy zone material points in the Lagrangian thermo-mechanical model as described by [92]. The solidification front velocity is calculated analytically according to [61], based on the classic analytical solution for solid-control solidification with superheat from [171].

A.2.3 Mold Distortion Model

As the solidifying steel-shell moves down in the casting direction, heat leaving its surface is continuously extracted by water-cooling that flows through rectangular slots and channels in the copper mold. The mold also supports the steel shell and determines the shell shape. In this multiphysics model, a separate 3D finite-element model of a symmetric quarter of the mold system was developed to consider the influences of narrow face mold distortion and different mold surface temperatures. The mold geometry includes taper of the mold narrow face, which is applied to accommodate shrinkage of the solid steel shell. This methodology has been used in previous work by [172]. In addition to calculating the temperature, this model also calculates thermal distortion of the mold, which is applied with its taper as a boundary condition on the contact surface of the solidifying shell model via the DISP subroutine in ABAQUS. The shell solidification model in turn provides heat flux as a thermal boundary condition for this model, as presented in Figure A.1.

A.2.4 Boundary Conditions and Shell/Mold Interface Treatment

Full thermal-mechanical coupling between the mold and solidifying steel shell is applied in this multiphysics model system to find the heat transferred across the interfacial gap, which in turn greatly depends on the gap size calculated from the mechanical solution. As the shell cools and shrinks, an air gap may open up near the corners due to non-optimized mold-taper. Gap formation greatly affects final product quality, especially if it causes insufficient heat removal, a thinner shell, and defects such as longitudinal cracks, or even a catastrophic breakout if the molten steel penetrates through the shell. In this work, a resistor model is used to calculate heat transport across the interfacial gap. To find accurate interfacial

heat fluxes, measurements of mold thermocouple temperatures and heat flux from water heatup are needed. For some previous models, such as [87, 173], an inverse heat conduction problem (IHCP) is solved to match the surface boundary conditions with specific plant measurements. In the current work, the two-way thermal-mechanical coupling between the solidifying steel shell and mold is modeled in detail to find the heat transferred across the interfacial gap between the mold and steel shell, which depends strongly on the local gap distance calculated from the mechanical solution. Measurements are used here for model calibration and validation.

The gap heat flux, , includes two parallel contributions, from radiation, , and conduction, :

$$q_{gap} = -k\partial T/\partial n = -\left(h_{rad} + h_{cond}\right)\left(T_{shell} - T_{mold}\right) \tag{A.8}$$

where is the normal surface unit vector . The heat transfer coefficient due to radiation through the semi-transparent liquid part of the slag is:

$$h_{rad} = \frac{\sigma_{SB}}{\frac{1}{\varepsilon_{shell}} + \frac{1}{\varepsilon_{mold}} - 1}\left(T_{shell} + T_{mold}\right)\left(T_{shell}^2 + T_{mold}^2\right) \tag{A.9}$$

where the Stefan-Boltzmann constant, is , and are the shell and the mold surface emissivities, taken to be 0.8; and are the surface temperatures. The heat transfer coefficient due to conduction is calculated with four resistances connected in series:

$$\frac{1}{h_{cond}} = \frac{1}{h_{mold}} + \frac{\left(d_{gap} - d_{slag}\right)}{k_{air}} + \frac{d_{slag}}{k_{slag}} + \frac{1}{h_{shell}} \tag{A.10}$$

where the first resistance, , is for contact between the mold hot face surface and the solidified mold-slag layer; the next resistance is due to conduction through the local air layer, , calculated from the thermal-mechanical model displacement results. The third resistance is conduction through the slag layer, and the final resistance is a temperature-dependent contact resistance between the slag and the outer surface of the steel shell. The specific

parameters for this resister model, given in Table 1, are taken mainly from [64]. These calculations are performed with CON1D and also calculated in the Abaqus models via the GAPCON user subroutine.

Ferrostatic pressure in the liquid steel pool, that pushes the continuously solidifying shell towards the contact surfaces of the mold, is implemented into the solidifying steel shell model via the DLOAD subroutine as a distributed load which increases linearly with vertical distance (time) down the mold. This methodology is described in more detail by [15]. Mechanical interaction between the shell and the mold contact surfaces is accounted for using coulomb friction with a friction factor of $\mu = 0.15$ based on measurements by[33]. Sliding contact that permits gap formation without permitting penetration is enforced using the contact algorithm in ABAQUS with the mold hotface as the "master" surface and the shell exterior as the "slave" surface.

Table A.1: CON1D interfacial gap parameters

Interfacial gap parameter	Value	Unit
Solidification temperature of slag	1083	°C
Conductivity of slag	1.5	W K/m
Contact resistance of slag layer/mold	5.0x10-9	m^2 K/W
Dynamic viscosity of slag at 1300 °C	1.8	Pa s
Exponent for temperature dependence of viscosity	0.9	-
Density of slag	2500	kg/m^3
Absorption factor of slag	250	1/m
Refraction index of slag	1.5	-
Emissivity of slag	0.9	-
Mold powder consumption Rate	0.399	kg/m^2
Oscillation mark depth	0.324	mm
Oscillation mark width	1.5	mm
Mold oscillation frequency	2.5	cps
Mold oscillation stroke	6.6	mm
Ratio of solid slag velocity/casting speed (WF)	0.16	-
Ratio of solid slag velocity/casting speed (NF)	0.167	-

A.3 Viscoplastic Model of Solidifying Steel

The total strain in this elastic-viscoplastic model is split into three components, written in rate form as:

$$\dot{\varepsilon} = \dot{\varepsilon}_{el} + \dot{\varepsilon}_{th} + \dot{\varepsilon}_{ie} \tag{A.11}$$

Where tensors contain the components of the elastic, thermal and inelastic (both rate-independent plasticity and rate-dependent creep) strain rates. The stress and strain rates then are related by the constitutive equations:

$$\dot{\sigma} = \underline{\underline{\mathbf{D}}} : (\dot{\varepsilon} - \alpha\dot{T} - \dot{\varepsilon}_{ie}) \tag{A.12}$$

where contains the isotropic elasticity constants based on the temperature-dependent elastic modulus and Poisson ratio, as given in [60]. The thermal strain term depends on the isotropic temperature-dependent thermal expansion coefficient tensor, found from the temperature-dependent density, as explained by [90], and the evolving temperature distribution calculated from the transient thermal model results, T. In case of finite deformation, the objective stress rate is provided by the Jaumann stress rate :

$$\hat{\sigma} = \dot{\sigma} + \sigma : W - W : \sigma \tag{A.13}$$

where W is the anti-symmetric part of the velocity gradient. Even though there is no explicit yield condition, like in classical plasticity, inelastic effects are assumed to follow “J2 plasticity" with isotropic hardening. The inelastic strain rate is found assuming the Prandtl-Reuss equations:

$$\dot{\varepsilon}_{ie} = \dot{\bar{\varepsilon}}_{ie} \frac{3}{2} \frac{\sigma'}{\bar{\sigma}} \tag{A.14}$$

where is the effective or von Mises stress:

$$\bar{\sigma} = \sqrt{\frac{3}{2}\,\sigma' : \sigma'} \tag{A.15}$$

while is a deviatoric stress tensor defined by:

$$\sigma' = \sigma - \frac{1}{3}pI \tag{A.16}$$

and the pressure portion of the Cauchy stress tensor is:

$$p = \frac{1}{3}tr(\sigma) \tag{A.17}$$

Unified viscoplastic models treat creep and plasticity as a combined "inelastic strain", whose instantaneous rate of change depends on the current stress, temperature, and "structure". Structure is represented by one or more scalar or tensor state variables, which evolve with time, and can include phenomena such as rate of phase transformation. [174] obtained traditional elastic-viscoplastic models when inelastic strain is selected as the structure parameter. Thus, the current model employs such a unified constitutive model, with inelastic strain as the single structure parameter. Here, inelastic strain rate is related to stress, temperature, inelastic strain, and carbon content, %C:

$$\dot{\bar{\varepsilon}}_{ie} = f(\,\bar{\sigma},\ T,\ \bar{\varepsilon}_{ie}, \tag{A.18}$$

Separate relations are used for each metallurgical phase: liquid, austenite, and ferrite.

A.3.1 Austenite Constitutive Model

For the austenite phase, a unified formulation proposed by [83] is used, which matches both the creep test data of [96] and the tensile test data measured by [80]:

$$
\begin{aligned}
&\dot{\bar{\varepsilon}}_{ie}[\sec^{-1}] = f_C\big(\bar{\sigma}[MPa] - f_1\,\bar{\varepsilon}_{ie}|\bar{\varepsilon}_{ie}|^{f2-1}\big)^{f3}\exp\left(-\frac{Q}{T[K]}\right)\\
&where:\\
&Q = 44,465\\
&f_1 = 130.5 - 5.128\times 10^{-3}T[K]\\
&f_2 = -0.6289 + 1.114\times 10^{-3}T[K]\\
&f_3 = 8.132 - 1.54\times 10^{-3}T[K]\\
&f_C = 46,550 + 71,400(\%C) + 12,000(\%C)^2
\end{aligned}
\tag{A.19}
$$

where Q is an activation energy constant, $\bar{\sigma}$ (MPa) is Von Mises effective stress, empirical functions f_1 ,f_2 ,f_3 ,f_c depend on absolute temperature K , and %C is carbon content (weight percent), which is one of the ways that steel grade (composition) is represented. [97] showed that section A.3.1 allows an algorithmic approximation of kinematic hardening, where $\bar{\sigma}$ and $\dot{\bar{\varepsilon}}_{ie}$ are signed according to the largest principal stress and strain rate component respectively. They demonstrated reasonable agreement with some cyclic fatigue test data at high temperatures.

Originally fitted to tensile-test and creep data for plain carbon steel, Figure A.3 compares the Kozlowski model III constitutive equation with data points measured by [80] for plain carbon steel at two different temperatures. The form of this austenite constitutive model is rather restrictive to allow inclusion of realistic behavior during cyclic loading, such as kinematic hardening, the Bauschinger effect and other realistic behavior in cyclic loading.

A.3.2 Ferrite cCnstitutive Model

For the δ-ferrite phase, a power law constitutive model proposed by [82], is implemented, as given in section A.3.2. This model was fitted to match tensile-test measurements of plain carbon steel made by [94].

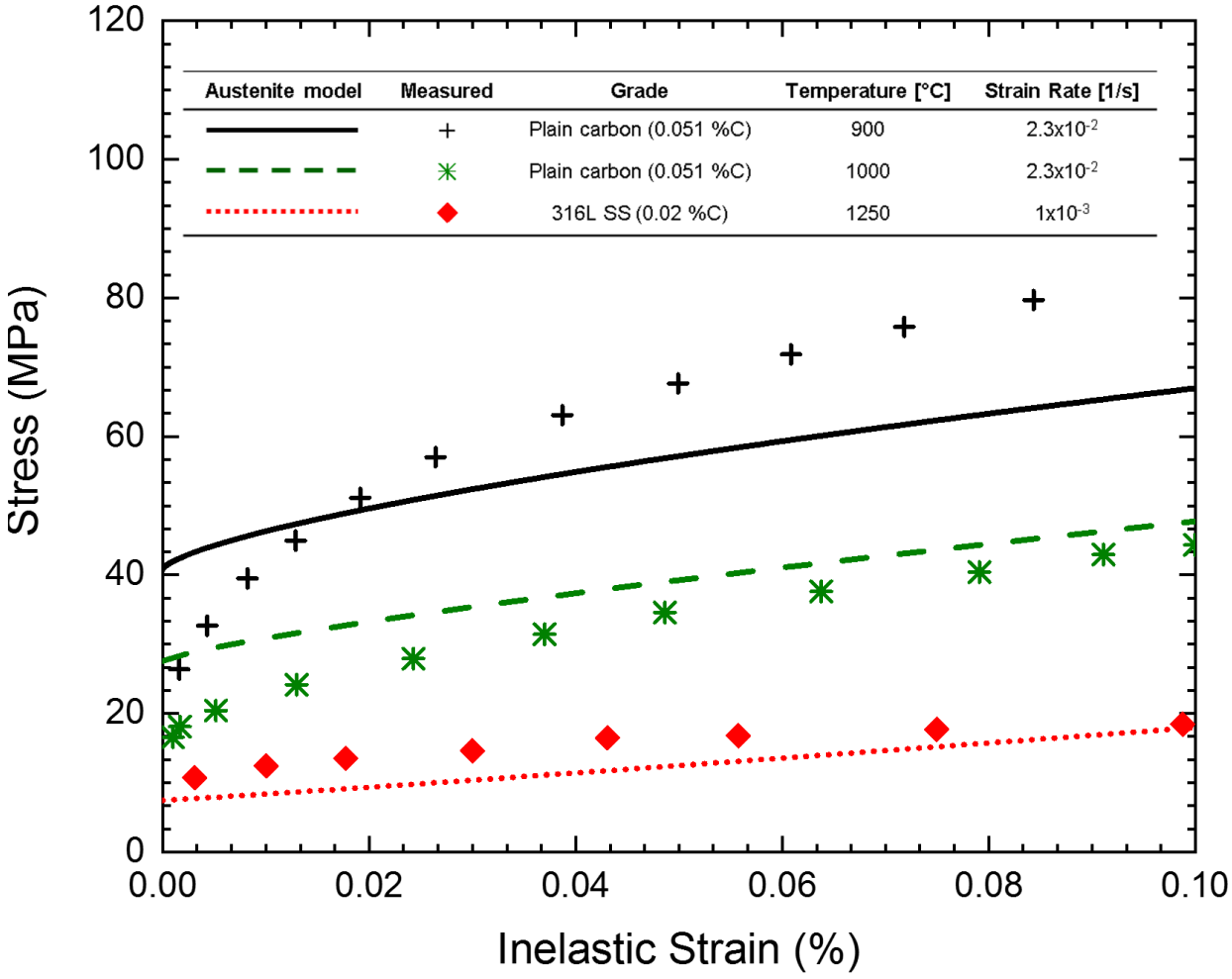


Figure A.3: Austenite constitutive model for plain carbon steel (Wray, 1982) compared with stainless steel data

$$\dot{\bar{\varepsilon}}_{ie}\,(1/sec.) = 0.1\left|\frac{\bar{\sigma}\,(MPa)}{f_{\delta c}(\%C)\left(\frac{T(^oK)}{300}\right)^{-5.52}(1+1000\bar{\varepsilon}_{ie})^m}\right|^n$$
$$where:$$
$$f_{\delta c}\,(\%C) = 1.3678\times 10^4(\%C)^{-5.56\times 10^{-2}}$$
$$m = -9.4156\times 10^{-5}T\,(^oK) + 0.3495$$
$$n = \frac{1}{1.617\times 10^{-4}T\,(^oK) - 0.06166} \tag{A.20}$$

Figure A.4 shows this ferrite model integrated within the relevant low strain range for a variety of constant temperatures and strain rates. For the same conditions, this phase is almost an order of magnitude weaker than austenite. As with the austenite model, the ferrite model is also restrictive to accommodate kinematic hardening and the Bauschinger effect in cyclic loading, which increases the difficulty of fitting the model accurately. Compositions for all steel grades discussed in this work can be found in Table 2.

A.3.3 Liquid and Mushy Phase Constitutive Model

Similar to the works of [90] and [41], the liquid and mushy zones are modeled with an isotropic elastic-perfectly-plastic rate-independent constitutive model, using a small, constant yield stress of 0.01 MPa, whenever temperature exceeds the solidus temperature.

A.3.4 Phase-Based Constitutive Model Selection

As different steel phases have greatly different mechanical properties, the choice of constitutive model in this work depends on the phase-fraction evolution with temperature of the particular steel grade of interest, and the transition between phases, as described by [41]. In two-phase regions, most thermal and mechanical properties are modeled based on a simple weighted average summation based on phase fraction. Constitutive equations are handled differently.

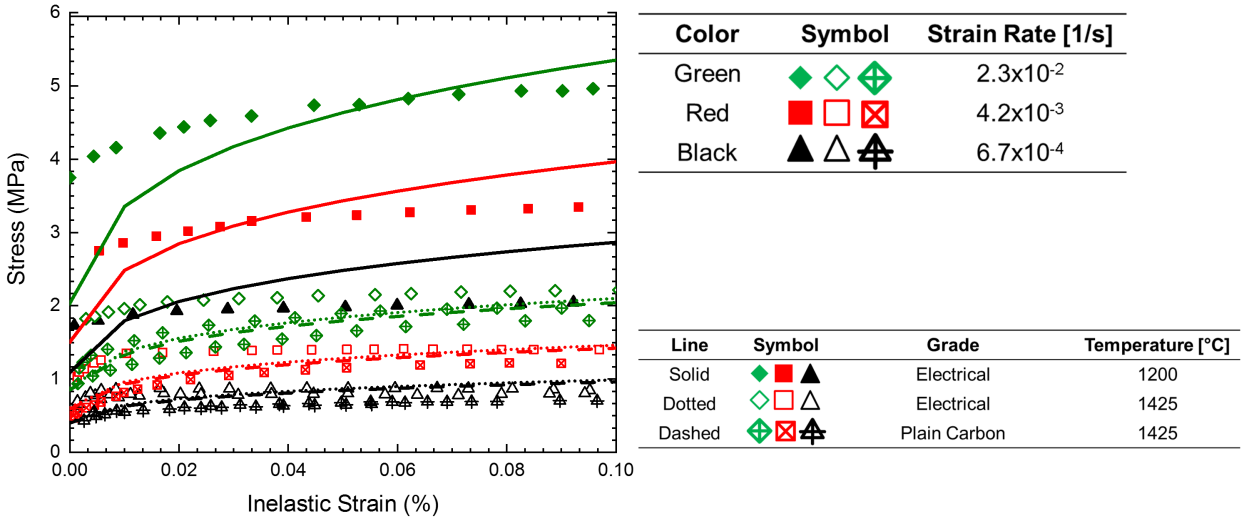


Figure A.4: Delta-ferrite constitutive model results for plain carbon steel (lines) compared with measurements (symbols) by (Wray, 1976) at 2 temperatures, and 3 strain rates, for two steel grades.

In austenite/ferrite mixtures, the Zhu model for ferrite is applied in the solid when the ferrite volume fraction exceeds 10%. Otherwise, the Kozlowski Eqn. (19) is used. This criterion was chosen over a mixture law based on phase fractions, because time-dependent inelastic response in the ferrite phase governs the local mechanical behavior if the ferrite domain is unbroken. The previous work of [89] found that a transition of 10% matched quite well with a more complicated transitional model using an Eshelby tensor with multiple phases. Details on the method devised to integrate these highly nonlinear constitutive equations are explained in [90], and were implemented via the UMAT subroutine in ABAQUS.

Figure A.5 shows the results of both constitutive models, integrated for the same conditions as data measured by [91] for 316L stainless steel. The austenite is observed to be about 10X stronger than the corresponding ferrite, and the Kozlowski model agrees with the measured data.

A.4 Phase-Based Material Properties for Stainless Steel

The composition of steel greatly influences its mechanical properties. Due to the many different types of steel, comprehensive mechanical-property experimental-data for the range

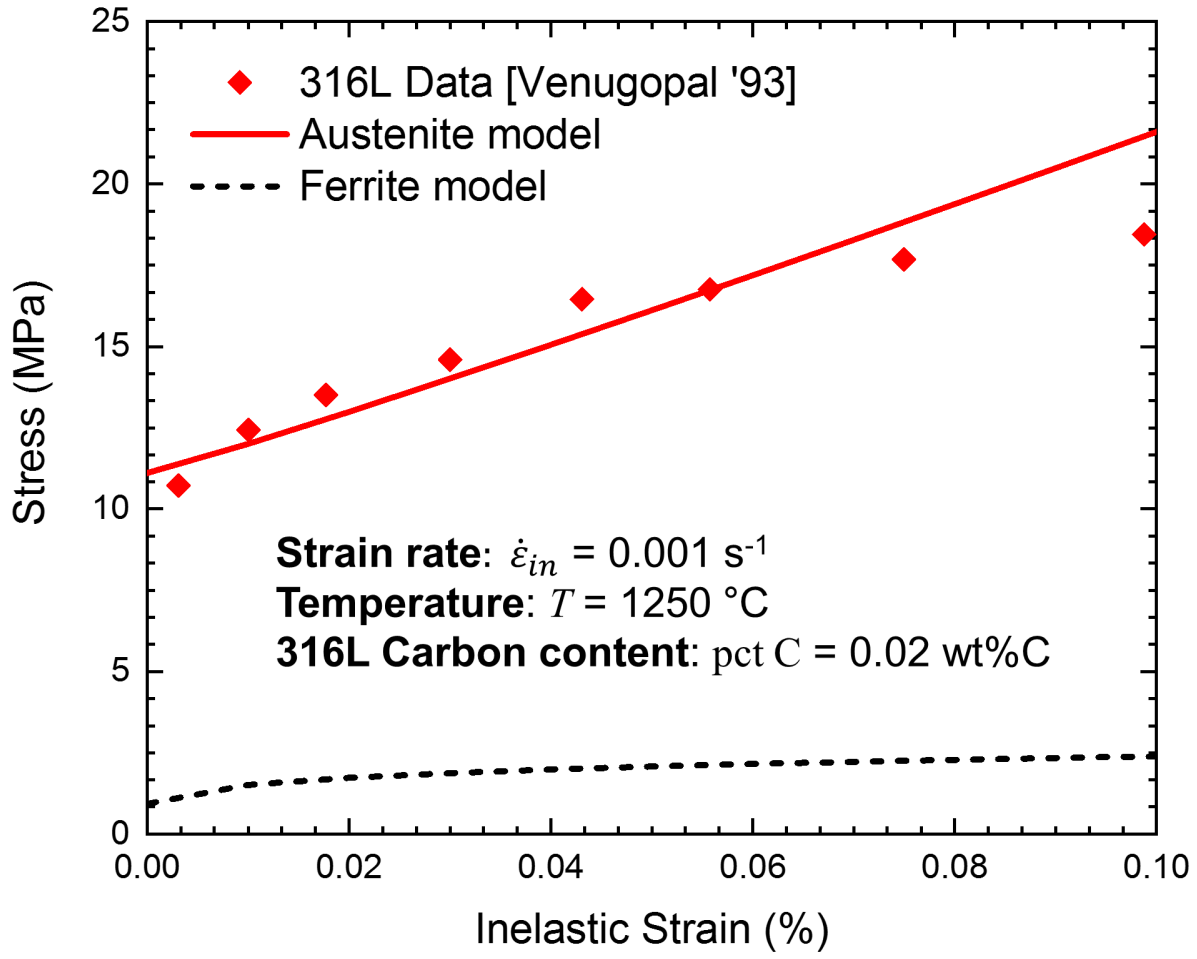


Figure A.5: Constitutive models of austenite and ferrite for 316L stainless steel with experimental data (Venugopal et al., 1993).

of high temperatures, low strains, and low strain rates of interest in casting processes is difficult to find for any given steel grade. Although plain carbon steels are defined by their carbon content, they also contain up to several weight percent of many other alloying elements, which depend heavily on the specific grade. Higher alloy steels such as next generation Advanced High-Strength Steels, tool steels, and stainless steels have substantially higher amounts of specific alloying elements (such as Si, Mn, Cr, and Ni) in order to achieve specific enhanced properties such as ductility-to-strength ratio, hardenability, hot working strength, and corrosion resistance.

Originally fit to data for specific plain carbon steels, both the austenite and ferrite models of the Kozlowski-Zhu constitutive laws exhibit good agreement with tensile-test data for other types of steel when the temperature, strain rate, and phase evolution are the same. Figure A.3 in section 3.1, which shows the austenite constitutive model and some of its plain-carbon fitting data, also compares the predictions of this model with tensile-test measurements for 316L stainless steel obtained by [91] at the appropriate temperature and strain rate. As also shown in Figure A.5, the agreement is remarkable and significant, considering the very different composition of this steel. Furthermore, Figure A.4 in section 3.2, which shows the δ-ferrite constitutive model and some of its fitting data, also compares the predictions of this model with tensile-test measurements for a high-silicon electrical steel, which falls in the ferrite regime. Again, a very close fit is obtained for this very different steel grade.

Very little mechanical property data can be found for specific steels at elevated temperatures. High temperature stress-strain data for the temperature-, strain-, and strain-rate conditions encountered during continuous casting for 409L could not be found in the literature. However, while high temperature steel properties depend on composition, the specific phase at a given temperature is substantially more relevant to its behavior as shown by the results presented above. Therefore, finding the proper phase diagram, more specifically the phase fraction history of a given steel grade, and using phase specific constitutive equations is

a sufficient and more convenient method for determining mechanical behavior during solidification, without the necessity of performing complete mechanical testing in this regime. This method has been previously validated by [86] comparing predictions using the Kozlowski-Zhu constitutive laws with force measurements in solidifying steel shells. Other similar studies, including those by [92] and [41] have applied this approach to investigate various aspects of the continuous casting process.

As with all steels, stainless steels can exhibit a wide range of thermal and mechanical properties during solidification. The steel of interest in this work, 409L, is a specific type of ferritic stainless steel. Stainless steels as a group are designed to withstand corrosive environments, due to high chromium and nickel contents, which help to create a strong protective oxide layer adhered tightly to the surface. These higher alloy contents also strongly affect phases as well as micro constituents, and depending upon the exact chemical composition of the steel, the high-temperature microstructure during casting may consist of austenite, ferrite, or a mix of the two phases.

Based on its composition shown in Table A.2, the evolution of the volume fractions of each phase with temperature during solidification and cooling of 409L stainless steel are shown in Figure A.6, calculated from the appropriate multi-dimensional equilibrium phase diagram based on free-energy minimization with JMatPro [93]. Specific transformation temperatures are given in Table A.3.

Compared to plain carbon steel grades, the phase history of 409L stainless has substantially different austenite and ferrite regions. Whereas in plain low-carbon steels, solidification to δ-ferrite is followed by complete transformation into austenite, in this particular ferritic stainless steel, ferrite is still stable all the way to room temperature. Figure A.6 shows that the cooling steel only partially transforms into austenite, reaching a maximum austenite fraction of about 60% at $\sim$1000 °C, followed by a complete transition back into ferrite.

The temperature-dependent thermal properties: conductivity and enthalpy, shown in Figure A.7, are calculated by JMatPro [93] and input into ABAQUS subroutines. The

Table A.2: Compositions (wt.%) of steel grades used in Stainless Steel Work

Steel grade	**Plain 1**[80]	**Plain 2**[94]	**Electrical**[94]	**316 SS**[91]	**409L SS**
C	0.051	0.028	0.017	0.02	0.005
Mn	0.82	0.01	0.01	1.7	0.27
Si	0.28	0.006	3.01	0.77	0.54
S	0.018	0.004	0.004	0.007	0.001
P	0.001	0.001	0.001	0.04	0.0224
Cr	-	-	-	18.2	11.2
Ni	-	-	-	11.6	0.1
Al	<0.002	0.001	0.002	-	0.003
Ti	-	-	-	-	0.22
N	0.001	0.001	0.003	-	0.008

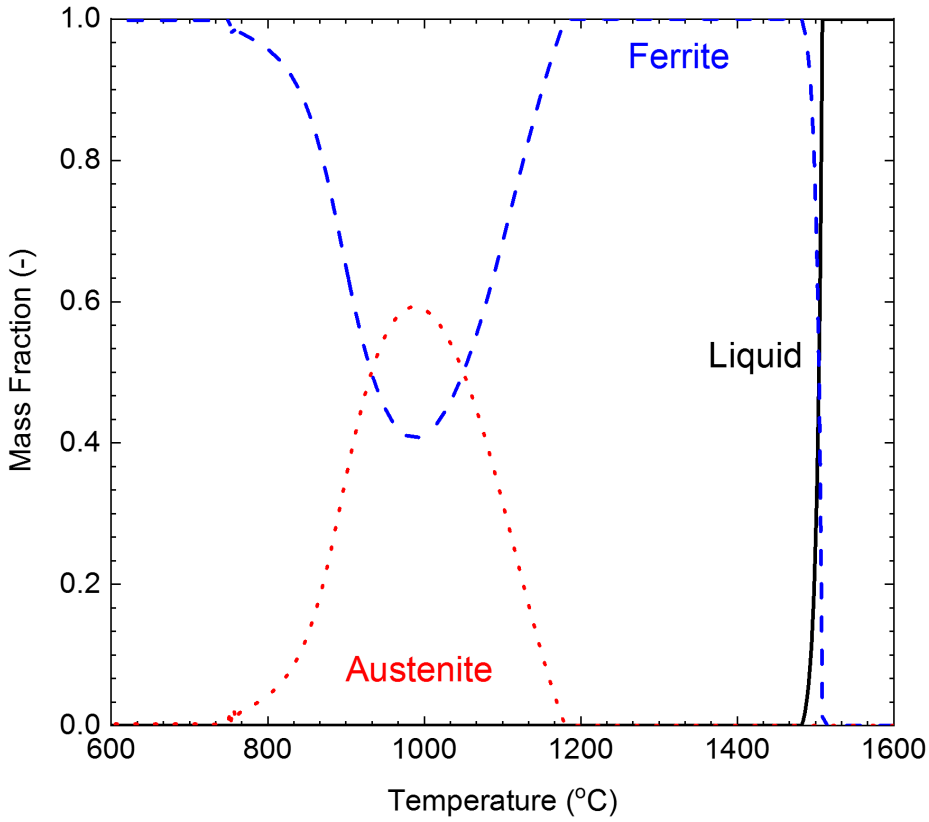


Figure A.6: Phase fractions for 409L stainless steel.

Table A.3: Transition temperatures for 409L stainless steel.

Pour temp.	1555.00 °C
Liquidus temp.	1508.63 °C
Solidus temp.	1481.93 °C
Mushy zone	26.7 °C
Austenite start	1180 °C
Austenite end	753 °C

temperature-dependent elastic modulus, density, and thermal linear expansion are shown in Figure A.8.

Decreasing temperature leads to increases in density and elastic modulus as the crystal structure become more tightly packed and stiffer. In addition, as the steel changes phase from δ-ferrite to γ-austenite, and thus from body-centered-cubic to close-packed face-centered-cubic, the atomic packing fraction also increases, so the density further increases, as the lattice spacing becomes smaller. This is accompanied by corresponding decreases in the thermal linear expansion, which is inversely related to the cube root of the density at a given temperature.

A.5 Results and Discussion

The coupled multiphysics model, including the Kozlowski-Zhu constitutive laws, was employed to quantify the thermo-mechanical nature of solidifying 409L stainless steel in a commercial continuous slab caster with a 220 mm (thickness) x 1260 mm (width) strand, cast at 1 m/min casting speed in a straight mold with working length of 0.8 m and 120 mm nozzle submergence depth. The slice domain of the shell model in Figure A.2 begins at the meniscus, with a uniform pouring temperature, and no initial displacement, strain, or stress. The 2D domain is discretized with ∼24,000 four-node, temperature-displacement generalized plane-strain elements, providing an average element size (0.3 mm) – which is sufficient to capture thermal-mechanical solidification phenomena on a fixed grid according to [41]. The 1D domain has a uniformly refined mesh of 0.1 mm square elements. The "slice"

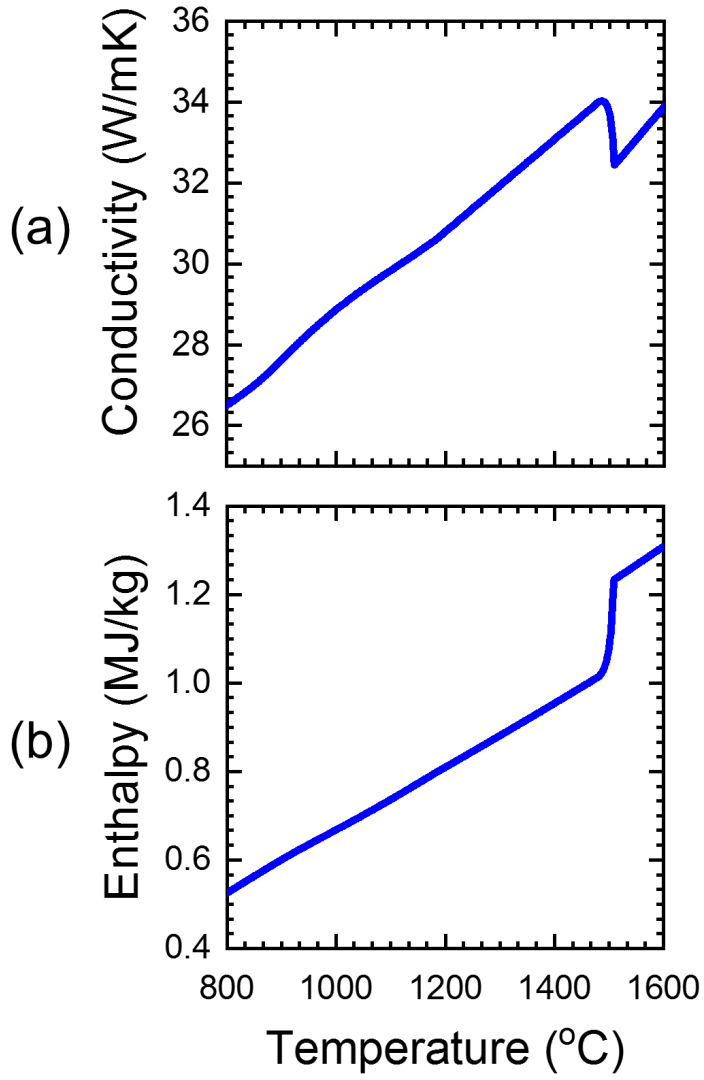


Figure A.7: Thermal properties of 409L stainless steel: (a) conductivity and (b) enthalpy.

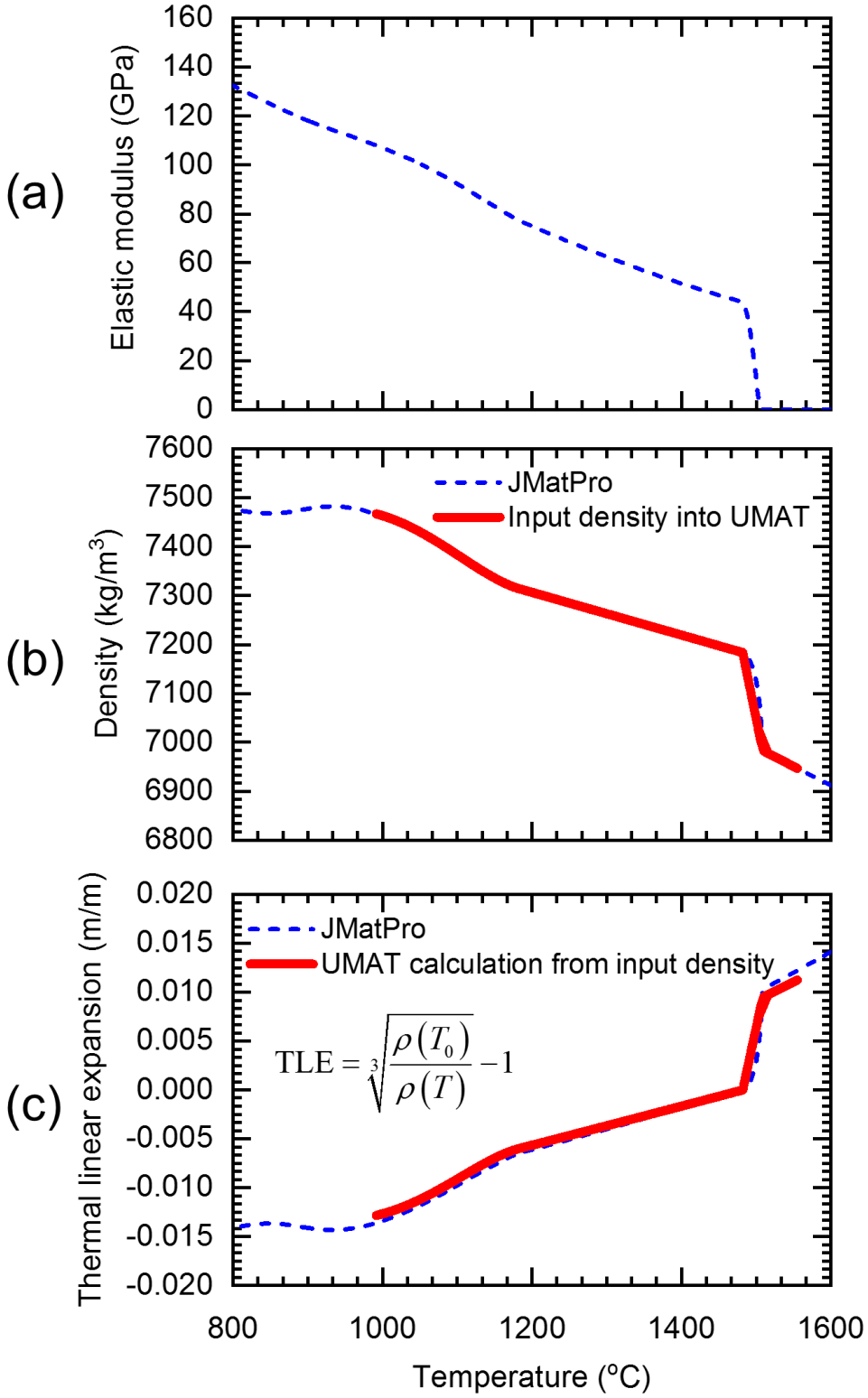


Figure A.8: Mechanical properties of 409L stainless steel: (a) elastic modulus, (b) density, (c) thermal linear expansion.

model approach is justified for the heat transfer analysis, due to insignificant axial (casting direction) conduction compared to heat advected by the casting velocity, *i.e.* large Péclet number. [97] and later [92] have found that generalized plane strain, with constant axial strain and negligible out of plane bending, is capable of reproducing the complete 3D stress state in continuous casting modeling, and is therefore applied as a suitable 2D mechanical approximation in this work as well.

A.5.1 Thermal Flow in Liquid Pool

Figure A.9 shows time-averaged flow patterns and temperature distributions in the liquid steel at horizontal and center-middle planes in the mold, calculated from the 3D turbulent thermal fluid flow model. Owing to the lower casting speed of stainless-steel casters, (relative to typical plain-carbon steel casters), the jet is angled upward (5°up), in order to increase surface velocity into an optimum range for good steel quality reviewed by [6].

The distribution of superheat is governed by the flow pattern in the mold region. The jet flowing from the nozzle traverses the mold interior to impact upon the narrow faces, transferring most of the superheat to the solidifying steel shell on the narrow faces. The jet then separates to flow upward towards the top surface and down the narrow faces deep into the strand. Temperature of the flowing steel continuously drops as superheat is removed at the solidification front, so the stagnant regions in the center of the lower recirculation zones are coldest.

The mold flow causes an uneven distribution of superheat flux, showing a peak at a region in the middle of the narrow face and 200 mm below meniscus, as shown in Figure A.10. The superheat flux delivered to the solidification front at the wide faces is observed in this figure to be much smaller. The heat flux removed from the outer surface of the solidifying shell, across the interfacial gap and into the mold, is naturally much larger than the superheat flux, and depends on the difference between the calculated mold-wall shape and the shrinking steel-shell size.

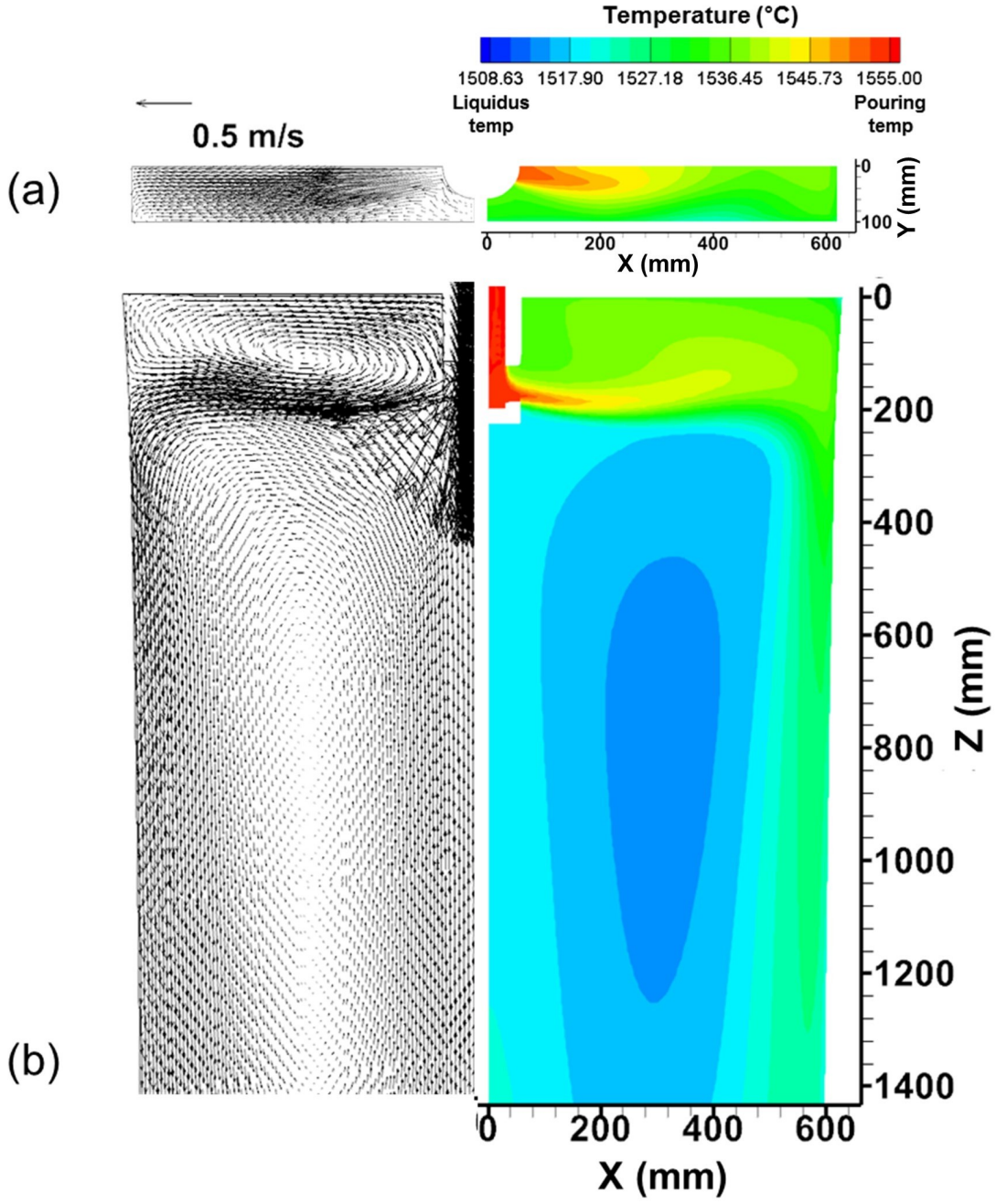


Figure A.9: Molten-steel flow patterns and temperature distributions at (a) horizontal plane 180 mm below the meniscus and (b) center plane between the wide faces in the mold.

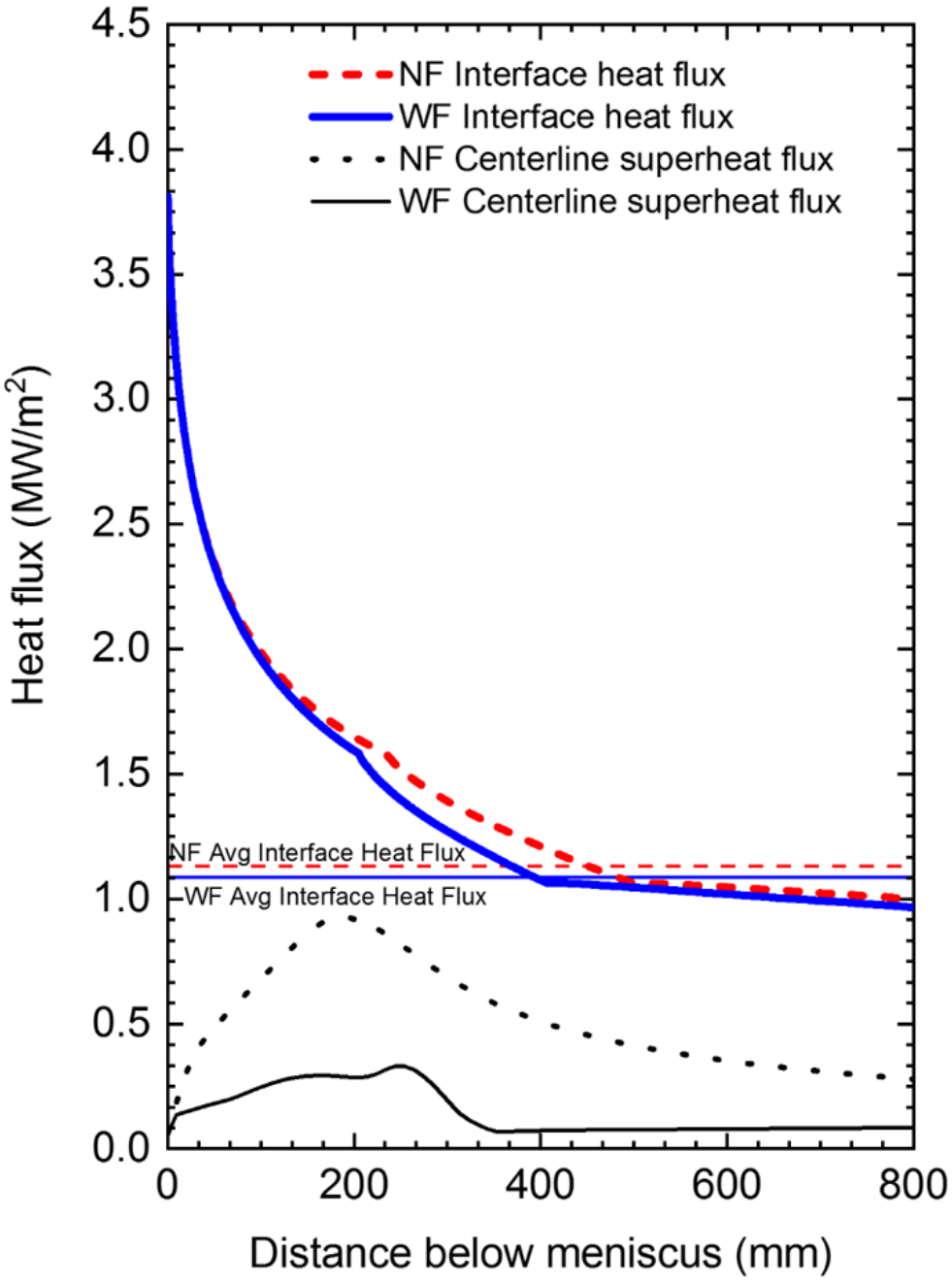


Figure A.10: Calculated interfacial and superheat flux profiles down mold centerlines

A.5.2 Heat Flux in the Mold and Model Validation

Measurements were obtained from the operating caster to enable calibration and validation of the heat transfer model. This includes the measured heatup of the cooling water between entering and leaving the mold wide faces and narrow faces and the measured temperatures from thermocouples in the mold walls during ∼3 hours of nearly steady casting in the real plant. Figure A.11 shows time histories of average heat flux leaving the mold, which are calculated from the water heatup, knowing the water flow rate and total mold surface area. The time averages of these heat fluxes are also given. Figure A.12 shows plant measurements from 13 thermocouples (TCs) located 110 mm below the meniscus, and 20 mm beneath the mold hot face. The time- and spatial- averages of these temperature histories are also included in Figure A.12(b). The thermocouple data of TCs 4-10 located in the central wide face region away from the corners average 120.4 °C with standard deviation of 3.7 °C.

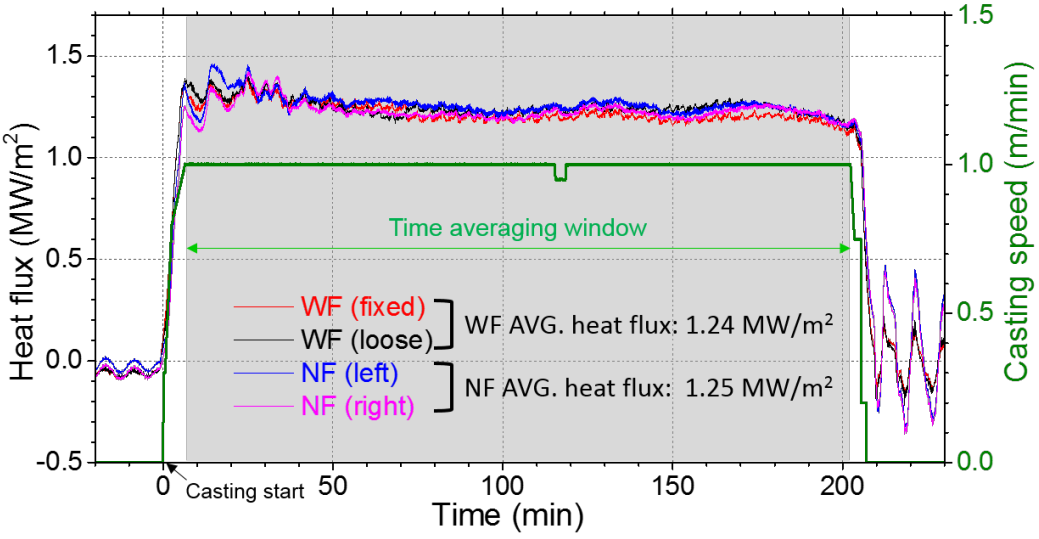


Figure A.11: Heat flux measurements from heatup of mold cooling water

The average heat flux across the interface between the steel shell and the mold hot face predicted by the CON1D model, is calculated by integrating the interface heat flux

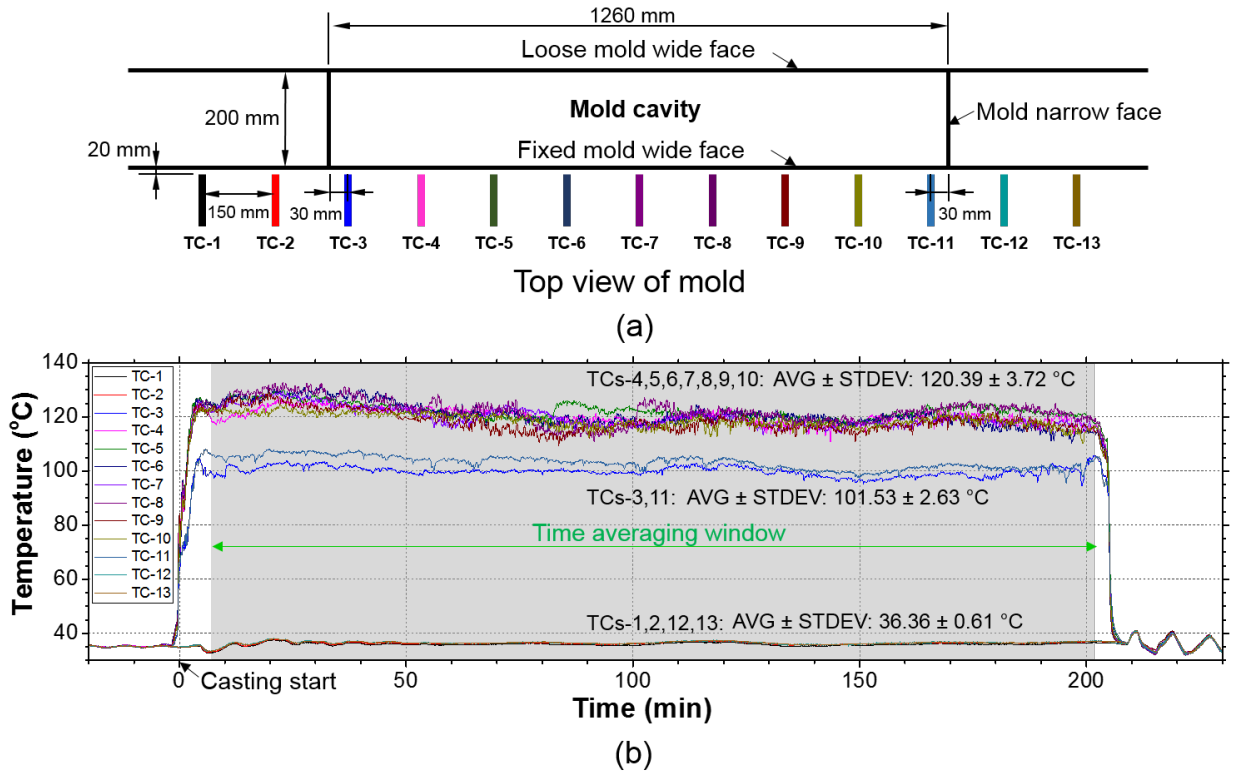


Figure A.12: Thermocouple measurements: (a) locations and (b) temperature histories of thermocouples inserted on the mold wide face

profile along the casting direction, shown in Figure A.10, and dividing by the total mold length (900 mm) and width. These calculated average heat fluxes agree reasonably with the measurements: WF: 1.10 (predicted) vs. 1.24 (measured) MW/m^2 and NF: 1.15 (predicted) vs. 1.25 (measured) MW/m^2. Furthermore, the temperature in the mold wide face predicted at the thermocouple location exactly matches the measured average thermocouple data, as shown in Figure A.13. Matching both average mold heat flux and thermocouple temperatures in the upper mold is significant because it suggests that the entire heat flux profile cannot be too far from reality. This was achieved by careful adjustment of model thermal parameters in Table A.1 such as fv.

The non-uniform superheat distributions, caused by the mold flow pattern, results in local thinning and temperature variations in the solidifying steel shell which greatly affects thermal stress behavior in the shell, and quality of the final steel products. As described previously, the superheat profile on the narrow-face centerline is higher than on the wide face, which makes the shell thickness of the narrow face substantially thinner than the wide face, as shown in Figure A.14. This is also influenced by heat transfer through the interfacial gap between the steel shell and mold contact surface.

Figure A.12 shows that the shell surface temperature starts to decrease faster at ∼400 mm below the meniscus, which is accompanied by corresponding decreases in slope of the mold wall temperatures. This is due to decreasing gap thickness, from better contact between the steel shell and the mold surfaces at that location. The model predictions of both shell thickness and mold temperature profiles are quantitatively verified by comparing the models (CON1D and ABAQUS), in addition to the validation of CON1D with plant measurements already discussed.

A.5.3 Stress and Deformation in Solidifying Steel Shell

Figure A.15 shows temperature and hoop stress profiles down the surface of the wide face and narrow face in the mold. The hoop stress acts tangentially to the surface around the strand circumference. Note that the hoop stress directions are different for the two mold

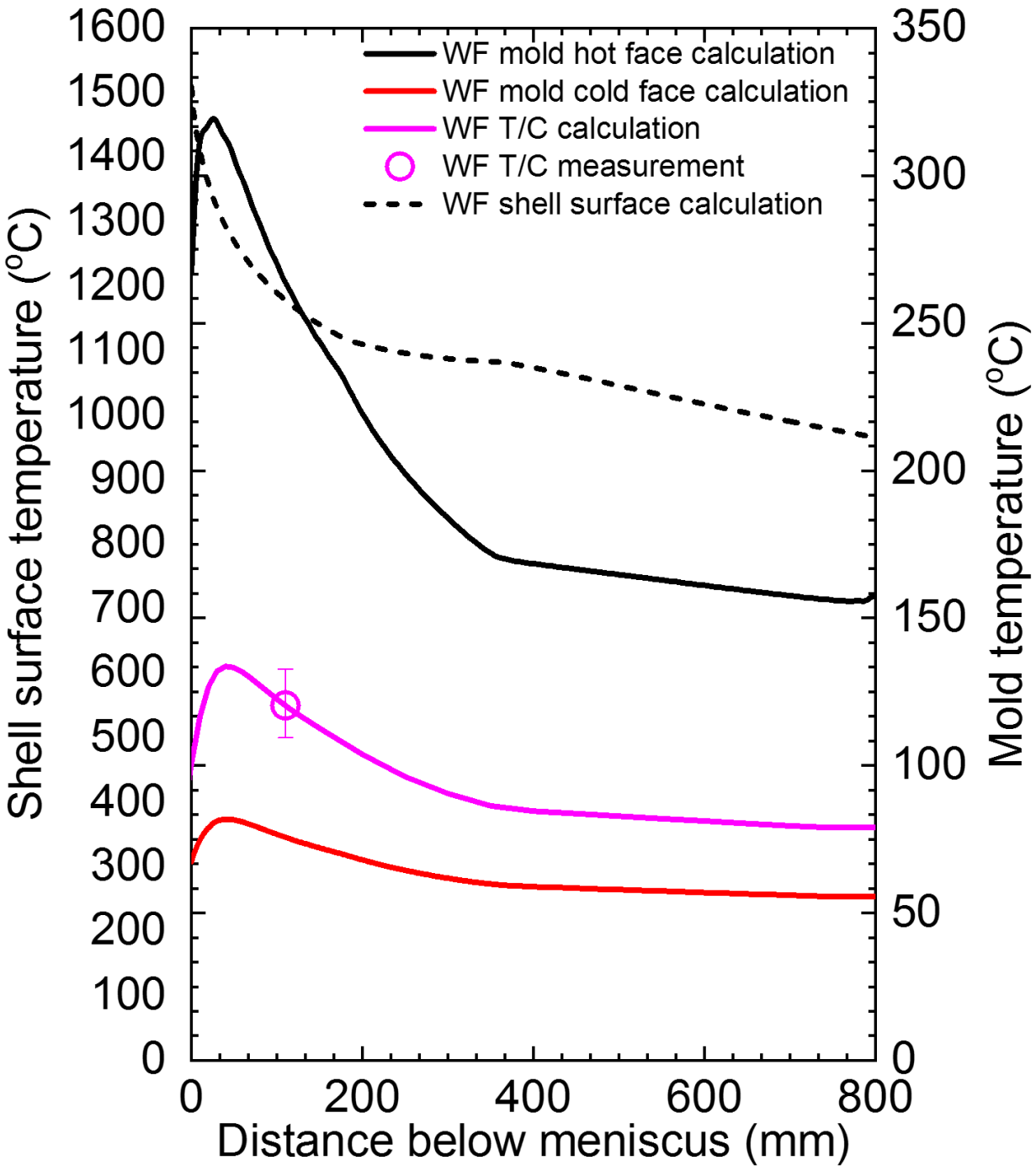


Figure A.13: Calculated mold and shell temperature results (wide face) with thermocouple validation.

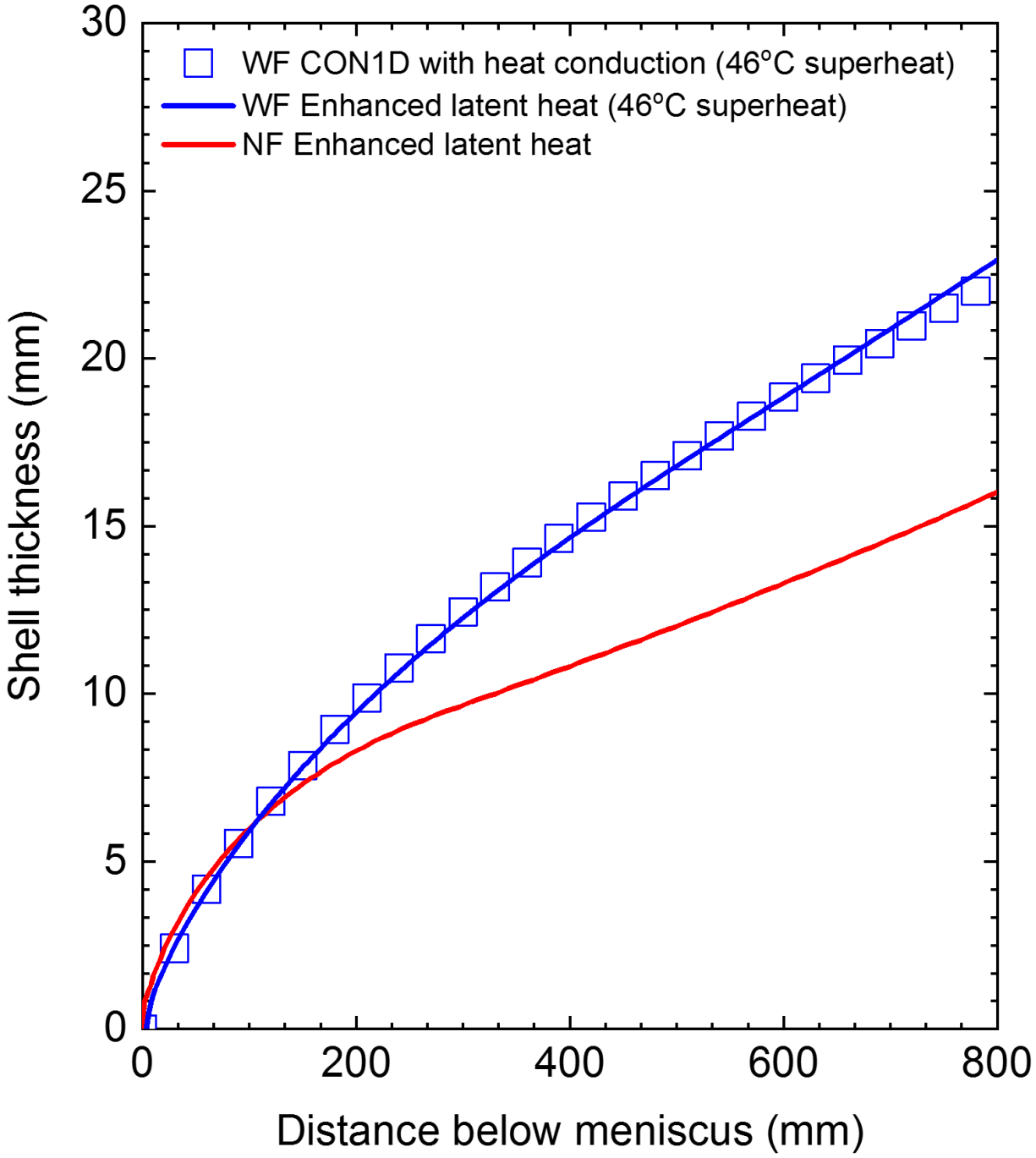
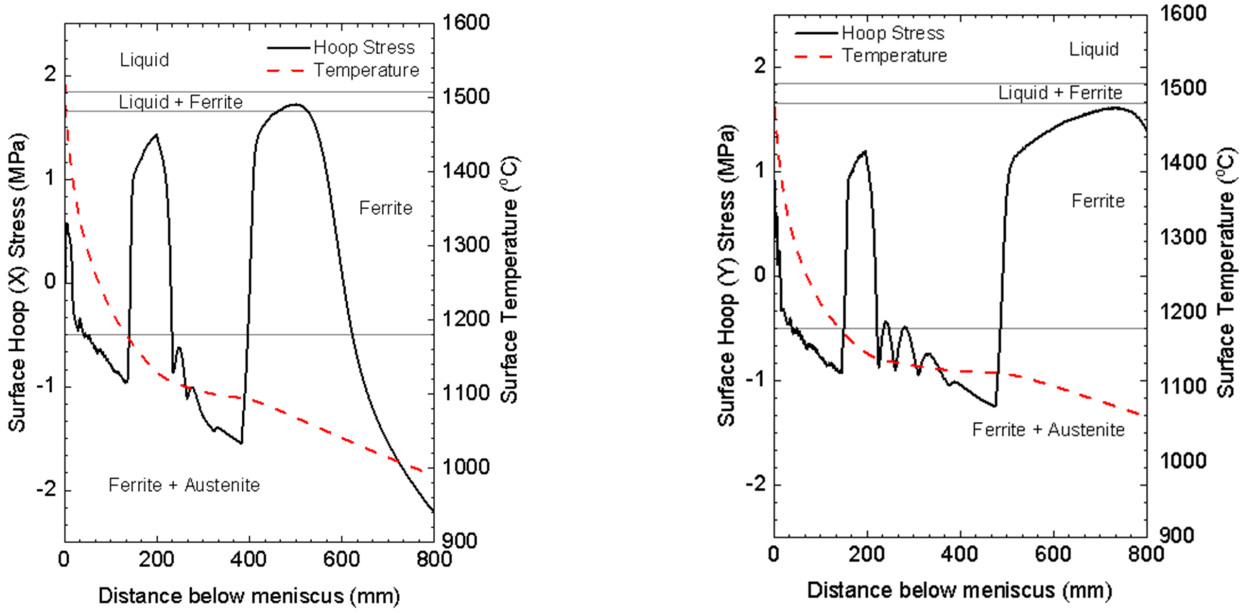


Figure A.14: Shell thickness results from CON1D and ABAQUS.

faces in the global coordinate system (ie x direction on WF and y direction on NF). Both locations experience similar but slightly different temperature histories, with the wide face dropping to a lower temperature by mold exit, while the narrow face remains hotter as a result of the higher superheat flux from the liquid. Stress results are qualitatively similar with both locations experiencing two tensile stress peaks. The first peak is initiated from the rapid shrinkage associated with the phase transformation from ferrite to austenite. The second peak is due to the small but sudden increase in cooling rate at the surface as a result of renewed contact with each respective mold wall. The delay in the compression of the narrow face is due to its higher temperature, and after a longer time, the surface stress there also drops back into compression.



(a) (b)

Figure A.15: Surface temperature and hoop stress results with superheat flux: (a) Wide face and (b) Narrow face.

Figure A.16 gives hoop stress results through the shell thickness at various times during solidification. The expected thermal-mechanical behavior for plain carbon steel, observed by several previous researchers including [41], is compression at the chilled surface, transitioning

into tension towards the solidification front, and then to nearly zero (the ferrostatic pressure) in the liquid. This behavior is also seen in the analytical solution of thermal stress during solidification of a single-phase material by [85]. In addition, a tensile peak often appears at the surface at early times when the cooling rate is high. The new stainless steel results generally exhibit both of these behaviors. However, as discussed previously and shown in Figure A.15, a secondary tensile peak appears at the surface, at later times. Another second tensile peak is also seen to appear inside the shell near the solidification front, moving further beneath the surface with time (Figure A.16).

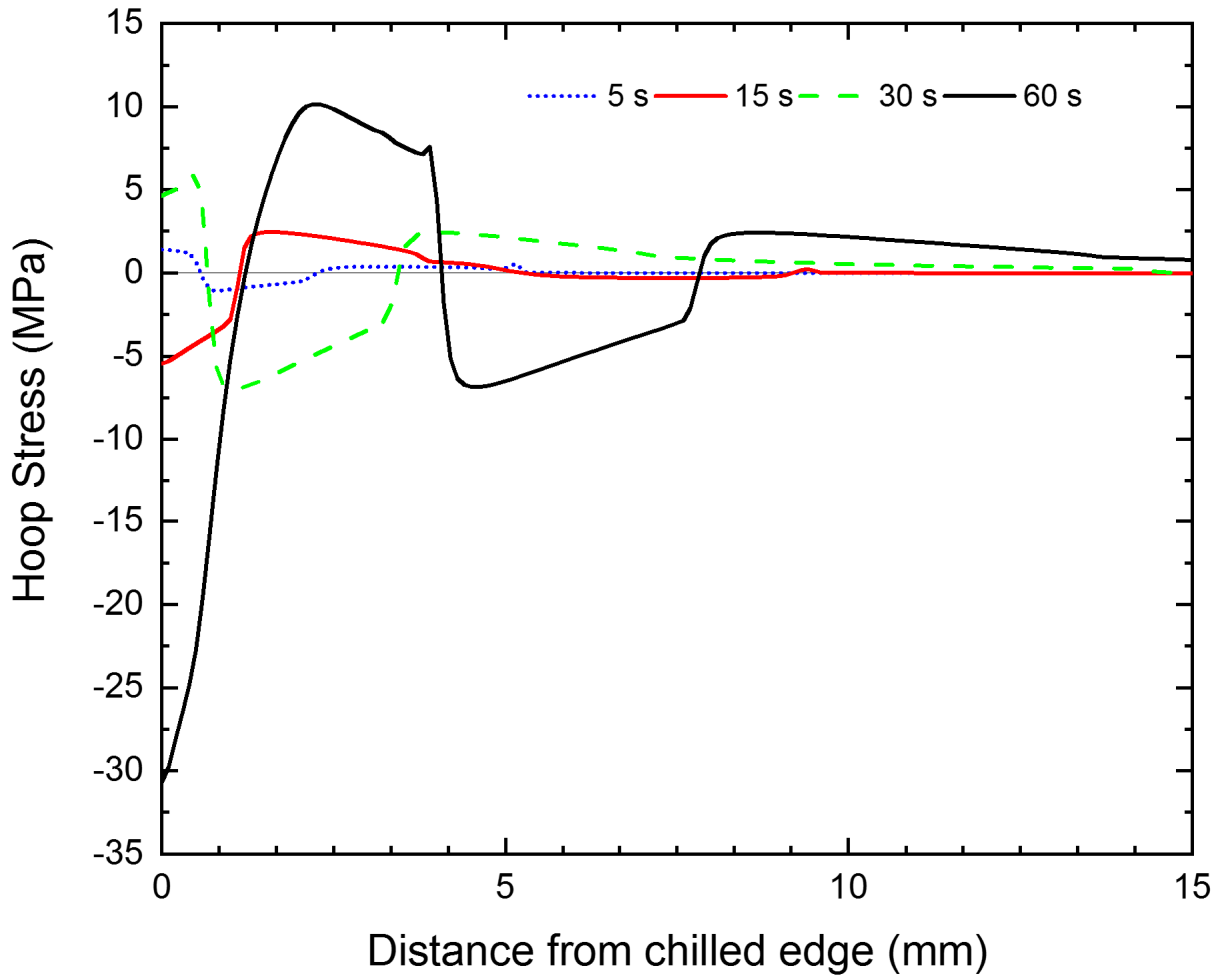


Figure A.16: Hoop stress profile through the thickness at different times below meniscus (WF centerline from slice model).

Figure A.17 shows a single snapshot of hoop stress through the thickness at 60 s below the meniscus of the wide face centerline, using the refined-mesh slice model. This snapshot also includes the phase fractions, in order to understand the stress profile. The difference between the classic behavior of plain carbon steels, surface compression and subsurface tension, is a second compression peak, which is explained by some γ-austenite transforming back into δ-ferrite between 3 and 8 mm beneath the surface, as shown in the inlaid plot of the γ-austenite and δ-ferrite phase fractions. The region transforming back into δ-ferrite experiences an expansion from a FCC to BCC crystal structure, and is forced into compression by the surrounding stronger material: the γ-austenite-rich region on the inside, and the δ-ferrite region at the surface (which becomes much stronger at the lower temperatures). This new compression peak divides the usual subsurface tensile region into two stress peaks. The first interior peak coincides with the maximum phase fraction of γ-austenite (the stronger phase) and the second is generated within the δ-ferrite region due the cooling (compressive) surface region.

These results show that differences in phase transformations between steel grades have a great effect on their stress evolution during solidification. In addition, changes in surface cooling rate are observed to have an equally-important effect on stress evolution at the surface. When considered together with the work by [95] on the grade effects in plain-carbon steels during solidification, the mechanical behavior of solidifying steels becomes more clear. Figure A.18 shows the deformed shell and its temperature contours at various times in the mold, calculated using the L-shaped domain, (Figure A.2). The shell contracts and shrinks away from the mold most at the corner region, which has the lowest temperatures due to 2D heat transfer and is strong enough to support the internal ferrostatic pressure. Similar corner behavior is reported in many previous works such as by [97] and subsequently by [92]. Shrinkage of the wide-face shell is more than the narrow-face mold taper can compensate within $\sim$100 mm below the narrow face meniscus, Figure A.18a, and near mold exit, Figure A.18d, so bulging is often experienced at those locations. Such bulging can lead

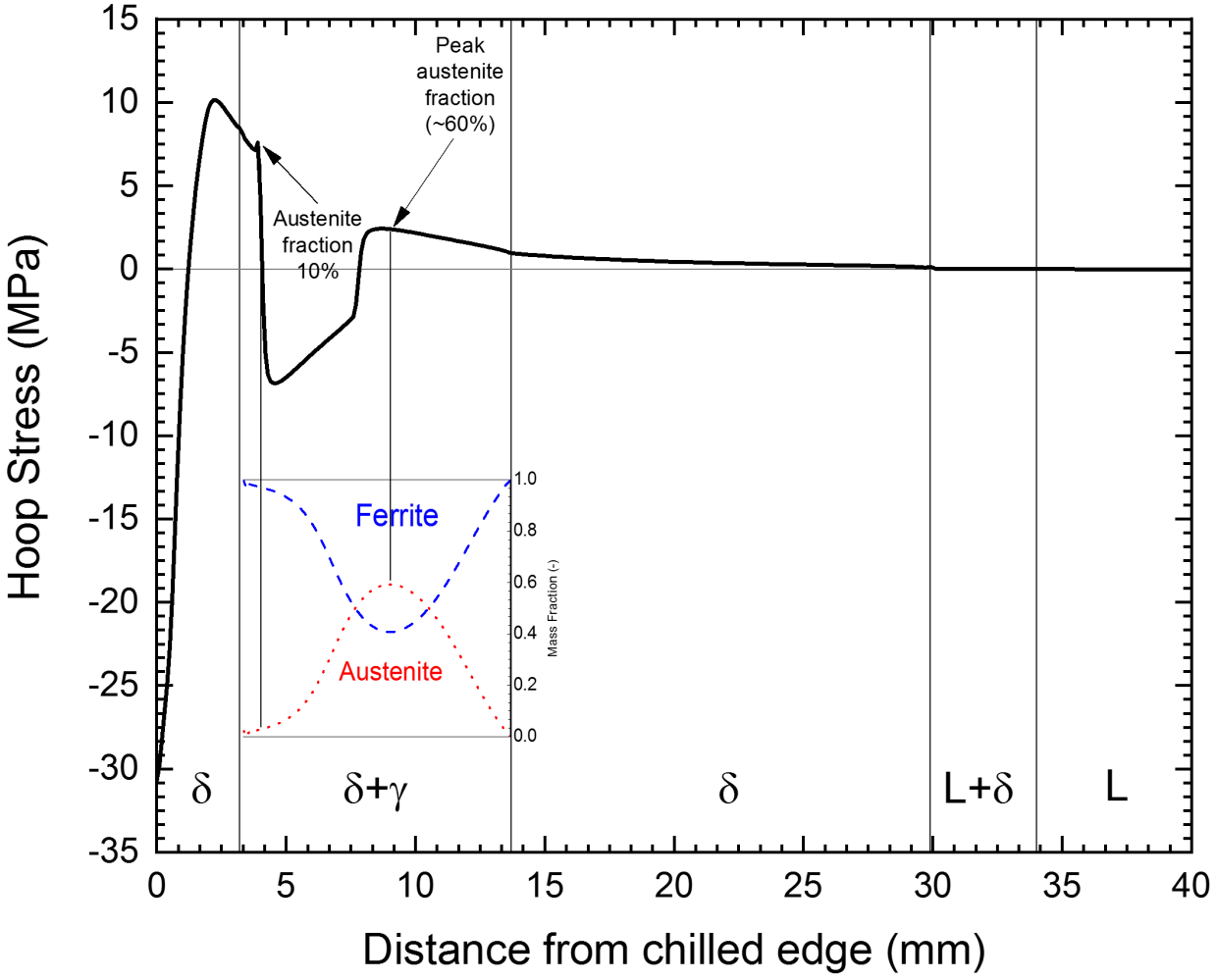


Figure A.17: Hoop stress and phase profile through the thickness 60 s below the meniscus (WF centerline from slice model).

to surface depressions, cracks and other problems below the mold, as explained previously by [55] followed by [175]. Improved taper design of the narrow faces, as suggested by [176] can help lessen these problems.

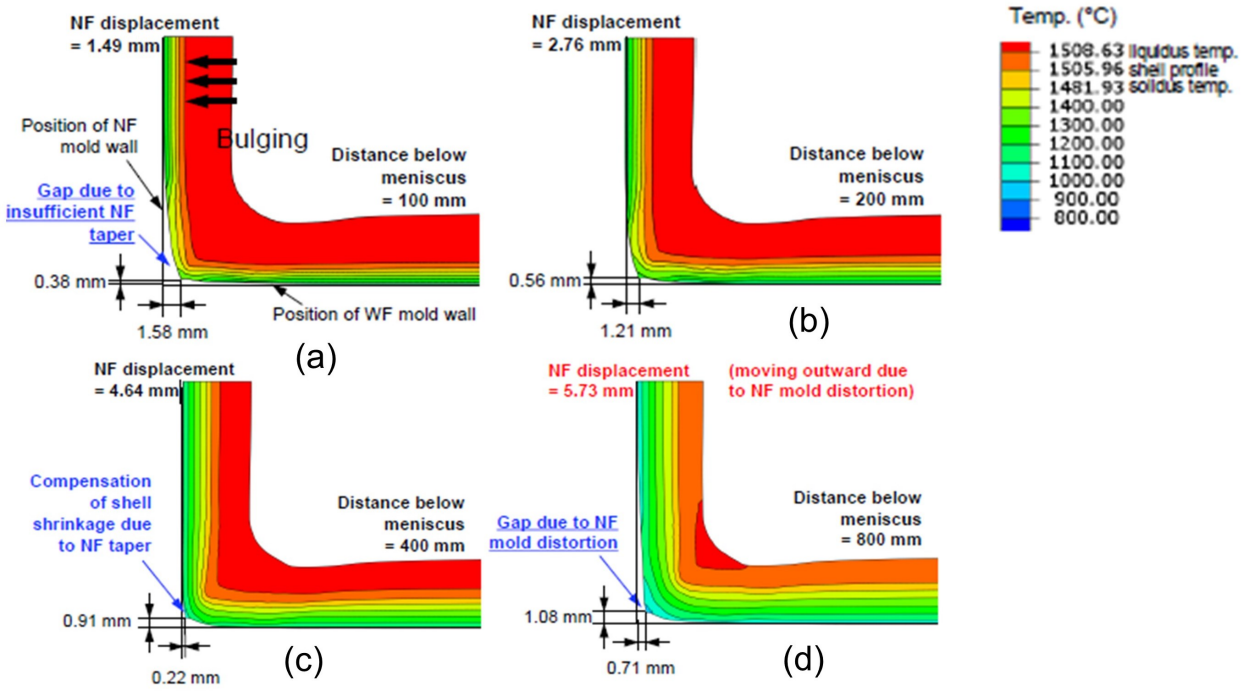


Figure A.18: Deformed shape with temperature contours: (a) 100 mm, (b) 200 mm, (c) 400 mm, and (d) 800 mm below meniscus.

A.5.4 Computational Considerations

Combined nonlinearities from the highly nonlinear material response, coupled distribution of superheat from the CFD model, and complex boundary and contact conditions between the shell and mold lead to significant ill-conditioning of the coupled thermal-mechanical global finite element stiffness matrix. ABAQUS uses the Newton-Raphson method to bring the system of nonlinear finite-element equations into equilibrium within each quasi-static increment. The direct multi frontal solver, used to solve linearized equations in ABAQUS/-Standard, is parallelized with the hybrid MPI/OpenMP implementation. The 150,000 DOF thermal-mechanical model took several days on 4 nodes (96 cores) of the 2016 iForge system at NCSA to reach 48 seconds of total simulation time down the mold length. The CFD

and 3D Mold calculations were larger, but with fewer nonlinearities and better parallel scalability on HPC. [177] have recently benchmarked a similar multi-frontal solver on a large supercomputer, and effectively scaled the solution time on several thousand processors. This shows that the accurate modeling of multiphysics solidification problems, such as presented in this work, is becoming increasingly feasible, using high performance, parallel computing resources.

A.6 Conclusions

A multiphysics model for the study of stainless steel alloy solidification processes has been developed, which features phase-dependent constitutive equations. Specifically, the thermal-mechanical behavior of a solidifying stainless-steel shell in a straight-walled continuous casting mold is simulated using thermo-elastic-viscoplastic constitutive models for the austenite, ferrite, and liquid phases during the solidification process, which are tightly coupled with phase fraction calculations, as well as with highly nonlinear temperature-dependent properties.

These constitutive equations, which were originally fitted from data for plain carbon steel, are shown to reproduce tensile-test measurements for stainless steels as well, so long as the phase, temperature, and strain rate are the same. While high temperature steel properties depend greatly on composition, the specific phase at a given temperature is the reason for this behavior. Using phase-specific constitutive equations is a sufficient and more convenient method to determine mechanical behavior of solidifying steel without the need for complete mechanical testing data in this difficult regime.

The simulation results show that the stresses arising during solidification of a 409L ferritic stainless steel shell include a second sub-surface compression peak through the shell thickness, due to the late phase change expansion from γ-austenite back to δ-ferrite, which is not seen in plain carbon steel. In addition to the phase change peak, it is found that abrupt changes in heat transfer, such as produced in this example by increases in the size of the evolving the shell/mold gap, and by the turbulent fluid flow, also lead to spikes in tensile stresses

at the surface. This multiphysics model can predict the evolving temperature distribution, shrinkage, shape and stress during solidification of steel for different compositions, including stainless steel. It can be used to better understand the fluid flow and thermal-mechanical behavior, and to optimize the continuous casting process, such as by providing ideal mold taper profiles to minimize the formation of defects such as depressions, hot spots and cracks.

A.7 Future Work

More work is needed to apply and couple additional physical phenomena into more comprehensive modeling systems, designed for a particular industrial solidification process of interest. While it is clear that the phase-dependent constitutive behavior approach demonstrated here is a valid method for handling these different steel grades, as newer advanced high strength steels grow in interest, more experimental measurements of mechanical behavior are needed to confirm this finding. Specifically, more tensile tests, creep tests, and reverse loading tests are needed in the high temperature, low strain, and low strain rate regimes experienced by these materials in commercial solidification processes. Finally, with the additional effort, multiphysics models such as this one will become increasingly valuable tools to understand how defects form, and to optimize solidification processes, such as stainless steel continuous-casting.

A.8 Acknowledgements

The authors thank the National Center for Supercomputing Applications (NCSA) Industry Program at the University of Illinois and its Blue Waters project funded by NSF and the state of Illinois as well as support from the Continuous Casting Center at the Colorado School of Mines, the Continuous Casting Consortium at University of Illinois at Urbana-Champaign, and two National Science Foundation GOALI grants (Grants No. CMMI-13-00907 and CMMI 18-08731). Financial support (Grant No. 4.0012983) and assistance in collecting plant data from POSCO are gratefully acknowledged. The ANSYS Inc. academic partnership program for providing Fluent licenses is also appreciated.

APPENDIX B

CON1D INPUT FILE

This section contains the CON1D input file used for the Tata Steel verification example. This model only calculates 900 mm below top of copper, and is not valid below the mold.

Copyright (c) <2020> <Matthew L.S. Zappulla> Permission is hereby granted, free of charge, to any person obtaining a copy of this software and associated documentation files (the "Software"), to deal in the Software without restriction, including without limitation the rights to use, copy, modify, merge, publish, distribute, sublicense, and/or sell copies of the Software, and to permit persons to whom the Software is furnished to do so, subject to the following conditions: The above copyright notice and this permission notice shall be included in all copies or substantial portions of the Software. THE SOFTWARE IS PROVIDED "AS IS", WITHOUT WARRANTY OF ANY KIND, EXPRESS OR IMPLIED, INCLUDING BUT NOT LIMITED TO THE WARRANTIES OF MERCHANTABILITY, FITNESS FOR A PARTICULAR PURPOSE AND NONINFRINGEMENT. IN NO EVENT SHALL THE AUTHORS OR COPYRIGHT HOLDERS BE LIABLE FOR ANY CLAIM, DAMAGES OR OTHER LIABILITY, WHETHER IN AN ACTION OF CONTRACT, TORT OR OTHERWISE, ARISING FROM, OUT OF OR IN CONNECTION WITH THE SOFTWARE OR THE USE OR OTHER DEALINGS IN THE SOFTWARE.

```
 CON1D15.11.01 Steel Continuous Casting Heat Transfer Analysis
 UI Version15.11.01 University of Illinois, Brian G. Thomas
 University of Illinois, Tata, 2-Aug-2018
 Tata Steel Caster 21 Far Field

#1 Parameters to update every call
//CASTING CONDITION:
  1.00 Number of time-cast speed data points
    (If=1, constant casting speed)
    Next 2 lines contain time(s) and vc(m/min) data points
  0.0
  1.440
  1554.000 Pour temperature (C)
  90.000 Distance of meniscus from top of mold (mm)
  200.000 Nozzle submergence depth (mm)


  900.00 Max. simulation length (must > z-distance)(mm)
```

```
  0 Calculate mold and interface (=0 flux casting, or =2 oil casting )
    or enter interface heat flux data starting at meniscus z=0 (=-1)
  or enter avg. mold flux (=-2), or enter cooling water temp. increase (=-3)
  6 Number of zmm and q data points (if above = -1)
    Next 2 lines contain zmm(mm) and q(kW/m2) data
  0.00 20.00 270.00 630.00 670.00 900.00
  1500.00 2900.00 1650.00 1300.00 1000.00 800.00
  1.560   1.329 Average mold heat flux (MW/m^2) (if above =-2)
2.30 0.07 0.40 Mold flux tuning parameters q_fac, tc_fac, q_n (if above =-2)
  5.558 7.499 Mold cooling water temp. increase (Deg C)(if above =-3)
  -1  Running mode (0=stop right now; -1=continue to run; positive integer ts
  = run the program for ts seconds.

//SPRAY ZONE VARIABLES:
  8.700 Minimum convection heat trans. coeff. (natural) (W/m^2K)
  right side (inside radius):
  25.000 Water and ambient temperature after spray zone(Deg C)
  spray zone condition:(heat tran.coeff.funct:h=A*C*W^n(1-bT))
  (Nozaki Model:A*C=0.3925,n=0.55,b=0.0075)
  1.5700 A(0=off)
  0.5500 n
  7.500E-03 b
  1 Number of zones
No. zone rol. water spray contct frac.of spray conv amb.
  starts # rad. flowrate width length angle q thr rol coeff coeff temp. z1 z2 z3 h1 h2 h3
  (mm) (m) (l/min/row) (m) (m) (Deg) (W/m^2K) (DegC)
1 856.0 1 0.0630 67.691 1.640 0.050 10.00 0.010 0.250 8.70 34.5 0.00 0.50 1.00 1.00 1.00 1.00
  900.0 End of last spray zone (mm)
  -1 Consider Leidenfrost effect? (-1=yes;0=no)
  5 Number of points in the Leidenfrost effect curve (if above =-1)
  Next 2 lines contain Leidenfrost effect h-multipliers and temperatures
  1.0 2.5 1.8 1.3 1.0
  500 600 700 800 900

  left side (outside radius):
  25.000 Water and ambient temperature after spray zone(Deg C)
  spray zone condition:(heat tran.coeff.funct:h=A*C*W^n(1-bT))
  (Nozaki Model:A*C=0.3925,n=0.55,b=0.0075)
  1.5700 A(0=off)
  0.5500 n
```

```
  7.500E-03 b
  1 Number of zones
No. zone rol. water        spray contct frac.of spray conv amb.
starts # rad. flowrate width length angle q thr rol coeff coeff temp. z1 z2 z3 h1 h2 h3
(mm) (m) (l/min/row) (m) (m) (Deg) (W/m^2K) (DegC)
1 856.0 1 0.0630 67.691 1.640 0.050 10.00 0.010 0.250 8.70 34.5 0.00 0.50 1.00 1.00 1.00 1.00
900.0 End of last spray zone (mm)
-1 Consider Leidenfrost effect? (-1=yes;0=no)
5 Number of points in the Leidenfrost effect curve (if above =-1)
Next 2 lines contain Leidenfrost effect h-multipliers and temperatures
1.0 2.5 1.8 1.3 1.0
500 600 700 800 900

//MOLD COOLING WATER PARAMETERS:
46.000 Cooling water temperature at mold top(C)
1.362 Cooling water pressure(MPa)
2 Form of cooling water velocity/flowrate(1=m/s ; 2=L/s)
71.000 9.100 Cooling water velocity/flowrate per face (WF,NF)
(> 0 cooling water from mold top to bottom
< 0 cooling water from mold bottom to top)



#2 Parameters to update every heat:
//SLAB GEOMETRY:
229.500 Slab thickness (mm)
1318.430 Slab width (mm)
900.000 Total mold length (mm)
45.000 WF Mold thickness with water channel (mm),(outer rad.,top)
45.000 WF Mold thickness with water channel (mm),(inner rad.,top)

//STEEL PROPERTIES:
0.0450 0.2050 0.0000 0.0000 0.0000 %C, %Mn, %S , %P , %Si
0.0000 0.0000 0.0000 0.0000 0.0000 %Cr, %Ni, %Cu, %Mo, %Ti
0.0450 0.0000 0.0330 0.0000 0.0000 %Al, %V, %N, %Nb, %W
0.0000 %Co,(additional components)
1000 Grade flag
(1000,304,316,317,347,410,419,420,430,999)
1 If CK simple Seg. Model wanted for default Tliq,Tsol
(1=yes,0=no)
10.000  Cooling rate used in Seg.Model(if above =1) (K/sec)
Override defaults with following constants(-1=default)
```

```
-1.00 Steel liquidus temperature (C)
-1.00 Steel solidus temperature (C)
-1.00 Steel density (g/cm^3)7000
-1.00 Heat fusion of steel (kJ/kg)243
-1.00 Steel emissivity (-)
-1.00 Steel specific heat (kJ/kg deg K)0.680
-1.00  Steel thermal conductivity (W/mK)
-1.00E+00 Steel thermal expansion coeff. (/K)



#3 Parameters to update when model is calibrated
//SIMULATION PARAMETERS:
1 Which version of Con1d to run?(1=OFF version;-1=ON version(CONONLINE))

0 New simulation or Restart (0=new; 1=restart)
800.000 Z-distance for heat balance  (mm)
0 Which shell to consider? (0=wide face; 1=narrow face)
0 What type of mold?(0=slab, 1=funnel, 2=billet, -1=shell only)
2 Which moldface to consider? (1=curved, 2=straight)
0 Is superheat treated as heatflux?
0=no; 1=yes (take default); -1=yes (enter data)
6 Number of zmm and q data points(if above = -1)
Next 2 lines contain zmm(mm) and q(kW/m2) data
0.00 25.00 480.00 780.00 1000.00 1118.00
170.00 70.00 720.00 250.00 125.00 100.00
1 Do you want (more accurate) 2d calculations in mold?
(0=no; 1=yes; 2=yes, one extra loop for better taper)
1.00 Relaxation factor for 2-D calcualtion
800.000 Max. dist. below meniscus for 2d mold calcs (mm)
(=mold length if above = 2)
4.00E-03 Time increment (s)
500 Number of slab sections
1.000 Printout interval (mm)
0.00E+00 Start output at (mm)
-1.000 Max. simulation thickness (mm)
(Usually the slab thickness)
200000 Max. number of iterations
3 Shell thermocouple numbers below hot face (less than 10)
 Next line gives the distance below surface of thermocouples(mm)
15.0 12.5 25.0
0.700 Fraction solid for shell thicknesss location (-)
```

```
1 Do you want to print all the files  for the related information for each slice?
(0=no; 1=yes;) (remark: choosing 1  would slow down the program)

//MOLD FLUX PROPERTIES:
30.00 36.40 1.20 13.40 0.80 %CaO, %SiO2, %MgO, %Na2O, %K2O
0.00 1.70 0.00 0.00 0.00 %FeO, %Fe2O3, %NiO, %MnO, %Cr2O3
5.30 0.20 0.00 0.00 0.00 %Al2O3, %TiO2, %B2O3, %Li2O, %SrO
0.00 10.80 0.00 0.00 0.00 %ZrO2,%F, %free C, %total C, %CO2
1 number of Tfsol and viscosity exponent n
Next 3 lines contain zmm(mm) and tfol and expn data
0.0
1045.00
0.850
0.30 Solid flux conductivity(W/mK)
1 number of Liquid flux conductivity data
Next 2 lines contain zmm and Tkliquid data
0.0
1.00
1.100 Flux viscosity at 1300C (poise)
2500.00 Mold flux density(kg/m^3)
250.00 Flux absorption coefficient(1/m)
-1.000 Flux index of refraction(-)
(-1 = take default f(composition)
0.900 Slag emissivity(-)
2 Form of mold powder consumption rate(1=kg/m^2; 2=kg/t)
0.400 Mold powder consumption rate
0.025 Location of peak heat flux (m)
0.800 Slag rim thickness at metal level (meniscus) (mm)
0.500 Slag rim thickness at heat flux peak (mm)
10.000 Liquid pool depth (mm)
8.000E+01 Solid flux tensile fracture strength (KPa)
8.000E+03 Solid flux compress fracture strength (KPa)
0.170 Solid flux Poisson ratio(-)
1 number of slag static friction coeff data
 Next 2 lines contain zmm and Static friction coeff
0.0
0.500
0.500 Moving friction coefficient between solid flux and mold wall

//INTERFACE HEAT TRANSFER VARIABLES:
1 Number of distance-vratio data points
```

```
(1=constant ratio of solid flux velocity
to casting speed)
Next 2 lines contain zmm(mm) and ratio(-) data
0.0
0.1750
5.000E-09 Flux/mold or shell/mold contact resistance(m^2K/W)
0.500 Mold surface emissivity(-)
6.000E-02 Air conductivity(in oscillation marks)(W/mK)
0 Osc.marks simulation flag(0=average,1=transient)
0.450 Oscillation mark depth(mm)
2.000 Width of oscillation mark (mm)
2.916 Oscillation frequency(cps)
(-1=take default cpm=2*ipm casting speed)
7.1999 Oscillation stroke(mm)

//MOLD WATER PROPERTIES:
-1.000 heat transfer coefficient(W/m^2K)
(-1=default=f(T), based on Sleicher and Rouse Eqn)
-1.000 Water heat capacity(J/kgK)(-1=default=f(T))
-1.000 Water density(kg/m3)(-1=default=f(T))

//MOLD GEOMETRY:
45.000 Narrow face (NF) mold thickness with water channel (mm)
40.000 Equivalent thickness of water box (mm)
-1.000 Mean temperature diff between hot & cold face of NF (C)
18.000 25.000 Cooling water channel depth(mm)(WF,NF)
5.000 5.000 Cooling water channel width(mm)(WF,NF)
16.500 29.000 Channel distance(center to center)(mm)(WF,NF)
-1.000 -1.000 Total channel cross sectional area(mm^2)(WF,NF)
(served by water flow line where temp rise measured)
315.000 315.000 Mold thermal conductivity(W/mK)(WF,NF)
1.60E-05 Mold thermal expansion coeff. (1/K)
0.000 funnel height (mm)
0.000 funnel width (mm)
0.000 funnel depth at mold top (mm)
8.000 Machine outer radius(m)
8.000 Machine inner radius(m)
-1 Mold offset to account for geometry simplification effect(-1=default, 1=user enter)
0.000 0.000  (mm, if above=1, user entered mold offset, WF and NF)
5 Number of mold coating/plating thickness changes down mold
No. Scale Ni Cr Others Air Z-positions unit
```

```
1 0.000 0     0     0.1     0     0     0
2 0.000 0     0     0.12 0    25.0000 0
3 0.000 0.000 0.000 0.200 0.000 150.000 0
4 0.000 0.000 0.000 0.300 0.000 450.000 0
5 0.000 0.000 0.000 0.600 0.000 900.000 0
0.550 72.100 67.000 17.500 0.060 Conductivity (W/mK)

//MOLD THERMOCOUPLES:
0.00E+00 Offset distance towards hot face (mm)
70 Total number of thermocouples
No. Distance beneath Distance below
hot surface(mm)  meniscus(mm)
1 10.5 -60
2 10.5 -55
3 10.5 -50
4 10.5 -45
5 10.5 -40
6 10.5 -35
7 10.5 -30
8 10.5 -25
9 10.5 -20
10 10.5 -15
11 10.5 -10
12 10.5 -5
13 10.5 0
14 10.5 5
15 10.5 10
16 10.5 15
17 10.5 20
18 10.5 25
19 10.5 30
20 10.5 35
21 10.5 40
22 10.5 45
23 10.5 50
24 10.5 55
25 10.5 60
26 10.5 65
27 10.5 70
28 10.5 75
29 10.5 80
```

```
30 10.5 85
31 10.5 90
32 10.5 95
33 10.5 100
34 10.5 105
35 10.5 110
36 10.5 115
37 10.5 120
38 10.5 125
39 10.5 130
40 10.5 135
41 10.5 140
42 10.5 145
43 10.5 150
44 10.5 155
45 10.5 160
46 10.5 165
47 10.5 170
48 10.5 175
49 10.5 180
50 10.5 185
51 10.5 190
52 10.5 195
53 10.5 200
54 10.5 205
55 10.5 210
56 10.5 215
57 10.5 220
58 10.5 225
59 10.5 230
60 10.5 235
61 10.5 240
62 10.5 245
63 10.5 250
64 10.5 255
65 10.5 260
66 10.5 265
67 10.5 270.00
68 10.5 275.00
69 10.5 280.00
70 10.5 285.00
```

APPENDIX C
ABAQUS INPUT FILES

This section contains example code from this work and the necessary input files needed to recreate the models described including the use of the MPC cracking subroutine which requires special treatment of the nodes to recreate the boundary condition at the symmetry plane and also allow for nodal separation.

Copyright (c) <2020> <Matthew L.S. Zappulla> Permission is hereby granted, free of charge, to any person obtaining a copy of this software and associated documentation files (the "Software"), to deal in the Software without restriction, including without limitation the rights to use, copy, modify, merge, publish, distribute, sublicense, and/or sell copies of the Software, and to permit persons to whom the Software is furnished to do so, subject to the following conditions: The above copyright notice and this permission notice shall be included in all copies or substantial portions of the Software. THE SOFTWARE IS PROVIDED "AS IS", WITHOUT WARRANTY OF ANY KIND, EXPRESS OR IMPLIED, INCLUDING BUT NOT LIMITED TO THE WARRANTIES OF MERCHANTABILITY, FITNESS FOR A PARTICULAR PURPOSE AND NONINFRINGEMENT. IN NO EVENT SHALL THE AUTHORS OR COPYRIGHT HOLDERS BE LIABLE FOR ANY CLAIM, DAMAGES OR OTHER LIABILITY, WHETHER IN AN ACTION OF CONTRACT, TORT OR OTHERWISE, ARISING FROM, OUT OF OR IN CONNECTION WITH THE SOFTWARE OR THE USE OR OTHER DEALINGS IN THE SOFTWARE.

C.1 Thermcouple Analysis Abaqus Input File

```
**********************************************************************************
**                                                                              **
**         INPUT FILE FOR 2D DEPRESSION MODEL SOLIDIFICATION STRESS PROBLEM     **
**                                                                              **
**           THIS FILE IS INTENDED FOR USE WITH THE CCC USER SUBROUTINE FILES    **
**                                                                              **
**                      CREATED BY MATTHEW L.S. ZAPPULLA                        **
**                                                                              **
**********************************************************************************
*PREPRINT, PARSUBSTITUTION=YES
*PARAMETER
# DEFINE THE DESIRED NUMBER OF ELEMENTS IN THE X AND Y DIRECTIONS (MUST BE INTEGER)
 EX = 40 # from study 'Mesh'
```

```
 EY = 160 # from study 'Mesh'

 WALL_EX = 1 # from study 'Mesh'
 WALL_EY = 320 # from study 'Mesh'

# DEFINE THE RUN TIME OF THE JOB IN SECONDS
 RUNTIME = 30.0


# DEFINE THE STARTING,MINIMUM, AND MAXIMUM STEP SIZE
 STARTSTEP = 1e-4
 MINSTEP   =  1e-30
 MAXSTEP   = 1.0

# DEFINE THE MAXIMUM NUMBER OF INCREMENTS FOR THE SIMULATION
 INCREMENTS = 10000000

# DEFINE THE TEMPERATURE CHANGE TO CONTROL THE STEP SIZE
 DELTATEMP = 10.0

# DEFINE THE LENGTH OF YOUR DOMAIN IN MM (MUST BE DECIMATED)
 LENGTH = 20.0

 WALL_LENGTH = 28.35

# DEFINE THE INITIAL TEMPERATURE OF THE DOMAIN (USUALLY AT LEAST 5DEG>LIQUIDUS)
 INITIALTEMP = 1554.0

# DEFINE THE OUTPUT FREQUENCY IN SECONDS
 OUTTIMEINT = 0.1

# WIDTH OF THE DOMAIN AUTOMATICALLY CALCULATED USING SQUARE ELEMENTS
 WIDTH = 80.0

 WALL_WIDTH = 80.0
**************************************************************
**************************************************************
**                       END OF USER INPUT AREA
**                  MODIFY BELOW AT YOUR OWN RISK
**************************************************************
**************************************************************
```

```
**                                MESH DEFINITION          **
**************************************************************
*PART, NAME=LINEAR_SLICE
  *PARAMETER
   L_NX = EX+1
   L_NY = EY+1
   L_SW = 1
   L_SE = L_NX
   L_NE = L_NX*L_NY
   L_NW = L_NE-L_NX+1
   L_NW_OFF = L_NW+1
   L_ND_REF = L_NE+1
   L_DX = LENGTH/EX
   L_DY = WIDTH/EY
   L_Y_BOT  = -0.5*WIDTH
   L_Y_TOP  =  0.5*WIDTH
   L_ME_SW = 1
   L_ME_SE = 2
   L_ME_NW = L_NX+1
   L_ME_NE = L_NX+2
   L_E_NE = (EX*EY)-EX+1
   SWALL_SIZE = EX*EY
  *NODE
   <L_SW>, 0.0, <L_Y_BOT>
   <L_NW>, 0.0, <L_Y_TOP>
  *NGEN, NSET=FREE
   <L_SW>, <L_NW>, <L_NX>
  *NODE
   <L_SE>, <LENGTH>, <L_Y_BOT>
   <L_NE>, <LENGTH>, <L_Y_TOP>
  *NGEN, NSET=WALL
   <L_SE>, <L_NE>, <L_NX>
  *NFILL, NSET=ALL
   FREE, WALL, <EX>, 1
  *NODE, NSET=RP
   <L_ND_REF>, 0.0, 0.0
  *NSET, NSET=BOTTOM_EDGE, GENERATE
   1,  <L_NX>, 1
  *NSET, NSET=TOP_EDGE, GENERATE
   <L_NW_OFF>, <L_NE>, 1
  *NSET, NSET=GPE_EDGE, GENERATE
```

```
   2, <L_NX>, 1
  *NSET, NSET=CENTER_HOLD, GENERATE
   3281, 3321, 1
  *ELEMENT, TYPE=CPEG4HT
   1, <L_ME_SW>, <L_ME_SE>, <L_ME_NE>, <L_ME_NW>
  *ELGEN, ELSET=ALL
   1, <EX>, 1, 1, <EY>, <L_NX>, <EX>
  *ELSET, ELSET=WALL, GENERATE
   <EX>, <SWALL_SIZE>, <EX>
  *SURFACE, NAME=WALL, TYPE=ELEMENT
   WALL, S2
*Solid Section, elset=ALL, material=STEEL, REF NODE=RP
1.,
*END PART
**############################################################*
*PART, NAME=WALL
  *PARAMETER
   WALL_NX = WALL_EX+1
   WALL_NY = WALL_EY+1
   WALL_SW = 1
   WALL_SE = WALL_NX
   WALL_NE = WALL_NX*WALL_NY
   WALL_NW = WALL_NE-WALL_NX+1
   WALL_NW_OFF = WALL_NW+1
   WALL_ND_REF = WALL_NE+1
   WALL_DX = WALL_LENGTH/WALL_EX
   WALL_DY = WALL_WIDTH/WALL_EY
   WALL_Y_BOT  = -0.5*WALL_WIDTH
   WALL_Y_TOP  =  0.5*WALL_WIDTH
   WALL_ME_SW = 1
   WALL_ME_SE = 2
   WALL_ME_NW = WALL_NX+1
   WALL_ME_NE = WALL_NX+2
   WALL_E_NE = (WALL_EX*WALL_EY)-WALL_EX+1
   WALL_SIZE = WALL_EX*WALL_EY
  *NODE
   <WALL_SW>, 0.0, <WALL_Y_BOT>
   <WALL_NW>, 0.0, <WALL_Y_TOP>
  *NGEN, NSET=FREE
   <WALL_SW>, <WALL_NW>, <WALL_NX>
  *NODE
```

```
   <WALL_SE>, <WALL_LENGTH>, <WALL_Y_BOT>
   <WALL_NE>, <WALL_LENGTH>, <WALL_Y_TOP>
  *NGEN, NSET=WALL
   <WALL_SE>, <WALL_NE>, <WALL_NX>
  *NFILL, NSET=ALL
   FREE, WALL, <WALL_EX>, 1
  *NODE, NSET=RP
   <WALL_ND_REF>, 0.0, 0.0
  *NSET, NSET=WALL
  1, <WALL_NW>, <WALL_NX>
  *NSET, NSET=BOTTOM_EDGE, GENERATE
   1, <WALL_SE>, 1
  *NSET, NSET=GPE_EDGE, GENERATE
   <WALL_NW_OFF>, <WALL_NE>, 1
  *ELEMENT, TYPE=CPEG4HT
   1, <WALL_ME_SW>, <WALL_ME_SE>, <WALL_ME_NE>, <WALL_ME_NW>
  *ELGEN, ELSET=ALL
   1, <WALL_EX>, 1, 1, <WALL_EY>, <WALL_NX>, <WALL_EX>
  *ELSET, ELSET=WALL, GENERATE
   1, <WALL_E_NE>, <WALL_EX>
  *SURFACE, NAME=WALL, TYPE=ELEMENT
   WALL, S4
  *ELSET, ELSET=ColdFace, GENERATE
   <WALL_EX>, <WALL_SIZE>, <WALL_EX>
  *SURFACE, NAME=ColdFace, TYPE=ELEMENT
   ColdFace, S2
*Solid Section, elset=ALL, material=MOLD, REF NODE=RP
1.,
*END PART
**##########################################################*
**                            ASSEMBLY DEFINITION                            **
**##########################################################*
*ASSEMBLY, NAME=ASSEMBLY
  *INSTANCE, NAME=STRAND, PART=LINEAR_SLICE
  *END INSTANCE
  *INSTANCE, NAME=WALL, PART=WALL
   <LENGTH>, 0.0
  *END INSTANCE
*EQUATION
  2
  STRAND.TOP_EDGE, 2, 1.0, STRAND.<L_NW>, 2, -1.0
```

```
*END ASSEMBLY
**##########################################################*
**                  MATERIAL PROPERTY DEFINITIONS
**##########################################################*
*Material, name=MOLD
*Conductivity
315.,
*Density
 8.9e-09,
*Elastic
120000., 0.2
*Specific Heat
 0.9e+07,
*HEAT GENERATION
*MATERIAL, NAME=STEEL
*DENSITY
 7.5e-09,
*EXPANSION, USER, TYPE=ISO
*USER MATERIAL, CONSTANTS=0, TYPE=THERMAL
*USER MATERIAL, CONSTANTS=0, TYPE=MECHANICAL
*DEPVAR
   23
    1, FL,    "FRACTION LIQUID"
    2, FD,    "FRACTION DELTA"
    3, FG,    "FRACTION GAMMA"
    4, FA,    "FRACTION ALPHA"
    5, EE11,  "ELASTIC STRAIN 11"
    6, EE22,  "ELASTIC STRAIN 22"
    7, EE33,  "ELASTIC STRAIN 33"
    8, EE12,  "ELASTIC STRAIN 12"
    9, EEBAR, "EFFECTIVE ELASTIC STRAIN"
   10, EP11,  "PLASTIC STRAIN 11"
   11, EP22,  "PLASTIC STRAIN 22"
   12, EP33,  "PLASTIC STRAIN 33"
   13, EP12,  "PLASTIC STRAIN 12"
   14, EPBAR, "EFFECTIVE PLASTIC STRAIN"
   15, EPDOT, "EFFECTIVE PLASTIC STRAIN RATE"
   16, EF11,  "FLUID STRAIN 11"
   17, EF22,  "FLUID STRAIN 22"
   18, EF33,  "FLUID STRAIN 33"
   19, EF12,  "FLUID STRAIN 12"
```

```
   20, EFBAR, "EFFECTIVE FLUID STRAIN"
   21, BTZ,   "BRITTLE TEMPERATURE ZONE"
   22, EC,    "CRITICAL STRAIN"
   23, ED22,  "DAMAGE STRAIN 22"
*PHYSICAL CONSTANTS, ABSOLUTE ZERO=-273.15, STEFAN BOLTZMANN=56.704e-09
**********************************************************************
**                     INTERACTION PROPERTIES                       *
**********************************************************************
****
*Contact Pair, interaction=MoldSteelFriction, type=SURFACE TO SURFACE, adjust=0.0
STRAND.Wall, WALL.WALL
*Surface Interaction, name=MoldSteelFriction
*FRICTION
0.15
*GAP CONDUCTANCE, USER
**************************************************************
**                     PREDEFINED FIELDS                        *
**************************************************************
*Initial Conditions, type=TEMPERATURE
STRAND.ALL, <INITIALTEMP>
WALL.ALL, 100.0
**************************************************************
**                     STEP DEFINITION                         *
**************************************************************
*STEP, NAME=STEP, INC=<INCREMENTS>, NLGEOM=YES
*Coupled Temperature-displacement, creep=none, deltmx=<DELTATEMP>
<STARTSTEP>, <RUNTIME>, <MINSTEP>, <MAXSTEP>
***CONTACT CONTROLS, STABILIZE
*SOLUTION TECHNIQUE, TYPE=SEPARATED
*CONTROLS, ANALYSIS=DISCONTINUOUS
*CONTROLS, PARAMETERS=FIELD
** 0.005, 0.01 are defaults, (inc displ/avg inc strain) and (cor inc displ/inc displ)
0.030, 0.06
*CONTROLS, PARAMETERS=TIME INCREMENTATION
10, , ,20,8,5, ,20, , , , ,
0.24,0.4,0.5, , ,0.2, ,
**************************************************************
**                     BOUNDARY CONDITIONS                      *
**************************************************************
*Boundary, TYPE=DISPLACEMENT
STRAND.BOTTOM_EDGE, 2, 2, 0.0
```

```
STRAND.RP, 4, 5, 0.0
WALL.RP, 4, 5, 0.0
WALL.ALL, 1, 2, 0.0
STRAND.CENTER_HOLD, 2,2, 0.0
STRAND.<L_NW>,2, 2, 0.0
**************************************************************
**                                   LOADS                                    *
**************************************************************
*DSLOAD
 STRAND.WALL, PNU
*SFILM
 WALL.ColdFace, FNU
**************************************************************
**                          OUTPUT REQUESTS
**************************************************************
*RESTART, WRITE, OVERLAY, NUMBER INTERVAL=250
*Output, field, time interval=<OUTTIMEINT>
    *NODE OUTPUT
     NT, UT, TF, RF, RT, VF
    *ELEMENT OUTPUT
     HFL, S, E, THE, EE, SDV, NFORC
    *CONTACT OUTPUT, VARIABLE=ALL
*END STEP
```

C.2 Tata Steel Cracking Model Input File

```
**********************************************************************************
**                                                                              #*
**   INPUT FILE FOR 2D CRACKED DEPRESSION MODEL SOLIDIFICATION STRESS PROBLEM    #*
**                                                                              #*
**           THIS FILE IS INTENDED FOR USE WITH THE CCC USER SUBROUTINE FILES    #*
**                                                                              #*
**                      CREATED BY MATTHEW L.S. ZAPPULLA                        #*
**                                                                              #*
**********************************************************************************
*PREPRINT, PARSUBSTITUTION=YES
*PARAMETER
# DEFINE THE DESIRED NUMBER OF ELEMENTS IN THE X AND Y DIRECTIONS (MUST BE INTEGER)
 EX = 40 # from study 'Mesh'
 EY = 160 # from study 'Mesh'

 WALL_EX = 1 # from study 'Mesh'
```

```
 WALL_EY = 320 # from study 'Mesh'

# DEFINE THE RUN TIME OF THE JOB IN SECONDS
 RUNTIME = 30.0

# DEFINE THE STARTING,MINIMUM, AND MAXIMUM STEP SIZE
 STARTSTEP = 1e-4
 MINSTEP   =  1e-30
 MAXSTEP   = 1.0

# DEFINE THE MAXIMUM NUMBER OF INCREMENTS FOR THE SIMULATION
 INCREMENTS = 10000000

# DEFINE THE TEMPERATURE CHANGE TO CONTROL THE STEP SIZE
 DELTATEMP = 10.0

# DEFINE THE LENGTH OF YOUR DOMAIN IN MM (MUST BE DECIMATED)
 LENGTH = 20.0

 WALL_LENGTH = 28.35

# DEFINE THE INITIAL TEMPERATURE OF THE DOMAIN (USUALLY AT LEAST 5DEG>LIQUIDUS)
 INITIALTEMP = 1554.0

# DEFINE THE OUTPUT FREQUENCY IN SECONDS
 OUTTIMEINT = 0.1

# WIDTH OF THE DOMAIN AUTOMATICALLY CALCULATED USING SQUARE ELEMENTS
 WIDTH = 80.0

 WALL_WIDTH = 80.0
**************************************************************
**************************************************************
**                      END OF USER INPUT AREA
**                 MODIFY BELOW AT YOUR OWN RISK
**************************************************************
**************************************************************
**                               MESH DEFINITION           **
**************************************************************
*PART, NAME=LINEAR_SLICE
  *PARAMETER
```

```
 L_NX = EX+1
 L_NY = EY+1
 L_SW = 1
 L_SE = L_NX
 L_NE = L_NX*L_NY
 L_NW = L_NE-L_NX+1
 L_NW_OFF = L_NW+1
 L_ND_REF = L_NE+1
 L_DX = LENGTH/EX
 L_DY = WIDTH/EY
 L_Y_BOT  = -0.5*WIDTH
 L_Y_TOP  =  0.5*WIDTH
 L_ME_SW = 1
 L_ME_SE = 2
 L_ME_NW = L_NX+1
 L_ME_NE = L_NX+2
 L_E_NE = (EX*EY)-EX+1
 SWALL_SIZE = EX*EY
*NODE
 <L_SW>, 0.0, <L_Y_BOT>
 <L_NW>, 0.0, <L_Y_TOP>
*NGEN, NSET=FREE
 <L_SW>, <L_NW>, <L_NX>
*NODE
 <L_SE>, <LENGTH>, <L_Y_BOT>
 <L_NE>, <LENGTH>, <L_Y_TOP>
*NGEN, NSET=WALL
 <L_SE>, <L_NE>, <L_NX>
*NFILL, NSET=ALL
 FREE, WALL, <EX>, 1
*NODE, NSET=RP
 <L_ND_REF>, 0.0, 0.0
*NSET, NSET=BOTTOM_EDGE, GENERATE
 1,  <L_NX>, 1
*NSET, NSET=TOP_EDGE, GENERATE
 <L_NW_OFF>, <L_NE>, 1
*NSET, NSET=GPE_EDGE, GENERATE
 2, <L_NX>, 1
*ELEMENT, TYPE=CPEG4HT
 1, <L_ME_SW>, <L_ME_SE>, <L_ME_NE>, <L_ME_NW>
*ELGEN, ELSET=ALL
```

```
   1, <EX>, 1, 1, <EY>, <L_NX>, <EX>
  *ELSET, ELSET=WALL, GENERATE
   <EX>, <SWALL_SIZE>, <EX>
  *ELSET, ELSET=BTM, GENERATE
   1, 40, 1
  *SURFACE, NAME=WALL, TYPE=ELEMENT
   WALL, S2
  *SURFACE, NAME=BTM, TYPE=ELEMENT
   BTM, S1
*Solid Section, elset=ALL, material=STEEL, REF NODE=RP
1.,
*END PART
**############################################################*
*PART, NAME=WALL
  *PARAMETER
   WALL_NX = WALL_EX+1
   WALL_NY = WALL_EY+1
   WALL_SW = 1
   WALL_SE = WALL_NX
   WALL_NE = WALL_NX*WALL_NY
   WALL_NW = WALL_NE-WALL_NX+1
   WALL_NW_OFF = WALL_NW+1
   WALL_ND_REF = WALL_NE+1
   WALL_DX = WALL_LENGTH/WALL_EX
   WALL_DY = WALL_WIDTH/WALL_EY
   WALL_Y_BOT  = -0.5*WALL_WIDTH
   WALL_Y_TOP  =  0.5*WALL_WIDTH
   WALL_ME_SW = 1
   WALL_ME_SE = 2
   WALL_ME_NW = WALL_NX+1
   WALL_ME_NE = WALL_NX+2
   WALL_E_NE = (WALL_EX*WALL_EY)-WALL_EX+1
   WALL_SIZE = WALL_EX*WALL_EY
  *NODE
   <WALL_SW>, 0.0, <WALL_Y_BOT>
   <WALL_NW>, 0.0, <WALL_Y_TOP>
  *NGEN, NSET=FREE
   <WALL_SW>, <WALL_NW>, <WALL_NX>
  *NODE
   <WALL_SE>, <WALL_LENGTH>, <WALL_Y_BOT>
   <WALL_NE>, <WALL_LENGTH>, <WALL_Y_TOP>
```

```
  *NGEN, NSET=WALL
   <WALL_SE>, <WALL_NE>, <WALL_NX>
  *NFILL, NSET=ALL
   FREE, WALL, <WALL_EX>, 1
  *NODE, NSET=RP
   <WALL_ND_REF>, 0.0, 0.0
  *NSET, NSET=WALL
  1, <WALL_NW>, <WALL_NX>
  *NSET, NSET=BOTTOM_EDGE, GENERATE
   1, <WALL_SE>, 1
  *NSET, NSET=GPE_EDGE, GENERATE
   <WALL_NW_OFF>, <WALL_NE>, 1
  *ELEMENT, TYPE=CPEG4HT
   1, <WALL_ME_SW>, <WALL_ME_SE>, <WALL_ME_NE>, <WALL_ME_NW>
  *ELGEN, ELSET=ALL
   1, <WALL_EX>, 1, 1, <WALL_EY>, <WALL_NX>, <WALL_EX>
  *ELSET, ELSET=WALL, GENERATE
   1, <WALL_E_NE>, <WALL_EX>
  *SURFACE, NAME=WALL, TYPE=ELEMENT
   WALL, S4
  *ELSET, ELSET=ColdFace, GENERATE
   <WALL_EX>, <WALL_SIZE>, <WALL_EX>
  *SURFACE, NAME=ColdFace, TYPE=ELEMENT
   ColdFace, S2
*Solid Section, elset=ALL, material=MOLD, REF NODE=RP
1.,
*END PART
*PART, NAME=FAKE
  *NODE
   1, 0.0, -20.5
   42, 0.0, -20.0
  *NODE
   41, 20.0, -20.5
   82, 20.0, -20.0
  *NGEN, NSET=FIX
   1, 41, 1
  *NGEN
   42, 82, 1
  *NSET, NSET=TOP, generate
   42, 82, 1
  *NODE, NSET=RP
```

```
   100, 0.0, 0.0
  *NSET, NSET=ALL, GENERATE
   1,82,1
  *ELEMENT, TYPE=CPEG4HT
   1, 1, 2, 43, 42
  *ELGEN, ELSET=ALL
   1, 40, 1, 1, 1, 41, 40
  *SURFACE, NAME=TOP, TYPE=ELEMENT
   ALL, S3
  *SURFACE, NAME=FIX, TYPE=ELEMENT
   ALL, S1
*Solid Section, elset=ALL, material=MOLD, REF NODE=RP
1.,
*END PART
**############################################################*
**                            ASSEMBLY DEFINITION                            **
**############################################################*
*ASSEMBLY, NAME=ASSEMBLY
  *INSTANCE, NAME=STRAND, PART=LINEAR_SLICE
  *END INSTANCE
  *INSTANCE, NAME=FAKE, PART=FAKE
   0.0, -20.0
  *END INSTANCE
  *INSTANCE, NAME=WALL, PART=WALL
   <LENGTH>, 0.0
  *END INSTANCE
*EQUATION
  2
  STRAND.TOP_EDGE, 2, 1.0, STRAND.<L_NW>, 2, -1.0
*MPC, MODE=DOF, USER
41,FAKE.42,STRAND.1
40,FAKE.43,STRAND.2
39,FAKE.44,STRAND.3
38,FAKE.45,STRAND.4
37,FAKE.46,STRAND.5
36,FAKE.47,STRAND.6
35,FAKE.48,STRAND.7
34,FAKE.49,STRAND.8
33,FAKE.50,STRAND.9
32,FAKE.51,STRAND.10
31,FAKE.52,STRAND.11
```

```
30,FAKE.53,STRAND.12
29,FAKE.54,STRAND.13
28,FAKE.55,STRAND.14
27,FAKE.56,STRAND.15
26,FAKE.57,STRAND.16
25,FAKE.58,STRAND.17
24,FAKE.59,STRAND.18
23,FAKE.60,STRAND.19
22,FAKE.61,STRAND.20
21,FAKE.62,STRAND.21
20,FAKE.63,STRAND.22
19,FAKE.64,STRAND.23
18,FAKE.65,STRAND.24
17,FAKE.66,STRAND.25
16,FAKE.67,STRAND.26
15,FAKE.68,STRAND.27
14,FAKE.69,STRAND.28
13,FAKE.70,STRAND.29
12,FAKE.71,STRAND.30
11,FAKE.72,STRAND.31
10,FAKE.73,STRAND.32
9,FAKE.74,STRAND.33
8,FAKE.75,STRAND.34
7,FAKE.76,STRAND.35
6,FAKE.77,STRAND.36
5,FAKE.78,STRAND.37
4,FAKE.79,STRAND.38
3,FAKE.80,STRAND.39
2,FAKE.81,STRAND.40
1,FAKE.82,STRAND.41
*END ASSEMBLY
**##########################################################*
**                 MATERIAL PROPERTY DEFINITIONS
**##########################################################*
*Material, name=MOLD
*Conductivity
315.,
*Density
 8.9e-09,
*Elastic
120000., 0.2
```

```
*Specific Heat
 0.9e+07,
*HEAT GENERATION
*MATERIAL, NAME=STEEL
*DENSITY
 7.5e-09,
*EXPANSION, USER, TYPE=ISO
*USER MATERIAL, CONSTANTS=0, TYPE=THERMAL
*USER MATERIAL, CONSTANTS=0, TYPE=MECHANICAL
*DEPVAR
   23
    1, FL,    "FRACTION LIQUID"
    2, FD,    "FRACTION DELTA"
    3, FG,    "FRACTION GAMMA"
    4, FA,    "FRACTION ALPHA"
    5, EE11,  "ELASTIC STRAIN 11"
    6, EE22,  "ELASTIC STRAIN 22"
    7, EE33,  "ELASTIC STRAIN 33"
    8, EE12,  "ELASTIC STRAIN 12"
    9, EEBAR, "EFFECTIVE ELASTIC STRAIN"
   10, EP11,  "PLASTIC STRAIN 11"
   11, EP22,  "PLASTIC STRAIN 22"
   12, EP33,  "PLASTIC STRAIN 33"
   13, EP12,  "PLASTIC STRAIN 12"
   14, EPBAR, "EFFECTIVE PLASTIC STRAIN"
   15, EPDOT, "EFFECTIVE PLASTIC STRAIN RATE"
   16, EF11,  "FLUID STRAIN 11"
   17, EF22,  "FLUID STRAIN 22"
   18, EF33,  "FLUID STRAIN 33"
   19, EF12,  "FLUID STRAIN 12"
   20, EFBAR, "EFFECTIVE FLUID STRAIN"
   21, BTZ,   "BRITTLE TEMPERATURE ZONE"
   22, EC,    "CRITICAL STRAIN"
   23, ED22,  "DAMAGE STRAIN 22"
*PHYSICAL CONSTANTS, ABSOLUTE ZERO=-273.15, STEFAN BOLTZMANN=56.704e-09
**********************************************************************
**                      INTERACTION PROPERTIES                        *
**********************************************************************
****
*Contact Pair, interaction=MoldSteelFriction, type=SURFACE TO SURFACE, adjust=0.0
STRAND.Wall, WALL.WALL
```

```
*Surface Interaction, name=MoldSteelFriction
*FRICTION
0.15
*GAP CONDUCTANCE, USER
*Contact Pair, interaction=DummyThing, type=SURFACE TO SURFACE, adjust=0.0
STRAND.BTM, FAKE.TOP
*Surface Interaction, name=DummyThing
** *GAP CONDUCTANCE
** 3.0E3, 0.0
** 3.0E3, 1.0
** *SURFACE BEHAVIOR, DIRECT, PRESSURE-OVERCLOSURE=HARD
**************************************************************
**                      PREDEFINED FIELDS                     *
**************************************************************
***Initial Conditions, type=solution, user
*Initial Conditions, type=TEMPERATURE
STRAND.ALL, <INITIALTEMP>
WALL.ALL, 100.0
FAKE.ALL, 100.0
**************************************************************
**                      STEP DEFINITION                       *
**************************************************************
*STEP, NAME=STEP, INC=<INCREMENTS>, NLGEOM=YES
*Coupled Temperature-displacement, creep=none, deltmx=<DELTATEMP>
<STARTSTEP>, <RUNTIME>, <MINSTEP>, <MAXSTEP>
***CONTACT CONTROLS, STABILIZE
*SOLUTION TECHNIQUE, TYPE=SEPARATED
*CONTROLS, ANALYSIS=DISCONTINUOUS
*CONTROLS, PARAMETERS=FIELD
** 0.005, 0.01 are defaults, (inc displ/avg inc strain) and (cor inc displ/inc displ)
0.030, 0.06
*CONTROLS, PARAMETERS=TIME INCREMENTATION
10, , ,20,8,5, ,20, , , , ,
0.24,0.4,0.5, , ,0.2, ,
**************************************************************
**                      BOUNDARY CONDITIONS                   *
**************************************************************
*Boundary, TYPE=DISPLACEMENT
**STRAND.BOTTOM_EDGE, 2, 2, 0.0
**STRAND-C.<L_SE>, 1, 1, 0.0
STRAND.RP, 4, 5, 0.0
```

```
WALL.RP, 4, 5, 0.0
WALL.ALL, 1, 2, 0.0
FAKE.FIX, 1, 2, 0.0
FAKE.RP, 4, 5, 0.0
**STRAND.<L_NW>,2, 2, 1.0
**STRAND.WALL, 1, 1, 0.0
***BOUNDARY
**WALL.ALL, 11, 11, 150.0
**STRAND.WALL, 1, 1, 0.0
**************************************************************
**                                   LOADS                                    *
**************************************************************
*DSLOAD
 STRAND.WALL, PNU
*SFILM
 WALL.ColdFace, FNU
**************************************************************
**                          OUTPUT REQUESTS
**************************************************************
*RESTART, WRITE, OVERLAY, NUMBER INTERVAL=250
*Output, field, time interval=<OUTTIMEINT>
**Output, field, FREQUENCY=1
    *NODE OUTPUT
     NT, UT, TF, RF, RT, VF
    *ELEMENT OUTPUT
     HFL, S, E, THE, EE, SDV, NFORC
    *CONTACT OUTPUT, VARIABLE=ALL
*END STEP
```

APPENDIX D

ABAQUS FORTRAN SUBROUTINES

This section contains example code from this work and the necessary subroutine needed to recreate the models described. Basic descriptions taken from the Abaqus subroutine manual and provided [77].

Copyright (c) <2020> <Matthew L.S. Zappulla> Permission is hereby granted, free of charge, to any person obtaining a copy of this software and associated documentation files (the "Software"), to deal in the Software without restriction, including without limitation the rights to use, copy, modify, merge, publish, distribute, sublicense, and/or sell copies of the Software, and to permit persons to whom the Software is furnished to do so, subject to the following conditions: The above copyright notice and this permission notice shall be included in all copies or substantial portions of the Software. THE SOFTWARE IS PROVIDED "AS IS", WITHOUT WARRANTY OF ANY KIND, EXPRESS OR IMPLIED, INCLUDING BUT NOT LIMITED TO THE WARRANTIES OF MERCHANTABILITY, FITNESS FOR A PARTICULAR PURPOSE AND NONINFRINGEMENT. IN NO EVENT SHALL THE AUTHORS OR COPYRIGHT HOLDERS BE LIABLE FOR ANY CLAIM, DAMAGES OR OTHER LIABILITY, WHETHER IN AN ACTION OF CONTRACT, TORT OR OTHERWISE, ARISING FROM, OUT OF OR IN CONNECTION WITH THE SOFTWARE OR THE USE OR OTHER DEALINGS IN THE SOFTWARE.

D.1 FILM for ROM mold

This subroutine is used to provide film coefficients and sink temperatures for fully coupled thermal-stress analysis.

```
CCCCCCCCCCCCCCCCCCCCCCCCCCCCCCCCCCCCCCCCCCCCCCCCCCCCCCCCCCCCCCCCCCCCCCCCCCCCCCC
C                                                                      C
C           INTERNAL ABAQUS FILM CONVECTION SUBROUTINE                 C
C           SETUP SPECIFICALLY FOR TATA STEEL CASTER 21                C
C                                                                      C
C            CREATED BY MATTHEW L.S. ZAPPULLA, MAY 2019                C
C                                                                      C
CCCCCCCCCCCCCCCCCCCCCCCCCCCCCCCCCCCCCCCCCCCCCCCCCCCCCCCCCCCCCCCCCCCCCCCCCCCCCCC
```

```
      subroutine film(h, sink, temp, kstep, kinc, time, noel, npt,
     &                coords, jltyp, field, nfield, sname, node, area)
c
      include 'aba_param.inc'
c
      dimension h(2), time(2), coords(3), field(nfield)
      character*80 sname

      double precision t, vcast, z, zmen
c
      DOUBLE PRECISION Kmold, Dcoat, Kcoat, Dfoul, Kfoul, Dc, Pc, Wc
      DOUBLE PRECISION Beta, Hfins, hwa, Hmold, Hroots, Hcold, Qhot
      DOUBLE PRECISION twa, Dmold
      DOUBLE PRECISION TWater(811), HWater(811), Tim(811)
CCCCCCCCCCCCCCCCCCCCCCCCCCCCCCCCCCCCCCCCCCCCCCCCCCCCCCCCCCCCCCCCCCCCCCCCCC
        Tim(1)=0.0d0
        Tim(2)=0.0458330d0
        Tim(3)=0.083330d0
        Tim(4)=0.1291660d0
        Tim(5)=0.1666660d0
        Tim(6)=0.20d0
        Tim(7)=0.20d0
        Tim(8)=0.291666660d0
        Tim(9)=0.3370d0
        Tim(10)=0.370d0
        Tim(11)=0.420833330d0
        Tim(12)=0.458333330d0
        Tim(13)=0.504166660d0
        Tim(14)=0.545833330d0
        Tim(15)=0.583333330d0
        Tim(16)=0.629166660d0
        Tim(17)=0.666666660d0
        Tim(18)=0.7120d0
```

```
Tim(19)=0.70d0
Tim(20)=0.791666660d0
Tim(21)=0.8370d0
Tim(22)=0.870d0
Tim(23)=0.920833330d0
Tim(24)=0.958333330d0
Tim(25)=1.0d0
Tim(26)=1.045833330d0
Tim(27)=1.083333330d0
Tim(28)=1.129166660d0
Tim(29)=1.166666660d0
Tim(30)=1.2120d0
Tim(31)=1.20d0
Tim(32)=1.291666660d0
Tim(33)=1.3370d0
Tim(34)=1.370d0
Tim(35)=1.420833330d0
Tim(36)=1.458333330d0
Tim(37)=1.0d0
Tim(38)=1.545833330d0
Tim(39)=1.583333330d0
Tim(40)=1.629166660d0
Tim(41)=1.666666660d0
Tim(42)=1.7120d0
Tim(43)=1.70d0
Tim(44)=1.791666660d0
Tim(45)=1.8370d0
Tim(46)=1.870d0
Tim(47)=1.920833330d0
Tim(48)=1.958333330d0
Tim(49)=2.0d0
Tim(50)=2.045833330d0
Tim(51)=2.083333330d0
```

```
Tim(52)=2.129166660d0
Tim(53)=2.166666660d0
Tim(54)=2.2120d0
Tim(55)=2.20d0
Tim(56)=2.291666660d0
Tim(57)=2.3370d0
Tim(58)=2.370d0
Tim(59)=2.420833330d0
Tim(60)=2.458333330d0
Tim(61)=2.0d0
Tim(62)=2.545833330d0
Tim(63)=2.583333330d0
Tim(64)=2.629166660d0
Tim(65)=2.666666660d0
Tim(66)=2.7120d0
Tim(67)=2.70d0
Tim(68)=2.791666660d0
Tim(69)=2.8370d0
Tim(70)=2.870d0
Tim(71)=2.920833330d0
Tim(72)=2.958333330d0
Tim(73)=3.0d0
Tim(74)=3.045833330d0
Tim(75)=3.083333330d0
Tim(76)=3.129166660d0
Tim(77)=3.166666660d0
Tim(78)=3.2120d0
Tim(79)=3.20d0
Tim(80)=3.291666660d0
Tim(81)=3.3370d0
Tim(82)=3.370d0
Tim(83)=3.420833330d0
Tim(84)=3.458333330d0
```

```
Tim(85)=3.0d0
Tim(86)=3.545833330d0
Tim(87)=3.583333330d0
Tim(88)=3.629166660d0
Tim(89)=3.666666660d0
Tim(90)=3.7120d0
Tim(91)=3.70d0
Tim(92)=3.791666660d0
Tim(93)=3.8370d0
Tim(94)=3.870d0
Tim(95)=3.920833330d0
Tim(96)=3.958333330d0
Tim(97)=4.0d0
Tim(98)=4.045833330d0
Tim(99)=4.083333330d0
Tim(100)=4.129166660d0
Tim(101)=4.166666660d0
Tim(102)=4.2120d0
Tim(103)=4.20d0
Tim(104)=4.291666660d0
Tim(105)=4.3370d0
Tim(106)=4.370d0
Tim(107)=4.420833330d0
Tim(108)=4.458333330d0
Tim(109)=4.50d0
Tim(110)=4.545833330d0
Tim(111)=4.583333330d0
Tim(112)=4.629166660d0
Tim(113)=4.666666660d0
Tim(114)=4.7120d0
Tim(115)=4.70d0
Tim(116)=4.791666660d0
Tim(117)=4.8370d0
```

```
Tim(118)=4.870d0
Tim(119)=4.920833330d0
Tim(120)=4.958333330d0
Tim(121)=5.0d0
Tim(122)=5.045833330d0
Tim(123)=5.083333330d0
Tim(124)=5.129166660d0
Tim(125)=5.166666660d0
Tim(126)=5.2120d0
Tim(127)=5.20d0
Tim(128)=5.291666660d0
Tim(129)=5.3370d0
Tim(130)=5.370d0
Tim(131)=5.420833330d0
Tim(132)=5.458333330d0
Tim(133)=5.0d0
Tim(134)=5.545833330d0
Tim(135)=5.583333330d0
Tim(136)=5.629166660d0
Tim(137)=5.666666660d0
Tim(138)=5.7120d0
Tim(139)=5.70d0
Tim(140)=5.791666660d0
Tim(141)=5.8370d0
Tim(142)=5.870d0
Tim(143)=5.920833330d0
Tim(144)=5.958333330d0
Tim(145)=6.004166660d0
Tim(146)=6.045833330d0
Tim(147)=6.083333330d0
Tim(148)=6.129166660d0
Tim(149)=6.166666660d0
Tim(150)=6.2120d0
```

```
Tim(151)=6.20d0
Tim(152)=6.291666660d0
Tim(153)=6.3370d0
Tim(154)=6.370d0
Tim(155)=6.420833330d0
Tim(156)=6.458333330d0
Tim(157)=6.504166660d0
Tim(158)=6.545833330d0
Tim(159)=6.583333330d0
Tim(160)=6.629166660d0
Tim(161)=6.666666660d0
Tim(162)=6.7120d0
Tim(163)=6.70d0
Tim(164)=6.791666660d0
Tim(165)=6.8370d0
Tim(166)=6.870d0
Tim(167)=6.920833330d0
Tim(168)=6.958333330d0
Tim(169)=7.004166660d0
Tim(170)=7.045833330d0
Tim(171)=7.083333330d0
Tim(172)=7.129166660d0
Tim(173)=7.166666660d0
Tim(174)=7.2120d0
Tim(175)=7.20d0
Tim(176)=7.291666660d0
Tim(177)=7.3370d0
Tim(178)=7.370d0
Tim(179)=7.420833330d0
Tim(180)=7.458333330d0
Tim(181)=7.504166660d0
Tim(182)=7.545833330d0
Tim(183)=7.583333330d0
```

```
Tim(184)=7.629166660d0
Tim(185)=7.666666660d0
Tim(186)=7.7120d0
Tim(187)=7.70d0
Tim(188)=7.791666660d0
Tim(189)=7.8370d0
Tim(190)=7.870d0
Tim(191)=7.920833330d0
Tim(192)=7.958333330d0
Tim(193)=8.004166660d0
Tim(194)=8.045833330d0
Tim(195)=8.083333330d0
Tim(196)=8.129166660d0
Tim(197)=8.166666660d0
Tim(198)=8.2120d0
Tim(199)=8.20d0
Tim(200)=8.291666660d0
Tim(201)=8.3370d0
Tim(202)=8.370d0
Tim(203)=8.420833330d0
Tim(204)=8.458333330d0
Tim(205)=8.504166660d0
Tim(206)=8.545833330d0
Tim(207)=8.583333330d0
Tim(208)=8.629166660d0
Tim(209)=8.666666660d0
Tim(210)=8.7120d0
Tim(211)=8.70d0
Tim(212)=8.791666660d0
Tim(213)=8.8370d0
Tim(214)=8.870d0
Tim(215)=8.920833330d0
Tim(216)=8.958333330d0
```

```
Tim(217)=9.004166660d0
Tim(218)=9.045833330d0
Tim(219)=9.083333330d0
Tim(220)=9.129166660d0
Tim(221)=9.166666660d0
Tim(222)=9.2120d0
Tim(223)=9.20d0
Tim(224)=9.291666660d0
Tim(225)=9.3370d0
Tim(226)=9.370d0
Tim(227)=9.420833330d0
Tim(228)=9.458333330d0
Tim(229)=9.504166660d0
Tim(230)=9.541666660d0
Tim(231)=9.583333330d0
Tim(232)=9.629166660d0
Tim(233)=9.666666660d0
Tim(234)=9.7120d0
Tim(235)=9.70d0
Tim(236)=9.791666660d0
Tim(237)=9.8370d0
Tim(238)=9.870d0
Tim(239)=9.920833330d0
Tim(240)=9.958333330d0
Tim(241)=10.00416660d0
Tim(242)=10.04166660d0
Tim(243)=10.08333330d0
Tim(244)=10.12916660d0
Tim(245)=10.16666660d0
Tim(246)=10.2120d0
Tim(247)=10.20d0
Tim(248)=10.29166660d0
Tim(249)=10.3370d0
```

```
Tim(250)=10.370d0
Tim(251)=10.42083330d0
Tim(252)=10.45833330d0
Tim(253)=10.50416660d0
Tim(254)=10.54166660d0
Tim(255)=10.58333330d0
Tim(256)=10.62916660d0
Tim(257)=10.66666660d0
Tim(258)=10.7120d0
Tim(259)=10.70d0
Tim(260)=10.79583330d0
Tim(261)=10.8370d0
Tim(262)=10.870d0
Tim(263)=10.92083330d0
Tim(264)=10.95833330d0
Tim(265)=11.00416660d0
Tim(266)=11.04166660d0
Tim(267)=11.08333330d0
Tim(268)=11.12916660d0
Tim(269)=11.16666660d0
Tim(270)=11.2120d0
Tim(271)=11.20d0
Tim(272)=11.29166660d0
Tim(273)=11.3370d0
Tim(274)=11.370d0
Tim(275)=11.42083330d0
Tim(276)=11.45833330d0
Tim(277)=11.50416660d0
Tim(278)=11.54166660d0
Tim(279)=11.58333330d0
Tim(280)=11.62916660d0
Tim(281)=11.66666660d0
Tim(282)=11.7120d0
```

```
Tim(283)=11.70d0
Tim(284)=11.79166660d0
Tim(285)=11.8370d0
Tim(286)=11.870d0
Tim(287)=11.92083330d0
Tim(288)=11.95833330d0
Tim(289)=12.00416660d0
Tim(290)=12.04583330d0
Tim(291)=12.08333330d0
Tim(292)=12.12916660d0
Tim(293)=12.16666660d0
Tim(294)=12.2120d0
Tim(295)=12.20d0
Tim(296)=12.29166660d0
Tim(297)=12.3370d0
Tim(298)=12.370d0
Tim(299)=12.42083330d0
Tim(300)=12.45833330d0
Tim(301)=12.50416660d0
Tim(302)=12.54583330d0
Tim(303)=12.58333330d0
Tim(304)=12.62916660d0
Tim(305)=12.66666660d0
Tim(306)=12.7120d0
Tim(307)=12.70d0
Tim(308)=12.79166660d0
Tim(309)=12.8370d0
Tim(310)=12.870d0
Tim(311)=12.92083330d0
Tim(312)=12.95833330d0
Tim(313)=13.00416660d0
Tim(314)=13.04583330d0
Tim(315)=13.08333330d0
```

```
Tim(316)=13.12916660d0
Tim(317)=13.16666660d0
Tim(318)=13.2120d0
Tim(319)=13.20d0
Tim(320)=13.29166660d0
Tim(321)=13.3370d0
Tim(322)=13.370d0
Tim(323)=13.42083330d0
Tim(324)=13.45833330d0
Tim(325)=13.50416660d0
Tim(326)=13.54583330d0
Tim(327)=13.58333330d0
Tim(328)=13.62916660d0
Tim(329)=13.66666660d0
Tim(330)=13.7120d0
Tim(331)=13.70d0
Tim(332)=13.79166660d0
Tim(333)=13.8370d0
Tim(334)=13.870d0
Tim(335)=13.92083330d0
Tim(336)=13.95833330d0
Tim(337)=14.00416660d0
Tim(338)=14.04583330d0
Tim(339)=14.08333330d0
Tim(340)=14.12916660d0
Tim(341)=14.16666660d0
Tim(342)=14.2120d0
Tim(343)=14.20d0
Tim(344)=14.29166660d0
Tim(345)=14.3370d0
Tim(346)=14.370d0
Tim(347)=14.42083330d0
Tim(348)=14.45833330d0
```

```
Tim(349)=14.50416660d0
Tim(350)=14.54583330d0
Tim(351)=14.58333330d0
Tim(352)=14.62916660d0
Tim(353)=14.66666660d0
Tim(354)=14.7120d0
Tim(355)=14.70d0
Tim(356)=14.79166660d0
Tim(357)=14.8370d0
Tim(358)=14.870d0
Tim(359)=14.92083330d0
Tim(360)=14.95833330d0
Tim(361)=15.0d0
Tim(362)=15.04583330d0
Tim(363)=15.08333330d0
Tim(364)=15.12916660d0
Tim(365)=15.16666660d0
Tim(366)=15.2120d0
Tim(367)=15.20d0
Tim(368)=15.29166660d0
Tim(369)=15.3370d0
Tim(370)=15.370d0
Tim(371)=15.42083330d0
Tim(372)=15.45833330d0
Tim(373)=15.50d0
Tim(374)=15.54583330d0
Tim(375)=15.58333330d0
Tim(376)=15.62916660d0
Tim(377)=15.66666660d0
Tim(378)=15.7120d0
Tim(379)=15.75416660d0
Tim(380)=15.79166660d0
Tim(381)=15.8370d0
```

```
Tim(382)=15.870d0
Tim(383)=15.92083330d0
Tim(384)=15.95833330d0
Tim(385)=16.0d0
Tim(386)=16.04583330d0
Tim(387)=16.08333330d0
Tim(388)=16.12916660d0
Tim(389)=16.16666660d0
Tim(390)=16.2120d0
Tim(391)=16.25416660d0
Tim(392)=16.29166660d0
Tim(393)=16.3370d0
Tim(394)=16.370d0
Tim(395)=16.42083330d0
Tim(396)=16.45833330d0
Tim(397)=16.50d0
Tim(398)=16.54583330d0
Tim(399)=16.58333330d0
Tim(400)=16.62916660d0
Tim(401)=16.66666660d0
Tim(402)=16.7120d0
Tim(403)=16.75416660d0
Tim(404)=16.79166660d0
Tim(405)=16.8370d0
Tim(406)=16.870d0
Tim(407)=16.92083330d0
Tim(408)=16.95833330d0
Tim(409)=17.0d0
Tim(410)=17.04583330d0
Tim(411)=17.08333330d0
Tim(412)=17.12916660d0
Tim(413)=17.16666660d0
Tim(414)=17.2120d0
```

```
Tim(415)=17.25416660d0
Tim(416)=17.29166660d0
Tim(417)=17.3370d0
Tim(418)=17.370d0
Tim(419)=17.42083330d0
Tim(420)=17.45833330d0
Tim(421)=17.50d0
Tim(422)=17.54583330d0
Tim(423)=17.58333330d0
Tim(424)=17.62916660d0
Tim(425)=17.66666660d0
Tim(426)=17.7120d0
Tim(427)=17.75416660d0
Tim(428)=17.79166660d0
Tim(429)=17.8370d0
Tim(430)=17.870d0
Tim(431)=17.92083330d0
Tim(432)=17.95833330d0
Tim(433)=18.0d0
Tim(434)=18.04583330d0
Tim(435)=18.08333330d0
Tim(436)=18.12916660d0
Tim(437)=18.16666660d0
Tim(438)=18.2120d0
Tim(439)=18.25416660d0
Tim(440)=18.29166660d0
Tim(441)=18.3370d0
Tim(442)=18.370d0
Tim(443)=18.42083330d0
Tim(444)=18.45833330d0
Tim(445)=18.50d0
Tim(446)=18.54583330d0
Tim(447)=18.58333330d0
```

```
Tim(448)=18.62916660d0
Tim(449)=18.66666660d0
Tim(450)=18.70833330d0
Tim(451)=18.75416660d0
Tim(452)=18.79166660d0
Tim(453)=18.8370d0
Tim(454)=18.870d0
Tim(455)=18.92083330d0
Tim(456)=18.95833330d0
Tim(457)=19.0d0
Tim(458)=19.04583330d0
Tim(459)=19.08333330d0
Tim(460)=19.12916660d0
Tim(461)=19.16666660d0
Tim(462)=19.20833330d0
Tim(463)=19.25416660d0
Tim(464)=19.29166660d0
Tim(465)=19.3370d0
Tim(466)=19.370d0
Tim(467)=19.42083330d0
Tim(468)=19.45833330d0
Tim(469)=19.50d0
Tim(470)=19.54583330d0
Tim(471)=19.58333330d0
Tim(472)=19.62916660d0
Tim(473)=19.66666660d0
Tim(474)=19.70833330d0
Tim(475)=19.75416660d0
Tim(476)=19.79166660d0
Tim(477)=19.8370d0
Tim(478)=19.870d0
Tim(479)=19.92083330d0
Tim(480)=19.9620d0
```

```
Tim(481)=20.0d0
Tim(482)=20.04583330d0
Tim(483)=20.08333330d0
Tim(484)=20.12916660d0
Tim(485)=20.16666660d0
Tim(486)=20.20833330d0
Tim(487)=20.25416660d0
Tim(488)=20.29166660d0
Tim(489)=20.3370d0
Tim(490)=20.370d0
Tim(491)=20.42083330d0
Tim(492)=20.4620d0
Tim(493)=20.50d0
Tim(494)=20.54583330d0
Tim(495)=20.58333330d0
Tim(496)=20.62916660d0
Tim(497)=20.66666660d0
Tim(498)=20.70833330d0
Tim(499)=20.75416660d0
Tim(500)=20.79166660d0
Tim(501)=20.8370d0
Tim(502)=20.870d0
Tim(503)=20.92083330d0
Tim(504)=20.9620d0
Tim(505)=21.00d0
Tim(506)=21.04583330d0
Tim(507)=21.08333330d0
Tim(508)=21.12916660d0
Tim(509)=21.16666660d0
Tim(510)=21.20833330d0
Tim(511)=21.25416660d0
Tim(512)=21.29166660d0
Tim(513)=21.3370d0
```

```
Tim(514)=21.370d0
Tim(515)=21.42083330d0
Tim(516)=21.4620d0
Tim(517)=21.50d0
Tim(518)=21.54583330d0
Tim(519)=21.58333330d0
Tim(520)=21.62916660d0
Tim(521)=21.66666660d0
Tim(522)=21.70833330d0
Tim(523)=21.75416660d0
Tim(524)=21.79166660d0
Tim(525)=21.8370d0
Tim(526)=21.870d0
Tim(527)=21.92083330d0
Tim(528)=21.9620d0
Tim(529)=22.0d0
Tim(530)=22.04583330d0
Tim(531)=22.08333330d0
Tim(532)=22.12916660d0
Tim(533)=22.16666660d0
Tim(534)=22.20833330d0
Tim(535)=22.25416660d0
Tim(536)=22.29166660d0
Tim(537)=22.3370d0
Tim(538)=22.370d0
Tim(539)=22.42083330d0
Tim(540)=22.4620d0
Tim(541)=22.50d0
Tim(542)=22.54583330d0
Tim(543)=22.58333330d0
Tim(544)=22.62916660d0
Tim(545)=22.66666660d0
Tim(546)=22.70833330d0
```

```
Tim(547)=22.75416660d0
Tim(548)=22.79166660d0
Tim(549)=22.8370d0
Tim(550)=22.870d0
Tim(551)=22.91666660d0
Tim(552)=22.9620d0
Tim(553)=23.0d0
Tim(554)=23.04583330d0
Tim(555)=23.08333330d0
Tim(556)=23.12916660d0
Tim(557)=23.16666660d0
Tim(558)=23.20833330d0
Tim(559)=23.25416660d0
Tim(560)=23.29166660d0
Tim(561)=23.3370d0
Tim(562)=23.370d0
Tim(563)=23.41666660d0
Tim(564)=23.4620d0
Tim(565)=23.50d0
Tim(566)=23.54583330d0
Tim(567)=23.58333330d0
Tim(568)=23.62916660d0
Tim(569)=23.67083330d0
Tim(570)=23.70833330d0
Tim(571)=23.75416660d0
Tim(572)=23.79166660d0
Tim(573)=23.8370d0
Tim(574)=23.870d0
Tim(575)=23.91666660d0
Tim(576)=23.9620d0
Tim(577)=24.0d0
Tim(578)=24.04583330d0
Tim(579)=24.08333330d0
```

```
Tim(580)=24.12916660d0
Tim(581)=24.17083330d0
Tim(582)=24.20833330d0
Tim(583)=24.25416660d0
Tim(584)=24.29166660d0
Tim(585)=24.3370d0
Tim(586)=24.370d0
Tim(587)=24.41666660d0
Tim(588)=24.4620d0
Tim(589)=24.50d0
Tim(590)=24.54583330d0
Tim(591)=24.58333330d0
Tim(592)=24.62916660d0
Tim(593)=24.67083330d0
Tim(594)=24.70833330d0
Tim(595)=24.75416660d0
Tim(596)=24.79166660d0
Tim(597)=24.8370d0
Tim(598)=24.870d0
Tim(599)=24.91666660d0
Tim(600)=24.9620d0
Tim(601)=25.0d0
Tim(602)=25.04583330d0
Tim(603)=25.08333330d0
Tim(604)=25.12916660d0
Tim(605)=25.17083330d0
Tim(606)=25.20833330d0
Tim(607)=25.25416660d0
Tim(608)=25.29166660d0
Tim(609)=25.3370d0
Tim(610)=25.370d0
Tim(611)=25.41666660d0
Tim(612)=25.4620d0
```

```
Tim(613)=25.50d0
Tim(614)=25.54583330d0
Tim(615)=25.58333330d0
Tim(616)=25.62916660d0
Tim(617)=25.67083330d0
Tim(618)=25.70833330d0
Tim(619)=25.75416660d0
Tim(620)=25.79166660d0
Tim(621)=25.8370d0
Tim(622)=25.870d0
Tim(623)=25.91666660d0
Tim(624)=25.9620d0
Tim(625)=26.0d0
Tim(626)=26.04583330d0
Tim(627)=26.08333330d0
Tim(628)=26.12916660d0
Tim(629)=26.17083330d0
Tim(630)=26.20833330d0
Tim(631)=26.25416660d0
Tim(632)=26.29166660d0
Tim(633)=26.3370d0
Tim(634)=26.370d0
Tim(635)=26.41666660d0
Tim(636)=26.4620d0
Tim(637)=26.50d0
Tim(638)=26.54583330d0
Tim(639)=26.58333330d0
Tim(640)=26.620d0
Tim(641)=26.67083330d0
Tim(642)=26.70833330d0
Tim(643)=26.75416660d0
Tim(644)=26.79166660d0
Tim(645)=26.8370d0
```

```
Tim(646)=26.870d0
Tim(647)=26.91666660d0
Tim(648)=26.9620d0
Tim(649)=27.0d0
Tim(650)=27.04583330d0
Tim(651)=27.08333330d0
Tim(652)=27.120d0
Tim(653)=27.17083330d0
Tim(654)=27.20833330d0
Tim(655)=27.25416660d0
Tim(656)=27.29166660d0
Tim(657)=27.3370d0
Tim(658)=27.37916660d0
Tim(659)=27.41666660d0
Tim(660)=27.4620d0
Tim(661)=27.50d0
Tim(662)=27.54583330d0
Tim(663)=27.58333330d0
Tim(664)=27.620d0
Tim(665)=27.67083330d0
Tim(666)=27.70833330d0
Tim(667)=27.75416660d0
Tim(668)=27.79166660d0
Tim(669)=27.8370d0
Tim(670)=27.87916660d0
Tim(671)=27.91666660d0
Tim(672)=27.9620d0
Tim(673)=28.0d0
Tim(674)=28.04583330d0
Tim(675)=28.08333330d0
Tim(676)=28.120d0
Tim(677)=28.17083330d0
Tim(678)=28.20833330d0
```

```
Tim(679)=28.25416660d0
Tim(680)=28.29166660d0
Tim(681)=28.3370d0
Tim(682)=28.37916660d0
Tim(683)=28.41666660d0
Tim(684)=28.4620d0
Tim(685)=28.50d0
Tim(686)=28.54583330d0
Tim(687)=28.58333330d0
Tim(688)=28.620d0
Tim(689)=28.67083330d0
Tim(690)=28.70833330d0
Tim(691)=28.75416660d0
Tim(692)=28.79166660d0
Tim(693)=28.8370d0
Tim(694)=28.87916660d0
Tim(695)=28.91666660d0
Tim(696)=28.9620d0
Tim(697)=29.0d0
Tim(698)=29.04583330d0
Tim(699)=29.08333330d0
Tim(700)=29.120d0
Tim(701)=29.17083330d0
Tim(702)=29.20833330d0
Tim(703)=29.25416660d0
Tim(704)=29.29166660d0
Tim(705)=29.3370d0
Tim(706)=29.37916660d0
Tim(707)=29.41666660d0
Tim(708)=29.4620d0
Tim(709)=29.50d0
Tim(710)=29.54583330d0
Tim(711)=29.58333330d0
```

```
Tim(712)=29.620d0
Tim(713)=29.67083330d0
Tim(714)=29.70833330d0
Tim(715)=29.75416660d0
Tim(716)=29.79166660d0
Tim(717)=29.8370d0
Tim(718)=29.87916660d0
Tim(719)=29.91666660d0
Tim(720)=29.9620d0
Tim(721)=30.0d0
Tim(722)=30.04583330d0
Tim(723)=30.08333330d0
Tim(724)=30.120d0
Tim(725)=30.17083330d0
Tim(726)=30.20833330d0
Tim(727)=30.25416660d0
Tim(728)=30.29166660d0
Tim(729)=30.33333330d0
Tim(730)=30.37916660d0
Tim(731)=30.41666660d0
Tim(732)=30.4620d0
Tim(733)=30.50d0
Tim(734)=30.54583330d0
Tim(735)=30.58333330d0
Tim(736)=30.620d0
Tim(737)=30.67083330d0
Tim(738)=30.70833330d0
Tim(739)=30.75416660d0
Tim(740)=30.79166660d0
Tim(741)=30.83333330d0
Tim(742)=30.87916660d0
Tim(743)=30.91666660d0
Tim(744)=30.9620d0
```

```
Tim(745)=31.0d0
Tim(746)=31.04583330d0
Tim(747)=31.08333330d0
Tim(748)=31.120d0
Tim(749)=31.17083330d0
Tim(750)=31.20833330d0
Tim(751)=31.25416660d0
Tim(752)=31.29166660d0
Tim(753)=31.33333330d0
Tim(754)=31.37916660d0
Tim(755)=31.41666660d0
Tim(756)=31.4620d0
Tim(757)=31.50d0
Tim(758)=31.54583330d0
Tim(759)=31.5870d0
Tim(760)=31.620d0
Tim(761)=31.67083330d0
Tim(762)=31.70833330d0
Tim(763)=31.75416660d0
Tim(764)=31.79166660d0
Tim(765)=31.83333330d0
Tim(766)=31.87916660d0
Tim(767)=31.91666660d0
Tim(768)=31.9620d0
Tim(769)=32.0d0
Tim(770)=32.04583330d0
Tim(771)=32.0870d0
Tim(772)=32.120d0
Tim(773)=32.17083330d0
Tim(774)=32.20833330d0
Tim(775)=32.25416660d0
Tim(776)=32.29166660d0
Tim(777)=32.33333330d0
```

```
Tim(778)=32.37916660d0
Tim(779)=32.41666660d0
Tim(780)=32.4620d0
Tim(781)=32.50d0
Tim(782)=32.54583330d0
Tim(783)=32.5870d0
Tim(784)=32.620d0
Tim(785)=32.67083330d0
Tim(786)=32.70833330d0
Tim(787)=32.75416660d0
Tim(788)=32.79166660d0
Tim(789)=32.83333330d0
Tim(790)=32.87916660d0
Tim(791)=32.91666660d0
Tim(792)=32.9620d0
Tim(793)=33.0d0
Tim(794)=33.04583330d0
Tim(795)=33.0870d0
Tim(796)=33.120d0
Tim(797)=33.17083330d0
Tim(798)=33.20833330d0
Tim(799)=33.25416660d0
Tim(800)=33.29166660d0
Tim(801)=33.33333330d0
Tim(802)=33.37916660d0
Tim(803)=33.41666660d0
Tim(804)=33.4620d0
Tim(805)=33.50d0
Tim(806)=33.54583330d0
Tim(807)=33.5870d0
Tim(808)=33.620d0
Tim(809)=33.67083330d0
Tim(810)=33.70833330d0
```

```
Tim(811)=33.75416660d0



Hwater(1)=50076.0d0
Hwater(2)=50077.0d0
Hwater(3)=50078.0d0
Hwater(4)=50079.0d0
Hwater(5)=50079.0d0
Hwater(6)=50080.0d0
Hwater(7)=50081.0d0
Hwater(8)=50082.0d0
Hwater(9)=50083.0d0
Hwater(10)=50083.0d0
Hwater(11)=50084.0d0
Hwater(12)=50085.0d0
Hwater(13)=50086.0d0
Hwater(14)=50087.0d0
Hwater(15)=50088.0d0
Hwater(16)=50089.0d0
Hwater(17)=50090.0d0
Hwater(18)=50091.0d0
Hwater(19)=50090d0
Hwater(20)=50092.0d0
Hwater(21)=50093.0d0
Hwater(22)=50094.0d0
Hwater(23)=50095.0d0
Hwater(24)=50096.0d0
Hwater(25)=50097.0d0
Hwater(26)=50090.0d0
Hwater(27)=50103.0d0
Hwater(28)=50109.0d0
Hwater(29)=50115.0d0
Hwater(30)=50121.0d0
```

```
Hwater(31)=50126.0d0
Hwater(32)=50132.0d0
Hwater(33)=50130.0d0
Hwater(34)=50143.0d0
Hwater(35)=50149.0d0
Hwater(36)=50154.0d0
Hwater(37)=50159.0d0
Hwater(38)=50164.0d0
Hwater(39)=50169.0d0
Hwater(40)=50170.0d0
Hwater(41)=50179.0d0
Hwater(42)=50185.0d0
Hwater(43)=50189.0d0
Hwater(44)=50194.0d0
Hwater(45)=50199.0d0
Hwater(46)=50204.0d0
Hwater(47)=50209.0d0
Hwater(48)=50214.0d0
Hwater(49)=50218.0d0
Hwater(50)=50223.0d0
Hwater(51)=50220.0d0
Hwater(52)=50232.0d0
Hwater(53)=50237.0d0
Hwater(54)=50242.0d0
Hwater(55)=50246.0d0
Hwater(56)=50250.0d0
Hwater(57)=50255.0d0
Hwater(58)=50259.0d0
Hwater(59)=50264.0d0
Hwater(60)=50268.0d0
Hwater(61)=50272.0d0
Hwater(62)=50277.0d0
Hwater(63)=50281.0d0
```

```
Hwater(64)=50285.0d0
Hwater(65)=50289.0d0
Hwater(66)=50294.0d0
Hwater(67)=50298.0d0
Hwater(68)=50302.0d0
Hwater(69)=50306.0d0
Hwater(70)=50310.0d0
Hwater(71)=50315.0d0
Hwater(72)=50310.0d0
Hwater(73)=50322.0d0
Hwater(74)=50327.0d0
Hwater(75)=50330.0d0
Hwater(76)=50335.0d0
Hwater(77)=50330.0d0
Hwater(78)=50343.0d0
Hwater(79)=50340.0d0
Hwater(80)=50350.0d0
Hwater(81)=50354.0d0
Hwater(82)=50358.0d0
Hwater(83)=50362.0d0
Hwater(84)=50366.0d0
Hwater(85)=50370.0d0
Hwater(86)=50374.0d0
Hwater(87)=50377.0d0
Hwater(88)=50381.0d0
Hwater(89)=50385.0d0
Hwater(90)=50389.0d0
Hwater(91)=50392.0d0
Hwater(92)=50396.0d0
Hwater(93)=50400.0d0
Hwater(94)=50400.0d0
Hwater(95)=50407.0d0
Hwater(96)=50411.0d0
```

```
Hwater(97)=50414.0d0
Hwater(98)=50418.0d0
Hwater(99)=50422.0d0
Hwater(100)=50420.0d0
Hwater(101)=50429.0d0
Hwater(102)=50433.0d0
Hwater(103)=50436.0d0
Hwater(104)=50440.0d0
Hwater(105)=50443.0d0
Hwater(106)=50447.0d0
Hwater(107)=50450.0d0
Hwater(108)=50454.0d0
Hwater(109)=50457.0d0
Hwater(110)=50461.0d0
Hwater(111)=50464.0d0
Hwater(112)=50468.0d0
Hwater(113)=50471.0d0
Hwater(114)=50475.0d0
Hwater(115)=50478.0d0
Hwater(116)=50481.0d0
Hwater(117)=50485.0d0
Hwater(118)=50488.0d0
Hwater(119)=50492.0d0
Hwater(120)=50495.0d0
Hwater(121)=50498.0d0
Hwater(122)=50502.0d0
Hwater(123)=50505.0d0
Hwater(124)=50508.0d0
Hwater(125)=50512.0d0
Hwater(126)=50515.0d0
Hwater(127)=50518.0d0
Hwater(128)=50521.0d0
Hwater(129)=50525.0d0
```

```
Hwater(130)=50528.0d0
Hwater(131)=50530.0d0
Hwater(132)=50535.0d0
Hwater(133)=50538.0d0
Hwater(134)=50541.0d0
Hwater(135)=50544.0d0
Hwater(136)=50548.0d0
Hwater(137)=50551.0d0
Hwater(138)=50554.0d0
Hwater(139)=50557.0d0
Hwater(140)=50560.0d0
Hwater(141)=50560.0d0
Hwater(142)=50560.0d0
Hwater(143)=50570.0d0
Hwater(144)=50573.0d0
Hwater(145)=50576.0d0
Hwater(146)=50579.0d0
Hwater(147)=50582.0d0
Hwater(148)=50585.0d0
Hwater(149)=50588.0d0
Hwater(150)=50592.0d0
Hwater(151)=50595.0d0
Hwater(152)=50598.0d0
Hwater(153)=50601.0d0
Hwater(154)=50604.0d0
Hwater(155)=50607.0d0
Hwater(156)=50610.0d0
Hwater(157)=50613.0d0
Hwater(158)=50616.0d0
Hwater(159)=50619.0d0
Hwater(160)=50622.0d0
Hwater(161)=50625.0d0
Hwater(162)=50628.0d0
```

```
Hwater(163)=50631.0d0
Hwater(164)=50634.0d0
Hwater(165)=50637.0d0
Hwater(166)=50640.0d0
Hwater(167)=50643.0d0
Hwater(168)=50646.0d0
Hwater(169)=50649.0d0
Hwater(170)=50652.0d0
Hwater(171)=50655.0d0
Hwater(172)=50658.0d0
Hwater(173)=50660.0d0
Hwater(174)=50664.0d0
Hwater(175)=50666.0d0
Hwater(176)=50669.0d0
Hwater(177)=50672.0d0
Hwater(178)=50675.0d0
Hwater(179)=50678.0d0
Hwater(180)=50681.0d0
Hwater(181)=50684.0d0
Hwater(182)=50687.0d0
Hwater(183)=50689.0d0
Hwater(184)=50692.0d0
Hwater(185)=50695.0d0
Hwater(186)=50698.0d0
Hwater(187)=50701.0d0
Hwater(188)=50700.0d0
Hwater(189)=50700.0d0
Hwater(190)=50709.0d0
Hwater(191)=50712.0d0
Hwater(192)=50715.0d0
Hwater(193)=50718.0d0
Hwater(194)=50720.0d0
Hwater(195)=50723.0d0
```

```
Hwater(196)=50726.0d0
Hwater(197)=50729.0d0
Hwater(198)=50732.0d0
Hwater(199)=50734.0d0
Hwater(200)=50737.0d0
Hwater(201)=50740.0d0
Hwater(202)=50740.0d0
Hwater(203)=50745.0d0
Hwater(204)=50748.0d0
Hwater(205)=50751.0d0
Hwater(206)=50754.0d0
Hwater(207)=50756.0d0
Hwater(208)=50759.0d0
Hwater(209)=50762.0d0
Hwater(210)=50760.0d0
Hwater(211)=50767.0d0
Hwater(212)=50770.0d0
Hwater(213)=50770.0d0
Hwater(214)=50775.0d0
Hwater(215)=50778.0d0
Hwater(216)=50780.0d0
Hwater(217)=50783.0d0
Hwater(218)=50786.0d0
Hwater(219)=50788.0d0
Hwater(220)=50791.0d0
Hwater(221)=50794.0d0
Hwater(222)=50797.0d0
Hwater(223)=50799.0d0
Hwater(224)=50802.0d0
Hwater(225)=50804.0d0
Hwater(226)=50807.0d0
Hwater(227)=50810.0d0
Hwater(228)=50812.0d0
```

```
Hwater(229)=50815.0d0
Hwater(230)=50810.0d0
Hwater(231)=50820.0d0
Hwater(232)=50823.0d0
Hwater(233)=50825.0d0
Hwater(234)=50828.0d0
Hwater(235)=50830.0d0
Hwater(236)=50833.0d0
Hwater(237)=50836.0d0
Hwater(238)=50838.0d0
Hwater(239)=50841.0d0
Hwater(240)=50843.0d0
Hwater(241)=50846.0d0
Hwater(242)=50840.0d0
Hwater(243)=50851.0d0
Hwater(244)=50854.0d0
Hwater(245)=50856.0d0
Hwater(246)=50859.0d0
Hwater(247)=50861.0d0
Hwater(248)=50864.0d0
Hwater(249)=50866.0d0
Hwater(250)=50869.0d0
Hwater(251)=50871.0d0
Hwater(252)=50874.0d0
Hwater(253)=50876.0d0
Hwater(254)=50879.0d0
Hwater(255)=50881.0d0
Hwater(256)=50884.0d0
Hwater(257)=50886.0d0
Hwater(258)=50889.0d0
Hwater(259)=50891.0d0
Hwater(260)=50894.0d0
Hwater(261)=50896.0d0
```

```
Hwater(262)=50899.0d0
Hwater(263)=50901.0d0
Hwater(264)=50904.0d0
Hwater(265)=50906.0d0
Hwater(266)=50909.0d0
Hwater(267)=50911.0d0
Hwater(268)=50910.0d0
Hwater(269)=50916.0d0
Hwater(270)=50910.0d0
Hwater(271)=50921.0d0
Hwater(272)=50923.0d0
Hwater(273)=50926.0d0
Hwater(274)=50928.0d0
Hwater(275)=50931.0d0
Hwater(276)=50933.0d0
Hwater(277)=50930.0d0
Hwater(278)=50938.0d0
Hwater(279)=50940.0d0
Hwater(280)=50943.0d0
Hwater(281)=50945.0d0
Hwater(282)=50940.0d0
Hwater(283)=50950.0d0
Hwater(284)=50952.0d0
Hwater(285)=50955.0d0
Hwater(286)=50957.0d0
Hwater(287)=50959.0d0
Hwater(288)=50962.0d0
Hwater(289)=50964.0d0
Hwater(290)=50960.0d0
Hwater(291)=50969.0d0
Hwater(292)=50971.0d0
Hwater(293)=50970.0d0
Hwater(294)=50976.0d0
```

```
Hwater(295)=50978.0d0
Hwater(296)=50980.0d0
Hwater(297)=50983.0d0
Hwater(298)=50985.0d0
Hwater(299)=50988.0d0
Hwater(300)=50990.0d0
Hwater(301)=50990.0d0
Hwater(302)=50995.0d0
Hwater(303)=50997.0d0
Hwater(304)=50999.0d0
Hwater(305)=51002.0d0
Hwater(306)=51004.0d0
Hwater(307)=51006.0d0
Hwater(308)=51000.0d0
Hwater(309)=51011.0d0
Hwater(310)=51013.0d0
Hwater(311)=51016.0d0
Hwater(312)=51018.0d0
Hwater(313)=51020.0d0
Hwater(314)=51020.0d0
Hwater(315)=51025.0d0
Hwater(316)=51027.0d0
Hwater(317)=51029.0d0
Hwater(318)=51032.0d0
Hwater(319)=51034.0d0
Hwater(320)=51036.0d0
Hwater(321)=51030.0d0
Hwater(322)=51041.0d0
Hwater(323)=51043.0d0
Hwater(324)=51045.0d0
Hwater(325)=51048.0d0
Hwater(326)=51050.0d0
Hwater(327)=51052.0d0
```

```
Hwater(328)=51054.0d0
Hwater(329)=51050.0d0
Hwater(330)=51059.0d0
Hwater(331)=51061.0d0
Hwater(332)=51063.0d0
Hwater(333)=51066.0d0
Hwater(334)=51068.0d0
Hwater(335)=51070.0d0
Hwater(336)=51072.0d0
Hwater(337)=51075.0d0
Hwater(338)=51077.0d0
Hwater(339)=51079.0d0
Hwater(340)=51081.0d0
Hwater(341)=51083.0d0
Hwater(342)=51086.0d0
Hwater(343)=51088.0d0
Hwater(344)=51090.0d0
Hwater(345)=51092.0d0
Hwater(346)=51094.0d0
Hwater(347)=51097.0d0
Hwater(348)=51099.0d0
Hwater(349)=51101.0d0
Hwater(350)=51103.0d0
Hwater(351)=51105.0d0
Hwater(352)=51108.0d0
Hwater(353)=51110.0d0
Hwater(354)=51112.0d0
Hwater(355)=51114.0d0
Hwater(356)=51116.0d0
Hwater(357)=51110.0d0
Hwater(358)=51121.0d0
Hwater(359)=51123.0d0
Hwater(360)=51125.0d0
```

```
Hwater(361)=51127.0d0
Hwater(362)=51129.0d0
Hwater(363)=51131.0d0
Hwater(364)=51134.0d0
Hwater(365)=51136.0d0
Hwater(366)=51138.0d0
Hwater(367)=51140.0d0
Hwater(368)=51142.0d0
Hwater(369)=51144.0d0
Hwater(370)=51140.0d0
Hwater(371)=51149.0d0
Hwater(372)=51151.0d0
Hwater(373)=51153.0d0
Hwater(374)=51155.0d0
Hwater(375)=51157.0d0
Hwater(376)=51159.0d0
Hwater(377)=51160d0
Hwater(378)=51164.0d0
Hwater(379)=51166.0d0
Hwater(380)=51168.0d0
Hwater(381)=51170.0d0
Hwater(382)=51172.0d0
Hwater(383)=51174.0d0
Hwater(384)=51176.0d0
Hwater(385)=51178.0d0
Hwater(386)=51181.0d0
Hwater(387)=51183.0d0
Hwater(388)=51185.0d0
Hwater(389)=51187.0d0
Hwater(390)=51189.0d0
Hwater(391)=51191.0d0
Hwater(392)=51193.0d0
Hwater(393)=51195.0d0
```

```
Hwater(394)=51197.0d0
Hwater(395)=51200.0d0
Hwater(396)=51201.0d0
Hwater(397)=51200.0d0
Hwater(398)=51206.0d0
Hwater(399)=51208.0d0
Hwater(400)=51210.0d0
Hwater(401)=51212.0d0
Hwater(402)=51214.0d0
Hwater(403)=51216.0d0
Hwater(404)=51218.0d0
Hwater(405)=51220.0d0
Hwater(406)=51222.0d0
Hwater(407)=51224.0d0
Hwater(408)=51226.0d0
Hwater(409)=51228.0d0
Hwater(410)=51230.0d0
Hwater(411)=51232.0d0
Hwater(412)=51230.0d0
Hwater(413)=51230.0d0
Hwater(414)=51239.0d0
Hwater(415)=51241.0d0
Hwater(416)=51243.0d0
Hwater(417)=51245.0d0
Hwater(418)=51247.0d0
Hwater(419)=51249.0d0
Hwater(420)=51251.0d0
Hwater(421)=51253.0d0
Hwater(422)=51255.0d0
Hwater(423)=51257.0d0
Hwater(424)=51259.0d0
Hwater(425)=51261.0d0
Hwater(426)=51263.0d0
```

```
Hwater(427)=51265.0d0
Hwater(428)=51267.0d0
Hwater(429)=51269.0d0
Hwater(430)=51271.0d0
Hwater(431)=51273.0d0
Hwater(432)=51275.0d0
Hwater(433)=51277.0d0
Hwater(434)=51279.0d0
Hwater(435)=51281.0d0
Hwater(436)=51283.0d0
Hwater(437)=51285.0d0
Hwater(438)=51287.0d0
Hwater(439)=51289.0d0
Hwater(440)=51291.0d0
Hwater(441)=51293.0d0
Hwater(442)=51295.0d0
Hwater(443)=51297.0d0
Hwater(444)=51299.0d0
Hwater(445)=51301.0d0
Hwater(446)=51303.0d0
Hwater(447)=51305.0d0
Hwater(448)=51307.0d0
Hwater(449)=51309.0d0
Hwater(450)=51311.0d0
Hwater(451)=51313.0d0
Hwater(452)=51315.0d0
Hwater(453)=51317.0d0
Hwater(454)=51319.0d0
Hwater(455)=51321.0d0
Hwater(456)=51323.0d0
Hwater(457)=51320.0d0
Hwater(458)=51327.0d0
Hwater(459)=51320.0d0
```

```
Hwater(460)=51331.0d0
Hwater(461)=51332.0d0
Hwater(462)=51334.0d0
Hwater(463)=51336.0d0
Hwater(464)=51338.0d0
Hwater(465)=51340.0d0
Hwater(466)=51342.0d0
Hwater(467)=51344.0d0
Hwater(468)=51346.0d0
Hwater(469)=51348.0d0
Hwater(470)=51350.0d0
Hwater(471)=51352.0d0
Hwater(472)=51354.0d0
Hwater(473)=51356.0d0
Hwater(474)=51358.0d0
Hwater(475)=51360.0d0
Hwater(476)=51361.0d0
Hwater(477)=51360.0d0
Hwater(478)=51365.0d0
Hwater(479)=51367.0d0
Hwater(480)=51369.0d0
Hwater(481)=51371.0d0
Hwater(482)=51373.0d0
Hwater(483)=51375.0d0
Hwater(484)=51377.0d0
Hwater(485)=51379.0d0
Hwater(486)=51381.0d0
Hwater(487)=51383.0d0
Hwater(488)=51384.0d0
Hwater(489)=51386.0d0
Hwater(490)=51388.0d0
Hwater(491)=51390.0d0
Hwater(492)=51392.0d0
```

```
Hwater(493)=51394.0d0
Hwater(494)=51396.0d0
Hwater(495)=51398.0d0
Hwater(496)=51400.0d0
Hwater(497)=51400.0d0
Hwater(498)=51403.0d0
Hwater(499)=51405.0d0
Hwater(500)=51407.0d0
Hwater(501)=51409.0d0
Hwater(502)=51411.0d0
Hwater(503)=51413.0d0
Hwater(504)=51415.0d0
Hwater(505)=51410.0d0
Hwater(506)=51410.0d0
Hwater(507)=51420.0d0
Hwater(508)=51422.0d0
Hwater(509)=51424.0d0
Hwater(510)=51426.0d0
Hwater(511)=51428.0d0
Hwater(512)=51430.0d0
Hwater(513)=51432.0d0
Hwater(514)=51433.0d0
Hwater(515)=51435.0d0
Hwater(516)=51437.0d0
Hwater(517)=51439.0d0
Hwater(518)=51441.0d0
Hwater(519)=51443.0d0
Hwater(520)=51445.0d0
Hwater(521)=51446.0d0
Hwater(522)=51448.0d0
Hwater(523)=51450.0d0
Hwater(524)=51452.0d0
Hwater(525)=51454.0d0
```

```
Hwater(526)=51456.0d0
Hwater(527)=51458.0d0
Hwater(528)=51459.0d0
Hwater(529)=51461.0d0
Hwater(530)=51463.0d0
Hwater(531)=51465.0d0
Hwater(532)=51467.0d0
Hwater(533)=51469.0d0
Hwater(534)=51470.0d0
Hwater(535)=51472.0d0
Hwater(536)=51474.0d0
Hwater(537)=51476.0d0
Hwater(538)=51478.0d0
Hwater(539)=51480.0d0
Hwater(540)=51481.0d0
Hwater(541)=51483.0d0
Hwater(542)=51485.0d0
Hwater(543)=51487.0d0
Hwater(544)=51489.0d0
Hwater(545)=51490.0d0
Hwater(546)=51492.0d0
Hwater(547)=51494.0d0
Hwater(548)=51496.0d0
Hwater(549)=51498.0d0
Hwater(550)=51500.0d0
Hwater(551)=51501.0d0
Hwater(552)=51503.0d0
Hwater(553)=51505.0d0
Hwater(554)=51507.0d0
Hwater(555)=51500.0d0
Hwater(556)=51510.0d0
Hwater(557)=51512.0d0
Hwater(558)=51514.0d0
```

```
Hwater(559)=51516.0d0
Hwater(560)=51510.0d0
Hwater(561)=51519.0d0
Hwater(562)=51521.0d0
Hwater(563)=51523.0d0
Hwater(564)=51525.0d0
Hwater(565)=51526.0d0
Hwater(566)=51528.0d0
Hwater(567)=51530.0d0
Hwater(568)=51532.0d0
Hwater(569)=51534.0d0
Hwater(570)=51535.0d0
Hwater(571)=51537.0d0
Hwater(572)=51539.0d0
Hwater(573)=51541.0d0
Hwater(574)=51540.0d0
Hwater(575)=51544.0d0
Hwater(576)=51546.0d0
Hwater(577)=51548.0d0
Hwater(578)=51550.0d0
Hwater(579)=51551.0d0
Hwater(580)=51553.0d0
Hwater(581)=51555.0d0
Hwater(582)=51557.0d0
Hwater(583)=51558.0d0
Hwater(584)=51560.0d0
Hwater(585)=51562.0d0
Hwater(586)=51564.0d0
Hwater(587)=51565.0d0
Hwater(588)=51567.0d0
Hwater(589)=51569.0d0
Hwater(590)=51571.0d0
Hwater(591)=51570.0d0
```

```
Hwater(592)=51574.0d0
Hwater(593)=51576.0d0
Hwater(594)=51578.0d0
Hwater(595)=51580.0d0
Hwater(596)=51581.0d0
Hwater(597)=51583.0d0
Hwater(598)=51585.0d0
Hwater(599)=51586.0d0
Hwater(600)=51588.0d0
Hwater(601)=51590.0d0
Hwater(602)=51592.0d0
Hwater(603)=51593.0d0
Hwater(604)=51595.0d0
Hwater(605)=51597.0d0
Hwater(606)=51599.0d0
Hwater(607)=51600.0d0
Hwater(608)=51602.0d0
Hwater(609)=51604.0d0
Hwater(610)=51606.0d0
Hwater(611)=51607.0d0
Hwater(612)=51609.0d0
Hwater(613)=51611.0d0
Hwater(614)=51610.0d0
Hwater(615)=51614.0d0
Hwater(616)=51616.0d0
Hwater(617)=51618.0d0
Hwater(618)=51619.0d0
Hwater(619)=51621.0d0
Hwater(620)=51623.0d0
Hwater(621)=51625.0d0
Hwater(622)=51626.0d0
Hwater(623)=51628.0d0
Hwater(624)=51630.0d0
```

```
Hwater(625)=51631.0d0
Hwater(626)=51633.0d0
Hwater(627)=51635.0d0
Hwater(628)=51637.0d0
Hwater(629)=51638.0d0
Hwater(630)=51640.0d0
Hwater(631)=51642.0d0
Hwater(632)=51643.0d0
Hwater(633)=51645.0d0
Hwater(634)=51647.0d0
Hwater(635)=51648.0d0
Hwater(636)=51650.0d0
Hwater(637)=51652.0d0
Hwater(638)=51654.0d0
Hwater(639)=51655.0d0
Hwater(640)=51657.0d0
Hwater(641)=51659.0d0
Hwater(642)=51660.0d0
Hwater(643)=51662.0d0
Hwater(644)=51664.0d0
Hwater(645)=51665.0d0
Hwater(646)=51667.0d0
Hwater(647)=51669.0d0
Hwater(648)=51670.0d0
Hwater(649)=51672.0d0
Hwater(650)=51674.0d0
Hwater(651)=51675.0d0
Hwater(652)=51677.0d0
Hwater(653)=51679.0d0
Hwater(654)=51680.0d0
Hwater(655)=51682.0d0
Hwater(656)=51684.0d0
Hwater(657)=51686.0d0
```

```
Hwater(658)=51687.0d0
Hwater(659)=51689.0d0
Hwater(660)=51690.0d0
Hwater(661)=51692.0d0
Hwater(662)=51694.0d0
Hwater(663)=51690.0d0
Hwater(664)=51697.0d0
Hwater(665)=51699.0d0
Hwater(666)=51700.0d0
Hwater(667)=51702.0d0
Hwater(668)=51704.0d0
Hwater(669)=51706.0d0
Hwater(670)=51707.0d0
Hwater(671)=51709.0d0
Hwater(672)=51710.0d0
Hwater(673)=51712.0d0
Hwater(674)=51714.0d0
Hwater(675)=51715.0d0
Hwater(676)=51717.0d0
Hwater(677)=51719.0d0
Hwater(678)=51720.0d0
Hwater(679)=51722.0d0
Hwater(680)=51724.0d0
Hwater(681)=51725.0d0
Hwater(682)=51727.0d0
Hwater(683)=51729.0d0
Hwater(684)=51730.0d0
Hwater(685)=51732.0d0
Hwater(686)=51734.0d0
Hwater(687)=51735.0d0
Hwater(688)=51737.0d0
Hwater(689)=51730.0d0
Hwater(690)=51740.0d0
```

```
Hwater(691)=51742.0d0
Hwater(692)=51743.0d0
Hwater(693)=51745.0d0
Hwater(694)=51747.0d0
Hwater(695)=51748.0d0
Hwater(696)=51750.0d0
Hwater(697)=51750.0d0
Hwater(698)=51753.0d0
Hwater(699)=51755.0d0
Hwater(700)=51756.0d0
Hwater(701)=51758.0d0
Hwater(702)=51760.0d0
Hwater(703)=51761.0d0
Hwater(704)=51763.0d0
Hwater(705)=51765.0d0
Hwater(706)=51766.0d0
Hwater(707)=51768.0d0
Hwater(708)=51770.0d0
Hwater(709)=51771.0d0
Hwater(710)=51773.0d0
Hwater(711)=51774.0d0
Hwater(712)=51776.0d0
Hwater(713)=51770.0d0
Hwater(714)=51779.0d0
Hwater(715)=51781.0d0
Hwater(716)=51782.0d0
Hwater(717)=51784.0d0
Hwater(718)=51786.0d0
Hwater(719)=51787.0d0
Hwater(720)=51789.0d0
Hwater(721)=51790.0d0
Hwater(722)=51792.0d0
Hwater(723)=51794.0d0
```

```
Hwater(724)=51795.0d0
Hwater(725)=51797.0d0
Hwater(726)=51798.0d0
Hwater(727)=51800.0d0
Hwater(728)=51802.0d0
Hwater(729)=51803.0d0
Hwater(730)=51805.0d0
Hwater(731)=51806.0d0
Hwater(732)=51808.0d0
Hwater(733)=51810.0d0
Hwater(734)=51811.0d0
Hwater(735)=51813.0d0
Hwater(736)=51814.0d0
Hwater(737)=51816.0d0
Hwater(738)=51818.0d0
Hwater(739)=51819.0d0
Hwater(740)=51821.0d0
Hwater(741)=51822.0d0
Hwater(742)=51824.0d0
Hwater(743)=51820.0d0
Hwater(744)=51827.0d0
Hwater(745)=51829.0d0
Hwater(746)=51830.0d0
Hwater(747)=51832.0d0
Hwater(748)=51833.0d0
Hwater(749)=51835.0d0
Hwater(750)=51837.0d0
Hwater(751)=51838.0d0
Hwater(752)=51840.0d0
Hwater(753)=51841.0d0
Hwater(754)=51843.0d0
Hwater(755)=51840.0d0
Hwater(756)=51846.0d0
```

```
Hwater(757)=51848.0d0
Hwater(758)=51849.0d0
Hwater(759)=51851.0d0
Hwater(760)=51852.0d0
Hwater(761)=51854.0d0
Hwater(762)=51850.0d0
Hwater(763)=51857.0d0
Hwater(764)=51859.0d0
Hwater(765)=51860.0d0
Hwater(766)=51862.0d0
Hwater(767)=51863.0d0
Hwater(768)=51865.0d0
Hwater(769)=51866.0d0
Hwater(770)=51868.0d0
Hwater(771)=51870.0d0
Hwater(772)=51871.0d0
Hwater(773)=51873.0d0
Hwater(774)=51874.0d0
Hwater(775)=51876.0d0
Hwater(776)=51877.0d0
Hwater(777)=51879.0d0
Hwater(778)=51880.0d0
Hwater(779)=51882.0d0
Hwater(780)=51884.0d0
Hwater(781)=51885.0d0
Hwater(782)=51887.0d0
Hwater(783)=51888.0d0
Hwater(784)=51890.0d0
Hwater(785)=51891.0d0
Hwater(786)=51893.0d0
Hwater(787)=51894.0d0
Hwater(788)=51896.0d0
Hwater(789)=51897.0d0
```

```
Hwater(790)=51899.0d0
Hwater(791)=51901.0d0
Hwater(792)=51902.0d0
Hwater(793)=51904.0d0
Hwater(794)=51905.0d0
Hwater(795)=51907.0d0
Hwater(796)=51908.0d0
Hwater(797)=51910.0d0
Hwater(798)=51911.0d0
Hwater(799)=51913.0d0
Hwater(800)=51914.0d0
Hwater(801)=51916.0d0
Hwater(802)=48690.0d0
Hwater(803)=48700.0d0
Hwater(804)=48701.0d0
Hwater(805)=48703.0d0
Hwater(806)=48704.0d0
Hwater(807)=48705.0d0
Hwater(808)=48707.0d0
Hwater(809)=48708.0d0
Hwater(810)=48710.0d0
Hwater(811)=48711.0d0


Twater(1)=40.0d0
Twater(2)=40.0d0
Twater(3)=40.0d0
Twater(4)=46.00d0
Twater(5)=46.00d0
Twater(6)=46.00d0
Twater(7)=46.00d0
Twater(8)=46.00d0
Twater(9)=46.00d0
```

```
Twater(10)=46.00d0
Twater(11)=46.00d0
Twater(12)=46.00d0
Twater(13)=46.00d0
Twater(14)=46.00d0
Twater(15)=46.00d0
Twater(16)=46.00d0
Twater(17)=46.00d0
Twater(18)=46.00d0
Twater(19)=46.00d0
Twater(20)=46.00d0
Twater(21)=46.00d0
Twater(22)=46.00d0
Twater(23)=46.00d0
Twater(24)=46.00d0
Twater(25)=46.00d0
Twater(26)=46.00d0
Twater(27)=46.00d0
Twater(28)=46.0d0
Twater(29)=46.10d0
Twater(30)=46.10d0
Twater(31)=46.10d0
Twater(32)=46.10d0
Twater(33)=46.10d0
Twater(34)=46.0d0
Twater(35)=46.20d0
Twater(36)=46.20d0
Twater(37)=46.20d0
Twater(38)=46.20d0
Twater(39)=46.20d0
Twater(40)=46.20d0
Twater(41)=46.0d0
Twater(42)=46.30d0
```

```
Twater(43)=46.30d0
Twater(44)=46.30d0
Twater(45)=46.30d0
Twater(46)=46.30d0
Twater(47)=46.30d0
Twater(48)=46.0d0
Twater(49)=46.40d0
Twater(50)=46.40d0
Twater(51)=46.40d0
Twater(52)=46.40d0
Twater(53)=46.40d0
Twater(54)=46.40d0
Twater(55)=46.0d0
Twater(56)=46.50d0
Twater(57)=46.50d0
Twater(58)=46.50d0
Twater(59)=46.50d0
Twater(60)=46.50d0
Twater(61)=46.50d0
Twater(62)=46.50d0
Twater(63)=46.0d0
Twater(64)=46.60d0
Twater(65)=46.60d0
Twater(66)=46.60d0
Twater(67)=46.60d0
Twater(68)=46.60d0
Twater(69)=46.60d0
Twater(70)=46.60d0
Twater(71)=46.60d0
Twater(72)=46.70d0
Twater(73)=46.70d0
Twater(74)=46.70d0
Twater(75)=46.70d0
```

```
Twater(76)=46.70d0
Twater(77)=46.70d0
Twater(78)=46.70d0
Twater(79)=46.70d0
Twater(80)=46.0d0
Twater(81)=46.80d0
Twater(82)=46.80d0
Twater(83)=46.80d0
Twater(84)=46.80d0
Twater(85)=46.80d0
Twater(86)=46.80d0
Twater(87)=46.80d0
Twater(88)=46.80d0
Twater(89)=46.0d0
Twater(90)=46.90d0
Twater(91)=46.90d0
Twater(92)=46.90d0
Twater(93)=46.90d0
Twater(94)=46.90d0
Twater(95)=46.90d0
Twater(96)=46.90d0
Twater(97)=46.90d0
Twater(98)=47.0d0
Twater(99)=47.00d0
Twater(100)=47.00d0
Twater(101)=47.00d0
Twater(102)=47.00d0
Twater(103)=47.00d0
Twater(104)=47.00d0
Twater(105)=47.00d0
Twater(106)=47.00d0
Twater(107)=47.00d0
Twater(108)=47.0d0
```

```
Twater(109)=47.10d0
Twater(110)=47.10d0
Twater(111)=47.10d0
Twater(112)=47.10d0
Twater(113)=47.10d0
Twater(114)=47.10d0
Twater(115)=47.10d0
Twater(116)=47.10d0
Twater(117)=47.10d0
Twater(118)=47.0d0
Twater(119)=47.20d0
Twater(120)=47.20d0
Twater(121)=47.20d0
Twater(122)=47.20d0
Twater(123)=47.20d0
Twater(124)=47.20d0
Twater(125)=47.20d0
Twater(126)=47.20d0
Twater(127)=47.20d0
Twater(128)=47.20d0
Twater(129)=47.0d0
Twater(130)=47.30d0
Twater(131)=47.30d0
Twater(132)=47.30d0
Twater(133)=47.30d0
Twater(134)=47.30d0
Twater(135)=47.30d0
Twater(136)=47.30d0
Twater(137)=47.30d0
Twater(138)=47.30d0
Twater(139)=47.0d0
Twater(140)=47.40d0
Twater(141)=47.40d0
```

```
Twater(142)=47.40d0
Twater(143)=47.40d0
Twater(144)=47.40d0
Twater(145)=47.40d0
Twater(146)=47.40d0
Twater(147)=47.40d0
Twater(148)=47.40d0
Twater(149)=47.40d0
Twater(150)=47.0d0
Twater(151)=47.50d0
Twater(152)=47.50d0
Twater(153)=47.50d0
Twater(154)=47.50d0
Twater(155)=47.50d0
Twater(156)=47.50d0
Twater(157)=47.50d0
Twater(158)=47.50d0
Twater(159)=47.50d0
Twater(160)=47.50d0
Twater(161)=47.50d0
Twater(162)=47.0d0
Twater(163)=47.60d0
Twater(164)=47.60d0
Twater(165)=47.60d0
Twater(166)=47.60d0
Twater(167)=47.60d0
Twater(168)=47.60d0
Twater(169)=47.60d0
Twater(170)=47.60d0
Twater(171)=47.60d0
Twater(172)=47.60d0
Twater(173)=47.0d0
Twater(174)=47.70d0
```

```
Twater(175)=47.70d0
Twater(176)=47.70d0
Twater(177)=47.70d0
Twater(178)=47.70d0
Twater(179)=47.70d0
Twater(180)=47.70d0
Twater(181)=47.70d0
Twater(182)=47.70d0
Twater(183)=47.70d0
Twater(184)=47.70d0
Twater(185)=47.0d0
Twater(186)=47.0d0
Twater(187)=47.80d0
Twater(188)=47.80d0
Twater(189)=47.80d0
Twater(190)=47.80d0
Twater(191)=47.80d0
Twater(192)=47.80d0
Twater(193)=47.80d0
Twater(194)=47.80d0
Twater(195)=47.80d0
Twater(196)=47.80d0
Twater(197)=47.80d0
Twater(198)=47.0d0
Twater(199)=47.90d0
Twater(200)=47.90d0
Twater(201)=47.90d0
Twater(202)=47.90d0
Twater(203)=47.90d0
Twater(204)=47.90d0
Twater(205)=47.90d0
Twater(206)=47.90d0
Twater(207)=47.90d0
```

```
Twater(208)=47.90d0
Twater(209)=47.90d0
Twater(210)=40d0
Twater(211)=40d0
Twater(212)=48.00d0
Twater(213)=48.00d0
Twater(214)=48.00d0
Twater(215)=48.00d0
Twater(216)=48.00d0
Twater(217)=48.00d0
Twater(218)=48.00d0
Twater(219)=48.00d0
Twater(220)=48.00d0
Twater(221)=48.00d0
Twater(222)=48.00d0
Twater(223)=48.0d0
Twater(224)=48.0d0
Twater(225)=48.10d0
Twater(226)=48.10d0
Twater(227)=48.10d0
Twater(228)=48.10d0
Twater(229)=48.10d0
Twater(230)=48.10d0
Twater(231)=48.10d0
Twater(232)=48.10d0
Twater(233)=48.10d0
Twater(234)=48.10d0
Twater(235)=48.10d0
Twater(236)=48.10d0
Twater(237)=48.0d0
Twater(238)=48.20d0
Twater(239)=48.20d0
Twater(240)=48.20d0
```

```
Twater(241)=48.20d0
Twater(242)=48.20d0
Twater(243)=48.20d0
Twater(244)=48.20d0
Twater(245)=48.20d0
Twater(246)=48.20d0
Twater(247)=48.20d0
Twater(248)=48.20d0
Twater(249)=48.20d0
Twater(250)=48.0d0
Twater(251)=48.0d0
Twater(252)=48.30d0
Twater(253)=48.30d0
Twater(254)=48.30d0
Twater(255)=48.30d0
Twater(256)=48.30d0
Twater(257)=48.30d0
Twater(258)=48.30d0
Twater(259)=48.30d0
Twater(260)=48.30d0
Twater(261)=48.30d0
Twater(262)=48.30d0
Twater(263)=48.30d0
Twater(264)=48.0d0
Twater(265)=48.40d0
Twater(266)=48.40d0
Twater(267)=48.40d0
Twater(268)=48.40d0
Twater(269)=48.40d0
Twater(270)=48.40d0
Twater(271)=48.40d0
Twater(272)=48.40d0
Twater(273)=48.40d0
```

```
Twater(274)=48.40d0
Twater(275)=48.40d0
Twater(276)=48.40d0
Twater(277)=48.40d0
Twater(278)=48.0d0
Twater(279)=48.0d0
Twater(280)=48.50d0
Twater(281)=48.50d0
Twater(282)=48.50d0
Twater(283)=48.50d0
Twater(284)=48.50d0
Twater(285)=48.50d0
Twater(286)=48.50d0
Twater(287)=48.50d0
Twater(288)=48.50d0
Twater(289)=48.50d0
Twater(290)=48.50d0
Twater(291)=48.50d0
Twater(292)=48.50d0
Twater(293)=48.0d0
Twater(294)=48.60d0
Twater(295)=48.60d0
Twater(296)=48.60d0
Twater(297)=48.60d0
Twater(298)=48.60d0
Twater(299)=48.60d0
Twater(300)=48.60d0
Twater(301)=48.60d0
Twater(302)=48.60d0
Twater(303)=48.60d0
Twater(304)=48.60d0
Twater(305)=48.60d0
Twater(306)=48.60d0
```

```
Twater(307)=48.60d0
Twater(308)=48.0d0
Twater(309)=48.70d0
Twater(310)=48.70d0
Twater(311)=48.70d0
Twater(312)=48.70d0
Twater(313)=48.70d0
Twater(314)=48.70d0
Twater(315)=48.70d0
Twater(316)=48.70d0
Twater(317)=48.70d0
Twater(318)=48.70d0
Twater(319)=48.70d0
Twater(320)=48.70d0
Twater(321)=48.70d0
Twater(322)=48.70d0
Twater(323)=48.0d0
Twater(324)=48.80d0
Twater(325)=48.80d0
Twater(326)=48.80d0
Twater(327)=48.80d0
Twater(328)=48.80d0
Twater(329)=48.80d0
Twater(330)=48.80d0
Twater(331)=48.80d0
Twater(332)=48.80d0
Twater(333)=48.80d0
Twater(334)=48.80d0
Twater(335)=48.80d0
Twater(336)=48.80d0
Twater(337)=48.80d0
Twater(338)=48.0d0
Twater(339)=48.0d0
```

```
Twater(340)=48.90d0
Twater(341)=48.90d0
Twater(342)=48.90d0
Twater(343)=48.90d0
Twater(344)=48.90d0
Twater(345)=48.90d0
Twater(346)=48.90d0
Twater(347)=48.90d0
Twater(348)=48.90d0
Twater(349)=48.90d0
Twater(350)=48.90d0
Twater(351)=48.90d0
Twater(352)=48.90d0
Twater(353)=48.90d0
Twater(354)=49.0d0
Twater(355)=49.0d0
Twater(356)=49.00d0
Twater(357)=49.00d0
Twater(358)=49.00d0
Twater(359)=49.00d0
Twater(360)=49.00d0
Twater(361)=49.00d0
Twater(362)=49.00d0
Twater(363)=49.00d0
Twater(364)=49.00d0
Twater(365)=49.00d0
Twater(366)=49.00d0
Twater(367)=49.00d0
Twater(368)=49.00d0
Twater(369)=49.00d0
Twater(370)=49.0d0
Twater(371)=49.0d0
Twater(372)=49.10d0
```

```
Twater(373)=49.10d0
Twater(374)=49.10d0
Twater(375)=49.10d0
Twater(376)=49.10d0
Twater(377)=49.10d0
Twater(378)=49.10d0
Twater(379)=49.10d0
Twater(380)=49.10d0
Twater(381)=49.10d0
Twater(382)=49.10d0
Twater(383)=49.10d0
Twater(384)=49.10d0
Twater(385)=49.10d0
Twater(386)=49.10d0
Twater(387)=49.0d0
Twater(388)=49.20d0
Twater(389)=49.20d0
Twater(390)=49.20d0
Twater(391)=49.20d0
Twater(392)=49.20d0
Twater(393)=49.20d0
Twater(394)=49.20d0
Twater(395)=49.20d0
Twater(396)=49.20d0
Twater(397)=49.20d0
Twater(398)=49.20d0
Twater(399)=49.20d0
Twater(400)=49.20d0
Twater(401)=49.20d0
Twater(402)=49.20d0
Twater(403)=49.0d0
Twater(404)=49.0d0
Twater(405)=49.30d0
```

```
Twater(406)=49.30d0
Twater(407)=49.30d0
Twater(408)=49.30d0
Twater(409)=49.30d0
Twater(410)=49.30d0
Twater(411)=49.30d0
Twater(412)=49.30d0
Twater(413)=49.30d0
Twater(414)=49.30d0
Twater(415)=49.30d0
Twater(416)=49.30d0
Twater(417)=49.30d0
Twater(418)=49.30d0
Twater(419)=49.30d0
Twater(420)=49.0d0
Twater(421)=49.0d0
Twater(422)=49.40d0
Twater(423)=49.40d0
Twater(424)=49.40d0
Twater(425)=49.40d0
Twater(426)=49.40d0
Twater(427)=49.40d0
Twater(428)=49.40d0
Twater(429)=49.40d0
Twater(430)=49.40d0
Twater(431)=49.40d0
Twater(432)=49.40d0
Twater(433)=49.40d0
Twater(434)=49.40d0
Twater(435)=49.40d0
Twater(436)=49.40d0
Twater(437)=49.40d0
Twater(438)=49.0d0
```

```
Twater(439)=49.50d0
Twater(440)=49.50d0
Twater(441)=49.50d0
Twater(442)=49.50d0
Twater(443)=49.50d0
Twater(444)=49.50d0
Twater(445)=49.50d0
Twater(446)=49.50d0
Twater(447)=49.50d0
Twater(448)=49.50d0
Twater(449)=49.50d0
Twater(450)=49.50d0
Twater(451)=49.50d0
Twater(452)=49.50d0
Twater(453)=49.50d0
Twater(454)=49.50d0
Twater(455)=49.0d0
Twater(456)=49.0d0
Twater(457)=49.60d0
Twater(458)=49.60d0
Twater(459)=49.60d0
Twater(460)=49.60d0
Twater(461)=49.60d0
Twater(462)=49.60d0
Twater(463)=49.60d0
Twater(464)=49.60d0
Twater(465)=49.60d0
Twater(466)=49.60d0
Twater(467)=49.60d0
Twater(468)=49.60d0
Twater(469)=49.60d0
Twater(470)=49.60d0
Twater(471)=49.60d0
```

```
Twater(472)=49.60d0
Twater(473)=49.0d0
Twater(474)=49.0d0
Twater(475)=49.70d0
Twater(476)=49.70d0
Twater(477)=49.70d0
Twater(478)=49.70d0
Twater(479)=49.70d0
Twater(480)=49.70d0
Twater(481)=49.70d0
Twater(482)=49.70d0
Twater(483)=49.70d0
Twater(484)=49.70d0
Twater(485)=49.70d0
Twater(486)=49.70d0
Twater(487)=49.70d0
Twater(488)=49.70d0
Twater(489)=49.70d0
Twater(490)=49.70d0
Twater(491)=49.0d0
Twater(492)=49.0d0
Twater(493)=49.80d0
Twater(494)=49.80d0
Twater(495)=49.80d0
Twater(496)=49.80d0
Twater(497)=49.80d0
Twater(498)=49.80d0
Twater(499)=49.80d0
Twater(500)=49.80d0
Twater(501)=49.80d0
Twater(502)=49.80d0
Twater(503)=49.80d0
Twater(504)=49.80d0
```

```
Twater(505)=49.80d0
Twater(506)=49.80d0
Twater(507)=49.80d0
Twater(508)=49.80d0
Twater(509)=49.80d0
Twater(510)=49.0d0
Twater(511)=49.0d0
Twater(512)=49.90d0
Twater(513)=49.90d0
Twater(514)=49.90d0
Twater(515)=49.90d0
Twater(516)=49.90d0
Twater(517)=49.90d0
Twater(518)=49.90d0
Twater(519)=49.90d0
Twater(520)=49.90d0
Twater(521)=49.90d0
Twater(522)=49.90d0
Twater(523)=49.90d0
Twater(524)=49.90d0
Twater(525)=49.90d0
Twater(526)=49.90d0
Twater(527)=49.90d0
Twater(528)=49.90d0
Twater(529)=50.0d0
Twater(530)=50.00d0
Twater(531)=50.00d0
Twater(532)=50.00d0
Twater(533)=50.00d0
Twater(534)=50.00d0
Twater(535)=50.00d0
Twater(536)=50.00d0
Twater(537)=50.00d0
```

```
Twater(538)=50.00d0
Twater(539)=50.00d0
Twater(540)=50.00d0
Twater(541)=50.00d0
Twater(542)=50.00d0
Twater(543)=50.00d0
Twater(544)=50.00d0
Twater(545)=50.00d0
Twater(546)=50.00d0
Twater(547)=50.00d0
Twater(548)=50.0d0
Twater(549)=50.0d0
Twater(550)=50.10d0
Twater(551)=50.10d0
Twater(552)=50.10d0
Twater(553)=50.10d0
Twater(554)=50.10d0
Twater(555)=50.10d0
Twater(556)=50.10d0
Twater(557)=50.10d0
Twater(558)=50.10d0
Twater(559)=50.10d0
Twater(560)=50.10d0
Twater(561)=50.10d0
Twater(562)=50.10d0
Twater(563)=50.10d0
Twater(564)=50.10d0
Twater(565)=50.10d0
Twater(566)=50.10d0
Twater(567)=50.0d0
Twater(568)=50.0d0
Twater(569)=50.20d0
Twater(570)=50.20d0
```

```
Twater(571)=50.20d0
Twater(572)=50.20d0
Twater(573)=50.20d0
Twater(574)=50.20d0
Twater(575)=50.20d0
Twater(576)=50.20d0
Twater(577)=50.20d0
Twater(578)=50.20d0
Twater(579)=50.20d0
Twater(580)=50.20d0
Twater(581)=50.20d0
Twater(582)=50.20d0
Twater(583)=50.20d0
Twater(584)=50.20d0
Twater(585)=50.20d0
Twater(586)=50.20d0
Twater(587)=50.0d0
Twater(588)=50.0d0
Twater(589)=50.30d0
Twater(590)=50.30d0
Twater(591)=50.30d0
Twater(592)=50.30d0
Twater(593)=50.30d0
Twater(594)=50.30d0
Twater(595)=50.30d0
Twater(596)=50.30d0
Twater(597)=50.30d0
Twater(598)=50.30d0
Twater(599)=50.30d0
Twater(600)=50.30d0
Twater(601)=50.30d0
Twater(602)=50.30d0
Twater(603)=50.30d0
```

```
Twater(604)=50.30d0
Twater(605)=50.30d0
Twater(606)=50.30d0
Twater(607)=50.0d0
Twater(608)=50.0d0
Twater(609)=50.40d0
Twater(610)=50.40d0
Twater(611)=50.40d0
Twater(612)=50.40d0
Twater(613)=50.40d0
Twater(614)=50.40d0
Twater(615)=50.40d0
Twater(616)=50.40d0
Twater(617)=50.40d0
Twater(618)=50.40d0
Twater(619)=50.40d0
Twater(620)=50.40d0
Twater(621)=50.40d0
Twater(622)=50.40d0
Twater(623)=50.40d0
Twater(624)=50.40d0
Twater(625)=50.40d0
Twater(626)=50.40d0
Twater(627)=50.0d0
Twater(628)=50.0d0
Twater(629)=50.50d0
Twater(630)=50.50d0
Twater(631)=50.50d0
Twater(632)=50.50d0
Twater(633)=50.50d0
Twater(634)=50.50d0
Twater(635)=50.50d0
Twater(636)=50.50d0
```

```
Twater(637)=50.50d0
Twater(638)=50.50d0
Twater(639)=50.50d0
Twater(640)=50.50d0
Twater(641)=50.50d0
Twater(642)=50.50d0
Twater(643)=50.50d0
Twater(644)=50.50d0
Twater(645)=50.50d0
Twater(646)=50.50d0
Twater(647)=50.50d0
Twater(648)=50.0d0
Twater(649)=50.0d0
Twater(650)=50.60d0
Twater(651)=50.60d0
Twater(652)=50.60d0
Twater(653)=50.60d0
Twater(654)=50.60d0
Twater(655)=50.60d0
Twater(656)=50.60d0
Twater(657)=50.60d0
Twater(658)=50.60d0
Twater(659)=50.60d0
Twater(660)=50.60d0
Twater(661)=50.60d0
Twater(662)=50.60d0
Twater(663)=50.60d0
Twater(664)=50.60d0
Twater(665)=50.60d0
Twater(666)=50.60d0
Twater(667)=50.60d0
Twater(668)=50.60d0
Twater(669)=50.0d0
```

```
Twater(670)=50.0d0
Twater(671)=50.70d0
Twater(672)=50.70d0
Twater(673)=50.70d0
Twater(674)=50.70d0
Twater(675)=50.70d0
Twater(676)=50.70d0
Twater(677)=50.70d0
Twater(678)=50.70d0
Twater(679)=50.70d0
Twater(680)=50.70d0
Twater(681)=50.70d0
Twater(682)=50.70d0
Twater(683)=50.70d0
Twater(684)=50.70d0
Twater(685)=50.70d0
Twater(686)=50.70d0
Twater(687)=50.70d0
Twater(688)=50.70d0
Twater(689)=50.70d0
Twater(690)=50.0d0
Twater(691)=50.0d0
Twater(692)=50.80d0
Twater(693)=50.80d0
Twater(694)=50.80d0
Twater(695)=50.80d0
Twater(696)=50.80d0
Twater(697)=50.80d0
Twater(698)=50.80d0
Twater(699)=50.80d0
Twater(700)=50.80d0
Twater(701)=50.80d0
Twater(702)=50.80d0
```

```
Twater(703)=50.80d0
Twater(704)=50.80d0
Twater(705)=50.80d0
Twater(706)=50.80d0
Twater(707)=50.80d0
Twater(708)=50.80d0
Twater(709)=50.80d0
Twater(710)=50.80d0
Twater(711)=50.0d0
Twater(712)=50.0d0
Twater(713)=50.0d0
Twater(714)=50.90d0
Twater(715)=50.90d0
Twater(716)=50.90d0
Twater(717)=50.90d0
Twater(718)=50.90d0
Twater(719)=50.90d0
Twater(720)=50.90d0
Twater(721)=50.90d0
Twater(722)=50.90d0
Twater(723)=50.90d0
Twater(724)=50.90d0
Twater(725)=50.90d0
Twater(726)=50.90d0
Twater(727)=50.90d0
Twater(728)=50.90d0
Twater(729)=50.90d0
Twater(730)=50.90d0
Twater(731)=50.90d0
Twater(732)=50.90d0
Twater(733)=50.0d0
Twater(734)=50.0d0
Twater(735)=51.00d0
```

```
Twater(736)=51.00d0
Twater(737)=51.00d0
Twater(738)=51.00d0
Twater(739)=51.00d0
Twater(740)=51.00d0
Twater(741)=51.00d0
Twater(742)=51.00d0
Twater(743)=51.00d0
Twater(744)=51.00d0
Twater(745)=51.00d0
Twater(746)=51.00d0
Twater(747)=51.00d0
Twater(748)=51.00d0
Twater(749)=51.00d0
Twater(750)=51.00d0
Twater(751)=51.00d0
Twater(752)=51.00d0
Twater(753)=51.00d0
Twater(754)=51.00d0
Twater(755)=51.0d0
Twater(756)=51.0d0
Twater(757)=51.0d0
Twater(758)=51.10d0
Twater(759)=51.10d0
Twater(760)=51.10d0
Twater(761)=51.10d0
Twater(762)=51.10d0
Twater(763)=51.10d0
Twater(764)=51.10d0
Twater(765)=51.10d0
Twater(766)=51.10d0
Twater(767)=51.10d0
Twater(768)=51.10d0
```

```
Twater(769)=51.10d0
Twater(770)=51.10d0
Twater(771)=51.10d0
Twater(772)=51.10d0
Twater(773)=51.10d0
Twater(774)=51.10d0
Twater(775)=51.10d0
Twater(776)=51.10d0
Twater(777)=51.10d0
Twater(778)=51.0d0
Twater(779)=51.0d0
Twater(780)=51.20d0
Twater(781)=51.20d0
Twater(782)=51.20d0
Twater(783)=51.20d0
Twater(784)=51.20d0
Twater(785)=51.20d0
Twater(786)=51.20d0
Twater(787)=51.20d0
Twater(788)=51.20d0
Twater(789)=51.20d0
Twater(790)=51.20d0
Twater(791)=51.20d0
Twater(792)=51.20d0
Twater(793)=51.20d0
Twater(794)=51.20d0
Twater(795)=51.20d0
Twater(796)=51.20d0
Twater(797)=51.20d0
Twater(798)=51.20d0
Twater(799)=51.20d0
Twater(800)=51.20d0
Twater(801)=51.0d0
```

```
        Twater(802)=51.0d0
        Twater(803)=51.30d0
        Twater(804)=51.30d0
        Twater(805)=51.30d0
        Twater(806)=51.30d0
        Twater(807)=51.30d0
        Twater(808)=51.30d0
        Twater(809)=51.30d0
        Twater(810)=51.30d0
        Twater(811)=51.30d0
CCCCCCCCCCCCCCCCCCCCCCCCCCCCCCCCCCCCCCCCCCCCCCCCCCCCCCCCCCCCCCCCCCCCCCC
      z     = coords(3)                  ! mm
      zmen  = 90.0d0                     ! meniscus position, mm
      vcast = 1.5d0*(1000.0d0/60.0d0)    ! vcast to mm/s
      t = (z-zmen)/vcast                 ! time corresponding to z

      call interp(Tim, Hwater, TIME(2), hwa, 811)    ! hw now convection coefficient
      call interp(Tim, Twater, TIME(2), twa, 811)    ! tw now water temperature

      hwa = hwa/1000.0D0

      Kmold = 315.0D0   ! CONDUCTIVITY OF THE COPPER MOLD

      Dcoat = 0.0D0     ! THICKNESS OF THE MOLD COATING
      Kcoat = 0.0D0     ! CONDUCTIVITY OF THE MOLD COATING
      Dfoul = 0.0D0     ! THICKNESS OF THE FOULING LAYER
      Kfoul = 0.0D0     ! CONDUCTIVITY OF THE FOULING LAYER

      Dc    = 13.920D0     ! Calibrated DEPTH OF THE WATER CHANNELS
      Wc    = 6.70D0     ! Calibrated WIDTH OF THE WATER CHANNELS
      Pc    = 18.8D0     ! PITCH OF THE WATER CHANNELS
CCCCCCCCCCCCCCCCCCCCCCCCCCCCCCCCCCCCCCCCCCCCCCCCCCCCCCCCCCCCCCCCCCCCCCC
      Beta = (hwa*Dc/Kmold)
```

```
      Beta = Beta/DSQRT((hwa*(Pc-Wc))/Kmold/2)
CCCCCCCCCCCCCCCCCCCCCCCCCCCCCCCCCCCCCCCCCCCCCCCCCCCCCCCCCCCCCCCCCCC

      Hfins = (Kmold/Dc)*Beta*DTANH(Beta)      !FIN EFFECT CALCULATION
      Hroots = 1/((1/hwa))                     !NO FOULING CASE
      Hcold = (Wc/Pc)*Hroots+(1-(Wc/Pc))*Hfins !FIN/CHANNEL EFFECTS CALCULATION
      Hmold = 1/((1/Hcold))                    !NO COATING CASE ALSO NO MOLD

      h(1) = Hmold  !FILM COEFFICIENT
      h(2) = 0.0d0  !FILM COEFFICIENT DERIVATIVE WRT TSURF
      sink = twa    !SINK TEMPERATURE

      return
      end subroutine film
CCCCCCCCCCCCCCCCCCCC
```

```
      CHARACTER*80 CMNAME
      DIMENSION TEMP(2),STATEV(*),PREDEF(*),TIME(2),FLUX(2),
     & DPRED(*)
      DOUBLE PRECISION STOPTIME, INITIALVAL, HVAL
CCCCCCCCCCCCCCCCCCCCCCCCCCCCCCCCCCCCCCCCCCCCCCCCCCCCCCCCCCCCCCCCCCCCCCCCCC
      STOPTIME = 10.0D0

      IF (TIME(2).LT.STOPTIME) THEN
        FLUX(1) = 0.0D0+0.13D0*TEMP(1)**1.18D0
        FLUX(1) = FLUX(1)*(1.0d0-ERF(TIME(1)/6.0d0))
        FLUX(1) = -1.0D0*FLUX(1)
      ELSE
        FLUX(1) = 0.0D0
      END IF

      FLUX(2) = 0.0D0

      RETURN
      END
CCCCCCCCCCCCCCCCCCCCCCCCCCCCCCCCCCCCCCCCCCCCCCCCCCCCCCCCCCCCCCCCCCCCCCCCCC
```

D.3 GAPCON for Resistor Model

The full details for GAPCON can be found in the ABAQUS User Subroutine Reference Guide [77]. The subroutine allows for the definition of k_{Gap} as a function of other input parameters. It assumes that the heat transfer between surfaces is modeled as $q'' = k_{Gap}(T_{Master} - T_{Slave})$. Where q'' is the heat flux per unit area flowing between corresponding points on the master and slave surfaces, k_{Gap} is the gap conductance, and T_{Master} and T_{Slave} are the master and slave surface temperature respectively. GAPCON is called for every increment at the slave nodes of a contact pair, in our case this means it is called for every node on the surface of the steel shell.

Note about the Abaqus Fortran environment: Within a subroutine call once a variable has been set to a value. Either initially, or from a previous calculation increment, it holds that value until it is set to a different value, is cleared, or the simulation is terminated. *However, each time a subroutine call is returned the stored values disappear. In order to make a variable value persist across subroutine calls the FORTRAN "save" keyword is necessary.* This is particularly important for the flag used in the example code to track whether the entire flux layer has become solid.

```
CCCCCCCCCCCCCCCCCCCCCCCCCCCCCCCCCCCCCCCCCCCCCCCCCCCCCCCCCCCCCCCCCCCCCCCCCC
C                                                                     C
C           INTERNAL ABAQUS GAP CONDUCTIVITY SUBROUTINE               C
C                                                                     C
C                 TEMPERATURE VARYING PROPERTIES                      C
C              SOLID/LIQUID FLUX AND AIR GAP FORMATION                C
C                                                                     C
C            CREATED BY MATTHEW L.S. ZAPPULLA, MARCH 2016             C
C                                                                     C
CCCCCCCCCCCCCCCCCCCCCCCCCCCCCCCCCCCCCCCCCCCCCCCCCCCCCCCCCCCCCCCCCCCCCCCCCC

      SUBROUTINE GAPCON(AK,D,FLOWM,TEMP,PREDEF,TIME,CINAME,SLNAME,
     1                  MSNAME,COORDS,NOEL,NODE,NPRED,KSTEP,KINC)

      INCLUDE 'ABA_PARAM.INC'
      CHARACTER*80 CINAME,SLNAME,MSNAME
      DIMENSION AK(5),D(2), FLOWM(2), TEMP(2), PREDEF(2,*),
     1 TIME(2), COORDS(3)

      DOUBLE PRECISION DGAP, DAIR, DSOL, DLIQ, SLAG
      DOUBLE PRECISION LiqThresh, AirThresh
      DOUBLE PRECISION TMOLD, TSHELL, TCRYSTAL, TMC, TLS
      DOUBLE PRECISION KAIR, KLIQ, KSOL
      DOUBLE PRECISION RAIR, RSOL, RLIQ, RTOT, RGAP
```

```
      DOUBLE PRECISION ShellIntR, RCONTACT
      DOUBLE PRECISION HGAP
      DOUBLE PRECISION FLAG
      DOUBLE PRECISION ITER, ITERS
      DOUBLE PRECISION STARTCOORD, ENDCOORD, STARTVAL, ENDVAL
      INTEGER KINC
      SAVE FLAG, TLS, TMC

CCCCCCCCCCCCCCCCCCCCCCCCCCCCCCCCCCCCCCCCCCCCCCCCCCCCCCCCCCCCCCCCCCCCCCC
C  DEFINE PARAMETERS
CCCCCCCCCCCCCCCCCCCCCCCCCCCCCCCCCCCCCCCCCCCCCCCCCCCCCCCCCCCCCCCCCCCCCCC
      TCRYSTAL = 1030.0D0   !FLUX CRYSTALLIZATION TEMPERATURE, DEG C

      KSOL = 0.5D0          !FIXED CONDUCTIVITY OF THE SOLID SLAG
      KLIQ = 3.0D0          !FIXED CONDUCTIVITY OF THE LIQUID SLAG

      ITER = 0.0D0          !SET THE ITERATION COUNTER TO ZERO
      ITERS = 20.0D0       !TOTAL NUMBER OF ITERATIONS

      LiqThresh = 0.00001D0 !MINIMUM LIQUID THRESHOLD SIZE [m]
      AirThresh = 0.00001D0 !MINIMUM AIR GAP THRESHOLD SIZE [m]

      IF (COORDS(2).LE.-15.0D0) THEN
        SLAG = 0.001D0
      ELSE
        SLAG = 0.002D0        !DEFINE THE SLAG LAYER THICKNESS
      END IF

   IF USING THE INPUT FILE TEMPLATE OF ZAPPULLA AND HIBBELER
   THE DOMAIN IS CENTERED AT 0, SO ALL NEGATIVE Y COORDINATES ARE
   IN THE DIRECTION OF THE DEPRESSION CENTERLINE

CCCCCCCCCCCCCCCCCCCCCCCCCCCCCCCCCCCCCCCCCCCCCCCCCCCCCCCCCCCCCCCCCCCCCCC
```

```
C  UNPACK VALUES FROM ABAQUS
CCCCCCCCCCCCCCCCCCCCCCCCCCCCCCCCCCCCCCCCCCCCCCCCCCCCCCCCCCCCCCCCCCCCCCC
      TSHELL = TEMP(1)  ! SLAVE SURFACE TEMPERATURE
      TMOLD  = TEMP(2)  ! MASTER SURFACE TEMPERATURE
CCCCCCCCCCCCCCCCCCCCCCCCCCCCCCCCCCCCCCCCCCCCCCCCCCCCCCCCCCCCCCCCCCCCCCC
C  THERMAL RESISTANCE OF AIR GAP
CCCCCCCCCCCCCCCCCCCCCCCCCCCCCCCCCCCCCCCCCCCCCCCCCCCCCCCCCCCCCCCCCCCCCCC

      DAIR = D(1)/1000.0D0

      IF (DAIR.LE.AirThresh) THEN
        DAIR = 0.0D0
        RAIR = 0.0D0
      ELSE
        DAIR = DAIR
        KAIR = 6.0D-2  ! mW/(mm*K)
        RAIR = DAIR/KAIR
      END IF

      DGAP   = SLAG     ! GAP SIZE

      IF (TSHELL.GT.1532.0D0) THEN
        TLS = 1400.0D0
        TMC = 250.0D0
        RSOL = (DGAP/2)/KSOL
        RLIQ = (DGAP/2)/KLIQ
        FLAG = 0.0D0
      END IF
CCCCCCCCCCCCCCCCCCCCCCCCCCCCCCCCCCCCCCCCCCCCCCCCCCCCCCCCCCCCCCCCCCCCCCC
C  MOLD-FLUX INTERFACE CONTACT RESISTANCE
CCCCCCCCCCCCCCCCCCCCCCCCCCCCCCCCCCCCCCCCCCCCCCCCCCCCCCCCCCCCCCCCCCCCCCC
      RCONTACT = 1.0D0/2500.0D0 !m2K/W
```

```
      IF (FLAG.EQ.1.0D0) THEN

        DSOL = DGAP
        RSOL = DSOL/KSOL
        ShellIntR = 1.0D0/1000.0D0
        RTOT = RCONTACT + RSOL + ShellIntR + RAIR
        TMC = TMOLD+(TSHELL-TMOLD)*(RCONTACT/RTOT)
        TLS = (TMC+(TSHELL-TMOLD)*((RSOL+RAIR)/RTOT))
        GOTO 1738
      END IF
CCCCCCCCCCCCCCCCCCCCCCCCCCCCCCCCCCCCCCCCCCCCCCCCCCCCCCCCCCCCCCCCCCCC
CCCCCCCCCCCCCCCCCCCCCCCCCCCCCCCCCCCCCCCCCCCCCCCCCCCCCCCCCCCCCCCCCCCC
C   START OF THE GAP LAYER ITERATION LOOP
CCCCCCCCCCCCCCCCCCCCCCCCCCCCCCCCCCCCCCCCCCCCCCCCCCCCCCCCCCCCCCCCCCCC
CCCCCCCCCCCCCCCCCCCCCCCCCCCCCCCCCCCCCCCCCCCCCCCCCCCCCCCCCCCCCCCCCCCC
      DO WHILE(ITER.LT.ITERS)
CCCCCCCCCCCCCCCCCCCCCCCCCCCCCC
C   SHELL INTERFACE RESISTANCE
CCCCCCCCCCCCCCCCCCCCCCCCCCCCCC
          ShellIntR = (3.8981D0*DEXP(0.0054D0*TLS))
          IF (ShellIntR.LT.1000.0D0) THEN
            ShellIntR = 1000.0D0
          END IF
          IF (ShellIntR.GT.20000.0D0) THEN
            ShellIntR = 20000.0D0
          END IF

          ShellIntR = 1.0D0/ShellIntR

CCCCCCCCCCCCCCCCCCCCC
C    TOTAL RESISTANCE
CCCCCCCCCCCCCCCCCCCCC
```

```
          RTOT = RCONTACT + RLIQ + RSOL + ShellIntR + RAIR

CCCCCCCCCCCCCCCCCCCCCCCCCCCCCCC
C    TEMPERATURES THROUGH GAP
CCCCCCCCCCCCCCCCCCCCCCCCCCCCCCCCC

        TMC = TMOLD+(TSHELL-TMOLD)*(RCONTACT/RTOT)
        TLS = (Tmc+(TSHELL-TMOLD)*((RSOL+RLIQ+RAIR)/RTOT))

CCCCCCCCCCCCCCCCCCCCCCCCCCCCCCCCCCCCCCCCCCCCCCC
C  DIVIDE GAP INTO LIQUID AND SOLID PARTS
CCCCCCCCCCCCCCCCCCCCCCCCCCCCCCCCCCCCCCCCCCCCCCC

        DSOL = (TCRYSTAL-TMC)*DGAP/(TLS-TMC)
        DLIQ = DGAP-DSOL
        IF ((DLIQ.LT.LiqThresh).OR.(FLAG.EQ.1.0D0)) THEN
            DSOL = DGAP
            DLIQ = 0.0D0
            RLIQ = 0.0D0
            RSOL = DSOL/KSOL
        ELSE
            RLIQ = DLIQ/KLIQ
            RSOL = DSOL/KSOL
        END IF

          ITER = ITER + 1.0D0

      END DO
CCCCCCCCCCCCCCCCCCCCCCCCCCCCCCCCCCCCCCCCCCCCCCCCCCCCCCCCCCCCCCCCCCCCCCCCCCC
CCCCCCCCCCCCCCCCCCCCCCCCCCCCCCCCCCCCCCCCCCCCCCCCCCCCCCCCCCCCCCCCCCCCCCCCCCC
C
C   END OF THE GAP LAYER ITERATION LOOP
C
```

```
CCCCCCCCCCCCCCCCCCCCCCCCCCCCCCCCCCCCCCCCCCCCCCCCCCCCCCCCCCCCCCCCCCCC
CCCCCCCCCCCCCCCCCCCCCCCCCCCCCCCCCCCCCCCCCCCCCCCCCCCCCCCCCCCCCCCCCCCC
1738  IF ((TSHELL.LT.1400.0D0).AND.(DSOL.EQ.DGAP)) THEN
        FLAG = 1.0D0
      END IF
CCCCCCCCCCCCCCCCCCCCCCCCCCCCCCCCCC
C  GAP HEAT TRANSFER COEFFICIENT
CCCCCCCCCCCCCCCCCCCCCCCCCCCCCCCCCC
      RGAP = RTOT
      HGAP = 1.0D0/RGAP
CCCCCCCCCCCCCCCCCCCCCCCCCCCCCCCCCCCC
C  PACK VALUES AND RETURN TO ABAQUS
CCCCCCCCCCCCCCCCCCCCCCCCCCCCCCCCCCCC
      AK(1) = HGAP/100.0D0  ! GAP CONDUCTANCE, mW/(mm^2*K)
      AK(2) = 0.0D0         ! DERIV WRT GAP SIZE
      AK(3) = 0.0D0         ! DERIV WRT PRESSURE
      AK(4) = 0.0D0         ! DERIV WRT SLAVE SURFACE TEMPERATURE
      AK(5) = 0.0D0         ! DERIV WRT MASTER SURFACE TEMPERATURE

      RETURN
      END SUBROUTINE GAPCON

CCCCCCCCCCCCCCCCCCCCCCCCCCCCCCCCCCCCCCCCCCCCCCCCCCCCCCCCCCCCCCCCCCCC
CCCCCCCCCCCCCCCCCCCCCCCCCCCCCCCCCCCCCCCCCCCCCCCCCCCCCCCCCCCCCCCCCCCC
```

D.4 MPC Cracking Subroutine

The MPC user subroutine is called to impose a user-defined multi-point constraint and is intended for use when general constraints cannot be defined with one of the MPC types provided by ABAQUS/Standard and is chosen primarily because it makes it possible to switch constraints on and off during an analysis. In this work it was used to allow dynamic changes to a boundary condition simulated with an MPC.

```
CCCCCCCCCCCCCCCCCCCCCCCCCCCCCCCCCCCCCCCCCCCCCCCCCCCCCCCCCCCCCCCCCCCCCCCCCCCC
C                                                                      C
C         INTERNAL ABAQUS MULTI-POINT CONSTRAINT SUBROUTINE            C
C                                                                      C
C            SPECIFIC CONDITION IS A CRACK FOLLOWING                   C
C                 A 3.3*SQRT(t)-3.0 PROFILE                            C
C                AND ARRESTING AT A LENGTH OF 4.5 MM                   C
C                                                                      C
C            CREATED BY MATTHEW L.S. ZAPPULLA, 2017                    C
C                                                                      C
CCCCCCCCCCCCCCCCCCCCCCCCCCCCCCCCCCCCCCCCCCCCCCCCCCCCCCCCCCCCCCCCCCCCCCCCCCCC

      SUBROUTINE MPC(UE,A,JDOF,MDOF,N,JTYPE,X,U,UINIT,MAXDOF,
     & LMPC,KSTEP,KINC,TIME,NT,NF,TEMP,FIELD,LTRAN,TRAN)

      INCLUDE 'ABA_PARAM.INC'

      DIMENSION A(N),JDOF(N),X(6,N),U(MAXDOF,N),UINIT(MAXDOF,N),
     & TIME(2),TEMP(NT,N),FIELD(NF,NT,N),LTRAN(N),TRAN(3,3,N)

      LMPC=1        !INITIALIZE ALL OF THE CONSTRAINTS TO REMAIN ACTIVE

      FARLIQCRV = 3.3D0*DSQRT(TIME(2))  !DEFINE THE CRACK PROPAGATION HISTORY
      FARSLDCRV = FARLIQCRV - 3.0D0     !DEFINE THE CRACK PROPAGATION HISTORY

      VL = FARSLDCRV/0.5D0      !ACCOUNT FOR THE SIZE OF ELEMENTS

      IF (JTYPE.LE.9.0D0) THEN  !ACCOUNT FOR AN ARRESTED CRACK
        IF (VL.GE.JTYPE) THEN
            LMPC=0              !DEACTIVATE GIVEN JTYPE(#) CONSTRAINT
        END IF
      END IF
```

```
C---------- Set Y displacement of node a = node b
      JDOF(1) = 2    !ESTABLISH WHICH DOF IS IN USE FOR THE FIRST  MPC NODE
      JDOF(2) = 2    !ESTABLISH WHICH DOF IS IN USE FOR THE SECOND MPC NODE

      A(1) = 1.0     !EQUAL AND OPPOSITE DISPLACEMENTS
      A(2) = -1.0    !EQUAL AND OPPOSITE DISPLACEMENTS

      UE = U(2,2)

       RETURN
       END
CCCCCCCCCCCCCCCCCCCCCCCCCCCCCCCCCCCCCCCCCCCCCCCCCCCCCCCCCCCCCCCCCCCCCCC
CCCCCCCCCCCCCCCCCCCCCCCCCCCCCCCCCCCCCCCCCCCCCCCCCCCCCCCCCCCCCCCCCCCCCCC
```

APPENDIX E

POST-PROCESSING SCRIPTS

This section contains example code from this work and helpful scripts to be used in the post processing of Abaqus results.

Copyright (c) <2020> <Matthew L.S. Zappulla> Permission is hereby granted, free of charge, to any person obtaining a copy of this software and associated documentation files (the "Software"), to deal in the Software without restriction, including without limitation the rights to use, copy, modify, merge, publish, distribute, sublicense, and/or sell copies of the Software, and to permit persons to whom the Software is furnished to do so, subject to the following conditions: The above copyright notice and this permission notice shall be included in all copies or substantial portions of the Software. THE SOFTWARE IS PROVIDED "AS IS", WITHOUT WARRANTY OF ANY KIND, EXPRESS OR IMPLIED, INCLUDING BUT NOT LIMITED TO THE WARRANTIES OF MERCHANTABILITY, FITNESS FOR A PARTICULAR PURPOSE AND NONINFRINGEMENT. IN NO EVENT SHALL THE AUTHORS OR COPYRIGHT HOLDERS BE LIABLE FOR ANY CLAIM, DAMAGES OR OTHER LIABILITY, WHETHER IN AN ACTION OF CONTRACT, TORT OR OTHERWISE, ARISING FROM, OUT OF OR IN CONNECTION WITH THE SOFTWARE OR THE USE OR OTHER DEALINGS IN THE SOFTWARE.

E.1 Abaqus Depression Shape Extraction Script

```
##############################################################################
def DepressionShape():
    import section
    import regionToolset
    import displayGroupMdbToolset as dgm
    import part
    import material
    import assembly
    import optimization
    import step
    import interaction
    import load
```

```
    import mesh
    import job
    import sketch
    import visualization
    import xyPlot
    import displayGroupOdbToolset as dgo
    import connectorBehavior
##############################################################################
#####                        End User Input Section                      #####
##############################################################################


##############################################################################
#####                        Variable Output Portion                     #####
##############################################################################

    # Get names of all open ODBs and loop through each one
    o = session.odbs.keys()
    outvars = []

    pathNodes = (('STRAND', '41:3321:41'),) #Path along the cooled surface

    for l, JobName in enumerate(o):

        varname = os.path.basename(JobName)

        session.Path(name='Tmp', type=NODE_LIST, expression=pathNodes)
        shellPath = session.paths['Tmp']

        odb_display = session.viewports['Viewport: 1'].odbDisplay
        odb = session.odbs[JobName]
        frameInfo = odb_display.lastFrame
        session.viewports['Viewport: 1'].setValues(displayedObject=odb)
```

```
thing = session.viewports['Viewport: 1'].odbDisplay.fieldSteps


TotalFrames = frameInfo[1]+1


JobName = re.sub('\.odb$','',varname)
print JobName


# Make the path
session.Path(name='SHELL_PATH', type=NODE_LIST, expression=pathNodes)
# Isolate the path handle
# Get odb and frame info from current context
odb_display = session.viewports['Viewport: 1'].odbDisplay
odbName = odb_display.name
odb = session.odbs[odbName]
frameInfo = odb_display.lastFrame
numFrames = frameInfo[1]
outVarName  = JobName + '-Shape'
xQuantity = visualization.QuantityType(type=TIME)
yQuantity = visualization.QuantityType(type=FORCE)


session.viewports['Viewport: 1'].odbDisplay.setFrame(step=0, frame=numFrames)
odb_display.display.setValues(plotState=(CONTOURS_ON_DEF,))
odb_display.setPrimaryVariable(variableLabel='UT',
                                    outputPosition=NODAL,
                                    refinement=(COMPONENT, 'UT1'), )


# Extract the temperature data along the path
print outVarName
session.XYDataFromPath(name=outVarName,
                                path=shellPath,
                                includeIntersections=False,
                                shape=DEFORMED,
```

```
                                        labelType=TRUE_DISTANCE)

        outvars.append(outVarName)


    for i in range(0, len(outvars)):
        xyp = session.xyPlots['XYPlot-1']
        chartName = xyp.charts.keys()[0]
        chart = xyp.charts[chartName]
        xy1 = session.xyDataObjects[outvars[i]]
        c1 = session.Curve(xyData=xy1)
        chart.setValues(curvesToPlot=(c1, ), )
        session.viewports['Viewport: 1'].setValues(displayedObject=xyp)


        session.curves[outvars[i]].setValues(useDefault=True,\
        legendSource=CURVE_NAME, suppressQuery=True)
        session.curves[outvars[i]].lineStyle.setValues(thickness=1.2)
##############################################################################################
```

E.2 Abaqus Interpolate Thermocouple Temperatures in Single Element ROM Mold

```
def InterpolateFarTCs():
    import section
    import regionToolset
    import displayGroupMdbToolset as dgm
    import part
    import material
    import assembly
    import step
    import interaction
    import load
    import mesh
    import optimization
    import job
```

```
    import sketch
    import visualization
    import xyPlot
    import displayGroupOdbToolset as dgo
    import connectorBehavior
##############################################################################
##############################################################################


    FDepthofInterest = 13.372    #FBG DEPTH
    MoldThickness = 28.35

    # 5 and 6 for the single layer slice
    # 309 IS BEST FOR SINGLE ELEMENT 40MM MODEL

    SurfNode = '309' #641 is the 80 mm hold domain end
    ColdNode = str(float(SurfNode) + 1)


##############################################################################
    # Get names of all open ODBs
    o = session.odbs.keys()

    # Loop through all of the open ODBs
    for l, JobName in enumerate(o):

        # Get the shortname of the current ODB
        varname = os.path.basename(JobName)

        # Switch focus to viewport 1
        odb_display = session.viewports['Viewport: 1'].odbDisplay

        # Make sure the current ODB is displayed
```

```
odb = session.odbs[JobName]
session.viewports['Viewport: 1'].setValues(displayedObject=odb)

# Extract string for the variable name
JobName = re.sub('\.odb$','',varname)
#print JobName

outvarname = JobName + '-FarFBG'

xy1,xy2 = session.xyDataListFromField(odb=odb, outputPosition=NODAL, variable=(('NT11',
    NODAL), ), nodeLabels=(('WALL', (SurfNode, ColdNode, )), ))

xy3 = xy1+FDepthofInterest*((xy2-xy1)/MoldThickness)
xy3.setValues(
    sourceDescription='Interpolated From Script')
tmpName = xy3.name

session.xyDataObjects.changeKey(tmpName, outvarname)

surfstring = 'NT11 PI: WALL N: ' + str(SurfNode)
coldstring = 'NT11 PI: WALL N: ' + str(ColdNode)

del xy1, xy2
del session.xyDataObjects[surfstring], session.xyDataObjects[coldstring]
```

APPENDIX F

MATLAB SCRIPTS

This section contains example code from this work used to process FBG data and numerical implementation of the Integral Defect Methodology.

Copyright (c) <2020> <Matthew L.S. Zappulla> Permission is hereby granted, free of charge, to any person obtaining a copy of this software and associated documentation files (the "Software"), to deal in the Software without restriction, including without limitation the rights to use, copy, modify, merge, publish, distribute, sublicense, and/or sell copies of the Software, and to permit persons to whom the Software is furnished to do so, subject to the following conditions: The above copyright notice and this permission notice shall be included in all copies or substantial portions of the Software. THE SOFTWARE IS PROVIDED "AS IS", WITHOUT WARRANTY OF ANY KIND, EXPRESS OR IMPLIED, INCLUDING BUT NOT LIMITED TO THE WARRANTIES OF MERCHANTABILITY, FITNESS FOR A PARTICULAR PURPOSE AND NONINFRINGEMENT. IN NO EVENT SHALL THE AUTHORS OR COPYRIGHT HOLDERS BE LIABLE FOR ANY CLAIM, DAMAGES OR OTHER LIABILITY, WHETHER IN AN ACTION OF CONTRACT, TORT OR OTHERWISE, ARISING FROM, OUT OF OR IN CONNECTION WITH THE SOFTWARE OR THE USE OR OTHER DEALINGS IN THE SOFTWARE.

F.1 Data File Import Function

```
function FBGArray = FBGimportFunction(str)

filename = strcat('E:\Zapp\Current Studies\TATA\RDatabase\',str);

delimiter = ',';
startRow = 2;

%% Format string for each line of text:
%   column2: double (%f)
formatSpec = '%*q%f%f%f%f%f%f%f%f%f%f%f%f%f%f%f...
             %f%f%f%f%f%f%f%f%f%f%f%f%f%f%f%f%f...
             %f%f%f%f%f%f%f%f%f%f%f%f%f%f%f%f%f...
             %f%f%f%f%f%f%f%f%f%f%f%f%f%f%f%f%f...
             %[^\n\r]';

%% Open the text file.
```

```
fileID = fopen(filename,'r');

%% Read columns of data according to format string.
% This call is based on the structure of the file used to generate this
% code. If an error occurs for a different file, try regenerating the code
% from the Import Tool.
dataArray = textscan(fileID, formatSpec, 'Delimiter', delimiter, 'HeaderLines' ,startRow-1, 'ReturnOnError', false);

%% Close the text file.
fclose(fileID);

%% Post processing for unimportable data.
% No unimportable data rules were applied during the import, so no post
% processing code is included. To generate code which works for
% unimportable data, select unimportable cells in a file and regenerate the
% script.

%% Create output variable
FBGArray = rot90([dataArray{1:end-1}]);
%% Clear temporary variables
clearvars filename delimiter startRow formatSpec fileID dataArray ans;

end
```

F.2 Integral Method Video Script

```
%%%%%%%%%%%%%%%%%%%%%%%%%%%%%%%%%%%%%%%%%%%%%%%%%%%%%%%%%%%%%%%%%%%%%%%%%%%%
%
%              INTEGRAL DEFECT METHODOLGY VIDEO SCRIPT
%
%        SETUP FOR USE ON TATA STEEL EUROPE FBG ARRAY
%
%           CREATED BY MATTHEW ZAPPULLA JUNE 2018
%
%%%%%%%%%%%%%%%%%%%%%%%%%%%%%%%%%%%%%%%%%%%%%%%%%%%%%%%%%%%%%%%%%%%%%%%%%%%%
clc
clear all

%%subplot setup
```

```
%SUBPLOTS WIDE
subW = 8;
%SUBPLOTS TALL
subT = 2;
%SUBPLOTS WIDTH FOR CONTOURS
subWW = 4;
%SUBPLOT IMAGE WIDTH
subIW = subW-subWW;

%left axis OF THE LEFT PLOTS
Lwidth = -640;
Rwidth = 0;

a = dir('*.txt');
b = {a.name};

testframes = length(b);
framerate = 4;

FBGMinus = 0;

slab = zeros(70-FBGMinus,38);
SLAB = slab;

cycle = 25



%%%%%%%%%%%%%%%%%%%%%%%%%%%%%
%DEFECT IMAGE ALTERATION AND DISPLAY
%%%%%%%%%%%%%%%%%%%%%%%%%%%%%
Defect = imread('DefectImage.jpg');
%FULL CROPPING RECTANGLE BEFORE ROTATION
%DEFINED AS  [xmin ymin width height]
rect = [0.51,0.51,5311.98,2746.98];

Defect = imcrop(Defect,rect);
DefectA = imrotate(Defect,-90);
%%%%%%%%%%%%%%%%%%%%%%%%%%%%%
%DEFECT IMAGE ALTERATION AND DISPLAY
%%%%%%%%%%%%%%%%%%%%%%%%%%%%%
```

```
counter = 0;
for (u = 1:numel(cycle))
    fiberlocation = cycle(u);
    Y = linspace(30,375,70);

    namething = fullfile(pwd,'Publication-Integral-Visualization-QuadPlotVideo.avi');

      writerObj = VideoWriter(namething);
      writerObj.FrameRate = 2;
      writeObj.Quality = 100;
      open(writerObj);

    tic

    %at 8:05 end of defect is at approx 280
    frames = 1;
    for i = 30:length(b)
        clf

        %i=1;
        str = b{i};

        FBGArray = FBGimportFunction(str);
        FBGArray = flipud(FBGArray);

         %UPDATED FOR WISTMOLD V2.5 FIBER LOCATIONS
         X = [-925 -875 -825 -775 -725 -675 -625 -575...
              -525 -475 -425 -375 -325 -275 -225 -175 -125 -75 -25];
         X = [X fliplr(-X)];
         Y = linspace(30,375,70);
         h1 = subplot(subT,subW,1:4);
        colormap(hot(20))
        [C,h]=contourf(-X,Y,fliplr(FBGArray),20);
        colorbar
        set(h,'LineColor','none')

         a = strsplit(str,'.');
         a = strsplit(char(a(1)),'-');
%
        title('Instantaneous Mold Temperatures [{\circ}C]','FontSize',14);
```

```
axis([Lwidth Rwidth 30 375])
set(gca,'Ydir','reverse')
set(gca,'XMinorTick','on','YMinorTick','on')
xlabel('Distance From WF Centerline [mm]','FontSize',12);
ylabel('Distance from Top of Mold [mm]','FontSize',12);
caxis([50 220])
 %GRID LINES
  yL = get(gca,'YLim');
  xL = get(gca,'XLim');
 %MOLD WIDTH and defect locations
 Primary = 469;
 Secondary = 394;
%         %size of either side of defects
 extrawide = 10;

 StandardProfile = [58.0700000000000;57.6150000000000;57.9250000000000;57.8300000000000;...
          58.5800000000000;59.4550000000000;60.3700000000000;62.5150000000000;...
          64.9100000000000;68.1700000000000;72.2400000000000;77.5650000000000;...
          84.5450000000000;93.4250000000000;104.195000000000;117.080000000000;...
          132.220000000000;148.855000000000;164.770000000000;178.905000000000;...
          189.075000000000;195.520000000000;199.465000000000;201.270000000000;...
          201.725000000000;200.885000000000;199.295000000000;196.685000000000;...
          194.525000000000;192.745000000000;190.615000000000;188.085000000000;...
          186.385000000000;184.600000000000;182.630000000000;181.250000000000;...
          179.745000000000;177.410000000000;175.400000000000;174.100000000000;...
          172.525000000000;171.115000000000;170.020000000000;169.165000000000;...
          167.425000000000;166.280000000000;164.915000000000;164.065000000000;...
          162.665000000000;161.580000000000;160.540000000000;159.440000000000;...
          158.570000000000;157.585000000000;157.320000000000;156.235000000000;...
          155.615000000000;154.715000000000;153.985000000000;153.915000000000;...
          153.080000000000;152.295000000000;152.060000000000;151.420000000000;...
          150.710000000000;150.375000000000;149.585000000000;149.315000000000;...
          148.375000000000;147.360000000000];

 inner = 8;
 deviator = 0;

for l = 1:size(FBGArray,1) %vertical direction
    lineavg = mean(FBGArray(l,1+inner:end-inner));
    %spaced 8 in from the sides take the average
    for k = 1:size(FBGArray,2) %horizontal direction
```

```
        slab(l,k) =  StandardProfile(l)-flipud(FBGArray(l,k));
        %get the difference between avg and local
        if slab(l,k)<=deviator
        else
            slab(l,k) = 0;
        end
    end
end

h8 = subplot(subT,subW,13:16)

for m = 5:70-FBGMinus
    SLAB(m,:) = SLAB(m,:)+slab(m,:);
end

SLAB = vertcat(slab(1:5,:),SLAB);

counter = counter+1;

weirdspace = linspace(0,size(SLAB,1)*5,size(SLAB,1));
[C,h] = contourf(X,weirdspace-375,SLAB(:,:),20);

xlabel('Distance from WF Centerline [mm]','FontSize',12);
ypos=ylabel('Distance Below Instrumented Mold Region [mm]','FontSize',12);

title('Integrated Temperature Deviation [{\circ}C{\cdot}s]','FontSize',14);

xlim([-640 0]);
set(gca,'XMinorTick','on','YMinorTick','on')
set(h,'LineColor','none')
colormap(hot);

caxis([-80 0])
hold on

 line([-800 800],[-345 -345],'Color','k','LineWidth',2,'LineStyle','-');
 text(-320,-330,'Top of Instrumentation','HorizontalAlignment'...
 ,'center','VerticalAlignment','top','FontSize',10);


 line([-800 800],[0 0],'Color','k','LineWidth',2);
```

```
          text(-320,-14,'Bottom of Instrumentation','HorizontalAlignment'...
          ,'center','VerticalAlignment','bottom','FontSize',10);

          set(h8,'ydir','reverse')

          % adjust position; the offset has to be determined visually by trial and error
          pos = get(h8, 'Position');
          posnew = pos; posnew(1) = posnew(1) + 0.015; set(h8, 'Position', posnew)
         hold off
         colorbar
%%%%%%%%%%%%%%%%%%%%%%%%%%%%%
%DEFECT IMAGE
%%%%%%%%%%%%%%%%%%%%%%%%%%%%%
         %DEFECT rectangle is 200 wide

         imageshifter = 7250;%1365;

         % TRY TO CROP TO THE VISIBLE RECTANGLE DEFECT AREA
         %     LEFT SIDE TOP SIDE WIDTH HEIGHT
         %rect = [10,i*100+imageshifter,1000,3000];
         cast = 100;
         h3 = subplot(subT,subW,subWW+1:subW);
         rect = [0,-i*cast+imageshifter,2600,1200];
         Defect = imcrop(DefectA,rect);

         imshow(imresize(Defect, [3000 1200]),'XData', -640:0,'YData', 30:375);

         thisdefect = 190;
         otherdefect = 265;
         yL = get(h3,'YLim');

         axis on
         xlabel('Distance from WF Centerline [mm]','FontSize',12);
         title('Final Slab Surface Appearance','FontSize',14);
         set(gca,'XMinorTick','on','YMinorTick','on')

         hold on
         patch([-640 0 0 -640],[90 90 30 30],'k' ,'FaceAlpha',0.5)
         hold off
%%%%%%%%%%%%%%%%%%%%%%%%%%%%%
%DEFECT IMAGE
```

```
%%%%%%%%%%%%%%%%%%%%%%%%%%%%

        h5 = subplot(subT,subW,9:12);

        [C,h]=contourf(X,Y,slab,20);
        set(h5,'ydir','reverse')
        set(h,'LineColor','none')
        set(gca,'XMinorTick','on','YMinorTick','on')
        ylim([30 375]);
        xlim([-640 0]);

        hc=colorbar('EastOutside');

        title('Instantaneous Difference from Standard Temperature Array [{\circ}C]','FontSize',14);
        ylabel('Distance From Top of Mold [mm]','FontSize',12);
        xlabel('Distance from WF Centerline [mm]','FontSize',12);
        caxis([-20 0])

        text(0,-35,'All dimensions and locations are approximate','HorizontalAlignment','center','FontSize',12);

        drawnow
        refresh

        set(gcf, 'Position', get(0, 'Screensize'));
        rect = [150 50 1430 900];
        frame(frames) = getframe(gcf,rect);

        frames = frames+1;

    end
    writeVideo(writerObj,frame(1,2:end));
    close(writerObj);
    toc
end
```

APPENDIX G

SELECTED LONGITUDINAL DEFECT PERSPECTIVE IMAGES



Figure G.1: Multiple longitudinal depressions across slab broadface

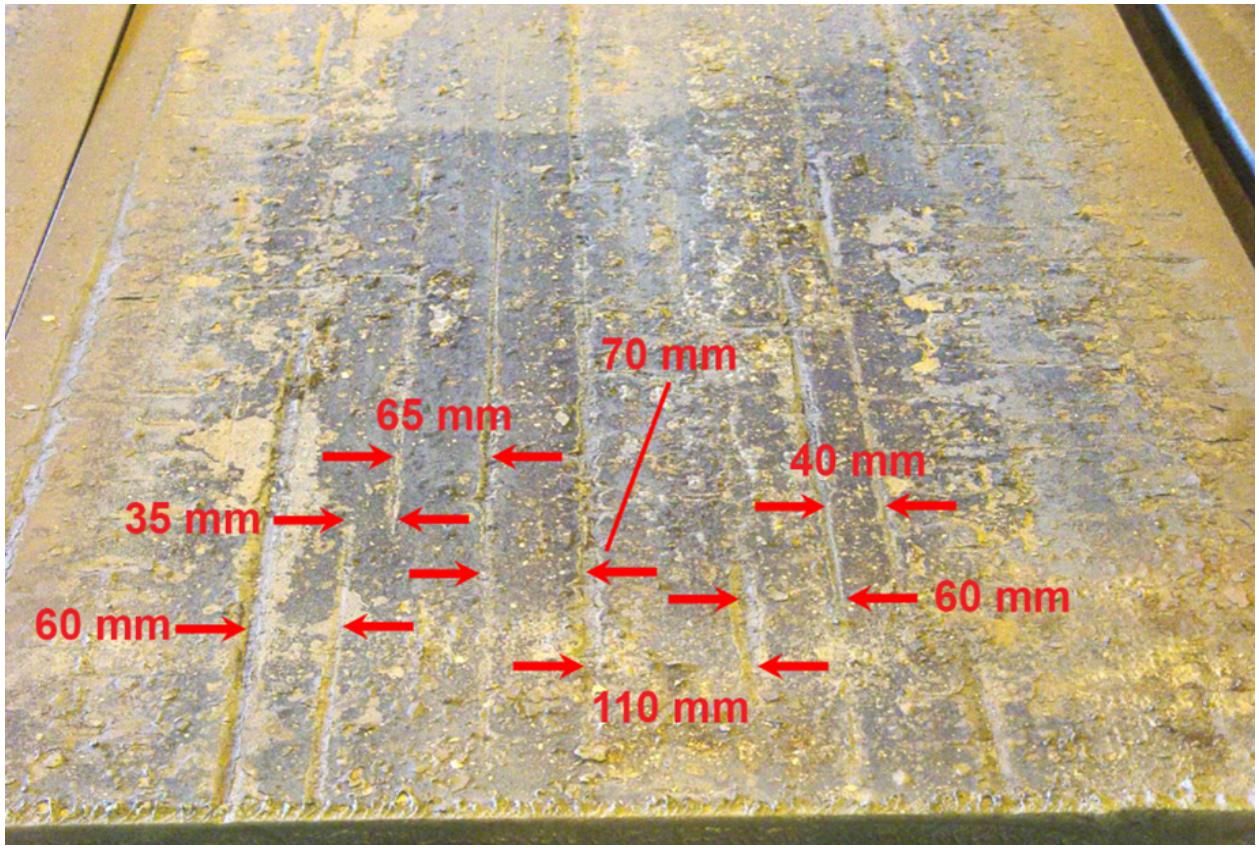


Figure G.2: Multiple longitudinal depressions across slab broadface - Dimensioned



Figure G.3: Multiple longitudinal cracks within a moving depression

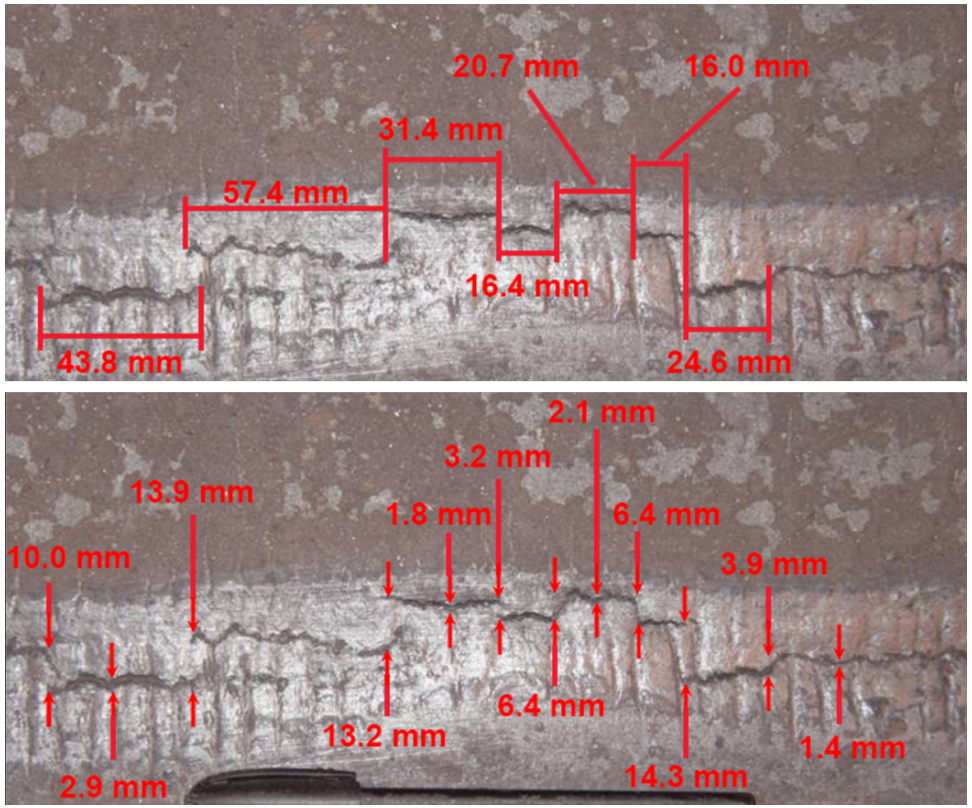


Figure G.4: Multiple longitudinal cracks within a moving depression - Dimensioned



Figure G.5: Multiple longitudinal cracks within a moving depression

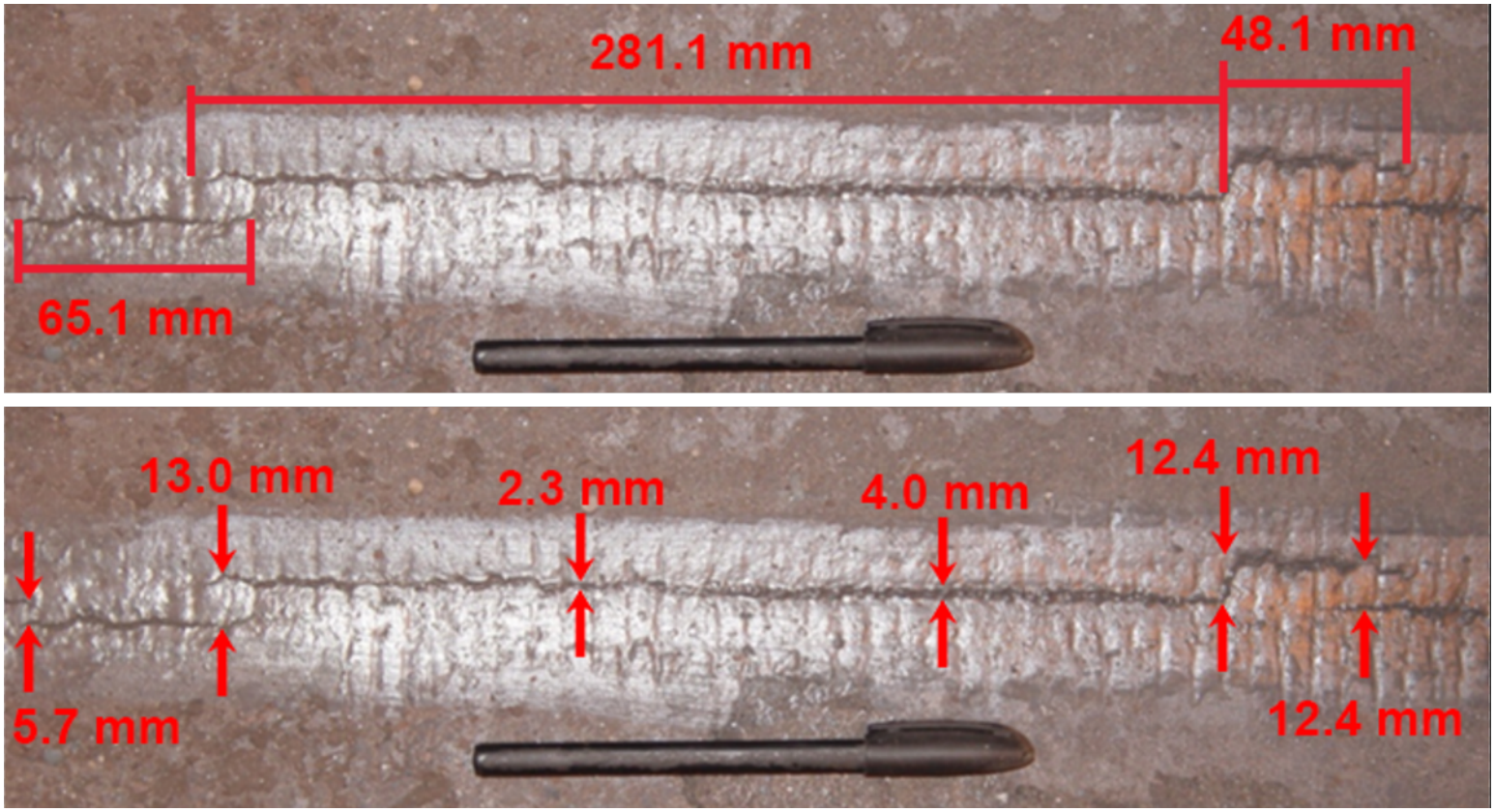


Figure G.6: Multiple longitudinal cracks within a moving depression - Dimensioned



Figure G.7: Longitudinal cracks on slab broadface, casting direction down. (scale unavailable)

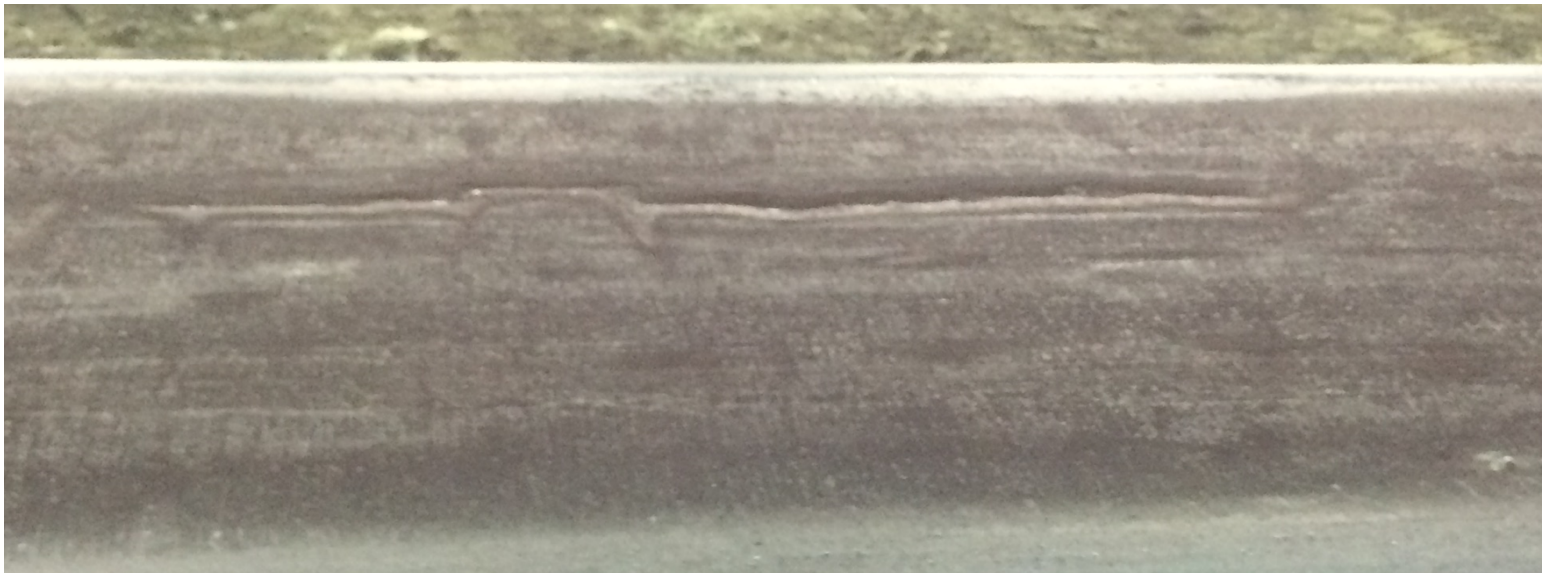


Figure G.8: Sharp longitudinal depression on slab broadface

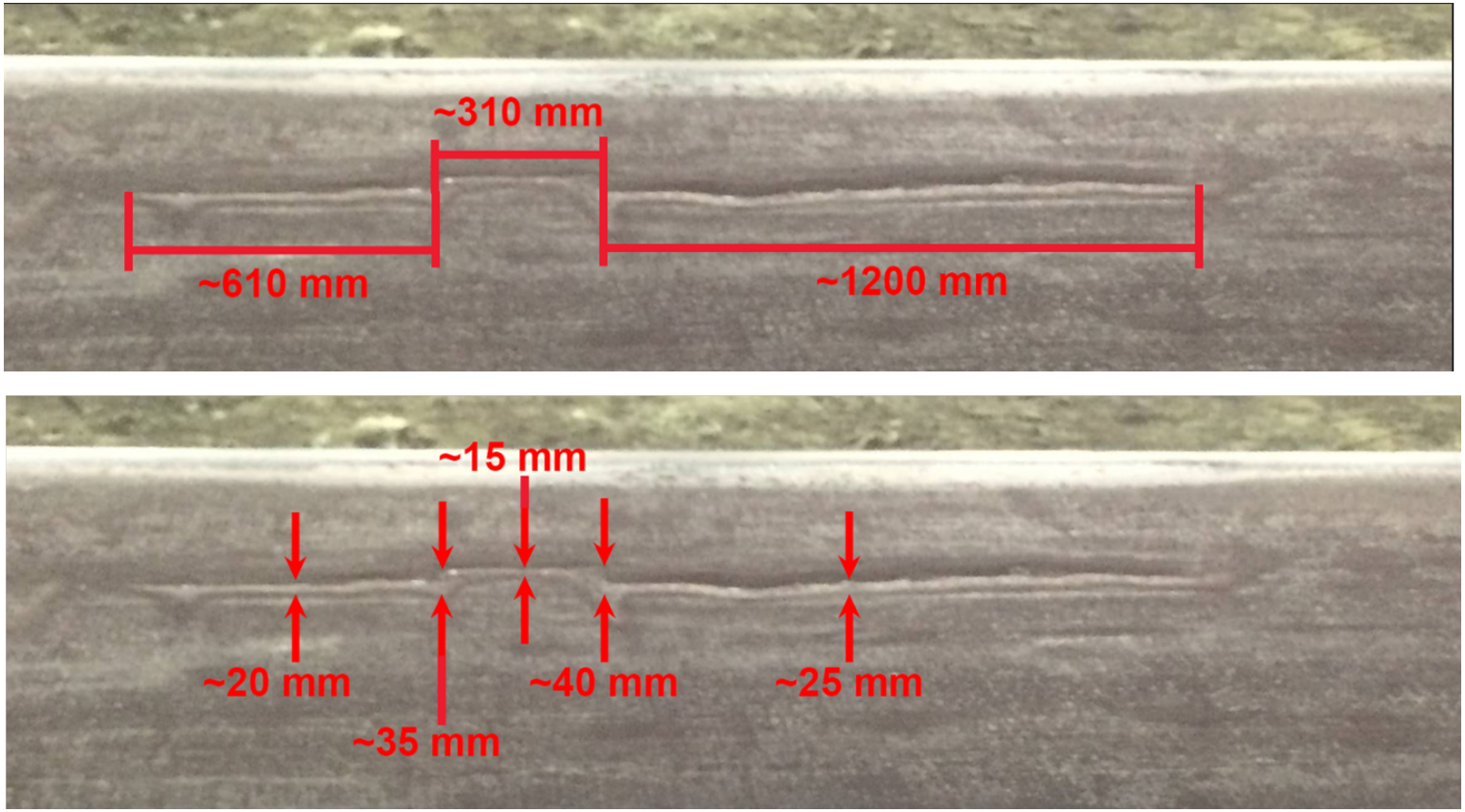


Figure G.9: Sharp longitudinal depression on slab broadface - Dimensioned



Figure G.10: Longitudinal crack at the base of deep U shape depression

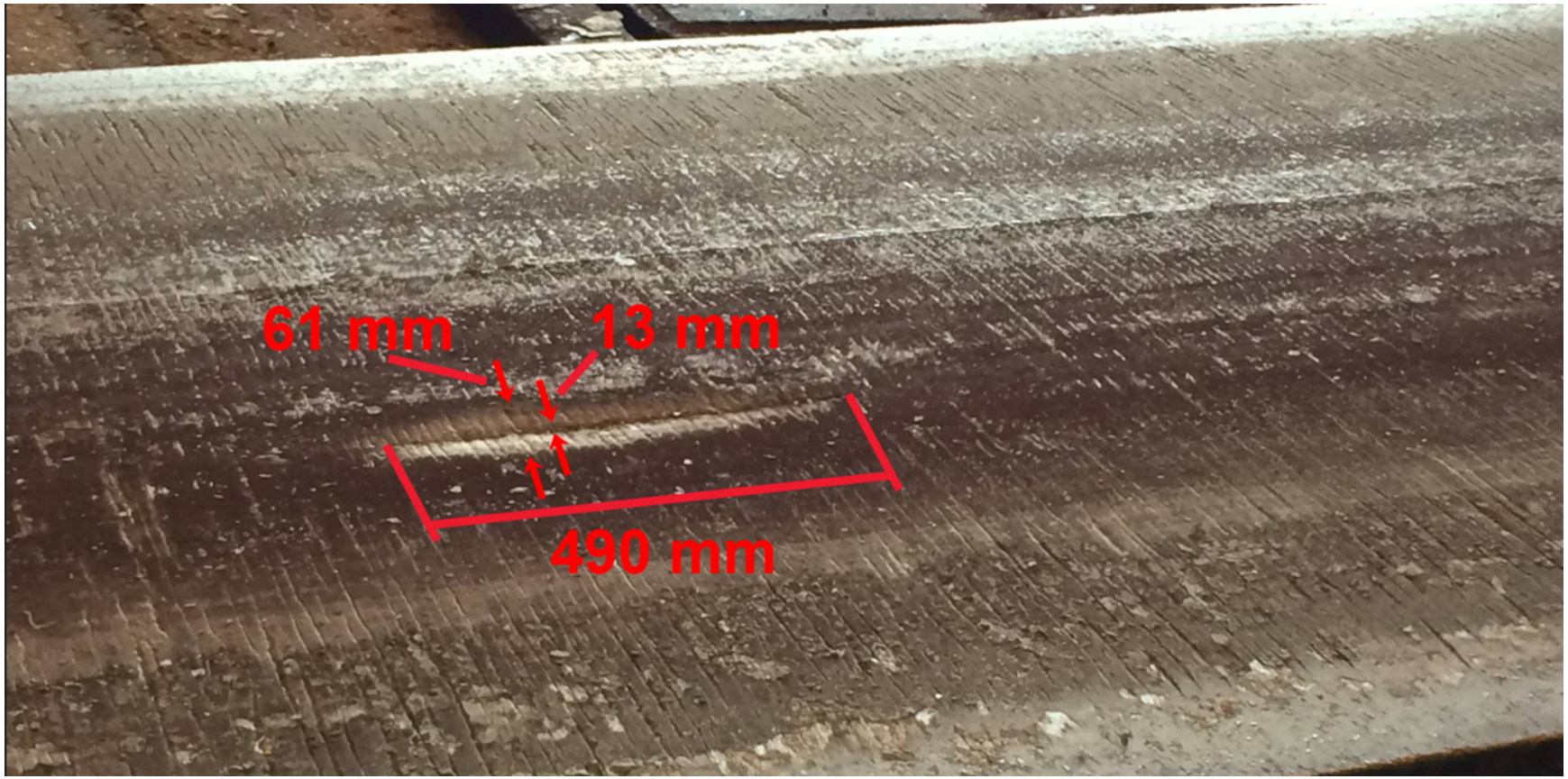


Figure G.11: Longitudinal crack at the base of deep U shape depression - Dimensioned

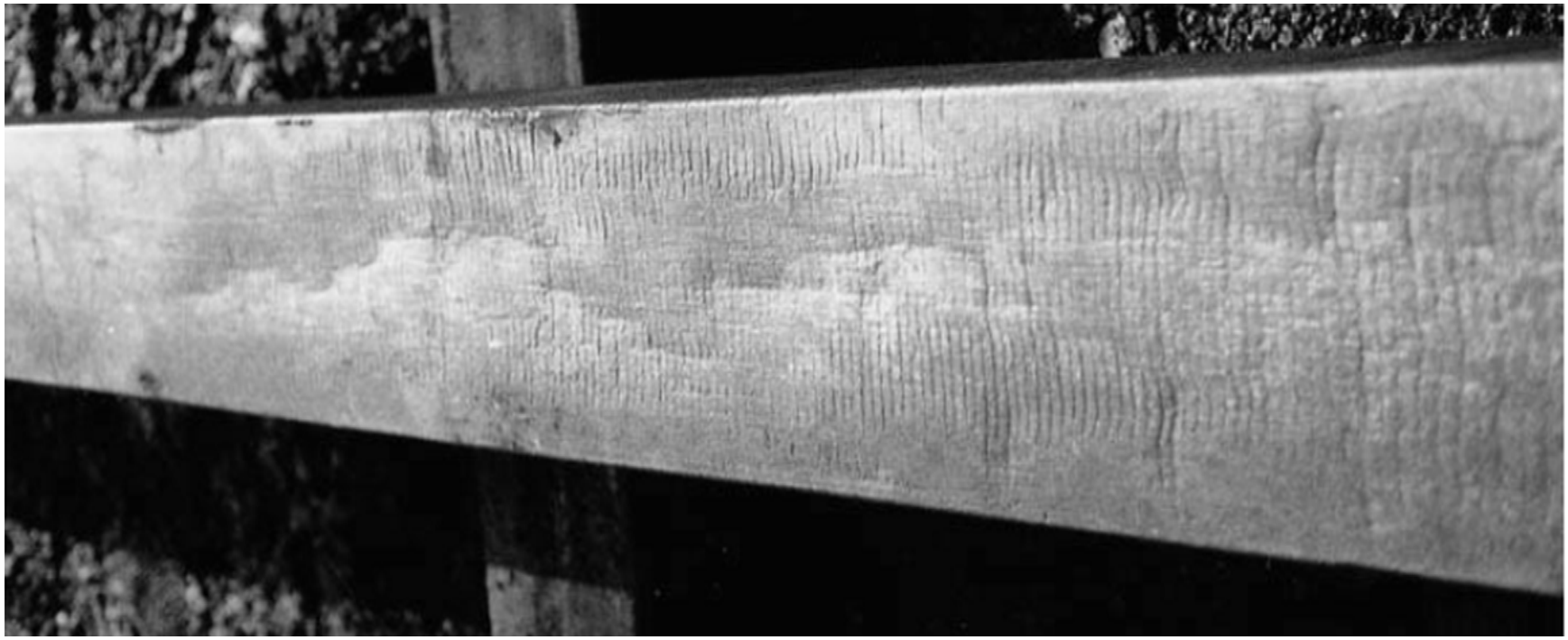


Figure G.12: Longitudinal midface W-shape depression and intermittent surface cracks on a 203 mm square billet, 0.8wt%C, lubrication changed from oil to flux [133]



Figure G.13: Sharp longitudinal depression with severe crack at the base wandering along slab broadface

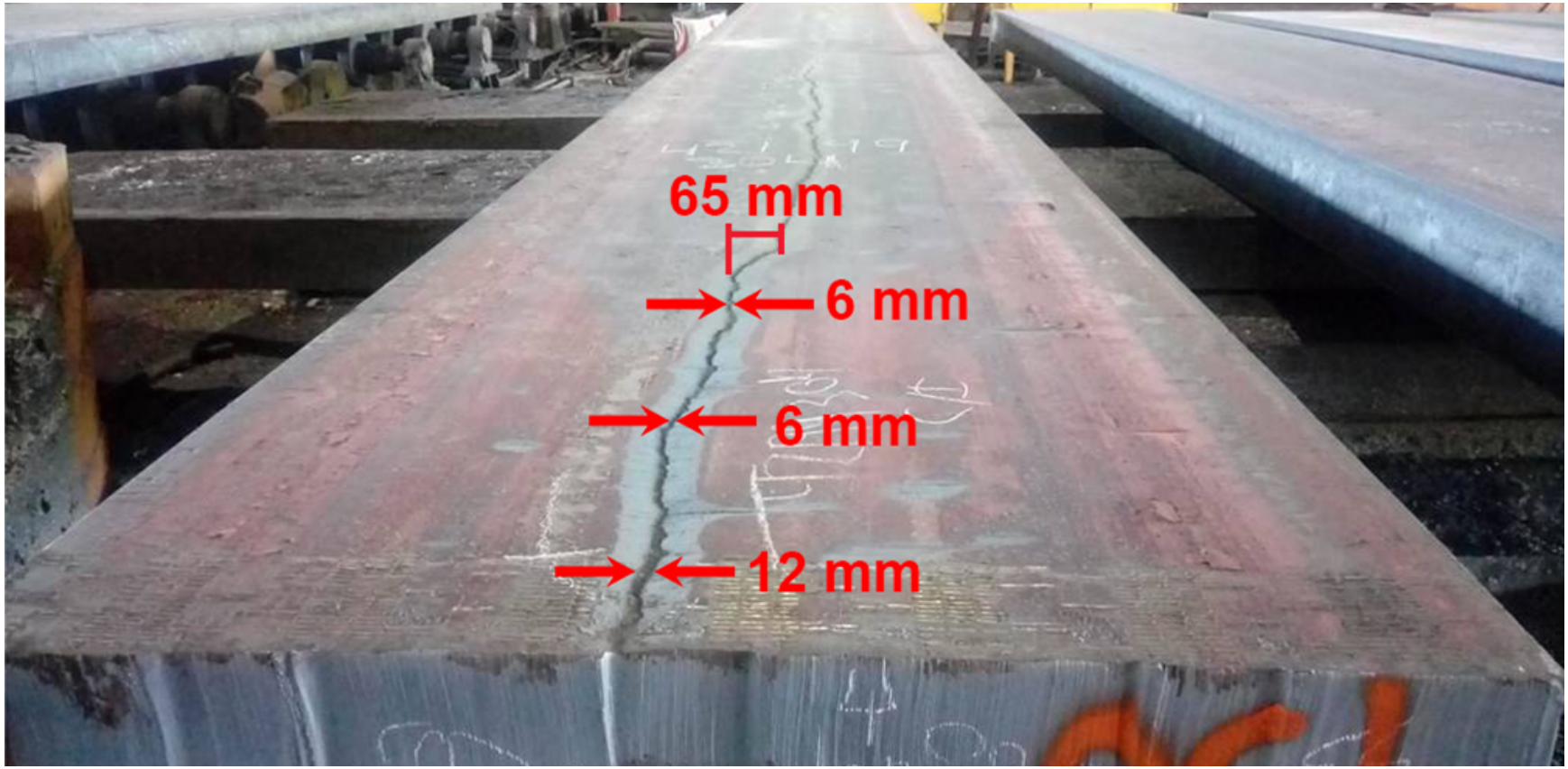


Figure G.14: Sharp longitudinal depression with severe crack at the base wandering along slab broadface - Dimensioned



Figure G.15: Sharp longitudinal depression with severe crack at the base wandering along slab broadface



Figure G.16: Sharp longitudinal depression with severe crack at the base wandering along slab broadface - Dimensioned



Figure G.17: Sharp longitudinal depression with severe crack at the base on slab broadface

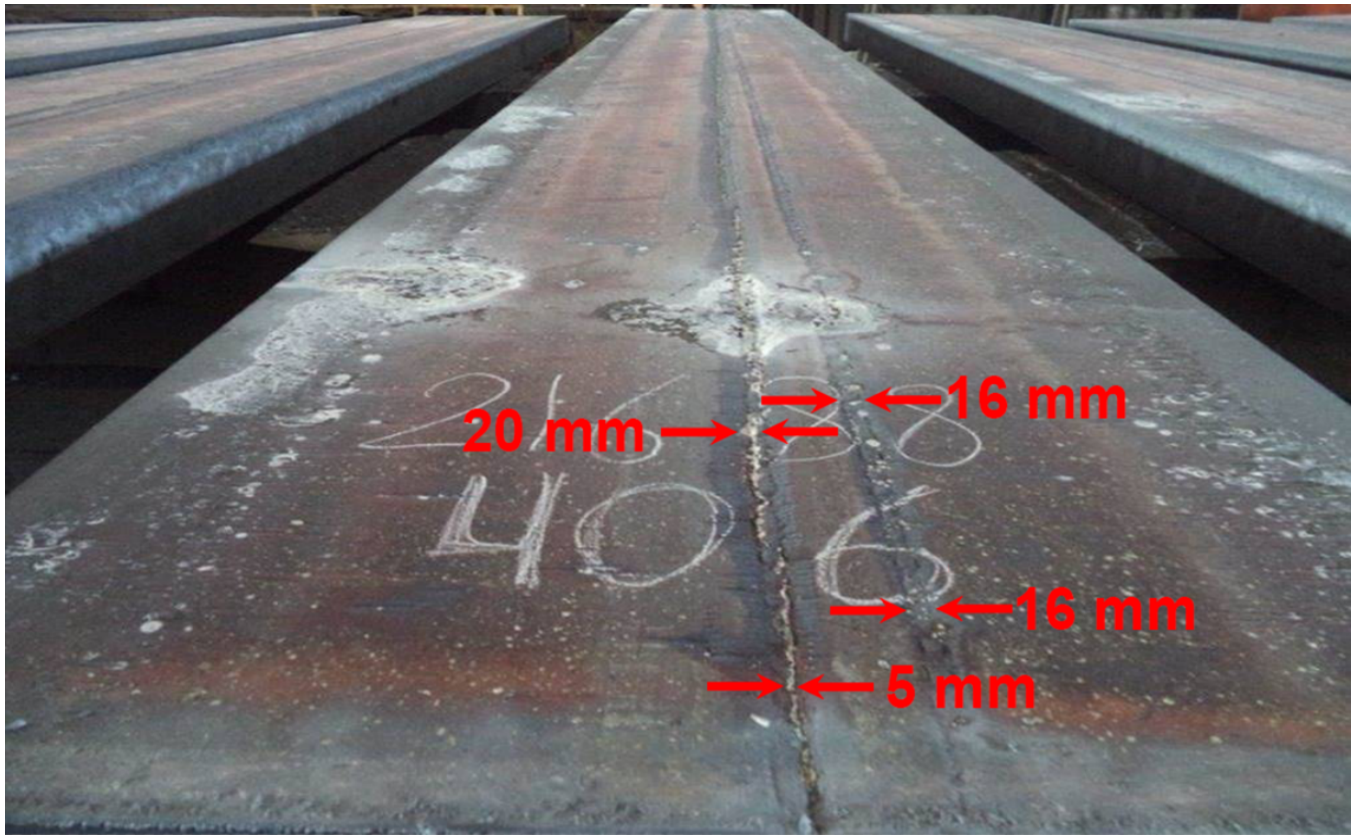


Figure G.18: Sharp longitudinal depression with severe crack at the base on slab broadface - Dimensioned

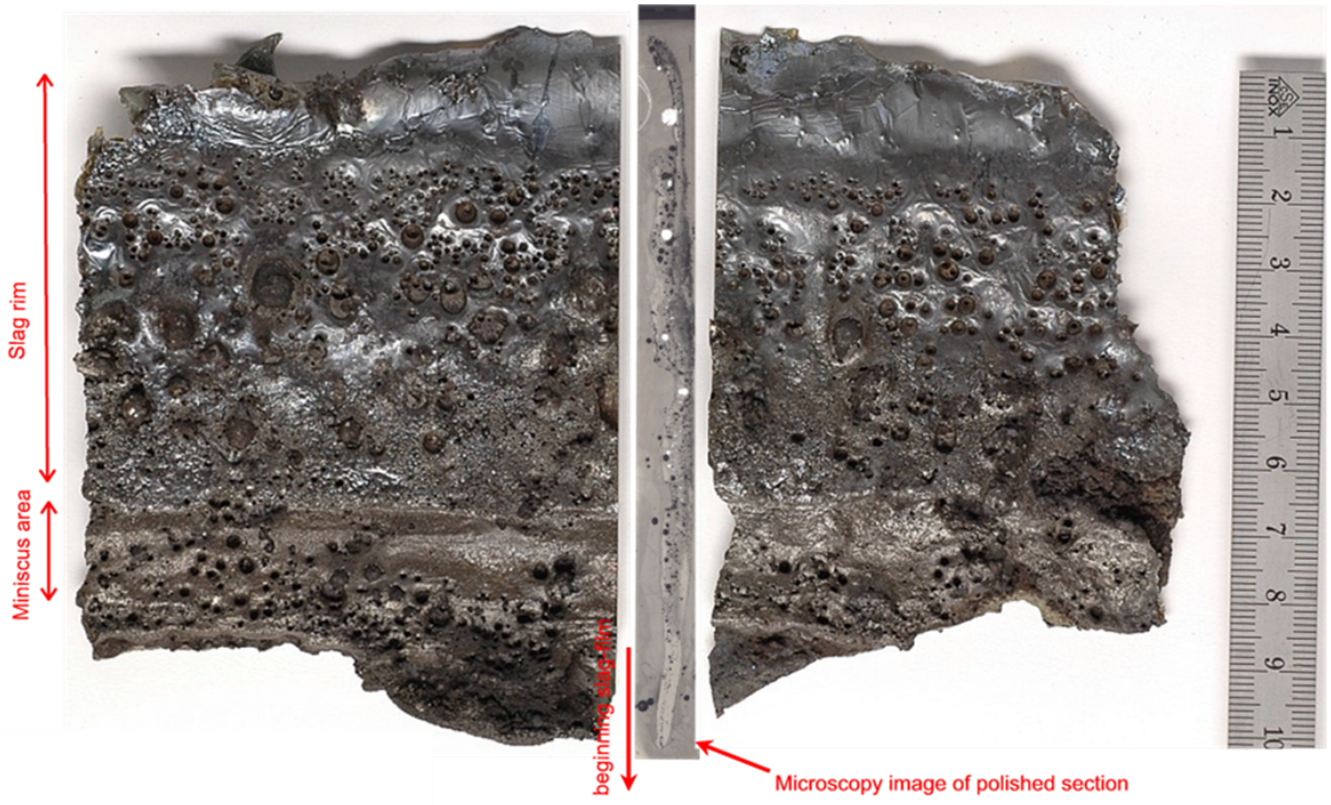


Figure G.19: Slag rim sample removed from a caster including polished light optical image (center)

APPENDIX H

SELECTED LONGITUDINAL DEFECT CROSS SECTION IMAGES

- The letter at the start of the sample name indicates which feature the sample contains, with A being the leftmost feature.
- The number that follows indicates the depth of the sample, with 00 being the surface sample, 01 being the sample beneath 00, etc.
- The saw kerf between samples ~1.6 mm (i.e. A01 "top" is 1.6 mm further from surface than A00 "bottom")

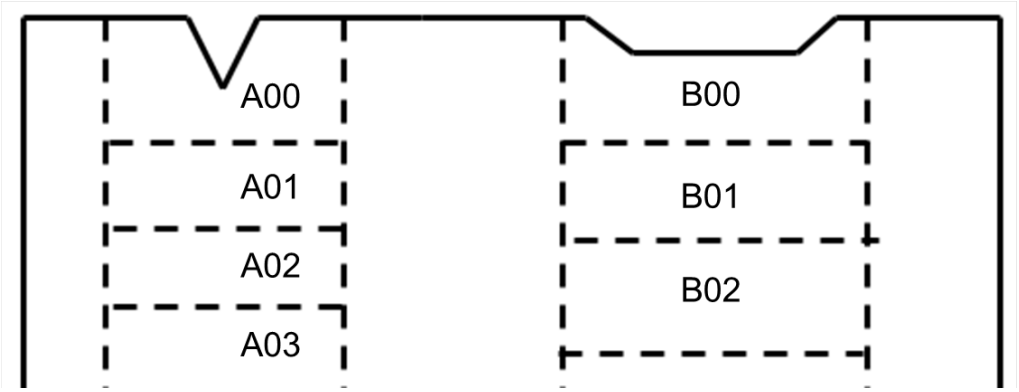


Figure H.1: Sample micrograph cross section naming convention



Figure H.2: Transverse cross section from a non-peritectic Al-Mn AHSS steel grade (0.2 wt %C). Sample name: 88-403

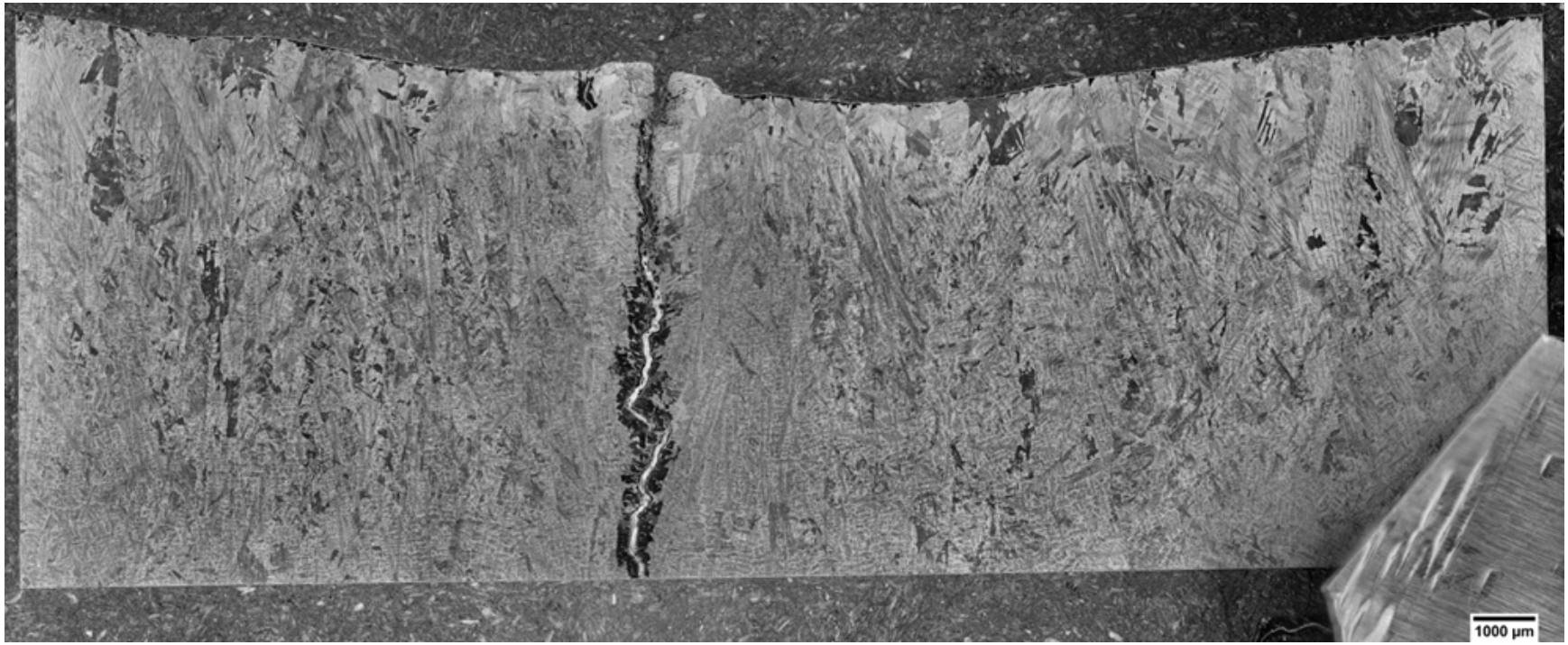


Figure H.3: Transverse cross section from a non-peritectic Al-Mn AHSS steel grade (0.2 wt %C) etched with 3% Nital. Sample name: 88-403-A00

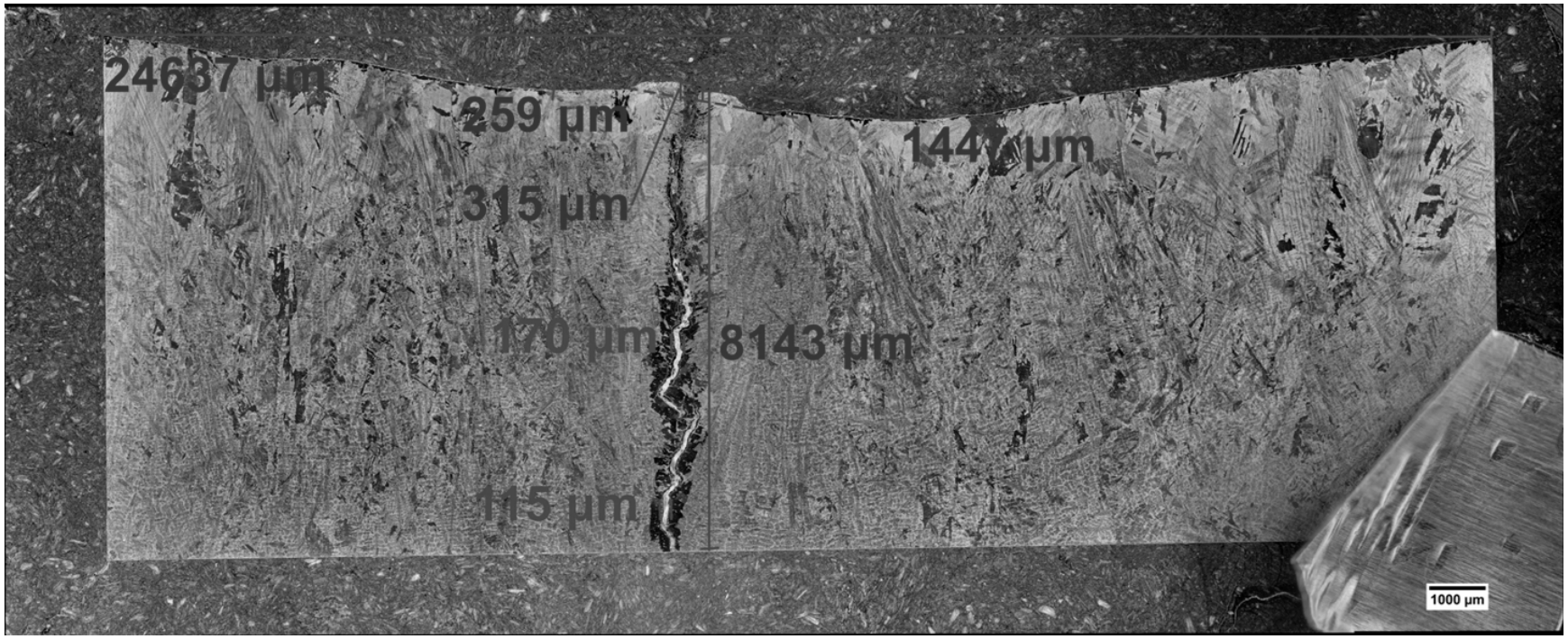


Figure H.4: Transverse cross section from a non-peritectic Al-Mn AHSS steel grade (0.2 wt %C) etched with 3% Nital. Sample name: 88-403-A00 - Dimensioned

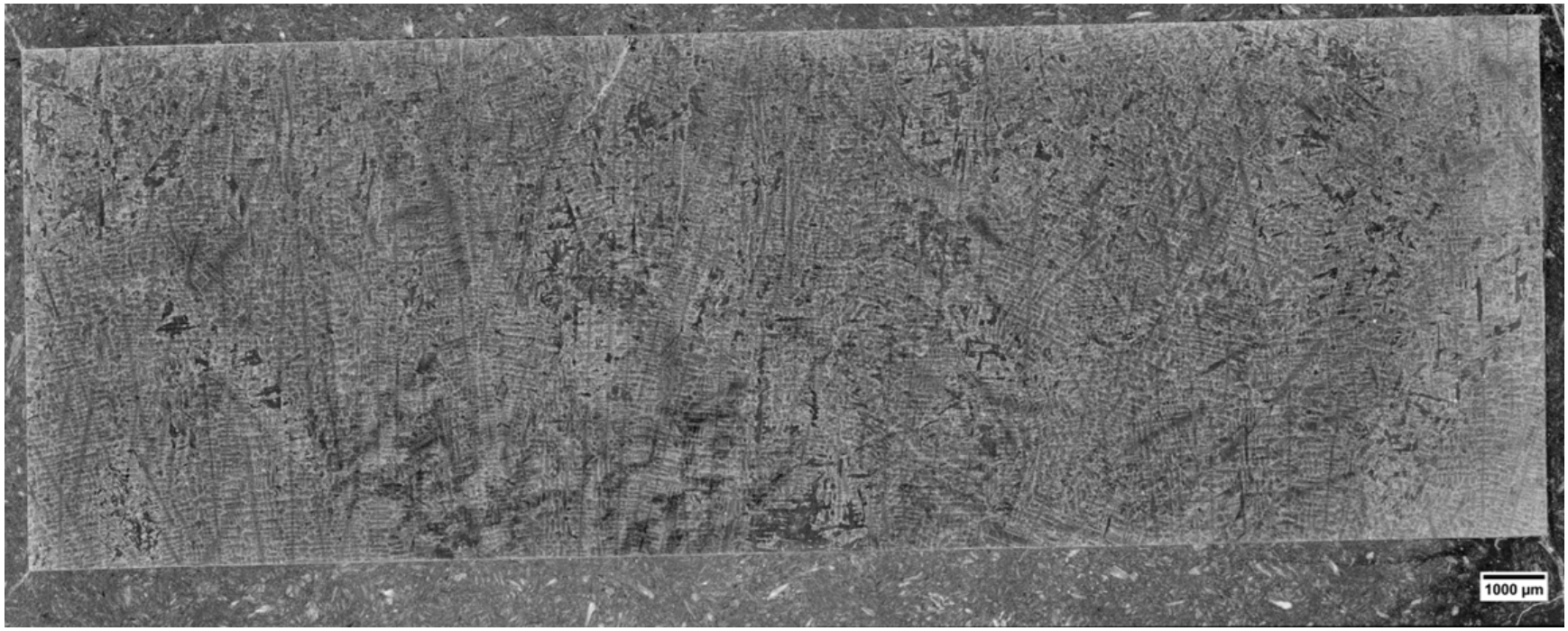


Figure H.5: Transverse cross section from a non-peritectic Al-Mn AHSS steel grade (0.2 wt %C) etched with 3% Nital. Sample name: 88-403-A01

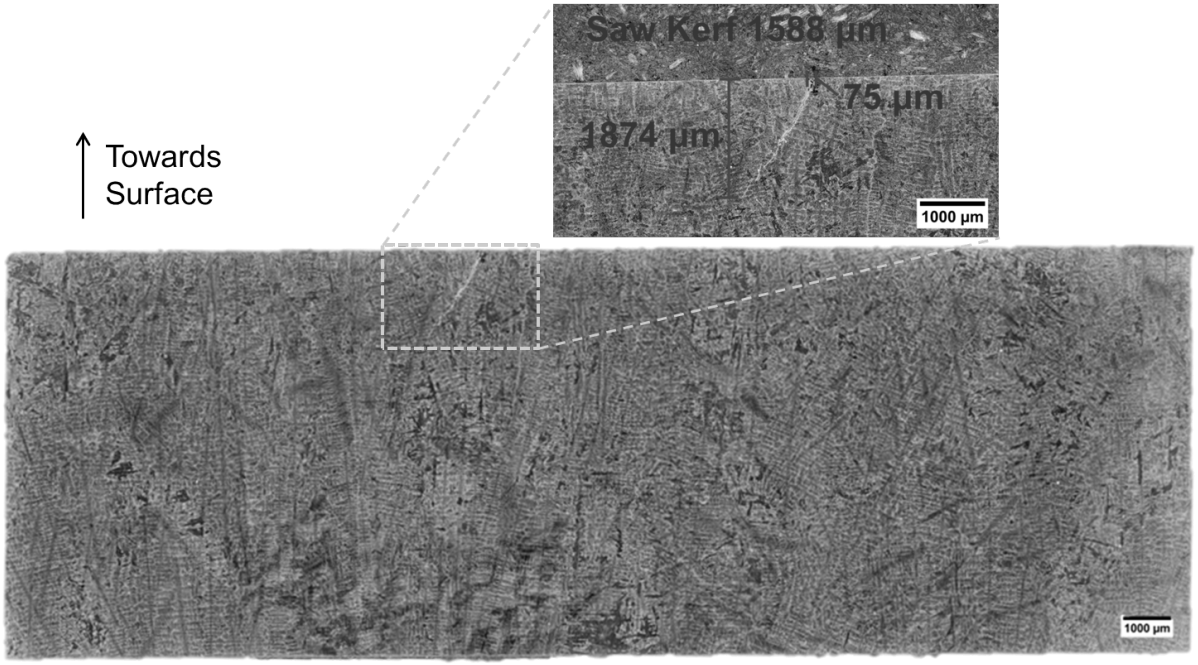


Figure H.6: Transverse cross section from a non-peritectic Al-Mn AHSS steel grade (0.2 wt %C) etched with 3% Nital. Sample name: 88-403-A01 - Dimensioned

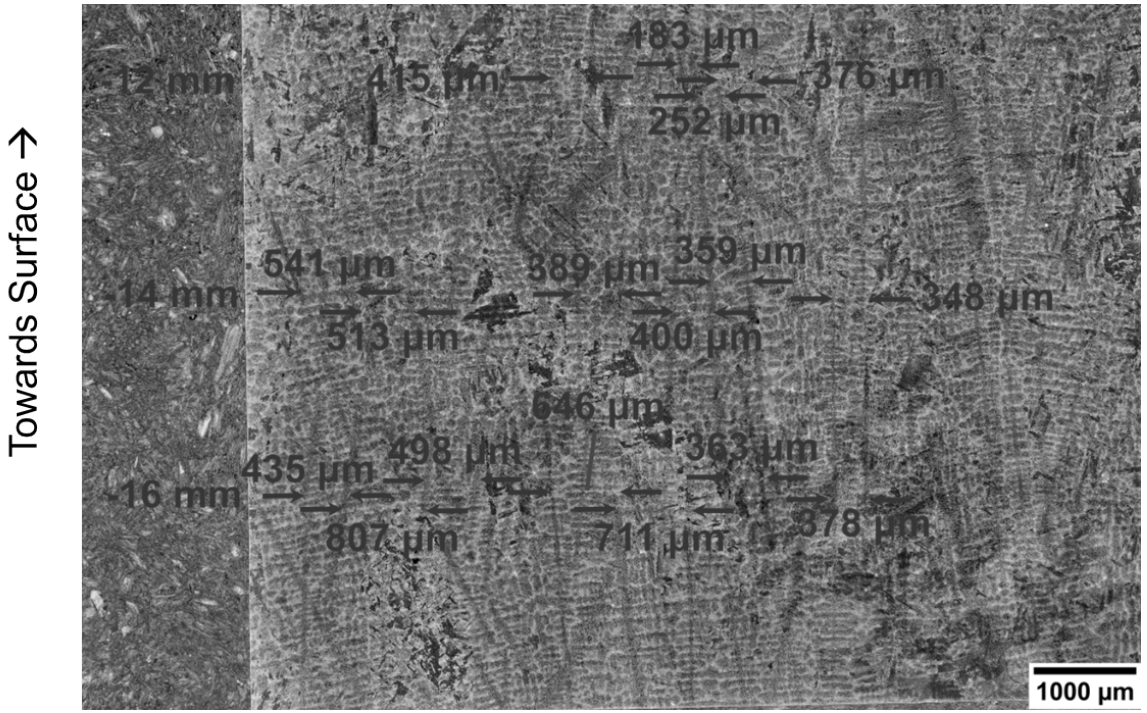


Figure H.7: Transverse cross section from a non-peritectic Al-Mn AHSS steel grade (0.2 wt %C) micrograph etched with 3% Nital, with primary dendrite arm spacing, sample name: 88-403-A01

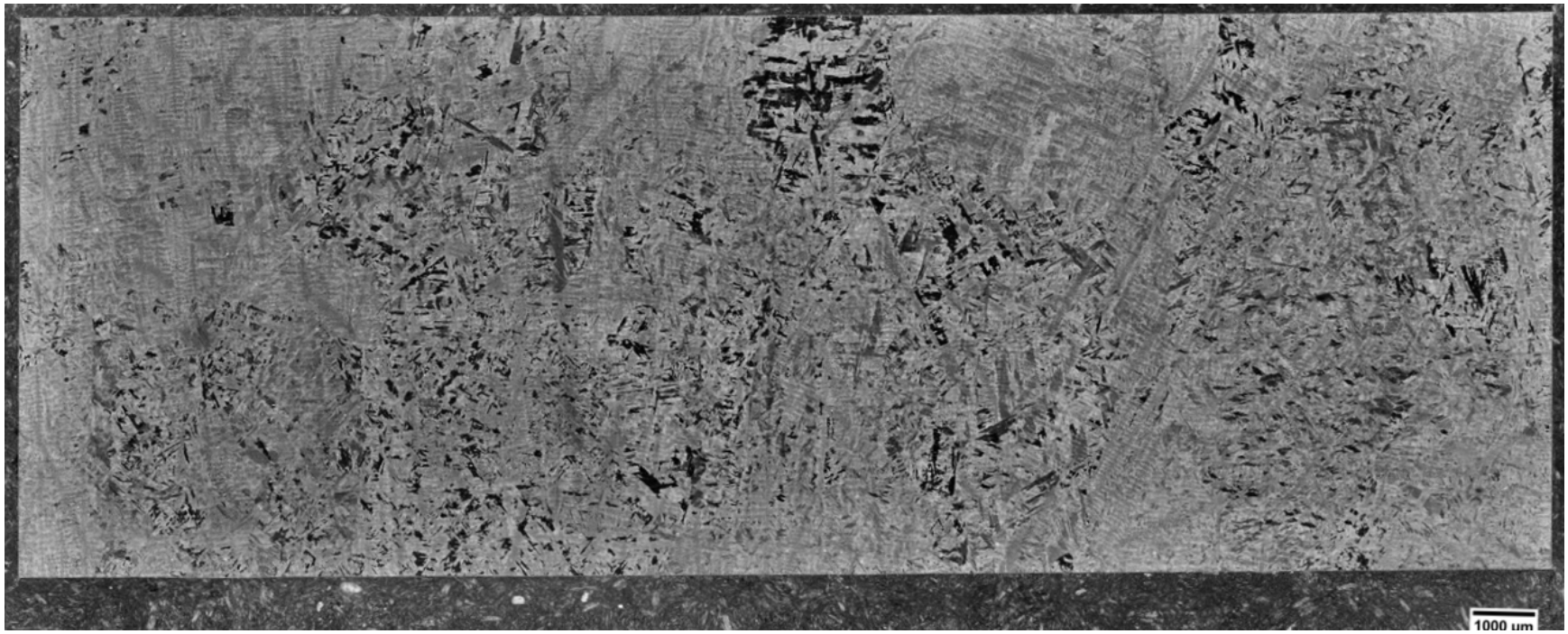


Figure H.8: Transverse cross section from a non-peritectic Al-Mn AHSS steel grade (0.2 wt %C) micrograph etched with 3% Nital sample name: 88-403-A02

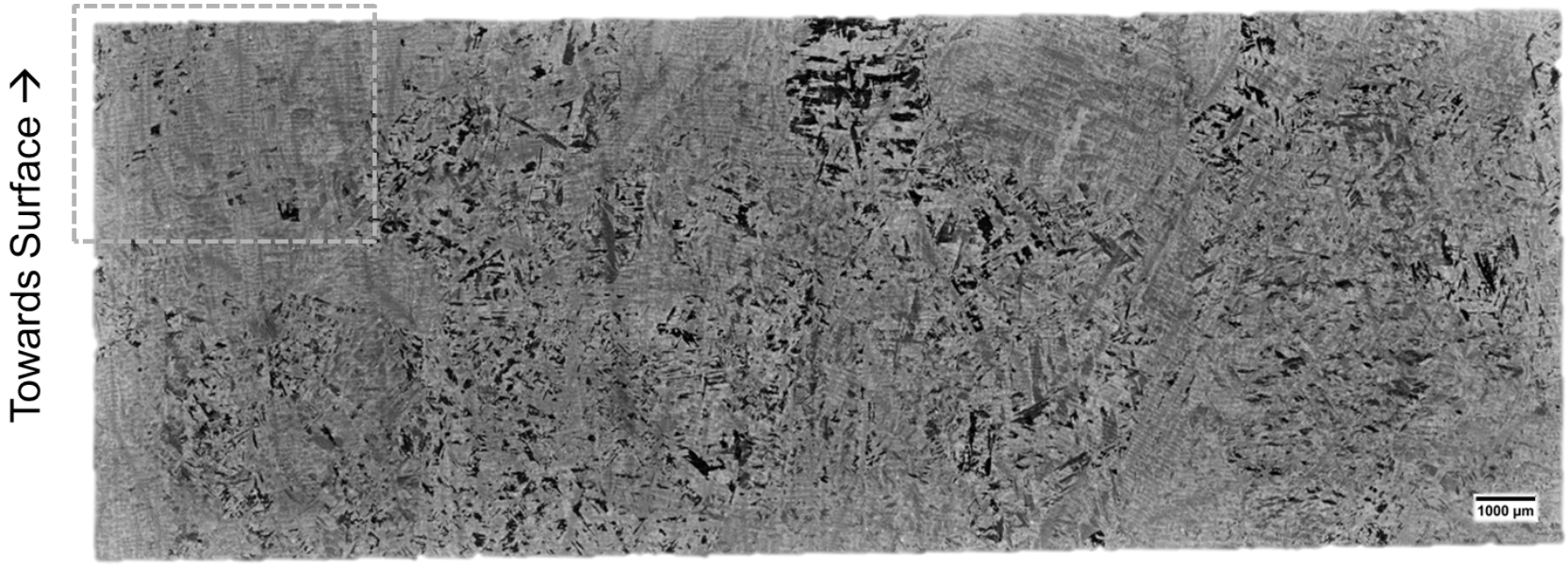


Figure H.9: Transverse cross section from a non-peritectic Al-Mn AHSS steel grade (0.2 wt %C) micrograph etched with 3% Nital sample name: 88-403-A02 - Dimensioned

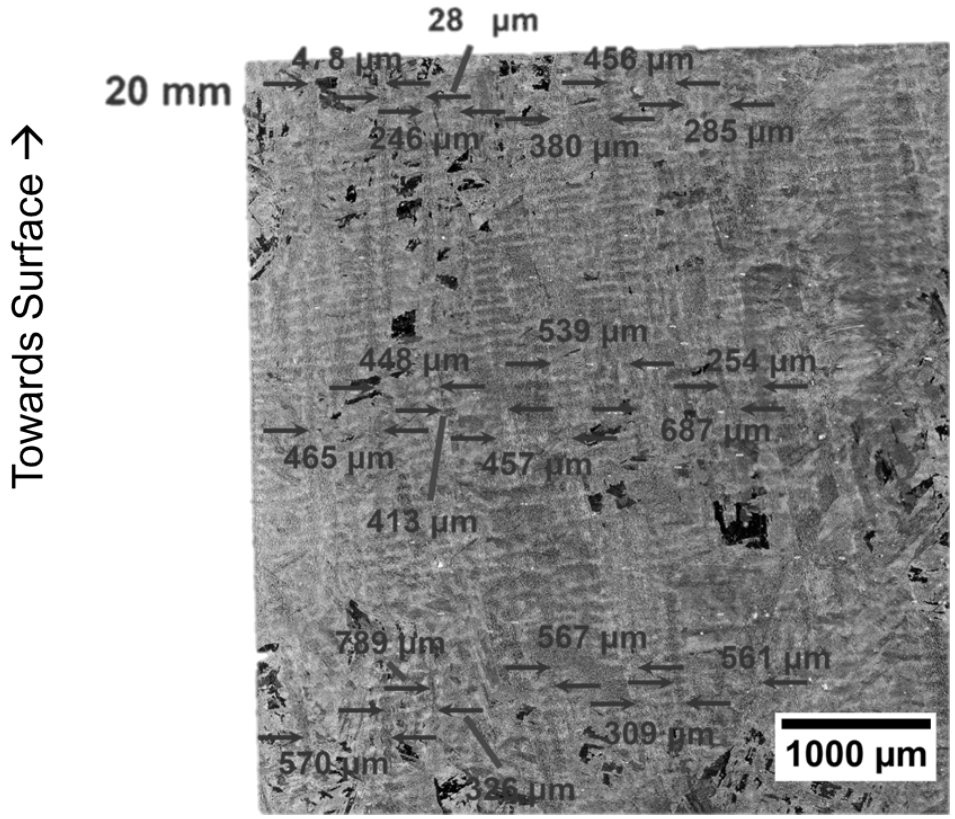


Figure H.10: Transverse cross section from a non-peritectic Al-Mn AHSS steel grade (0.2 wt %C) micrograph etched with 3% Nital, including primary dendrite arm spacing, sample name: 88-403-A02



Figure H.11: Transverse cross section from a non-peritectic Al-Mn AHSS steel grade (0.2 wt %C). Sample name: 91-303

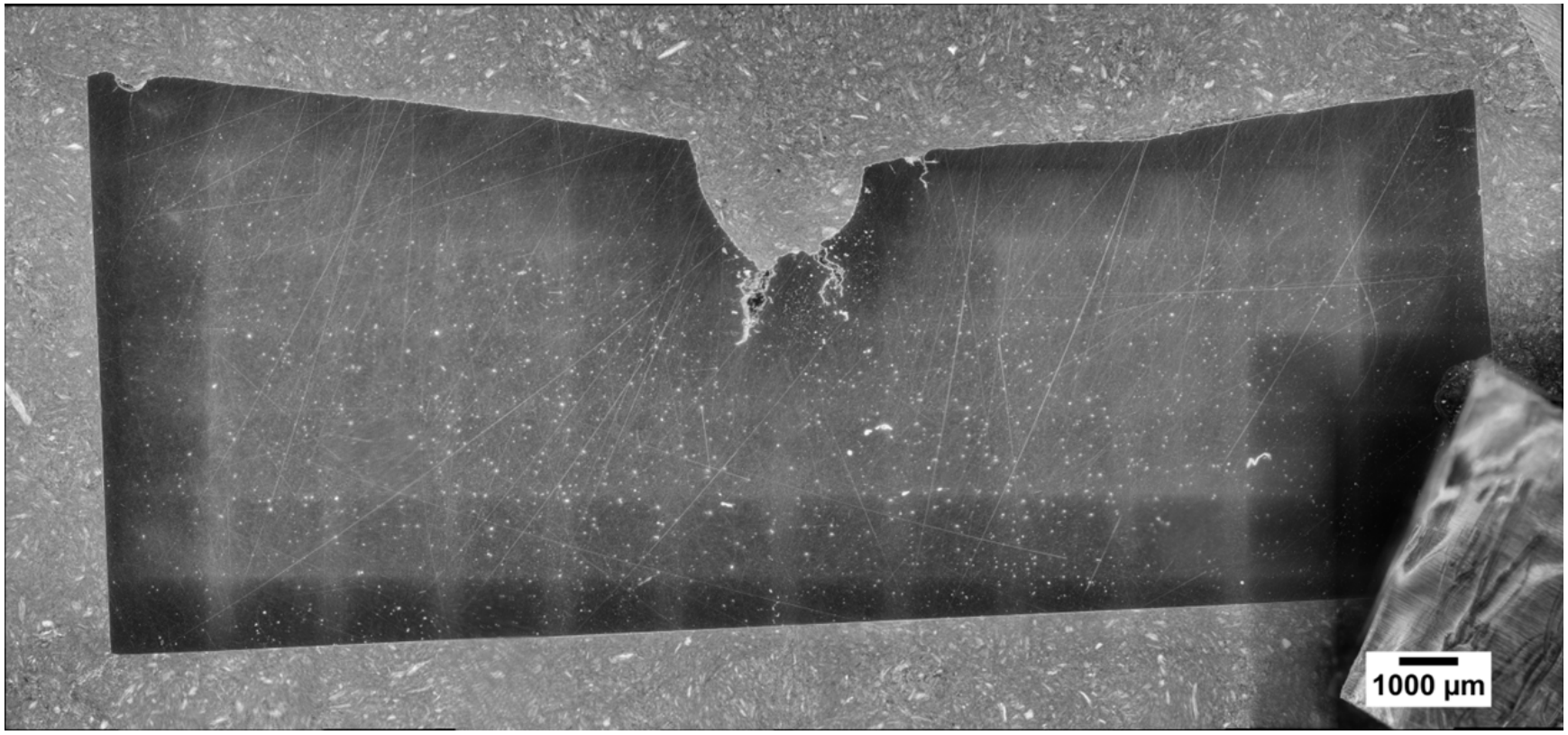


Figure H.12: Transverse cross section from a non-peritectic Al-Mn AHSS steel grade (0.2 wt %C). Sample name: 91-303-A00

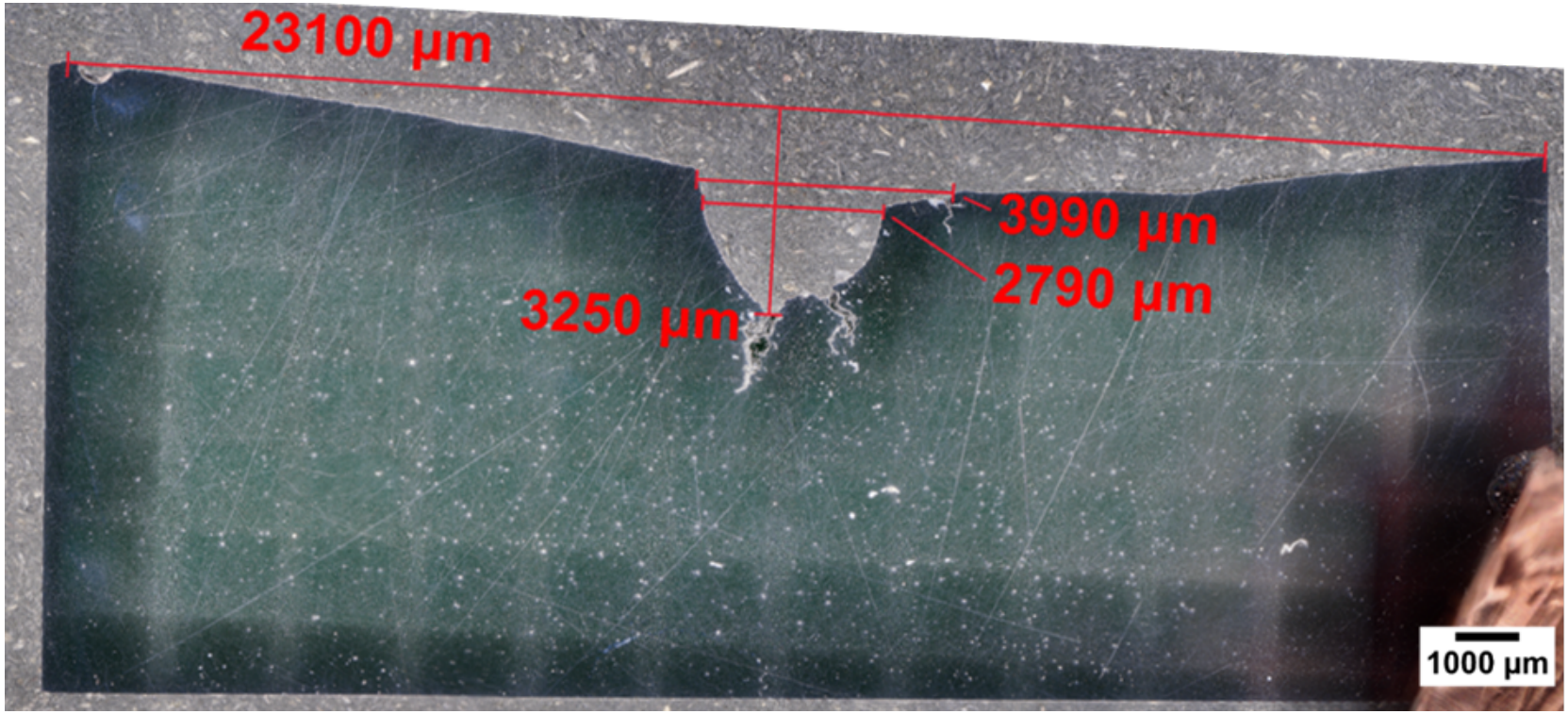


Figure H.13: Transverse cross section from a non-peritectic Al-Mn AHSS steel grade (0.2 wt %C). Sample name: 91-303-A00 - Dimensioned

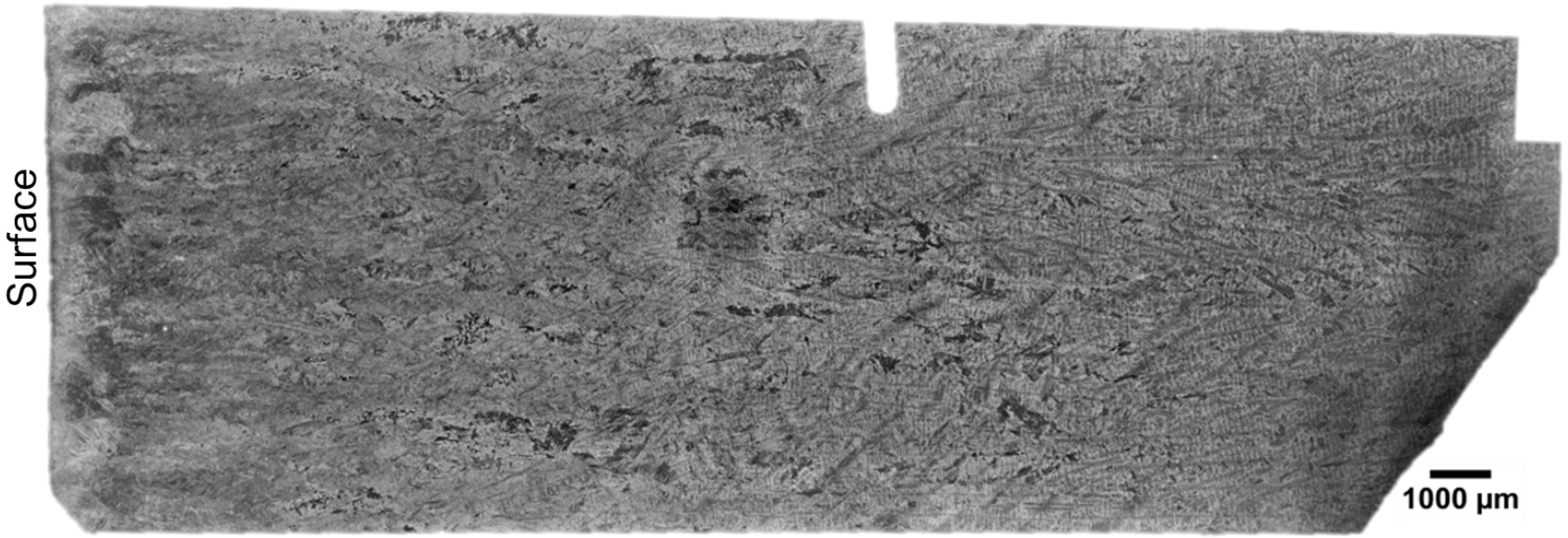


Figure H.14: Transverse cross section from a non-peritectic Al-Mn AHSS steel grade (0.2 wt %C) etched with 3% Nital. Sample name: 91-303-B00



Figure H.15: As cast image of Low carbon steel cast at 43 in/min, 121.3" wide, 52°F superheat, and 7.16" SEN submergence depth (Sample A)

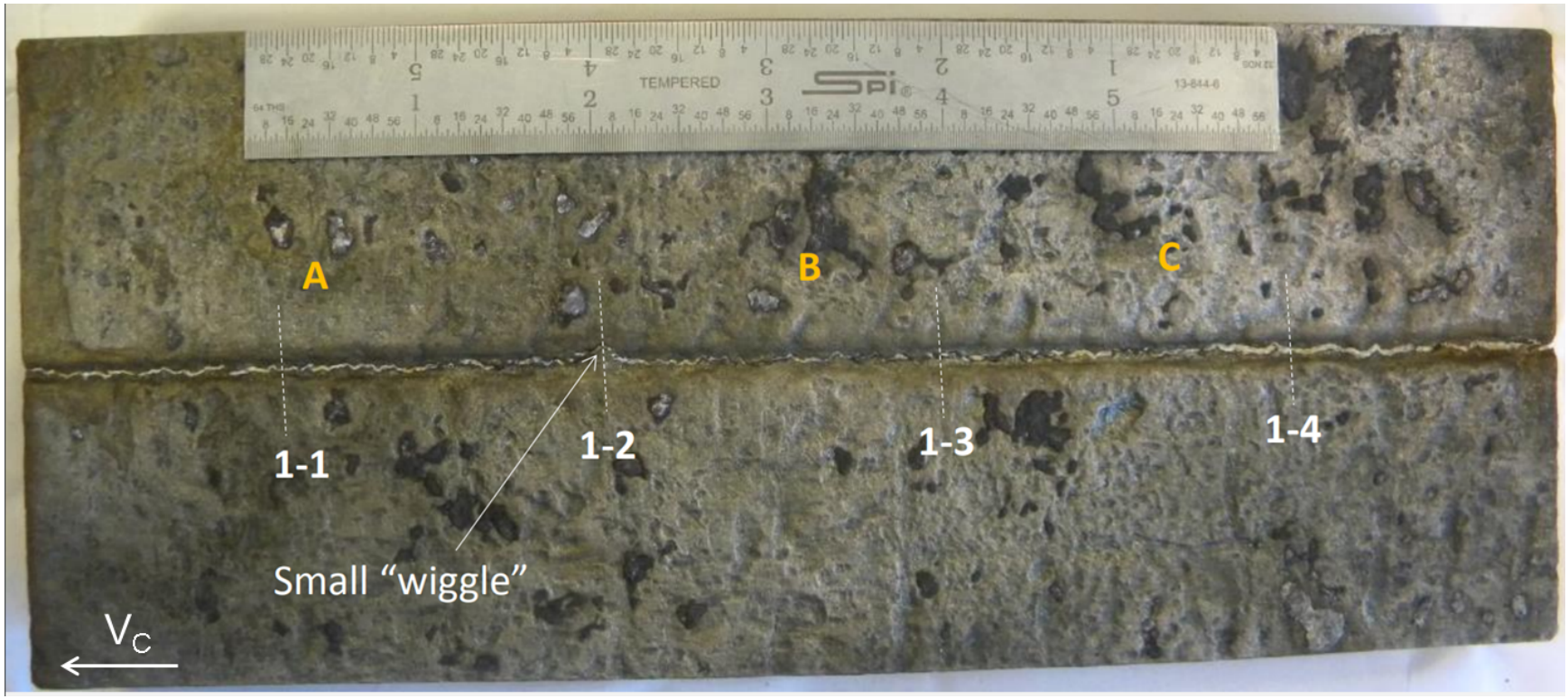


Figure H.16: 2% Nital etched Low carbon steel cast at 43 in/min, 121.3" wide, 52°F superheat, and 7.16" SEN submergence depth (Sample A)

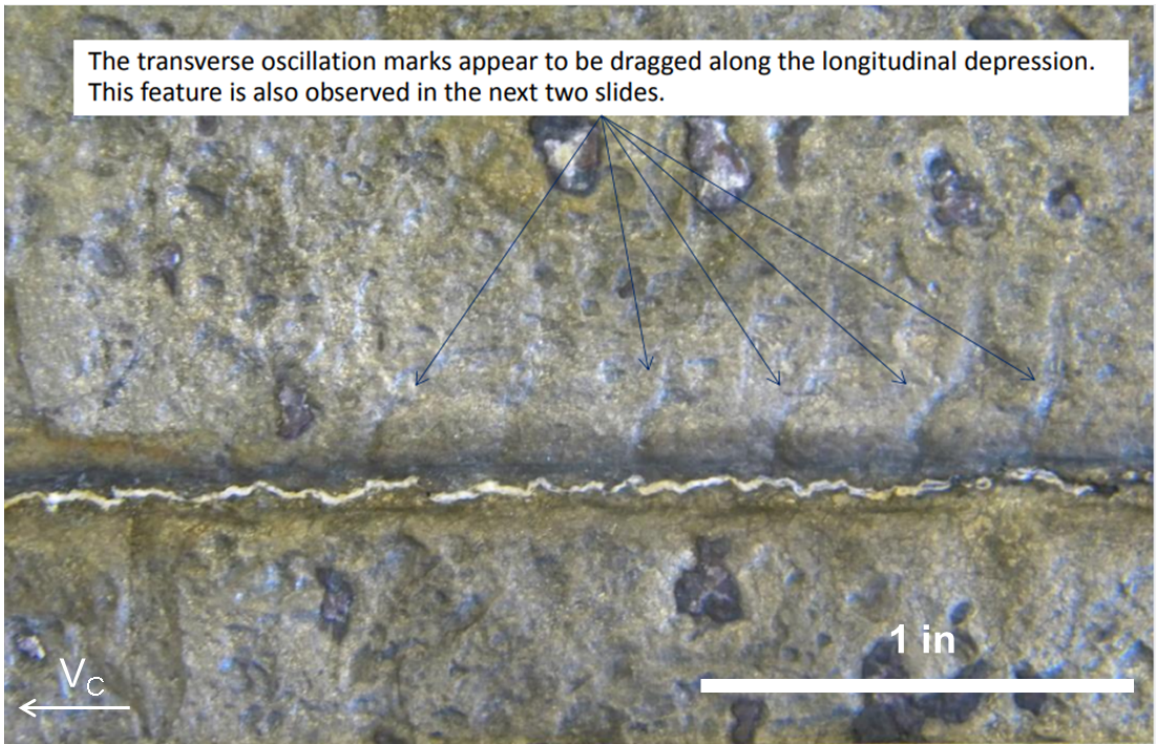


Figure H.17: 2% Nital etched Low carbon steel cast at 43 in/min, 121.3" wide, 52°F superheat, and 7.16" SEN submergence depth (Sample A – Region A)

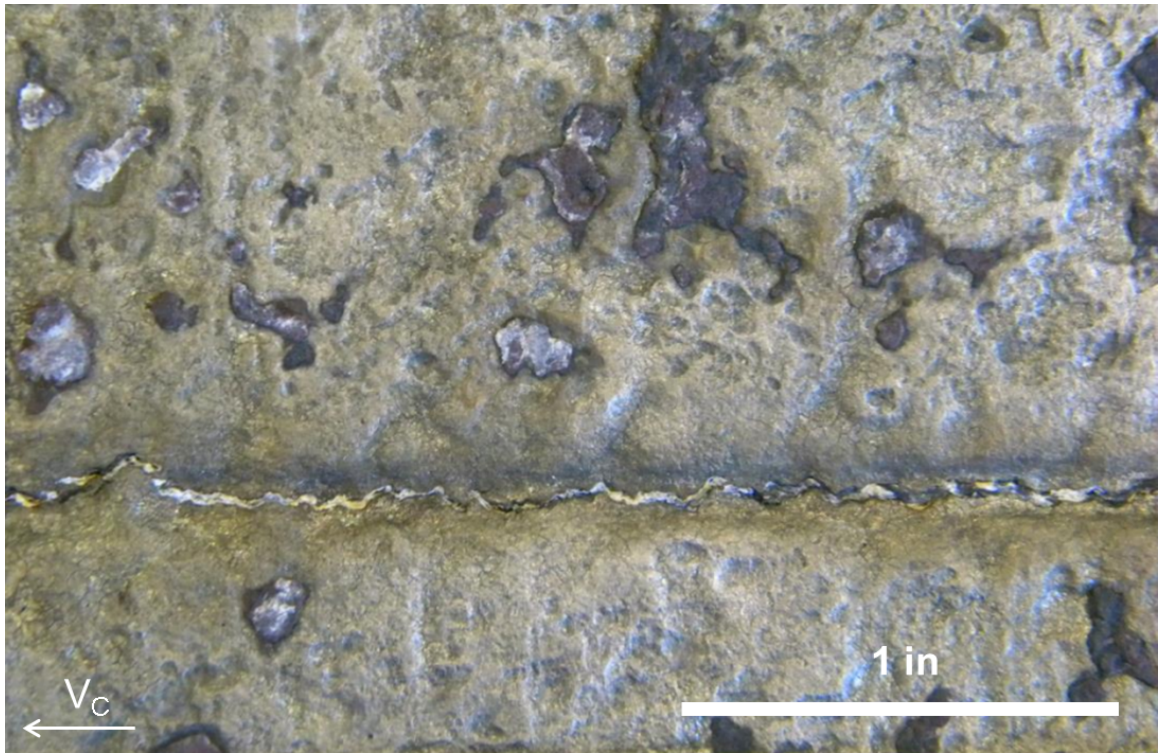


Figure H.18: 2% Nital etched Low carbon steel cast at 43 in/min, 121.3" wide, 52°F superheat, and 7.16" SEN submergence depth (Sample A – Region B)

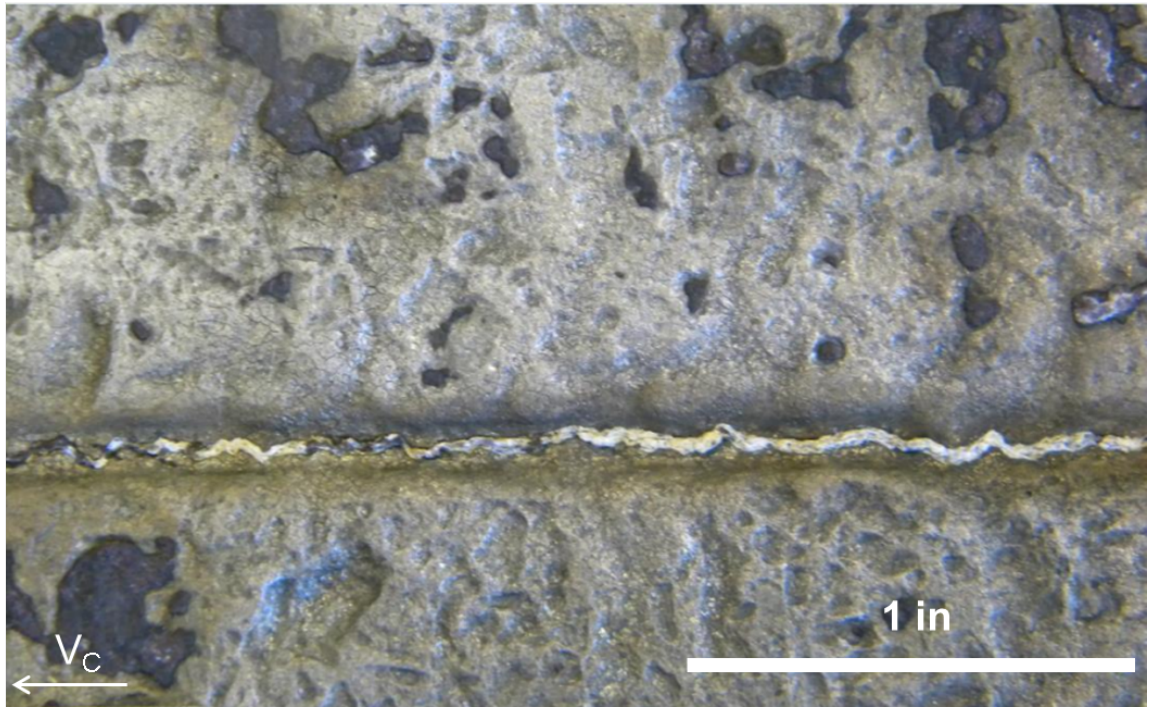


Figure H.19: 2% Nital etched Low carbon steel cast at 43 in/min, 121.3" wide, 52°F superheat, and 7.16" SEN submergence depth (Sample A – Region C)

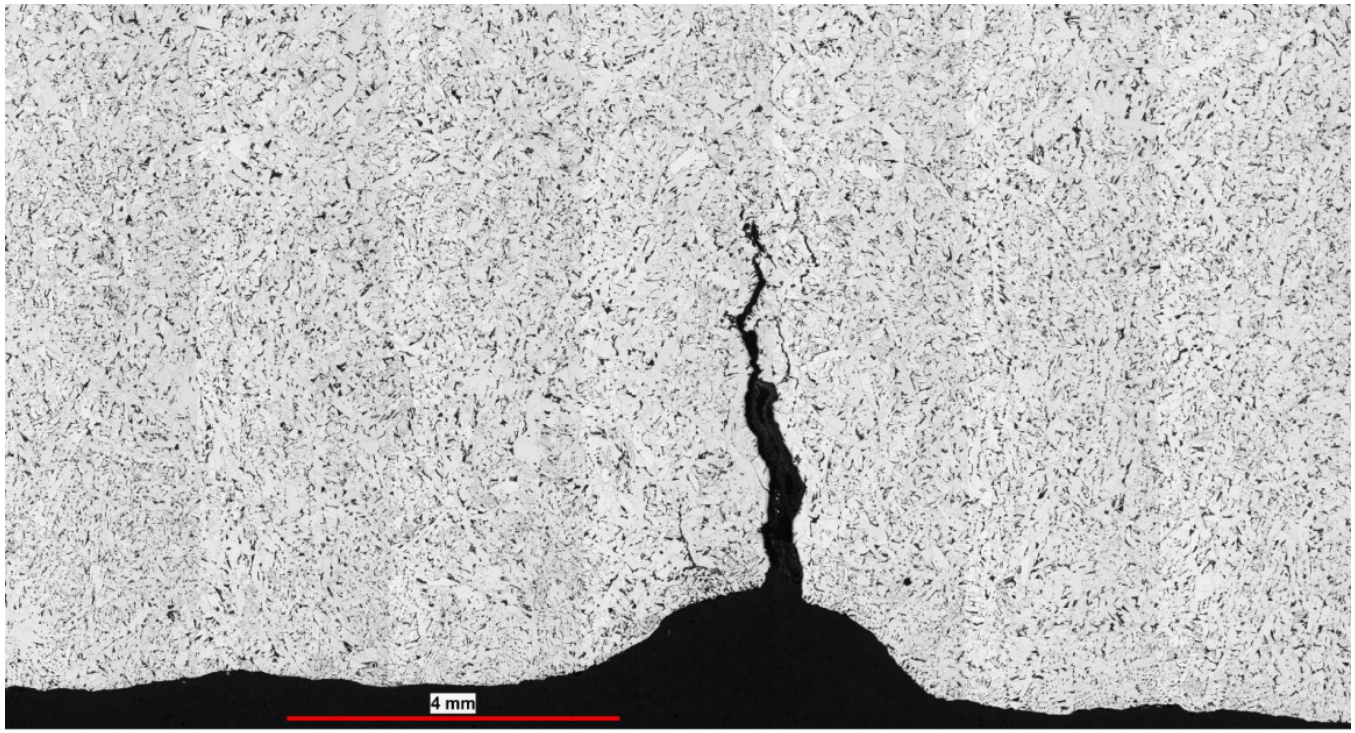


Figure H.20: 2% Nital etched Low carbon steel cast at 43 in/min, 121.3" wide, 52°F superheat, and 7.16" SEN submergence depth (Sample A – Cross Section 1-1)

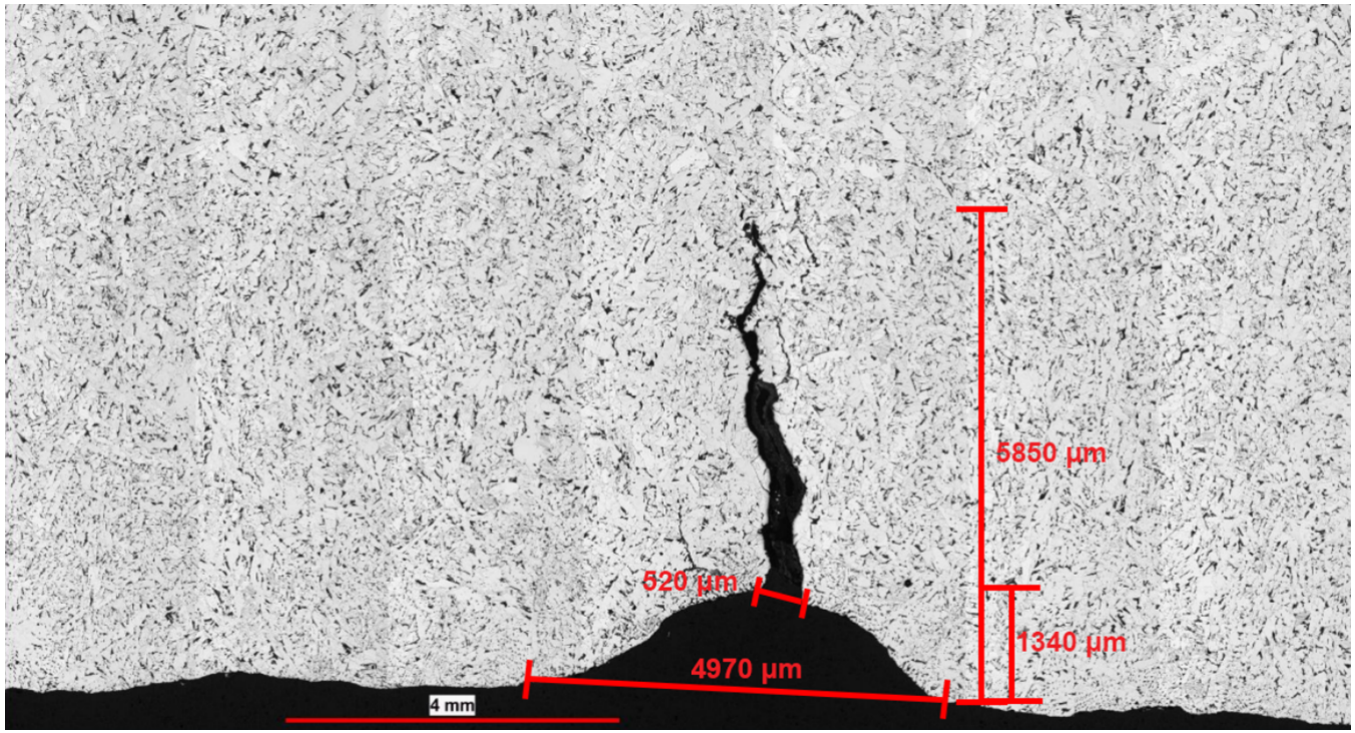


Figure H.21: 2% Nital etched Low carbon steel cast at 43 in/min, 121.3" wide, 52°F superheat, and 7.16" SEN submergence depth (Sample A – Cross Section 1-1) - Dimensioned

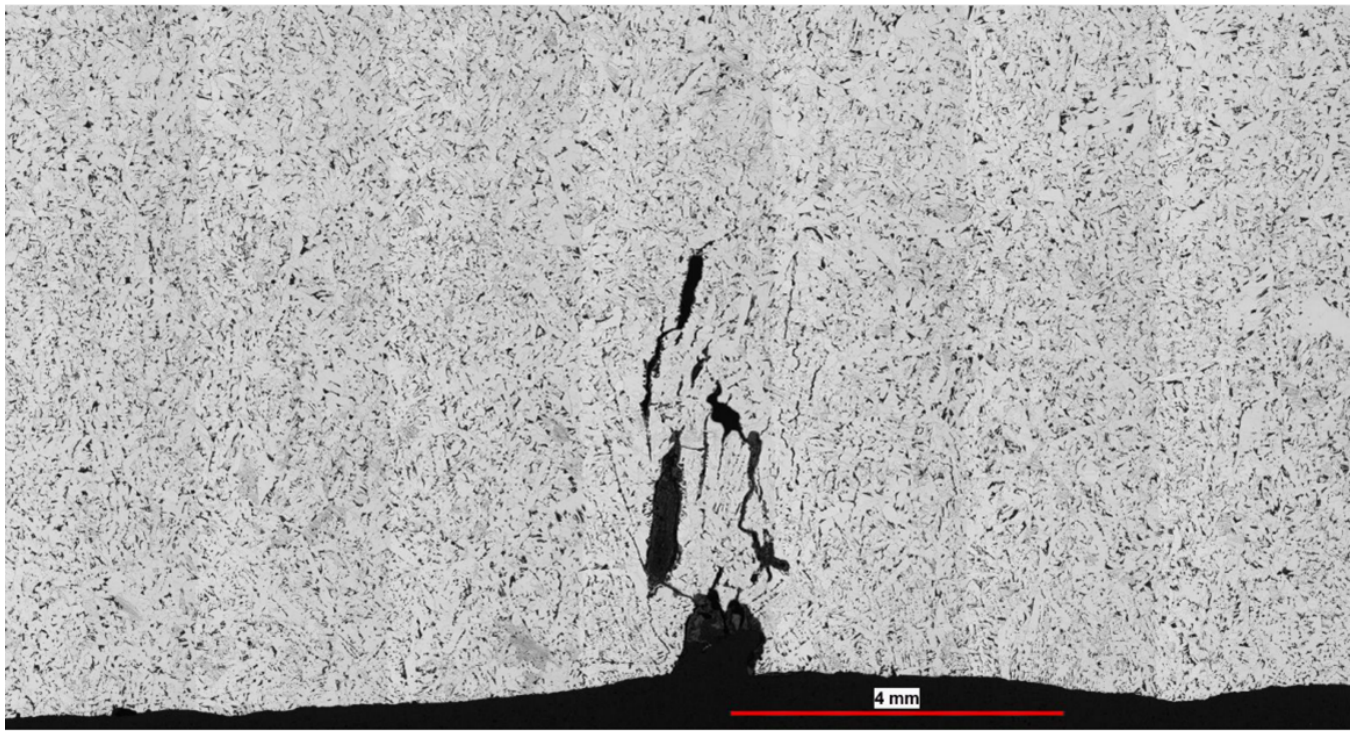


Figure H.22: 2% Nital etched Low carbon steel cast at 43 in/min, 121.3" wide, 52°F superheat, and 7.16" SEN submergence depth (Sample A – Cross Section 1-2)

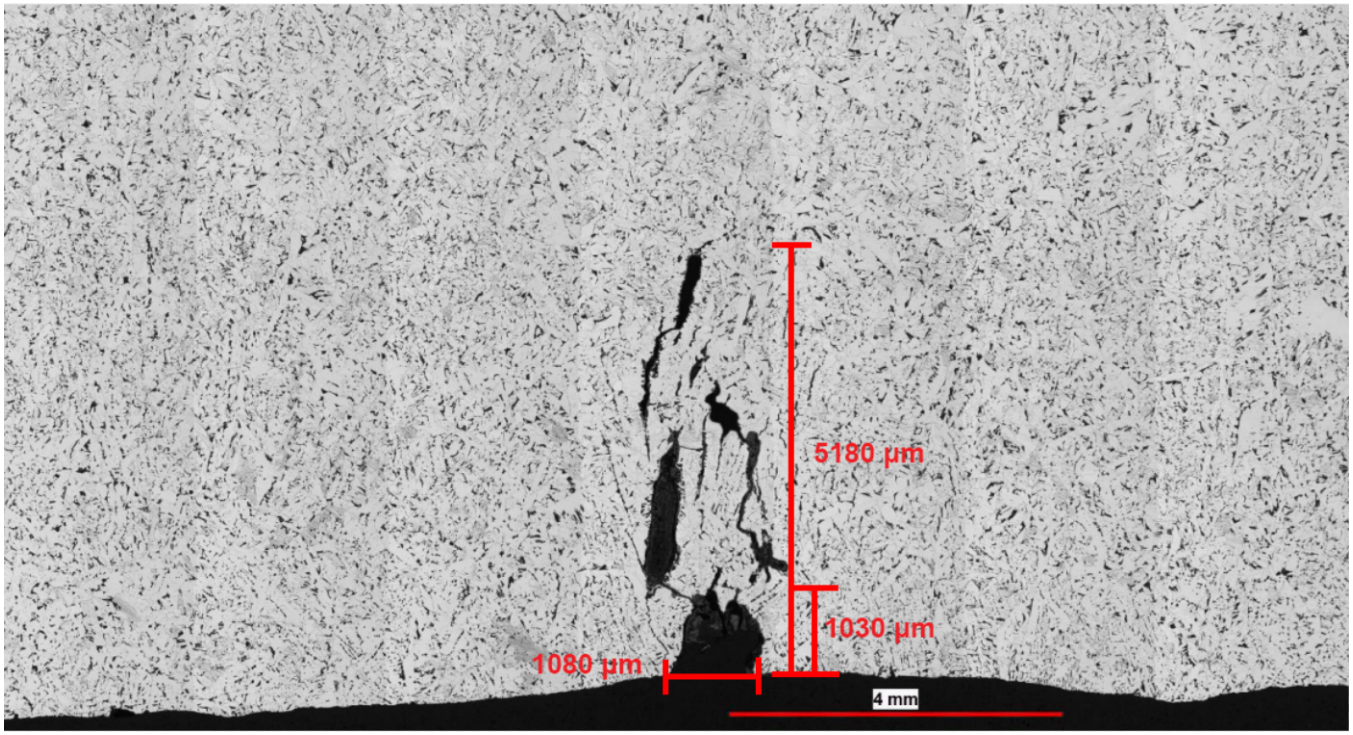


Figure H.23: 2% Nital etched Low carbon steel cast at 43 in/min, 121.3" wide, 52°F superheat, and 7.16" SEN submergence depth (Sample A – Cross Section 1-2) - Dimensioned

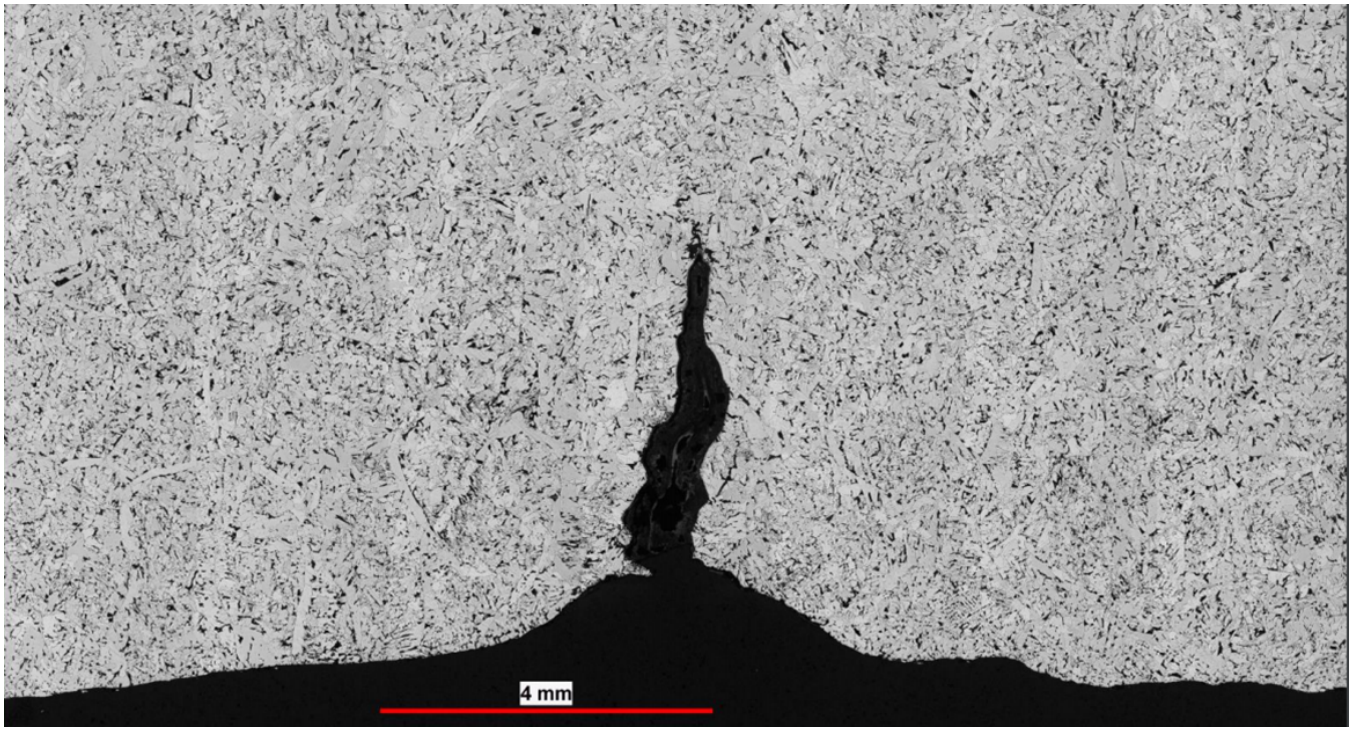


Figure H.24: 2% Nital etched Low carbon steel cast at 43 in/min, 121.3" wide, 52°F superheat, and 7.16" SEN submergence depth (Sample A – Cross Section 1-4)

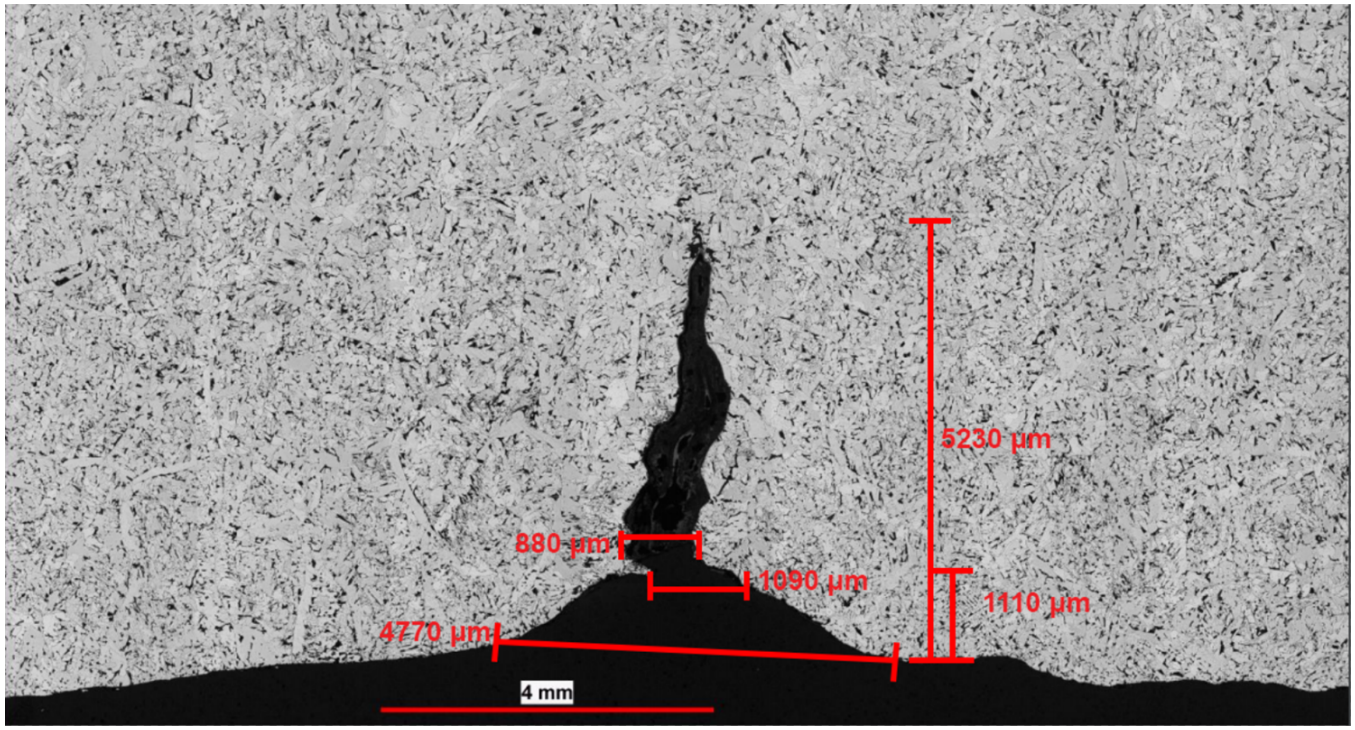


Figure H.25: 2% Nital etched Low carbon steel cast at 43 in/min, 121.3" wide, 52°F superheat, and 7.16" SEN submergence depth (Sample A – Cross Section 1-4) - Dimensioned

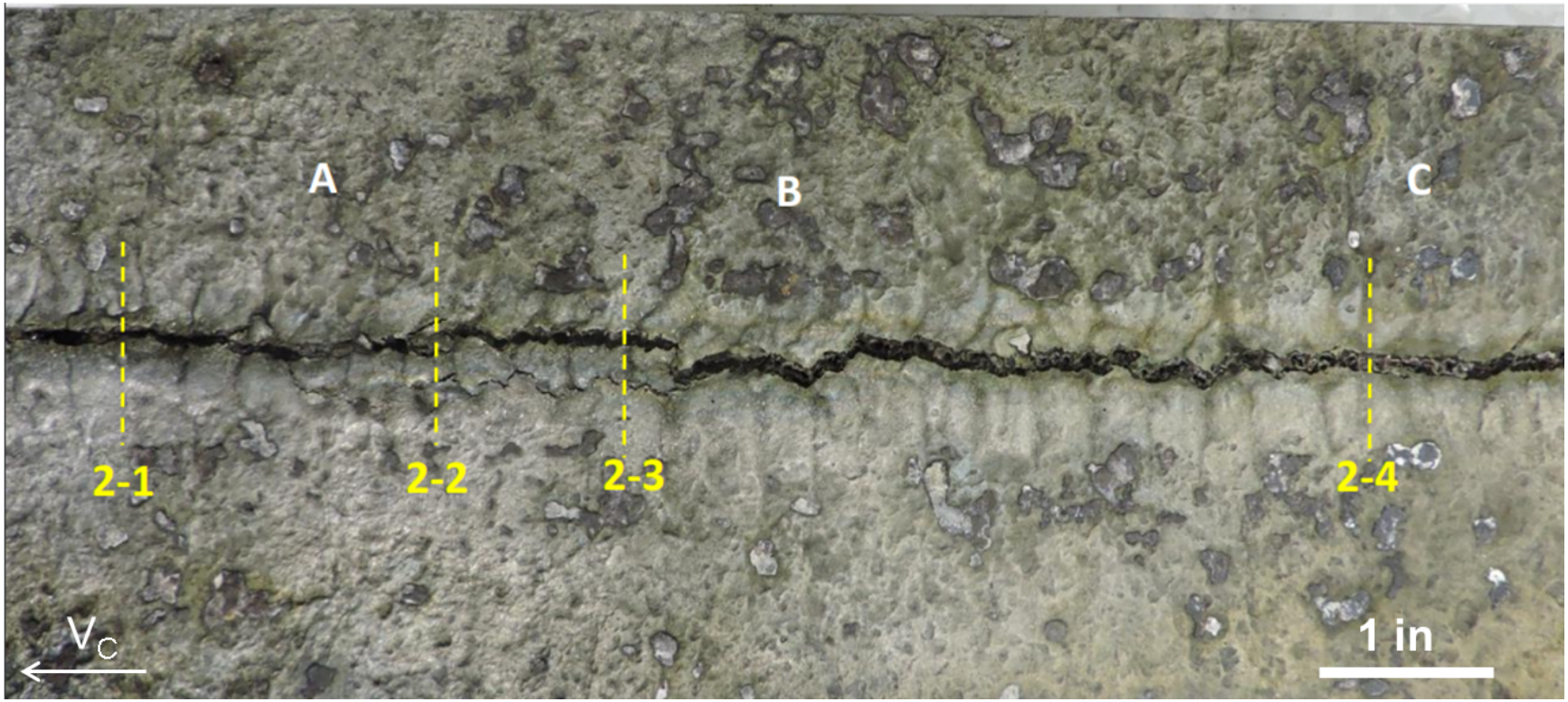


Figure H.26: 2% Nital etched Low carbon steel cast at 43 in/min, 121.3" wide, 52°F superheat, and 7.16" SEN submergence depth (Sample B)



Figure H.27: 2% Nital etched Low carbon steel cast at 43 in/min, 121.3" wide, 52°F superheat, and 7.16" SEN submergence depth (Sample B – Region A)



Figure H.28: 2% Nital etched Low carbon steel cast at 43 in/min, 121.3" wide, 52°F superheat, and 7.16" SEN submergence depth (Sample B – Region B)

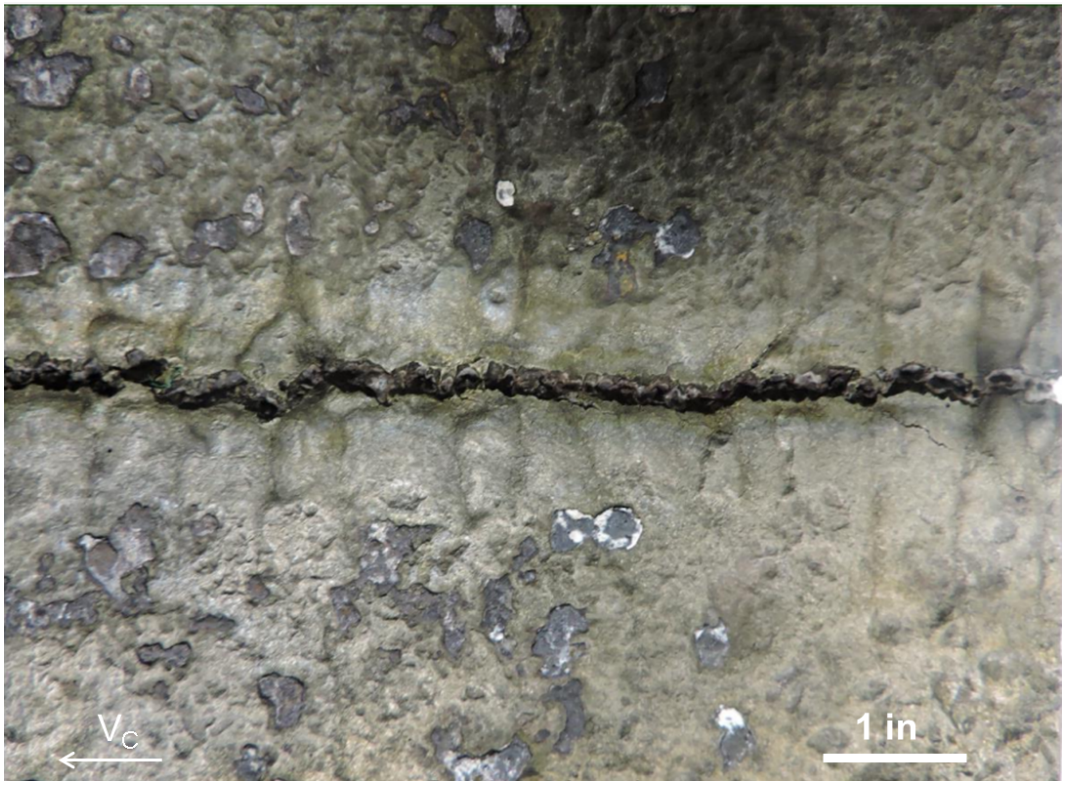


Figure H.29: 2% Nital etched Low carbon steel cast at 43 in/min, 121.3" wide, 52°F superheat, and 7.16" SEN submergence depth (Sample B – Region C)



Figure H.30: 2% Nital etched Low carbon steel cast at 43 in/min, 121.3" wide, 52°F superheat, and 7.16" SEN submergence depth (Sample B – Cross Section 2-1)

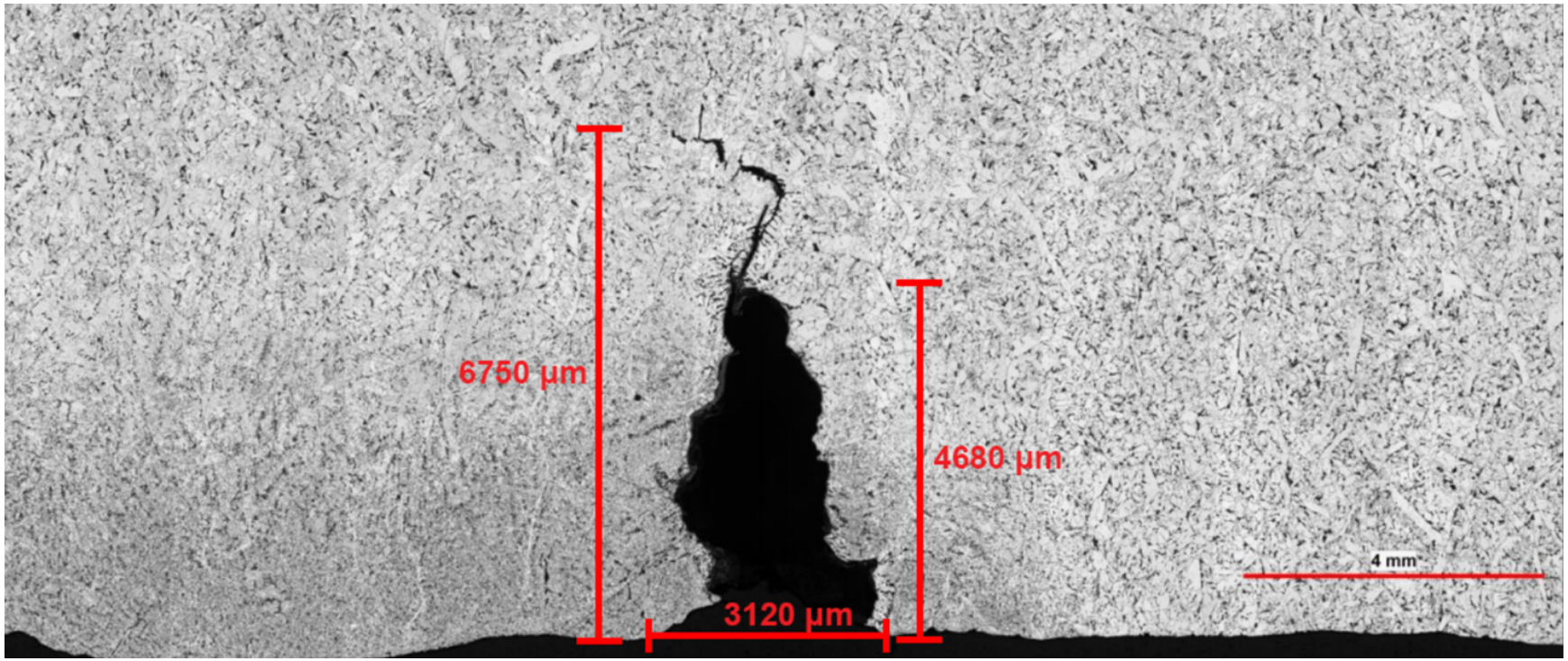


Figure H.31: 2% Nital etched Low carbon steel cast at 43 in/min, 121.3" wide, 52°F superheat, and 7.16" SEN submergence depth (Sample B – Cross Section 2-1) - Dimensioned

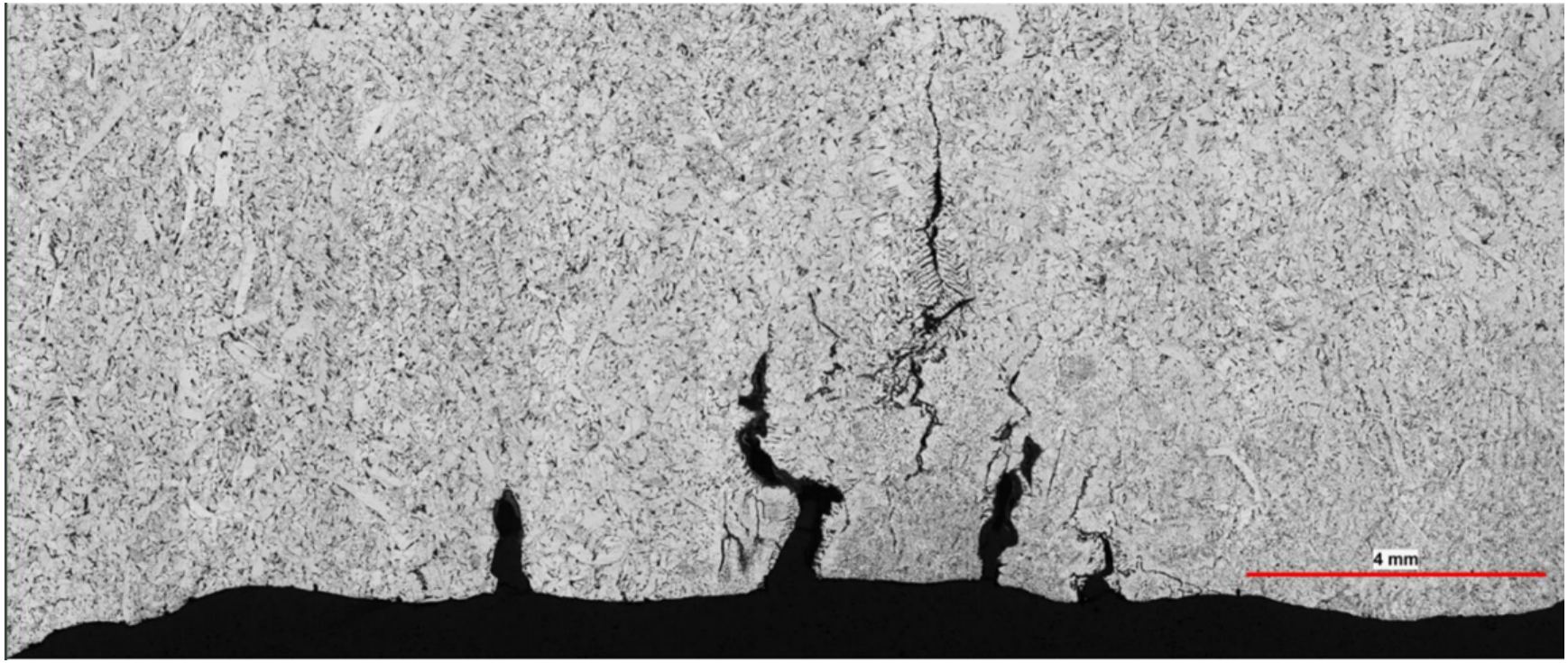


Figure H.32: 2% Nital etched Low carbon steel cast at 43 in/min, 121.3" wide, 52°F superheat, and 7.16" SEN submergence depth (Sample B – Cross Section 2-2)

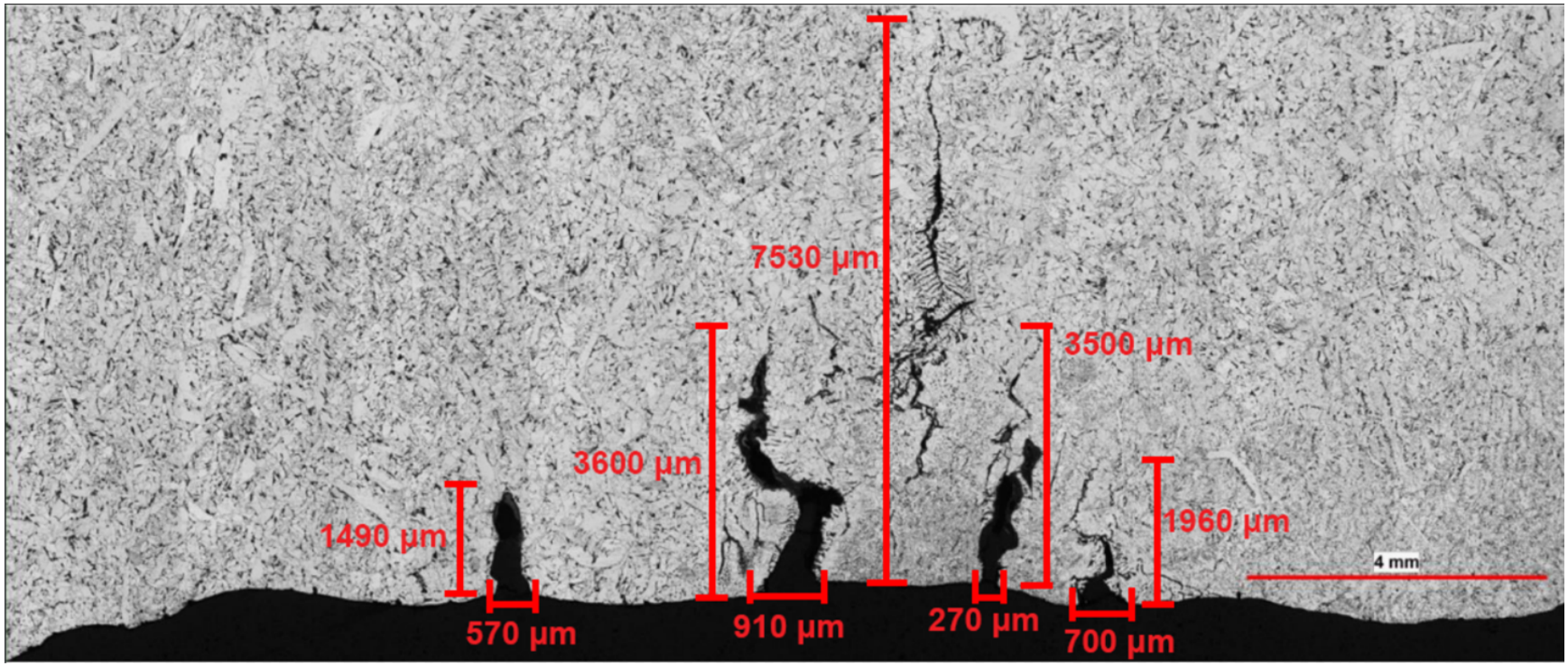


Figure H.33: 2% Nital etched Low carbon steel cast at 43 in/min, 121.3" wide, 52°F superheat, and 7.16" SEN submergence depth (Sample B – Cross Section 2-2) - Dimensioned



Figure H.34: 2% Nital etched Low carbon steel cast at 43 in/min, 121.3" wide, 52°F superheat, and 7.16" SEN submergence depth (Sample B – Cross Section 2-3)

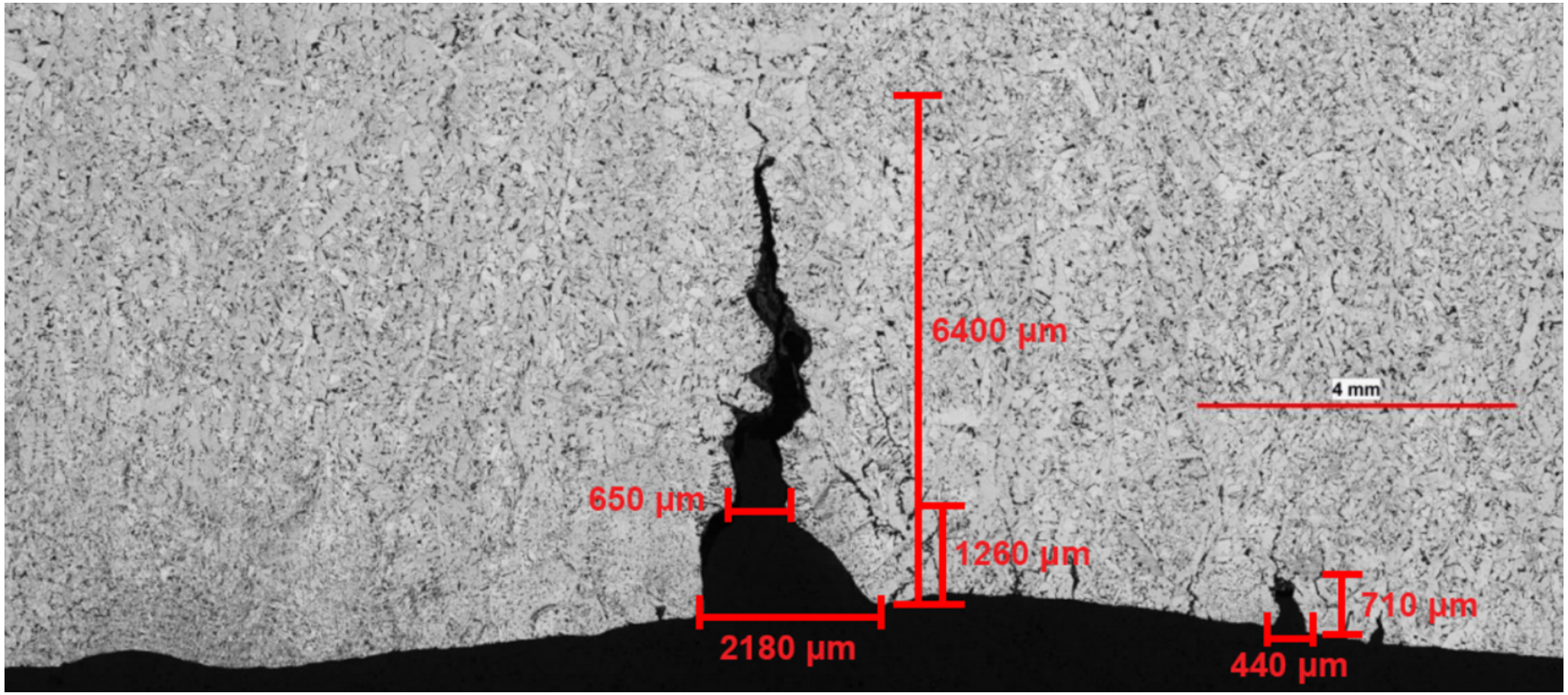


Figure H.35: 2% Nital etched Low carbon steel cast at 43 in/min, 121.3" wide, 52°F superheat, and 7.16" SEN submergence depth (Sample B – Cross Section 2-3) - Dimensioned

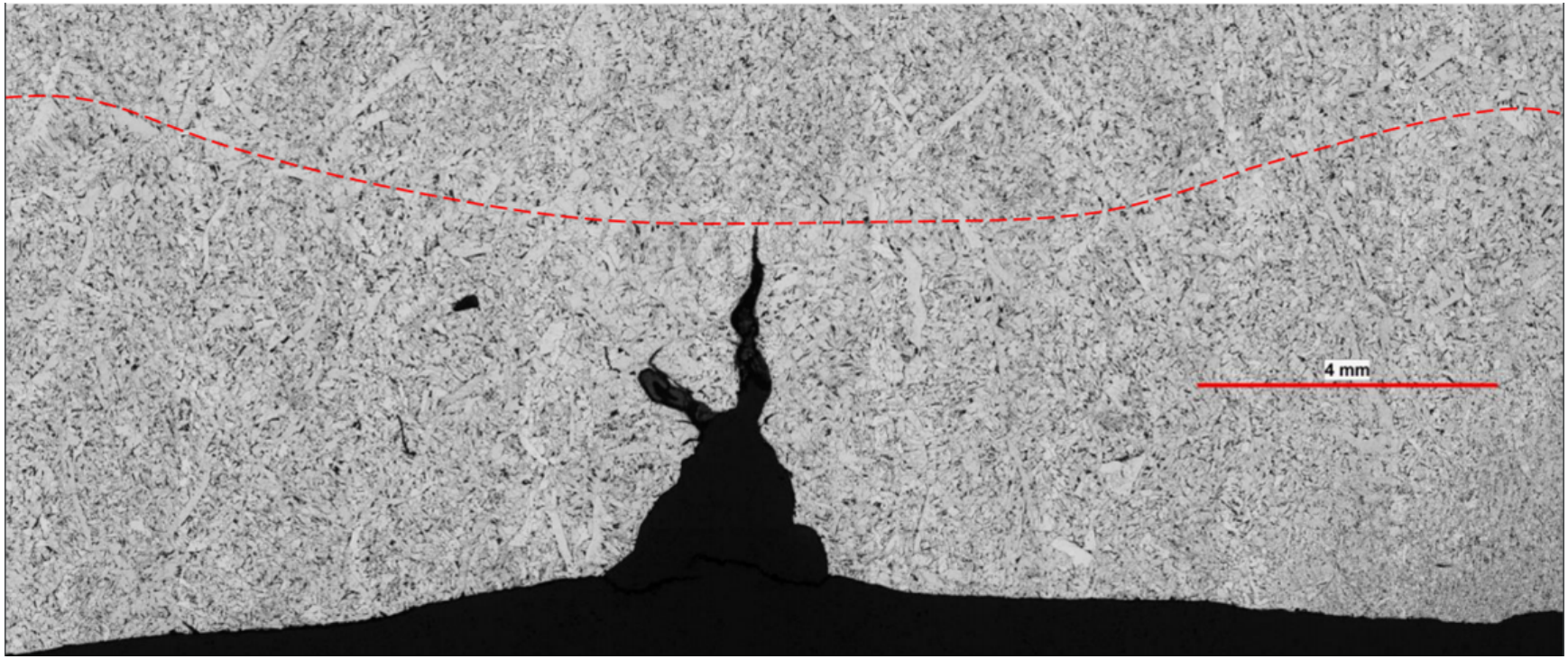


Figure H.36: 2% Nital etched Low carbon steel cast at 43 in/min, 121.3" wide, 52°F superheat, and 7.16" SEN submergence depth (Sample B – Cross Section 2-4)

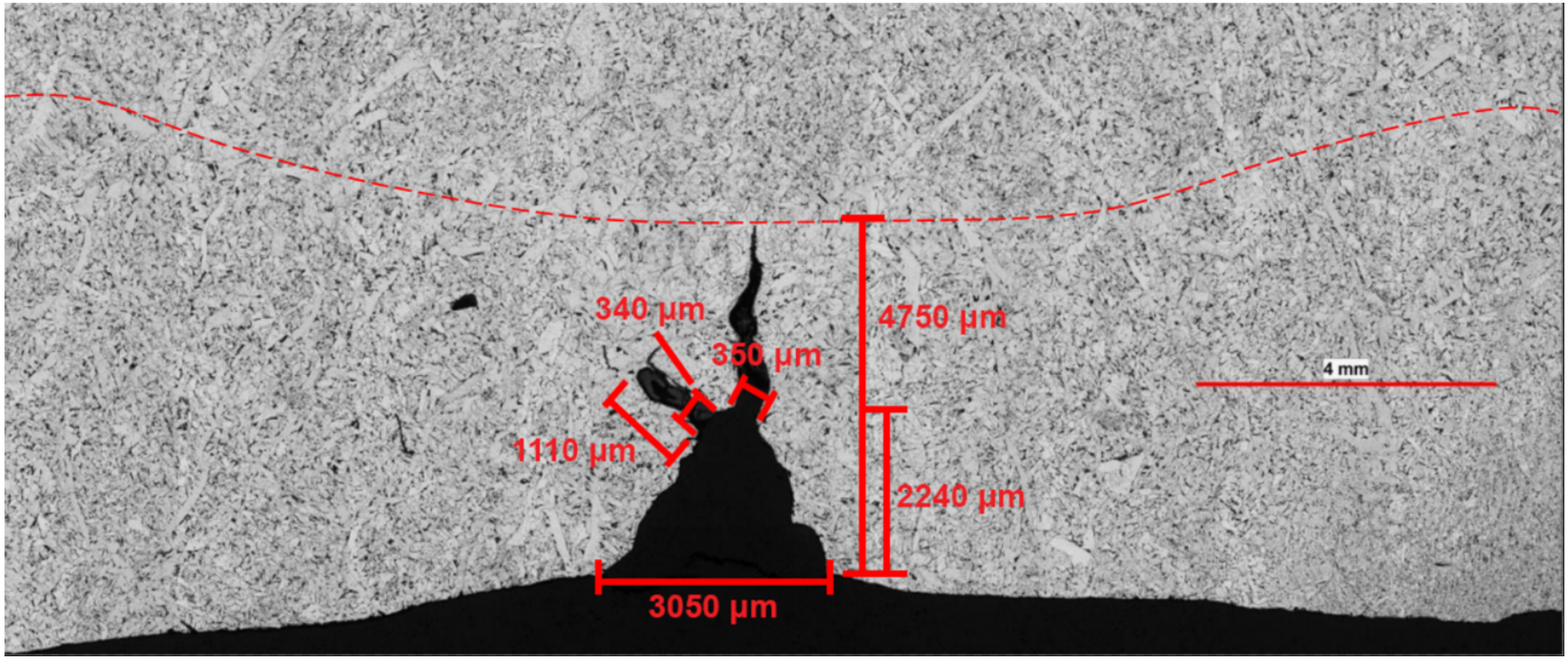


Figure H.37: 2% Nital etched Low carbon steel cast at 43 in/min, 121.3" wide, 52°F superheat, and 7.16" SEN submergence depth (Sample B – Cross Section 2-4) - Dimensioned

APPENDIX I

SUPPLEMENTAL ELECTRONIC FILES

There is one attached supplemental electronic file related to this dissertation. The attached file is an .avi video file of the integral defect prediction methodology introduced in Chapter 5 and Chapter 7. Selected individual frames of this video can be found in Chapter 5 and Chapter 7 where they are also discussed in detail. The .avi video file is ∼7.71 MB, 20 seconds long, and shows 40 frames of data taken from the operating caster 21 at Tata Steel Europe in Ijmuiden, Netherlands with the defect prediction methodolgy applied.

Audio Video Interleave (AVI) Files	
Integral Defect Prediction Method Video.avi	AVI file of the integral defect prediction methodology.